UNIVERSIDAD DE CANTABRIA

Departamento de Ciencias y Técnicas
del Agua y del Medio Ambiente

TESIS DOCTORAL

Aplicación de la Dinámica de Fluidos Computacional a la Acción del Oleaje Sobre Estructuras

Presentada por: **Pablo Higuera Caubilla**

Dirigida por: **Javier López Lara**

Iñigo J. Losada Rodríguez

Enero 2015

Agradecimientos

Esta tesis doctoral es el fruto de varios años de trabajo y sacrificios, de días buenos y de días menos buenos, de semanas de 60 horas, pero afortunadamente de ninguna noche sin dormir. Sin embargo, no es mi intención atribuirme el mérito completo, puesto que hay personas detrás que han contribuido en gran medida a su éxito, sin siquiera imaginárselo.

En primer lugar me gustaría agradecer a mi familia por todo el cariño y la comprensión que me han brindado a lo largo de mis años de vida. Papá y Mamá, gracias por tener siempre palabras bonitas y convencerme de que el tiempo pone todo en su sitio. David, Miguel, gracias por las sonrisas que me arrancáis. Pilli, Mimi, Marta, Moncho, Elías, Lucía, Mari, Chiqui y tantos otros, gracias por estar siempre pendientes y por preguntar cómo va todo. Y por supuesto gracias a Yaya, no hay palabras. Esta tesis está dedicada especialmente a ella.

Quizá no sea lo más apropiado separar a los amigos de la familia, pero solo en un apartado en solitario destacan como se merecen. Hay tres personas que han jugado un papel muy especial para mí y que se merecen no sólo una breve línea en este trabajo, sino una gratitud eterna. Estos amigo son como plantas crasas, porque aunque en ocasiones no los haya regado suficiente, no se han marchitado. Fito, la música y los viajes nos ha unido y aunque seas la única persona que practica las catas de agua se te quiere igual. Jaime, gran fotógrafo y mejor persona, anfitrión como ninguno en São Miguel. Largas han sido las decenas de noches de fotografía, las docenas de puesta de sol en la Arnía y un par de amaneceres tratando de "disparar" a los ciervos en Sejos y Richmond Park, habrá que seguir trabajando la técnica y buscando La Foto. Íñigo, hace ya mucho tiempo del Campus de Química y todavía conseguirnos reírnos como aquella noche. No lo perdamos nunca, porque ciertamente los sueños de una tarde de verano se pueden hacer realidad, y especialmente los que vendrán... brindaremos otra vez más cuando los dos

seamos doctores.

Me gustaría también agradecer a mis directores de tesis, Javier L. Lara e Íñigo Losada por su continuo tutelaje. Sin su amplia experiencia solo habría podido aspirar a perderme en el bosque del modelado numérico, un bosque que me han dejado recorrer en solitario, pero acompañado de una excelente brújula. En especial tengo el placer de agradecer a Javi todos los buenos ratos que hemos compartido en mil y un viajes de congreso, y todas las anécdotas que como piezas de un puzzle me han ayudado a montar un panorama del pasado, presente y futuro de la investigación. No sería justo dejar de nombrar en este apartado a mi "tercer director", Raúl Medina, gracias por todo.

Tampoco puedo dejar pasar esta ocasión sin agradecer al resto de compañeros del IH Cantabria. Son muchas las personas que a lo largo de estos años de trabajo me han mostrado y demostrado lo mejor de ellas. Por eso, ya haya sido en discusiones de trabajo, en la comida y en el café, en ambientes más distendidos o escalando una montaña, siempre las tendré presentes. Gracias César Vidal, Edurne, Manu, Jorge, Alexia, Nico, Mar, David, María y tantos otros.

Finalmente me encuentro en gratitud con el Ministerio de Educación, Cultura y Deporte por la financiación brindada en el marco del Programa de Formación del Profesorado Universitario (FPU12-04354), que me ha permitido llevar a cabo esta tesis. Asimismo no puedo más que agradecer de nuevo al IH Cantabria por los medios que me ha ofrecido a lo largo de estos años, con los que he podido realizar los ensayos físicos y numéricos de la tesis, además de presentar mi trabajo en numerosas conferencias y revistas internacionales.

Índice general

Capítulo 1

Introducción

Las estructuras costeras juegan un papel de alta importancia en la actualidad como un elemento clave en la defensa de la costa. Bajo esta denominación se pueden encontrar todo tipo de obras marítimas, como diques verticales y de escollera, espigones, muelles o playas y arrecifes artificiales. Todas las estructuras comparten un fin último, la protección de las zonas costeras frente a las dinámicas del mar (oleaje y corriente).

Uno de las aplicaciones por las que se construyen obras marítimas es para desarrollar áreas portuarias. Actualmente hay gran número de infraestructuras portuarias repartidas por todo el litoral, sin embargo el hecho de que el incremento del transporte marítimo haya inducido el crecimiento de los barcos, hace que sólo algunos puedan proveer las condiciones de accesibilidad y capacidad operativa que necesitan.

El incremento del tamaño de los buques requiere una respuesta a nivel del puerto. De esta forma los puertos más pequeños intentan adaptarse a las nuevas industrias en auge y cumplir con los nuevos estándares. Por ello, una de las preguntas más complicadas a las que tienen que enfrentarse los planificadores es decidir entre construir una expansión del puerto en aguas más profundas para mejorar el acceso, el área de maniobra y permitir el atraque a barcos de mayor calado, o bien mejorar las infraestructuras actuales, para cambiar su uso o niveles de funcionalidad. Esta segunda opción suele implicar un menor coste que la construcción de una obra nueva en grandes profundidades y a la vez supone un reto técnico de diseño que da lugar a estructuras no convencionales.

De cualquier forma, el proceso de diseño en ambos cases es igualmente desafiante. Construir una estructura en aguas profundas requiere de unos estándares muy altos y es muy costoso económicamente. A cambio, ofrece mejor acceso y maniobrabilidad para

grandes barcos. Adaptar una estructura existente para cumplir otro propósito o mejorar sus niveles de funcionalidad u operatividad es generalmente más económico, pero da lugar a estructuras no convencionales, que tienen que ser probadas en detalle.

De la misma manera, la modificación de estructuras no solo es aplicable para cambios de uso, sino que puede servir para afianzar estructuras históricas. Además, la adaptación de obras de defensa por cambio climático se perfila como un campo con gran crecimiento en el futuro. En este caso se proyecta un añadido a la estructura para que mantenga o mejore sus niveles de funcionalidad ante los efectos producidos por la variabilidad climática: aumento del nivel del mar y de la frecuencia y magnitud de los temporales. Esta situación ha quedado patente este año con la gran cantidad de temporales que han azotado la costa cantábrica y que han dañado sobre todo paseos marítimos expuestos y las estructuras de protección de puertos pesqueros y deportivos más vulnerables.

Tradicionalmente, el diseño y verificación de las estructuras marítimas se fundamenta en dos pilares básicos: las formulaciones semiempíricas y el modelado físico. Ambas permiten caracterizar los regímenes de operatividad, funcionalidad y fiabilidad.

La forma más sencilla es aplicar formulaciones semiempíricas basadas en análisis dimensional ajustado de ensayos de de laboratorio, que modelan el comportamiento hidráulico de la estructura cuando se ve solicitada por el oleaje. Además, permiten obtener parámetros de comportamiento de las mismas de una manera simple y rápida. Entre las más conocidas se encuentran: Tanimoto et al. (1976) para el diseño de diques mixtos, Goda (1985) y Takahashi et al. (1994) para diques verticales o van der Meer (1987) para diques de escollera. Su principal ventaja es su simplicidad y su bajo coste. Sin embargo, no son aplicables fuera de su rango de estudio, a estructuras con secciones no convencionales o con efectos locales importantes.

El segundo método clásico es el estudio experimental en laboratorio, que sigue siendo una pieza clave en el desarrollo del sector. Con el modelado físico a escala se pueden obtener formulaciones específicas ad hoc, aplicables para el caso concreto de estudio. Este es especialmente necesario cuando la estructura es no convencional o está sometida a efectos tridimensionales. Un ejemplo ilustrativo es el Dique Torres del Puerto de Gijón, que posee un entronque entre una sección en talud que pasa a cajones, caso para el que no existen formulaciones semiempíricas. No obstante esta aproximación presenta ciertas

limitaciones operativas. Sus grandes inconvenientes son los efectos de escala y el alto coste (temporal y económico) asociado a la ejecución de los ensayos. La adquisición de datos también es un factor limitante, debido a que por lo general se dispone de un número limitado de sensores y en la mayoría de las ocasiones son elementos de medida intrusiva que modifican el flujo a su alrededor.

Ha sido recientemente cuando se ha incorporado el modelado numérico a este campo, por lo que todavía no está estadarizado. No obstante, este método se recoge ya en el catálogo de "Diques de Abrigo en los Puertos de Interés General del Estado", editado por Puertos del Estado en 2012. El catálogo lo añade como elemento de verificación diferenciador, en referencia a los trabajos que se han llevado a cabo con el software MARIFE, de desarrollo conjunto entre Puertos del Estado y la Universidad de Cantabria, para verificar el diseño del dique exterior del Puerto de La Coruña. Sin embargo estas herramientas también presentan limitaciones, ya que las simulaciones bidimensionales no son capaces de representar todos los procesos, mientras que las simulaciones tridimensionales requieren de altos recursos computacionales. Además el modelado numérico requiere de una validación para demostrar que es capaz de simular las dinámicas de interés, y generalmente estos datos proceden de experimentos.

Es como complemento y extensión al modelado físico donde mayor sentido cobra el modelado numérico. Esta simbiosis ha derivado en un nuevo campo de estudio denominado modelado híbrido (*composite modelling*, (Gerritsen and Sutherland, 2011)) cuyo objetivo es replicar y extender los ensayos físicos mediante modelos numéricos. El uso combinado de ambas técnicas puede ayudar a identificar los pros y contras de cada aproximación, ya que hay procesos que no se pueden simular físicamente pero sí numéricamente (y viceversa) por conflictos de su escala espacial o temporal.

Un modelo numérico tiene dos funciones principales en la fase de diseño:

- Asistir en el prediseño de experimentos, señalando los casos más importantes o ayudando a localizar los sensores en zonas relevantes.
- Extender la base de datos experimental con resultados de detalle mediante nuevos ensayos puramente numéricos, y por lo tanto más económicos.

El continuo desarrollo del modelado numérico hace que en este momento esté completamente preparado no solo para verificar sino para poder asistir en el diseño de estruc-

turas, ya que es posible simular distintas condiciones de oleaje y diferentes alternativas estructurales simultáneamente. Además los resultados se pueden obtener a escala de prototipo, evitando los efectos de escala y reduciendo la incertidumbre asociada a este tipo de medidas.

Los resultados extraídos de las simulaciones, en conjunción con técnicas avanzadas como redes neuronales y algoritmos genéticos, se pueden aplicar después para optimizar el diseño de las estructuras con el fin de obtener soluciones constructivas más funcionales y a la vez más económicas, ecológicas y sostenibles. Además, estas tecnologías no son solo aplicables en el ámbito de ingeniería de costas o portuaria, sino que otras industrias como la offshore, pueden beneficiarse del modelado numérico por las mismas razones.

El caso del modelo IH2VOF (**?**), ilustra esta situación perfectamente. No obstante, IH2VOF es un modelo bidimensional, lo que limita su aplicación a estructuras en las que se puede asumir incidencia normal del oleaje, y en las que los efectos tridimensionales no juegan un papel relevante. A día de hoy no hay un modelo 3D que esté en una situación tan avanzada como el IH2VOF, capaz de simular estados de mar completos en tiempos razonables.

Es por ello que se necesita desarrollar un modelo numérico tridimensional validado con la capacidad de simular los procesos físicos que rigen la interacción del oleaje con las estructuras marítimas, que cumpla con las características enunciadas. Para ello será necesaria una metodología que racionalice su uso para obtener resultados de detalle, en tres dimensiones y en un tiempo asumible, de forma que esta tecnología pueda integrarse en el proceso de diseño de estructuras marítimas, como complemento a las técnicas actuales.

Para concluir, es necesario recalcar que el modelado numérico avanzado de interacción del oleaje con las estructuras marítimas ofrece todavía grandes retos y oportunidades para la investigación. Esta tesis está dedicada a afrontar algunos de los desafíos más apremiantes para hacer el modelado numérico tridimensional accesible a la comunidad de ingeniería costera y portuaria.

1.1. Estructura de la tesis

Este documento es un resumen extendido de la tesis completa, escrita en inglés, con el fin de cumplir la normativa de la Universidad de Cantabria. Por ello no debe verse como un trabajo completo, sino como un documento donde se explican los puntos más relevantes. En cualquier caso, para obtener una explicación o desarrollo íntegros véase el documento en inglés.

En primer lugar se revisa brevemente el estado de la técnica en simulación numérica de interacción del oleaje con las estructuras en el Capítulo 2. Con las carencias que se encuentran se procede a enunciar los objetivos del trabajo junto con la metodología aplicada para conseguirlos en el Capítulo 3.

Posteriormente, en el Capítulo 4, se describe en detalle el funcionamiento del modelo numérico desarrollado en este trabajo: **IHFOAM**. Seguidamente, se demuestra que el modelo es capaz de replicar los procesos físicos implicados en la interacción del oleaje con las estructuras mediante una serie de casos de validación.

A continuación, en el Capítulo 5, el modelo se incorpora en el marco de una novedosa metodología híbrida para evaluar procesos tridimensionales en estructuras reales, con una aplicación práctica en la que se simula el dique exterior del Puerto de Laredo en toda su extensión.

Finalmente, las principales conclusiones de este trabajo se recogen en el Capítulo 6.

Capítulo 2

Estado del arte en simulación de interacción oleaje-estructura

Actualmente existen tres tipos de modelado principales para simular procesos de interacción flujo-estructura. Dentro de ellos se encuentran los modelos basados en teoría de flujo potencial como Boussinesq o Nonlinear Shallow Water (NLSW), y los basados en las ecuaciones de Navier-Stokes, tanto Eulerianos (Reynolds Averaged Navier-Stokes, RANS) como Lagrangianos (Smooth Particle Hidrodynamics, SPH), como viene recogido en la Figura 2.1. Cada procedimiento parte de una serie de consideraciones o simplificaciones iniciales, y se encuentra en un diferente grado de desarrollo, por lo que su campo de aplicación es distinto.

2.1. Modelos basados en teoría de flujo potencial

Antes de la generalización de los modelos de Navier-Stokes, los modelos más extendidos eran los de teoría de flujo potencial o 2DH (bidimensional de plano horizontal) (Liu and Losada, 2002). Esta denominación general incluye los modelos de Boussinesq (FUNWAVE, Wei and Kirby (1995) o COULWAVE, Lynett and Liu (2002)) y los modelos NLSW (SWASH, Zijlema and Stelling (2011)). En ambos casos son programas que resuelven una versión simplificada de las ecuaciones de Navier-Stokes promediadas en vertical. Estos modelos son ideales para la propagación del oleaje incluyendo refracción, difracción y asomeramiento. Debido a la simplicidad relativa de sus ecuaciones, permiten simular grandes extensiones (de centenares de metros a kilómetros) y series temporales (estados

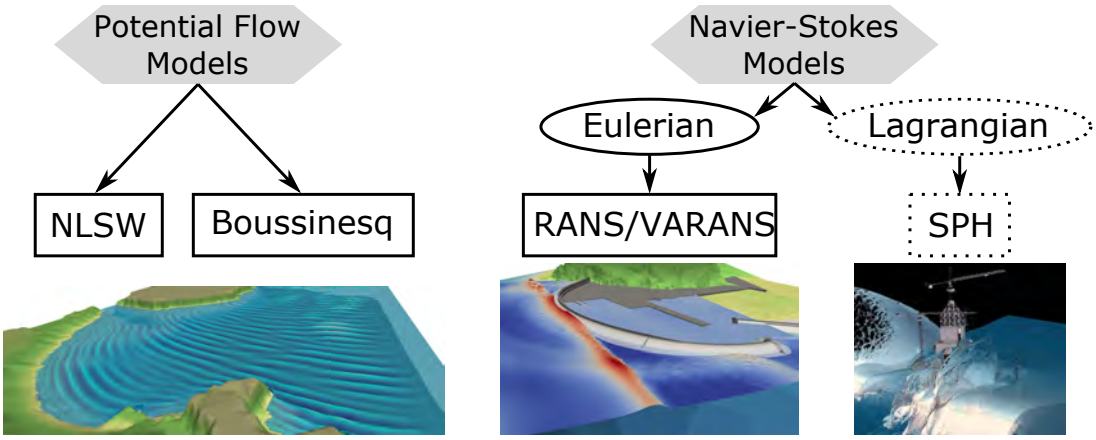

Figura 2.1: Tipos de modelos numéricos aplicados en interacción oleaje-estructura. [Imagen SPH tomada de www.dual.sphysics.org]

de mar de varias horas) en tiempos muy competitivos (horas).

Probablemente la mayor desventaja de este tipo de modelos es la limitación para simular velocidades verticales y gradientes complejos de velocidades horizontales a lo largo de la columna de agua, debido a sus hipótesis de partida. Esto imposibilita caracterizar zonas con alto grado de reflexión o procesos como la rotura del oleaje. Para tratar de emular esta última aplican procedimientos numéricos con los que la altura de ola decrece como si hubiese disipación de energía. Pese a continuar mejorando, todavía están muy lejos del realismo en interacción flujo-estructura ofrecido por los RANS o SPH.

2.2. Modelos de Navier-Stokes

Los modelos de Navier-Stokes se pueden distinguir en función de cómo se trata el flujo. Si los fluidos se consideran continuos en el espacio, los modelos se denominan Eulerianos, mientras que si se representan como un conjunto de partículas individuales, los modelos se llaman Lagrangianos.

2.2.1. Modelos Eulerianos de Navier-Stokes

El segundo tipo de modelos son los RANS. Sus ecuaciones provienen de aplicar la descomposición de Reynolds a las ecuaciones de Navier-Stokes, por lo que consideran el fluido como un medio continuo (aproximación Euleriana) y tienen la capacidad de reproducir correctamente los perfiles de presión y velocidad a lo largo de la columna de

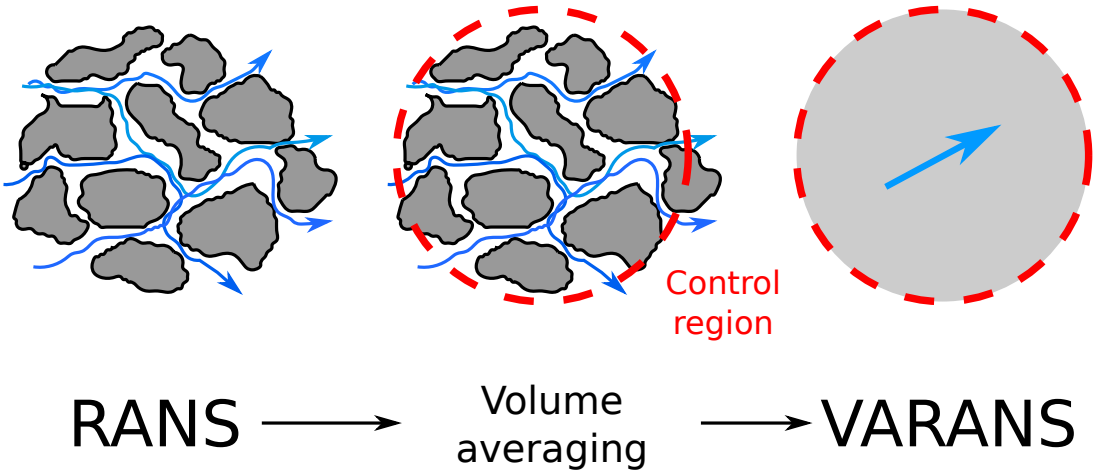

Figura 2.2: Método de promediación volumétrica.

agua, al carecer de hipótesis de partida simplificadas. De este modo nos encontramos con unas ecuaciones altamente no lineales que pueden simular completamente los procesos que afectan al oleaje: refracción, difracción, reflexión, asomeramiento, rotura, interacción no lineal entre olas, ascenso (run-up), rotura del oleaje...

Otra de las grandes ventajas de esta aproximación son las denominadas ecuaciones VARANS (Volume Averaged Reynolds Averaged Navier-Stokes) o ecuaciones RANS promediadas en volumen. El proceso esquemático para su obtención viene recogido en la Figura 2.2. Con ellas es posible caracterizar el movimiento medio de los fluidos en el interior de medios porosos sin tener en cuenta su complicada geometría, sino considerándolos como medios continuos. De esta forma se puede simular la interacción del oleaje con los mantos en diques de escollera o banquetas en diques verticales.

Los modelos RANS iniciales fueron los 2DV (bidimensionales de plano vertical), destacando el COBRAS (Lin, 1998), VOFbreak (Troch and De Rouck, 1998) o IH2VOF (Lara et al. (2008), Losada et al. (2008)). Por su bajo coste computacional son adecuados tanto para replicar ensayos en un canal físico como para simular estructuras a escala de prototipo. Es por ello que son ampliamente usados a día de hoy, incluso para el diseño de estructuras como demuestra el modelo IH2VOF. Como referencia, este modelo usado posteriormente en el trabajo, es capaz de simular estados de mar horarios a escala de prototipo (750 m de longitud) en menos de 24 horas en un PC.

La revolución en el sector ha llegado con la generalización de uso de modelos RANS 3D, ya que los procesos de interacción flujo-estructura son altamente tridimensionales. Entre

los modelos más usados se encuentran el CADMAS-SURF (Kim et al., 2010), FLOW-3D (Choi et al., 2007), IH3VOF (del Jesus et al., 2012). Debido a su alto coste computacional, estos modelos requieren del uso de técnicas de computación en paralelo. De esta forma se acelera el proceso de resolución y los tiempos de computación son lo más ajustados posibles para que puedan usarse en aplicaciones reales. Como orden de magnitud, **IHFOAM**, el modelo desarrollado en este trabajo, es capaz de simular un dominio real de 500 x 500 m a razón de unos 30 s por día con un entorno de paralelización HPC (cluster).

Los modelos RANS no están preparados para simular dominios tan extensos como los modelos potenciales, sino que ofrecen una mayor resolución y representan los procesos físicos de manera más exacta al rebajarse el número de hipótesis de partida. El análisis de los datos permite obtener resultados de detalle como leyes de presiones sobre la estructura, rebase, reflexión, transmisión, ascenso-descenso...

2.2.2. Modelos Lagrangianos de Navier-Stokes

El tercer tipo de modelos se denomina SPH y también se basa en las ecuaciones de Navier-Stokes, pero en este caso en su forma discreta (aproximación Lagrangiana) tanto en 2D como en 3D. El comportamiento medio de las ecuaciones se reproduce mediante la interacción de un gran número de partículas esféricas. La precisión final depende del número total de partículas y de su tamaño.

Este tipo de modelos no se encuentra tan desarrollado como los dos anteriores, pero presenta algunas ventajas notables con respecto a ellos. En primer lugar, el SPH es un método "meshless", porque no resuelve las ecuaciones en una malla. Esto minimiza el tiempo necesario de preproceso y elimina ciertos errores numéricos. Además, la aproximación Lagrangiana no requiere resolver aceleraciones convectivas, altamente no lineales, y que presentan problemas numéricos a la hora de resolverlas. Es por ello que su forma de resolución es menos compleja que en el caso Euleriano, por lo que se pueden paralelizar mediante tarjetas gráficas, que poseen un rendimiento y velocidad mucho mayores con respecto a los procesadores convencionales: dominios de 50 x 50 m se pueden simular a razón de decenas de segundos por hora.

Los modelos más extendidos a día de hoy son el SPHYSICS (Dalrymple and Rogers, 2006) e ISPH (Shao, 2010). Su principal desventaja es que todavía no están preparados

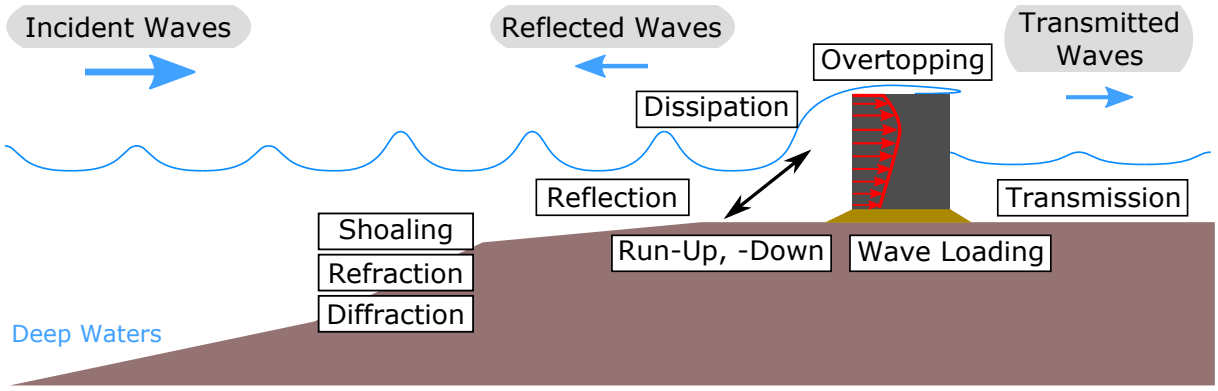

Figura 2.3: Procesos de propagación del oleaje y de su interacción con estructuras marinas.

para simular dominios tan extensos como los vistos anteriormente por su alta difusividad numérica, que induce una pérdida artificial de cantidad de movimiento. Además, el modelo de flujo a través de medios porosos sólo está desarrollado en dos dimensiones, impidiendo simular estructuras porosas tridimensionales, limitando por tanto su aplicación a casos reales.

2.3. Necesidades de diseño en interacción entre el oleaje y las estructuras

El diseño de una estructura marítima implica caracterizar y establecer unos niveles de funcionalidad y estabilidad. Tradicionalmente este proceso se ha llevado a cabo mediante formulaciones semiempíricas y ensayos de laboratorio. El modelado numérico es un factor novedoso que puede servir de asistencia en todas las fases de diseño. Esto es lo que se conoce como modelado híbrido. Para que un modelo numérico se integre en la metodología global de diseño debe ser capaz de evaluar la estabilidad y funcionalidad de las estructuras. Este es el requerimiento último, que se fundamenta en otros más básicos, como reproducir los procesos que aparecen en la interacción del oleaje y las estructuras, recogidos en la Figura 2.3

En primer lugar, es evidente que un modelo numérico aplicable a ingeniería de costas necesita ser capaz de generar oleaje. Puesto que las condiciones reales de oleaje dependen del periodo, altura de ola y profundidad de generación, el modelo ha de ser lo más generalista posible y cubrir todo el espectro de oleajes. Asimismo, al generar el oleaje se

introduce energía en el sistema. Si la energía no se disipa de algún modo, acabará incidiendo de nuevo en los contornos, y produciendo reflexiones que distorsionarán los resultados. Por ello es necesario un sistema de absorción del oleaje. Existen numerosos sistemas de generación y absorción del oleaje, entre ellos generación mediante función fuente y esponjas numéricas (Lin and Liu, 1999), zonas de relajación (Jacobsen et al., 2012) y generación y absorción activas (Troch and De Rouck, 1999). Este último método puede considerarse el más avanzado, ya que comparado con los anteriores, no incrementa el coste computacional del modelo. No obstante, en el estado del arte no hay una forma clara de implementarlo de forma que absorba oleaje direccional en tres dimensiones.

Además el modelo debe poseer la capacidad de simular los procesos primarios de transformación del oleaje tales como refracción, difracción, asomeramiento o reflexión, y los más complejos como las interacciones no lineales ola a ola. Además, debe ser capaz de simular correctamente la rotura del oleaje, capturando las grandes variaciones de velocidad y presión existentes a lo largo de la columna de agua, las situaciones de superficie libre multiconexas y la correcta disipación de la energía asociada a este complejo proceso. Solo en ese caso el oleaje que llegue a la estructura estará apropiadamente representado.

Para conseguir el fin anterior se ha de modelar la superficie libre que separa la fase agua de la fase aire. Para ello existen numerosas técnicas como Marker-and-Cell (MAC) desarrollada por Harlow and Welch (1965) y otras más recientes como Volume of Fluid (VOF, Hirt and Nichols (1981)). Esta última se caracteriza por ser capaz de representar configuraciones de superficie libre muy complejas con suma facilidad, tanto mediante la reconstrucción geométrica de la superficie libre (Rider and Kothe, 1998) como mediante la simple advección como pasivo escalar. En la técnica VOF, se representa la fracción de la celda ocupada por el fluido de interés, por lo que 0 indica que la celda no contiene dicho fluido, y 1 que está llena completamente.

Otro factor importante es que el modelo sea capaz de simular correctamente el flujo dentro de medios porosos, como los mantos y el núcleo de los diques, ya que éste afecta en gran medida a las variables asociadas a estabilidad y funcionalidad: las presiones sobre la estructura y el rebase. Para ello existen formulaciones específicas como las ecuaciones VARANS. En la literatura existen un gran número de ecuaciones VARANS (Liu et al. (1999), Hsu and Liu (2002), Nikora et al. (2007), del Jesus et al. (2012), Jensen et al.

(2014)) derivadas teniendo en cuenta determinadas hipótesis. Sin embargo, se ha detectado que ninguna de ellas deriva las ecuaciones acorde con la técnica desarrollada por Slattery (1967) y Whitaker (1967), altamente aceptadas en otros campos, y teniendo en cuenta la variación temporal de la porosidad. Con estas nuevas ecuaciones se podrían tratar nuevos problemas, como el transporte de sedimentos.

En la misma línea, una adecuada caracterización de la estabilidad estructural implica obtener presiones que recojan los efectos no lineales del impacto, especialmente cuando son causados por olas ya rotas.

A priori, los modelos RANS 3D son los únicos que cumplen con las necesidades enumeradas, mientras que los demás no son plenamente aplicables. Por ejemplo, los modelos potenciales no reproducen correctamente el oleaje no lineal, ni son capaces de simular la rotura. Los modelos SPH puede que sean aplicables en un futuro, pero a día de hoy son excesivamente difusivos, lo que limita el tamaño de los dominios de cálculo, y sólo son capaces de simular el flujo en el interior de medios porosos de forma bidimensional.

Algunas de las ventajas de incluir el modelado RANS 3D en la metodología de diseño ya han sido enunciadas: se pueden aplicar para el prediseño, para obtener resultados en detalle de ensayos físicos o para extender la base de datos experimental con bajo coste. Además, la adquisición de datos no está limitada y se pueden localizar un gran número de sensores sin perturbar el flujo. El análisis de los datos permite obtener resultados tridimensionales y ver su variación a lo largo de toda la estructura. Como se verá en el caso práctico del Puerto de Laredo (Capítulo 5), esto permite la optimización de la sección en base a un método cuantificable, que puede suponer un ahorro considerable en la fase de construcción.

Capítulo 3

Objetivos y Metodología

Los objetivos de la presente tesis se han formulado para rellenar los vacíos que se han detectado en el estado del arte, así como para extender o mejorar ciertas capacidades ya existentes.

Sin embargo, todos los objetivos pueden ser integrados en uno global: desarrollar un modelo numérico tridimensional capaz de simular un gran espectro de procesos de ingeniería de costas, con una implementación robusta, realista, totalmente validado y preparado para ser aplicado para el diseño de estructuras marítimas reales.

Los objetivos primarios y secundarios, así como la metodología seguida para conseguirlos se detallan a continuación:

3.1. Objetivo 1

Desarrollar un modelo numérico tridimensional capaz de transformación del oleaje para su uso en ingeniería de costas.

El modelo debe ser universal, capaz de simular cualquier condición de oleaje, presentar una implementación robusta y un comportamiento realista, de forma que sea pueda caracterizar los procesos de transformación del oleaje en su interacción con las estructuras marítimas.

Este primer objetivo principal se compone de otros sub-objetivos que ofrecen una clara línea para el desarrollo del modelo.

- **Objetivo 1.1: Implementar una generación de oleaje realista y robusta.** Las olas son la principal dinámica en ingeniería de costas. Como ya se apuntó en el

Estado del Arte, los métodos de generación más avanzados tienen lugar en los contornos (tanto como condiciones de contorno de Dirichlet o como contornos móviles). Asimismo, la absorción activa del oleaje es necesaria para evitar los efectos secundarios de esta técnica: el incremento del nivel medio del agua (Torres-Freyermuth et al., 2010). Se persigue, por tanto, obtener unas condiciones de contorno capaces de producir estados de mar realistas en cualquier profundidad relativa.

- **Objetivo 1.2: Implementar una absorción del oleaje eficiente en los contornos.** La generación del oleaje induce un incremento de la energía total del sistema. Las olas que se propagan pueden finalmente romper, disipando parte de esa energía, pero siempre hay una fracción de la energía incidente que se refleja y alcanza los contornos. Si estas olas no se absorben, se reflejarán y se propagarán de nuevo hacia el dominio de cálculo, distorsionando los resultados. De nuevo la revisión de la literatura muestra que la absorción activa (i.e. que se lleva a cabo en los contornos) es el método más avanzado y conveniente, comparado con la absorción pasiva. Es por ello que se desarrollará un sistema de absorción activa (en contornos estáticos y móviles) que permita realizar simulaciones más largas, estables y realistas.

- **Objetivo 1.3: Enlazar los métodos de generación y absorción activa para funcionar simultáneamente.** La generación activa del oleaje funcionando en contornos estáticos presenta una desventaja: debido a la física de las olas, existe un desequilibrio entre el agua que se introduce para crear las crestas y la que se extrae para generar los senos. Es por ello que en simulaciones largas se puede producir un incremento en el nivel medio del agua. Con el uso de la absorción activa conectada y funcionando simultáneamente con la generación de olas se corrige este fenómeno. Además, en el caso de contornos móviles, esta es la forma en la que funcionan en los dispositivos de generación del oleaje en los laboratorios.

- **Objetivo 1.4: Derivar unas nuevas ecuaciones VARANS para representar flujo bifásico a través de medios porosos.** Las ecuaciones VARANS han probado ser el método más avanzado para simular estructuras porosas complejas sin tener en cuenta la geometría exacta de los obstáculos en los mantos. Puesto que existen un gran número de formulaciones en la literatura se puede demostrar que

las VARANS son capaces de considerar procesos físicos adicionales si se derivan sin asumir que la porosidad no varía en el tiempo. Esta mejora puede ayudar a incluir en las ecuaciones, por ejemplo, el transporte del sedimento. Otra de las necesidades en las simulaciones costeras es tener en cuenta el efecto de los medios porosos sobre la turbulencia. Para ello es necesario promediar volumétricamente los modelos de turbulencia.

- **Objetivo 1.5: Implementar las nuevas ecuaciones y enlazar la generación y absorción en un nuevo modelo.** OpenFOAM® se ha perfilado como un código de CFD (dinámica de fluidos computacional) en volúmenes finitos con capacidades excepcionales. Sin embargo hay que enfatizar que OpenFOAM® no está preparado por defecto para simular procesos de ingeniería de costas, ya que carece de métodos de generación y absorción del oleaje, así como de flujo bifásico dentro de medios porosos. Por estas razones se decidió desarrollar este trabajo en OpenFOAM®, y llamar el nuevo solver **IHFOAM**.

3.2. Objetivo 2

Validar el modelo numérico tridimensional para probar que es capaz de simular procesos de ingeniería de costas.

Todos los modelos numéricos deben estar validados para demostrar que producen resultados correctos. En este caso, se han llevado a cabo diferentes pruebas de validación, ya que hay un gran número de procesos físicos implicados:

- **Objetivo 2.1: Validar la generación y absorción del oleaje.** El primer paso es probar que las nuevas condiciones de contorno desarrolladas son capaces de generar todo tipo de olas, en función de diferentes teorías. Asimismo, la absorción tiene que mostrar un correcto desempeño, con coeficientes de reflexión lo suficientemente bajos.

- **Objetivo 2.2: Validar los procesos de transformación del oleaje.** Es necesario simular los procesos básicos de transformación del oleaje (i.e. asomeramiento, refracción, difracción, interacciones no lineales y rotura del oleaje) inducidos por

geometrías simples para demostrar que el modelo es capaz de reproducirlas de una forma físicamente correcta. Para ello hay que comparar los resultados numéricos con medidas de laboratorio para demostrar su eficiencia.

- **Objetivo 2.3: Validar el flujo a través de medios porosos.** El nuevo módulo debe ser capaz de representar todos los procesos que los flujos bifásicos producen al moverse en el interior de los medios porosos. Este paso implica caracterizar los factores de fricción para varios tipos de medios porosos y bajo diferentes condiciones de flujo por comparación directa con datos experimentales.

- **Objetivo 2.4: Validar todos los procesos al unísono.** Como paso definitivo para demostrar la aplicación total del modelo, tiene que demostrar su habilidad para simular todos los procesos de interacción del oleaje con las estructuras a la vez, de la misma forma que suceden en situaciones reales.

3.3. Objetivo 3

Aplicar el modelo numérico tridimensional para simular estructuras reales a escala de prototipo.

El último objetivo es probablemente el más ambicioso, ya que si no fuera posible realizarlo el modelo desarrollado sólo sería aplicable a un rango limitado de aplicaciones. La posibilidad de simular estructuras reales abre nuevas perspectivas para el diseño de nuevas obras marítimas.

Generalmente, los modelos numéricos muestran largos tiempos de cálculo y requieren del uso de medios computacionales intensivos. De esta forma, para obtener las condiciones óptimas de integración en diseños reales se han de reducir ambos condicionantes. La manera más completa para realizar este objetivo es:

- **Objetivo 3.1: Desarrollar una metodología para integrar el uso del modelo en el proceso de diseño de estructuras marítimas.** La nueva metodología debe integrar diferentes modelos que sean capaces de, primero, propagar el oleaje en un dominio extenso y sin tener en cuenta la estructura para reducir el dominio a simular con el modelo RANS 3D, y segundo, simular la interacción detallada entre un estado

de mar y la estructura, para extraer los instantes pésimos de cara a la inestabilidad de la estructura. Ambos modelos deben poder ejecutarse en tiempos competitivos. Con la consecución de este objetivo, los ingenieros dispondrán de una herramienta avanzada para asistir en la toma de decisiones y con la que obtener diseños más óptimos.

Capítulo 4

Modelado Numérico

4.1. Introducción

En este trabajo se ha desarrollado un modelo RANS 3D denominado IHFOAM. Su concepción comienza en el año 2011 con el fin de adaptar OpenFOAM® para simular procesos de transformación del oleaje y de interacción con estructuras marítimas. Las continuas mejoras introducidas desde entonces lo convierten en uno de los modelos más avanzados en el estado del arte actual, y plenamente preparado para resolver los procesos enunciados en el apartado anterior.

¿Por qué usar como elemento de partida OpenFOAM®? Porque es un código de CFD universal, avanzado, robusto y cuyo uso se encuentra ampliamente instaurado en gran variedad de industrias. Básicamente es una librería multipropósito con aplicaciones para mallar, resolver y analizar problemas complejos como la turbulencia, el movimiento de fluidos... Además, es completamente gratuito y de código abierto, por lo que puede ser modificado. De este modo, y contrariamente a los códigos comerciales, OpenFOAM® no es una "caja negra": los usuarios pueden controlar y modificar todos y cada uno de los pasos del proceso de resolución.

IHFOAM, modelo desarrollado en esta tesis, resuelve las ecuaciones VARANS en dominios tridimensionales para dos fases incompresibles (agua y aire) mediante la tecnología VOF (Volume Of Fluid), aplicando una discretización en volúmenes finitos. Asimismo, permite el cálculo con gran cantidad de modelos de turbulencia ($k-\epsilon$, $k-\omega$ SST...)

4.2. Ecuaciones de gobierno

Las ecuaciones VARANS desarrolladas en este trabajo incluyen términos que tienen en cuenta la variación temporal de la porosidad, sin embargo la parte de transporte de sedimento se ha dejado fuera de la tesis (véase Sección 6.4).

Es por ello que las VARANS presentadas en este capítulo no consideran variación temporal de la porosidad. Las ecuaciones de gobierno comprenden la ecuación de continuidad (4.1) y las de conservación de momento (4.2):

$$\frac{\partial \langle u_i \rangle}{\partial x_i} = 0 \tag{4.1}$$

$$\begin{aligned} \frac{1+C}{\phi}\frac{\partial \rho \langle u_i \rangle}{\partial t} + \frac{1}{\phi}\frac{\partial}{\partial x_j}\left[\frac{1}{\phi}\rho \langle u_i \rangle \langle u_j \rangle\right] = \\ - \frac{\partial \langle p^* \rangle^f}{\partial x_i} - g_j X_j \frac{\partial \rho}{\partial x_i} + \frac{1}{\phi}\frac{\partial}{\partial x_j}\left[\mu_{\text{eff}}\frac{\partial \langle u_i \rangle}{\partial x_j}\right] + F_i^{\text{ST}} \\ - \alpha\frac{(1-\phi)^3}{\phi^3}\frac{\mu}{D_{50}^2}\langle u_i \rangle - \beta\left(1+\frac{7{,}5}{\text{KC}}\right)\frac{1-\phi}{\phi^3}\frac{\rho}{D_{50}}\sqrt{\langle u_j \rangle \langle u_j \rangle}\langle u_i \rangle \end{aligned} \tag{4.2}$$

En ellas ϕ representa la porosidad del material; ρ es la densidad; $\langle u_i \rangle$ es la velocidad promediada en volumen; $\langle p^* \rangle^f$ es la presión pseudo-dinámica; g_j es la aceleración de la gravedad; X_j es el vector posición; μ_{eff} es la viscosidad dinámica efectiva, que tiene en cuenta la viscosidad molecular y la turbulenta; y F_i^{ST} es la fuerza debida a la tensión superficial.

Finalmente también aparecen una serie de términos de cierre que representan la fricción adicional creada por los medios porosos. Puesto que no es posible calcularlos, hay que modelarlos mediante las características de los medios (D_{50} es el tamaño medio de grano). Para ello en IHFOAM se aplica la formulación de Burcharth and Andersen (1995). El término del factor α corresponde a la fricción lineal con respecto a la velocidad. El término β es la fricción no lineal, e incluye una mayoración dependiente del número de Keulegan-Carpenter para flujos oscilatorios. El último término, transitorio, se ha incluido en la aceleración local mediante el factor C.

Cuando en las ecuaciones anteriores $\phi = 1$ (es decir, fuera de los medios porosos),

resultan idénticas a las clásicas ecuaciones RANS.

4.3. Características distintivas de IHFOAM

La principal característica distintiva de IHFOAM es que se han desarrollado unas condiciones de contorno específicas para la generación y absorción activa tridimensional del oleaje. Puesto que el oleaje es la dinámica principal en las simulaciones de estructuras marítimas, estas técnicas son elementos clave. Con este procedimiento, absorción y generación se llevan a cabo únicamente en los contornos de la malla, por lo que no incrementan el coste computacional significativamente. Tampoco necesitan extender el dominio numérico. Esto supone un gran avance respecto a los métodos pasivos como el recogido en Jacobsen et al. (2012), que implican aumentar el tamaño del dominio en alrededor de 1–2 longitudes de onda.

Una generación realista del oleaje sienta las bases de un resultado final lo más preciso posible. Es por ello que se han desarrollado gran cantidad de teorías de oleaje que se pueden aplicar en 2D y 3D, mediante contornos estáticos o móviles. Esto incluye la generación de estados de mar irregulares, con teoría de segundo orden y dispersión direccional.

La absorción activa permite que las olas que inciden en un contorno, en muchos casos previamente reflejadas en las estructuras, desaparezcan con una reflexión mínima, como lo harían en mar abierto. Su funcionamiento es similar al de los sistemas de generación en laboratorio, midiendo la elevación de la superficie libre en el contorno para, mediante filtros digitales, generar una velocidad de corrección que absorbe el oleaje, tanto en dos como en tres dimensiones. Si no se asegura una correcta absorción, el oleaje puede volver a reflejarse en los contornos y contaminar los resultados.

IHFOAM también posee otra forma de generación novedosa: un módulo para emular los generadores de oleaje de laboratorio mediante contorno móvil, replicando el movimiento real de la palas. Este método también incluye absorción activa del oleaje, que modifica el movimiento de los generadores de oleaje.

La generación dinámica requiere de un complejo sistema para que el modelo sea capaz de desplazar el contorno y ajustar la malla interna. Asimismo, esta técnica permite simular estructuras flotantes, como la presentada en la Figura 6.1, e incluso elementos rotatorios

como hélices.

Otra de las características asociadas a las mallas dinámicas es el refinamiento dinámico simultáneo a la simulación, que permite obtener mejor resolución en zonas de interés, como a lo largo de la superficie libre.

4.4. Validación

La validación es un proceso que todos los modelos numéricos necesitan desarrollar para demostrar que son capaces de replicar las físicas que simulan.

IHFOAM es un modelo ampliamente validado. La generación y absorción activa sobre contornos estáticos demuestra sus capacidades en Higuera et al. (2013a), con un análisis detallado de las diferentes teorías de absorción (2D, Cuasi-3D y 3D) bajo distintas condiciones de oleaje. En Higuera et al. (2013b) se valida el modelo replicando un gran número de procesos de transformación del oleaje (difracción, refracción, rotura, interacciones no lineales...) y de interacción con estructuras impermeables (presiones, efectos hidrodinámicos, ascenso...), en su mayoría tridimensionales.

En referencias más recientes, Higuera et al. (2014a), se valida el módulo de flujo en el interior de medios porosos. Para ello, primero se calibran los coeficientes de fricción de los medios con un ensayo muy simple en el que el único forzamiento es la gravedad. Posteriormente, se simulan dos casos en los que se prueba que el modelo poroso funciona correctamente también para flujos oscilatorios, en 2D y 3D.

En el artículo más reciente (Higuera et al., 2015) se valida el sistema de generación y absorción multi-pala. Para ello se realiza una serie de ensayos puramente numéricos, con los que se estima el grado de absorción de la condición de contorno. Además se replican 2 ensayos de laboratorio, con sendas concentraciones de oleaje en 2D y 3D.

Capítulo 5

Aplicaciones

La parte final de este resumen extendido está dedicada a aplicar todos los avances desarrollados para simular estructuras reales a escala de prototipo.

Los modelos RANS tridimensionales requieren grandes recursos computacionales para ejecutarse. A pesar de que los tiempos de simulación de los casos de validación son razonables, se necesita al menos una simulación tridimensional de un estado de mar irregular de una hora de duración para diseñar una estructura no convencional en base a los criterios establecidos.

Sin embargo, con un ritmo típico de simulación de IHFOAM de 2 segundo por hora, la simulación completa necesitaría 75 días de cálculo, demasiado larga para ser aplicada en el contexto de una consultoría. Asimismo, cuanto más extenso sea el dominio a simular, mayor será la cantidad de datos que se obtendrán cada paso de tiempo, por lo que se requeriría una capacidad de almacenamiento considerable. En resumen, las capacidades computacionales actuales no son suficientes para este tipo de simulaciones.

Se hace necesaria una metodología para reducir el tiempo y dominio de las simulaciones al máximo, con el fin de racionalizar el uso de recursos computacionales y el tiempo de simulación para obtener resultados.

El primer caso tratado en este capítulo corresponde con una estructura idealizada y que sirve de ejemplo para comprobar los beneficios de aplicar la hibridación de dos modelos RANS: IH2VOF (2D) e IHFOAM (3D). El objetivo no es solamente probar que la hibridación de modelos puede ayudar a reducir los tiempos computacionales significativamente, sino también analizar cómo las variables ligadas a estabilidad y funcionalidad pueden variar ampliamente a lo largo de la estructura bajo condiciones de alta tridimen-

sionalidad.

El segundo caso corresponde con la aplicación de una metodología integral para simular estructuras reales bajo condiciones ambientales reales (e.g. batimetría, clima marítimo...). La metodología desarrollada en la sección anterior se integra en una más completa, que incluye el uso de diferentes modelos numéricos y técnicas estadísticas avanzadas. La metodología propuesta permite reducir la incertidumbre asociada a este tipo de cálculos.

5.1. Interacción de oleaje oblicuo con un dique mixto

Este primer caso práctico muestra una estructura realista en toda su extensión, sometida a un estado de mar con incidencia oblicua de 30 grados. Además se introduce una metodología de uso conjunto de los modelos IH2VOF e IHFOAM que permite racionalizar el uso de los recursos y ahorrar mucho tiempo de cálculo.

En este momento con IH2VOF (Lara et al. (2008), Losada et al. (2008)) es posible simular estados de mar de una a tres horas de duración a escala real en apenas 24 horas en 2D. Este rendimiento sobrepasa las posibilidades de IHFOAM considerando las capacidades técnicas actuales. Como se ha visto anteriormente los tiempos de simulación del modelo tridimensional son muy competitivos, pero simular un estado de mar en 3D llevaría demasiado tiempo y recursos de almacenamiento. Por ello se propone el uso de una metodología combinada 2D-3D. Con ella se simula el estado de mar completo con el modelo 2D y se seleccionan los instantes más desfavorables para la estabilidad de la estructura. Posteriormente se simulan solamente esos instantes con el modelo 3D y se obtienen los resultados que caracterizan el estado límite último de la estructura, incluyendo efectos tridimensionales.

5.1.1. Modelado numérico

La estructura simulada es un dique mixto cuya sección se puede ver en el panel superior de la Figura 5.1. El manto principal está formado por cubos de hormigón de 1.7 m de lado y se define como un medio poroso. La estructura está girada 30 grados respecto de la incidencia del oleaje y se somete a un oleaje irregular definido por un espectro JONSWAP de $H_s = 4.5$ m, $T_p = 10$ s y $\gamma = 3.3$.

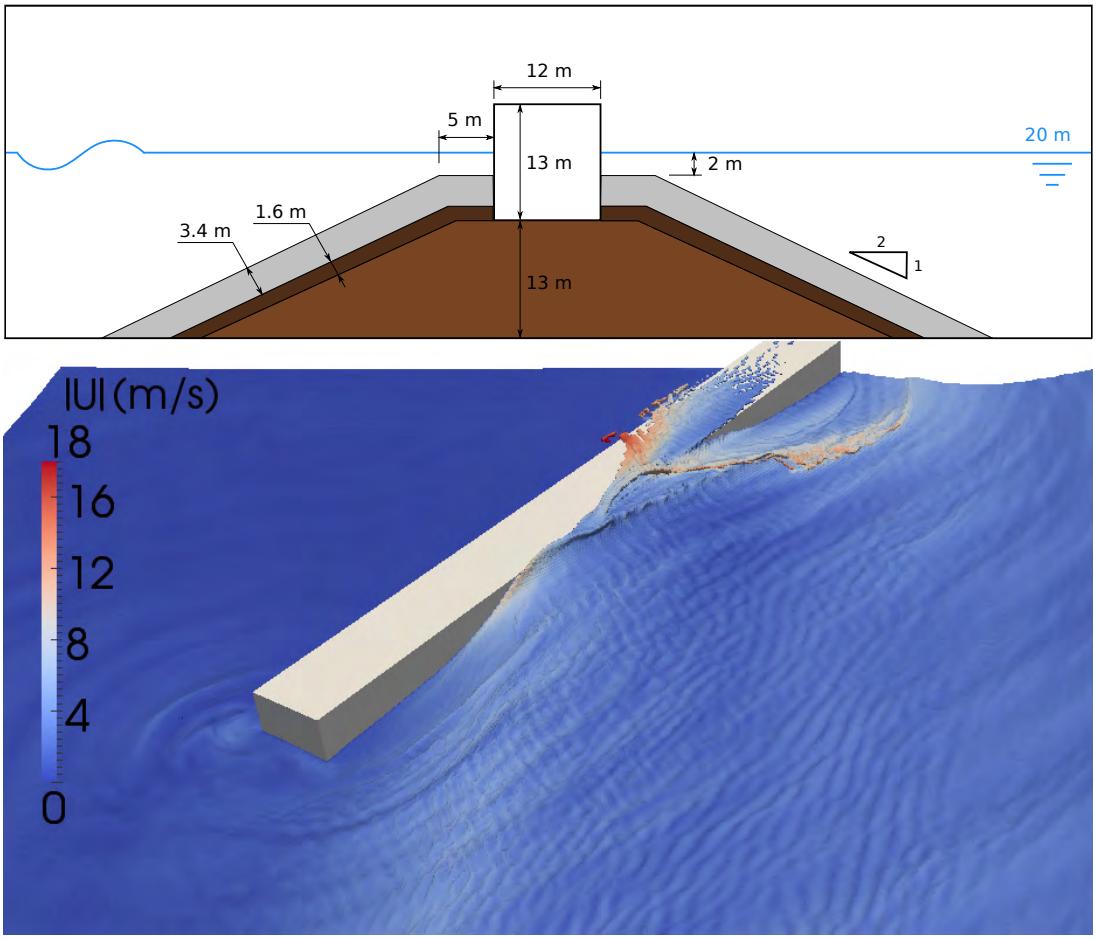

Figura 5.1: Sección y dominio del dique mixto.

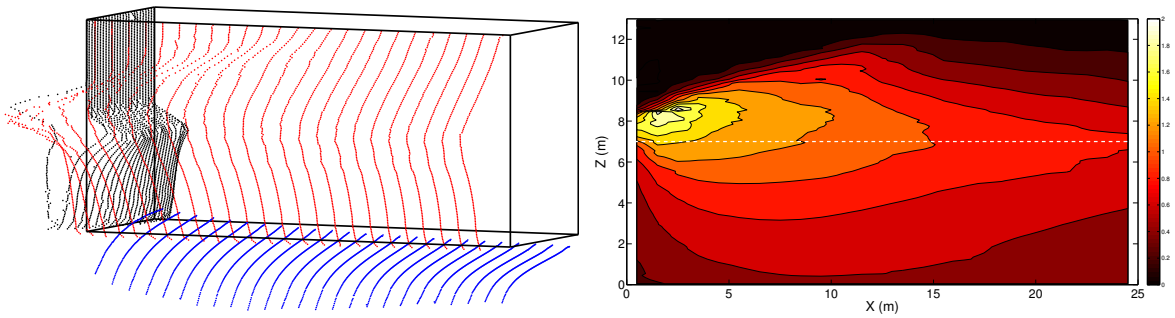

Figura 5.2: Presiones dinámicas adimensionales ($p_{din}/\rho g H_s$) sobre el cajón del morro.

El dominio de la simulación 3D se muestra casi completo en el panel inferior de la Figura 5.1. En total tiene 345 x 225 x 35 m y presenta un mallado variable, con celdas mayores (2 x 1 x 1 m) en generación y más finas (0.5 x 0.5 x 0.5 m) en la zona de detalle alrededor de la estructura. Esta malla base suma unos 10 millones de celdas.

En la simulación de IHFOAM se aplica la técnica de refinamiento dinámico a lo largo de la superficie libre, por lo que las celdas de la interfaz aire-agua presentan una resolución doble con respecto a la malla base, y van cambiando de forma dinámica. La malla final tiene una media de alrededor 20 millones de elementos, con una discretización máxima de 25 cm.

La malla del IH2VOF corresponde a un transecto en perpendicular al dique, con dimensiones análogas a la malla 3D y con el doble de resolución respecto a la malla base ya vista. En total tiene algo menos de 100,000 celdas y el estado de mar completo de 1 hora de duración se simula en 19 horas. El análisis de los datos permite obtener los coeficientes de seguridad instantáneos frente a vuelco y deslizamiento. La simulación de IHFOAM se lanza 70 s antes del instante en que se obtiene la menor estabilidad en IH2VOF, de forma que el agua esté ya en movimiento cuando lleguen las olas a estudiar. La simulación 3D finaliza a los 110 s y tarda 4 días en 96 procesadores (2.6 GHz).

5.1.2. Resultados

Para el estudio detallado del dique se ha dividido en 5 cajones de 25 m de largo. Las mayores solicitaciones, que inducen el estado más desfavorable para la estabilidad de la estructura, ocurren en el cajón del morro. Sólo se estudiará este evento, entendiendo que se pueden obtener resultados análogos para todos los cajones en cualquier paso de tiempo.

Las presiones dinámicas para el estado más desfavorable se muestran en la Figura 5.2. En el panel izquierdo se representa la distribución tridimensional sobre las caras expuestas del cajón. Las presiones de la cara de barlomar también se representan, de forma adimensional ($p_{din}/\rho g H_s$) y en 2D, en el panel de la derecha. La línea blanca a trazos indica el nivel inicial del agua en reposo.

En ambos paneles se pueden observar diferentes tipos de presiones. En primer lugar, las presiones de la cara de barlomar (puntos rojos) muestran un comportamiento distinto en función de su cercanía al extremo del dique. En la parte más alejada, la ley de presiones se asemeja a la obtenida con la teoría de Goda-Takahashi (Takahashi et al. (1994)). Sin embargo, en la zona más cercana al morro se puede observar un gran pico de presión de impacto causado por la cresta de la ola. Su magnitud sostenida casi dobla a la máxima prevista por la formulación semiempírica y se mantiene durante medio segundo, aproximadamente. Las subpresiones (puntos azules) presentan una forma similar a lo largo de todo el cajón, sin variaciones reseñables. Finalmente, las presiones de la cara frontal (puntos negros) tienen una distribución representativa. Como se puede observar, el primer transecto vertical, el más cercano a la esquina, tiene una forma similar a lo que ocurre en la cara de barlomar. El resto, sin embargo, muestran presiones negativas (representadas hacia el interior del cajón). Este fenómeno es debido a la gran separación de flujo existente en esa zona al pasar la cresta de la ola, que tiende a arrastrar el cajón.

En la Figura 5.1 se puede ver uno de los eventos de rebase, que ocurren a medida que la cresta de la ola recorre la estructura. Mediante sensores posicionados a lo largo de toda ella se puede estudiar la variación espacial y temporal de magnitudes como el caudal instantáneo o acumulado de rebase o el espesor y velocidades de la lámina de agua que rebasa.

En este caso se ha estudiado el caudal instantáneo de rebase por metro lineal de dique, tal y como se refleja en la Figura 5.3. El punto de referencia de distancias del eje X es el arranque de la estructura. Las grandes diferencias que aparecen ola a ola se deben a que el oleaje de estudio es irregular, por lo que no todas las olas tienen la misma altura y forma. Sin embargo, la primera y segunda son similares y sus diferencias son fruto de la interacción del oleaje incidente con el reflejado por la estructura.

Con la primera ola del grupo de estudio aparece un rebase máximo de unos 9.0 m^3/s

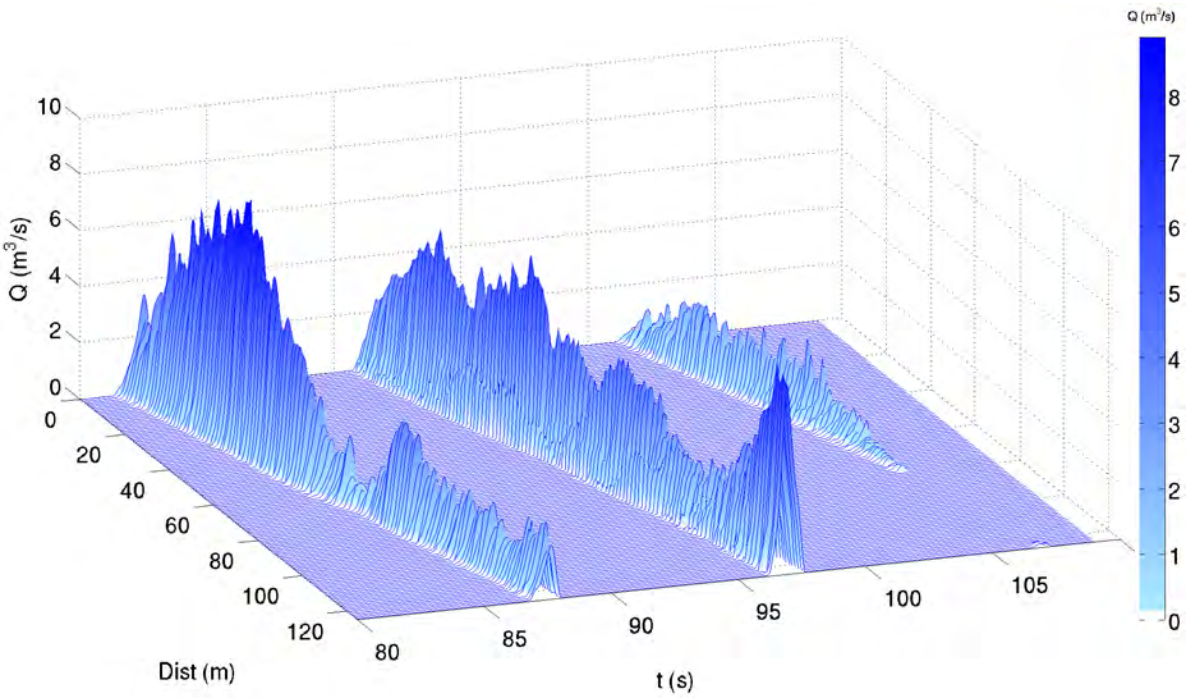

Figura 5.3: Caudales de rebase instantáneos por metro lineal.

cerca del arranque para luego pasar a ser aproximadamente constante hasta el morro, con un valor medio de 2.0 m^3/s. La siguiente ola es del mismo orden de magnitud y produce una distribución muy similar pero con dos peculiaridades. El pico del arranque no aparece, ya que esta ola interacciona con la reflejada de la primera y llega ya rota a la estructura. Además aparece un pico muy alto, de 7.0 m^3/s justamente sobre el morro. La ola final es mucho más pequeña que las anteriores y el rebase se reduce acordemente.

5.2. Simulación completa del Puerto de Laredo

El caso final pone de manifiesto todo el potencial del modelo, con un análisis tridimensional del dique exterior del Puerto de Laredo (Cantabria). Una situación tan compleja, que incluye la geometría de la estructura y batimetría reales, necesita una metodología que defina los pasos a seguir para fijar las condiciones que se simulan en detalle. Por ello, en este trabajo se propone una metodología de trabajo que se esquematiza en la Figura 5.4 y se desarrolla a continuación.

5.2.1. Metodología

1. Caracterización del clima marítimo en una localización cercana a la estructura no afectada por procesos costeros (refracción, difracción...) ni por rotura del oleaje. Puede provenir de una serie de datos observacionales, de medidas de una boya o de reanálisis. Es conveniente que la base de datos sea lo más extensa posible y esté calibrada.

2. Selección de un cluster de oleajes de la base de datos disponible mediante técnicas estadísticas de clasificación como SOM, k-medias, MaxDiss...

3. Propagación del cluster seleccionado desde el punto original hasta el pie de estructura mediante modelos integrados en la fase.

4. Reconstrucción del clima marítimo en el pie de la estructura y selección del estado de mar de diseño, conforme al periodo de retorno y condiciones establecidas por la ROM (Nivel I).

5. Determinación del oleaje de diseño en el punto inicial.

6. Propagación del oleaje mediante modelos no integrados en fase desde el punto inicial hasta el pie de la estructura. El resultado es una serie temporal de superficie libre y velocidades.

7. Simulación RANS en 2D con los datos de entrada del modelo no integrado en fase.

    a) Cálculo de las variables asociadas a la estabilidad estructural: coeficientes de seguridad frente a deslizamiento y vuelco.

    b) Identificación de los grupos de oleaje que originan los mínimos coeficientes de seguridad.

8. Simulación RANS en 3D de los grupos más desfavorables.

    a) Estudio de detalle en tres dimensiones de las variables de interés: run-up, rebases, fuerzas, coeficientes de seguridad...

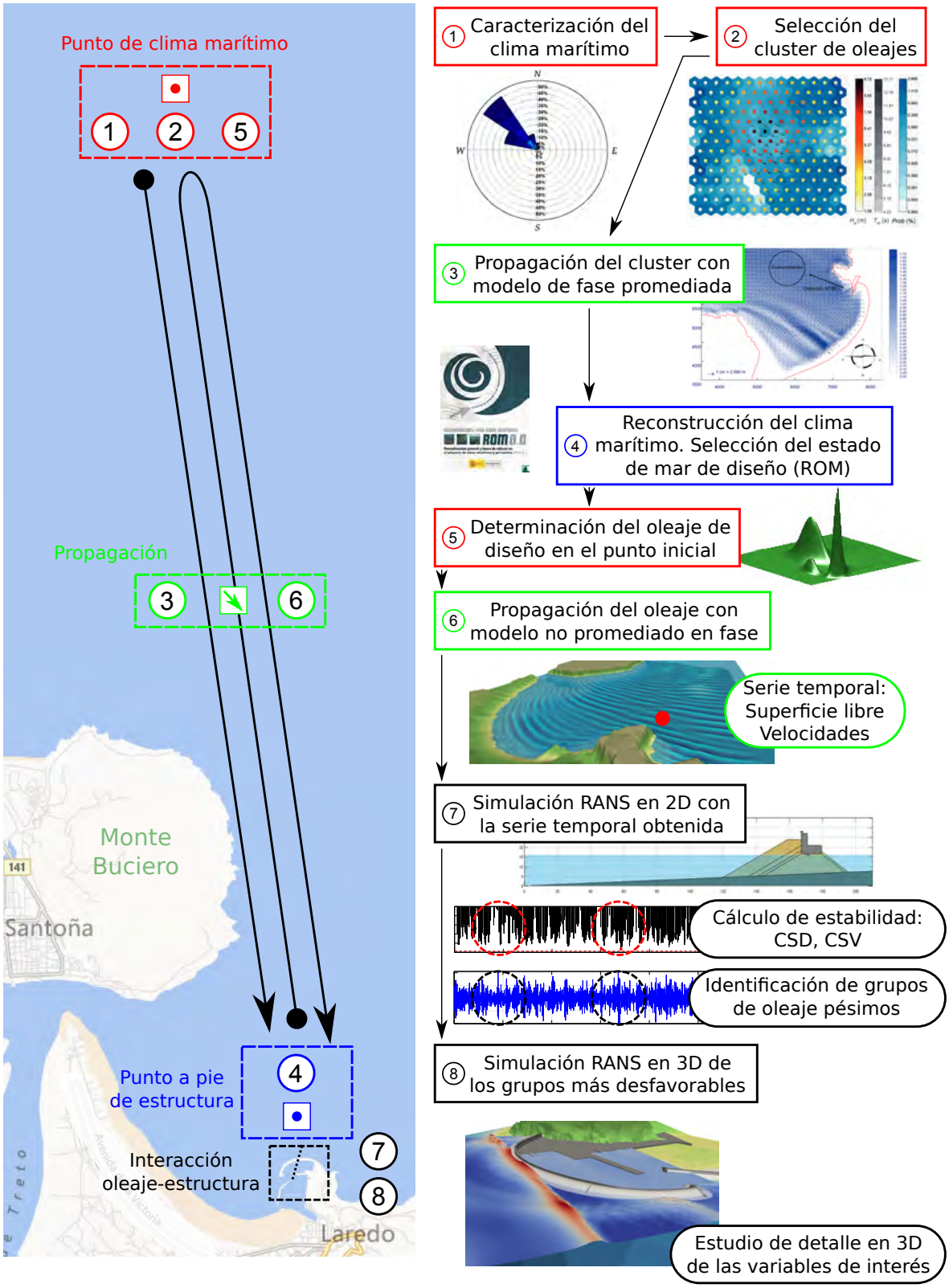

Figura 5.4: Metodología de trabajo para el modelado 3D de estructuras reales.

El proceso seguido en este caso en particular se ilustra en la Figura 5.4. El punto de partida es el clima marítimo de la base de datos DOW (Camus et al., 2013) en un punto en aguas profundas próximo al puerto. Aplicando MaxDiss se han seleccionado 214 de los estados de mar más energéticos. La propagación de este cluster (paso 3) se ha llevado a cabo con el modelo espectral OLUCA, con el objeto de caracterizar los temporales a pie de dique tras sufrir la transformación.

Un puerto deportivo típico, de una importancia similar a la que puede tener el de Laredo, se calcula para un periodo de retorno de alrededor de 475 años. El clima marítimo al pie de la estructura, según el ajuste GEV, indica que la altura significante de ola correspondiente al periodo de retorno de 475 años es de 6 m. Este tipo de oleajes viene asociado a periodos de 18 s, con una dirección dominante del NW en aguas profundas. La difracción del oleaje en el saliente del Monte Buciero y la refracción en un cañón submarino, que concentra el oleaje, hacen que la dirección de incidencia al pie del dique se encuentre alrededor de N15E. Se comprueba que la mayor ola más probable para este oleaje (10.8 m) es compatible con la profundidad (8 m + 5.5 m de marea), y corresponde con la altura máxima de ola que puede alcanzar la estructura sin romper.

Una vez determinado el estado de mar de diseño, se propaga con el modelo IHBouss, que resuelve las ecuaciones de Boussinesq (paso 6) y no considera la reflexión de la estructura para evitar efectos artificiales en la propagación. Los resultados son unas series temporales de superficie libre y velocidades en varios puntos a aproximadamente una longitud de onda de la estructura. Estos se usan como datos de entrada para forzar el oleaje en el modelado RANS con IH2VOF (paso 7). La simulación en 2D permite obtener una representación idealizada de la estructura, con la que calcular los coeficientes de seguridad al deslizamiento y vuelco de una sección tipo. Posteriormente se identifica los grupos de oleaje que inducen los mínimos coeficientes de seguridad, para simularlos en detalle en el modelo 3D. Finalmente se simulan los instantes críticos para la estructura con IHFOAM, forzando la generación con las series de IHBouss.

Como antecedentes se puede comentar que el Puerto de Laredo es de reciente construcción. El dique exterior presenta un talud 1:2, está formado por tres curvas enlazadas y lo corona un espaldón de hormigón en masa, como se ve en la Figura 5.4. El manto principal está formado por bloques cúbicos de 65 t, que aumentan a 70 t en la parte

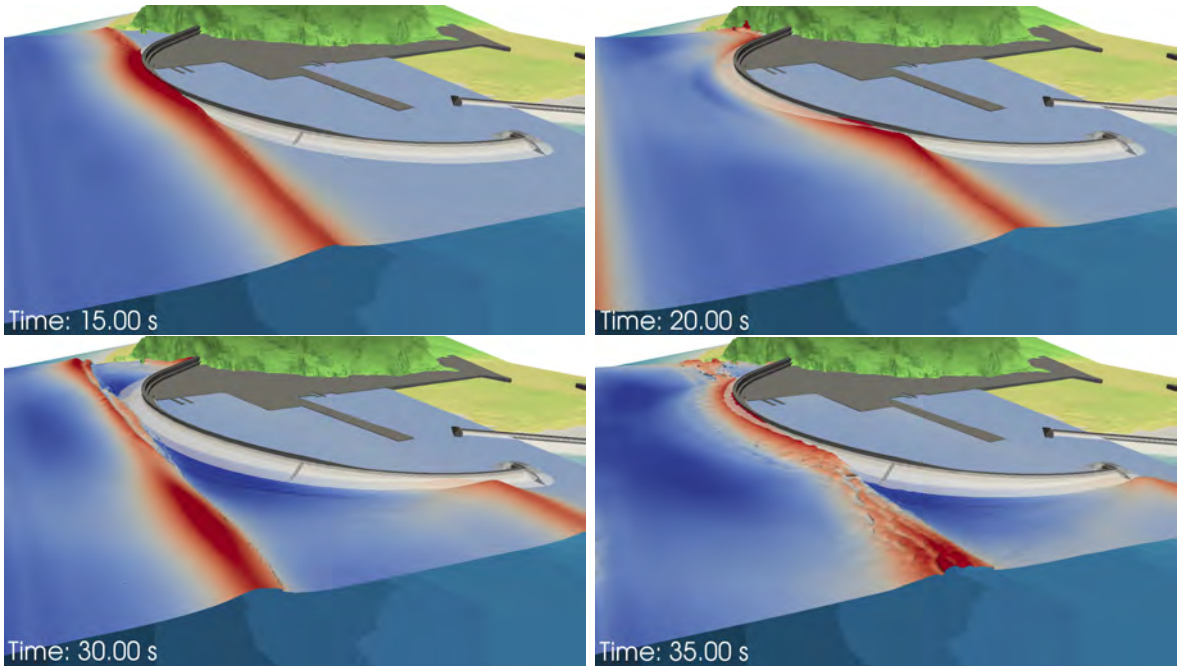

Figura 5.5: Propagación e impacto del grupo contra el dique de Laredo.

exterior del morro. Bajo él se localizan un manto secundario con cubos de 6 t, un manto terciario (escollera de 300–1000 kg) y el núcleo. El talud de sotamar tiene pendiente 1:1.5 y es de escollera de 300–1000 kg. El espaldón está cimentado a la cota +5.5 m, coronado a la +17 m y posee un botaolas en su parte más expuesta. A medida que se acerca hacia el morro, la cota de coronación desciende hasta la +14 m y desaparece el botaolas.

La malla de IHFOAM está orientada en la dirección de propagación del oleaje (N15E) y cubre una extensión de 500 x 700 x 34 m. El contorno de generación se localiza a aproximadamente una longitud de onda del dique y el punto más bajo de la malla corresponde con la cota -11 m de la batimetría. El tamaño de celda general se sitúa en 1.5 x 1.5 x 1 m, mientras que en la zona de detalle (alrededor de la estructura y próxima a la superficie libre) se reduce hasta 1 x 1.5 x 0.5 m. Para que el espaldón quede perfectamente definido y obtener un gran detalle del flujo y presiones a su alrededor, se refinan las celdas adyacentes hasta 0.25 x 0.375 x 0.125 m. En total esta malla contiene 10 millones de celdas. Su rendimiento en la simulación es de unos 25 s por día en 128 procesadores.

5.2.2. Resultados

En la Figura 5.5 aparecen varias instantáneas con una vista general del dique a medida que el grupo de oleaje se propaga. Es la primera ola del grupo la que induce las

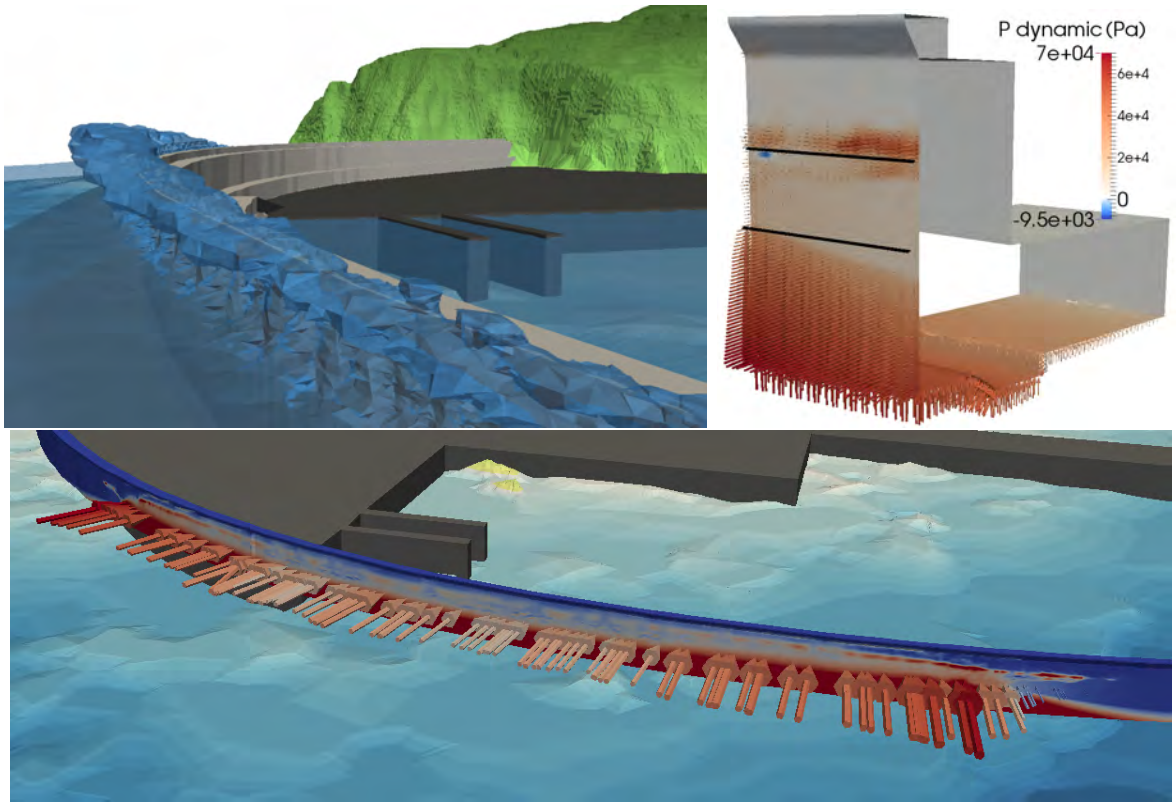

Figura 5.6: Resultados tridimensionales de rebase, presiones y fuerzas sobre el dique de Laredo.

mayores solicitaciones, ya que la segunda llega ya rota por su mayor altura. Se pueden ver también procesos tan complejos como el impacto del oleaje con el acantilado ($t = 20$ s), la interacción ola incidente-reflejada ($t = 30$ s), la propagación de un frente roto ($t = 35$ s) o la difracción a medida que se sobrepasa el morro ($t = 35$ s).

En la Figura 5.6 se muestran los resultados del impacto de la primera ola del grupo. En ellos se puede apreciar la gran tridimensionalidad de los procesos. En el panel superior izquierdo aparece representada la superficie libre cuando la ola impacta en el espaldón y la lámina de agua alcanza su máxima elevación. Pese a que el nivel del agua proyectada se encuentra muy por encima de la cota de coronación el rebase es casi inexistente. Esto es debido a que la cota superior de la cresta de la ola no excede el nivel de coronación, y por lo tanto la ola que impacta es deflectada por el botaolas. El resultado es que el momento vertical que posee la ola en ese punto se proyecta hacia barlomar, lo que evita el rebase sobre la estructura. También se puede ver el efecto que juega el aire atrapado en la interacción con la estructura, ya que la zona de contacto del manto principal con el espaldón presenta a lo largo de todo el dique pequeñas bolsas de aire ocluido.

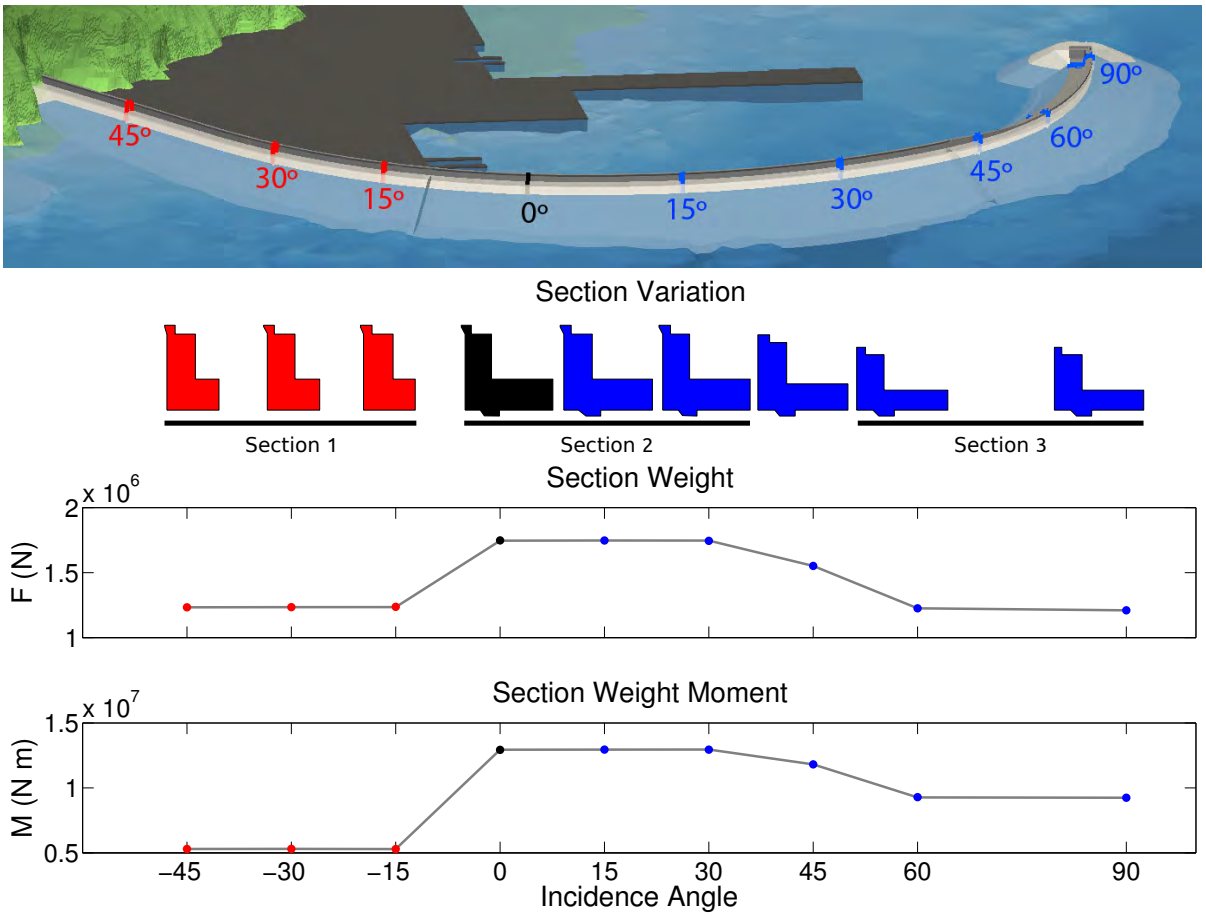

Figura 5.7: Secciones de referencia del dique de Laredo.

En el panel inmediatamente a su derecha se ha representado la ley de presiones sobre una sección del espaldón de 5 m de ancho. Las líneas negras indican la localización del manto principal. La distribución varía tanto a lo ancho como a lo alto de la sección. Es especialmente relevante el efecto protector del manto principal, ya que la presión dinámica (sobrepresión con respecto a la inicial) en su interior es casi nula. Por encima de su límite superior sí que aparecen presiones positivas por el impacto de la ola y una pequeña zona de presión dinámica negativa, probablemente causada por una bolsa de aire atrapada en el manto. También es reseñable la gran complejidad de las subpresiones, debido al talón del espaldón. En el panel inferior se pueden observar las presiones sobre el espaldón completo, así como unas flechas que indican la fuerza total que actúa sobre diferentes secciones verticales. Se calculan integrando las presiones en transectos definidos. Las mayores solicitaciones se localizan en el frente de ola, donde éste ataca de forma transversal al espaldón.

También se ha llevado a cabo un estudio detallado de la estabilidad estructural, con-

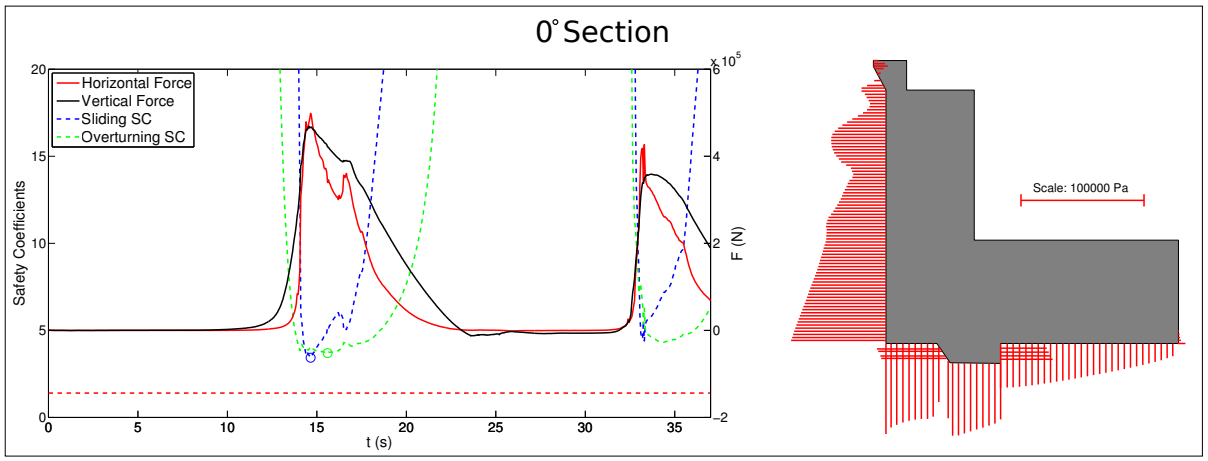

Figura 5.8: Resultados tridimensionales de estabilidad en el dique de Laredo.

siderando distintas secciones a lo largo de la traza de la estructura, mostradas en la Figura 5.7. Al tratarse de un dique curvo es posible analizar la variación en las solicitaciones causadas por el distinto ángulo de incidencia del oleaje, de 0 a 90 grados. En el panel superior se muestra una vista en perspectiva del dique exterior con todas las secciones de estudio. Cada una de ellas tiene 5 m de ancho (análogas a las vistas en la Figura 5.6). El código de colores indica la posición de la sección, ya que hay dos localizaciones (rojo/azul) en las que el oleaje incide en las direcciones 15, 30 y 45 grados, una a cada lado de la sección con incidencia normal del oleaje (color negro, 0 grados). En el panel inferior se muestran las propiedades de cada una de las secciones. Puesto que el análisis se realiza sobre la geometría real, esta ha sido optimizada en su fase de diseño, y las secciones se han aligerado en los lugares en los que se ha determinado que no están sometidas a grandes solicitaciones. Se pueden distinguir 3 tipologías, dependiendo de su altura de coronación y de si tienen botaolas o no.

El panel izquierdo de la Figura 5.8 muestra la evolución temporal de las fuerzas medias en la sección por metro lineal (escala de la derecha). En rojo aparecen las fuerzas horizontales, que muestran picos cuando la ola impacta. Las fuerzas verticales, en negro, son más suavizadas y de una magnitud similar a las horizontales. En el mismo gráfico también se representa el coeficiente de seguridad al deslizamiento de la sección, en línea azul discontinua y con escala a la izquierda. Se aprecia que su mínimo global (círculo azul) está asociado al impacto de la primera ola, y su valor es de 3.4, muy alejado del valor crítico representado en línea roja discontinua. A su derecha se muestra la ley de presiones media sobre dicha sección para el instante crítico. Su forma es prácticamente

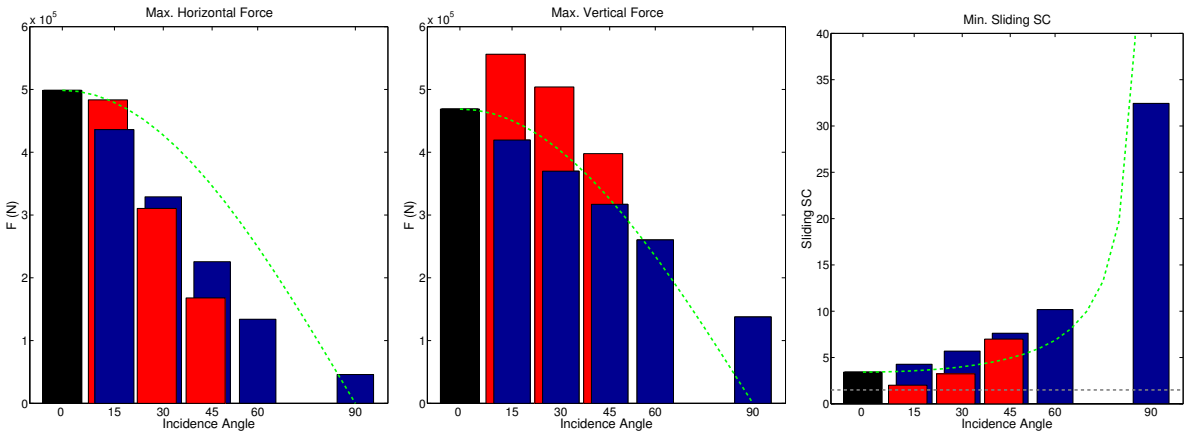

Figura 5.9: Variación de las solicitaciones en función del ángulo de incidencia del oleaje en el dique de Laredo.

hidrostática en la parte del espaldón protegida por los mantos y presenta dos máximos locales en la parte expuesta, causados por del impacto del frente. También se aprecian presiones negativas en el botaolas, causadas por el arrastre al deflectar la salpicadura.

En la Figura 5.9 aparece una comparativa de fuerza máxima horizontal y vertical, y de mínimo coeficiente de seguridad al deslizamiento para todas las secciones estudiadas. La línea verde es la evolución esperada tomando como referencia la sección de incidencia normal y la evolución típica asociada al coseno del ángulo de incidencia, como en la formulación de Takahashi et al. (1994).

La evolución de las máximas fuerzas horizontales es pareja en ambas direcciones y los resultados están siempre por debajo de la línea verde. Sin embargo, las fuerzas verticales muestran un desarrollo diferente en función del lateral hacia el que se propagan, ya que las rojas son hasta un 30 % mayores que las del lado azul. Esta discordancia puede explicarse por dos factores: efectos locales de la batimetría y que la sección del dique no es homogénea, sino que su cota de coronación varía a lo largo de su longitud para optimizar costes. La variación del coeficiente al deslizamiento es creciente en el lateral azul, lo que indica que la estructura es más estable cuanto más alejada se encuentre de la incidencia normal del oleaje. Los valores rojos son notablemente inferiores a los azules, puesto que las fuerzas verticales eran mayores. De nuevo, los efectos locales son los causantes de este comportamiento. No obstante, el coeficiente de seguridad mínimo global que se alcanza es de 2, por lo que todavía existe margen de seguridad.

5.2.3. Análisis del diseño

Basado en los resultados tridimensionales, y si esta fuera una alternativa de prediseño, el siguiente paso sería estudiar y proponer una sección modificada, aligerada donde los coeficientes de seguridad muestran mayores valores. De esta forma los coeficientes de seguridad se reducirían (dentro de un margen aceptable y seguro) y se obtendría una estructura más optimizada: tan funcional y estable como la anterior, pero más económica en términos de material.

Hay un gran número de factores que se tienen que tener en consideración cuando se planea una estructura óptima. Quizá la idea más importante que hay que resaltar es que el diseño perfecto desde el punto de vista teórico da lugar a la alternativa constructivamente más cara. Esto sucede debido a que el hormigonado del espaldón es un proceso semi-automático mediante encofrados deslizantes. Cambiar la sección constantemente impediría el automatismo y elevaría los costes (en términos de tiempo, materiales de encofrado y ajustes) por encima de las ganancias en hormigón. Además, retrasar o bajar el ritmo de construcción del espaldón eleva considerablemente el riesgo al que está sometida la estructura, ya que en el caso de que llegue una tormenta, la estructura se encuentra desprotegida y el rebase puede llevarse los materiales.

Estas consideraciones iniciales dan lugar a unas conclusiones claras: para diques cortos, una sección única es probablemente la opción más segura y económica. Para diques largos, probablemente sea más beneficioso tener varias secciones. La clave en este caso está en diseñar todas las secciones para que puedan ser construidas con pequeñas variaciones del mismo encofrado modular, de forma que sea fácil de construir y de amortizar.

La cuestión relevante es ahora cómo determinar si un dique es “corto” o “largo”. La respuesta no es trivial, ya que necesita un análisis integral económico y de riesgo. Los principales factores a tener en cuenta son los siguientes:

- Tiempo y coste adicional para diseñar y construir el encofrado.
- Tiempo adicional para manejar el nuevo encofrado.
- Tiempo adicional necesario para construir la transición entre diferentes secciones.
- Restricciones de plazo incluidas en el contrato.

- Riesgo climático (daños) debido a los tiempos adicionales.
- Ahorro económico debido al uso de menos hormigón.

En este caso en particular, el dique de Laredo tiene 730 m de longitud y posee 3 diferentes secciones, con 2 transiciones (véase la Figura 5.7). En vista de los resultados, el diseño actual es óptimo. La sección 1 está coronada a la cota +17 m, incluye un botaolas y la losa inferior es corta y sin talón. La sección número 2 es idéntica a la primera, pero la losa es más larga e incluye un talón para evitar que deslice. La sección número 3 está coronada a la cota +14 m, no posee botaolas y la losa inferior es más fina. A pesar de todo las anchuras de la pared vertical y de la losa de la base son iguales a las de la sección anterior. La forma similar de todas las secciones, que sólo varía en la altura de ciertos elementos, es muy conveniente de cara a usar un encofrado único que se adapte, ahorrando tiempo y dinero.

La cantidad total de hormigón necesario para construir el espaldón es de aproximadamente 47000 m^3. Si todo el espaldón se construyese con una sección única (sección número 2), se necesitarían 57000 m^3, dando lugar a una estructura sobredimensionada. La optimización que se ha llevado a cabo por los diseñadores supone un ahorro del 20 % en hormigón, que considerando a un precio típico de 130 €/m^3, supone 1,300,000 €.

Se podría considerar una sección más aligerada cerca del morro del dique, pero esto supondría un nuevo cambio de encofrado para una parte muy corta de la estructura. Esto incrementaría el coste y tiempo de construcción, no compensándose con el ahorro del material.

5.2.4. Conclusiones

Esta simulación pone de manifiesto la importancia de los efectos tridimensionales locales y la gran capacidad del modelado numérico tridimensional para asistir en el diseño de estructuras reales. Se ha probado que el botaolas del dique de Laredo funciona correctamente, ya que el rebase para grandes olas es mínimo. En la portada del trabajo se puede comparar la forma del impacto de una ola durante los temporales de este año y la de la simulación. También se ha demostrado que todas las secciones son estables, con coeficientes de seguridad adecuados.

En base a los datos tridimensionales, el siguiente paso sería proponer una sección modificada, más aligerada a medida que se acerque la zona del morro. Con ella se reduciría el coeficiente de seguridad (dentro de unos límites razonables) en las zonas menos solicitadas y se obtendría una estructura optimizada: igual de funcional y estable, pero más económica.

Capítulo 6

Conclusiones

6.1. Conclusiones generales

Este trabajo se ha centrado en completar y mejorar el conocimiento existente, así como en perfeccionar las técnicas asociadas al modelado numérico de interacción flujo-estructura. Para ello se han enunciado una serie de objetivos y una metodología para lograrlos, descrita en el Capítulo 3. Las conclusiones que se pueden extraer son:

En la primera parte de esta tesis se presenta OpenFOAM®, un código de CFD multipropósito gratuito, de código abierto y plenamente establecido, que se ha adaptado para incluir nuevas características.

El nuevo modelo desarrollado, IHFOAM, que resuelve las ecuaciones VARANS para dos fases incompresibles en tres dimensiones, se presenta validado y listo para simular todo tipo de procesos de interacción del oleaje con estructuras de protección costera a escala real, con tiempos de cálculo muy competitivos. Las características distintivas que lo sitúan entre los modelos más punteros del estado del arte incluyen la generación y absorción activas del oleaje, sin las que no se podrían obtener resultados de tan alta calidad. Además, las técnicas de mallado dinámico permiten simular dinámicas complejas y mejorar el detalle de los resultados en zonas concretas, ayudando a conseguir un elevado rendimiento.

En vista de los resultados se ha conseguido una generación y absorción de olas realista, estable y robusta. Además su implementación en forma de condiciones de contorno ha demostrado ser una de las más avanzadas del estado del arte, puesto que no incrementa el coste computacional del modelo.

Las nuevas condiciones de contorno incluyen las teorías de oleaje más extendidas, cubriendo con ellas todo el espectro de profundidades relativas, así como generación de primer y segundo orden. Además, puesto que los estados de mar reales son aleatorios y tridimensionales, uno de los avances mostrados es la capacidad de generar espectros frecuencia-dirección, discretizados en sus componentes.

El módulo de absorción activa presenta un excelente rendimiento y es incluso capaz de lidiar con oleaje reflejado con grandes amplitudes. Este método se ha asociado también a contornos de generación de oleaje, mejorando la estabilidad de las simulaciones largas permitiendo que una gran parte de la energía fluya hacia el exterior y evitando el incremento del nivel medio.

El desarrollo de una condición de contorno móvil para la generación de oleaje es otra de las novedades de esta tesis. Este procedimiento puede ayudar a obtener simulaciones numéricas más detalladas, ya que replica las máquinas de generación de laboratorio (pala de tipo pistón), e incluye absorción activa.

El movimiento de las palas numéricas se puede prescribir mediante una serie teórica o una serie de "feedback" de un generador de laboratorio. La absorción activa se puede conectar para evitar que el oleaje se refleje en las palas. También se pueden tener en cuenta las limitaciones físicas de las máquinas reales (máxima carrera, velocidades, aceleraciones...) para realizar simulaciones previas realistas con señales teóricas.

Se han replicado correctamente experimentos de concentración del oleaje en 2D y 3D. Los resultados presentan un alto grado de realismo, a pesar de que se han encontrado limitaciones en OpenFOAM® a la hora de simular la propagación de olas muy peraltadas.

La absorción activa es también aplicable a contornos móviles y su efectividad es tan alta como cuando se aplica en contornos estáticos. Los coeficientes de reflexión obtenidos son generalmente menores al 10 %, y sólo mayores en los casos cuyas condiciones de oleaje se alejan de las hipótesis de partida de esta técnica. Sin embargo, la eficiencia de las condiciones de contorno móviles es menor que las estáticas, puesto que el modelo tiene que resolver el movimiento de la malla.

También se han desarrollado unas nuevas ecuaciones VARANS que tienen en cuenta los gradientes espaciales y temporales de la porosidad, suponiendo un avance con respecto a una de las últimas referencias en la literatura (Jensen et al., 2014). Esta nueva capa-

cidad permite, por ejemplo, la simulación de sedimento que se mueve. Asimismo, se han promediado dos modelos de turbulencia, $k-\epsilon$ y $k-\omega$ SST, para considerar la producción de turbulencia en el interior de los medios porosos.

La implementación práctica de las ecuaciones en OpenFOAM® incluye una formulación de arrastre específica para ingeniería de costas y soluciona problemas conocidos en la versión distribuida por OpenFOAM®, que no es conservativa con la masa.

La validación es uno de los puntos fuertes de esta tesis. Con ella se prueba que IHFOAM es un modelo adecuado para simular procesos de interacción entre el oleaje y las estructuras, no sólo por los buenos resultados obtenidos, sino también por las razonables necesidades computacionales y tiempo de simulación

El verdadero potencial de los modelos RANS radica en su capacidad de asistir en el diseño de estructuras reales, superando las limitaciones de formulaciones semi-empíricas y experimentales. Este es el objetivo último de la presente tesis.

En el Capítulo 5, el uso conjunto de los modelos numéricos IH2VOF e IHFOAM muestra notables ventajas de cara a racionalizar los recursos y obtener tiempos de simulación más competitivos. En este aspecto, el altísimo rendimiento del modelo bidimensional permite calcular un gran número de estados de mar, de entre los que seleccionar los casos más desfavorables para la estabilidad de la estructura, y después simularlos en 3D. Así, se limitan las simulaciones de grandes dominios a unos cientos de segundos, lo que supone obtener resultados hasta en 36 veces menos de tiempo, que solo incluyen los grupos de oleaje con mayor incidencia en la estabilidad estructural. Con las simulaciones en detalle se pueden obtener resultados como distribuciones de presiones, rebase, transmisión o patrones de reflexión tridimensionales a lo largo de toda la estructura.

La metodología final propuesta para la simulación de estructuras íntegras combina todo tipo de herramientas y técnicas estadísticas para reducir el rango de incertidumbre asociado a este tipo de cálculos. El uso del modelo IHBouss permite propagar el oleaje teniendo en cuenta los efectos locales ocasionados por la batimetría y la interacción ola a ola, y obtener series temporales reales a pie de estructura en lugar de un espectro como se viene haciendo hasta ahora. La introducción del modelado 2D para seleccionar los casos más desfavorables cobra una mayor relevancia con su integración en esta metodología, ya que es el elemento clave para permitir la aplicación del modelo 3D. Finalmente, el

uso de IHFOAM para simular la estructura en toda su extensión supone un hito en el campo del modelado numérico ya que es la primera vez que se calcula una estructura real tan compleja con un modelo RANS 3D. Además, los resultados indican el correcto funcionamiento del dique, ya que no se han medido rebases y los coeficientes de seguridad se ajustan a la norma.

En conclusión, el modelado híbrido se perfila como un factor clave en el futuro del diseño de estructuras marítimas, especialmente no convencionales. No hay que perder de vista que en la metodología híbrida el uso del modelado numérico es siempre complementario al modelado físico. Los beneficios de la simbiosis aparecen desde el principio, con la asistencia en el prediseño de los ensayos. Posteriormente, se extienden tras el fin de los experimentos, con la obtención de resultados de alto nivel de detalle y la ampliación de la base de datos de los casos de estudio.

La capacidad del modelado numérico para evaluar los efectos tridimensionales abre nuevas perspectivas en los estudios de detalle. Sin duda, la generalización de estas tecnologías supondrá un gran avance en el diseño de estructuras no convencionales de un modo óptimo, con funcionalidad y estabilidad mejoradas, más ecológicas y con menores costes.

6.2. Contribuciones científicas

El trabajo de esta tesis ha dado lugar a varias contribuciones científicas en forma de artículos y ponencias en congresos.

En Higuera et al. (2013a) se presenta el desarrollo de las condiciones de contorno de generación y absorción para contornos estáticos. Este trabajo supone un hito en el campo de la ingeniería de costas porque no sólo se detalla la teoría sino que se dan indicaciones prácticas de la implementación numérica, válidas para cualquier modelo RANS. En un segundo artículo publicado inmediatamente a continuación (Higuera et al., 2013b) se incluye una extensa recopilación de casos de validación de IHFOAM. La importancia de este artículo radica en que es la primera vez que OpenFOAM® se valida como una herramienta aplicada a procesos de ingeniería de costas en 3D.

La implementación y validación de las ecuaciones VARANS de del Jesus et al. (2012) fue presentada en Higuera et al. (2014a). Pese a que en la presente tesis se han encontrado y

corregido ciertas discrepancias con el procedimiento clásico de promediación volumétrica, los resultados en ambos casos son idénticos, con la única diferencia de los factores de fricción usados.

Higuera et al. (2014b) constituye una aplicación práctica de la primera metodología híbrida presentada en este trabajo, y muestra el verdadero potencial de IHFOAM para simular estructuras tridimensionales. Hasta donde saben los autores es la primera vez que se presentan leyes de presiones tridimensionales y series espacio-temporales de rebase sobre una estructura, obtenidas mediante modelo numérico.

Higuera et al. (2015) se ha enviado recientemente para ser publicado e incluye todos los detalles acerca de la implementación y validación de la generación y absorción de oleaje mediante contorno móvil.

6.3. Transferencia tecnológica

El desarrollo de IHFOAM comenzó en 2011 como una versión ligeramente modificada de *interFoam*. Como parte del trabajo asociado a esta tesis se ha desarrollado un curso intensivo de formación que incluye todos los materiales necesarios para aprender a utilizar OpenFOAM® e IHFOAM. Hasta la fecha se han llevado a cabo 5 ediciones de dicho curso, para asistentes tanto de el ámbito universitario y de investigación como de consultoría, en Santander, Madrid y Chennai (India).

La primera versión de IHFOAM se liberó en el marco del primer curso de formación, en Octubre de 2012. Ese solver incluía una versión inicial de las condiciones de contorno de generación y absorción desarrolladas en este documento, pero carecía de modelado de flujo a través de medios porosos.

IHFOAM 2.0 es la versión actual, y fue liberada gratis bajo la licencia GNU GPL el 15 de julio de 2014, con avances significativos y nuevas características. Las instrucciones para la descarga del modelo se encuentran en su página web[1].

Gracias al continuo desarrollo, IHFOAM es uno de los modelos RANS más avanzados que se pueden encontrar en el estado del arte, totalmente capaz de simular los procesos de interacción oleaje-estructura, tal y como se ha probado en esta tesis. Algunas de las capacidades más relevantes de IHFOAM se encuentran recogidas en la Figura 6.1.

[1] http://ihfoam.ihcantabria.com/source-download/

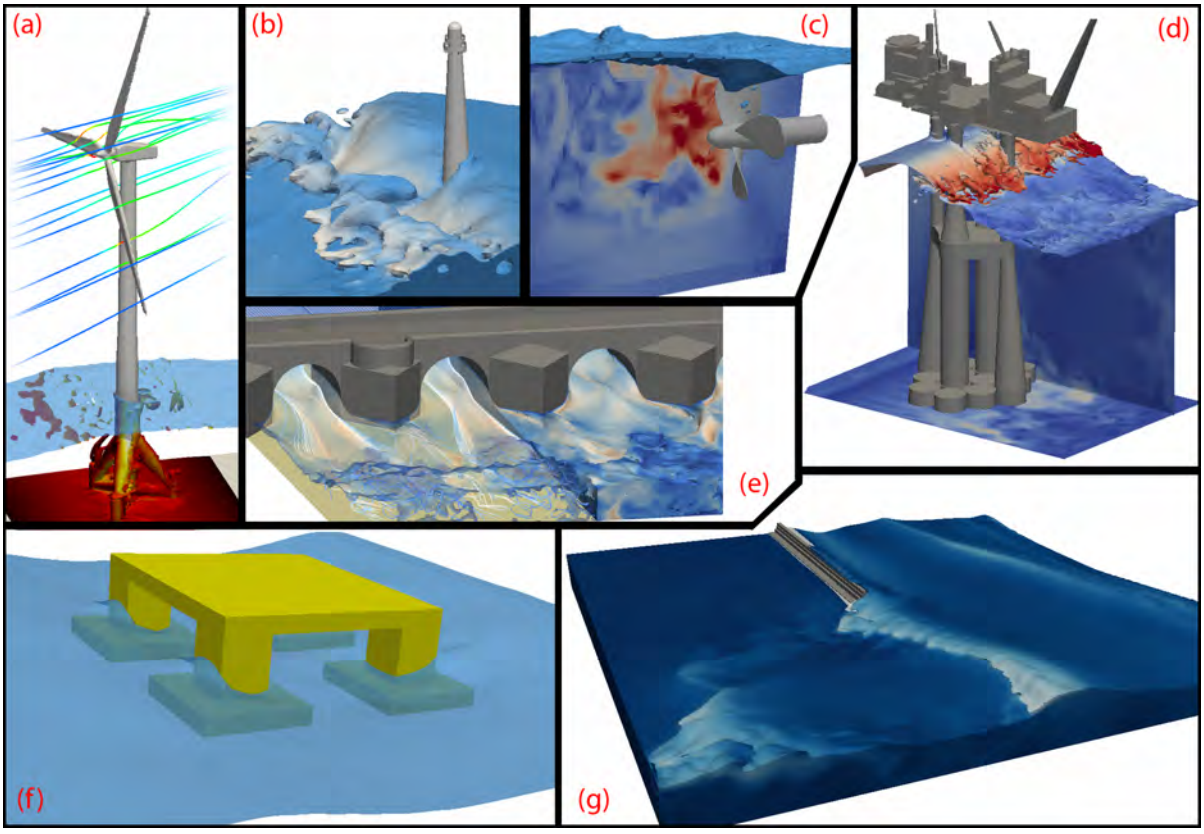

Figura 6.1: Capacidades más relevantes de IHFOAM: (a) cimentaciones offshore de aerogeneradores (hidrodinámica + aerodinámica); (b) interacción del oleaje con estructuras impermeables como faros; (c) dinámicas externas como hélices de barco; (d) impactos sobre plataformas offshore; (e) hidráulica fluvial alrededor de puentes; (f) plataformas offshore flotantes; (g) estructuras marítimas.

Gracias a ellas el modelo constituye un ejemplo de transferencia tecnológica entre centros de investigación y empresas, ya que se han impartido cursos de formación a los que han asistido personas del ámbito académico y de consultorías. Además el código fuente del modelo es abierto y está disponible para todo el que lo desee en su página web[2]. Actualmente cuenta con más de 280 usuarios en 49 países (España, Estados Unidos, Canadá, Dinamarca, Singapur...)

El modelo es también un ejemplo de transferencia tecnológica entre centros de investigación y empresas. Las estadísticas de las descargas en la web indican que IHFOAM tiene más de 280 usuarios en 49 países diferentes (España, USA, Dinamarca, Reino Unido, China...)

6.4. Futuras líneas de trabajo

El desarrollo de IHFOAM continúa, añadiendo nuevas características, mejorando las existentes y corrigiendo bugs.

Las líneas futuras de trabajo implican continuar con el estudio de las posibilidades que OpenFOAM® puede ofrecer en todos los campos relacionados con el oleaje (e.g. costas, offshore, energías renovables...) con especial énfasis en el acoplamiento de modelos para ofrecer capacidades adicionales y mejores rendimientos.

La línea de trabajo más avanzada que no se ha incluido en esta tesis es el transporte de sedimento. La nueva versión de IHFOAM incluye la implementación completa de las ecuaciones VARANS derivadas en este trabajo, incluyendo la variación temporal de la porosidad.

La técnica usada para simular el sedimento también es novedosa. Cada partícula de sedimento se simula independientemente mediante una técnica Lagrangiana denominada DEM (Discrete Element Method), en la que las partículas tienen un comportamiento mecánico y que considera la interacción completa fluido-partícula y partícula-fluido.

Una aplicación práctica, el socavamiento causado por una corriente uniforme (0.5 m/s) de agua bajo un cilindro (10 cm de diámetro), se muestra en la Figura 6.2.

En el panel superior se puede apreciar como el sedimento ha sido arrastrado y la erosión es ya patente bajo el cilindro. Es reseñable que algunas partículas (1 mm de diámetro)

[2] http://ihfoam.ihcantabria.com

se encuentran en suspensión. El panel central muestra las líneas de corriente y la interfaz del sedimento. En el panel inferior aparece un paso de tiempo anterior, con perfiles de velocidad a lo largo de la columna de agua e isolíneas de vorticidad. Los valores más altos de vorticidad aparecen alrededor de la estructura y cerca de los lugares erosionados, que siguen creciendo.

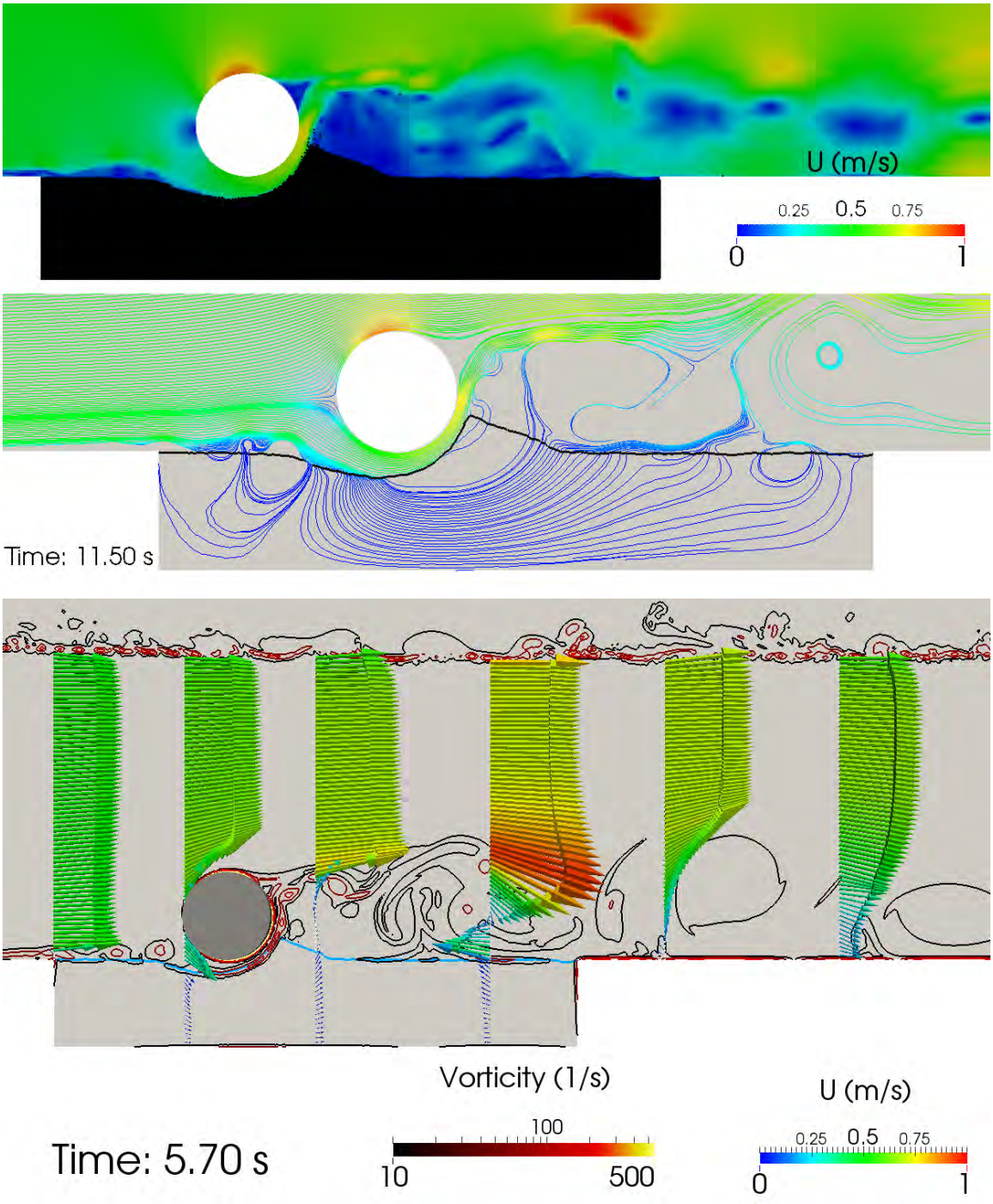

Figura 6.2: Volume averaging domain for several phases and obstacles.

Bibliografía

Burcharth, H. and Andersen, O. (1995). On the one-dimensional steady and unsteady porous flow equations. *Coastal Engineering*, 24(3-4):233–257.

Camus, P., Mendez, F. J., Medina, R., Tomas, A., and Izaguirre, C. (2013). High resolution downscaled ocean waves (DOW) reanalysis in coastal areas. *Coastal Engineering*, 72:56–68.

Choi, B. H., Kim, D. C., Pelinovsky, E., and Woo, S. B. (2007). Three-dimensional simulation of tsunami run-up around conical island. *Coastal Engineering*, 54(8):618–629.

Dalrymple, R. A. and Rogers, B. D. (2006). Numerical modeling of water waves with the SPH method. *Coastal Engineering*, 53:141–147.

del Jesus, M., Lara, J. L., and Losada, I. J. (2012). Three-dimensional interaction of waves and porous structures. Part I: Numerical model formulation. *Coastal Engineering*, 64:57–72.

Gerritsen, H. and Sutherland, J. (2011). *Users guide to physical modelling and experimentation. Experience of the HYDRALAB network.*, chapter Composite Modelling. IAHR.

Goda, Y. (1985). *Random seas and design of maritime structures.* University of Tokio Press.

Harlow, F. and Welch, J. E. (1965). Numerical calculation of time-dependent viscous incompressible flow of fluid with a free surface. *Physics of Fluids*, 8:191–203.

Higuera, P., Lara, J. L., and Losada, I. J. (2013a). Realistic wave generation and active wave absorption for Navier–Stokes models: Application to OpenFOAM. *Coastal Engineering*, 71:102–118.

Higuera, P., Lara, J. L., and Losada, I. J. (2013b). Simulating coastal engineering processes with OpenFOAM. *Coastal Engineering*, 71:119–134.

Higuera, P., Lara, J. L., and Losada, I. J. (2014a). Three–dimensional interaction of waves and porous coastal structures using OpenFOAM. Part I: Formulation and validation. *Coastal Engineering*, 83:243–258.

Higuera, P., Lara, J. L., and Losada, I. J. (2014b). Three–dimensional interaction of waves and porous coastal structures using OpenFOAM. Part II: Applications. *Coastal Engineering*, 83:259–270.

Higuera, P., Losada, I. J., and Lara, J. L. (2015). Three-dimensional numerical wave generation with moving boundaries. *Coastal Engineering (Submitted)*.

Hirt, C. W. and Nichols, B. D. (1981). Volume of fluif (VOF) method for the dynamics of free boundaries. *Journal of Computational Physics*, 39:201–225.

Hsu, T., S. T. and Liu, P. (2002). A numerical model for wave motions and turbulence flows in front of a composite breakwater. *Coastal Engineering*, 46(1):25–50.

Jacobsen, N. G., Fuhrman, D. R., and Fredsøe, J. (2012). A wave generation toolbox for the open-source CFD library: OpenFOAM. *International Journal for Numerical Methods in Fluids.*, 70(9):1073–1088.

Jensen, B., Jacobsen, N. G., and Christensen, E. D. (2014). Investigations on the porous media equations and resistance coefficients for coastal structures. *Coastal Engineering*, 84:56–72.

Kim, S.-H., Yamashiro, M., and Yoshida, A. (2010). A simple two-way coupling method of BEM and VOF model for random wave calculations. *Coastal Engineering*, 57(11-12):1018–1028.

Lara, J. L., Losada, I. J., and Guanche, R. (2008). Wave interaction with low mound breakwaters using a RANS model. *Ocean Engineering*, 35:1388–1400.

Lin, P. (1998). *Numerical modeling of breaking waves*. PhD thesis, Cornell University.

Lin, P. and Liu, P.-F. (1999). Internal wave-maker for Navier–Stokes equations models. *Journal of Waterway, Port, Coastal, and Ocean Engineering*, 125:207–215.

Liu, P.-F., Lin, P., Chang, K., and Sakakiyama, T. (1999). Numerical modeling of wave interaction with porous structures. *Journal of Waterway, Port, Coastal, and Ocean Engineering*, 125:322–330.

Liu, P.-F. and Losada, I. J. (2002). Wave propagation modeling in coastal engineering. *Journal of Hydraulic Research*, 40(3):229–240.

Losada, I. J., Lara, J. L., Guanche, R., and Gonzalez-Ondina, J. M. (2008). Numerical analysis of wave overtopping of rubble-mound breakwaters. *Coastal Engineering*, 55(1):47–62.

Lynett, P. J. and Liu, P. L.-F. (2002). A two-dimensional, depth-integrated model for internal wave propagation over variable bathymetry. *Wave Motion*, 36(3):221–240.

Nikora, V., McEwan, I., McLean, S., Coleman, S., Pokrajac, D., and Walters, R. (2007). Double-averaging concept for rough-bed open-channel and overland flows: Theoretical background. *Journal of Hydraulic Engineering*, 133(8):873–883.

Rider, W. J. and Kothe, D. B. (1998). Reconstructing volume tracking. *Journal of Computational Physics*, 141:112–152.

Shao, S. (2010). Incompressible SPH flow model for wave interactions with porous media. *Coastal Engineering*, 57(3):304–316.

Slattery, J. C. (1967). Flow of viscoelastic fluids through porous media. *American Institute of Chemical Engineers Journal*, 13(6):1066–1071.

Takahashi, S., Tanimoto, K., and Shimosako, K. (1994). A proposal of impulsive pressure coefficient for design of composite breakwaters. *Proceedings of the International Conference on Hydro-technical Engineering for Port and Harbour Construction.*, pages 489–504.

Tanimoto, K., Moto, K., Ishizuka, S., and Goda, Y. (1976). An investigation on design wave force formulae of composite-type breakwaters. *Proceedings of the 23rd Japanese Conference on Coastal Engineering.*, pages 11–16. (in Japanese).

Torres-Freyermuth, A., Lara, J. L., and Losada, I. J. (2010). Numerical modelling of short- and long-wave transformation on a barred beach. *Coastal Engineering*, 57:317–330.

Troch, P. and De Rouck, J. (1998). Development of 2D numerical wave flume for simulation of wave interaction with rubble mound breakwaters. *Proceedings 26th ICCE, Copenhagen.*

Troch, P. and De Rouck, J. (1999). An active wave generating-absorbing boundary condition for VOF type numerical model. *Coastal Engineering*, 38(4):223–247.

van der Meer, J. W. (1987). Stability of breakwater armour layers–design formulae. *Coastal Engineering*, 11(3):219–239.

Wei, G. and Kirby, J. T. (1995). Time-dependent numerical code for extended Boussinesq equations. *Journal of Waterway, Port, Coastal and Ocean Engineering*, 121(5):251–261.

Whitaker, S. (1967). Diffusion and dispersion in porous media. *American Institute of Chemical Engineers Journal*, 13(3):420–427.

Zijlema, M. and Stelling, G. S. (2011). Swash: an operational public domain code for simulationg wave fields and rapidly varied flows in coastal waters. *Coastal Engineering*, 58(10):92–1012.

UNIVERSIDAD DE CANTABRIA

Departamento de Ciencias y Técnicas
del Agua y del Medio Ambiente

DOCTORAL THESIS

Application of Computational Fluid Dynamics to Wave Action on Structures

Presented by: **Pablo Higuera Caubilla**

Directed by: **Javier López Lara**

Iñigo J. Losada Rodríguez

January 2015

Acknowledgements

The present doctoral thesis is the result of several years of continuous work and sacrifices, of good days and not so good days, of weeks with more than 60 working hours, but fortunately, this thesis is not the result of sleepless nights. Nevertheless, I do not want to take full credit on it. There are people that have made a difference and contributed to its success, even without realizing.

In first place I would like to thank my family for all the love and understanding they have given me throughout my lifetime. Mom and Dad, thanks for always having nice words and convincing me that time puts everything in place. David, Miguel, thanks for making me smile. Pilli, Mimi, Marta, Moncho, Elías, Lucía, Mari, Chiqui and many others, thanks for always being attentive and asking how everything is going. And of course, thanks to Yaya, no words can describe it. This thesis is dedicated especially to her.

It may not be the most appropriate procedure to separate friends from family, but with a whole section for them they really get the importance they require. There are three people who have played a special role for me and they deserve not only a short line in this work, but eternal gratitude. These friends are like succulent plants, because even though sometimes I have not watered them enough, they have not faded. Fito, music and travel united us and even if you are the only person who practices water-tasting you are still much appreciated. Jaime, great photographer and a better person, host as no other in São Miguel. Long were the tens of photography nights, dozens the sunsets in La Arnía and a couple the sunrises trying to "shoot" deer in Sejos and Richmond Park, we will always need to further develop our photo techniques and continue looking for The Picture. Iñigo, we met long time ago in the Chemistry Campus and we still manage to laugh like that night. Let's not lose it, ever, because certainly the dreams of a summer

afternoon can come true, especially those to come... we will toast once again when we both are doctors.

I would also like to thank my thesis supervisors, Javier L. Lara and Iñigo Losada for their continued tutelage. Without their extensive experience I could have only managed to get lost in the forest of numerical modelling, a forest that I had to walk alone, but with an excellent compass. In particular I have the pleasure to thank Javi for all the good times we shared in a thousand and one congress travels, and for all the anecdotes that like pieces of a puzzle helped me set up an overview of past, present and future of research. It would be unfair to forget to mention in this section "my third director", Raúl Medina, thanks for everything.

I can not let this occasion pass without thanking the other colleagues at IH Cantabria. There are many people who throughout these years of work have shown and proven the best of them for me. Therefore, even if it were discussing work matters, during lunch and coffee times, in more relaxed environments or even climbing a mountain, they will always be present for me. Thanks César Vidal, Edurne, Manu, Jorge, Alexia, Nico, Mar, David, María and many others.

Finally I am indebted to the Ministry of Education for the funding provided under the Program "Formación del Profesorado Universitario" (FPU12-04354), which has enabled me to carry out this thesis. Also I can only thank again the IH Cantabria for everything that offered me throughout these years, with which I have been able to perform the physical and numerical tests of this thesis, besides presenting my work at numerous conferences and journals international.

Contents

Chapter 1

Introduction

1.1 Motivation

Coastal structures play an important role in the world of today. Under this denomination different kinds of structures may be found, such as dikes, breakwater, jetties, docks, artificial beaches and reefs... Each of them may have its own purpose, but they all share a main objective of sheltering a location from the action of the harmful sea dynamics (e.g. waves, currents...).

One of the principal tasks for which coastal structures are built is to create harbours. Currently, there is a large number of ports along the coasts of all world, but the growing sea transport volume drives the tendency to increase the size of ships and only few of them can accommodate the largest vessels in the globe.

The growing size of ships requires a response at the port level, therefore, smaller ports are trying to accommodate new industries and to comply with the new shipping standards. This factor is driving a change in the traditional hierarchy of ports, generating competition among them. The most difficult question that port planners are facing is to decide whether to build an expansion in deeper waters or to improve existing infrastructures.

Either way, the design process is challenging. Building a structure in deep waters requires high standards and is more expensive. In return, it offers better access and maneuvering capabilities for larger vessels. Adapting an existing structure to modify its purpose or functionality levels is cheaper, but it often yields a non-conventional design, which has to be tested thoroughly.

The adaptation of coastal structures can have three main purposes. The first has

already been introduced, and is changing the use of the facility. A second function is to consolidate and protect historical structures, to avoid a collapse under sea action. Finally, adaptations can also be planned to overcome the effects of climate change.

In this last field, that seems to have a promising future, a modification of an existing infrastructure is planned to enhance its functionality and stability levels against the effects of climate: sea level rise and in the number and magnitude of extreme events (storms). The 2013 winter season is a perfect example of such a situation. An unusually large number of storms reached the north coast of Spain and damaged the protection structures of small marinas. The damage was almost non-existing for large infrastructures, although significant overtopping discharges were observed due to high total water levels.

The design of coastal structures is traditionally founded on two basic tools: semi-empirical formulations and physical modelling. They both allow characterizing the operability, functionality and reliability requirements.

Semi-empirical formulations model the hydraulic behaviour of a structure affected by waves with a mathematical expression. They provide the structural response in a simple and fast way, based on adjusted dimensional analysis of sets of laboratory experiments. The best known semi-empirical formulations are: Tanimoto et al. (1976) for composite breakwaters, Goda (1985) and Takahashi et al. (1994) for vertical breakwaters or van der Meer (1987) for rubble-mounds. The advantages of this procedure are clear, as it is a very fast and inexpensive method. However, semi-empirical formulations are not strictly applicable outside the conditions that they were derived for. Therefore, this method is not applicable to design structures with non conventional sections or with important local effects.

Scaled physical modelling in a laboratory is still the key method in the design of coastal structures. This technique is advantageous because it reduces the uncertainty when obtaining the structural response of a structure and is specially necessary when the structures are non-conventional or present three-dimensional effects. With it, ad hoc formulations can be obtained for a specific design problem. Nevertheless, this approach presents certain limitations: intrusive measuring devices, scale effects and high cost (in time and money) of the experiments. An illustrative example of physical modelling for designing a coastal structure is the main breakwater of Gijón's Port (Spain), which was

planned with a section changing from a rubble mound breakwater to a vertical breakwater. Since no semi-empirical formulations existed, it had to be tested in the laboratory.

In recent times a third tool has been introduced in the design process of coastal structures: numerical modelling. This is a novel technique with which tests can be carried out in computers, instead of in experimental facilities. Numerical modelling encompasses numerous approaches and models, which will be introduced in Section 2.2. For example, one of the most advanced approaches in numerical modelling of wave and structure interaction, the Reynolds Averaged Navier–Stokes (RANS) equations, has already been applied in 2D to assist in the design of the exterior port of La Coruña (Spain) and is also considered a distinguished method in the catalogue of the Spanish coastal structures, edited in 2012 by the Spanish Port Authorities. Nevertheless, these newer tools also present limitations, as RANS models sometimes require large computational resources and long times to run.

Besides, in order to obtain accurate numerical results, the model must be validated to prove that it is capable of reproducing the processes of interest. Moreover, if the model depends on calibration parameters, they need to be adjusted. In either case this is to be performed by comparing the model results with experimental results. In conclusion, numerical modelling must be regarded as a tool complementary to physical modelling. The combined use of both techniques can help to identify the pros and cons of each method, as there are processes than can only be replicated experimentally or numerically because of their time or space scales.

In fact, there is a field called composite modelling that promotes the integrated and balanced use of physical and numerical models (Gerritsen and Sutherland, 2011), offering countless advantages. Within this symbiotic framework, numerical modelling unveils its full potential with two main roles:

- Assisting with the pre-design of the physical experiments.
- Extending the experimental database with detailed results, after validation.

The benefits of composite modelling appear at every stage of the design projects. Before starting the study itself, the numerical model can help in the predesign of the experiments in an approximate way. Numerical modelling is significantly cheaper than

physical experiments and it can be applied as a tool to characterize the hydrodynamics around the structure beforehand to highlight the zones of interest, to find the most suitable places where the measuring devices can be placed, to anticipate problems or even to select the most relevant cases to be tested physically.

While the experiments are ongoing, the model can be validated to create a numerical mirror of the experimental facility. A numerical mirror is a setup (mesh, boundary conditions, calibrated parameters...) of a model that has proven to mimic the physical processes that take place at a given experimental facility. This conception may seem novel in coastal engineering, but it has been applied for long time in other fields. The paradigm is aerodynamics, in which composite modelling is fully developed, as numerical mirrors of wind tunnels are extensively applied.

Once the experiments have ended, numerical modelling can be applied to extend the database obtained with purely numerical results, simulating different wave conditions and structural alternatives at the same time and at a fraction of the cost of performing them in the laboratory. Additional numerical measurements can also be collected at this final stage, overcoming some experimental restrictions, as probing can be performed for any field or location without disturbing the flow. Moreover, the new cases can be run at prototype scale, avoiding scale effects, hence, reducing the uncertainty linked to this kind of calculations.

Finally, the analysis of the experimental plus numerical results or by feeding neuronal networks and genetic algorithms can be used to optimize the structural design, producing solutions with enhanced functionality, more economical, environmentally friendly and sustainable.

Obviously, the most interesting range of application of physical and numerical models is cases in which three-dimensional effects play a significant role. Unfortunately, and unlike 2D RANS models, that have already been applied to simulate wave action on structures for complete sea states, there is no 3D RANS model that can be applied for that general purpose.

Concluding, it can be said that the advanced numerical modelling of wave and coastal structures interaction still offers a wealth of challenges and research opportunities. This thesis is devoted to overcome some of the most pressing challenges to make three-dimensional

numerical modelling available for the coastal and port engineering community.

1.2 Structure of the thesis

The present document is structured as follows:

This introductory chapter serves to motivate the topics studied in this thesis, stressing the advantages that three-dimensional numerical modelling could offer to the design of coastal structures.

In Chapter 2, a review of the state of knowledge in numerical modelling of waves interacting with structures is presented. First, the literature review focuses on the different types of models, comparing the pros, cons and limitations of each approach. Once the most suitable technique is found, three key elements are analyzed in detail: the governing equations, the porous media models and the methods for generating and absorbing waves.

Chapter 3 defines the objectives of the present work, according to the gaps found in the state of the art of previous chapter. Also, the methodology followed to complete this study is enunciated.

Chapter 4 is devoted to the mathematical derivation of a new set of volume-averaged equations to simulate wave flow through porous zones (e.g. the layers of breakwaters). Additionally, two turbulence models are also volume averaged to account for the turbulence enhancement caused by the elements that conform the porous media. Finally, this chapter concludes with a technical discussion, comparing the newly developed equations with others found in literature.

In Chapter 5 a complete description of the numerical modelling tool developed and used in this work, **IHFOAM**, is given. Since the model is developed in the computational fluid dynamics (CFD) frame of OpenFOAM®, the first section includes a brief introduction to this open source library. Then, full details are given on the equations solved and how the model operates. Next comes the description of the boundary conditions that have been developed for wave generation and absorption.

Chapters 6 and 7 include an extensive set of validation cases, for which the capabilities of **IHFOAM** are demonstrated. First, the performance of the wave generation and absorption boundary conditions, both static and moving, is tested. Next, coastal

processes such as wave transformation (e.g. refraction, diffraction, shoaling and breaking) are reproduced and compared with experimental data. Wave interaction with porous structures is validated next, replicating laboratory experiments in 2D and 3D. This last section also describes the calibration process for the friction parameters that represent the porous media.

Chapter 8 is where the methodological part of this thesis is developed and applied. In the first part, a case where a train of oblique irregular waves interacts with a vertical breakwater in 3D is calculated applying a 2D-3D hybrid methodology. Results include three-dimensional pressure distributions on the caissons and the overtopping flow rate along the breakwater.

In the second part of this chapter, the previous methodology is incorporated into a global methodology that enables the simulation of wave interaction with real structures at prototype scale. The new methodology is applied to the non-conventional case of the curved breakwater in the Port of Laredo (Spain), a highly three-dimensional case for which semi-empirical formulations do not exist.

Finally, the conclusions of this work are discussed in Chapter 8, analysing the results obtained for the initial objectives and the doors that the new model opens.

Chapter 2

State of the Art

This chapter serves as a reference guide for the state of knowledge of different elements that are involved in the numerical modelling of wave-structure interaction.

First, the requirements for numerical models to obtain a detailed description of the wave-structure interaction processes are analysed. The three main approaches in which numerical simulation of wave-structure interaction is founded are studied next. Finally, once a suitable type of models has been found, the literature regarding wave generation, wave absorption and treatment of porous structures is reviewed.

2.1 Requirements for wave-structure interaction

Traditionally the design of coastal structures has been carried out applying semi-empirical formulations and laboratory experiments. They both allow characterizing the operability, functionality and reliability regimes. If a numerical model aims to perform the same operations it needs certain capabilities.

Wave-structure interaction involves studying all the processes derived from the action of waves impacting on coastal structures. This includes local wave propagation and wave transformation prior to the impact on the structures. Once waves reach the structure, both elements need to be studied to analyse the mutual effects. A selection of the most important wave-structure interaction processes is represented in Fig. 2.1.

In the first place, a model for wave-structure interaction needs to be able to simulate the primary processes of wave transformation at a local scale (e.g. shoaling, refraction, diffraction and breaking, plus nonlinear interaction between waves), so that the waves

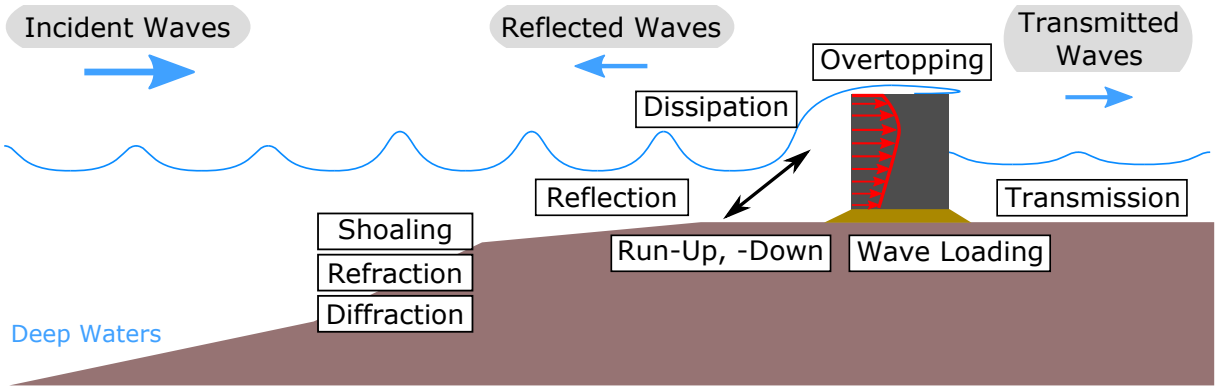

Figure 2.1: Wave propagation and wave-structure interaction processes.

that reach the structure are represented correctly. Wave transformation is induced by the bathymetry, by wave and current interaction or by wave-to-wave interaction. It encompasses important phenomena, with different degrees of complexity. For example, on the one hand shoaling can be studied with simple mathematical formulations and is easy to simulate. On the other hand, a correct representation of wave breaking needs to capture the large and intricate variations of velocity and pressure that exist along the water column and the dissipation of energy associated to it, being one of the most complex processes to reproduce numerically.

Another key factor is that the model should be able to simulate flow inside porous media (e.g. armour layers and the nucleus of the breakwaters) to correctly characterize the wave characteristics near the structure. Determining the physical processes that take place around and inside the structure involves a twofold study, as waves and the structure are mutually influenced. Failure to characterize the local hydrodynamics will mean that wave processes as for example reflection, transmission or breaking, and structural processes as run-up, overtopping or forces and moments will not be correctly calculated. Moreover, in order to obtain a correct description of structural stability, the pressure around the structure should also include the nonlinear effects of the impact, especially when originated by broken waves.

Needless to say, most of the aforementioned processes are highly three-dimensional. Therefore, if 2D simplifications are not reasonable for a specific project, the model would need to simulate a 3D case to obtain more realistic results.

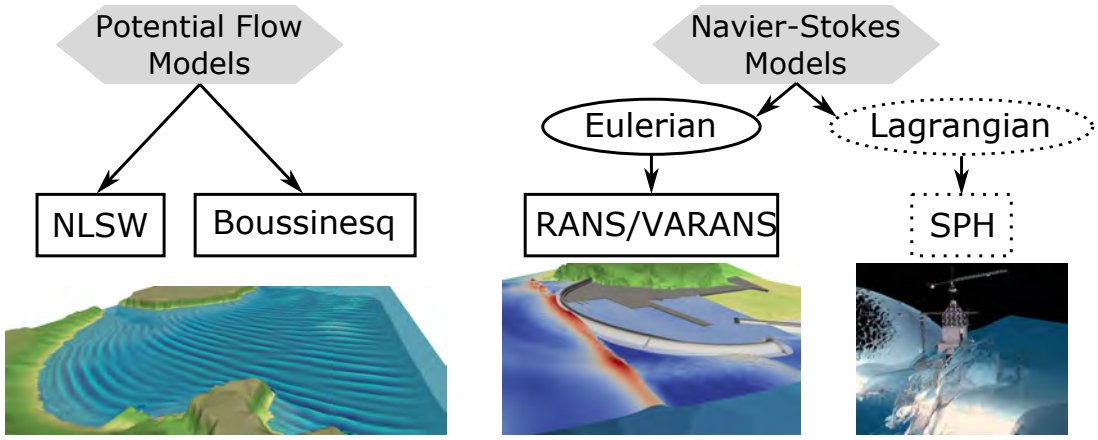

Figure 2.2: Types of numerical models applied in wave-structure interaction. [SPH image taken from www.dual.sphysics.org]

2.2 Numerical approaches for wave-structure interaction processes

Currently three main modelling approaches exist to simulate the interaction between waves and structures, as shown in Fig. 2.2. Ideally, the models need to be able to reproduce as many physics and as close to reality as possible. However, since each technique has its own initial assumptions or simplifications and presents a different degree of development, the field of application of each model is different.

2.2.1 Potential flow models

The potential flow models include, among others, the Boussinesq type (FUNWAVE, Wei and Kirby (1995) or COULWAVE, Lynett and Liu (2002)) and the Nonlinear Shallow Water (NLSW) type (SWASH, Zijlema and Stelling (2011)) models. Both resolve simplified versions of the Navier–Stokes equations averaged in vertical, under the Eulerian (continuous fluid) hypothesis. Being also called 2DH (two-dimensional horizontal plane) models (Liu and Losada, 2002), they are ideal to simulate wave propagation, involving refraction, diffraction and shoaling. Due to their relatively simple equations, they are suitable to simulate large domains (hundreds of metres to kilometres) and time series (sea states of several hours) in very competitive times (a few hours).

The potential flow models present limitations derived from their initial hypotheses,

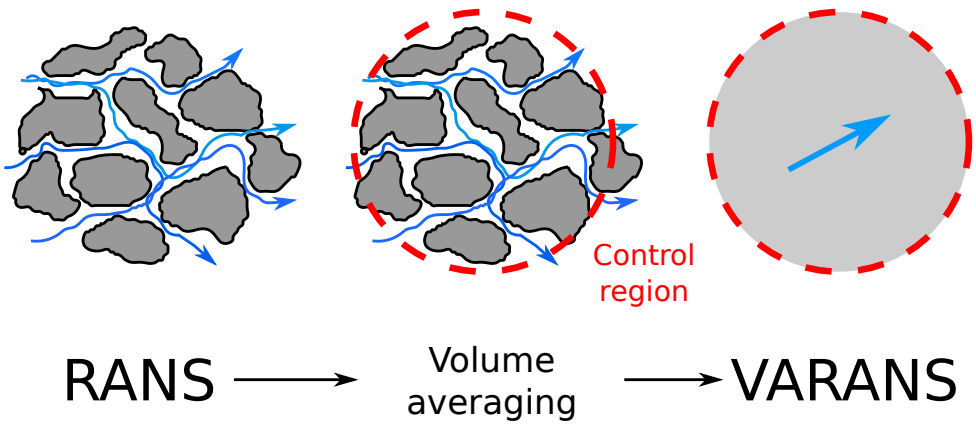

Figure 2.3: Volume averaging technique.

as considering a uniform (or piecewise linear) velocity profile along the water column. Since vertical velocities are not accounted for, it is not possible to fully characterize regions where they are the dominant dynamic, as for example, close to highly reflective structures.

These models are also unable to consider complex free surface configurations as plunging breakers. Moreover, wave breaking cannot be simulated and needs to be triggered, with the associated dissipation being modelled by means of an additional viscosity.

Several techniques exist to treat wave interaction with porous media. For example, a weakly nonlinear Boussinesq model with quadratic drag losses inside a porous layer was introduced in Cruz et al. (1997).

2.2.2 Navier–Stokes models

Models based in the Navier–Stokes equations can be distinguished depending on how the flow is treated. If the fluids are considered continuous in space the models are called Eulerian. On the contrary, if the fluids are considered as an ensemble of different particles, the models are called Lagrangian.

2.2.2.1 Eulerian Navier–Stokes models

The first subtype corresponds to the Reynolds Averaged Navier–Stokes (RANS) models. These highly nonlinear equations consider the fluid as a continuum (Eulerian approach). Moreover, they are capable of reproducing the vertical profiles of pressure and velocity, as they lack simplified initial hypotheses.

The VARANS (Volume Averaged RANS) equations are a modified version of RANS. This technique characterizes the mean flow inside porous media, disregarding the complex porous geometry by considering each medium as homogeneous. The schematic process to obtain the VARANS equations is shown in Fig. 2.3. Later in this section, a number of VARANS formulations is reviewed. Moreover, in Chapter 4, the full mathematical derivation of a new set of VARANS equations is developed.

Historically, the first RANS models were 2DV (two-dimensional vertical plane), for example, COBRAS (Lin (1998)), VOFbreak (Troch and De Rouck (1998)) or **IH2VOF** (Lara et al. (2008), Losada et al. (2008b)). Due to their low computational cost they are adequate for engineering applications. This is the main reason why they are widely used today, even as a design tool for real structures. As a reference **IH2VOF**, later applied in this work, can simulate 1 hour long sea states at real scale (around 750–1000 m long) in less than 24 hours in a regular PC.

The generalization of 3D RANS models is resulting in a revolution, as 3D wave-structure interaction processes can now be accurately captured. Among the most advanced 3D models are: CADMAS-SURF (Kim et al. (2010)), FLOW-3D (Choi et al. (2007)) and IH3VOF (del Jesus et al. (2012)). As an order of magnitude the model developed and applied in this work, **IHFOAM**, is capable of simulating a real domain of 500 x 500 m at a rate of 30 s per day with a HPC (cluster).

RANS models are not yet prepared to simulate domains as large as the potential flow models can, even when the simulations are parallelized. However, they offer finer detail.

2.2.2.2 Lagrangian Navier–Stokes models

The second subtype of Navier–Stokes models is called Smooth Particle Hydrodynamics (SPH). In SPH the Navier–Stokes equations are also solved in 2D or 3D, but in a discrete way (Lagrangian approach; i.e. the movement and interaction between spherical particles reproduces the behaviour of the equations). The best-known models are SPHYSICS (Dalrymple and Rogers, 2006), GPUSPH (Dalrymple et al., 2010) and ISPH (Shao, 2010).

These models are not as developed as the previously introduced types, but they present some noticeable advantages with respect to them. First of all, SPH does not depend on a mesh, eliminating certain kinds of numerical errors. On top of that, the solution

procedure is less complex than for Eulerian models, therefore, these models present much higher performance. As a reference, domains of 50 x 50 m can be simulated at a rate of tenths of seconds per hour.

SPH models are still in an early stage of development. Yet they are able to provide similar standards as that of the RANS models. Since SPH methods were first developed for astronomical applications, such as galaxy collisions, they present an inherent highly compressible behaviour, that needs to be reduced numerically to accurately represent incompressible flows (Becker and Teschner, 2007). Therefore, their main disadvantage is the high diffusivity, which induces an artificial loss in wave height, limiting the size of the simulation domains to avoid numerical wave damping. At the same time, this feature enables the simulation of impulsive loading on wave impacts.

On top of that, the technique to calculate flow through porous media (Shao, 2010) is only developed for two-dimensional domains, hindering the simulation of real coastal structures.

2.2.3 Conclusions

In view of the results, it can be concluded that the RANS equations are the most comprehensive method for simulating the processes involved in wave-structure interaction into detail. The main reasons supporting this choice include that they are able to simulate complex processes as wave braking, they can account for domains large enough to be representative for most real structures and they provide tools to simulate flow inside porous media in 3D.

2.3 RANS modelling

Since it has been concluded that the RANS equations are currently the most suitable method to simulate wave-structure interaction, a full description of them plus how they treat turbulence will be given.

2.3.1 Governing equations

The Reynods Averaged Navier–Stokes (RANS) equations are a set of mathematical expressions that describe the mean behaviour of fluid flows. The equations were formulated by Osborne Reynolds under the assumption that an instantaneous quantity (a) could be decomposed into a time-averaged part ($\bar{a}$) plus a fluctuating part (a') (Reynolds, 1895). Mathematically:

$$a = \bar{a} + a' \tag{2.1}$$

The time-averaging process should be performed for a time time interval long enough to filter out the "random" turbulent fluctuations and short enough to preserve the flow details of interest.

RANS equations can be obtained by differential analysis of the flow. The first equation derives from applying the mass conservation law to a control volume (CV): the change in mass inside the CV is a result of the mass flux across the boundaries. For a 3D cartesian problem:

$$\frac{\partial \rho}{\partial t} + \frac{\partial \rho u}{\partial x} + \frac{\partial \rho v}{\partial y} + \frac{\partial \rho w}{\partial z} = 0 \tag{2.2}$$

where ρ is the density of the fluid and the velocity vector is defined as: $\mathbf{U} = (u, v, w)$.

If the fluid is incompressible, as it can be considered for most fluids at subsonic speeds, the Eq. 2.2 can be simplified because density does not change in time or space. The result, in normal notation and Einstein notation, is as follows:

$$\nabla \cdot \mathbf{U} = 0 \tag{2.3}$$

$$\frac{\partial u_i}{\partial x_i} = 0 \tag{2.4}$$

It is easy to see that applying the Reynolds decomposition ($a = \bar{a} + a'$) to the equations above and time-averaging the equations again yields the same equations, but formulated in terms of the time-averaged velocity.

Differential analysis can also be performed to enforce the conservation of momentum

law. A general analysis yields Cauchy's equation:

$$\frac{\partial \rho u_i}{\partial t} + \frac{\partial \rho u_i u_j}{\partial x_j} = \rho\, g_i + \frac{\partial \sigma_{ij}}{\partial x_j} \tag{2.5}$$

in which the new terms are the acceleration vector due to gravity (g_i) and the stress tensor (σ_{ij}), which is symmetric and has 6 independent components. At this point there are 10 unknowns (3 velocity components and 6 stresses) and the equations are only 4. Either 6 more equations are needed to close the problem, or further assumptions must be taken.

The first step is to separate the stress tensor into the stresses induced by pressure (p) and and by viscosity:

$$\sigma_{ij} = -p\,\delta_{ij} + \tau_{ij} \tag{2.6}$$

so that τ_{ij} is the viscous or deviatoric stress tensor.

Next, since the most common fluids are Newtonian (i.e. the viscous stresses, τ_{ij}, are linearly proportional to the strain, ϵ_{ij}). Mathematically:

$$\tau_{ij} = 2\mu\epsilon_{ij} \tag{2.7}$$

for which μ is the dynamic viscosity of the fluid. Since ϵ_{ij} is defined as:

$$\epsilon_{ij} = \frac{1}{2}\left(\frac{\partial u_i}{\partial x_j} + \frac{\partial u_j}{\partial x_i}\right) \tag{2.8}$$

the final expression of the stress tensor is:

$$\sigma_{ij} = -p\,\delta_{ij} + \mu\left(\frac{\partial u_i}{\partial x_j} + \frac{\partial u_j}{\partial x_i}\right) \tag{2.9}$$

Under the incompressible flow regime it can be proved that the last term can be simplified because the antisymmetric part of the deviatoric stress tensor represents the fluid rotation and cannot generate stress by itself (Kundu and Cohen, 2004). Additionally, if the viscosity is constant along the fluid:

$$\frac{\partial \rho u_i}{\partial t} + \frac{\partial \rho u_i u_j}{\partial x_j} = -\frac{\partial p\delta_{ij}}{\partial x_j} + \rho\, g_i + \mu\frac{\partial}{\partial x_j}\frac{\partial u_i}{\partial x_j} \tag{2.10}$$

Introducing the Reynolds decomposition is not as straightforward as for the continuity

equation, because some cross terms appear. Before going any further the term $u_i u_j$ is going to be averaged:

$$\overline{u_i u_j} = \overline{(\overline{u_i} + u_i')(\overline{u_j} + u_j')} = \overline{\overline{u_i}\,\overline{u_j}} + \overline{\overline{u_i} u_j'} + \overline{u_i' \overline{u_j}} + \overline{u_i' u_j'} = \overline{u_i}\,\overline{u_j} + \overline{u_i' u_j'} \tag{2.11}$$

Note that the time average of u_i' is zero, but the time average of $u_i' u_j'$ cannot be anticipated, as it may be different from zero. With this expression, the final form of the RANS equations can be obtained. Note that the bars over the time-averaged variables have been dropped:

$$\frac{\partial \rho u_i}{\partial t} + \frac{\partial \rho u_i u_j}{\partial x_j} + \frac{\partial \rho \overline{u_i' u_j'}}{\partial x_j} = -\frac{\partial p}{\partial x_i} + \rho\, g_i + \mu \frac{\partial}{\partial x_j}\frac{\partial u_i}{\partial x_j} \tag{2.12}$$

The new term $(\rho \overline{u_i' u_j'})$ generates the so called Reynolds stresses and is usually included with the viscous term:

$$\frac{\partial \rho u_i}{\partial t} + u_j \frac{\partial \rho u_i}{\partial x_j} = -\frac{\partial p}{\partial x_i} + \rho\, g_i + \frac{\partial}{\partial x_j}\left[\mu \frac{\partial u_i}{\partial x_j} - \rho \overline{u_i' u_j'}\right] \tag{2.13}$$

Considering that this term appears when time-averaging the equations and involves the turbulent fluctuations of velocity (u_i'), it can be thought of as a contribution from turbulence. Since the turbulent fluctuations cannot be solved with the RANS equations, this term has to be modelled, using a turbulence model.

A turbulence model is an independent set of differential equations that accounts for the effect of Reynolds stresses, and is the standard way to take turbulence into account in RANS simulations. Some well known turbulence models ($k-\epsilon$ and $k-\omega$ SST) will be reviewed in next subsection.

Since turbulence has a role in dissipating energy, the most usual output of a turbulence model is an additional viscosity:

$$\overline{u_i' u_j'} = -\nu_t \frac{\partial u_i}{\partial x_j} \tag{2.14}$$

The turbulent viscosity (ν_t, also known as eddy viscosity) is then added to the molecular one, resulting in an effective viscosity: $\mu_{\text{eff}} = \mu + \rho\,\nu_t = \mu + \mu_t$.

Other external forces can be also taken into account directly into the equations. The final RANS equations, with a generic force F_i, are as follows:

$$\frac{\partial \rho u_i}{\partial t} + u_j \frac{\partial \rho u_i}{\partial x_j} = -\frac{\partial p}{\partial x_i} + \rho g_i + \frac{\partial}{\partial x_j}\left[\mu_{\text{eff}} \frac{\partial u_i}{\partial x_j}\right] + F_i \tag{2.15}$$

The left hand side of these equations represents the change in momentum of the fluid. The first term, the time derivative, takes the unsteadiness into account, while the second corresponds to the momentum advection by the mean flow. On the right hand side, the pressure gradient appears first, next comes the body forces (e.g. gravity). Then, the stresses account for the viscosity of the fluid and additional turbulent effects. Finally, any other additional forces (e.g. surface tension) can also be included.

2.3.2 Turbulence modelling

Turbulence is not easy to define, although its effects are well known. From Kundu and Cohen (2004), turbulence is a state which the flow shows the following processes/effects entwined:

- **Randomness**: Turbulent flows seem irregular, chaotic and unpredictable.
- **Nonlinearity**: Turbulent flows are highly nonlinear. The nonlinearity serves two purposes:
  - It causes the relevant nonlinearity parameter (e.g. Reynolds number) to exceed a critical value. In unstable flows small perturbations grow spontaneously and frequently equilibrate as finite amplitude disturbances. On further exceeding the stability criteria, the new state can become unstable to more complicated disturbances, and the flow eventually reaches a chaotic state.
  - It results in vortex stretching, a key process by which three-dimensional turbulent flows maintain their vorticity.
- **Diffusivity**: Due to the macroscopic mixing of fluid particles, turbulent flows are characterized by a rapid rate of diffusion of momentum and heat.
- **Vorticity**: Turbulence is characterized by high levels of fluctuating vorticity. The identifiable structures in a turbulent flow are vaguely called eddies. The vortical

structures appear coalescing, dividing, stretching and above all spinning. A characteristic feature of turbulence is the existence of an enormous range of eddy sizes. The larger eddies have a size of order of the width of the region of turbulence flow, and contain most of the energy. The energy is handles down from large to small eddies by nonlinear interactions, until it is dissipated by viscous diffusion in the smallest eddies, whose size is of the order of millimetres.

- **Dissipation**: The vortex stretching mechanism transfers energy and vorticity to increasingly smaller scales, until the gradients become so large that they are smeared out by viscosity. Turbulent flows therefore require a continuous supply of energy to make up for the viscous losses.

As already introduced, the flow regime is controlled by the Reynolds number. This dimensionless is an indicator of the ratio between inertial forces to viscous forces. Mathematically, it is defined as follows:

$$\mathrm{Re} = \frac{\rho U L}{\mu} = \frac{U L}{\nu} \tag{2.16}$$

where U is the modulus of velocity and L is a length scale. For example, in pipe flows the length scale is the diameter of the pipe.

For small Reynolds numbers (viscous forces dominate over the inertial forces), the flow is in the laminar regime, and does not show relevant turbulent effects. In pipe flows this occurs for $\mathrm{Re} < 2100$. For large Reynolds number the inertial forces dominate over the viscous forces and the characteristics listed before appear. In pipe flows this occurs for $\mathrm{Re} > 4000$. A transitional state exists between the laminar and turbulent regimes, showing some of the turbulent effects.

There are several approaches to take turbulence into account in numerical modelling. All of the ones reviewed here involve solving the Navier–Stokes equations.

The most rigorous technique is the Direct Numerical Simulation (DNS). In DNS, the Navier–Stokes equations are solved directly, therefore, extremely small cells are required to account for the correct transfer of energy to the smallest vortex scales. This approach solves the turbulence, but it requires enormous computational resources. Just a little number of applications of DNS for wave dynamics exist in literature, and Lubin et al.

(2003) is the main reference.

A less computationally demanding technique is Large Eddy Simulation (LES), first proposed by Smagorinsky (1963). In LES, the Navier–Stokes equations are filtered to eliminate the smallest scales. This reduces the computational cost of the simulation and yields two different zones: the grid scale, that is represented by the mesh, in which the turbulence is simulated; and the sub-grid scale, below the maximum discretization, in which the effects of turbulence need to be modelled. LES still requires small cells, although not as fine as DNS. This way LES representation of reality is more realistic than alternative approaches such as RANS or DES (Detached Eddy Simulation, introduced next). An example of the application of LES to numerical simulation of waves is Christensen and Deigaard (2001).

Detached Eddy Simulation (DES) is a modification of the RANS approach in which the model switches to a sub-grid scale formulation in regions where the resolution is fine enough to perform a LES. Therefore, it can be thought of as a hybrid LES-RANS type of modelling. The regions where the turbulent length scale is smaller than the one defined are solved applying RANS. The complementary domain, where the turbulence scales are greater are solved using LES.

Finally, in RANS modelling, turbulence is not simulated, but is modelled instead. As noted in the previous methods, the turbulent multi-scale flows require small-scale cells to account for the correct dissipation, therefore, RANS is the computationally cheapest approach. The turbulence effects are accounted for in RANS as an additional eddy viscosity. Applications in literature of RANS to simulate waves are by far the most numerous: Lin and Liu (1999), Troch and De Rouck (1999), Lara et al. (2006b).

A large number of RANS turbulence models exist. The two used in this thesis are reviewed next.

2.3.2.1 The $k-\epsilon$ model

The $k-\epsilon$ model is one of the most widely used in CFD. It was initially developed to deal with free-shear flows under the assumption that the turbulent viscosity (ν_t) is isotropic. This means that it is specially indicated for flows with relatively small pressure gradients. Its performance is also adequate for confined flows where the Reynolds shear

$D_k = \nu + \frac{\nu_t}{\sigma_k}$	$D_\epsilon = \nu + \frac{\nu_t}{\sigma_\epsilon}$
$\beta_k = \frac{\epsilon}{k}$	$\beta_\epsilon = C_{\epsilon_2}\frac{\epsilon}{k}$
$F_k = 2\nu_t \mathbf{S}^2$	$F_\epsilon = 2C_{\epsilon_1}\nu_t\frac{\epsilon}{k}\mathbf{S}^2$

Table 2.1: $k-\epsilon$ intermediate expressions.

stresses prevail. The $k-\epsilon$ model underperforms in cases with large adverse pressure gradients such as unconfined flows, where curved boundary layers exist or flow separation occurs.

In this section the equations will be written following the normal notation instead of using the index notation, for a more compact representation.

$k-\epsilon$ is a two-equation turbulence model, mathematically represented as follows:

$$\frac{\partial k}{\partial t} + \mathbf{u}\cdot\nabla k - \nabla\cdot(D_k\nabla k) + \beta_k k = F_k \tag{2.17}$$

$$\frac{\partial \epsilon}{\partial t} + \mathbf{u}\cdot\nabla \epsilon - \nabla\cdot(D_\epsilon\nabla \epsilon) + \beta_\epsilon \epsilon = F_\epsilon \tag{2.18}$$

where k is the turbulent kinetic energy; it indicates the mean kinetic energy per unit mass linked with the eddies and is physically characterized by the root mean square of the velocity fluctuations.ϵ is the turbulent dissipation rate and represents the rate at which turbulence kinetic energy is converted into thermal internal energy. D_k and D_ϵ are the diffusion coefficients, β_k and β_ϵ are the dissipation (or reaction) coefficients and F_k and F_ϵ are the production (source) terms. All the expressions are provided in Table 2.1. The production terms include the strain rate tensor ($\mathbf{S}$), defined as follows:

$$\mathbf{S} = \left|\frac{\nabla\mathbf{u} + (\nabla\mathbf{u})^t}{2}\right| \tag{2.19}$$

The only new variable is the turbulent kinematic viscosity (ν_t), which introduces the dissipative effects of turbulence in the RANS equations. ν_t is a function of k and ϵ:

$$\nu_t = C_\mu \frac{k^2}{\epsilon} \tag{2.20}$$

The rest of unreferenced terms are constants, which take a value by default as shown in Table 2.2.

σ_k	1	C_μ	0.09
σ_ϵ	1.3	C_{ϵ_1}	1.44
		C_{ϵ_2}	1.92

Table 2.2: $k-\epsilon$ constants.

$D_k = \nu + \sigma_k\,\nu_t$	$D_\omega = \nu + \sigma_\omega\,\nu_t$
$\beta_k = \beta^*\,\omega$	$\beta_\omega = \beta\,\omega$
$F_k = min\left[2\nu_t\left\lvert\frac{\nabla\mathbf{u}+(\nabla\mathbf{u})^t}{2}\right\rvert^2; c_1\beta^* k\,\omega\right]$	$F_\omega = 2\gamma\left\lvert\frac{\nabla\mathbf{u}+(\nabla\mathbf{u})^t}{2}\right\rvert^2$

Table 2.3: $k-\omega$ SST intermediate expressions.

2.3.2.2 The $k-\omega$ SST model

$k-\omega$ SST is a turbulence model introduced by Menter (1994) that combines the best features of $k-\epsilon$ and $k-\omega$ models. The main advantage of $k-\omega$ SST is that it can separate the zones in which $k-\epsilon$ and $k-\omega$ each model yields the best results by applying a set of blending functions. As previously introduced, $k-\epsilon$ does not represent boundary layers and flow separation correctly, hence, $k-\omega$ is used in that areas. In the free flow region $k-\epsilon$ presents a better performance, and it is used instead of $k-\omega$.

As in $k-\epsilon$, $k-\omega$ SST is also a two-equation model, represented mathematically as follows:

$$\frac{\partial k}{\partial t} + \mathbf{u}\cdot\nabla k - \nabla\cdot(D_k\nabla k) + \beta_k\,k = F_k \tag{2.21}$$

$$\frac{\partial \omega}{\partial t} + \mathbf{u}\cdot\nabla \omega - \nabla\cdot(D_\omega\nabla \omega) - (1-F_1)\ \mathrm{CD}_{k\omega} + \beta_\omega\,\omega = F_\omega \tag{2.22}$$

where k is the turbulent kinetic energy and ω is the turbulent frequency scale. D_k and D_ω are the diffusion coefficients, β_k and β_ω are the dissipation coefficients and F_k and F_ω are the production terms. The values of the intermediate expressions are provided in Table 2.3.

The $k-\omega$ SST equations look very much alike the $k-\epsilon$ and $k-\omega$ ones. It is sensible to think that since $k-\omega$ SST is able to represent both turbulence models, and the only common equation is k-equation, this should be the same in the three models. Therefore, by comparing Eq. 2.17 with Eq. 2.21 an expression linking ϵ and ω can be derived:

$$\epsilon = \beta^* k\,\omega \tag{2.23}$$

There is only one major difference that deviates from the regular $k-\epsilon$ or $k-\omega$ expressions and is the cross-diffusion term ($\mathrm{CD}_{k\omega}$, the fourth term in Eq. 2.22). This term is needed to switch smoothly between turbulence models from the boundary layer zones ($k-\omega$) to the free flow region ($k-\epsilon$). In fact, the F_1 function in that term is one of the model blending functions, to be introduced later.

The turbulent kinematic viscosity (ν_t), that is responsible for the energy dissipation due to turbulence in the RANS equations, is now calculated as follows:

$$\nu_t = \frac{a_1\,k}{max\left[a_1\,\omega; F_2\,\sqrt{2}\left|\frac{\nabla\mathbf{u}+(\nabla\mathbf{u})^t}{2}\right|\right]} = min\left[\frac{k}{\omega}; \frac{a_1\,k}{F_2\,\sqrt{2}\left|\frac{\nabla\mathbf{u}+(\nabla\mathbf{u})^t}{2}\right|}\right] \tag{2.24}$$

Two blending functions, ranging from 0 to 1, appear in the previous equations: $F_1 = \tanh(arg_1^4)$ and $F_2 = \tanh(arg_2^2)$. The arguments are calculated as follows:

$$arg_1 = min\left\{min\left[max\left(\frac{\sqrt{k}}{\beta^*\omega\,y}; \frac{500\,\nu}{\omega\,y^2}\right); \frac{4\,\sigma_{\omega_2} k}{\mathrm{CD}_{k\omega}\,y^2}\right]; 10\right\} \tag{2.25}$$

$$\mathrm{CD}_{k\omega} = max\left(\frac{2\,\sigma_{\omega_2}}{\omega}\nabla k\cdot\nabla\omega; 10^{-10}\right) \tag{2.26}$$

$$arg_2 = min\left[max\left(\frac{2\sqrt{k}}{\beta^*\omega\,y}; \frac{500\,\nu}{\omega\,y^2}\right); 100\right] \tag{2.27}$$

where the variable y in the previous equations represents the distance from a given point to the nearest wall. The rest of the terms that have not been introduced are constants that take a value by default, as shown in Table 2.4.

In literature γ_n is generally not taken as a pair of constants (although it results in an easier treatment), but its general expression is used instead:

Constant	Value	
	$n = 1$ $(k - \omega)$	$n = 2$ $(k - \epsilon)$
σ_{k_n}	0.85	1
σ_{ω_n}	0.5	0.856
β_n	0.075	0.0828
γ_n	0.5532	0.4403
β^*	0.09	
a_1	0.31	
c_1	10.0	
κ	0.41	

Table 2.4: $k - \omega$ SST constants.

$$\gamma = \frac{\beta}{\beta^*} - \sigma_\omega \frac{\kappa^2}{\sqrt{\beta^*}} \tag{2.28}$$

Still there are some variables that have not been introduced, namely those without a numeric subscript on their name (i.e. σ_k, σ_ω, β and γ). It is reasonable to think that they must be linked with the four pairs of constants sharing their name but with an additional subscript (n), all gathered in Table 2.4. In fact the blending function F_1 is the one used to calculate their value. For an arbitrary function ψ_n:

$$\psi_n = F_1 \, \psi_1 + (1 - F_1) \, \psi_2 \tag{2.29}$$

As F_1 ranges from 0 ($k - \epsilon$ value, free stream, $y >> 0$) to 1 ($k - \omega$ value, boundary layer, $y \simeq 0$), ψ_n changes its value accordingly.

2.3.3 Conclusions

It can be concluded that RANS modelling is an advanced method to simulate hydrodynamic processes, as it yields the pressure, velocity and turbulent effects. However, the RANS equations cannot describe per se the free surface between two different flows or the flow through porous media. These two factors will be addressed in the next sections.

2.4 Flow through porous media

There is not a universal or unique way to simulate flow through porous media in Navier–Stokes equations. Therefore, the two main methods to treat porous media flow,

the microscopic and macroscopic approaches will be introduced in this section.

The most intuitive way to simulate the flow through a porous material is the microscopic approach, in which each of the elements that form the material is represented in the mesh. This approach has been introduced recently, because sophisticate techniques are required to obtain the geometries to work with, the meshing process is complicated and the simulations are computationally demanding due to the large number of cells involved, even when only simulating several cubic centimetres.

It is impossible to apply such procedures in coastal engineering for several reasons: there is no way to obtain the complete and exact description of the geometry of a real structure, and it is not possible to mesh such a great variation of scales (from blocks to sand grains). Furthermore, it is of greater interest to understand the global effects of porous media in the flow than obtaining an accurate solution in submillimetric scale.

However, research fields as those linked with the oil and gas industry perform pore-scale multiphase flow simulations. An example can be found in Bogdanov et al. (2011), where the real geometry of a porous medium is obtained by reconstructing a stack of microtomographic images taken from a sample with X-rays and neutron tomography. The goal in most of these works is to simulate the action of pumping water at high pressures into fractured rocks that contain oil or gas pockets to determine how they are driven. The complexity lies, then, in simulating the microfluidics, for which representing correctly several physics, as the surface tension and drag forces between the different phases, is vital.

The second procedure is the macroscopic approach. It consists in obtaining the mean behaviour of the flow within the porous media disregarding the internal geometry, by averaging their properties.

2.4.1 Drag forces

Some of the present approaches involve a complex mathematical treatment of the equations. However, flow through porous media has been addressed for more than one hundred years just by considering a set of drag forces generated by the material, that opposes to the flow movement. In this sense, the first expression that defined the flow within a porous medium is as follows:

$$I = A\,\mathbf{u} \tag{2.30}$$

where I is the hydraulic gradient (proportional to the pressure drop) and $\mathbf{u}$ is the velocity of the flow. This very simple equation was derived by Darcy (1856) while he was experimenting with sand filters in Dijon (France). The coefficient A is a parameter to adjust the pressure loss to different materials, and needs to be calibrated. Since flow inside sand is laminar (very low Reynolds number), the dependence of head loss with velocity is linear.

Almost half a century later, during the first years of the XX$^{\text{th}}$ century, scientists discovered that Darcy's law failed to describe faster flows inside other kinds of porous media. Forcheimer (1901) proposed an extension:

$$I = A\,\mathbf{u} + B\,|\mathbf{u}|\,\mathbf{u} \tag{2.31}$$

The mechanics of the hydraulic gradient are the same, but now they depend on a second parameter, B, with which transitional and fully turbulent flows (larger Reynolds number range) could be better described.

Finally, in the early sixties, Polubarinova-Kochina (1962) proposed a third term, to extend the formulation for unsteady flows:

$$I = A\,\mathbf{u} + B\,|\mathbf{u}|\,\mathbf{u} + C\frac{\partial \mathbf{u}}{\partial t} \tag{2.32}$$

The three coefficients (A, B and C) need to be calibrated, because they depend on the physical properties of the porous material and on the flow regime. A large number of formulations exist in literature to characterize the parameters, as for example, Ergun (1952), Engelund (1953), Ward (1964), Burcharth and Andersen (1995), van Gent (1995) or Liu et al. (1999). For example, in Engelund (1953) the friction coefficients are calculated according to the following formulas:

$$A = \alpha\frac{(1-\phi)^3}{\phi^2}\frac{\nu}{D_{50}^2} \tag{2.33a}$$

$$B = \beta\frac{1-\phi}{\phi^3}\frac{1}{D_{50}} \tag{2.33b}$$

where ϕ is the porosity of the material, defined as the volume that may be occupied by the fluid over the total volume; D_{50} is the mean nominal diameter of the porous material; and ν is the flow kinematic viscosity.

The parameters that characterize the linear and nonlinear friction terms are α and β. They are not only dependent on the porous media physical properties but also on the flow regime. Therefore, they need to be calibrated from physical tests. The factor C has proven to be less significant to variations than A or B and a value of $C = 0.34$ is often applied by default (del Jesus, 2011).

There are two cases for which drag forces by themselves are able to represent two phase flows through porous media. The first one when no porosity gradients exist (i.e. the whole domain is a single porous medium, there are no interfaces). The second case, although not mathematically accurate, is for high porosity (0.85–1) materials because the small porosity gradient between the clear flow region ($\phi = 1$) and the porous media induces minor effects that can sometimes be neglected (e.g. canopy flow).

2.4.2 Averaging RANS equations

Drag forces alone fail to fully represent two phase flows through regular porous materials because the fluid is constraint and able to pass only through the voids left by the solid matrix of the material. Therefore, the Navier–Stokes equations need also some modifications (averaging process) to account for low porosity materials (0.35–0.65), that can normally be found in coastal engineering structures.

Two kinds of averaging exist: time-averaging the volume-averaged Navier–Stokes equations (de Lemos and Pedras, 2001) and volume-averaging the Reynolds-Averaged Navier–Stokes equations (Liu et al., 1999). This work is based on the second type.

The first efforts to obtain a set of volume-averaged Reynolds Averaged Navier–Stokes (VARANS) equations originated from the chemical and oil and gas industries during the mid-late sixties. The works by Whitaker (1967) and Slattery (1967) are the foundations of this field, as they established the mathematical fundamentals of volume-averaging.

Volume averaging Navier–Stokes equations allows considering the porous zones as continuous media, characterized by their macroscopic properties only, thus eliminating the need for a detailed description of their complex internal geometry. Hence, this technique

can be thought of as a spatial filter to obtain an average flow behaviour inside porous zones, as already sketched in Fig. 2.3.

The mathematical process is carried out inside pre-defined volumes, known as control volumes. All the insights and definitions regarding the process to obtain a set of VARANS equations will be provided in Section 4.

This procedure introduces new terms in the equations that describe real physics, as the frictional forces, pressure forces and added mass of the individual components of the porous media. Unfortunately, these contributions cannot be solved, and need to be modelled. Closure models for volume-averaged equations have been traditionally addressed by means of drag forces, as that of Eq. 2.32.

Apart from all the different closure models, that have been cited, the VARANS equations can present diverse terms, depending on the assumptions applied by the authors. A brief introduction to several works will be given here, understanding that a thorough comparison will be shown in Section 4.6.

One of the first VARANS works in coastal engineering is Liu et al. (1999). They developed a set of volume-averaged equations that constituted a breakthrough in the field because previous works, as Troch and De Rouck (1998), did not consider the effect of porosity in the equations, just the drag forces. However, during Liu et al. (1999) derivation, porosity is taken out of the differential operators, which is not strictly applicable if spatial gradients of porosity exist. This is a very important effect to take into account for coastal engineering, as the structures can present several layers of different porous materials. Therefore, with these equations the flux across the interfaces of porous media is not solved accurately.

Improvements in Liu et al. (1999) formulation were performed by Hsu and Liu (2002). Since then, this work has been the main reference in coastal engineering for more than 10 years. The principal upgrade of Hsu and Liu (2002) is to introduce a volume-averaged $k-\epsilon$ turbulence model, featuring the closure presented in Nakayama and Kuwahara (1999). Therefore, turbulence enhancement is considered within the porous media. Still, porosities persist outside the differential operators.

The large number of applications of VARANS in coastal engineering published during the last years of the 2000's decade (Lara et al. (2006a), Lara et al. (2008), Losada et al.

(2008b), Guanche et al. (2009)) prove their growing importance. This kind of equations is also known in other fields, as for example in environmental hydraulics. In Nikora et al. (2007a), a set of double-averaged equations was derived. This formulation considers porosity as a field in which space and time gradients may appear, therefore, it is kept inside the differential operators to obtain more realistic results at the interfaces between different materials. Several practical applications were presented in the second part of the paper (Nikora et al., 2007b).

There is also another approach that takes into account the porosity gradients, Hur et al. (2008). In this work of the coastal engineering field, although the Navier–Stokes equations are not volume-averaged per se, the resistance due to the porous materials is represented using drag forces. The momentum equation is also modified to include area and volume fractions to represent the porosity.

One of the most recent works, devoted to perform a rigorous mathematical derivation of the volume-averaged RANS equations is del Jesus et al. (2012). This reference extended the range of applicability of VARANS to a general scenario in which spatial variations of porosity are taken into account. The equations were developed maintaining the porosity inside the differential operators, which is especially relevant for wave-structure simulations in coastal engineering. These equations were implemented in a new model called **IH3VOF**, validated in Lara et al. (2012).

At the same time, works that still relied on representing the effects of porous media with drag forces without accounting for porosity in the equations, were being developed (Vanneste, 2012).

One of the most recent works in literature is Jensen et al. (2014). In it, a new set of VARANS was presented, and were compared against the equations of del Jesus et al. (2012). Dissimilarities were found based on the fact that the volume-averaging math was not applied as intended by Whitaker (1967) and Slattery (1967) in del Jesus et al. (2012). Therefore, Jensen et al. (2014) must be viewed as the most advanced version of the VARANS equations, under their assumptions. Further discussion on this topic can be found in Section 4.6.

Generally, VARANS are applied in finite volume discretization solvers. Larese et al. (2014) recently presented another version of the equations similar to Hur et al. (2008),

applied to finite element discretization. Therefore, apart from the regular equations, the weak form was also derived.

2.4.3 Conclusions

In conclusion, the advantages of VARANS equations are numerous. Since they are derived from the RANS, the solving process yields very detailed solutions, both in time and space. Pressure and velocity fields are obtained cell-wise, even inside the porous zones, so the whole three-dimensional flow structure is solved. Moreover, non-linearity is inherent to the equations, and therefore, all the complex interactions among the different processes are also taken into consideration. Finally, the effects of turbulence within the porous zones can also be easily incorporated with closure models.

However, there is an interesting feature that is not extended yet in coastal engineering: time-varying porosity. Under this assumption, additional terms must appear in the equations to be able to describe important physics as for example sediment transport.

Moreover, in this review it has been detected that the only formulation that accounts for a time-varying porosity (Nikora et al., 2007a) is not based on the rules and theorems established by the pioneers of this field Whitaker (1967) and Slattery (1967).

2.5 Numerical methods in coastal engineering

The analysis of the two previous sections indicates that the numerical modelling of coastal engineering processes involves solving a system of partial differential equations.

In fact, neither the RANS or VARANS equations can be solved under the most general conditions. There are only certain sorts of problems that can be solved in an exact way, but they involve simplifications and assumptions that are not often met in coastal engineering (e.g. laminar flow regime, simple geometries...).

Therefore, the system of equations that govern the physical phenomena needs to be approximated and converted into a system of algebraic equations applying numerical methods. According to Kundu and Cohen (2004), numerical methods always present four types of errors:

- Discretization error: it appears because a continuum (flow) is represented in a dis-

crete fashion (space and time discretization). It is highly dependent on the grid size and shape, and on the numerical schemes, that may yield different orders of magnitude of errors.

- Input data error: it appears because the flow geometry or its properties might not be exactly those of the real case.
- Initial and boundary condition error: it appears because most often the initial and boundary conditions represent the flow behaviour in an approximate way, due to the high complexity of real flows.
- Modelling error: it appears because flows are complex and involve physics that cannot be fully represented by the equations that are solved (e.g. turbulence, free surface...).

The most widely known numerical methods that will be reviewed in this section are finite differences, finite volumes or finite elements. It must be noted that the goal of this study is to give the basic details of each method. For a full mathematical description, the reader is referred to Kundu and Cohen (2004) (finite differences and finite elements) and Jasak (1996) (finite volumes).

2.5.1 Finite differences

Finite differences is the simplest technique to discretize the system of partial differential equations. Discretization is obtained by evaluating the equations at fixed grid points (in time and space). The differential operators are approximated by means of truncated Taylor series.

The finite differences is one of the most widely spread numerical methods in coastal engineering. Its implementation and solving procedure are quite straightforward, therefore, the models that rely in the finite differences method usually show an excellent performance in terms of simulation time.

A large number of finite differences numerical models applied for coastal engineering applications in 2D and 3D can be found in literature: COBRAS (Lin, 1998), VOFbreak (Troch and De Rouck, 1998), **IH2VOF** (Lara et al., 2006a), FLOW-3D (Choi et al., 2007) and CADMAS-SURF (2D version) (Kim et al., 2010).

2.5.2 Finite volumes

Finite volumes is a more advanced technique. The discretization is performed by means of small volumes (finite volumes) that are defined by a centroid and external faces.

In this case the volume integrals that appear in the partial differential equations are converted to surface integrals with the divergence theorem. Therefore, the new terms can be represented as fluxes at the surfaces of each finite volume. The two main advantages of this method are that it is conservative, because a unique flux is calculated at each of the faces that are shared between two finite volumes, and that it can handle unstructured meshes in an easy way.

Finite volumes discretization is yet not so widely applied in coastal engineering. However, some of the most advanced results published to the date have been obtained with finite volume codes: waves2FOAM (Jacobsen, 2011), COMFLOW (Wellens, 2012) and IH3VOF (del Jesus et al., 2012).

2.5.3 Finite elements

Finite elements is also an advanced numerical method that is based on subdividing the whole domain in simpler parts (finite elements). This sophisticate technique uses the connection of the small finite elements to approximate the complex equations over large domains by means of variational methods whose goal is to minimize an error function. Since there are a large amount of elements available, depending on the type selected, the solution can be closer to reality.

The finite elements technique has a peculiarity; it does not act on the general set of governing partial differential equations (called strong form), but the problem has to be reformulated into a so-called weak form. The weak form is a variational form of the problem, in which the equations are integrated against any chosen function. The implications of this procedure is that instead of finding an exact solution everywhere, the problem gets relaxed and the final solution satisfies the strong form on average over the domain. Moreover, it is not a conservative method by default.

Finite element models are not yet commonly applied for coastal engineering applications, but some examples can be found in literature: PFEM (Larese et al., 2008) and

CADMAS-SURF/3D (Okumura and Arikawa, 2014).

2.5.4 Conclusions

This section points out that the most widely used technique in coastal engineering is currently finite differences, however, it is not as advanced as finite volumes or finite elements. Since the most most spread technique among these other two numerical methods is finite volumes it should be regarded as a prospective new standard in the field.

2.6 Free surface modelling

The result of several types of fluids coexisting in a domain is a multiphase system. If the fluids are immiscible a free surface appears at the contact region between each of the pairs. If the fluids can mix, then a free surface is not formed.

The free surface can be defined as a surface of a fluid where a discontinuity occurs (i.e. a sharp change in density and fluid properties), but in which the pressure and shear stresses of both fluids is identical (compatibility condition). Generally in coastal engineering there are only two phases: water and air, but note that sometimes, when the effects of air are negligible it can be substituted by void, a special fluid with zero properties (e.g. density, viscosity...).

Numerically, there are different techniques to track where the free surface is located at any instant, and they vary depending on the type of model. For example, in most potential flow models air is not taken into account, hence free surface is tracked by a function that provides the elevation at each of the nodes of the mesh in a very simple way, linked with the continuity equation. Therefore, if the global flux is positive, the free surface raises, and if the total flux is negative, the free surface falls. The main drawback of this technique is that it is not possible to describe complex free surface configurations in which the free surface is vertical or even steeper (e.g. more than two free surface elevations at the same vertical line, as in plunging breaking waves).

SPH models do not usually consider air either, but there are some examples that start to incorporate this technology (Sun et al., 2012). Generally surface tracking in these Lagrangian models is performed by the identification of the particles that belong to the

interface by means of a kernel function, but more sophisticated options, as applying a level set method (LSM, to be introduced later) can be also applied as in Marrone et al. (2010).

The most advanced free surface tracking techniques have been developed for RANS models. Even though the RANS models follow the Eulerian approach, the first of these techniques is a particle method. The Marker-and Cell (MAC) developed by Harlow and Welch (1965) as an extension of the Particle in Cell (PIC) method and uses massless particles to track the position of the interface. Since the tracers have no mass or inertia, they move following the instantaneous streamlines at every time step, therefore, it is mostly suitable for flow regimes deriving from potential flows.

One of the most versatile methods to track the free surface location is the Volume Of Fluid (VOF) technique (Hirt and Nichols, 1981). In VOF, each phase is described by an indicator function (ϕ), that represents the fraction of the volume of a cell that is occupied by a given fluid. If $\phi = 1$ means that the cell is full of the fluid of interest, while if $\phi = 0$ indicates that the cell does not contain any of that fluid. A different VOF function must be defined for each type of fluid, although when working with two phases only, the system can be represented with a single indicator function ϕ, because the other one would be $1 - \phi$.

The main advantage of the VOF technique is that it is a simple approach that allows complex free surface configurations to be represented very easily and without requiring mesh motion. A minor disadvantage is that it becomes less effective as surface tension effects increase.

The movement of the phases is determined by a simple advection equation:

$$\frac{\partial \phi}{\partial t} + \nabla \cdot (\phi \mathbf{u}) = 0 \tag{2.34}$$

where $\mathbf{u}$ is the velocity of the fluid. However, some restrictions apply to the solution of this equation, so that the final results are physical. First, the output must be bounded between 0 and 1. Second, the interface (zone where $0 < \phi < 1$) must be kept as thin as possible, because free surface in real liquids is a sharp discontinuity. There are several options to fulfil the second requirement, because Eq. 2.34 is diffusive. One is adding a counter-diffusive term to avoid the smearing of the interface, another one is reconstructing

the free surface. Both of them have pros and cons.

On the one hand, the counter-diffusion term can be a compressive force that acts on the interface. The sharp transition between the fluids cannot be readily identified, because it is not reconstructed (thus saving computational cost), but it can be assimilated as the isosurface where $\phi = 0.5$. Therefore, in this approach the transition between phases is not sharp, but relatively smooth. Since the indicator function is only advected, this technique does not increase the computational cost as the next method. Moreover, having a smooth variation involves a continuous pressure distribution that does not produce pressure spikes.

On the other hand, the free surface can be reconstructed, so that the transition is kept perfectly sharp. The simplest reconstruction algorithm is the simple line interface calculation (SLIC) (Noh and Woodward, 1976). In SLIC the interface inside a cell can either be vertical or horizontal. In Hirt and Nichols (1981) some enhancements were presented, so that the orientation of the horizontal and vertical lines were also taken into account. For that purpose, the derivatives of the ϕ field are analyzed.

More sophisticated advances include Kothe et al. (1999), in which a more general procedure for interface reconstruction was developed to work with unstructured meshes, under the assumption that the free surface is a plane inside each cell. The orientation of the plane is calculated according to the derivatives of the ϕ field, and the location of the plane inside the cell depends on its ϕ value. This method yields very accurate solutions (second order accuracy). The fluxes can be calculated independently for each fluid, as the intersection of the free surface plane with the cell faces is available. However, having an internal surface inside the domain involves applying an internal boundary condition that makes the pressure and velocity of the water and air phases compatible. This process often yields false peaks of pressure that need to be filter when postprocessing. It must be noted that this technique increases the computational cost, because the reconstruction process takes additional time.

Finally, there is still room for developments in this field. One of the most recent references that opens new perspectives and seems a promising approach is the geometrical VOF function (Maric et al., 2013). This work includes a new parallelized algorithm that supports arbitrary unstructured meshes and dynamic local Adaptive Mesh Refinement (AMR), making it especially suitable for flow domains of arbitrary geometrical complexity.

The third approach is level set method (LSM) developed in Sussman et al. (1994) and Sussman et al. (1999)). LSM is based in defining a function (ϕ) that represents the arbitrary free surface position by means of a smooth function. Most often this function is a field with the signed distance from each cell to the free surface (e.g. positive in the water phase and negative in the air phase), therefore, the free surface is represented as the zero level (value) of that function. The movement of the level set function is calculated by solving the same simple advection equation shown before (Eq. 2.34).

The clearest advantages of LSM is that it avoids numerical diffusion to some extent, because it advects a smooth field instead of a field with large gradients (e.g. 1000 factor between density of water and air). At the same time this method does not present any restriction to the movement or shape of the free surface, allowing different portions to detach or coalesce as required.

There is also another technique that combines the best features from VOF and LSM, presented in Sussman and Puckett (2000).

The previous procedures do not require remeshing for the advection of free surface. There are specific implementations that apply in the case in which free surface is tracked with mesh deformation or even remeshing. One of the most advanced ones is presented in Mindel et al. (2007), in which an arbitrary Lagrangian-Eulerian (ALE) technique is applied to obtain a sharp free surface that drives mesh changes as it evolves. In ALE, the nodes of the mesh can either move with the fluid (as if they were Lagrangian) or be fixed, as in regular Eulerian applications.

2.7 Wave generation

Waves are the main driving dynamics in most coastal engineering cases. Therefore, wave generation is a key element of numerical modelling that lays the foundations for realistic final results.

If the starting point of a simulation is not accurate, all the errors introduced in this initial step will propagate until the end. Should this occur, the results may be completely different, as wave interaction can exhibit very important second order effects. Moreover, several processes that affect waves, mainly shoaling and breaking, are highly influenced

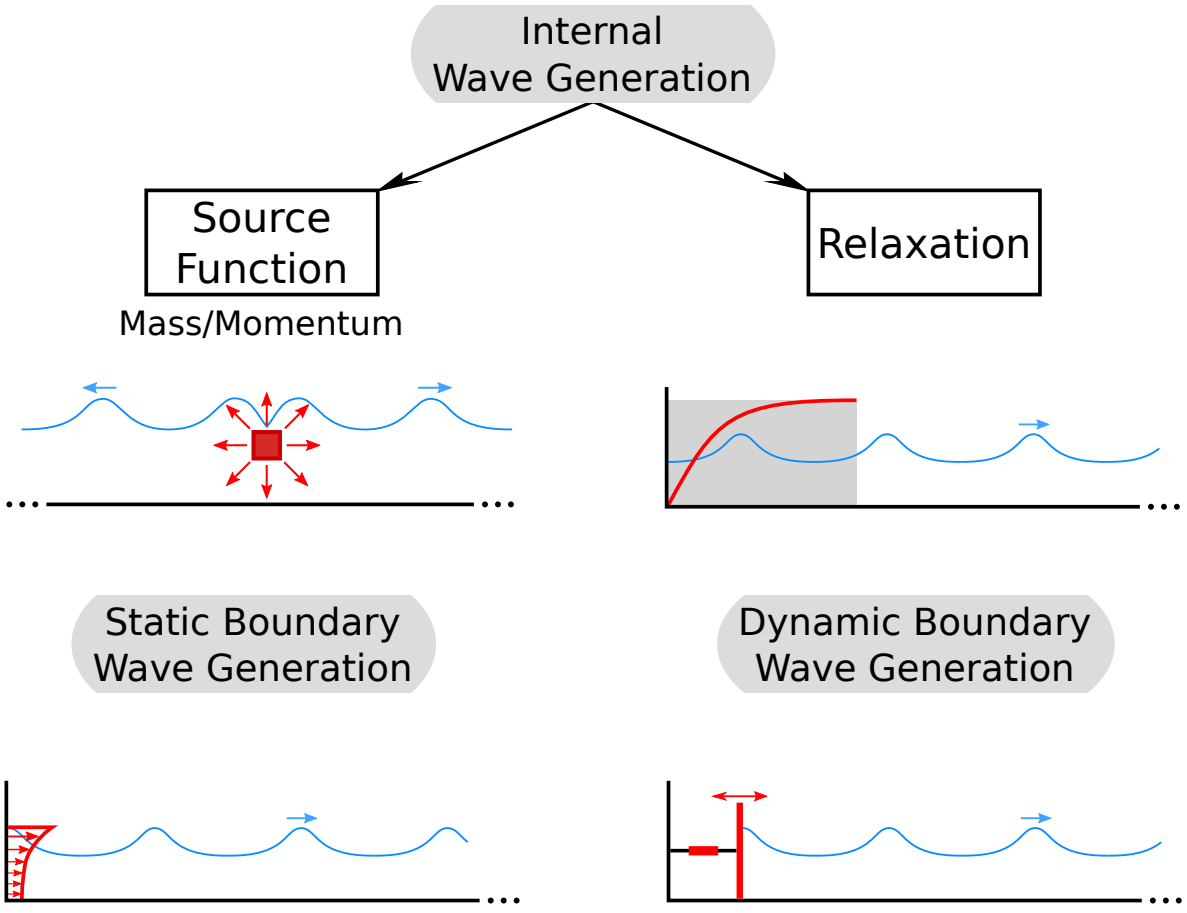

Figure 2.4: Wave generation methods for numerical models.

by the shape and height of waves. If these are not accurately replicated, chances are that the simulation will end up nowhere close to reality.

There are 3 main approaches to generate waves in numerical models: internal wave generation, static boundary wave generation (Dirichlet-type) and moving boundary wave generation. As sketched in Fig. 2.4.

2.7.1 Internal wave generation

The first wave generation procedure is internal wave generation. As its name indicates, the oscillatory flow is generated within a region defined inside the numerical domain. There are two different techniques to generate waves internally, as noted in Fig. 2.4.

The first of them involves a source function, either acting on the mass or momentum equations. A source function is an additional term in the equations, that is capable of pumping water in or out by creating or destroying mass (mass source function, Lin and

Liu (1999)) or by generating inwards or outwards velocities (momentum source functions, Choi and Yoon (2009)) according to mathematical expressions that can be designed to match certain wave conditions.

As an example, the mass source function by Lin and Liu (1999) gets included in the continuity equation:

$$\frac{\partial u_i}{\partial x_i} = S(t) \tag{2.35}$$

in which $S(t)$ is the time dependent source function.

The region over which the source function is defined (Ω) needs to be small compared to the wavelength of the target waves. Under the assumption that mass flow rate, positive or negative, introduced by the source function contributes to the generation of crests and troughs, respectively, the expression of the source function can be linked to the time series of free surface elevation. The equation for a two-dimensional case is:

$$\int_0^t \int_\Omega S(t)\, d\Omega\, dt = 2 \int_0^t C\, \eta(t)\, dt \tag{2.36}$$

where C is the celerity of the target wave; and $\eta(t)$ is the time series of free surface elevation. The factor 2 in Eq. 2.36 accounts for the fact that as water is pumped in all directions, the resulting waves are also radiated in the two directions, as in Fig. 2.4.

Finally, the expression of the source function for a linear wave is very simple:

$$S(t) = \frac{C\, H}{A} \cos\left(-\omega\, t + \psi\right) \tag{2.37}$$

The new variables introduced are H, the wave height; A, the area of the source function region; ω, the wave angular frequency; and ψ, the phase shift.

Wave generation with source functions is closely linked to numerical dissipation zones (also known as sponge layers, to be defined later), since those waves that are propagating away from the region of interest need to be absorbed. Otherwise, they would reach the end of the domain and reflect back, contaminating the results. Sponge layers serve for that purpose.

A mass or momentum source function does not add significant computational cost to the model per se. However, the need to enlarge the domain to include a sponge layer

increases the total number of cells and produces that undesirable effect.

The second option for internal wave generation is a relaxation zone (Mayer et al., 1998). In this approach, a region adjacent to a boundary is selected and a blending function (β) ranging from 0 to 1 is defined inside. The $\beta = 0$ value takes place at the boundary and the value $\beta = 1$ occurs at the interface between the relaxation zone and the regular domain, as shown in red in Fig. 2.4. This function needs to vary smoothly to avoid discontinuities and it usually presents a very slow decay first near 1 and more abrupt closer to the 0. The blending function is applied each time step to combine the theoretical solution and the one calculated by the numerical model. For a particular field F:

$$F = \beta\, F_{\text{calc}} + (1 - \beta) F_{\text{theo}} \tag{2.38}$$

In wave generation the fields (F) that are modified inside the relaxation zones are, at least, pressure, velocity and the indicator function for free surface elevation.

A relaxation zone serves also as a wave absorption region, as it will be presented in next section.

Examples of internal wave generation exist for RANS models (2D: Lin and Liu (1999), Jacobsen et al. (2012); 3D: Ha et al. (2013)), but also for potential flow models (Wei et al. (1999), Schäffer and Sørensen (2006)) and very recently for SPH models (Liu et al. (2015)).

2.7.2 Static boundary wave generation

The second type is static boundary wave generation. For this approach, waves are produced at a fixed boundary by means of special Dirichlet-type (i.e. fixed value) boundary conditions, following any wave theory formulation. Some of the large number of wave theories that can be found in literature are gathered in Section 5.3.

Wave theories provide mathematical expressions for free surface elevation, particle velocity or pressure along the water column. Hence, the boundary conditions apply those theoretical values to the flow. Generally, only velocities and free surface elevation are fixed, allowing pressure to be calculated. Otherwise, the mathematical problem would be overspecified and could present stability problems.

For example, the Stokes I wave theory provides the following expressions for free surface elevation (η) and the horizontal and vertical velocity components (u and v):

$$\eta = \frac{H}{2}\cos(kx - \omega t + \psi) \tag{2.39}$$

$$u = \frac{H}{2}\omega\frac{\cosh(kz)}{\sinh(kh)}\cos(kx - \omega t + \psi) \tag{2.40a}$$

$$w = \frac{H}{2}\omega\frac{\sinh(kz)}{\sinh(kh)}\sin(kx - \omega t + \psi) \tag{2.40b}$$

where H is the wave height; k is the wave number; x and z are the horizontal and vertical coordinates of the boundary; ω is the angular frequency; and ψ is the phase shift.

The principal advantage of static boundary wave generation is that all the processes are handled at a boundary. Therefore, it does not increase the computational cost of the model. Moreover, active wave absorption can also be applied simultaneously at the same boundary. Hence, dissipation zones are not needed, minimizing the domain size with respect to internal wave generation and absorption methods.

There is also a drawback linked to the fact that there is an imbalance between the velocities below wave crests and wave troughs. When generating a wave crest, water is introduced from to bottom to the crest ($\eta > 0$), while when a wave trough is generated, water is only taken out from the bottom to the trough ($\eta < 0$). This causes an excess of water that is introduced each wave period. If no corrections are introduced, the mean water level will increase as the simulation progresses. Active wave absorption, introduced in next section, is the solution. Consequently, static wave generation must be linked with active wave absorption.

The most remarkable application examples of static wave generation for RANS models include Troch and De Rouck (1999), Torres-Freyermuth et al. (2010) and Lara et al. (2011) in 2D and del Jesus et al. (2012) in 3D. Static boundary wave generation can also be applied in potential flow models (Wei and Kirby (1995)), but not in SPH models.

2.7.3 Dynamic boundary wave generation

The third procedure results from replicating the exact wave generation mechanisms of the experimental facilities (i.e. the actual wave-making machines). This involves a moving element driving the generation and absorption of water waves.

There are two main approaches for dynamic wave generation: virtual forces and mesh movement.

The first procedure is a variation of immersed boundary method (Mittal and Iaccarino, 2005). It enables the simulation of an obstacle of arbitrary shape moving inside the numerical domain, without modifying the mesh. This method involves defining an openness function, as in the cutting cell method, first introduced by Clarke et al. (1986). The openness function (θ) represents the fraction of open volume (i.e. not occupied by the obstacle) in a cell/face. It acts as a tracer to define the cells or faces inside ($\theta = 0$) and outside ($\theta = 1$) the obstacle. Then, a direct forcing method (Mohd-Yusof (1997), Mittal and Iaccarino (2005)) applies an explicit virtual force (momentum source) in the cells intercepted by the obstacle boundaries ($0 < \theta < 1$), to obtain a fixed velocity, equal to the velocity of the obstacle. This process can be regarded as applying a virtual boundary condition internal to the domain. The reader is referred to Lara et al. (2011) for further reference.

The second technique involves several requirements, as follows:

- A specific boundary condition to prescribe the displacement on the generation boundary (e.g. displacement of the piston-type wavemaker or tilting of the flap wavemaker).

- Dynamic mesh capabilities to handle the actual movement of the boundary, most often by deforming the mesh.

- A boundary condition to impose the velocity of the moving boundary to the flow, enforcing the dynamic non-slip boundary condition.

The virtual force method presents a great advantage over the mesh movement procedure, as solving the mesh deformation significantly increases the computational cost. This results in an average increment in simulation times of over 30%.

In both cases a time series of displacement needs to be provided, and the virtual force method requires the velocity time series as well. For example, the Stokes I displacement of a piston-type wavemaker (X), as derived in Hughes (1993), is:

$$X = \frac{S_0}{2} \cos\left(-\omega t + \phi\right) \tag{2.41}$$

where S_0 is the stroke of the paddle, that can be obtained with the expression for the height-to-stroke ratio:

$$\frac{H}{S_0} = \frac{4 \sinh^2 k\,h}{\sinh 2k\,h + 2k\,h} \tag{2.42}$$

Moving-boundary wave generation is an advantageous procedure for meshless methods, as SPH, because no mesh deformation is involved. Two-dimensional (Mahmoudi et al. (2014)) and three-dimensional (Farahani et al. (2014), applying a single paddle, though) examples can be found in literature. In fact, this wave generation procedure used to be the only one available for SPH models until Liu et al. (2015) adapted an internal wave generation procedure.

Moving-boundary wave generation is not so common yet for Eulerian potential flow and RANS models. Nevertheless, this procedure may prove important for cases very sensitive to the change in the length of the domain due to the movement of the paddles, as when reproducing seiches or harbour resonance. Applications have been published for potential flow models (Grilli et al. (2002), Orszaghova et al. (2012)) and for RANS models as well (2D: Lara et al. (2011); 3D: Kiku et al. (2014)).

2.7.4 Conclusions

In view of the pros and cons of each wave generation method, some conclusions can be extracted. In principle, the internal wave generation should be avoided because it noticeably increases the computational cost of numerical models (by enlarging the domain) and offer fewer advantages compared to static boundary wave generation. Nevertheless, internal generation is still perfectly valid.

Moving wave generation may also prove advantageous to replicate better the dynamics of physical wave flumes and basins, with additional computational cost due to dynamic

meshing techniques.

2.8 Wave absorption

In this section some of the most relevant contributions to the field of wave absorption are presented. Two main approaches are distinguished: passive and active absorption. The first type does not adapt to different wave conditions, while the second one responds to a feedback from the flow.

The reader will find that most of the absorption methods are reviewed from an experimental point of view. The main reason is because the first efforts in this discipline were applied to physical wave flumes and basins, as numerical models were still being developed. Another factor to take into account is that implementing these active absorption methods for moving boundaries would be straightforward. Moreover, implementing these procedures for static boundaries is also possible, in a similar way as for wave generation.

2.8.1 Passive wave absorption

The first attempts to dissipate waves in experimental facilities involved building dissipative beaches with gentle slopes (1:10 and milder), generally made of gravel or stones. Wave breaking dissipates most of the energy of the incident waves, but long waves are still reflected on them. Additional disadvantages include the large space occupied by the dissipative structure, that cannot be used to perform the tests. The work by Ouellet and Datta (1986) indicates that dissipative beaches were the most popular approach at that time.

From the numerical point of view, it is possible to replicate this experimental setup, to include the dissipative beaches, either as impervious or porous slopes. However, simulating these zones, which most often are located outside the zone of interest, increases the domain and number of cells of the model.

Other physical devices that function based in a similar principle to that of dissipative beaches are mesh screens. In this method, arrays of porous materials, generally perforated plates, are mounted near the wave tank walls to dissipate the energy by splitting the flow as the waves pass through them. The effectiveness of this system depends on several factors,

including the type of plates, the size of the holes (i.e. porosity), the layout, separation, gradations... Pioneering works (Goda and Ippen, 1963) indicated a higher dependency in terms of performance for the separation of the plates than for the total number, under deep water conditions. They also recommended an effective length of the porous baffles of at least one wavelength. Tests for other high-porosity materials, as aluminium wool or polyurethane foam were introduced in Keulegan (1972).

Jamieson and Mansard (1987) performed a large number of tests to derive the general rules to dissipate a wide range of wave conditions. Their wave absorber was made of wire mesh screens of different porosity. The goal was to minimize the reflections and the length of the absorber at the same time. The most important conclusions are listed next:

- The frontal area of the supporting framework should be as small as possible.
- High porosity screens work best for dissipating high steepness waves. Low porosity screens work best for low steepness waves
- The porosity of the screens should decrease towards the wall.
- The screens should be located approximately at the nodes of the resulting partial standing waves.
- The optimum absorber length varies between 0.35 and 1.0 times the wavelength.

Similarly to what occurs with dissipative beaches, the mesh screen absorbers are also efficient when absorbing gravity waves, but not quite for long waves, that may pass through them with minor energy loss.

The design of mesh screen absorbers has not only been performed from the theoretical and experimental point of view, but also using numerical models. For example, Klinghammer et al. (2012) applied RANS numerical modelling to characterize the dissipative capabilities of a number of perforated screens. Different layouts and configurations were then tested to obtain an optimal solution. The final design was later constructed and is currently being used in the Cantabria Coastal and Ocean Basin (CCOB).

This absorption procedure is not generally addressed in numerical modelling by replicating each of the mesh screens individually, as in Klinghammer et al. (2012). Instead, dissipation zones, also known as relaxation zones or sponge layers, are defined as regions

of the domain in which smooth-varying functions act on the fluid by removing momentum and/or mass. Practical applications of relaxation zones for RANS codes can be found in Lin and Liu (1999), Lara et al. (2006a) or Jacobsen et al. (2012) and for Boussinesq-type models in Wei and Kirby (1995) or Losada et al. (2008a).

The first efforts in wave damping regions were formulated modifying the momentum equation. Two main options exist to add momentum sink terms, either in the form of drag forces or as an additional viscosity on the fluid. Therefore, they can be assimilated as having a continuous porous media with a varying porosity dependent on the location inside the mesh. This type of dissipation regions is known to produce an increment of the mean water level inside it (Mendez et al., 2001), reducing its performance significantly.

More recent formulations, as Jacobsen et al. (2012), implemented in OpenFOAM® and based in Mayer et al. (1998), deal with this issue by modifying the mass conservation equation or the fluid indicator function as well. The relaxation technique relies on a blending function, as already shown in Eq. 2.38, to combine the theoretical values of the fields and those calculated by the model. Since the theoretical value always presents the same water depth, an increase in water level does no longer appear.

Numerical dissipation zones present several drawbacks. First, as for dissipative beaches, they increase the computational domain because the solution inside them is not physical. In fact, they need to be around one wave length to be efficient (Wei and Kirby, 1995), which is quite inconvenient for applications at prototype scale. A way to minimize this effect is applying a growing gradation in cell size towards the end of the dissipation zone, but still the number of additional cells with respect to other techniques is significantly higher. Moreover, Mayer et al. (1998) formulation involves multiplying the quantities inside the dissipation region by a factor smaller than 1 each time step, therefore, precision errors can be significant as time advances, especially when time steps are very small (i.e. more frequent multiplications).

2.8.2 2D active wave absorption

2.8.2.1 Introduction

According to Schäffer and Klopman (2000) there are six main authors who worked out different 2D active wave absorption methods in the early years. Most of them were

developed for experimental facilities, but can be easily transposed to numerical models. Further development has also been performed from year 2000 until today. As a result, more recent references will also be analysed.

The pioneering work in this field was carried out by Milgram (1970), who identified four criteria for the adequate design of an experimental active absorption system, as follows:

1 The system has to be stable.

2 Drift of the wave paddle must be prevented.

3 The frequency domain transfer function of the actual feedback filter has to be less than the theoretical one for high frequencies to prevent high-frequency noise.

4 The reflection coefficient should be less than one for all frequencies in order to prevent high frequency amplification of the superharmonics in nonlinear waves. (Experimental result).

His system featured a hinged wavemaker with a wave gauge near the paddle, and a recursive analog filter derived from linear wave theory, including evanescent modes. The filter was then approximated by a digital one, minimizing the mean square error over a certain frequency range.

The next remarkable work is Salter (1981) and Salter (1984). He used the force acting on the wave paddle as the hydrodynamic feedback, and an analog recursive filter to convert it into the wavemaker correction velocity. The main advantage is that since force is an integral quantity, it is less sensitive to local disturbances or cross-waves and it incorporates nonlinear effects to some extent.

Then, Bullock and Murton (1989) developed an active absorption system for a wedge-type wavemaker. The feedback was provided by a wave gauge which moved back and forth with the front part of the wedge, but always at the same height. Once again the correction is calculated by means of an analog recursive filter.

One year later, Hirakuchi et al. (1990) applied the same method of locating a wave gauge mounted on a piston-type wavemaker. An analog circuit controlled the velocity correction. They accounted for the evanescent modes by including the paddle acceleration in the formulation.

Several years later, Christensen and Frigaard (1994) developed a theory that relies on two wave gauges located at some distance from the wavemaker. One of them would be sufficient, but two are necessary to obtain stability. By manipulating the signals of both gauges the reflected waves are isolated and the absorption signal is obtained by means of a finite impulse response digital filter.

To conclude with the 2D absorption systems analysed in the aforementioned paper, there is another one by Schäffer et al. (1994) in which the wave gauge was also mounted on the paddle front. Both piston- and hinged-type wavemakers were supported, including the evanescent modes. The system used a recursive digital filter fitted to match the target transfer function for a wide range of frequencies. The name given was AWACS (Active Wave Absorption Control System) and it was developed for the Danish Hydraulics Institute (DHI).

Three years after writing the review paper, Schäffer and Jakobsen (2003) improved the system to allow simultaneous wave generation and absorption in a more accurate way. Since the transfer function is approximated, it will affect both the generation and absorption signals. However, the wave generation part should remain unaffected by these imperfections. This is achieved by splitting the paddle position into two independent signals: generation and absorption.

Finally the most recent works, Luppes et al. (2010) and Wellens (2012), take another approach, based on the Sommerfeld condition. This leads to a system that is mainly applicable in numerical models, as it takes the pressure and velocities and their gradients all over the water column as inputs.

The most relevant methods of 2D wave absorption are reviewed in detail next, with a specific order to show the improvements of each technique.

2.8.2.2 Schäffer and Klopman (2000)

First, the method proposed in Schäffer and Klopman (2000) is based on linear shallow water wave theory and is the easiest to understand. It is also the simplest to implement because the adjustment of the digital filter is immediate and it is very efficient at the same time.

It is convenient to use shallow water wave linear theory because the velocity along the

water column height is constant, matching the generation with a piston-type wavemaker. This also makes the evanescent modes to cancel out because the paddle motion makes an exact fit to the velocity profile of the desired progressive wave component.

From this wave theory two key expressions can be derived, as seen in Eq. 2.43 and 2.45.

$$U\,h = c\,\eta \tag{2.43}$$

where h is the water depth, η is the free surface elevation measured with respect to the still water level and c is the wave celerity, which in general form is:

$$c = \sqrt{g\,h}\,\sqrt{\frac{\tanh(k\,h)}{k\,h}}. \tag{2.44}$$

but taking into account the shallow water wave theory it can be applied as:

$$c = \sqrt{g\,h} \tag{2.45}$$

In order to cancel out the waves incident to a wavemaker, the paddle must generate a velocity equal to the incident one but in the opposite direction. Arranging both equations so that the free surface corresponds to the reflected one (the one to cancel out) leads to the active wave absorption expression presented in Eq. 2.46:

$$U(t) = -\sqrt{\frac{g}{h}}\,\eta_R(t) \tag{2.46}$$

where the reflected wave height ($\eta_R(t)$) is calculated by subtracting the measured elevation in the gauge from the target one according to the expected reflection-free wave generation: $\eta_R = \eta_M - \eta_T$. Both the reflected wave height ($\eta_R(t)$) and the correction velocity (U) are dependent of time.

Now it will be shown that this result can also be obtained with the application of a digital filter. The first step is to convert Eq. 2.46 into the movement of the wavemaker. This is done by integrating both parts, since wavemaker velocity is the derivative of its displacement. The result is Eq. 2.47.

$$X(t) = -\sqrt{\frac{g}{h}} \int_{-\infty}^{t} \eta_R(\tau)\, d\tau \tag{2.47}$$

Small deviations from a zero mean of $\eta_R(t)$ will contribute to a slow positive drift of the paddle position, leading eventually to saturation. This means that the paddle will end up in the position of maximum stroke, preventing any further movement. The solution is to force the paddle to go back to the zero position in a short time scale that avoids saturation, but long enough to allow some degree of absorption for low frequencies.

This transformation may be viewed as a filtering process. Therefore, there is a need to shift between the time domain and the frequency domain. This is performed by means of a Fourier transform, as follows:

$$\begin{aligned} X(t) &\overset{Fourier\,Transform}{\Longleftrightarrow} X_a(\omega) \\ \eta(t) &\overset{Fourier\,Transform}{\Longleftrightarrow} A(\omega) \end{aligned} \tag{2.48}$$

where $X(t)$ is the paddle position, $\eta(t)$ is the free surface elevation at the wave paddle and $X_a(\omega)$ and $A(\omega)$ are their equivalent complex amplitudes. ω denotes angular frequency.

The relation between $X_a(\omega)$ and $A(\omega)$ may generally be written as:

$$X_a = -F\, A \tag{2.49}$$

in which F represents a complex transfer function. By converting Eq. 2.47 to the frequency domain and identifying it with the terms in Eq. 2.49 the value of F can be obtained for this case, yielding Eq. 2.50.

$$F = \sqrt{\frac{g}{h}}\, \frac{1}{i\,\omega} \tag{2.50}$$

Analog filters can be designed from Eq. 2.50, by expressing it in terms of the complex frequency $s = i\,\omega$. Nowadays the development of electronics has made very simple to create electronic control devices that perform digital filtering. As a result, it is easier to to develop a digital formulation by fitting the digital filter to the analogic expression. In general, the transfer function is a rational function in terms of Z^{-1} with real coefficients (a_n, b_n), as follows:

$$F = \frac{\sum_{k=0}^{M} a_k \, Z^{-k}}{1 - \sum_{k=1}^{N} b_k \, Z^{-k}} \tag{2.51}$$

Eq. 2.51 is general, and covers both recursive and nonrecursive physically realizable digital filters, explained in the last part of this section.

The first step towards the fitting of the digital filter is to apply the Eq. 2.52, which is an approximation given by bilinear transformations, as seen in Section 11.6 of Antoniou (2006) book:

$$s = i\,\omega = \frac{2}{\Delta t} \frac{1 - Z^{-1}}{1 + Z^{-1}} \tag{2.52}$$

where $Z = e^{i\,\omega\,\Delta t}$ and$\Delta\ t$ is the sampling interval. If this equation is substituted into Eq. 2.50 it yields the expression which can be mapped directly to the digital filter.

$$F = \sqrt{\frac{g}{h}} \frac{\Delta t}{2} \frac{1 + Z^{-1}}{1 - Z^{-1}} \tag{2.53}$$

Identifying Eq. 2.51 and 2.53, and making $M = N = 1$ leads to the coefficients of the digital filter:

$$a_0 = a_1 = \sqrt{\frac{g}{h}} \frac{\Delta t}{2}, \; b_1 = 1 \tag{2.54}$$

Translating the analogic formulation to the digital one is performed for simplicity, as it is preferable to fit Eq. 2.51 with the target transfer function directly. Furthermore, as active absorption theory for dispersive waves starts in the frequency domain, the procedure shown above is suitable for a more general approach.

Finally some characteristics of digital filters are given:

Recursive filters:

- Also called infinite impulse response filters.
- Not all b-coefficients are equal to 0.
- They can be more compact than nonrecursive filters (smaller M and N).
- Stability is an issue that has to be taken into account upon design.

Nonrecursive filters:

- Also called finite impulse response filters.
- All b-coefficients are equal to 0.
- They require a large number of filter weight (large M).
- They have a time delay equal to half of the filter width. Hence, the wave gauge has to be placed far enough from the wavemaker for the system to react.
- Stability is not a problem. There are no poles in the transfer function.

As a general rule the sample rate with which the wavemaker is controlled has to be quite high compared to the wave frequencies to absorb in order to have a smooth control signal.

2.8.2.3 Schäffer and Jakobsen (2003)

Schäffer and Jakobsen (2003) presented a more general case with an enhanced method for generating and absorbing waves at the same time. Their method also allows extending the formulation to non-linear wave generation.

To shift between the time domain and the frequency domain the same method of section 2.8.2.2 is applied (Eq. 2.48). This time the only difference is in the nomenclature. Variable η (and therefore A) carries the following subscripts:

- "I" for the target, progressive, incident waves.
- "0" for waves measured right at the wavemaker front.
- "R" for progressive reflected waves.
- "RR" for progressive re-reflected waves.

Using linear wavemaker theory and assuming full re-reflection on the wave paddle, the equations that control the problem are:

$$A_I = i\, c_0\, X_a + A_{RR} \tag{2.55a}$$

$$A_0 = i\, X_a \sum_{j=0}^{\infty} c_j + A_R + A_{RR} \tag{2.55b}$$

$$A_R = A_{RR} \tag{2.55c}$$

In these equations c_0 is a real transfer function for paddle position to free surface elevation, often called Biésel transfer function. The others, c_j with $(j >= 1)$ denote the purely imaginary transfer function for the j'th evanescent mode. According to Biésel and Suquet (1951) for a piston-type wavemaker the transfer function is:

$$c_j = \frac{4\, \sinh^2(k_j\, h)}{2\, k_j\, h + \sinh(2\, k_j\, h)} \tag{2.56}$$

in which k_j satisfies the linear dispersion relation generalised to complex wave numbers (Eq. 2.57), while k_0 still represents the ordinary real wave number for progressive waves.

$$\omega^2 = g\, k_j\, \tanh(k_j\, h) \tag{2.57}$$

Solving Eqs. 2.55 directly for the wavemaker movement (X_0) with the goal to cancel out re-reflected waves, leads to the so called single mode solution:

$$X_a = (2A_I - A_0)\, F \tag{2.58}$$

where

$$F = \frac{-i}{c_0 - \sum_{j=1}^{\infty} c_j} \tag{2.59}$$

In addition to the data of the theoretical wave amplitude in the wavemaker, given in A_I, there is a need to obtain the measured amplitude A_0, which will be given by a free surface sensor mounted on the wavemaker.

As it was shown in Eq. 2.51, the mapping of the general F function by means of a digital filter is always an approximation. Accuracy increases as more terms are considered, but as it can be seen in Eq. 2.59 the theory involves an infinite number of terms, which

can never be achieved. Following the single mode solution presented above will result in deviation errors from the prescribed wavemaker position.

Since wave generation is the known part of the problem it should be carried out, in theory, without any errors if it is conveniently treated. Then, only the signal involved in the absorption of waves should be affected by the approximation of the transfer function. This is called dual mode and it is the main advantage presented in this paper because it offers improved wave generation.

The starting point is to decompose the position of the wavemaker in two terms. The first one controls the generation of the waves, and the second one controls the absorption of the reflected waves:

$$X_a = X_a^{gen} + X_a^{abs} \tag{2.60}$$

Eq. 2.55a leads to the following expressions, when cancelling out re-reflections:

$$X_a^{gen} = \frac{A_I}{i\, c_0} \tag{2.61}$$

and

$$X_a^{abs} = (A_{I,0} - A_0)\, F \tag{2.62}$$

where

$$A_{I,0} = \frac{A_I}{c_0} \sum_{j=0}^{\infty} c_j = A_I + \frac{A_I}{c_0} \sum_{j=1}^{\infty} c_j \tag{2.63}$$

Clearly, only the absorption part is affected by the infinite sum of terms, while the generation part only depends on the real transfer function for wavemaker position to free surface elevation. It can be easily proved that by adding both terms and considering Eq. 2.59, the single mode solution (Eq. 2.58) is obtained:

$$
\begin{aligned}
X_a =& X_a^{gen} + X_a^{abs} = \frac{A_I}{i\,c_0} + \left[A_I + \frac{A_I}{c_0} \sum_{j=1}^{\infty} c_j - A_0 \right] F \\
=& \left[\frac{A_I}{i\,c_0}\,\frac{1}{F} + A_I + \frac{A_I}{c_0} \sum_{j=1}^{\infty} c_j - A_0 \right] F \\
=& \left[\frac{A_I}{c_0} \left(c_0 - \sum_{j=1}^{\infty} c_j \right) + A_I + \frac{A_I}{c_0} \sum_{j=1}^{\infty} c_j - A_0 \right] F = (2\,A_I - A_0)\,F
\end{aligned}
\tag{2.64}
$$

In order for the system to work in real time it is necessary to shift this Fourier-domain formulation into the real time domain. This is done by means of a 1-dimensional recursive digital filter of the form:

$$
v_n = \sum_{k=0}^{M} a_k\, u_{n-k} + \sum_{k=1}^{N} b_k\, v_{n-k} \tag{2.65}
$$

where M is the order of the filter and a_k, b_k are the filter coefficients. u_n corresponds to the input, equal to $2\,\eta_I - \eta_0$ for the simple mode and $\eta_{I,0} - \eta_0$ for the dual mode. v_n is the total X of the wavemaker in the simple mode and X^{abs} (component of the position due to the absorption procedure) for the dual mode. All of the terms evaluated at the n^{th} time step ($t = n\,\Delta t$ in case of constant sampling rate). The second term is the recursive part of the filter, as it takes into account the input of the previous time steps.

Recalling Eq. 2.51, it continues to be the one that controls the process, so the goal is to map the target transfer function (2.59) fulfilling the stability conditions of such filters: locating the poles of the filter within the unit circle in the z-plane.

2.8.2.4 Christensen and Frigaard (1994)

The method proposed by Christensen and Frigaard (1994) is studied next. This one is also general, but it involves two measurements as well as two finite impulse response (FIR) digital filters. The general method to adjust the coefficients of the digital filter is explained as well.

Free surface elevations are measured by two gauges located in front of the wavemaker (Fig. 2.5), but the approach is still the same as before: the reflected wave train is separated from the sum of the incident and the re-reflected waves by means of two digital filters,

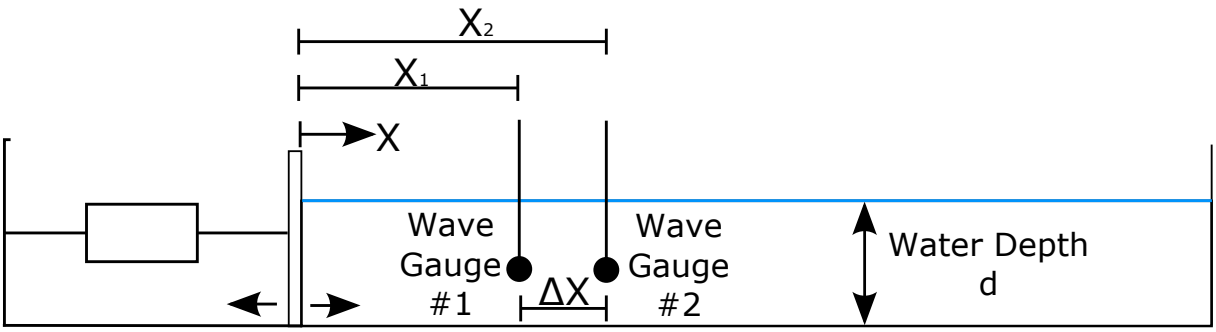

Figure 2.5: Christensen and Frigaard (1994) wave channel with piston-type wave maker.

which will then output the correction signal to absorb the waves, when added to the original wave paddle control signal.

The surface elevation at a position x may be considered as a sum of harmonic components. For simplicity just an isolated component of frequency f is considered, therefore the surface elevation is the sum of the incident and reflected wave components:

$$\begin{aligned} \eta(x,t) &= \eta_I(x,t) + \eta_R(x,t) \\ &= a_I \cos(2\,\pi\,f\,t - k\,x + \phi_I) + a_R \cos(2\,\pi\,f\,t + k\,x + \phi_R) \end{aligned} \tag{2.66}$$

where a is the wave amplitude, k is the wave number and ϕ is the phase.

It exists a linear relation between a given wavemaker displacement signal and its corresponding surface elevation, hence the wavemaker correction signal $X_{corr}(t)$ can be expressed as:

$$X_{corr}(t) \;=\; B\,a_R\;\cos(2\,\pi\,f\,t + \phi_R + \phi_B + \pi) \tag{2.67}$$

in which B is the piston stroke-to-wave-height relation and ϕ_B is the phaseshift between the paddle displacement and the surface elevation on the face of the paddle. At this time both are kept as generic quantities, but following Biésel and Suquet (1951) linear transfer functions for the case of a piston-type wave maker will be substituted by:

$$\begin{aligned} B &= \frac{2\;k\;h + \sinh(2\;k\;h)}{4\;\sinh^2(k\;h)} \\ \phi_B &= \frac{\pi}{2} \end{aligned} \tag{2.68}$$

Carrying out several simple operations on the measured signals of the gauges, such as amplification and modification of their phase, it can be derived that the sum of both signals is equal to the correction signal needed to absorb the reflected component of the waves.

At the two gauges the free surface is:

$$\begin{aligned}
\eta(x_1,t) &= a_I\cos(2\,\pi\,f\,t - k\,x_1 + \phi_I) + a_R\cos(2\,\pi\,f\,t + k\,x_1 + \phi_R)\\
\eta(x_2,t) &= a_I\cos(2\,\pi\,f\,t - k\,x_2 + \phi_I) + a_R\cos(2\,\pi\,f\,t + k\,x_2 + \phi_R)\\
&= a_I\cos(2\,\pi\,f\,t - k\,x_1 - k\,\Delta x + \phi_I) + a_R\cos(2\,\pi\,f\,t + k\,x_1 + k\,\Delta x + \phi_R)
\end{aligned} \tag{2.69}$$

where the geometrical identity $x_2 = x_1 + \Delta x$, shown in Fig. 2.5, is used.

Now an amplification of C and a theoretical phase shift ϕ^{theo} are introduced into the previous expressions of $\eta(x,t)$. The modified signal is denoted $\eta^*(x,t)$ and this is applied in the following way:

$$\begin{aligned}
\eta^*(x_i,t) &= C\,a_I\cos(2\,\pi\,f\,t - k\,x_i + \phi_I + \phi_i^{theo}) +\\
&\quad C\,a_R\cos(2\,\pi\,f\,t + k\,x_i + \phi_R + \phi_i^{theo})
\end{aligned} \tag{2.70}$$

The sum of $\eta^*(x_1,t)$ and $\eta^*(x_2,t)$ is denoted $\eta^{calc}(t)$ and equals:

$$\begin{aligned}
\eta^{calc}(t) &= \eta^*(x_1,t) + \eta^*(x_2,t)\\
&= 2\,C\,a_I\cos\left(\frac{k\,\Delta x + \phi_1^{theo} - \phi_2^{theo}}{2}\right)\\
&\quad \cos\left(2\,\pi\,f\,t - k\,x_1 + \phi_I + \frac{-k\,\Delta x + \phi_1^{theo} + \phi_2^{theo}}{2}\right) +\\
&\quad 2\,C\,a_R\cos\left(\frac{-k\,\Delta x + \phi_1^{theo} - \phi_2^{theo}}{2}\right)\\
&\quad \cos\left(2\,\pi\,f\,t + k\,x_1 + \phi_R + \frac{k\,\Delta x + \phi_1^{theo} + \phi_2^{theo}}{2}\right)
\end{aligned} \tag{2.71}$$

It is clear that $\eta^{calc}(t)$ equals $X_{corr}(t)$ when the following condition holds:

$$2\,C\cos\left(\frac{k\,\Delta x-\phi_1^{theo}+\phi_2^{theo}}{2}\right)=B \tag{2.72a}$$

$$k\,x_1+\frac{k\,\Delta x+\phi_1^{theo}+\phi_2^{theo}}{2}=\phi_B+\pi+n\cdot 2\pi \tag{2.72b}$$

$$\frac{k\,\Delta x+\phi_1^{theo}-\phi_2^{theo}}{2}=\frac{\pi}{2}+m\cdot\pi \tag{2.72c}$$

Solving Eq. 2.72 with respect to ϕ_1^{theo}, ϕ_2^{theo} and C with $n=m=0$ yields to:

$$\phi_1^{theo}=\phi_B-k\,\Delta x-k\,x_1+\frac{3\pi}{2} \tag{2.73a}$$

$$\phi_2^{theo}=\phi_B-k\,x_1+\frac{\pi}{2} \tag{2.73b}$$

$$C=\frac{B}{2\,\cos\left(-k\,\Delta x+\frac{\pi}{2}\right)} \tag{2.73c}$$

Eqs. 2.73 specify the amplification factors and phase shifts for the FIR filters of each wave gauge.

2.8.2.5 Luppes et al. (2010)

Finally, one of the most recent methods to simulate a wave transmissive boundary condition is presented in Luppes et al. (2010), and further developed in Wellens (2012) PhD thesis. This one is more prone to be developed in numerical models because of the measurements needed, and since it does not involve the calculation of the free surface elevation it can be applied cell by cell.

Its starting point is the Sommerfeld condition for the potential, given in the following equation:

$$\left(\frac{\partial}{\partial t}+c^{\text{out}}\frac{\partial}{\partial x}\right)\Phi^{out}=0 \tag{2.74}$$

in which c^{out} is the phase velocity of an outgoing wave component. This boundary condition is perfectly absorbent for this single wave component, but it will cause reflections for wave components with other phase velocities. This expression has been improved in Wellens (2012). Eq. 2.75 is used as a rational approximation for c^{out} in Eq. 2.44.

$$c^* = \sqrt{g\,h}\,\frac{a_0 + a_1(k\,h)^2}{1 + b_1(k\,h)^2}. \tag{2.75}$$

A thorough work to adjust a_i and b_i coefficients has been carried out in Wellens (2012).

Moreover, the reflection for all the wave components can be reduced by one order of magnitude if condition 2.74 is expanded to second order as shown:

$$\prod_{j=1}^{2}\left(\frac{\partial}{\partial t} + c_j\frac{\partial}{\partial x}\right)\Phi = 0 \tag{2.76}$$

2.8.3 3D active wave absorption

3D active wave absorption has two different branches, quasi-3D systems, in which there is no need to compute the angle of incident waves because it is fixed in advance, and true 3D systems, which estimate the angle of incidence each time step. Both theories are identical in form, indeed they derive from corrected formulation of 2D absorption. Quasi-3D absorption is simpler, and it works as 2D absorption does, while the true 3D absorption is more complex. It increases complexity by 1 order, since the general approach uses two-dimensional digital filters.

2.8.3.1 Quasi-3D method

Following the example presented in Schäffer and Klopman (2000) a method to absorb oblique waves is presented. As already mentioned, this is only a correction of 2D absorption accounting for a preset angle of incidende, reducing (projecting) the absorption velocity by a factor $cos(\theta)$. The general equation using shallow water wave theory is:

$$U(t) = -\cos(\theta)\sqrt{\frac{g}{h}}\cdot\eta_R(t) \tag{2.77}$$

Note that when incidence is normal ($\theta = 0°$), absorption velocity remains completely unaffected, since it is a true 2D condition. As waves approach to the parallel direction to the boundary the theory is expected to decrease its performance, not being able to absorb the tangential velocity component of the waves. This will finally lead to a stationary wave along the wavemaker if the situation is not handled correctly at the lateral boundaries.

2.8.3.2 Schäffer and Skourup (1996)

The work developed by Schäffer and Skourup (1996) is the extrapolation of the work presented in Schäffer et al. (1994) to 3D. Its fulfilment led to the well-known DHI 3D-AWACS, a proprietary system of the Danish Hydraulic Institute which is still in use today. The starting point is very close to the one presented in Eq. 2.58. When shifted to amplitudes it becomes:

$$\hat{X}_a = (2\hat{A}_I - \hat{A}_0)\,\frac{\cos(\theta)}{i\,c_0} \tag{2.78}$$

this transformation is performed in the following way:

$$(\hat{X}_a(y), \hat{A}_0(y), \hat{A}_I(y)) \equiv (X_a, A_0, A_I)e^{-i\,k_y\,y} \tag{2.79}$$

with $k_y = k\ \sin(\theta)$. Then, the preceding expression is differentiated in order to obtain directional information. The n'th derivative results:

$$\frac{\partial^n}{\partial y^n}\left(2\hat{A}_I - \hat{A}_0\right) = (i\,k\,sin(\theta))^n\left(2\hat{A}_I - \hat{A}_0\right) \tag{2.80}$$

For convenience, and since the cosine needs to be evaluated, the following expansion can be used:

$$\cos(\theta) = \sum_{n=0}^{N} a_{2n} sin^{2n}(\theta) \tag{2.81}$$

where a_{2n} are the expansion coefficients and N is the order of the expansion. Then joining Eqs. 2.80 and 2.81 the input for the absorption system is obtained:

$$\left(2\hat{A}_I - \hat{A}_0\right)\ cos(\theta) = \sum_{n=0}^{N} \frac{b_{2n}}{k^{2n}}\frac{\partial^{2n}}{\partial y^{2n}}\left(2\hat{A}_I - \hat{A}_0\right) \tag{2.82}$$

where $b_{2n} = (-1)^n a_{2n}$. When this expression is shifted to the time domain, amplitudes are replaced by elevations of the free surface at each of the paddles of the wavemaker, and therefore, are discrete both in time and space. Derivatives are computed using a given scheme, normally a centred one, which will involve at least $2n+1$ points to evaluate the $2n$'th derivative. Also for irregular waves the terms $1/k^{2n}$ have to be replaced with time

domain recursive filters, by approximation with the frequency domain transfer function. Therefore, the general method needs a two-dimensional digital filter in time and space, as follows:

$$v_{n,m} = \sum_{l=-M_2}^{M_2} \sum_{k=0}^{M1} a_{k,l}\, u_{n-k,m-l} + \sum_{l=-N_2}^{N_2} \sum_{k=1}^{N1} b_{k,l}\, v_{n-k,m-l} \tag{2.83}$$

As already mentioned the position and time at which free surface is evaluated are discrete. Measurements take place at the centre of the paddles, therefore y is sampled at $m\ \Delta y$ and t at $n\ \Delta t$. The input is $u_{n,m}$, which corresponds to $2\eta_I - \eta_0$ at $y = m\ \Delta y$ and $t = n\ \Delta t$. The output is $v_{n,m}$, which is the movement of the paddle: $X(n\Delta t, m\Delta y)$. Note that always k is greater than zero, which makes the filter causal, as future values are unknown until they are measured.

Since stability conditions for two-dimensional filters are not trivial and in order to avoid problems, Schäffer and Skourup omit the recursive element with respect to the spatial part of the filter ($N_2 = 0$). Moreover, they only take into account what happens in the immediate neighbours of each paddle ($M_2 = 1$). Also, since the transfer function F is even with respect to k_y this means that $a_{k,l} = a_{k,-l}$. The only step left is to obtain the coefficients so that the filter maps the transfer function F.

2.8.3.3 Klopman et al. (1996)

The full 3D absorption method presented in Klopman et al. (1996) is also based on shallow water wave theory. As seen in the previous reference, directional information comes from the spatial and temporal derivatives of free surface levels along the wavemaker. The cosine factor is approximated as a Taylor series in the Fourier space, as follows:

$$\cos(\theta) = \sqrt{1 - \frac{k_y^2}{k^2}} \approx 1 - \frac{1}{2} gh \frac{(i\, k_y)^2}{(i\, \omega)^2} \tag{2.84}$$

to obtain such a transformation the shallow water wave theory expression $c = \sqrt{gh} = \frac{\omega}{k}$ has been applied. Note that in Eq. 2.84, when shifting from the Fourier space to the physical one $(i\, k_y)^2$ corresponds to a second spatial derivative in the wavemaker (y) direction, and $\frac{1}{(i\, \omega)^2}$ corresponds to a double integration in time. Plugging Eq. 2.84 into Eq. 2.77 the main formulation of Klopman is obtained:

$$\frac{d^2U_j}{dt^2} = -\sqrt{\frac{g}{h}}\,\frac{d^2\eta_j}{dt^2} + \frac{1}{2}\,g\,\sqrt{gh}\,\frac{d^2\eta_j}{dy^2} \tag{2.85}$$

The final expression corresponds to a 2D recursive digital filter. In order to apply it the derivatives need to be discretized up to the desired order of approximation. Normally the time derivative is calculated using a second order backward scheme, and the spatial derivative applying a centred scheme, depending on the number of neighbours available. Klopman takes only one neighbour at each side into account.

2.8.4 Conclusions

Similarly to what occurred with wave generation, passive wave absorption must be regarded as less advantageous than active wave absorption, because it requires an increase of the computational domain.

Regarding active wave absorption, 2D and 3D theories are necessary to cover the cases that can appear in coastal engineering. In that sense, having a feedback that can be measured right at the boundary mimics the system implemented in the most modern experimental facilities and could offer a similar performance. Therefore, the system provided in Schäffer and Klopman (2000) is the most suitable for 2D cases. Prove can be obtained from references in which it is applied, even for different numerical models as in VOFbreak (Troch and De Rouck, 1999) and IH2VOF (Lara et al., 2006a). On top of that, it could be improved with Wellens (2012) advances, that have already been implemented in COMFLOW.

With respect to active 3D absorption, there is no formulation that steps on front of others. Moreover, attempts to absorb waves in 3D in numerical models are based in relaxation zones, because a general framework for active absorption does not exist. In fact, some of the attempts to absorb directional waves are based in the previous 2D theories.

Generally, for a real 3D behaviour each of the independent absorbing elements needs to communicate with adjacent ones. An improvement in 3D absorption could be eliminating the need to link paddles altogether, allowing each one to move independently depending on its own feedback.

Chapter 3

Objectives and Methodology

The objectives of the present work have been formulated to fill the gaps that have been found in the state of knowledge and to extend or enhance features that currently exist.

Nevertheless, all of them can be integrated into an ultimate goal: developing a three-dimensional numerical model capable of simulating the most diverse coastal engineering processes, with a robust, realistic implementation, fully validated and ready to be applied in the design process of real coastal structures.

The primary and secondary objectives of this work and the methodology to achieve them are formulated as follows.

3.1 Objective 1

Develop a three-dimensional numerical model capable of simulating coastal engineering processes.

The new model must be universal, capable of simulating any kind of real wave conditions and present a robust implementation and a realistic behaviour, to be able to characterize wave processes involved in the interaction with coastal structures.

This first global objective comprises other sub-objectives that characterize the whole model development process.

- **Objective 1.1: Implement robust and realistic wave generation.** Waves are the main driving factor in coastal engineering. As pointed out during the review of the state of the art, the most advanced wave generation procedures take place

at the boundaries (either as a Dirichlet-type boundary condition or as a moving boundary). Therefore, active wave generation needs to be implemented. The goal of this objective is obtaining a boundary condition able to produce realistic wave conditions all over the relative water depth regimes.

- **Objective 1.2: Implement efficient wave absorption.** The generation of waves induces an increase in the total energy of the system. The waves propagate and may eventually break, dissipating part of their energy. However, there is always a part of the energy that reflects back and reaches the boundaries. If these last waves are not absorbed, they will be reflected back into the domain, increasing the energetic level of the system and distorting the results. The literature shows again that active wave absorption (i.e. working at the boundaries) is the most advanced and convenient method, compared to passive absorption. Therefore, a pure active wave absorption system (both static and moving) needs to be implemented to allow for longer and more stable simulations.

- **Objective 1.3: Link wave generation and active wave absorption to work together.** Active wave generation at static boundaries presents a drawback. Due to the physics of waves, an excess of water is introduced when the crests are created, and it is not taken out when the troughs are generated. Therefore, in long simulations the mean water level would rise. With active wave absorption functioning simultaneously, this effect is corrected. Moreover, in the case of a moving boundary, this is how the experimental facilities function, with active wave absorption working at the wavemaker.

- **Objective 1.4: Derive a set of equations to represent two-phase flow through porous media.** VARANS equations have proven to be the most comprehensive method to simulate complex porous structures, disregarding the real geometry of the layers. Moreover, VARANS can also account for additional physics, if they are derived without assuming a zero time derivative of porosity. This improvement can help, for example, to simulate sediment transport. Another remarkable feature that is required for coastal simulations is volume-averaging turbulence models, to account for the enhancement of turbulence induced by the porous media.

- **Objective 1.5: Implement the new equations and link wave generation and absorption in the new solver.** OpenFOAM® stands out as a CFD finite volume framework with promising capabilities. It must be noted that it is not prepared to deal with coastal engineering processes by default, as it lacks wave generation and absorption, and porous media flow modules. That is the reason why it was chosen to be further developed. A solver for the new equations must be created, and it must include the wave generation and absorption boundary conditions: **IHFOAM**.

3.2 Objective 2

Validate the new three-dimensional numerical model to prove that it is capable of simulating coastal engineering processes.

All numerical models must undergo a validation process to demonstrate that they yield correct results. In this case, several types of validation must be performed, as a number of different physics are involved:

- **Objective 2.1: Validate wave generation and absorption.** The first step is to prove that the newly developed boundary conditions are able to generate all kind of waves according to different theories. Moreover, wave absorption has to show a correct performance, with significantly low reflection coefficients.

- **Objective 2.2: Validate wave transformation processes.** It is necessary to simulate basic wave transformation processes (i.e. shoaling, refraction, diffraction, nonlinear wave-to-wave interaction and wave breaking) induced by simple impervious geometries, to check that the model is able to represent them in a physical way. Comparisons with experimental results must be performed.

- **Objective 2.3: Validate flow through porous media.** The new module needs to be able to represent all the processes that two-phase flows undergo inside porous media. This step involves characterizing the friction factor for several porous materials and under different flow conditions by direct comparison with experimental data.

- **Objective 2.4: Validate all the processes at once.** Prior to applying the model to simulate coastal structures, it has to demonstrate its ability to deal with all the processes that wave interaction with coastal structures involves at the same time, as they take place in real cases.

3.3 Objective 3

Apply the three-dimensional numerical model to simulate real structures at prototype scale.

The last objective is probably the most ambitious, as if it were not achieved, the model would only be suitable for a limited range of applications. The possibility of simulating real coastal structures opens new perspectives for design purposes.

Generally, three-dimensional models present long runtimes and they require intensive computational resources. Therefore, in order to obtain the most suitable conditions to integrate the model in real designs is reducing both. The most comprehensive way to achieve this objective is:

- **Objective 3.1: Develop a methodology to integrate the use of the model in the design process of coastal structures.** The new methodology needs to integrate different models that should be able to, first, propagate wave conditions in a large domain but disregarding the structure itself to reduce the domain covered by the 3D RANS model, and second, to simulate the detailed interaction between sea states and the structure, so that the most critical moments can be extracted. These models should run in competitive times. By achieving this objective the engineers will benefit from an advanced tool to assist in taking decisions and to obtain more optimal designs.

Chapter 4

Mathematical Modelling - Volume-Averaged RANS equations

4.1 Introduction

A new set of Volume-Averaged Reynods-Averaged Navier–Stokes (VARANS) equations is derived in this section. While this is, obviously, a strongly mathematical process, especial emphasis is given to the physical meaning of each term. The goal is twofold, correcting the derivation in del Jesus et al. (2012) and reducing the number of underlying assumptions of the existing formulations.

Regarding the first goal, del Jesus et al. (2012) formulation was initially implemented with excellent results (a comparison between both derivations is shown in Appendix B). However, after discovering discrepancies with Slattery (1967) and Whitaker (1967), a rederivation was needed.

The second goal broadens the range of problems that can be solved with the equations. As it was remarked in the State of the Art chapter, the references in coastal engineering lack to describe a time-varying porosity, considering that the porous media are rigid. Moreover, the only reference that considers a time-varying porosity relies in a formulation that does not follow the Slattery (1967) and Whitaker (1967) prescriptions.

The novelty of this work consists in deriving the volume-averaged equations for two incompressible fluids in a domain with porous zones, considering a general case in which porosity may vary both in time and space, by means of the classic volume-averaging techniques.

In order to do so, two different kinds of porosity will be distinguished:

- The set of obstacles that do not move, which belong to the porous media of coastal structures (e.g. rubble mounds, core...). These will be the so-called rigid porosity, or static porosity, from now on.
- The set of particles that can move, representing for example, sediment that can be transported by wave dynamics. This kind encompasses the unsteady part of porosity, and will be called dynamic porosity.

4.2 General considerations

In this section the basic variables, theorems and mathematical operators used for the derivation of the VARANS equations are introduced.

Volume-averaging is a mathematical operation that when applied to a field yields a value at a point. Prior to applying the volume averaging technique the information of the field is local and dependent on the closest neighbours only. Such dependency can be obtained by evaluating the gradient at the point. This process takes into account an ensemble average of the field values enclosed by a given volume centred at the point, and not only the value at that specific point, extending the information provided by the field.

Volume averaging can be expressed mathematically as:

$$\langle a \rangle = \frac{1}{V} \int_{V_f} a \, \mathrm{dV} \tag{4.1}$$

in which $\langle\ \rangle$ is the volume averaging operator, a is a given field, V is the total (fixed) volume in which the averaging process takes place and V_f is the volume of fluid contained within the total volume. These variables are sketched in Fig. 4.1. The volume of fluid (V_f) defined here must not be confused with the Volume Of Fluid (VOF) technique (Hirt and Nichols, 1981), later represented by α.

A significant difference must be noted between the two volumes that have been introduced. While the total volume V is constant everywhere, the volume of fluid V_f may vary both in time and space, depending on the amount of solids or obstacles enclosed by the original V.

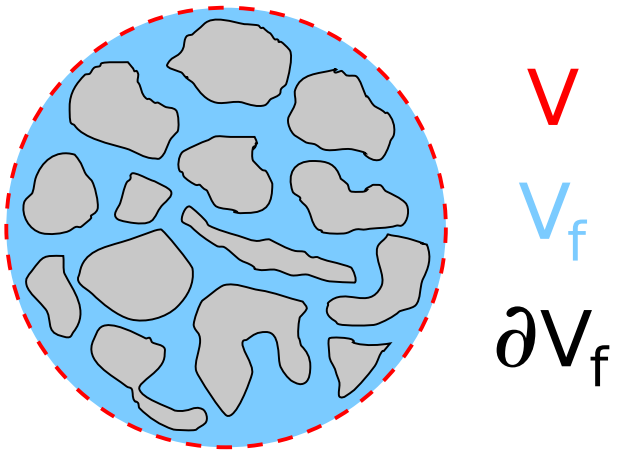

Figure 4.1: Volume averaging domain. V is the total volume, V_f is the volume occupied by the fluid and ∂V_f represents the solid boundaries in contact with the fluid.

The volume averaging procedure presented in Eq. 4.1 is called extended or superficial averaging. It introduces an inconvenient effect because it inherently includes the variations of V_f. Therefore, the volume-average of a constant field will yield space or time gradients due to the variations of V_f itself. The intrinsic volume average can be defined to overcome this effect:

$$\langle a \rangle^f = \frac{1}{V_f} \int_{V_f} a \, \mathrm{dV} \tag{4.2}$$

In order to stablish a connection between the extended and intrinsic average, a new variable has to be introduced. Porosity is defined as the fraction of volume of fluid that is contained in a control volume (or one minus the fraction of obstacles), namely:

$$\phi = \frac{V_f}{V} \tag{4.3}$$

Therefore, for a location outside the obstacles (clear fluid region) $V = V_f$ and $\phi = 1$. On the contrary, a region entirely located inside a solid obstacle yields $\phi = 0$. With this new variable, the relation between the extended average and intrinsic average is straightforward:

$$\langle a \rangle = \phi \, \langle a \rangle^f \tag{4.4}$$

A convenient decomposition of the variables will be adopted during the derivations in this work:

$$a = \langle \bar{a} \rangle^f + a' + a'' \tag{4.5}$$

where a is the real value of the magnitude, either obtained by direct measurement or by solving the original Navier–Stokes equations. This magnitude can be divided into three terms: $\langle \bar{a} \rangle^f$ is the intrinsic volume-averaged value, a' is the Reynolds turbulent fluctuation and a'' is the spatial fluctuation. This last term contains the information of the small-scale processes of the flow that are lost when volume-averaging. The decomposition can also be written as:

$$\bar{a} = \langle \bar{a} \rangle^f + a'' \tag{4.6}$$

in which $\bar{a}$ is the Reynolds-averaged variable. This artefact permits the application of the volume-averaging technique directly on the RANS equations. For convenience the over-bars will be dropped throughout this work understanding that the volume-averaging process is carried out on the Reynolds-averaged variables.

The composition of volume-averaging operators plays an important role in future derivations. The process can be started by volume-averaging each term in Eq. 4.6:

$$\begin{aligned} \langle \bar{a} \rangle^f &= \left\langle \langle \bar{a} \rangle^f \right\rangle^f + \langle a'' \rangle^f \\ \left\langle \langle \bar{a} \rangle^f \right\rangle^f &= \langle \bar{a} \rangle^f - \langle a'' \rangle^f \end{aligned} \tag{4.7}$$

The double volume average results in the single volume average minus the volume averaged spatial fluctuations. Applying this expression strictly will yield a large number of higher order terms when averaging the RANS equations. Therefore, Gray (1975) and Whitaker (1996) propose an approximation to consider the volume-averaged value constant within the control volume, and then:

$$\left\langle \langle a \rangle^f \right\rangle^f = \frac{1}{V_f} \int_{V_f} \langle a \rangle^f \, \mathrm{dV} = \langle a \rangle^f \frac{1}{V_f} \int_{V_f} \mathrm{dV} = \frac{V_f}{V_f} \langle a \rangle^f = \langle a \rangle^f \tag{4.8}$$

Comparing Eq. 4.7 and Eq. 4.8 it can be noted that:

$$\langle a'' \rangle^f = \langle a'' \rangle = 0 \tag{4.9}$$

this way, similarly to the turbulent fluctuation of the Reynolds decomposition, that has a time mean equals zero by definition, the spatial fluctuation is approximated to present an analogous property, a spatial mean equals zero. Simple algebra produces the rest of double averaging composition, gathered in the following table:

$\left\langle \langle a \rangle^f \right\rangle^f = \langle a \rangle^f$	$\left\langle \langle a \rangle^f \right\rangle = \phi \, \langle a \rangle^f = \langle a \rangle$
$\langle \langle a \rangle \rangle^f = \langle a \rangle$	$\langle \langle a \rangle \rangle = \phi \, \langle a \rangle = \phi^2 \, \langle a \rangle^f$

Table 4.1: Volume-averaging composition.

There is a particular situation in which Eq. 4.6 does not hold, when a is a composite variable (e.g. result of a product or a quotient of other variables, a_k). In that specific case, second order terms must be accounted for, as follows:

$$\bar{a} = \langle \bar{a_k} \rangle^f + a_k'' + a_k'^* \tag{4.10}$$

With this new formulation Eq. 4.9 is still applicable, but the volume average of the parent variable becomes:

$$\langle \underline{\bar{a}} \rangle = \langle \bar{a_k} \rangle + \langle a_k'^* \rangle \tag{4.11}$$

All the relevant expressions used throughout this work resulting from volume averaging composite variables are provided in Appendix A.1.

Two important theorems presented in Whitaker (1967) and Slattery (1967), that will appear several times along this work, need to be presented for fully understanding the development of the equations. They are the theorem for the local volume average of a gradient (Eq. 4.12) and the theorem for the local volume average of a time derivative (Eq. 4.13). For a given variable a which is differentiated with respect to time and space, and volume-averaged:

$$\left\langle \frac{\partial a}{\partial x_i} \right\rangle = \frac{\partial \langle a \rangle}{\partial x_i} + \frac{1}{V} \int_{\partial V_f} a \, \mathbf{dS} \tag{4.12}$$

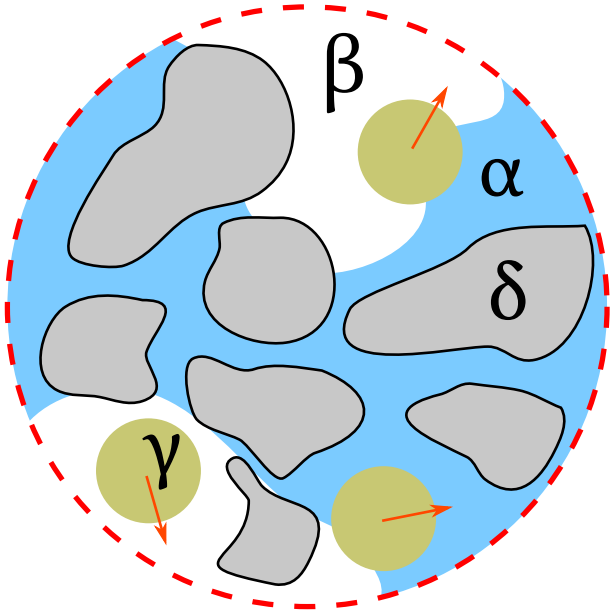

Figure 4.2: Volume averaging domain for several phases and obstacles.

$$\left\langle \frac{\partial a}{\partial t} \right\rangle = \frac{\partial \langle a \rangle}{\partial t} - \frac{1}{V} \int_{\partial V_f} a \, \mathbf{v} \cdot \mathbf{dS} \tag{4.13}$$

where the integral terms are defined over the solid surface of the obstacles (∂V_f, see Fig. 4.1 for reference). $\mathbf{dS} = \mathbf{n}\, dS$ is the outwardly-pointing normal vector to the interface ∂V_f, and $\mathbf{v}$ is the velocity of such interface. Later on, in application of the no-slip boundary condition at the interface, the velocity of the fluid $\mathbf{u}$ will be equal to that of the solid boundary $\mathbf{v}$.

Some interesting results can be obtained when developing the previous expressions for a constant field with unit value ($a = 1$, $\langle 1 \rangle = \phi$):

$$\left\langle \frac{\partial 1}{\partial x_i} \right\rangle = 0 = \frac{\partial \langle 1 \rangle}{\partial x_i} + \frac{1}{V} \int_{\partial V_f} \mathbf{dS} \longrightarrow \frac{\partial \phi}{\partial x_i} = -\frac{1}{V} \int_{\partial V_f} \mathbf{dS} \tag{4.14}$$

$$\left\langle \frac{\partial 1}{\partial t} \right\rangle = 0 = \frac{\partial \langle 1 \rangle}{\partial t} - \frac{1}{V} \int_{\partial V_f} \mathbf{v} \cdot \mathbf{dS} \longrightarrow \frac{\partial \phi}{\partial t} = \frac{1}{V} \int_{\partial V_f} \mathbf{v} \cdot \mathbf{dS} \tag{4.15}$$

Sometimes a single porosity (ϕ) does not suffice to represent a complex situation, as it is only enough to define a system with only a single obstacle type. In this case two phases, water (α) and air (β) and two solids, moving sediment (γ) and rigid elements (δ), must be represented as in Fig. 4.2. For a complete treatment a new variable has to be

introduced. Volume fraction (ϵ_i, also called saturation when applied to fluids) is defined as the fraction of material (or volume of fluid) "i" that is contained within the control volume. With this new variable an arbitrary number of phases can be accounted for at the same time. The main property of volume fraction is that:

$$\epsilon_\alpha + \epsilon_\beta + \epsilon_\gamma + \epsilon_\delta = 1 \tag{4.16}$$

Later in this chapter a distinction between the portion of porosity which does not move or change in time (static porosity ϕ_{ST}, from now on) and the unsteady part (dynamic porosity ϕ_{DY}) which may move, will be made. As already commented, the static porosity represents the porous media from coastal structures (e.g. mantles and core) and the dynamic porosity corresponds to the particles of sediment, which may move. Porosity is linked with volume fraction, mathematically:

$$\phi = \epsilon_\alpha + \epsilon_\beta = 1 - \epsilon_\gamma - \epsilon_\delta \tag{4.17}$$

$$\phi_{\text{ST}} = 1 - \epsilon_\delta \tag{4.18}$$

$$\phi_{\text{DY}} = 1 - \epsilon_\gamma \tag{4.19}$$

therefore, the total porosity can defined as:

$$\phi = \phi_{\text{ST}} + \phi_{\text{DY}} - 1 \tag{4.20}$$

The integration on the boundaries in Eqs. 4.12–4.13 is now extended to the bounds of both obstacles: $\partial V_f = \partial V_{f-\text{ST}} + \partial V_{f-\text{DY}}$. Moreover, by definition of the static porosity: $\frac{\partial \phi_{\text{ST}}}{\partial t} = \frac{\partial \epsilon_\delta}{\partial t} = 0$.

The following derivations will be performed for a single phase fluid. The Volume Of Fluid (VOF) technique permits this treatment, as proven in Appendix A.2. VOF helps tracking the different fluids by means of an indicator function (α_i). This new variable is defined as the volume of the fluid i per volume of the total fluid mixture (i.e. the total averaging volume minus the volume of the obstacles):

$$\alpha_i = \frac{V_{f_i}}{\sum_{j=1}^{n} V_{f_j}} \tag{4.21}$$

or formulated in terms of saturation for the α (water) phase:

$$\alpha_\alpha = \frac{V_\alpha}{V_\alpha + V_\beta} = \frac{\epsilon_\alpha}{\epsilon_\alpha + \epsilon_\beta} \tag{4.22}$$

In this work only 2 fluid phases (water and air) are considered, and just a single indicator function (α_α, α only from now on for simplicity) is needed, because that of the air is directly $(1-\alpha)$. The main advantage of VOF is that the fluids are treated globally as a mixture of others. The fluid properties can be calculated as a weighted average, for example, to obtain the density:

$$\rho = \rho_\alpha \alpha + \rho_\beta (1-\alpha) = \rho_\beta + (\rho_\alpha - \rho_\beta)\alpha \tag{4.23}$$

4.3 Derivation of the VARANS equations

4.3.1 Conservation of mass

The starting point of the derivation is to consider the classical conservation of mass equation, which holds in a point in space. According to Hassanizadeh and Gray (1979):

$$\frac{\partial \rho}{\partial t} + \frac{\partial \rho u_i}{\partial x_i} = 0 \tag{4.24}$$

Studying the terms of Eq. 4.24, they can be identified as the density rate of change and the density flow rate. Starting the volume averaging process:

$$\left\langle \frac{\partial \rho}{\partial t} \right\rangle + \left\langle \frac{\partial \rho u_i}{\partial x_i} \right\rangle = 0 \tag{4.25}$$

and then operating in each term:

$$\frac{\partial \langle \rho \rangle}{\partial t} - \frac{1}{V} \int_{\partial V_f} \rho\, u_i \, \mathrm{dS}_i + \frac{\partial \langle \rho u_i \rangle}{\partial x_i} + \frac{1}{V} \int_{\partial V_f} \rho\, u_i \, \mathrm{dS}_i = 0 \tag{4.26}$$

Two new integral terms appear due to the theorems presented in Eqs. 4.12 and 4.13. These integrals are defined over the surface of the obstacles that lie within the averaging volume. Both terms are equal to zero for the static porosity part because $v_i = 0$. For the moving obstacles ($v_i \neq 0$), one cancels the other out. Further developing the expression:

$$\frac{\partial \phi \, \langle \rho \rangle^f}{\partial t} + \frac{\partial \rho \, \langle u_i \rangle}{\partial x_i} = 0 \tag{4.27}$$

$$\frac{\partial \phi \, \rho}{\partial t} + \frac{\partial \rho \, \langle u_i \rangle}{\partial x_i} = 0 \tag{4.28}$$

Under the incompressible fluid regime and taking into account the different porosities defined ($\phi = \phi_{\text{ST}} + \phi_{\text{DY}} - 1$) the expression can be streamlined:

$$\frac{\partial \left(\phi_{\text{ST}} + \phi_{\text{DY}} - 1 \right)}{\partial t} + \frac{\partial \, \langle u_i \rangle}{\partial x_i} = 0 \tag{4.29}$$

$$\frac{\partial \phi_{\text{DY}}}{\partial t} + \frac{\partial \, \langle u_i \rangle}{\partial x_i} = 0 \tag{4.30}$$

this solution is similar to the classic equation, but it includes an additional term that accounts for the time variation in porosity. If porosity does not change in time the expression is reduced to:

$$\frac{\partial \, \langle u_i \rangle}{\partial x_i} = 0 \tag{4.31}$$

or in terms of the intrinsic velocities:

$$\frac{\partial \phi \, \langle u_i \rangle^f}{\partial x_i} = 0 \tag{4.32}$$

4.3.2 Conservation of mass II (VOF function)

Taking Eq. 4.24 as a starting point and plugging the expression in Eq. 4.23, the initial VOF advection equation can be obtained:

$$\frac{\partial}{\partial t}[\rho_\beta + (\rho_\alpha - \rho_\beta)\,\alpha] + \frac{\partial}{\partial x_i}\left[\rho_\beta\, u_i + (\rho_\alpha - \rho_\beta)\,\alpha\, u_i\right] = 0 \tag{4.33}$$

where the α subscript indicates the water phase and the β subscript indicates the air phase. Note that this equation includes now an averaged-in-volume variable, α, the VOF indicator function.

Expanding the expression accounting that ρ_α and ρ_β are constants and under the incompressible fluids assumption:

$$(\rho_\alpha - \rho_\beta)\frac{\partial \alpha}{\partial t} + \rho_\beta \frac{\partial u_i}{\partial x_i} + (\rho_\alpha - \rho_\beta)\frac{\partial \alpha u_i}{\partial x_i} = 0 \tag{4.34}$$

$$(\rho_\alpha - \rho_\beta)\left[\frac{\partial \alpha}{\partial t} + \frac{\partial \alpha u_i}{\partial x_i}\right] + \rho_\beta \frac{\partial u_i}{\partial x_i} = 0 \tag{4.35}$$

Starting the volume-averaging process and leaving the constants outside, as a result of Eq. A.6:

$$(\rho_\alpha - \rho_\beta)\left[\left\langle \frac{\partial \alpha}{\partial t} \right\rangle + \left\langle \frac{\partial \alpha u_i}{\partial x_i} \right\rangle\right] + \rho_\beta \left\langle \frac{\partial u_i}{\partial x_i} \right\rangle = 0 \tag{4.36}$$

$$(\rho_\alpha - \rho_\beta)\left[\frac{\partial \langle \alpha \rangle}{\partial t} - \frac{1}{V}\int_{\partial V_f} \alpha\, u_i \,\mathrm{d}S_i + \frac{\partial \langle \alpha u_i \rangle}{\partial x_i} + \frac{1}{V}\int_{\partial V_f} \alpha\, u_i \,\mathrm{d}S_i\right] + \rho_\beta \frac{\partial \langle u_i \rangle}{\partial x_i} + \rho_\beta \frac{1}{V}\int_{\partial V_f} u_i \,\mathrm{d}S_i = 0 \tag{4.37}$$

Applying Eq. 4.15, the second terms cancels out because of the conservation of mass equation (Eq. 4.30):

$$(\rho_\alpha - \rho_\beta)\left[\frac{\partial \phi\ \langle \alpha \rangle^f}{\partial t} + \frac{\partial \langle \alpha u_i \rangle}{\partial x_i}\right] + \rho_\beta \cancelto{0}{\left[\cancel{\frac{\partial \langle u_i \rangle}{\partial x_i}} + \cancel{\frac{\partial \phi}{\partial t}}\right]} = 0 \tag{4.38}$$

Identifying the expression in Eq. 4.30 further simplification can be achieved:

$$\frac{\partial \phi\ \langle \alpha \rangle^f}{\partial t} + \frac{\partial \langle \alpha u_i \rangle}{\partial x_i} = 0 \tag{4.39}$$

And finally the general expression, where $\langle \alpha \rangle^f = \alpha$, as noted in Appendix A.2:

$$\frac{\partial \phi\, \alpha}{\partial t} + \frac{\partial \alpha\ \langle u_i \rangle}{\partial x_i} = 0 \tag{4.40}$$

Obviously, this equation resembles the previously developed Eq. 4.30, with *alpha* instead of ρ.

If porosity does not change in time:

$$\begin{aligned} \phi\frac{\partial \alpha}{\partial t} + \alpha\cancelto{0}{\frac{\partial \phi}{\partial t}} + \frac{\partial \alpha\ \langle u_i \rangle}{\partial x_i} = \\ \frac{\partial \alpha}{\partial t} + \frac{1}{\phi}\frac{\partial \alpha\ \langle u_i \rangle}{\partial x_i} = 0 \end{aligned} \tag{4.41}$$

or alternatively, applying the continuity equation:

$$\begin{aligned} \frac{\partial \alpha}{\partial t} + \frac{1}{\cancel{\phi}}\alpha\cancelto{0}{\frac{\partial \langle u_i \rangle}{\partial x_i}} + \frac{1}{\phi}\langle u_i \rangle \frac{\partial \alpha}{\partial x_i} = \\ \frac{\partial \alpha}{\partial t} + \frac{1}{\phi}\langle u_i \rangle \frac{\partial \alpha}{\partial x_i} = 0 \end{aligned} \tag{4.42}$$

4.3.3 Conservation of momentum

The starting point of the derivation is to consider the classical equation of momentum conservation as in Hassanizadeh and Gray (1979), which is applicable in a point in space:

$$\frac{\partial \rho u_i}{\partial t} + u_j \frac{\partial \rho u_i}{\partial x_j} - \frac{\partial \sigma_{ij}}{\partial x_j} - \rho g_i = 0 \tag{4.43}$$

When this expression is expanded, it yields the general RANS equations:

$$\frac{\partial \rho u_i}{\partial t} + u_j \frac{\partial \rho u_i}{\partial x_j} = -\frac{\partial p}{\partial x_i} + \rho g_i + \frac{\partial}{\partial x_j}\left[\mu \frac{\partial u_i}{\partial x_j}\right] - \frac{\partial}{\partial x_j}\left[\rho \overline{u_i' u_j'}\right] \tag{4.44}$$

The terms in Eq. 4.44 are, from left to right, the local acceleration, the convective acceleration, the pressure gradient, the body forces (i.e. gravity), the viscous stresses and the Reynolds stresses. This last term includes the effects of turbulence, often represented

as an additional viscosity, as reported in Section 2.3.1.

$$\frac{\partial \rho u_i}{\partial t} + u_j \frac{\partial \rho u_i}{\partial x_j} = -\frac{\partial p}{\partial x_i} + \rho g_i + \frac{\partial}{\partial x_j}\left[(\mu + \mu_t)\frac{\partial u_i}{\partial x_j}\right] \tag{4.45}$$

The volume-averaging process of these equations is analogous to the previous ones, but with increasing complexity due to the large number of terms. On top of that, some terms cannot be solved and have to be modelled using closure laws.

Getting started with the local and convective accelerations, joined for convenience:

$$\begin{aligned}
\left\langle \frac{\partial \rho u_i}{\partial t} \right\rangle + \left\langle u_j \frac{\partial \rho u_i}{\partial x_j} \right\rangle = & \\
\left\langle \frac{\partial \rho u_i}{\partial t} \right\rangle + \left\langle \frac{\partial \rho u_i u_j}{\partial x_j} \right\rangle - \left\langle \rho u_i \frac{\partial u_j}{\partial x_j} \right\rangle = & \\
\frac{\partial \langle \rho u_i \rangle}{\partial t} - \frac{1}{V}\int_{\partial V_f} \rho u_i \, u_j \, \mathrm{dS}_j + \frac{\partial \langle \rho u_i u_j \rangle}{\partial x_j} + \frac{1}{V}\int_{\partial V_f} \rho u_i u_j \, \mathrm{dS}_j & \\
- \rho \frac{1}{\phi}\langle u_i \rangle \left\langle \frac{\partial u_j}{\partial x_j} \right\rangle - \rho \left\langle u_i'' \frac{\partial u_j''}{\partial x_j} \right\rangle = & \\
\frac{\partial \rho \langle u_i \rangle}{\partial t} + \frac{\partial \rho \langle u_i u_j \rangle}{\partial x_j} - \rho \frac{1}{\phi}\langle u_i \rangle \left(\frac{\partial \langle u_j \rangle}{\partial x_j} + \frac{1}{V}\int_{\partial V_f} u_j \, \mathrm{dS}_j \right) - \rho \left\langle u_i'' \frac{\partial u_j''}{\partial x_j} \right\rangle = & \\
\frac{\partial \rho \langle u_i \rangle}{\partial t} + \frac{\partial}{\partial x_j}\left[\frac{1}{\phi}\rho \langle u_i \rangle \langle u_j \rangle + \rho \langle u_i'' u_j'' \rangle\right] & \\
- \rho \frac{1}{\phi}\langle u_i \rangle \cancelto{0}{\left(\frac{\partial \phi}{\partial t} + \frac{\partial \langle u_j \rangle}{\partial x_j} \right)} - \rho \left\langle u_i'' \frac{\partial u_j''}{\partial x_j} \right\rangle = & \\
\frac{\partial \rho \langle u_i \rangle}{\partial t} + \frac{\partial}{\partial x_j}\left[\frac{1}{\phi}\rho \langle u_i \rangle \langle u_j \rangle\right] + \frac{\partial}{\partial x_j}\left[\rho \langle u_i'' u_j'' \rangle\right] - \rho \left\langle u_i'' \frac{\partial u_j''}{\partial x_j} \right\rangle &
\end{aligned} \tag{4.46}$$

Next is the pressure gradient:

$$\begin{aligned}
\left\langle \frac{\partial p}{\partial x_i} \right\rangle = \frac{\partial \langle p \rangle}{\partial x_i} + \frac{1}{V}\int_{\partial V_f} p \, \mathrm{dS}_j & \\
= \frac{\partial \phi \langle p \rangle^f}{\partial x_i} + \frac{1}{V}\int_{\partial V_f} (\langle p \rangle^f + p'') \, \mathrm{dS}_j & \\
= \phi \frac{\partial \langle p \rangle^f}{\partial x_i} + \langle p \rangle^f \frac{\partial \phi}{\partial x_i} + \frac{1}{V}\int_{\partial V_f} \langle p \rangle^f \, \mathrm{dS}_j + \frac{1}{V}\int_{\partial V_f} p'' \, \mathrm{dS}_j &
\end{aligned} \tag{4.47}$$

Under the assumption that the intrinsic pressure ($\langle p \rangle^f$) can be considered constant

along the integration surface (∂V_f) (Whitaker, 1986) and applying Eq. 4.14, the first integral term can be converted into:

$$\frac{1}{V}\int_{\partial V_f} \langle p\rangle^f \, \mathrm{dS}_j = \langle p\rangle^f \frac{1}{V}\int_{\partial V_f} \mathrm{dS}_j = -\langle p\rangle^f \frac{\partial \phi}{\partial x_i} \tag{4.48}$$

yielding the final expression for the volume-averaged pressure gradient:

$$\left\langle \frac{\partial p}{\partial x_i} \right\rangle = \phi \frac{\partial \langle p\rangle^f}{\partial x_i} + \frac{1}{V}\int_{\partial V_f} p'' \, \mathrm{dS}_j \tag{4.49}$$

Then the body forces:

$$\langle \rho g_i \rangle = \phi \rho g_i \tag{4.50}$$

For the viscous stresses, the Eq. 4.12 has to be applied twice:

$$\begin{aligned}\left\langle \frac{\partial}{\partial x_j}\left[\mu \frac{\partial u_i}{\partial x_j}\right]\right\rangle &= \frac{\partial}{\partial x_j}\left\langle \mu \frac{\partial u_i}{\partial x_j}\right\rangle + \frac{1}{V}\int_{\partial V_f} \mu \frac{\partial u_i}{\partial x_j}\,\mathrm{dS}_j = \\ &\frac{\partial}{\partial x_j}\left[\mu \frac{\partial \langle u_i\rangle}{\partial x_j} + \mu \frac{1}{V}\int_{\partial V_f} u_i \,\mathrm{dS}_j\right] + \frac{1}{V}\int_{\partial V_f} \mu \frac{\partial u_i}{\partial x_j}\,\mathrm{dS}_j \\ &= \frac{\partial}{\partial x_j}\left[\mu \frac{\partial \langle u_i\rangle}{\partial x_j}\right] + \frac{\partial}{\partial x_j}\left[\mu \frac{1}{V}\int_{\partial V_{f-\mathrm{DY}}} \left(\phi \langle u_i\rangle + u_i''\right)\,\mathrm{dS}_j\right] \\ &\quad + \frac{1}{V}\int_{\partial V_f} \mu\left(\frac{\partial \phi \langle u_i\rangle}{\partial x_j} + \frac{\partial u_i''}{\partial x_j}\right)\,\mathrm{dS}_j\end{aligned} \tag{4.51}$$

And finally the Reynolds stresses:

$$\begin{aligned}\left\langle \frac{\partial}{\partial x_j}\left[\rho \overline{u_i' u_j'}\right]\right\rangle &= \frac{\partial}{\partial x_j}\left[\rho \langle \overline{u_i' u_j'}\rangle\right] + \frac{1}{V}\int_{\partial V_f} \rho \overline{u_i' u_j'}\,\mathrm{dS}_j \\ &= \frac{\partial}{\partial x_j}\left[\rho \langle \overline{u_i' u_j'}\rangle\right] + \frac{1}{V}\int_{\partial V_{f-\mathrm{DY}}} \rho \overline{u_i' u_j'}\,\mathrm{dS}_j\end{aligned} \tag{4.52}$$

Gathering all these terms, the general Volume–Averaged Reynolds–Averaged Navier–Stokes (VARANS) equations can be assembled:

$$\frac{\partial \rho \langle u_i \rangle}{\partial t} + \frac{\partial}{\partial x_j}\left[\frac{1}{\phi}\rho \langle u_i \rangle \langle u_j \rangle\right] = - \phi \frac{\partial \langle p \rangle^f}{\partial x_i} + \phi \rho g_i + \frac{\partial}{\partial x_j}\left[\mu \frac{\partial \langle u_i \rangle}{\partial x_j}\right] - \frac{\partial}{\partial x_j}\left[\rho \langle \overline{u_i' u_j'} \rangle\right] + [CT]_{\mathrm{ST}} + [CT]_{\mathrm{DY}} \quad (4.53)$$

where the closure terms [CT] refer to:

$$[CT]_{\mathrm{ST}} = - \frac{\partial}{\partial x_j}\left[\rho \langle u_i'' u_j'' \rangle\right] + \rho \left\langle u_i'' \frac{\partial u_j''}{\partial x_j} \right\rangle - \frac{1}{V}\int_{\partial V_{f-\mathrm{ST}}} p'' \, \mathrm{dS}_j + \frac{1}{V}\int_{\partial V_{f-\mathrm{ST}}} \mu \left(\frac{\partial \phi \langle u_i \rangle}{\partial x_j} + \frac{\partial u_i''}{\partial x_j}\right) \mathrm{dS}_j \quad (4.54)$$

$$[CT]_{\mathrm{DY}} = - \frac{1}{V}\int_{\partial V_{f-\mathrm{DY}}} p'' \, \mathrm{dS}_j + \frac{\partial}{\partial x_j}\left[\mu \frac{1}{V}\int_{\partial V_{f-\mathrm{DY}}} \left(\langle u_i \rangle + u_i''\right) \mathrm{dS}_j\right] + \frac{1}{V}\int_{\partial V_{f-\mathrm{DY}}} \mu \left(\frac{\partial \phi \langle u_i \rangle}{\partial x_j} + \frac{\partial u_i''}{\partial x_j}\right) \mathrm{dS}_j - \frac{1}{V}\int_{\partial V_{f-\mathrm{DY}}} \rho \overline{u_i' u_j'} \, \mathrm{dS}_j \quad (4.55)$$

4.4 Closure of the VARANS equations

The volume-averaging technique yields terms that cannot be simulated. Such elements describe physics as the frictional forces, pressure forces and added mass of the individual components of the porous media, and need a closure model to be represented. Traditionally, they are addressed with drag forces, as already reviewed in Section 2.4:

$$I = A \langle u_i \rangle + B \, |\langle u \rangle| \langle \, u_i \rangle + C \frac{\partial \langle u_i \rangle}{\partial t} \quad (4.56)$$

A large number of closure models exist in literature. In this work, the formulation developed by Engelund (1953), as applied in Burcharth and Andersen (1995), will be employed. The friction coefficients are calculated according to the following formulas:

$$A = \alpha \frac{(1-\phi)^3}{\phi^2} \frac{\mu}{D_{50}^2} \tag{4.57a}$$

$$B = \beta \left(1 + \frac{7.5}{\mathrm{KC}}\right) \frac{1-\phi}{\phi^2} \frac{\rho}{D_{50}} \tag{4.57b}$$

where D_{50} is the mean nominal diameter of the porous material. KC is the Keulegan-Carpenter number $\left(\frac{T_o}{D_{50}} \frac{u_M}{\phi}\right)$, which introduces additional friction due to the oscillatory nature and unsteadiness of the system when waves are present. u_M is the maximum oscillatory velocity, and T_o is the period of the oscillation.

The parameters that characterize the linear and nonlinear friction terms are α and β. They are not only dependent on the porous media physical properties but also on the flow regime inside them. Therefore, most of the times they need to be calibrated from physical tests. The factor C has proven to be less significant to variations than A or B and a value of $C = 0.34$ is often applied by default (del Jesus, 2011).

Eq. 4.56 does only represent the effects of the static porous materials (i.e. the terms in Eq. 4.54). Additional terms need to be included to account for the dynamic components in Eq. 4.55. A drag force field ($\mathbf{F}_D$) can describe the effects of the moving particles. This term is a function of the relative velocity between the particle and the fluid, hence, if the particle is travelling faster than the fluid, momentum will be added to the fluid, and it will be subtracted otherwise. Drag forces are out of the scope of this work.

To conclude with, all the closure terms are gathered in the following expression:

$$[CT] = [CT]_{\mathrm{ST}} + [CT]_{\mathrm{DY}} = - \alpha \frac{(1-\phi_{\mathrm{ST}})^3}{\phi_{\mathrm{ST}}^2} \frac{\mu}{D_{50,\mathrm{ST}}^2} \langle u_i \rangle - \beta \left(1 + \frac{7.5}{\mathrm{KC}_{\mathrm{ST}}}\right) \frac{1-\phi_{\mathrm{ST}}}{\phi_{\mathrm{ST}}^2} \frac{\rho}{D_{50,\mathrm{ST}}} |\langle u \rangle| \langle u_i \rangle - C \frac{\partial \langle u_i \rangle}{\partial t} - \mathbf{F}_D \quad (4.58)$$

4.5 Volume Averaging of Turbulence Equations

4.5.1 The $k - \epsilon$ model

The $k - \epsilon$ model is one of the most widely used in CFD. A complete description can be found in Section 2.3.2.1. Here, a full rederivation of Nakayama and Kuwahara (1999) work is made, taking into account a time-varying porosity.

4.5.1.1 Volume averaging procedure

A change in notation is performed in the following two sections, from the Einstein (index) notation used before to the normal notation, for a more compact treatment of the equations. Just before starting the volume averaging process, the advection terms can be reformulated using a convenient mathematical artefact:

$$\frac{\partial k}{\partial t} + \mathbf{u} \cdot \nabla k = \frac{\partial k}{\partial t} + \mathbf{u} \cdot \nabla k + k \nabla \cdot \mathbf{u} - k \nabla \cdot \mathbf{u} = \frac{\partial k}{\partial t} + \nabla \cdot (k\,\mathbf{u}) - k \nabla \cdot \mathbf{u} \quad (4.59)$$

The first step is the averaging of the advection terms (local plus convective):

$$\begin{aligned}
\left\langle \frac{\partial k}{\partial t} \right\rangle + \langle \nabla\cdot\ (k\,\mathbf{u}) \rangle - \langle k \nabla \cdot \mathbf{u} \rangle = \\
\frac{\partial \langle k \rangle}{\partial t} - \frac{1}{V}\int_{\partial V_f} k\,\mathbf{u}\cdot\mathbf{dS} \\
+ \nabla \cdot \left(\frac{1}{\phi} \langle k \rangle \langle \mathbf{u} \rangle \right) + \frac{1}{V}\int_{\partial V_f} k\,\mathbf{u}\cdot\mathbf{dS} + \nabla \cdot \langle k'' \mathbf{u}'' \rangle \\
- \frac{1}{\phi} \langle k \rangle \nabla \cdot \langle \mathbf{u} \rangle - \frac{1}{\phi} \langle k \rangle \frac{1}{V}\int_{\partial V_f} \mathbf{u}\cdot\mathbf{dS} - \langle k'' \nabla \cdot \mathbf{u}'' \rangle = \\
\frac{\partial \langle k \rangle}{\partial t} + \nabla \cdot \left(\frac{1}{\phi} \langle k \rangle \langle \mathbf{u} \rangle \right) + \nabla \cdot \langle k'' \mathbf{u}'' \rangle \\
- \frac{1}{\phi} \langle k \rangle \nabla \cdot \langle \mathbf{u} \rangle - \frac{1}{\phi} \langle k \rangle \frac{\partial \phi}{\partial t} - \langle k'' \nabla \cdot \mathbf{u}'' \rangle = \\
\frac{\partial \langle k \rangle}{\partial t} + \nabla \cdot \left(\frac{1}{\phi} \langle k \rangle \langle \mathbf{u} \rangle \right) - \frac{1}{\phi} \langle k \rangle \left(\frac{\partial \phi}{\partial t} + \nabla \cdot \langle \mathbf{u} \rangle \right) \\
+ \nabla \cdot \langle k'' \mathbf{u}'' \rangle - \langle k'' \nabla \cdot \mathbf{u}'' \rangle
\end{aligned} \tag{4.60}$$

Which by means of Eq. 4.30 can be simplified, yielding:

$$\begin{aligned}
\left\langle \frac{\partial k}{\partial t} \right\rangle + \langle \nabla\cdot\ (k\,\mathbf{u}) \rangle - \langle k \nabla \mathbf{u} \rangle = \\
\frac{\partial \langle k \rangle}{\partial t} + \nabla \cdot \left(\frac{1}{\phi} \langle k \rangle \langle \mathbf{u} \rangle \right) + \nabla \cdot \langle k'' \mathbf{u}'' \rangle - \langle k'' \nabla \cdot \mathbf{u}'' \rangle
\end{aligned} \tag{4.61}$$

Continuing with the diffusion term, to be split into two others:

$$\left\langle \nabla \cdot \left[\left(\nu + \frac{\nu_t}{\sigma_k} \right) \nabla k \right] \right\rangle = \langle \nabla\cdot\ [\nu \nabla k] \rangle + \left\langle \nabla \cdot \left[\frac{\nu_t}{\sigma_k} \nabla k \right] \right\rangle \tag{4.62}$$

For the first one, the viscosity ν is treated as a constant as for density (ρ), because it is obtained in the same way:

$$\langle \nabla\cdot\ [\nu\nabla k]\rangle = \nabla\cdot\langle\nu\nabla k\rangle + \frac{1}{V}\int_{\partial V_f}\nu\nabla k\cdot\mathbf{dS} = \nabla\cdot(\nu\langle\nabla k\rangle) + \frac{1}{V}\int_{\partial V_f}\nu\nabla k\cdot\mathbf{dS} = \nabla\cdot(\nu\nabla\langle k\rangle) + \nabla\cdot\left(\nu\frac{1}{V}\int_{\partial V_{f-\mathrm{DY}}}k\,\mathbf{dS}\right) + \frac{1}{V}\int_{\partial V_f}\nu\nabla k\cdot\mathbf{dS} \quad (4.63)$$

The second term:

$$\left\langle\nabla\cdot\left[\frac{\nu_t}{\sigma_k}\nabla k\right]\right\rangle = \nabla\cdot\left\langle\frac{\nu_t}{\sigma_k}\nabla k\right\rangle + \frac{1}{V}\int_{\partial V_f}\frac{\nu_t}{\sigma_k}\nabla k\cdot\mathbf{dS} = \nabla\cdot\left(\frac{1}{\phi}\frac{\langle\underline{\nu_t}\rangle}{\sigma_k}\langle\nabla k\rangle\right) + \nabla\cdot\left(\frac{\nu_t''}{\sigma_k}\nabla k''\right) + \frac{1}{V}\int_{\partial V_f}\frac{\nu_t}{\sigma_k}\nabla k\cdot\mathbf{dS} = \nabla\cdot\left(\frac{1}{\phi}\frac{\langle\underline{\nu_t}\rangle}{\sigma_k}\nabla\langle k\rangle\right) + \nabla\cdot\left(\frac{1}{\phi}\frac{\langle\underline{\nu_t}\rangle}{\sigma_k}\frac{1}{V}\int_{\partial V_{f-\mathrm{DY}}}k\,\mathbf{dS}\right) + \nabla\cdot\left(\frac{\nu_t''}{\sigma_k}\nabla k''\right) + \frac{1}{V}\int_{\partial V_f}\frac{\nu_t}{\sigma_k}\nabla k\cdot\mathbf{dS} \quad (4.64)$$

On the previous equation there is a composite variable, ν_t, to be volume-averaged separately, applying Eq. A.24:

$$\langle\underline{\nu_t}\rangle = \langle\nu_t\rangle + \langle\nu_t'^*\rangle = \left\langle C_\mu\frac{k^2}{\epsilon}\right\rangle = C_\mu\left\langle\frac{k^2}{\epsilon}\right\rangle = \underbrace{C_\mu\frac{\langle k\rangle^2}{\langle\epsilon\rangle}}_{\langle\nu_t\rangle} + \underbrace{C_\mu\,\phi\frac{\langle k''k''\rangle}{\langle\epsilon\rangle} - 2\,C_\mu\,\phi\frac{\langle k\rangle\langle k''\epsilon''\rangle}{\langle\epsilon\rangle^2} + C_\mu\,\phi\frac{\langle k\rangle^2\langle\epsilon''\epsilon''\rangle}{\langle\epsilon\rangle^3}}_{\langle\nu_t'^*\rangle} \quad (4.65)$$

and the term that does not appear would be:

$$\nu_t'' = \frac{2\,\langle k\rangle\,k''}{\langle\epsilon\rangle} - \frac{\langle k\rangle^2\,\epsilon''}{\langle\epsilon\rangle^2} \quad (4.66)$$

Next is the dissipation coefficient:

$$\langle \beta_k k \rangle = \left\langle \frac{\epsilon}{k} k \right\rangle = \langle \epsilon \rangle \tag{4.67}$$

And finally the production term. The main difference compared to the other elements is that in this case the volume average operator is applied to the squared modulus of the strain rate tensor ($\mathbf{S}$). The squared modulus can be substituted by the double inner product, that will be represented in the following way:

$$\mathbf{S}^2 = \mathbf{S} : \mathbf{S} \tag{4.68}$$

First, the derivation up to second order yields three general terms applying Eq. A.13, two of which still need further development.

$$\begin{aligned}
\langle F_k \rangle = \left\langle 2\nu_t \mathbf{S}^2 \right\rangle = \\
&\frac{2}{\phi^2} \left\langle \underline{\nu_t} \right\rangle \langle \mathbf{S} \rangle^2 + \frac{2}{\phi} \left\langle \underline{\nu_t} \right\rangle \left\langle (\mathbf{S}'')^2 \right\rangle + \frac{4}{\phi} \langle \mathbf{S} \rangle : \langle \nu_t'' \mathbf{S}'' \rangle = \\
&\frac{2}{\phi^2} \left\langle \underline{\nu_t} \right\rangle \langle \mathbf{S} \rangle^2 + \frac{2}{\phi} \langle \nu_t \rangle \left\langle (\mathbf{S}'')^2 \right\rangle + \cancel{\frac{2}{\phi} \langle \nu_t'^* \rangle \left\langle (\mathbf{S}'')^2 \right\rangle} \to O(\theta^4) \\
&+ \frac{4}{\phi} \langle \mathbf{S} \rangle : \langle \nu_t'' \mathbf{S}'' \rangle = \\
&\frac{2}{\phi^2} \left\langle \underline{\nu_t} \right\rangle \left\langle \left| \frac{\nabla \mathbf{u} + (\nabla \mathbf{u})^t}{2} \right| \right\rangle^2 + \frac{2}{\phi} \langle \nu_t \rangle \left\langle \left| \frac{\nabla \mathbf{u}'' + (\nabla \mathbf{u}'')^t}{2} \right|^2 \right\rangle \\
&+ \frac{4}{\phi} \left\langle \left| \frac{\nabla \mathbf{u} + (\nabla \mathbf{u})^t}{2} \right| \right\rangle : \left\langle \nu_t'' \left| \frac{\nabla \mathbf{u}'' + (\nabla \mathbf{u}'')^t}{2} \right| \right\rangle = \\
&\frac{2}{\phi^2} \left\langle \underline{\nu_t} \right\rangle \left| \frac{\langle \nabla \mathbf{u} \rangle + \left\langle (\nabla \mathbf{u})^t \right\rangle}{2} \right|^2 + \frac{2}{\phi} \langle \nu_t \rangle \left\langle \left| \frac{\nabla \mathbf{u}'' + (\nabla \mathbf{u}'')^t}{2} \right|^2 \right\rangle \\
&+ \frac{4}{\phi} \left| \frac{\langle \nabla \mathbf{u} \rangle + \left\langle (\nabla \mathbf{u})^t \right\rangle}{2} \right| : \left\langle \nu_t'' \left| \frac{\nabla \mathbf{u}'' + (\nabla \mathbf{u}'')^t}{2} \right| \right\rangle
\end{aligned} \tag{4.69}$$

The first element of the production term originates a main contribution to the final equation, plus two other sub-terms, for the dynamic closure:

$$\frac{2}{\phi^2}\left\langle \underline{\nu_t} \right\rangle \left| \frac{\langle \nabla \mathbf{u} \rangle + \left\langle (\nabla \mathbf{u})^t \right\rangle}{2} \right|^2 =$$
$$\frac{2}{\phi^2}\left\langle \underline{\nu_t} \right\rangle \left| \frac{\nabla \langle \mathbf{u} \rangle + (\nabla \langle \mathbf{u} \rangle)^t}{2} + \frac{1}{2V}\int_{\partial V_{f-\mathrm{DY}}} \mathbf{u}\,\mathbf{dS} + \frac{1}{2V}\int_{\partial V_{f-\mathrm{DY}}} (\mathbf{u}\,\mathbf{dS})^t \right|^2 =$$
$$\frac{2}{\phi^2}\left\langle \underline{\nu_t} \right\rangle \left| \frac{\nabla \langle \mathbf{u} \rangle + (\nabla \langle \mathbf{u} \rangle)^t}{2} \right|^2$$
$$+ \frac{2}{\phi^2}\left\langle \underline{\nu_t} \right\rangle \left| \frac{1}{2V}\int_{\partial V_{f-\mathrm{DY}}} \mathbf{u}\,\mathbf{dS} + \frac{1}{2V}\int_{\partial V_{f-\mathrm{DY}}} (\mathbf{u}\,\mathbf{dS})^t \right|^2$$
$$+ \frac{4}{\phi^2}\left\langle \underline{\nu_t} \right\rangle \left| \frac{\nabla \langle \mathbf{u} \rangle + (\nabla \langle \mathbf{u} \rangle)^t}{2} \right| : \left| \frac{1}{2V}\int_{\partial V_{f-\mathrm{DY}}} \mathbf{u}\,\mathbf{dS} + \frac{1}{2V}\int_{\partial V_{f-\mathrm{DY}}} (\mathbf{u}\,\mathbf{dS})^t \right| \quad (4.70)$$

Note how the second and third elements vanish when the porous structures are static, because the velocity of the interface is zero.

Going back to Eq. 4.69, the second term does not need to be expanded, while the last one does:

$$\frac{4}{\phi}\left| \frac{\langle \nabla \mathbf{u} \rangle + \left\langle (\nabla \mathbf{u})^t \right\rangle}{2} \right| : \left\langle \nu_t'' \left| \frac{\nabla \mathbf{u}'' + (\nabla \mathbf{u}'')^t}{2} \right| \right\rangle =$$
$$\frac{4}{\phi}\left| \frac{\nabla \langle \mathbf{u} \rangle + (\nabla \langle \mathbf{u} \rangle)^t}{2} + \frac{1}{2V}\int_{\partial V_{f-\mathrm{DY}}} \mathbf{u}\,\mathbf{dS} + \frac{1}{2V}\int_{\partial V_{f-\mathrm{DY}}} (\mathbf{u}\,\mathbf{dS})^t \right| :$$
$$\left\langle \nu_t'' \left| \frac{\nabla \mathbf{u}'' + (\nabla \mathbf{u}'')^t}{2} \right| \right\rangle =$$
$$\frac{4}{\phi}\left| \frac{\nabla \langle \mathbf{u} \rangle + (\nabla \langle \mathbf{u} \rangle)^t}{2} \right| : \left\langle \nu_t'' \left| \frac{\nabla \mathbf{u}'' + (\nabla \mathbf{u}'')^t}{2} \right| \right\rangle$$
$$+ \frac{4}{\phi}\left| \frac{1}{2V}\int_{\partial V_{f-\mathrm{DY}}} \mathbf{u}\,\mathbf{dS} + \frac{1}{2V}\int_{\partial V_{f-\mathrm{DY}}} (\mathbf{u}\,\mathbf{dS})^t \right| : \left\langle \nu_t'' \left| \frac{\nabla \mathbf{u}'' + (\nabla \mathbf{u}'')^t}{2} \right| \right\rangle \quad (4.71)$$

Gathering all the contributions:

$$\begin{aligned}\langle F_k\rangle = \frac{2}{\phi^2}\langle\nu_t\rangle\left|\frac{\nabla\langle\mathbf{u}\rangle+(\nabla\langle\mathbf{u}\rangle)^t}{2}\right|^2 + \frac{2}{\phi^2}\langle\nu_t'^*\rangle\left|\frac{\nabla\langle\mathbf{u}\rangle+(\nabla\langle\mathbf{u}\rangle)^t}{2}\right|^2 \\ + \frac{2}{\phi^2}\langle\underline{\nu_t}\rangle\left|\frac{1}{2V}\int_{\partial V_{f-\mathrm{DY}}}\mathbf{u}\,\mathbf{dS}+\frac{1}{2V}\int_{\partial V_{f-\mathrm{DY}}}(\mathbf{u}\,\mathbf{dS})^t\right|^2 \\ + \frac{4}{\phi^2}\langle\underline{\nu_t}\rangle\left|\frac{\nabla\langle\mathbf{u}\rangle+(\nabla\langle\mathbf{u}\rangle)^t}{2}\right| : \left|\frac{1}{2V}\int_{\partial V_{f-\mathrm{DY}}}\mathbf{u}\,\mathbf{dS}+\frac{1}{2V}\int_{\partial V_{f-\mathrm{DY}}}(\mathbf{u}\,\mathbf{dS})^t\right| \\ + \frac{2}{\phi}\langle\nu_t\rangle\left\langle\left|\frac{\nabla\mathbf{u}''+(\nabla\mathbf{u}'')^t}{2}\right|^2\right\rangle \\ + \frac{4}{\phi}\left|\frac{\nabla\langle\mathbf{u}\rangle+(\nabla\langle\mathbf{u}\rangle)^t}{2}\right| : \left\langle\nu_t''\left|\frac{\nabla\mathbf{u}''+(\nabla\mathbf{u}'')^t}{2}\right|\right\rangle \\ + \frac{4}{\phi}\left|\frac{1}{2V}\int_{\partial V_{f-\mathrm{DY}}}\mathbf{u}\,\mathbf{dS}+\frac{1}{2V}\int_{\partial V_{f-\mathrm{DY}}}(\mathbf{u}\,\mathbf{dS})^t\right| : \left\langle\nu_t''\left|\frac{\nabla\mathbf{u}''+(\nabla\mathbf{u}'')^t}{2}\right|\right\rangle \quad (4.72)\end{aligned}$$

Only one term of the production contribution will be included in the final k equation. The rest of them, as they cannot be simulated, have to be accounted for as closure terms. The previous equation can be reformulated as:

$$\langle F_k\rangle = \frac{2}{\phi^2}\langle\nu_t\rangle\left|\frac{\nabla\langle\mathbf{u}\rangle+(\nabla\langle\mathbf{u}\rangle)^t}{2}\right|^2 + \langle F_k\rangle_{[CTST]} + \langle F_k\rangle_{[CTDY]} \quad (4.73)$$

where $\langle F_k\rangle_{[CTDY]}$ represents all the terms that include the integrals, and $\langle F_k\rangle_{[CTST]}$ the rest of them.

Next comes the volume averaging process for the ϵ–equation, term by term. Following the same procedure, the advection terms yield a result analogous to the previous one:

$$\begin{aligned}\left\langle\frac{\partial\epsilon}{\partial t}\right\rangle + \langle\nabla\cdot\,(\epsilon\,\mathbf{u})\rangle - \langle\epsilon\nabla\mathbf{u}\rangle = \\ \frac{\partial\langle\epsilon\rangle}{\partial t} + \nabla\cdot\left(\frac{1}{\phi}\langle\epsilon\rangle\langle\mathbf{u}\rangle\right) + \nabla\cdot\langle\epsilon''\mathbf{u}''\rangle - \langle\epsilon''\nabla\cdot\mathbf{u}''\rangle \quad (4.74)\end{aligned}$$

The diffusion term calculation is identical:

$$\left\langle \nabla \cdot \left[\left(\nu + \frac{\nu_t}{\sigma_\epsilon} \right) \nabla \epsilon \right] \right\rangle = \langle \nabla \cdot \left[\nu \nabla \epsilon \right] \rangle + \left\langle \nabla \cdot \left[\frac{\nu_t}{\sigma_\epsilon} \nabla \epsilon \right] \right\rangle =$$
$$\nabla \cdot \left(\nu \nabla \langle \epsilon \rangle \right) + \nabla \cdot \left(\nu \frac{1}{V} \int_{\partial V_{f-\mathrm{DY}}} \epsilon \, \mathbf{dS} \right) + \frac{1}{V} \int_{\partial V_f} \nu \nabla \epsilon \cdot \mathbf{dS}$$
$$+ \nabla \cdot \left(\frac{1}{\phi} \frac{\langle \underline{\nu_t} \rangle}{\sigma_\epsilon} \nabla \langle \epsilon \rangle \right) + \nabla \cdot \left(\frac{1}{\phi} \frac{\langle \underline{\nu_t} \rangle}{\sigma_\epsilon} \frac{1}{V} \int_{\partial V_{f-\mathrm{DY}}} \epsilon \, \mathbf{dS} \right)$$
$$+ \nabla \cdot \left(\frac{\nu_t''}{\sigma_\epsilon} \nabla \epsilon'' \right) + \frac{1}{V} \int_{\partial V_f} \frac{\nu_t}{\sigma_\epsilon} \nabla \epsilon \cdot \mathbf{dS} \quad (4.75)$$

Some differences arise on the volume averaging of the dissipation term, due to the different structure, but Eq. A.24 can be applied, similarly to Eq. 4.65:

$$\langle \beta_\epsilon \epsilon \rangle = \left\langle C_{\epsilon_2} \frac{\epsilon^2}{k} \right\rangle =$$
$$C_{\epsilon_2} \frac{\langle \epsilon \rangle^2}{\langle k \rangle} + C_{\epsilon_2} \phi \frac{\langle \epsilon'' \epsilon'' \rangle}{\langle k \rangle} - 2\, C_{\epsilon_2} \phi \frac{\langle \epsilon \rangle \langle k'' \epsilon'' \rangle}{\langle k \rangle^2} + C_{\epsilon_2} \phi \frac{\langle \epsilon \rangle^2 \langle k'' k'' \rangle}{\langle k \rangle^3} \quad (4.76)$$

Finally, the production term also resembles the previous one. Eq. A.13 is applied up to the second order terms, without decomposing ν_t, being the second term a quotient $(\frac{\epsilon}{k})$ and the third one a squared variable $(\mathbf{S}^2)$.

$$\langle F_\epsilon \rangle = \left\langle 2 C_{\epsilon_1} \nu_t \frac{\epsilon}{k} \mathbf{S}^2 \right\rangle =$$
$$\frac{2 C_{\epsilon_1}}{\phi^2} \langle \underline{\nu_t} \rangle \left\langle \frac{\epsilon}{\underline{k}} \right\rangle \langle \underline{\mathbf{S}^2} \rangle + \frac{2 C_{\epsilon_1}}{\phi} \langle \nu_t \rangle \left\langle \left(\frac{\epsilon}{k} \right)'' \left(\mathbf{S}^2 \right)'' \right\rangle$$
$$+ \frac{2 C_{\epsilon_1}}{\phi} \left\langle \frac{\epsilon}{k} \right\rangle \left\langle \nu_t'' \left(\mathbf{S}^2 \right)'' \right\rangle + \frac{2 C_{\epsilon_1}}{\phi} \langle \mathbf{S}^2 \rangle \left\langle \nu_t'' \left(\frac{\epsilon}{k} \right)'' \right\rangle \quad (4.77)$$

The four terms are treated independently. First element:

$$\frac{2C_{\epsilon_1}}{\phi^2}\left\langle \underline{\nu_t}\right\rangle \left\langle \frac{\epsilon}{\underline{k}}\right\rangle \left\langle \underline{\mathbf{S}^2}\right\rangle = \frac{2C_{\epsilon_1}}{\phi^2}\left\langle \nu_t\right\rangle \frac{\left\langle \epsilon\right\rangle}{\left\langle k\right\rangle}\left\langle \mathbf{S}\right\rangle^2 + \frac{2C_{\epsilon_1}}{\phi^2}\left\langle \nu_t'^*\right\rangle \frac{\left\langle \epsilon\right\rangle}{\left\langle k\right\rangle}\left\langle \mathbf{S}\right\rangle^2 + \frac{2C_{\epsilon_1}}{\phi}\left\langle \nu_t\right\rangle \frac{\left\langle \epsilon\right\rangle}{\left\langle k\right\rangle}\left\langle \left(\mathbf{S}''\right)^2\right\rangle - \frac{2C_{\epsilon_1}}{\phi}\left\langle \nu_t\right\rangle \left\langle \mathbf{S}\right\rangle^2 \frac{\left\langle \epsilon'' k''\right\rangle}{\left\langle k\right\rangle^2} + \frac{2C_{\epsilon_1}}{\phi}\left\langle \nu_t\right\rangle \left\langle \mathbf{S}\right\rangle^2 \frac{\left\langle \epsilon\right\rangle \left\langle k'' k''\right\rangle}{\left\langle k\right\rangle^3} \quad (4.78)$$

Noting that

$$\left\langle \mathbf{S}\right\rangle = \left|\frac{\left\langle \nabla \mathbf{u}\right\rangle + \left\langle \left(\nabla \mathbf{u}\right)^t\right\rangle}{2}\right| = \left|\frac{\nabla\left\langle \mathbf{u}\right\rangle + \left(\nabla\left\langle \mathbf{u}\right\rangle\right)^t}{2}\right| + \left|\frac{1}{2V}\int_{\partial V_{f-\mathrm{DY}}} \mathbf{u}\,\mathbf{dS} + \frac{1}{2V}\int_{\partial V_{f-\mathrm{DY}}} \left(\mathbf{u}\,\mathbf{dS}\right)^t\right| \quad (4.79)$$

the expression continues to grow up resulting in 13 terms:

$$
\begin{aligned}
\frac{2C_{\epsilon_1}}{\phi^2}\left\langle \underline{\nu_t}\right\rangle \left\langle \frac{\epsilon}{\underline{k}}\right\rangle \left\langle \underline{\mathbf{S}^2}\right\rangle = \\
&\frac{2C_{\epsilon_1}}{\phi^2}\left\langle \nu_t\right\rangle \frac{\langle\epsilon\rangle}{\langle k\rangle}\left|\frac{\nabla\left\langle \mathbf{u}\right\rangle + \left(\nabla\left\langle \mathbf{u}\right\rangle\right)^t}{2}\right|^2 + \frac{4C_{\epsilon_1}}{\phi^2}\left\langle \nu_t\right\rangle \frac{\langle\epsilon\rangle}{\langle k\rangle}\left|\frac{\nabla\left\langle \mathbf{u}\right\rangle + \left(\nabla\left\langle \mathbf{u}\right\rangle\right)^t}{2}\right| : \\
&\qquad \left|\frac{1}{2V}\int_{\partial V_{f-\mathrm{DY}}} \mathbf{u}\,\mathbf{dS} + \frac{1}{2V}\int_{\partial V_{f-\mathrm{DY}}} \left(\mathbf{u}\,\mathbf{dS}\right)^t\right| \\
&\qquad + \frac{2C_{\epsilon_1}}{\phi^2}\left\langle \nu_t\right\rangle \frac{\langle\epsilon\rangle}{\langle k\rangle}\left|\frac{1}{2V}\int_{\partial V_{f-\mathrm{DY}}} \mathbf{u}\,\mathbf{dS} + \frac{1}{2V}\int_{\partial V_{f-\mathrm{DY}}} \left(\mathbf{u}\,\mathbf{dS}\right)^t\right|^2 \\
&+ \frac{2C_{\epsilon_1}}{\phi^2}\left\langle \nu_t'^*\right\rangle \frac{\langle\epsilon\rangle}{\langle k\rangle}\left|\frac{\nabla\left\langle \mathbf{u}\right\rangle + \left(\nabla\left\langle \mathbf{u}\right\rangle\right)^t}{2}\right|^2 + \frac{4C_{\epsilon_1}}{\phi^2}\left\langle \nu_t'^*\right\rangle \frac{\langle\epsilon\rangle}{\langle k\rangle}\left|\frac{\nabla\left\langle \mathbf{u}\right\rangle + \left(\nabla\left\langle \mathbf{u}\right\rangle\right)^t}{2}\right| : \\
&\qquad \left|\frac{1}{2V}\int_{\partial V_{f-\mathrm{DY}}} \mathbf{u}\,\mathbf{dS} + \frac{1}{2V}\int_{\partial V_{f-\mathrm{DY}}} \left(\mathbf{u}\,\mathbf{dS}\right)^t\right| \\
&\qquad + \frac{2C_{\epsilon_1}}{\phi^2}\left\langle \nu_t'^*\right\rangle \frac{\langle\epsilon\rangle}{\langle k\rangle}\left|\frac{1}{2V}\int_{\partial V_{f-\mathrm{DY}}} \mathbf{u}\,\mathbf{dS} + \frac{1}{2V}\int_{\partial V_{f-\mathrm{DY}}} \left(\mathbf{u}\,\mathbf{dS}\right)^t\right|^2 \\
&\qquad + \frac{2C_{\epsilon_1}}{\phi}\left\langle \nu_t\right\rangle \frac{\langle\epsilon\rangle}{\langle k\rangle}\left\langle\left|\frac{\nabla\mathbf{u"} + \left(\nabla\mathbf{u"}\right)^t}{2}\right|^2\right\rangle \\
&- \frac{2C_{\epsilon_1}}{\phi}\left\langle \nu_t\right\rangle \frac{\langle\epsilon''k''\rangle}{\langle k\rangle^2}\left|\frac{\nabla\left\langle \mathbf{u}\right\rangle + \left(\nabla\left\langle \mathbf{u}\right\rangle\right)^t}{2}\right|^2 - \frac{4C_{\epsilon_1}}{\phi}\left\langle \nu_t\right\rangle \frac{\langle\epsilon''k''\rangle}{\langle k\rangle^2}\left|\frac{\nabla\left\langle \mathbf{u}\right\rangle + \left(\nabla\left\langle \mathbf{u}\right\rangle\right)^t}{2}\right| : \\
&\qquad \left|\frac{1}{2V}\int_{\partial V_{f-\mathrm{DY}}} \mathbf{u}\,\mathbf{dS} + \frac{1}{2V}\int_{\partial V_{f-\mathrm{DY}}} \left(\mathbf{u}\,\mathbf{dS}\right)^t\right| \\
&\qquad - \frac{2C_{\epsilon_1}}{\phi}\left\langle \nu_t\right\rangle \frac{\langle\epsilon''k''\rangle}{\langle k\rangle^2}\left|\frac{1}{2V}\int_{\partial V_{f-\mathrm{DY}}} \mathbf{u}\,\mathbf{dS} + \frac{1}{2V}\int_{\partial V_{f-\mathrm{DY}}} \left(\mathbf{u}\,\mathbf{dS}\right)^t\right|^2 \\
&\qquad + \frac{2C_{\epsilon_1}}{\phi}\left\langle \nu_t\right\rangle \frac{\langle\epsilon\rangle\langle k''k''\rangle}{\langle k\rangle^3}\left|\frac{\nabla\left\langle \mathbf{u}\right\rangle + \left(\nabla\left\langle \mathbf{u}\right\rangle\right)^t}{2}\right|^2 \\
&\qquad + \frac{4C_{\epsilon_1}}{\phi}\left\langle \nu_t\right\rangle \frac{\langle\epsilon\rangle\langle k''k''\rangle}{\langle k\rangle^3}\left|\frac{\nabla\left\langle \mathbf{u}\right\rangle + \left(\nabla\left\langle \mathbf{u}\right\rangle\right)^t}{2}\right| : \\
&\qquad \left|\frac{1}{2V}\int_{\partial V_{f-\mathrm{DY}}} \mathbf{u}\,\mathbf{dS} + \frac{1}{2V}\int_{\partial V_{f-\mathrm{DY}}} \left(\mathbf{u}\,\mathbf{dS}\right)^t\right| \\
&\qquad + \frac{2C_{\epsilon_1}}{\phi}\left\langle \nu_t\right\rangle \frac{\langle\epsilon\rangle\langle k''k''\rangle}{\langle k\rangle^3}\left|\frac{1}{2V}\int_{\partial V_{f-\mathrm{DY}}} \mathbf{u}\,\mathbf{dS} + \frac{1}{2V}\int_{\partial V_{f-\mathrm{DY}}} \left(\mathbf{u}\,\mathbf{dS}\right)^t\right|^2
\end{aligned}
\tag{4.80}
$$

The second term:

$$\frac{2C_{\epsilon_1}}{\phi}\left\langle\nu_t\right\rangle\left\langle\left(\frac{\epsilon}{k}\right)''\left(\mathbf{S}^2\right)''\right\rangle=$$
$$\frac{4C_{\epsilon_1}}{\phi}\left\langle\nu_t\right\rangle\frac{1}{\left\langle k\right\rangle}\left\langle\mathbf{S}\right\rangle:\left\langle\mathbf{S}''\epsilon''\right\rangle-\frac{4C_{\epsilon_1}}{\phi}\left\langle\nu_t\right\rangle\frac{\left\langle\epsilon\right\rangle}{\left\langle k\right\rangle^2}\left\langle\mathbf{S}\right\rangle:\left\langle\mathbf{S}''k''\right\rangle=$$
$$\frac{4C_{\epsilon_1}}{\phi}\left\langle\nu_t\right\rangle\frac{1}{\left\langle k\right\rangle}\left|\frac{\nabla\left\langle\mathbf{u}\right\rangle+\left(\nabla\left\langle\mathbf{u}\right\rangle\right)^t}{2}\right|:\left\langle\left|\frac{\nabla\mathbf{u"}+\left(\nabla\mathbf{u"}\right)^t}{2}\right|\epsilon''\right\rangle$$
$$+\frac{4C_{\epsilon_1}}{\phi}\left\langle\nu_t\right\rangle\frac{1}{\left\langle k\right\rangle}\left|\frac{1}{2V}\int_{\partial V_{f-\mathrm{DY}}}\mathbf{u}\,\mathbf{dS}+\frac{1}{2V}\int_{\partial V_{f-\mathrm{DY}}}\left(\mathbf{u}\,\mathbf{dS}\right)^t\right|:$$
$$\left\langle\left|\frac{\nabla\mathbf{u"}+\left(\nabla\mathbf{u"}\right)^t}{2}\right|\epsilon''\right\rangle$$
$$-\frac{4C_{\epsilon_1}}{\phi}\left\langle\nu_t\right\rangle\frac{\left\langle\epsilon\right\rangle}{\left\langle k\right\rangle^2}\left|\frac{\nabla\left\langle\mathbf{u}\right\rangle+\left(\nabla\left\langle\mathbf{u}\right\rangle\right)^t}{2}\right|:\left\langle\left|\frac{\nabla\mathbf{u"}+\left(\nabla\mathbf{u"}\right)^t}{2}\right|k''\right\rangle$$
$$-\frac{4C_{\epsilon_1}}{\phi}\left\langle\nu_t\right\rangle\frac{\left\langle\epsilon\right\rangle}{\left\langle k\right\rangle^2}\left|\frac{1}{2V}\int_{\partial V_{f-\mathrm{DY}}}\mathbf{u}\,\mathbf{dS}+\frac{1}{2V}\int_{\partial V_{f-\mathrm{DY}}}\left(\mathbf{u}\,\mathbf{dS}\right)^t\right|:$$
$$\left\langle\left|\frac{\nabla\mathbf{u"}+\left(\nabla\mathbf{u"}\right)^t}{2}\right|k''\right\rangle \quad (4.81)$$

The third term:

$$\frac{2C_{\epsilon_1}}{\phi}\left\langle\frac{\epsilon}{k}\right\rangle\left\langle\nu_t''\left(\mathbf{S}^2\right)''\right\rangle=\frac{4C_{\epsilon_1}}{\phi}\frac{\left\langle\epsilon\right\rangle}{\left\langle k\right\rangle}\left\langle\mathbf{S}\right\rangle:\left\langle\nu_t''\mathbf{S}''\right\rangle=$$
$$\frac{4C_{\epsilon_1}}{\phi}\frac{\left\langle\epsilon\right\rangle}{\left\langle k\right\rangle}\left|\frac{\nabla\left\langle\mathbf{u}\right\rangle+\left(\nabla\left\langle\mathbf{u}\right\rangle\right)^t}{2}\right|:\left\langle\nu_t''\left|\frac{\nabla\mathbf{u"}+\left(\nabla\mathbf{u"}\right)^t}{2}\right|\right\rangle$$
$$+\frac{4C_{\epsilon_1}}{\phi}\frac{\left\langle\epsilon\right\rangle}{\left\langle k\right\rangle}\left|\frac{1}{2V}\int_{\partial V_{f-\mathrm{DY}}}\mathbf{u}\,\mathbf{dS}+\frac{1}{2V}\int_{\partial V_{f-\mathrm{DY}}}\left(\mathbf{u}\,\mathbf{dS}\right)^t\right|:$$
$$\left\langle\nu_t''\left|\frac{\nabla\mathbf{u"}+\left(\nabla\mathbf{u"}\right)^t}{2}\right|\right\rangle \quad (4.82)$$

And the fourth term:

$$\frac{2C_{\epsilon_1}}{\phi}\left\langle \mathbf{S}^2\right\rangle \left\langle \nu_t''\left(\frac{\epsilon}{k}\right)''\right\rangle =$$

$$\frac{2C_{\epsilon_1}}{\phi}\frac{1}{\langle k\rangle}\left\langle \mathbf{S}\right\rangle^2\left\langle \nu_t''\epsilon''\right\rangle - \frac{2C_{\epsilon_1}}{\phi}\frac{\langle\epsilon\rangle}{\langle k\rangle^2}\left\langle \mathbf{S}\right\rangle^2\left\langle \nu_t'' k''\right\rangle =$$

$$\frac{2C_{\epsilon_1}}{\phi}\frac{1}{\langle k\rangle}\left|\frac{\nabla\langle\mathbf{u}\rangle+(\nabla\langle\mathbf{u}\rangle)^t}{2}\right|^2\left\langle \nu_t''\epsilon''\right\rangle + \frac{4C_{\epsilon_1}}{\phi}\frac{1}{\langle k\rangle}\left|\frac{\nabla\langle\mathbf{u}\rangle+(\nabla\langle\mathbf{u}\rangle)^t}{2}\right| :$$

$$\left|\frac{1}{2V}\int_{\partial V_{f-\mathrm{DY}}}\mathbf{u}\,\mathbf{dS}+\frac{1}{2V}\int_{\partial V_{f-\mathrm{DY}}}(\mathbf{u}\,\mathbf{dS})^t\right|\left\langle \nu_t''\epsilon''\right\rangle$$

$$+\frac{2C_{\epsilon_1}}{\phi}\frac{1}{\langle k\rangle}\left|\frac{1}{2V}\int_{\partial V_{f-\mathrm{DY}}}\mathbf{u}\,\mathbf{dS}+\frac{1}{2V}\int_{\partial V_{f-\mathrm{DY}}}(\mathbf{u}\,\mathbf{dS})^t\right|^2\left\langle \nu_t''\epsilon''\right\rangle$$

$$-\frac{2C_{\epsilon_1}}{\phi}\frac{\langle\epsilon\rangle}{\langle k\rangle^2}\left|\frac{\nabla\langle\mathbf{u}\rangle+(\nabla\langle\mathbf{u}\rangle)^t}{2}\right|^2\left\langle \nu_t'' k''\right\rangle - \frac{4C_{\epsilon_1}}{\phi}\frac{\langle\epsilon\rangle}{\langle k\rangle^2}\left|\frac{\nabla\langle\mathbf{u}\rangle+(\nabla\langle\mathbf{u}\rangle)^t}{2}\right| :$$

$$\left|\frac{1}{2V}\int_{\partial V_{f-\mathrm{DY}}}\mathbf{u}\,\mathbf{dS}+\frac{1}{2V}\int_{\partial V_{f-\mathrm{DY}}}(\mathbf{u}\,\mathbf{dS})^t\right|\left\langle \nu_t'' k''\right\rangle$$

$$-\frac{2C_{\epsilon_1}}{\phi}\frac{\langle\epsilon\rangle}{\langle k\rangle^2}\left|\frac{1}{2V}\int_{\partial V_{f-\mathrm{DY}}}\mathbf{u}\,\mathbf{dS}+\frac{1}{2V}\int_{\partial V_{f-\mathrm{DY}}}(\mathbf{u}\,\mathbf{dS})^t\right|^2\left\langle \nu_t'' k''\right\rangle \quad (4.83)$$

Finally, all the terms can be gathered into a single expression:

$$\langle F_\epsilon\rangle \quad = \quad \frac{2C_{\epsilon_1}}{\phi^2}\langle\nu_t\rangle\frac{\langle\epsilon\rangle}{\langle k\rangle}\left|\frac{\nabla\langle\mathbf{u}\rangle+(\nabla\langle\mathbf{u}\rangle)^t}{2}\right|^2 \quad + \quad \langle F_\epsilon\rangle_{[CT,ST]} \quad + \quad \langle F_\epsilon\rangle_{[CT,DY]} \quad (4.84)$$

There is only one term that contributes to the main equation, the rest of them, although numerous, count as closure terms. Those elements that include the integrals are accounted for at $\langle F_\epsilon\rangle_{[CT,DY]}$, and the others in $\langle F_\epsilon\rangle_{[CT,ST]}$.

4.5.1.2 Averaged form

Joining all the terms in the volume-averaged k and ϵ equations:

$$\frac{\partial \langle k \rangle}{\partial t} + \nabla \cdot \left(\frac{1}{\phi} \langle k \rangle \langle \mathbf{u} \rangle \right) - \nabla \cdot \left[\left(\nu + \frac{1}{\phi} \frac{\langle \nu_t \rangle}{\sigma_k} \right) \nabla \langle k \rangle \right] + \langle \epsilon \rangle = \frac{2}{\phi^2} \langle \nu_t \rangle \left| \frac{\nabla \langle \mathbf{u} \rangle + (\nabla \langle \mathbf{u} \rangle)^t}{2} \right|^2 + [CT]_{k_{\mathrm{ST}}} + [CT]_{k_{\mathrm{DY}}} \quad (4.85)$$

$$\frac{\partial \langle \epsilon \rangle}{\partial t} + \nabla \cdot \left(\frac{1}{\phi} \langle \epsilon \rangle \langle \mathbf{u} \rangle \right) - \nabla \cdot \left[\left(\nu + \frac{1}{\phi} \frac{\langle \nu_t \rangle}{\sigma_k} \right) \nabla \langle \epsilon \rangle \right] + C_{\epsilon_2} \frac{\langle \epsilon \rangle^2}{\langle k \rangle} = \frac{2C_{\epsilon_1}}{\phi^2} \langle \nu_t \rangle \frac{\langle \epsilon \rangle}{\langle k \rangle} \left| \frac{\nabla \langle \mathbf{u} \rangle + (\nabla \langle \mathbf{u} \rangle)^t}{2} \right|^2 + [CT]_{\epsilon_{\mathrm{ST}}} + [CT]_{\epsilon_{\mathrm{DY}}} \quad (4.86)$$

where:

$$[CT]_{k_{\mathrm{ST}}} = \langle k'' \nabla \cdot \mathbf{u}'' \rangle - \nabla \cdot \langle k'' \mathbf{u}'' \rangle + \frac{1}{V} \int_{\partial V_{f-\mathrm{ST}}} \left(\nu + \frac{\nu_t}{\sigma_k} \right) \nabla k \cdot \mathbf{dS} + \nabla \cdot \left(\frac{1}{\phi} \frac{\langle \nu_t'^* \rangle}{\sigma_k} \nabla \langle k \rangle \right) + \nabla \cdot \left(\frac{\nu_t''}{\sigma_k} \nabla k'' \right) + \langle F_k \rangle_{[CT,ST]} \quad (4.87)$$

$$[CT]_{k_{\mathrm{DY}}} = \nabla \cdot \left[\left(\nu + \frac{1}{\phi} \frac{\langle \nu_t \rangle}{\sigma_k} \right) \frac{1}{V} \int_{\partial V_{f-\mathrm{DY}}} k \, \mathbf{dS} \right] + \frac{1}{V} \int_{\partial V_{f-\mathrm{DY}}} \left(\nu + \frac{\nu_t}{\sigma_k} \right) \nabla k \cdot \mathbf{dS} + \langle F_k \rangle_{[CT,DY]} \quad (4.88)$$

and

$$[CT]_{\epsilon_{\mathrm{ST}}} = \langle \epsilon'' \nabla \cdot \mathbf{u}'' \rangle - \nabla \cdot \langle \epsilon'' \mathbf{u}'' \rangle + \frac{1}{V} \int_{\partial V_{f-\mathrm{ST}}} \left(\nu + \frac{\nu_t}{\sigma_\epsilon} \right) \nabla \epsilon \cdot \mathbf{dS} + \nabla \cdot \left(\frac{1}{\phi} \frac{\langle \nu_t'^* \rangle}{\sigma_\epsilon} \nabla \langle \epsilon \rangle \right) + \nabla \cdot \left(\frac{\nu_t''}{\sigma_\epsilon} \nabla \epsilon'' \right) - C_{\epsilon_2} \phi \frac{\langle \epsilon'' \epsilon'' \rangle}{\langle k \rangle} + 2\, C_{\epsilon_2} \phi \frac{\langle \epsilon \rangle \langle k'' \epsilon'' \rangle}{\langle k \rangle^2} - C_{\epsilon_2} \phi \frac{\langle \epsilon \rangle^2 \langle k'' k'' \rangle}{\langle k \rangle^3} + \langle F_\epsilon \rangle_{[CT,ST]} \quad (4.89)$$

$$[CT]_{\epsilon_{\mathrm{DY}}} = \nabla \cdot \left[\left(\nu + \frac{1}{\phi} \frac{\langle \nu_t \rangle}{\sigma_\epsilon} \right) \frac{1}{V} \int_{\partial V_{f-\mathrm{DY}}} \epsilon \, \mathbf{dS} \right] + \frac{1}{V} \int_{\partial V_{f-\mathrm{DY}}} \left(\nu + \frac{\nu_t}{\sigma_\epsilon} \right) \nabla \epsilon \cdot \mathbf{dS} + \langle F_\epsilon \rangle_{[CTDY]} \quad (4.90)$$

4.5.1.3 Closure model

Similarly to what occurs when volume averaging the RANS equations, averaging the $k - \epsilon$ turbulence model produces a number of terms that cannot be solved, and have to be accounted for using a closure model.

Nakayama and Kuwahara (1999) presented a study in which a correlation between the $k - \epsilon$ closure terms and the flow and porous medium characteristics was obtained. The closure model proposed is as follows:

$$[CT]_{k_{\mathrm{ST}}} = \epsilon_\infty \quad (4.91)$$

$$[CT]_{\epsilon_{\mathrm{ST}}} = C_{\epsilon_2} \frac{\epsilon_\infty^2}{k_\infty} \quad (4.92)$$

with ϵ_∞ and k_∞ being:

$$k_\infty = 3.7 \frac{1 - \phi}{\sqrt{\phi}} \left| \langle u_i \rangle \right|^2 \quad (4.93)$$

$$\epsilon_\infty = 39 \frac{(1 - \phi)^{\frac{5}{2}}}{\phi} \frac{\left| \langle u_i \rangle \right|^3}{D_{50}} \quad (4.94)$$

Nakayama and Kuwahara (1999) experiments were carried out for static porous media. To the author's knowledge there is currently no closure model available in literature for the case in which dynamic porosity exists. Therefore, $[CT]_{k_{\mathrm{DY}}}$ and $[CT]_{\epsilon_{\mathrm{DY}}}$ would need

to be left out, disregarding the turbulence enhancement caused by the movement of the particles by the moment.

4.5.2 The $k-\omega$ SST model

$k-\omega$ SST is a turbulence model introduced by Menter (1994) that combines the best features of $k-\epsilon$ and $k-\omega$ models. A complete description can be found in Section 2.3.2.2. Here, a full rederivation of del Jesus (2011) work is made, taking into account a time-varying porosity.

4.5.2.1 Volume averaging

The volume averaging process starts with the k–equation. This is similar enough to $k-\epsilon$'s k–equation to show the final result only for most of the terms.

A simplification has been made to avoid excessive complexity which would yield a great number of high order terms. This artefact is to consider σ_k, σ_ω, β and γ as constant within a given control volume. The main result is that some of the terms can be treated as shown in the previous $k-\epsilon$ averaging process.

First come the advection terms:

$$\left\langle \frac{\partial k}{\partial t} \right\rangle + \langle \nabla \cdot \ (k\,\mathbf{u}) \rangle - \langle k \nabla \mathbf{u} \rangle = \frac{\partial \langle k \rangle}{\partial t} + \nabla \cdot \left(\frac{1}{\phi} \langle k \rangle \langle \mathbf{u} \rangle \right) + \nabla \cdot \langle k'' \mathbf{u}'' \rangle - \langle k'' \nabla \cdot \mathbf{u}'' \rangle \quad (4.95)$$

The diffusion term calculation is also quite similar:

$$\langle \nabla\cdot\ [(\nu+\sigma_k\,\nu_t)\,\nabla k]\rangle = \langle \nabla\cdot\ [\nu\nabla k]\rangle + \langle \nabla\cdot\ [\sigma_k\,\nu_t\nabla k]\rangle =$$
$$\nabla\cdot(\nu\nabla\langle k\rangle) + \nabla\cdot\left(\nu\frac{1}{V}\int_{\partial V_{f-\mathrm{DY}}} k\,\mathbf{dS}\right) + \frac{1}{V}\int_{\partial V_f}\nu\nabla k\cdot\mathbf{dS}$$
$$+\nabla\cdot\left(\frac{1}{\phi}\sigma_k\,\langle\nu_t\rangle\,\nabla\langle k\rangle\right) + \nabla\cdot\left(\frac{1}{\phi}\sigma_k\ \langle\nu_t\rangle\,\frac{1}{V}\int_{\partial V_{f-\mathrm{DY}}} k\,\mathbf{dS}\right)$$
$$+\nabla\cdot(\sigma_k\,\nu_t''\nabla k'') + \frac{1}{V}\int_{\partial V_f}\sigma_k\,\nu_t\nabla k\cdot\mathbf{dS} \quad (4.96)$$

Since the expression of ν_t is different from $k-\epsilon$ model, the volume averaging also changes. Moreover, using a *maximum* function between two values doubles the amount of work needed, as either term can be taken. The first is straightforward:

$$\langle\nu_{tA}\rangle = \left\langle\frac{k}{\omega}\right\rangle \quad (4.97)$$

$$\langle\nu_{tA}\rangle = \phi\frac{\langle k\rangle}{\langle\omega\rangle} - \phi^2\frac{\langle k''\omega''\rangle}{\langle\omega\rangle^2} + \phi^2\frac{\langle k\rangle\,\langle\omega''\omega''\rangle}{\langle\omega\rangle^3} \quad (4.98)$$

$$\nu_{tA}'' = \phi\frac{k''}{\langle\omega\rangle} + \phi\frac{\langle k\rangle\,\omega''}{\langle\omega\rangle^2} \quad (4.99)$$

The second is extremely complex. Hence, only the main part (not the spatial fluctuations or second order terms) are going to be obtained, because they will end up in the closure part:

$$\langle\nu_{tB}\rangle = \left\langle\frac{a_1\,k}{F_2\,\sqrt{2}\left|\frac{\nabla\mathbf{u}+(\nabla\mathbf{u})^t}{2}\right|}\right\rangle \quad (4.100)$$

$$\langle\nu_{tB}\rangle + \nu_{tB}'' = \phi\frac{a_1\ \langle k\rangle}{F_2^+\,\sqrt{2}\left|\frac{\nabla\langle\mathbf{u}\rangle+(\nabla\langle\mathbf{u}\rangle)^t}{2}\right|} + \nu_{tB}'' \quad (4.101)$$

It can be noted that function F_2 has not been volume averaged per se, but taken as a constant instead and changed to another function F_2^+. This is an implication of F_2 being a blending function that ranges from 0 to 1. The same situation occurs for F_1. However, since the equations will likely be solved in volume-averaged variables, the arguments of

the hyperbolic tangents yielding F_1^+ and F_2^+ will be volume-averaged afterwards. It has to be acknowledged that this procedure modifies the nature of the blending, but there is no evident way around in order to maintain the 0 and 1 bounds.

Next comes the dissipation coefficient:

$$\langle \beta_k k \rangle = \langle \beta^* k\, \omega \rangle = \frac{\beta^*}{\phi} \langle k \rangle \langle \omega \rangle + \beta^* \langle k'' \omega'' \rangle \tag{4.102}$$

And finally the production term, also double due to the *minimum* function. The first option is the same as in $k - \epsilon$:

$$\langle F_{kA} \rangle = \left\langle 2\nu_t \left| \frac{\nabla \mathbf{u} + (\nabla \mathbf{u})^t}{2} \right|^2 \right\rangle \tag{4.103}$$

the reader is referred to the result shown in Eq. 4.73. Alternatively, the second option is:

$$\langle F_{kB} \rangle = \langle c_1\, \beta^* k\, \omega \rangle = \frac{c_1\, \beta^*}{\phi} \langle k \rangle \langle \omega \rangle + c_1\, \beta^* \langle k'' \omega'' \rangle \tag{4.104}$$

Next comes the volume averaging of the ω–equation. Following an identical procedure, the advection terms yield a result analogous to the previous one:

$$\left\langle \frac{\partial \omega}{\partial t} \right\rangle + \langle \nabla \cdot\ (\omega\, \mathbf{u}) \rangle - \langle \omega \nabla \mathbf{u} \rangle = \frac{\partial \langle \omega \rangle}{\partial t} + \nabla \cdot \left(\frac{1}{\phi} \langle \omega \rangle \langle \mathbf{u} \rangle \right) + \nabla \cdot \langle \omega'' \mathbf{u}'' \rangle - \langle \omega'' \nabla \cdot \mathbf{u}'' \rangle \tag{4.105}$$

The diffusion term calculation is also alike:

$$\begin{aligned} \langle \nabla \cdot\ [(\nu + \sigma_\omega\, \nu_t)\, \nabla \omega] \rangle = \langle \nabla \cdot\ [\nu \nabla \omega] \rangle + \langle \nabla \cdot\ [\sigma_\omega\, \nu_t \nabla \omega] \rangle = \\ \nabla \cdot (\nu \nabla \langle \omega \rangle) + \nabla \cdot \left(\nu \frac{1}{V} \int_{\partial V_{f-\mathrm{DY}}} \omega\, \mathbf{dS} \right) + \frac{1}{V} \int_{\partial V_f} \nu \nabla \omega \cdot \mathbf{dS} \\ + \nabla \cdot \left(\frac{1}{\phi} \sigma_\omega \langle \nu_t \rangle \nabla \langle \omega \rangle \right) + \nabla \cdot \left(\frac{1}{\phi} \sigma_\omega\ \langle \nu_t \rangle \frac{1}{V} \int_{\partial V_{f-\mathrm{DY}}} \omega\, \mathbf{dS} \right) \\ + \nabla \cdot (\sigma_\omega\, \nu_t'' \nabla \omega'') + \frac{1}{V} \int_{\partial V_f} \sigma_\omega\, \nu_t \nabla \omega \cdot \mathbf{dS} \end{aligned} \tag{4.106}$$

The cross-diffusion term is also quite complex, so only the main contribution is going to be derived. The spatial fluctuations would be accounted for in the closure terms.

$$\begin{aligned}\langle (1-F_1)\ \mathrm{CD}_{k\omega}\rangle = \left(1-F_1^+\right)\langle \mathrm{CD}_{k\omega}\rangle = \\ \left(1-F_1^+\right) max\left(\left\langle \frac{2\,\sigma_{\omega_2}}{\omega}\nabla k\cdot\nabla\omega\right\rangle ; 10^{-10}\right) = \\ \left(1-F_1^+\right) max\left(2\,\sigma_{\omega_2}\frac{\nabla\langle k\rangle\cdot\nabla\langle\omega\rangle}{\langle\omega\rangle}; 10^{-10}\right)\end{aligned} \tag{4.107}$$

The dissipation coefficient comes next:

$$\langle \beta_\omega \omega\rangle = \left\langle \beta\,\omega^2\right\rangle = \frac{\beta}{\phi}\langle\omega\rangle^2 + \beta\langle\omega''\omega''\rangle \tag{4.108}$$

And finally the production term, very similar to previous results:

$$\begin{aligned}\langle F_\omega\rangle = \left\langle 2\gamma\left|\frac{\nabla\mathbf{u}+(\nabla\mathbf{u})^t}{2}\right|^2\right\rangle = \\ \frac{2\gamma}{\phi}\left\langle\left|\frac{\nabla\mathbf{u}+(\nabla\mathbf{u})^t}{2}\right|\right\rangle^2 + 2\gamma\left\langle\left|\frac{\nabla\mathbf{u''}+(\nabla\mathbf{u''})^t}{2}\right|^2\right\rangle = \\ \frac{2\gamma}{\phi}\left|\frac{\langle\nabla\mathbf{u}\rangle+\left\langle(\nabla\mathbf{u})^t\right\rangle}{2}\right|^2 + 2\gamma\left\langle\left|\frac{\nabla\mathbf{u''}+(\nabla\mathbf{u''})^t}{2}\right|^2\right\rangle = \\ \frac{2\gamma}{\phi}\left|\frac{\nabla\langle\mathbf{u}\rangle+(\nabla\langle\mathbf{u}\rangle)^t}{2}\right|^2 + \frac{4\gamma}{\phi}\left|\frac{\nabla\langle\mathbf{u}\rangle+(\nabla\langle\mathbf{u}\rangle)^t}{2}\right| : \\ \left|\frac{1}{2V}\int_{\partial V_{f-\mathrm{DY}}}\mathbf{u}\,\mathbf{dS} + \frac{1}{2V}\int_{\partial V_{f-\mathrm{DY}}}(\mathbf{u}\,\mathbf{dS})^t\right| \\ + \frac{2\gamma}{\phi}\left|\frac{1}{2V}\int_{\partial V_{f-\mathrm{DY}}}\mathbf{u}\,\mathbf{dS} + \frac{1}{2V}\int_{\partial V_{f-\mathrm{DY}}}(\mathbf{u}\,\mathbf{dS})^t\right|^2 \\ + 2\gamma\left\langle\left|\frac{\nabla\mathbf{u''}+(\nabla\mathbf{u''})^t}{2}\right|^2\right\rangle\end{aligned} \tag{4.109}$$

Before merging all the terms, some special elements still need to be volume-averaged (Eqs. 2.25 and 2.27). No spatial fluctuations are considered, though.

$$\langle arg_{1A} \rangle = \left\langle \frac{\sqrt{k}}{\beta^* \omega \, y} \right\rangle = \phi \left\langle \frac{\sqrt{\langle k \rangle^f}}{\beta^* y \, \langle \omega \rangle^f} \right\rangle^f = \phi \frac{\sqrt{\frac{1}{\phi} \langle k \rangle}}{\beta^* y \frac{1}{\phi} \langle \omega \rangle} = \phi^{\frac{3}{2}} \frac{\sqrt{\langle k \rangle}}{\beta^* y \, \langle \omega \rangle} \tag{4.110}$$

$$\langle arg_{1B} \rangle = \left\langle \frac{500 \, \nu}{\omega \, y^2} \right\rangle = \phi \left\langle \frac{500 \, \nu}{\langle \omega \rangle^f \; y^2} \right\rangle^f = \phi \frac{500 \, \nu}{\frac{1}{\phi} \langle \omega \rangle \; y^2} = \phi^2 \frac{500 \, \nu}{\langle \omega \rangle \; y^2} \tag{4.111}$$

$$\langle arg_{1C} \rangle = \left\langle \frac{4 \, \sigma_{\omega_2} k}{\mathrm{CD}_{k\omega} \, y^2} \right\rangle = \phi \left\langle \frac{4 \, \sigma_{\omega_2} \langle k \rangle^f}{\langle \mathrm{CD}_{k\omega} \rangle^f \; y^2} \right\rangle^f = \phi \frac{4 \, \sigma_{\omega_2} \langle k \rangle}{\langle \mathrm{CD}_{k\omega} \rangle \; y^2} \tag{4.112}$$

$$\langle arg_{2A} \rangle = \left\langle \frac{2\sqrt{k}}{\beta^* \omega \, y} \right\rangle = 2 \, \phi^{\frac{3}{2}} \frac{\sqrt{\langle k \rangle}}{\beta^* y \, \langle \omega \rangle} \tag{4.113}$$

$$\langle arg_{2B} \rangle = \left\langle \frac{500 \, \nu}{\omega \, y^2} \right\rangle = \phi^2 \frac{500 \, \nu}{\langle \omega \rangle \; y^2} \tag{4.114}$$

4.5.2.2 Averaged form

Gathering all the terms in the volume-averaged k and ω SST equations:

$$\frac{\partial \langle k \rangle}{\partial t} + \nabla \cdot \left(\frac{1}{\phi} \langle k \rangle \langle \mathbf{u} \rangle \right) - \nabla \cdot \left[\left(\nu + \frac{\sigma_k}{\phi} \langle \nu_t \rangle \right) \nabla \langle k \rangle \right] + \frac{\beta^*}{\phi} \langle k \rangle \langle \omega \rangle = min \left[\frac{2}{\phi^2} \langle \nu_t \rangle \left| \frac{\nabla \langle \mathbf{u} \rangle + (\nabla \langle \mathbf{u} \rangle)^t}{2} \right|^2 ; \frac{c_1 \, \beta^*}{\phi} \langle k \rangle \langle \omega \rangle \right] + [CT]_k \tag{4.115}$$

$$\frac{\partial \langle \omega \rangle}{\partial t} + \nabla \cdot \left(\frac{1}{\phi} \langle \omega \rangle \langle \mathbf{u} \rangle \right) - \nabla \cdot \left[\left(\nu + \frac{\sigma_\omega}{\phi} \langle \nu_t \rangle \right) \nabla \langle \omega \rangle \right] - \left(1 - F_1^+ \right) \langle \mathrm{CD}_{k\omega} \rangle + \frac{\beta}{\phi} \langle \omega \rangle^2 = \frac{2}{\phi} \gamma \left| \frac{\nabla \langle \mathbf{u} \rangle + (\nabla \langle \mathbf{u} \rangle)^t}{2} \right|^2 \tag{4.116}$$

For which:

$$\langle \nu_t \rangle = min \left[\phi \frac{\langle k \rangle}{\langle \omega \rangle} ; \phi \frac{a_1 \; \langle k \rangle}{F_2^+ \sqrt{2} \left| \frac{\nabla \langle \mathbf{u} \rangle + (\nabla \langle \mathbf{u} \rangle)^t}{2} \right|} \right] \tag{4.117}$$

$$\langle arg_1 \rangle = min\left\{ min\left[max\left(\phi^{\frac{3}{2}} \frac{\sqrt{\langle k \rangle}}{\beta^* y \langle \omega \rangle}; \phi^2 \frac{500\,\nu}{\langle \omega \rangle\ y^2} \right); \phi \frac{4\,\sigma_{\omega_2} \langle k \rangle}{\langle \mathrm{CD}_{k\omega} \rangle\ y^2} \right]; 10 \right\} \tag{4.118}$$

$$\langle \mathrm{CD}_{k\omega} \rangle = max\left(2\,\sigma_{\omega_2} \frac{\nabla \langle k \rangle \cdot \nabla \langle \omega \rangle}{\langle \omega \rangle}; 10^{-10} \right) \tag{4.119}$$

$$\langle arg_2 \rangle = min\left[max\left(2\,\phi^{\frac{3}{2}} \frac{\sqrt{\langle k \rangle}}{\beta^* y \langle \omega \rangle}; \phi^2 \frac{500\,\nu}{\langle \omega \rangle\ y^2} \right); 100 \right] \tag{4.120}$$

The new blending functions still take values from 0 to 1, and are calculated as follows: $F_1^+ = \tanh(\langle arg_1 \rangle^4)$ and $F_2^+ = \tanh(\langle arg_2 \rangle^2)$. Furthermore, the blended variables (i.e. σ_k, σ_ω, β, γ) are now calculated as: $\psi_n = F_1^+\,\psi_1 + (1 - F_1^+)\,\psi_2$

4.5.2.3 Closure

Unlike for $k - \epsilon$, no closure model is available in literature for $k - \omega$ SST. Therefore, $[CT]_k$ and $[CT]_\omega$ will not be accounted for in the following work, disregarding both the turbulence enhancement caused by the static porous media and the movement of the sediment particles.

4.6 Equations discussion

In this section, the new set of VARANS equations derived in this work is compared to others, available in literature. The discussion will be centred on the general form of the equations, disregarding turbulence models or closure terms.

It must be noted that for any of the sets of the equations presented, any of the closure models available in literature could be applied and a correct calibration of the friction factors will yield very similar solutions.

First, the present VARANS derivation, recalled from Eqs. 4.30 and 4.53 and slightly rearranged is shown:

$$\frac{\partial \phi_{\mathrm{DY}}}{\partial t} + \frac{\partial \langle u_i \rangle}{\partial x_i} = 0 \tag{4.121}$$

$$\frac{1}{\phi}\frac{\partial \rho \langle u_i \rangle}{\partial t} + \frac{\langle u_j \rangle}{\phi}\frac{\partial}{\partial x_j}\left[\frac{1}{\phi}\rho \langle u_i \rangle\right] = -\frac{\partial \langle p \rangle^f}{\partial x_i} + \rho g_i + \frac{1}{\phi}\frac{\partial}{\partial x_j}\left[\mu \frac{\partial \langle u_i \rangle}{\partial x_j}\right] - [CT] \tag{4.122}$$

Chronologically, the first work to be reviewed is Liu et al. (1999), also used in Hsu and Liu (2002), where a more sophisticate turbulence treatment was introduced:

$$\frac{\partial \langle u_i \rangle}{\partial x_i} = 0 \tag{4.123}$$

$$\frac{1}{\phi}\frac{\partial \rho \langle u_i \rangle}{\partial t} + \frac{\langle u_j \rangle}{\phi^2}\frac{\partial \rho \langle u_i \rangle}{\partial x_j} = -\frac{\partial \langle p \rangle^f}{\partial x_i} + \rho g_i + \frac{1}{\phi}\frac{\partial}{\partial x_j}\left[\mu \frac{\partial \langle u_i \rangle}{\partial x_j}\right] - [CT] \tag{4.124}$$

As it can be noted, the continuity equations are identical, when considering that porosity does not change in time. The only major difference appears in the momentum equations. Comparing Eqs. 4.124 and 4.122, there is a discordance, as porosity is only outside the gradient in the convective acceleration term of Liu et al. (1999), instead of being inside and outside. This fact produces differences at the interface between different porous media, or between a porous medium and the clear flow region. Therefore, convective acceleration is not correctly replicated at that locations, and a deficit in momentum transport is expected.

The next formulation is Nikora et al. (2007a), with the double-averaged formulation, given in intrinsic magnitudes:

$$\frac{\partial \phi}{\partial t} + \frac{\partial \phi \langle u_i \rangle^f}{\partial x_i} = 0 \tag{4.125}$$

$$\frac{\partial \rho \langle u_i \rangle^f}{\partial t} + \langle u_j \rangle^f \frac{\partial \rho \langle u_i \rangle^f}{\partial x_j} = -\frac{1}{\phi}\frac{\partial \phi \langle p \rangle^f}{\partial x_i} + \rho g_i + \frac{1}{\phi}\frac{\partial}{\partial x_j}\left[\phi \left\langle \mu \frac{\partial u_i}{\partial x_j} \right\rangle\right] - [CT] \tag{4.126}$$

For an easier comparison, these equations will be posed in terms of the extended

average:

$$\frac{\partial \phi}{\partial t} + \frac{\partial \langle u_i \rangle}{\partial x_i} = 0 \tag{4.127}$$

$$\frac{\partial}{\partial t}\left[\frac{1}{\phi}\rho \langle u_i \rangle\right] + \frac{\langle u_j \rangle}{\phi}\frac{\partial}{\partial x_j}\left[\frac{1}{\phi}\rho \langle u_i \rangle\right] = - \frac{1}{\phi}\frac{\partial \phi \langle p \rangle^f}{\partial x_i} + \rho g_i + \frac{1}{\phi}\frac{\partial}{\partial x_j}\left[\phi \left\langle \mu \frac{\partial u_i}{\partial x_j} \right\rangle\right] - [CT] \tag{4.128}$$

Nikora et al. (2007a) derived the equations for environmental hydraulics and, the continuity equation includes the time variation of porosity as in the present formulation. The differences are very significant in the momentum equation, comparing Eqs. 4.122 and 4.128. The acceleration terms are completely different because the local derivative lacks the division by porosity. Since porosity is always equal or lower than 1, the contribution of this term is reduced, but at the same time porosity is introduced dividing inside the operator, which would balance some part of the reduction. The convective acceleration is identical. The effect of the pressure gradient is maximized because the term is divided by porosity. At the same time, being multiplied by porosity inside the gradient operator will affect the flow at the interface between porous media. Finally, the viscous term is also reduced, as porosity is introduced multiplying inside it.

Hur et al. (2008) formulation is next:

$$\frac{\partial \phi \langle u_i \rangle^f}{\partial x_i} = 0 \tag{4.129}$$

$$\phi \frac{\partial \rho \langle u_i \rangle^f}{\partial t} + \langle u_j \rangle^f \frac{\partial \rho \phi \langle u_i \rangle^f}{\partial x_j} = -\phi \frac{\partial \langle p \rangle^f}{\partial x_i} + \rho \phi g_i + \frac{\partial}{\partial x_j}\left[\phi \mu \frac{\partial \langle u_i \rangle^f}{\partial x_j}\right] - [CT] \tag{4.130}$$

Shifted into extended-average variables:

$$\frac{\partial \langle u_i \rangle}{\partial x_i} = 0 \tag{4.131}$$

$$\frac{\partial}{\partial t}\left[\rho\frac{1}{\phi}\left\langle u_i\right\rangle\right]+\frac{\left\langle u_j\right\rangle}{\phi^2}\frac{\partial\rho\left\langle u_i\right\rangle}{\partial x_j}=-\frac{\partial\left\langle p\right\rangle^f}{\partial x_i}+\rho g_i+\frac{1}{\phi}\frac{\partial}{\partial x_j}\left[\phi\mu\frac{\partial}{\partial x_j}\left(\frac{1}{\phi}\left\langle u_i\right\rangle\right)\right]-[CT] \quad (4.132)$$

The continuity equation is the same as for all the works. Discordances appear in the first term of the momentum equation, because the porosity appears inside the differential operator, instead of outside. However, since Hur et al. (2008) do not account for time-varying porosity, their approach would yield the same solution. The convective acceleration is identical to that on Liu et al. (1999), and presents the same effects: differences at the interface between different porous media. Finally, some differences are also expected where gradients of porosity appear for the viscous stresses, due to the presence of porosities inside the differential operators. Outside that zones, no differences with respect to the derivation on this document will be experienced.

del Jesus et al. (2012) formulation put effort in following a rigorous mathematical process, but the volume-averaging algebra was not applied as intended by Slattery (1967) and Whitaker (1967):

$$\frac{\partial}{\partial x_i}\frac{\left\langle u_i\right\rangle}{\phi}=0 \quad (4.133)$$

$$\frac{1}{\phi}\frac{\partial\rho\left\langle u_i\right\rangle}{\partial t}+\frac{\left\langle u_j\right\rangle}{\phi}\frac{\partial}{\partial x_j}\left[\frac{1}{\phi}\rho\left\langle u_i\right\rangle\right]=-\frac{\partial\left\langle p\right\rangle^f}{\partial x_i}+\rho g_i+\frac{\partial}{\partial x_j}\left[\mu\frac{\partial}{\partial x_j}\left(\frac{1}{\phi}\left\langle u_i\right\rangle\right)\right]-[CT] \quad (4.134)$$

The continuity equation is not correct, as the extended average must be constant to conserve mass. However, comparing the momentum equation, the only difference is in the viscous term, where porosity divides inside the differential operator, instead of outside.

The implementation of del Jesus et al. (2012) was initially developed in OpenFOAM® as a part of this thesis, before re-deriving the VARANS equations. In this previous work, the term $\frac{\langle u_i\rangle}{\phi}$ was converted to a modified velocity ($\langle u_i\rangle^*$). Therefore, considering no change in porosity in time, the equations will look as follows:

$$\frac{\partial\left\langle u_i\right\rangle^*}{\partial x_i}=0 \quad (4.135)$$

$$\frac{\partial \rho \langle u_i \rangle^*}{\partial t} + \langle u_j \rangle^* \frac{\partial \rho \langle u_i \rangle^*}{\partial x_j} = -\frac{\partial \langle p \rangle^f}{\partial x_i} + \rho g_i + \frac{\partial}{\partial x_j}\left[\mu \frac{\partial \langle u_i \rangle^*}{\partial x_j}\right] - [CT] \tag{4.136}$$

Comparing this alternative version with the one derived in the present thesis, some interesting conclusions can be obtained. First, continuity is the same, therefore, no problems of mass loss or gain are experienced. Second, regarding the momentum equation, the inverse of porosity (factor greater than 1) does not appear in the local and convective accelerations. In the latter case it is missing twice, inside and outside the gradient. Moreover, it is also not present outside the viscous stresses term. These differences can explain why the friction factors were so large in del Jesus et al. (2012) and Higuera et al. (2014a), compared to those obtained now, while the results were the same.

One of the latest works in coastal engineering is Jensen et al. (2014):

$$\frac{\partial \langle u_i \rangle}{\partial x_i} = 0 \tag{4.137}$$

$$\frac{\partial}{\partial t}\left[\frac{1}{\phi}\rho \langle u_i \rangle\right] + \frac{\langle u_j \rangle}{\phi}\frac{\partial}{\partial x_j}\left[\frac{1}{\phi}\rho \langle u_i \rangle\right] = -\frac{\partial \langle p \rangle^f}{\partial x_i} + \rho g_i + \frac{1}{\phi}\frac{\partial}{\partial x_j}\left[\mu \frac{\partial \langle u_i \rangle}{\partial x_j}\right] - [CT] \tag{4.138}$$

When compared to the VARANS equations in this work, it is clear that they yield the same results in the case when porosity does not change in time. Otherwise, the present formulation must be applied in order to obtain physical results.

4.7 Conclusions

The set of VARANS equations that have been derived in this chapter can be considered as one of the most advanced available in literature. Not only the new equations correct known deficiencies from other implementations when dealing with space gradients of porosity, which were already discussed in the most recent reference (Jensen et al., 2014), but also they incorporate two key elements.

The first one is the two volume-averaged turbulence models, correctly rederived, that can help in modelling the turbulence enhancement induced by porous media. The second

distinctive feature is the inclusion of time gradients of porosity. The new terms can help in broadening the range of physics that can be simulated. For example, sediment transport can now be incorporated in a numerical model, and is taken into account directly in the VARANS equations.

Chapter 5

Numerical Implementation

As noted in the introduction of this thesis, numerical modelling is a technique that was not introduced long ago in coastal engineering. During the last decade, important advances have been made. As computational resources increased their performance and lowered their cost, this approach has been generalized and applied to solve real problems, especially in 2D. From the usability point of view, three types of CFD models can be distinguished: academic, commercial and open source.

Academic models are usually created by universities and research institutes for their own use. Developers have access to the source code, which most often has been created as an in-house project, and may sometimes be distributed as open source to external users. Generally, academic models are an exceptional tool to test new numerical techniques and can present features that surpass the state of the art. The drawbacks of this type of models are, generally, a lack of documentation, combined with an uneven coding style and the difficulty to set up and run the cases.

Commercial models are completely opposite to academical models. They are developed by companies, that charge a (quite high) fee for licenses. Sometimes, restrictions exist to access particular features depending on the license purchased. This may include modules to solve particular problems, constrains to the maximum number of cells that can be computed, etc. Commercial models are closed source, this means that the user cannot access the source code to add functionalities or to check the algorithms, therefore, this kind of models are regarded as "black boxes". Generally, users can only create custom boundary conditions from some predefined templates, so the capabilities of the model are not easily extended. The real advantages of commercial codes are the reference materials,

the technical support and the simplicity to use them, as most include well-designed point-and-click GUIs.

The open source models can be found in the middle way between academical and commercial models, although there might be a thin line separating open source and academical models. They share some of the best features of both worlds. Generally, open source models are developed by an entity (university, foundation or company) that makes the source code available to the general public for free and is devoted to development following a business model. Along with the model, documentation is also released. While not as easy to use as commercial codes, open source models are often easier to master than academic ones. Moreover, the code is usually well written and organized. The process of adding new capabilities to the model is, firstly, possible and secondly, not extremely difficult. An additional vantage point is the broad spectrum of users that are willing to contribute to the project. The active community in forums and conferences can help finding bugs and developing new techniques in less time.

As previously noted, prior to this thesis an open source model, OpenFOAM®, was explored as a CFD finite volume framework with promising capabilities. It must be noted that in the beginning it was not prepared to deal with coastal engineering processes, as it lacked wave generation and absorption, and porous media flow modules. For all these reasons, the numerical modelling in this work has been carried out with the open source model OpenFOAM®.

5.1 Introduction to OpenFOAM®

OpenFOAM® (**Open F**ield **O**peration **A**nd **M**anipulation) is a free and open source finite volume CFD toolbox originally developed at the Imperial College (Jasak (1996), Rusche (2002)). It consists in a bundle of libraries and codes to solve complex problems such as turbulence, fluid flows, electromagnetics, chemical reactions, combustion... It also features applications to pre- and post-process the cases, including mesh generation tools (*blockMesh*, *snappyHexMesh*), setting and modifying field values, mesh decomposition, sampling data (e.g. isosurfaces, gauges...). OpenFOAM® is prepared to run cases in parallel, allowing an easy set up and a straightforward calculation method, handling the

decomposition process and the final (optional) reconstruction process.

This library is written in C++ and is object oriented. Its modular structure is an advantage to program new solvers, boundary conditions or applications, allowing not to digging deeply in the source code to add new functionalities. Moreover, the syntax to discretize the equations is very similar to the mathematical notation, and the names of the variables are meaningful, resulting in an easily-readable and compact programming style. This is a result of the data types and classes, specific of OpenFOAM®, which help to handle the fields in a more compact and easy way, avoiding unnecessary loops to perform certain operations. This approach has countless advantages, but its main drawback is the difficulty to locate and understand the most basic classes located several levels below the first layer.

Being open source means that OpenFOAM® is not a "black box". Unlike commercial codes, the user can control and modify each of the steps of the solving process by changing the source code. This is a great advantage, since the solvers can be easily adapted to deal with custom problems, and boundary conditions can be developed without restrictions. Moreover OpenFOAM® includes several modules for mesh and data conversion from and to commercial CFD codes formats (Ansys®, Fluent®, CFX®) or other standards (VTK), which allows cross comparisons.

Other extended capabilities are added by third party programs. The most representative case is undoubtedly ParaView®, which is the main program used for postprocessing.

5.2 IHFOAM Solver

5.2.1 Description

IHFOAM is the numerical tool that has been created within the frame of this thesis, and can currently be considered a state-of-the-art software.

The model itself is based on *interFoam*, one of the solvers included in OpenFOAM®. **IHFOAM** solves the three-dimensional Volume Averaged Reynolds Averaged Navier–Stokes (VARANS) equations that have been developed in Chapter 4, for two incompressible phases (water + air) using a finite volume discretization and the Volume of Fluid

(VOF, Hirt and Nichols (1981)) technique. It also supports a large number of turbulence models out of the box (e.g. $k-\epsilon$, $k-\omega$ SST, LES...), and the two first have been volume averaged in this work to be applied inside porous media.

In VOF, each phase is described by a fraction α_i occupied by the volume of fluid of the i^{th} material in the cell. Its principal advantages are that it is a simple approach, allowing very complex free surface configurations to be represented easily, and that it does not require mesh motion. A minor disadvantage is that it becomes less effective as surface tension effects increase. However, most of the times coastal engineering practical applications deal with relatively long wavelengths, so that only for very specific phenomena are surface tension forces not negligible.

The distinctive capabilities of **IHFOAM**, which are not present in OpenFOAM® are: free surface flow through porous media, wave generation and active wave absorption (for static and dynamic meshes) and an enhanced version of dynamic meshing.

The porous media modelling is a key feature in coastal engineering, as it enables the calculation of real structures. Without the new set of equations OpenFOAM® was only capable of simulating impervious structures, limiting the spectrum of cases that could be solved. With the new VARANS formulation it is possible to simulate rubble-mound breakwaters and vertical breakwaters. The latter ones can be thought of as impervious, but they lay on top of porous foundations, therefore, the model is apt to calculate the uplift forces and the safety coefficients against sliding and overturning. Moreover, the turbulence effects inside the mantles can be calculated with one of the volume averaged turbulence models available.

IHFOAM features active wave generation and absorption, that have proven to be the most advanced methods in the current state of the art. With this technique both processes are handled at the boundaries of the mesh, hence, without increasing the computational cost. **IHFOAM** implementation is specially advantageous compared to Jacobsen et al. (2012) passive approach, that requires enlarging the domain up to several wave lengths. With the current implementation waves can be generated with a large number of theories, covering the full spectrum of relative water depths, as detailed later in this section.

Active wave absorption permits that the waves incident to a boundary flow out the domain, as they would in the open sea. If wave absorption was not performed, waves

will reflect at the boundaries, increasing the energy inside the system and contaminating the results. Moreover, this approach is able to prevent the increase of the mean water level due to the effects of mass imbalance between waves and troughs in static wave generation. Currently, two types of absorption theories are available, one based on a 2D theory (applicable in 2D and 3D) and another one based on a newly developed 3D theory, to account for oblique incident waves. These Dirichlet-type boundary condition modules have been implemented to work indistinctly with static or dynamic meshes.

IHFOAM is prepared to solve cases in which the mesh does not change. An enhanced version of it is *IHDYMFOAM*, which handles dynamic meshes ("DYM" stands for Dynamic Mesh). Dynamic meshing presents two main advantages. First, it enables the simulation of floating structures with 6 degrees of freedom, as offshore platforms or ships, and rotating elements as propellers. And second, it also permits dynamic mesh refinement simultaneously to the simulation, with which the resolution can be increased automatically at relevant locations (e.g. the free surface) to obtain enhanced flow details.

Another novel wave generation procedure, recently included, is a module to emulate the laboratory wavemakers. The real displacement of the wave paddles can be simulated with a moving boundary and a dynamic mesh. This method also includes active wave absorption.

The moving-boundary wave generation relies in a mesh deformation technique. By default, the deformation affects the whole mesh, and is of greater magnitude closer to the moving edge. However, as the mesh can contain porous zones, that should not move, a routine to prevent the displacement at that locations has also been implemented.

5.2.2 Governing equations

The variables used in the development of the governing equations in this chapter are gathered in Table 5.1.

RANS

The RANS equations are the governing mathematical expressions that link pressure and velocity, and are implemented by default in OpenFOAM®. They encompass the mass conservation (5.1) and momentum conservation (5.2) equations. Under the assumption

ρ	Density, which is calculated as presented in equation 5.11
$\mathbf{U}$	Velocity vector
p	Total pressure
p^*	Pseudo-dynamic pressure
$\mathbf{g}$	Acceleration due to gravity
$\mathbf{X}$	Position vector
$\sigma\kappa\nabla\alpha$	Surface tension term
σ	Surface tension coefficient
κ	Curvature of the interface: $\kappa = \nabla \cdot \frac{\nabla\alpha}{\lvert\nabla\alpha\rvert}$
α	Indicator (VOF) function
μ_{eff}	Efficient dynamic viscosity, which takes into account the molecular dynamic viscosity plus the turbulent effects: $\mu_{\text{eff}} = \mu + \rho\,\nu_{\text{turb}}$
ν_{turb}	Turbulent kinetic viscosity, given by the chosen turbulence model

Table 5.1: Variables used in this chapter.

of incompressible fluids they are as follows:

$$\nabla \cdot \mathbf{U} = \mathbf{0} \tag{5.1}$$

$$\begin{aligned} \frac{\partial \rho \mathbf{U}}{\partial t} + \nabla \cdot (\rho \mathbf{U}\mathbf{U}) \quad - \quad \nabla \quad (\mu_{\text{eff}} \nabla \mathbf{U}) = \\ -\nabla p^* - \mathbf{g} \cdot \mathbf{X}\, \nabla \rho + \nabla \mathbf{U} \cdot \nabla \mu_{\text{eff}} + \sigma\kappa\nabla\alpha \end{aligned} \tag{5.2}$$

where the bold letters indicate a vector field and all the variables are referenced in Table 5.1.

The elements in Eq. 5.2 have a particular disposition: those placed on the left hand side of the equal sign are used by OpenFOAM® to assemble the coefficients matrix, and the ones on the right side are calculated explicitly, yielding the independent term of the equations.

The form of the momentum equation differs slightly from the regular RANS equations seen in Section 2.3.1, whereas the continuity equation is identical:

$$\frac{\partial u_i}{\partial x_i} = 0 \tag{5.3}$$

$$\frac{\partial \rho u_i}{\partial t} + u_j \frac{\partial \rho u_i}{\partial x_j} = -\frac{\partial p}{\partial x_i} + \rho g_i + \frac{\partial}{\partial x_j}\left[\mu_{\text{eff}} \frac{\partial u_i}{\partial x_j}\right] + F_i^{\text{ST}} \tag{5.4}$$

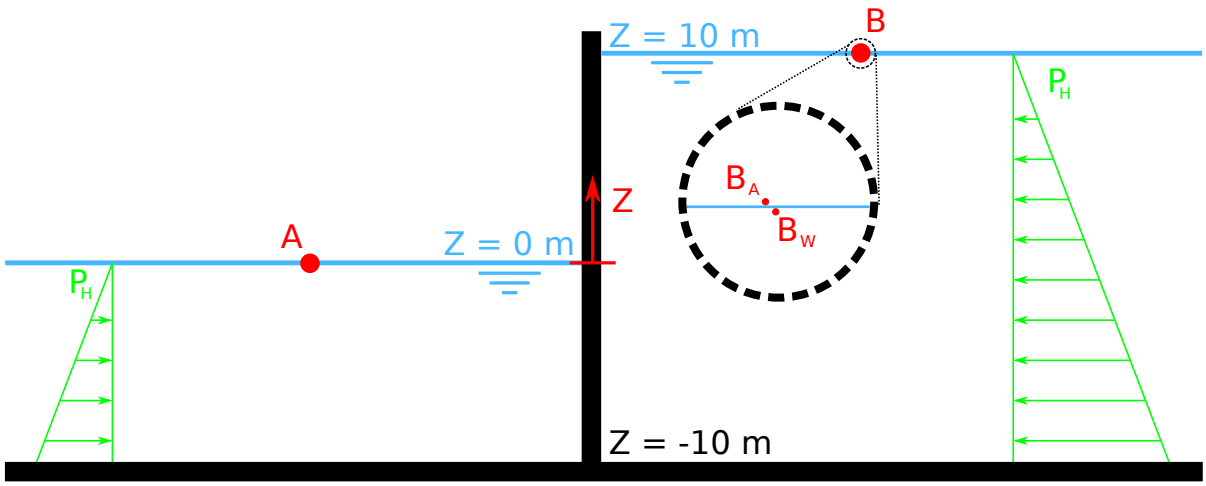

Figure 5.1: Simplified case to evaluate p^*.

where the surface tension force (F_i^{ST}) has been included.

The main difference derives from the fact that OpenFOAM® solves the RANS equations using a pseudo-dynamic pressure (p^*), which is defined as follows:

$$p = p^* + \rho\,\mathbf{g}\cdot\mathbf{X} \tag{5.5}$$

The pseudo-dynamic pressure does not have any physical meaning, it is just the result of a convenient numerical technique. In some references it is wrongfully defined as the pressure in excess of the hydrostatic (i.e. dynamic pressure) (Jacobsen et al., 2012). This will only be true if the free surface is located at $Z = 0$ (reference system) and under very limiting conditions, because no integration is performed.

A practical example can clarify this fact. Imagine two reservoirs at rest and open to the atmosphere (i.e. total pressure equal zero at the free surface). Reservoir A has the water level at $Z = 0$ m and reservoir B at $Z = 10$ m. Gravity acts in the negative Z axis, with an acceleration of 9.8 m/s. The setup is represented in Fig. 5.1.

Eq. 5.5 is rearranged and can be simplified for this particular case:

$$p^* = p - \rho\,g\,z \tag{5.6}$$

According to the sketch, the hydrostatic pressure ($\mathrm{P_H}$) and total pressure (p) at the points A and B are zero due to the atmospheric pressure condition. Hence, if p^* really were the pressure in excess of the hydrostatic it should be zero as well. This is true for

point A because $z = 0$. However, it is not true for point B:

$$p_B^* = 0 - \rho \cdot 9.8 \cdot 10 = -98\rho$$

Moreover, since no integration is carried out to calculate the real hydrostatic pressure, the value of p_B^* can vary up to a factor of 1000 depending if the point selected is inside the water ($\mathrm{B_W}$, $\rho = 1000$ kg/m^3) or air phase ($\mathrm{B_A}$, $\rho = 1$ kg/m^3).

This example highlights that p^* can be viewed as a pseudo-dynamic pressure, but in order to obtain physical results, the post-processing calculations need to be carried out using the total pressure (p).

The process to obtain Eq. 5.2 from Eq. 5.4 is straightforward. The pressure gradient and the gravity body force are taken from Eq. 5.4 and developed with Eq. 5.6 transformation:

$$\begin{aligned}
-\nabla p + \rho\,\mathbf{g} = -\nabla\left(p^* + \rho\,\mathbf{g}\cdot\mathbf{X}\right) + \rho\,\mathbf{g} = \\
-\nabla p^* - \nabla\left(\rho\,\mathbf{g}\cdot\mathbf{X}\right) + \rho\,\mathbf{g} = \\
-\nabla p^* - \rho\,\mathbf{g}\cdot\nabla\mathbf{X} - \rho\,\mathbf{X}\cdot\nabla\mathbf{g} - \mathbf{g}\cdot\mathbf{X}\,\nabla\rho + \rho\,\mathbf{g} = \\
-\nabla p^* - \rho\,\mathbf{g}\cdot[\mathbf{I}] - \rho\,\mathbf{X}\cdot[\mathbf{0}] - \mathbf{g}\cdot\mathbf{X}\,\nabla\rho + \rho\,\mathbf{g} = \\
-\nabla p^* - \rho\,\mathbf{g} - \mathbf{g}\cdot\mathbf{X}\,\nabla\rho + \rho\,\mathbf{g} \\
= -\nabla p^* - \mathbf{g}\cdot\mathbf{X}\,\nabla\rho = -\frac{\partial p^*}{\partial x_i} - g_j\,X_j\frac{\partial\rho}{\partial x_i}
\end{aligned} \tag{5.7}$$

in which $[\mathbf{I}]$ is the identity tensor and $[\mathbf{0}]$ is the zero tensor. The result can be introduced into Eq. 5.4 to obtain the final momentum equation adapted to OpenFOAM® formulation in Einstein notation:

$$\frac{\partial\rho u_i}{\partial t} + u_j\frac{\partial\rho u_i}{\partial x_j} = -\frac{\partial p^*}{\partial x_i} - g_j\,X_j\frac{\partial\rho}{\partial x_i} + \frac{\partial}{\partial x_j}\left[\mu_{\mathrm{eff}}\frac{\partial u_i}{\partial x_j}\right] + F_i^{\mathrm{ST}} \tag{5.8}$$

VARANS

The VARANS equations are the ones implemented in **IHFOAM**. Note that the version referenced in this section does not take time-varying porosity into account. The reader is

referred to Section 9.4 for further details.

First, mass conservation, which is the same as before, but for the volume averaged velocity:

$$\frac{\partial \langle u_i \rangle}{\partial x_i} = 0 \tag{5.9}$$

And second, the momentum conservation equations:

$$\begin{aligned}\frac{1+C}{\phi}\frac{\partial \rho \langle u_i \rangle}{\partial t} + \frac{1}{\phi}\frac{\partial}{\partial x_j}\left[\frac{1}{\phi}\rho \langle u_i \rangle \langle u_j \rangle\right] = \\ - \frac{\partial \langle p^* \rangle^f}{\partial x_i} - g_j X_j \frac{\partial \rho}{\partial x_i} + \frac{1}{\phi}\frac{\partial}{\partial x_j}\left[\mu_{\text{eff}}\frac{\partial \langle u_i \rangle}{\partial x_j}\right] + F_i^{\text{ST}} \\ - \alpha\frac{(1-\phi)^3}{\phi^3}\frac{\mu}{D_{50}^2}\langle u_i \rangle - \beta\left(1+\frac{7.5}{\text{KC}}\right)\frac{1-\phi}{\phi^3}\frac{\rho}{D_{50}}\sqrt{\langle u_j \rangle \langle u_j \rangle}\langle u_i \rangle\end{aligned} \tag{5.10}$$

Eqs. 5.9 and 5.10 are solved with a two-step method (predictor-corrector). In the original versions of OpenFOAM® the solving algorithm for two-phase flows was PISO (Pressure Implicit with Splitting of Operators) (Issa, 1986). The current solving procedure is called PIMPLE because it is actually a mixture between PISO and SIMPLE (Semi-Implicit Method for Pressure-Linked Equations) algorithms. Its main structure is inherited from the original PISO, but it allows equation under-relaxation to ensure the convergence of all the equations at each time step. The PIMPLE technique is described in detail in Section 5.2.3.

VOF equation

An additional equation must also be taken into account to describe the movement of the different fluid phases. Since for the vast majority of coastal engineering applications only water and air are present, the following analysis is carried out for those two phases. For a more general approach and further details the reader is referred to Berberovic et al. (2009) and Kissling et al. (2010).

As a result of this initial assumption, just one indicator phase function (α) is needed, and is defined as the quantity of water per unit of volume in each cell. This means that if $\alpha = 1$ the cell is full of water, if $\alpha = 0$ the cell is full of air, and in any other case

it belongs to the interface. It is straightforward to calculate any of the properties of the fluid in each cell, just by weighting them by the VOF function. For example, density of the fluid in a cell is computed as follows:

$$\rho = \alpha\,\rho_{\text{water}} + (1-\alpha)\,\rho_{\text{air}} \tag{5.11}$$

The starting point for the expression that tracks the fluid movement is a classic advection equation:

$$\frac{\partial \alpha}{\partial t} + \nabla \cdot \mathbf{U}\,\alpha = 0 \tag{5.12}$$

However, some restrictions apply in order to obtain physical results: a sharp interface must be maintained and α must be conservative and bounded between 0 and 1. OpenFOAM® makes use of an artificial compression term ($\nabla \cdot \mathbf{U}_c\,\alpha(1-\alpha)$) instead of applying a compressing differencing scheme. This approach is conservative and takes non-zero values only at the interface. Furthermore, the flow is only compressed in the normal direction to the interface: $\left(\frac{\nabla\alpha}{|\nabla\alpha|}\right)$, which points towards greater values of α (i.e. from the air to the water phase). This yields the final expression:

$$\frac{\partial \alpha}{\partial t} + \nabla \cdot \mathbf{U}\,\alpha + \nabla \cdot \mathbf{U}_c\,\alpha(1-\alpha) = 0 \tag{5.13}$$

in which the compression velocity is $|\mathbf{U}_c| = min\left[c_\alpha|\mathbf{U}|, max(|\mathbf{U}|)\right]$, where the user can specify factor c_α. By default it takes value 1, but it can be greater to enhance the compression of the interface, or zero to eliminate it.

Eq. 5.13 is implemented by default in OpenFOAM® and can be thought of as part of the RANS equations. The volume-averaged VOF advection equation (Eq. 4.41) that has been derived for **IHFOAM** can be extended to include the compression term:

$$\frac{\partial \alpha}{\partial t} + \frac{1}{\phi}\frac{\partial \alpha\ \langle u_i \rangle}{\partial x_i} + \frac{1}{\phi}\frac{\partial \alpha\,(1-\alpha)\ \langle u_i \rangle}{\partial x_i} = 0 \tag{5.14}$$

The boundedness of this equation is achieved by means of a specially designed solver called MULES (Multidimensional Universal Limiter for Explicit Solution). It makes use

of a limiter factor on the fluxes of the discretized divergence term to ensure a final value between 0 and 1. MULES is also analysed in Section 5.2.3.

5.2.3 Solving procedure

A detailed flow chart, Fig. 5.2, has been developed in order to show the full procedure for solving each time step. The main loop is presented enclosed by a gray rectangle. The VOF function subcycle and the PIMPLE loop are further developed outside it. Both of them include a basic description of the wave generation boundary conditions. Within it, some variables that appear in the source code (e.g. *nAlphaSubCycles*, *nCorrectors*...) are defined. These are set in the program control files and govern the performance of the model's solving procedures.

MULES

The Multidimensional Universal Limiter for Explicit Solution is a module based on the flux-corrected transport (FCT) technique by Rudman (1997). The solver has been especially designed to perform the advection of the VOF indicator function, ensuring that conservation of mass is fulfilled and that the solution is bounded between 0 and 1, unless other limits are specified.

MULES takes the VOF equation (5.13) in a semi-discretized form:

$$\frac{\partial \alpha}{\partial t} + \sum_f \phi_u + \sum_f \lambda_f \phi_h = 0 \tag{5.15}$$

where ϕ is the explicit flux of α at the faces (f) of the cell. The subscript u indicates an upwind scheme and h is a higher order scheme. λ_f is a limiter, therefore, the second term can be thought of as a limiting term to bound α between $\alpha_{\min}$ and $\alpha_{\max}$. Moreover, it can be split into two terms for convenience, one for positive fluxes and one for negative fluxes, as shown next. The time derivative of the VOF function is discretized with an explicit integration scheme. For the current time index n and a time step$\Delta\, t$:

$$\frac{\alpha^{n+1} - \alpha^n}{\Delta t} + \sum_f \phi_u + \sum_{f^+} \lambda_f^+ \phi_h^+ + \sum_{f^-} \lambda_f^- \phi_h^- = 0 \tag{5.16}$$

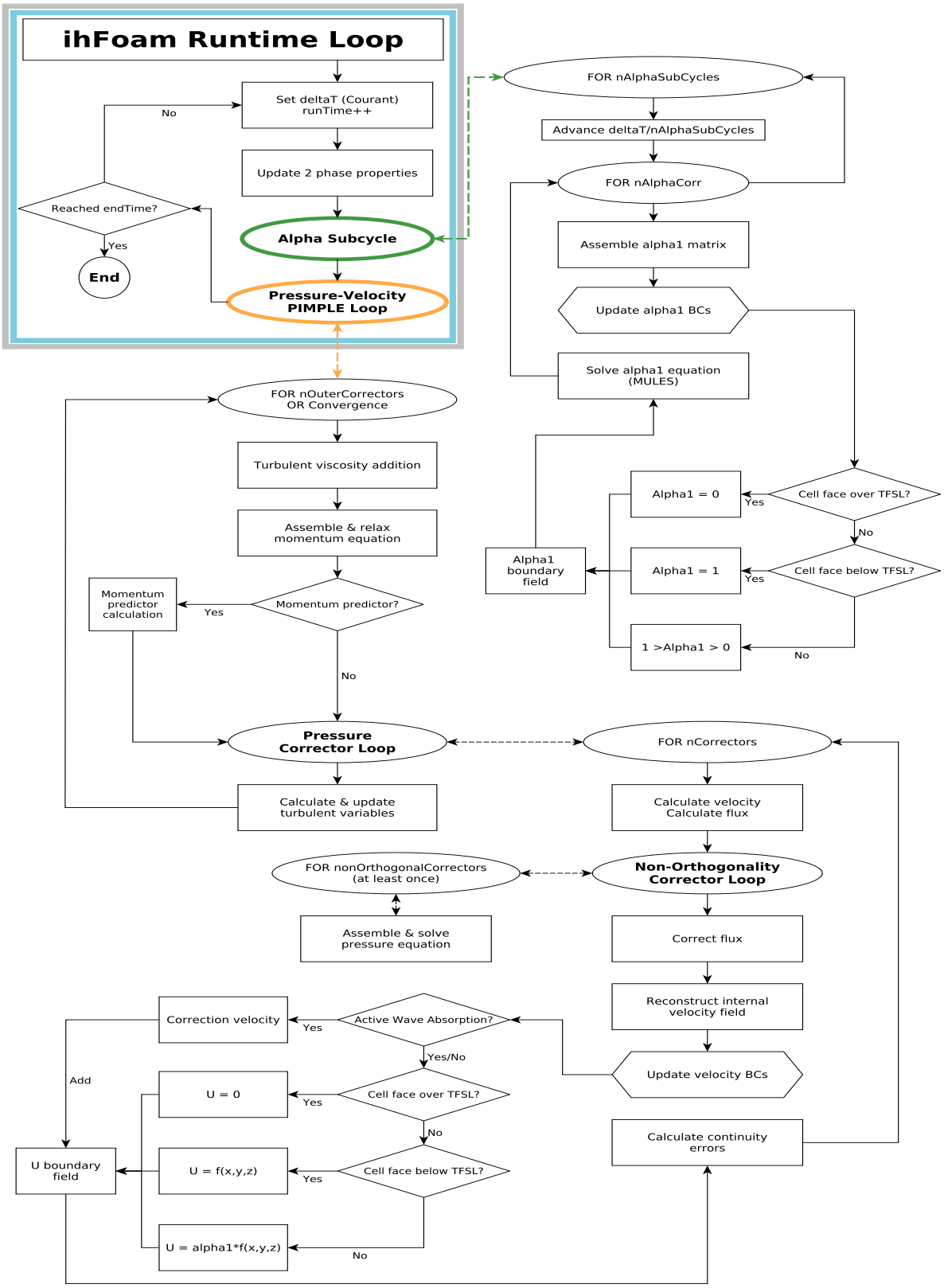

Figure 5.2: **IHFOAM** solving flow chart. "TFSL" stands for Theoretical Free Surface Level.

The value of the face limiters is calculated iteratively. Each iteration the limiters in each cell (λ_C) are established as a metric from 0 to 1, applying the following expressions:

$$\lambda_C^+ = -\frac{1}{\sum_{f^+} \phi_h^+} \left(\frac{\partial \alpha}{\partial t} + \sum_f \phi_u + \sum_{f^-} \lambda_f^- \phi_h^- \right) \quad \text{for } \alpha = \alpha_{\min} \tag{5.17a}$$

$$\lambda_C^- = -\frac{1}{\sum_{f^-} \phi_h^-} \left(\frac{\partial \alpha}{\partial t} + \sum_f \phi_u + \sum_{f^+} \lambda_f^+ \phi_h^+ \right) \quad \text{for } \alpha = \alpha_{\max} \tag{5.17b}$$

and then the face limiters are obtained as the minimum/maximum of the cell values sharing the face (owner cell C and its neighbouring cell N):

$$\lambda_f^+ = \min\left(\lambda_C^+, \lambda_N^-\right) \tag{5.18a}$$

$$\lambda_f^- = \max\left(\lambda_C^-, \lambda_N^+\right) \tag{5.18b}$$

This way, having common face limiters between adjacent cells ensures the conservation of mass. The results from the MULES solver are the new α field and the new flux of α.

For a more detailed description of MULES, the reader is referred to Márquez (2013).

PIMPLE

The RANS equations are a system of 4 partial differential equations (continuity + 3 of momentum conservation). The equations that couple the pressure and velocities are elliptical and implicit in space. Fortunately, the system is closed, as there are only 4 unknowns (pressure + 3 velocity components). Therefore, the equations can be solved without further assumptions.

The solving procedure in OpenFOAM®is called PIMPLE, and is a two-step method (predictor-corrector). Its workflow is as follows:

a. Discretization of the momentum equation. The momentum equation can be represented in matrix form:

$$M\, U_* = -\nabla P_* + T_U\, U + T_I \tag{5.19}$$

where M is the coefficient matrix that represents the implicit terms; U_* is the unknown velocity; P_* is the also unknown pseudo-dynamic pressure; T_U is the coefficient matrix of the explicit terms; U is the known velocity; $T_U\,U$ represents the velocity-dependent source term; and T_I is the source term that does not depend on velocity, which includes the surface tension and buoyancy effects.

In this step, the matrices M and T_U are assembled.

b. Relaxation of the momentum equation. It is possible to apply under-relaxation in the momentum equation, as inherited from the SIMPLE algorithm. This technique can be performed to improve the stability of the simulation, especially for steady-state problems. The under-relaxation mechanism limits the variation of velocity from one time step to the next one by modifying the coefficient matrix M and source T_U.

c. Momentum predictor. The momentum predictor consists in an intermediate solution of the momentum equation, applying the pressure (P) and velocity (U) fields from the previous time step (n), namely:

$$M\,U^* = -\nabla P_n + T_U\,U_n + T_I \tag{5.20}$$

The result is a new velocity field U^*, that does not fulfil the mass conservation equation ($\nabla \cdot \mathbf{U} \neq \mathbf{0}$). This field serves as an approximation and will be used in the next stages of the PIMPLE loop to calculate the explicit sources. If the momentum predictor is switched off, the velocity field from the previous time step will be used instead.

d. Pressure equation solution. The PIMPLE method involves a convenient decomposition of the equations to simplify the whole solving process. First, the M matrix is decomposed into two, one of them containing the terms of the diagonal (A) and a second one with the off-diagonal terms (H'): $M = A + H'$. Then, the off-diagonal terms are passed to the other side in Eq. 5.19 and combined with the other sources, yielding:

$$A\,U_{n+1} = -\nabla P_{n+1} + T_U\,U^* + T_I - H'\,U^* = H - \nabla P_{n+1} \tag{5.21}$$

U_{n+1} is the velocity of the new time step and H gathers all the terms except the pressure gradient. Note how the velocity of the predictor step is used to calculate the terms of the right hand side, including H'. Next, the unknown velocity (U_{n+1}) can be isolated by

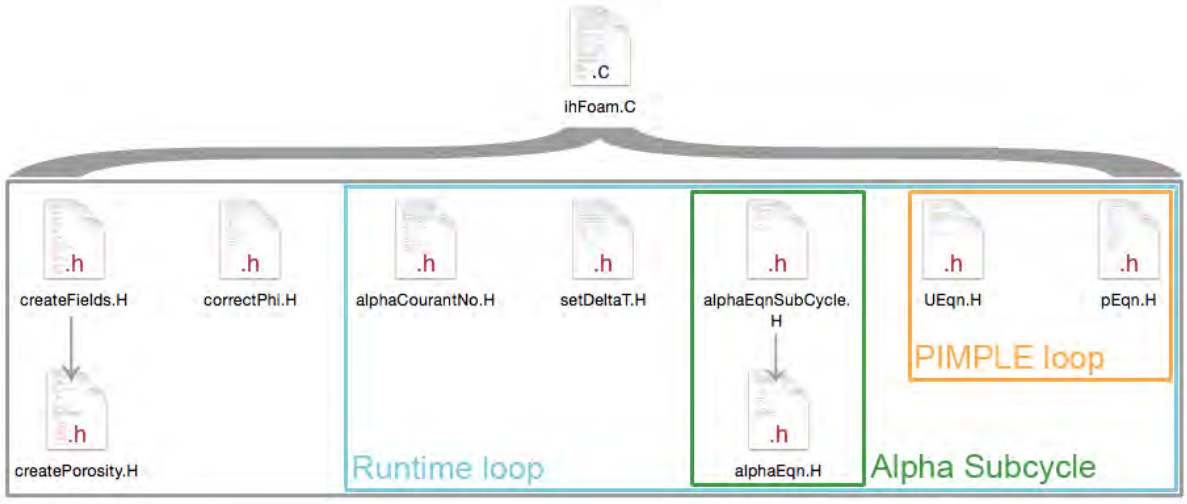

Figure 5.3: **IHFOAM** source code tree.

pre-multiplying each term by A^{-1}:

$$U_{n+1} = -\frac{\nabla P_{n+1}}{A} + \frac{H}{A} \tag{5.22}$$

So far, only the momentum equations have been taken into account. The continuity equation indicates that the divergence of the velocity field must be zero. Hence, applying the divergence operator to the whole equation results in a Poisson equation, where the only unknown is the pressure:

$$\nabla \cdot U_{n+1} = 0 = -\nabla \cdot \frac{\nabla P_{n+1}}{A} + \nabla \cdot \frac{H}{A} \quad \rightarrow \quad \nabla \frac{\nabla P_{n+1}}{A} = \nabla \cdot \frac{H}{A} \tag{5.23}$$

The solving process is iterative, and P_{n+1} is obtained when the solution has reached the established convergence criteria.

e. Velocity corrector. In this last stage, the velocity is updated to be solenoidal. This step is performed explicitly, substituting the newly-obtained pressure field into Eq. 5.22.

5.2.4 Numerical implementation

As an overview, the source code files that compose **IHFOAM** are represented in Fig. 5.3.

The basic structure of the solver is contained in **ihFoam.C** file, which starts with an extensive header including a brief description of the solver. From line 40, before the start

of the main program, some dependencies are loaded:

ihFoam.C

```
64 #include "fvCFD.H"
65 #include "MULES.H"
66 #include "subCycle.H"
67 #include "interfaceProperties.H"
68 #include "twoPhaseMixture.H"
69 #include "turbulenceModel.H"
70 #include "interpolationTable.H"
71 #include "pimpleControl.H"
```

These *include* statements load general purpose header files (**fvCFD.H**, **turbulenceModel.H**) and specific modules to solve two-phase flows (**MULES.H**, **twoPhaseMixture.H**).

The program itself starts at line 75, with the usual definition of *int main*.

ihFoam.C

```
75 int main(int argc, char *argv[])
76 {
77     #include "setRootCase.H"
78     #include "createTime.H"
79     #include "createMesh.H"
80
81     pimpleControl pimple(mesh);
82
83     #include "initContinuityErrs.H"
84     #include "createFields.H"
85     #include "readTimeControls.H"
86     #include "correctPhi.H"
87     #include "CourantNo.H"
88     #include "setInitialDeltaT.H"
```

The first lines of the program are committed to create objects to store the mesh, the time variables, the numerical parameters... The fields to be solved are created in **createFields.H**, reading them from the case folder. These include velocity (U), VOF indicator function ($alpha1$), pressure (p_rgh), gravity, and others derived from them: density (rho), mass flow rate ($rhoPhi$)...

createFields.H

```
1 #include "createPorosity.H"
2
3 Info<< "Reading field p_rgh\n" << endl;
```

```
4  volScalarField p_rgh
5  (
6      IOobject
7      (
8          "p_rgh",
9          runTime.timeName(),
10         mesh,
11         IOobject::MUST_READ,
12         IOobject::AUTO_WRITE
13     ),
14     mesh
15 );
```

Most importantly, in the first line, the **createPorosity.H** file is called to read and create the porosity variables (i.e. indices of the porous media and their properties):

createPorosity.H

```
1  Info<< "Reading field porosityIndex\n" << endl;
2
3  volScalarField porosityIndex
4  (
5      IOobject
6      (
7          "porosityIndex",
8          runTime.timeName(),
9          mesh,
10         IOobject::READ_IF_PRESENT,
11         IOobject::NO_WRITE
12     ),
13     mesh,
14     0.0
15 );
16
17 scalar nPor = gMax(porosityIndex); // Number of porous
       media
18 bool activePorosity = (nPor > 0.0);
19
20 volScalarField porosity
21 (
22     IOobject
23     (
24         "porosity",
25         runTime.timeName(),
26         mesh,
27         IOobject::NO_READ,
28         IOobject::NO_WRITE
29     ),
30     mesh,
31     1.0
32 );
33
34 surfaceScalarField porosityF = fvc::interpolate(porosity);
```

Before continuing the review of the source code, it is convenient to understand the way to define the porous media and their properties in **IHFOAM**.

A scalar field of integers called *porosityIndex* needs to be created. As indicated by its name, this field provides the index of the material that each cell contains. By default it is filled with zeroes, which is the index of the clear fluid region (i.e. outside porous media). The first type of porous material is introduced with index 1, the second one with index 2... The initialization procedure is similar to that of setting the initial conditions with the *setFields* utility.

The porosity variables (drag coefficients, porosity, mean nominal diametre) are defined in a dictionary file called **porosityDict**. As an example, a **porosityDict** dictionary looks as follows:

porosityDict

```
18 // Materials: clear region, core, secondary armour layer,
      primary armour layer
19 a                4(0 50   50   50);
20 b                4(0 1.2  2.0  0.6);
21 c                4(0 0.34 0.34 0.34);
22
23 D50              4(1 0.01 0.035 0.12);
24 porosity         4(1 0.49 0.493 0.5);
```

The magnitudes defined are the linear friction (a), nonlinear friction (b) and added mass (c), plus the mean size of the elements conforming the porous medium (D50, given in m) and the porosity of the material.

Three different porous materials (primary and secondary armour layers and the core) are defined. Additionally, as already discussed, the clear flow region corresponds to the index 0 (first index in C++). Therefore, the first values of each vector are applied to the zone outside the porous media, and must always have the value shown. The rest of the values can vary, depending on the material and flow conditions.

Back into the source code again, in the beginning the *porosityIndex* field is read. When it does not exist, it defaults to a zero value. In that case, the boolean variable *activePorosity* is set false and the rest of the porosity variables are not used in subsequent calculations. Hence, **IHFOAM** will be solving the regular RANS equations, and the user will get exactly the same results than using *interFoam*.

In line 20, the scalar field that stores the *porosity* is created with a default value of 1. The real porosity values will be introduced later, if needed. The implementation of the VARANS formulation in OpenFOAM® requires that the porosity field, which is defined

inside the cells, is interpolated to the faces. This is performed with a simple instruction in line 34.

If porosity is activated, the variables need to be read from **porosityDict** and converted into fields:

createPorosity.H

```
68  // Define dictionary
69  IOdictionary porosityDict
70  (
71      IOobject
72      (
73          "porosityDict",
74          runTime.constant(),
75          mesh,
76          IOobject::MUST_READ,
77          IOobject::NO_WRITE
78      )
79  );
80
81  // Read porosity variables
82  aPor = porosityDict.lookupOrDefault("a", List<scalar>(1,
        0.0));
83  bPor = porosityDict.lookupOrDefault("b", List<scalar>(1,
        0.0));
84  cPor = porosityDict.lookupOrDefault("c", List<scalar>(1,
        0.0));
85  D50Por  = porosityDict.lookupOrDefault("D50", List<scalar
        >(1, 1.0));
86  phiPor  = porosityDict.lookupOrDefault("porosity", List<
        scalar>(1, 1.0));
87  debugPor = porosityDict.lookupOrDefault<bool>("debugPor",
        false );
88  useTransient = porosityDict.lookupOrDefault<bool>("
        useTransient", false);
89  KC = porosityDict.lookupOrDefault<scalar>("KC", 1.0);

103 if (aPor.size()!=bPor.size() || aPor.size()!=cPor.size()
104     || aPor.size()!=phiPor.size() ||
105     aPor.size()!=D50Por.size() || aPor.size()!=nPor+1)
106 {
107     FatalError
108         << "Check the number of components for aPor, bPor,"
109         << "dPor, phiPor and D50Por within porosityDict or"
110         << " the maximum index within porosityIndex field."
111     << exit(FatalError);
112 }

117 forAll(porosityIndex, item)
118 {
119     if( porosityIndex[item] > 0.0 )
120     {
121         aPorField[item] = aPor[porosityIndex[item]];
122         bPorField[item] = bPor[porosityIndex[item]];
```

```
123             cPorField[item] = cPor[porosityIndex[item]];
124             KCPorField[item] = KC;
125             D50Field[item]  = D50Por[porosityIndex[item]];
126             porosity[item]  = phiPor[porosityIndex[item]];
127             if ( useTransient )
128             {
129                 useTransMask[item] = 1.0;
130             }
131         }
132     }
133
134     porosityF = fvc::interpolate(porosity);
135
136     // Write out porosity
137     porosity.write();
```

The object representing the **porosityDict** dictionary is created first, and all the porosity variables are then read as lists from it. If any of the variables is not defined in the dictionary, it is set to a single number list. After a message in the log reporting the values read, a consistency check is made (line 103). All the lists must have the same length, equal to the number of porous media plus one (for the clear flow region). If this condition is not met, the program stops and the user is prompt to review the inputs.

Once everything has been checked, the fields representing the porosity variables are set (line 117). Since they were originally created with the default values corresponding to the clear flow region, they only need to be changed where the porous media are defined (line 119). Finally, the porosity field is written to the time folder (line 137).

Back in **createFields.H**, this file also generates the objects and pointers necessary to handle the free surface calculations and the turbulence modelling. Note how this last operation is performed in an abstract way so that any incompressible model can be plugged in without any changes in the code:

createFields.H

```
88  // Construct interface from alpha1 distribution
89  interfaceProperties interface(alpha1, U, twoPhaseProperties
        );
90
91
92  // Construct incompressible turbulence model
93  autoPtr<incompressible::turbulenceModel> turbulence
94  (
95      incompressible::turbulenceModel::New(U, phi,
            twoPhaseProperties)
96  );
```

Another important file is **correctPhi.H**, with a twofold mission:

correctPhi.H

```
2  #include "continuityErrs.H"

35 adjustPhi(phi, U, pcorr);
36
37 while (pimple.correctNonOrthogonal())
38 {
39     fvScalarMatrix pcorrEqn
40     (
41         fvm::laplacian(rAUf, pcorr) == fvc::div(phi)
42     );
43
44     pcorrEqn.setReference(pRefCell, pRefValue);
45     pcorrEqn.solve();
46
47     if (pimple.finalNonOrthogonalIter())
48     {
49         phi -= pcorrEqn.flux();
50     }
51 }
52
53 #include "continuityErrs.H"
```

First, in line 2, it checks that the current flux obeys mass conservation. Note that the continuity equation is not solved per-se, but used as a condition in the final steps of the PIMPLE loop. If minor failures to comply are detected, the code tries to adjust the fluxes (line 35). Additionally, non-orthogonality correction is applied at this stage, if defined. The procedure involves solving a pressure correction equation, from which the flux correction can be obtained and finally added to the total flux.

The runtime loop, referenced in Fig. 5.2, starts some lines below:

ihFoam.C

```
95  while (runTime.run())
96  {
97      #include "readTimeControls.H"
98      #include "CourantNo.H"
99      #include "alphaCourantNo.H"
100     #include "setDeltaT.H"
101
102     runTime++;
103
104     Info<< "Time = " << runTime.timeName() << nl << endl;
105
106     twoPhaseProperties.correct();
107
108     #include "alphaEqnSubCycle.H"
```

The regular Courant number and the Courant number of the flow interface ($0.01 \leq \alpha \leq 0.99$) are calculated and reported in the simulation log. The procedure to calculate

the interface Courant number is as follows:

alphaCourantNo.H

```
42 scalarField sumPhi
43 (
44     pos(alpha1 - 0.01)*pos(0.99 - alpha1)
45    *fvc::surfaceSum(mag(phi))().internalField()
46 );
47
48 alphaCoNum = 0.5*gMax(sumPhi/mesh.V().field())*runTime.
      deltaTValue();
49
50 meanAlphaCoNum =
51     0.5*(gSum(sumPhi)/gSum(mesh.V().field()))*runTime.
         deltaTValue();
```

The code performs a summation of the magnitude of the velocity flux (i.e. flow rate) on the faces of each cell that belongs to the interface, yielding a scalar field called *sumPhi* (m^3/s). Afterwards, the mean and maximum Courant numbers are obtained dividing this field by the cell volume (m^3) and multiplying it by the time step (s) and a factor equal to 0.5. Generally, the Courant number for a 3D geometry is defined in a manner that takes into account the three velocity components:

$$\mathrm{Co} = \frac{u_i \, \Delta t}{\Delta c_i} \tag{5.24}$$

where u_i is each of the velocity components at the cell centre andΔ c_i is each of the cell dimensions. Since in OpenFOAM® formulation the magnitude of the flux is used, the 0.5 factor acts to average the in- and out-fluxes. In the end, both formulations are equivalent.

Note also how parallel computing is handled by means of the *gMax* and *gSum* functions, which are ready to gather values from multiple processors and obtain the global maximum value and the sum of the field values respectively.

After the calculation of the Courant numbers, the new time step may be re-set. One of the advantageous features of the model is the possibility to select an adjustable time step. This allows for a longer time step if velocities are low and shorter ones when higher dynamics are detected, saving computational efforts when possible. The time step can alternatively be fixed beforehand in the control file. In the latter case **setDeltaT.H** is not triggered, otherwise:

setDeltaT.H

```
34 if (adjustTimeStep)
35 {
36     scalar maxDeltaTFact =
37         min(maxCo/(CoNum + SMALL), maxAlphaCo/(alphaCoNum +
               SMALL));
38
39     scalar deltaTFact = min(min(maxDeltaTFact, 1.0 + 0.1*
          maxDeltaTFact), 1.2);
40
41     runTime.setDeltaT
42     (
43         min
44         (
45             deltaTFact*runTime.deltaTValue(),
46             maxDeltaT
47         )
48     );
49
50     Info<< "deltaT = " <<  runTime.deltaTValue() << endl;
51 }
```

This means that the time step (Δt) can decrease unboundedly, but when it gets to grow it is limited to 1.2 times the previous time step (Δt_{n-1}). Mathematically:

$$f_{\Delta t,\max} = \min\left[\frac{\mathrm{Co}_{\max}}{\mathrm{Co}_{n-1}}, \frac{\mathrm{Co}_{\alpha,\max}}{\mathrm{Co}_{\alpha,n-1}}\right] \tag{5.25a}$$

$$f_{\Delta t} = \min\left[1.2, \min\left(f_{\Delta t,\max}, 1 + 0.1 f_{\Delta t,\max}\right)\right] \tag{5.25b}$$

$$\Delta t_n = \min\left[f_{\Delta t}\Delta t_{n-1}, \Delta t_{\max}\right] \tag{5.25c}$$

Back in the main **ihFoam.C** code, the solver advances a time step (line 102), updates the kinematic viscosity value (line 106) and in line 108 it enters the VOF solving subcycle via the **alphaEqnSubCycle.H** file:

alphaEqnSubCycle.H

```
5  if (nAlphaSubCycles > 1)
6  {
7      dimensionedScalar totalDeltaT = runTime.deltaT();
8      surfaceScalarField rhoPhiSum(0.0*rhoPhi);
9
10     for
11     (
12         subCycle<volScalarField> alphaSubCycle(alpha1,
               nAlphaSubCycles);
13         !(++alphaSubCycle).end();
14     )
15     {
16         #include "alphaEqn.H"
17         rhoPhiSum += (runTime.deltaT()/totalDeltaT)*rhoPhi;
18     }
19
20     rhoPhi = rhoPhiSum;
21 }
22 else
23 {
24     #include "alphaEqn.H"
25 }
26
27 interface.correct();
28
29 rho == alpha1*rho1 + (scalar(1) - alpha1)*rho2;
```

This code calls **alphaEqn.H** to solve the advection equation of the VOF function. This solving process can be carried out all at once, or splitting the time step in several sub-steps for increased accuracy. The procedure, in any case, is as follows:

alphaEqn.H

```
5  surfaceScalarField phic(mag(phi/mesh.magSf()));
6  phic = min(interface.cAlpha()*phic, max(phic));
7  surfaceScalarField phir(phic*interface.nHatf());
8
9  for (int aCorr=0; aCorr<nAlphaCorr; aCorr++)
10 {
11     surfaceScalarField phiAlpha
12     (
13         fvc::flux
14         (
15             phi,
16             alpha1,
17             alphaScheme
18         )
19       + fvc::flux
20         (
21             -fvc::flux(-phir, scalar(1) - alpha1,
                   alpharScheme),
22             alpha1,
23             alpharScheme
24         )
25     );
26
27     //MULES::explicitSolve(alpha1, phi, phiAlpha, 1, 0);
28     MULES::explicitSolve
29     (
30         porosity,
31         alpha1,
32         phi,
33         phiAlpha,
34         zeroField(),
35         zeroField(),
36         1.0,
37         0.0
38     );
39
40     rhoPhi = phiAlpha*(rho1 - rho2) + phi*rho2;
41 }
42
43 Info<< "Phase-1 volume fraction = "
44     << alpha1.weightedAverage(mesh.Vsc()).value()
45     << "  Phase-1 total volume = "
46     << gSum(alpha1*porosity*mesh.Vsc())
47     << "  Min(alpha1) = " << min(alpha1).value()
48     << "  Max(alpha1) = " << max(alpha1).value()
49     << endl;
```

Here, the Eq. 5.13 is discretized in terms of the flux (*phi*) of the previous time step. Note that the time derivative term is not included explicitly in the *phiAlpha* field, because it is introduced by the MULES solver, as seen in Section 5.2.3.

The regular explicit resolution process used to be called in line 27, but it has been commented out. The VOF indicator function, the velocity flux, the flux of VOF and the

maximum and minimum bounds of the solution, respectively, were provided.

As shown before, the VOF advection equation is different from the default one because of the porosity. The MULES solver has another built-in procedure to account for the porosity and source terms. This is the constructor shown in line 28, where *porosity* has been introduced, and since the no source terms are needed, they are set to zero (*zeroField*). Calling MULES in such away, overcomes the well-known reported bug for OpenFOAM® *porousInterFoam* solver, in which porosity is not taken into account in the VOF equation. The outputs of this function are the new *alpha1* and *phiAlpha* fields.

Apart from the new way to solve for *alpha1*, the integration of the total volume needs to be adjusted to account for porosity as well. With the modification of line 46, the reported values are correct.

After the solution has been obtained, the mass flux field (*rhoPhi*) is updated, and back in **alphaEqnSubCycle.H** so are the curvature of the interface (line 27) and the density (line 29), which is recalculated using Eq. 5.11.

The main program continues with the PIMPLE loop, which calculates the new velocity and pressure fields.

ihFoam.C

```
110 // --- Pressure-velocity PIMPLE corrector loop
111 while (pimple.loop())
112 {
113     #include "UEqn.H"
114
115     // --- Pressure corrector loop
116     while (pimple.correct())
117     {
118         #include "pEqn.H"
119     }
120
121     if (pimple.turbCorr())
122     {
123         turbulence->correct();
124     }
125 }
126
127 runTime.write();
128 // Write Porous Variables
129 if( activePorosity && runTime.outputTime() )
130 {
131     porosity.write();
132     porosityIndex.write();
133 }
```

The line number 111 serves as an example to illustrate the level of abstractness of the

OpenFOAM® code after version 2.0. Instead of having the conditions explicitly defined in the main loop (i.e. number of iterations and convergence criteria, as noted in Fig. 5.2), an auxiliary function is called to check them.

The first stage in the PIMPLE loop is to assemble the equation for velocities and to perform the predictor step:

UEqn.H (*ihFoam*)

```
8  fvVectorMatrix UEqn
9  (
10     (1.0 + cPorField) / porosity * fvm::ddt(rho, U)
11     + 1.0/porosity * fvm::div(rhoPhi/porosityF, U)
12     - fvm::laplacian(muEff/porosityF , U)
13     - 1.0/porosity * ( fvc::grad(U) & fvc::grad(muEff) )
14     // Closure Terms
15     + aPorField * pow(1.0 - porosity, 3) / pow(porosity,3)
16         * twoPhaseProperties.mu() / pow(D50Field,2) * U
17     + bPorField * rho * (1.0 - porosity) / pow(porosity,3)
          / D50Field
18         * mag(U) * U *
19     // Transient formulation
20     (1.0 + useTransMask * 7.5 / KCPorField)
21 );
22
23 UEqn.relax();
24
25 if (pimple.momentumPredictor())
26 {
27     solve
28     (
29         UEqn
30      ==
31         fvc::reconstruct
32         (
33             (
34                 fvc::interpolate(interface.sigmaK())*fvc::
                      snGrad(alpha1)
35               - ghf*fvc::snGrad(rho)
36               - fvc::snGrad(p_rgh)
37             ) * mesh.magSf()
38         )
39     );
40 }
```

This piece of code is also very representative of the simplicity to discretize equations in OpenFOAM®. The *fvVectorMatrix* object created includes the coefficients matrix (implicit terms, denoted by *fvm*) and the independent terms (explicit terms, denoted by *fvc*) of the momentum equations. The porosity is introduced in all the terms, sometimes cell-wise and others face-wise, depending on the discretization procedure. The three friction terms are also implemented, a and b explicitly and c implicitly. Note also the

transient formulation with the Keulegan-Carpenter number (line 20), multiplying the b term.

The VARANS formulation is identical to the RANS equations, outside the porous media, therefore, both can be compared:

UEqn.H (*interFoam*)

```
8  fvVectorMatrix UEqn
9  (
10     fvm::ddt(rho, U)
11   + fvm::div(rhoPhi, U)
12   - fvm::laplacian(muEff, U)
13   - (fvc::grad(U) & fvc::grad(muEff))
14 //- fvc::div(muEff*(fvc::interpolate(dev(fvc::grad(U))) &
       mesh.Sf()))
15 );
```

Note how the Eq. 5.2 (lacking some terms) can almost be read literally from lines 10–13.

Line 23 of **UEqn.H** includes an instruction that allows the relaxation of the coefficients matrix, as allowed in SIMPLE loops. This is the main reason to call this loop PIMPLE (PISO + SIMPLE). However, relaxation is not usually enabled in transient calculations (i.e. all the simulations in this work), resulting in a regular PISO solving loop.

The predictor of the two-step method can be switched on or off (line 25). If connected, the system solves an intermediate equation that updates the velocity field of the system with the information of the previous time step pressure (*p_rgh*). The new velocity obtained does not fulfil continuity ($\nabla \cdot \mathbf{U} \neq \mathbf{0}$), but it will be adjusted in the next step. If the predictor is not connected, the velocity field from the previous time step will be used to solve the pressure equation.

It is remarkable that the terms of Eq. 5.2 that were not included before, are now accounted for (lines 31–37) without modifying the original *UEqn* object. Also note the easy way to solve the equation, by using the *solve* function.

The pressure loop starts in line 116 of **ihFoam.C** and is coded in **pEqn.H**:

pEqn.H

```
2  volScalarField rAU(1.0/UEqn.A());
3  surfaceScalarField rAUf(fvc::interpolate(rAU));
4
5  U = rAU*UEqn.H();
6  surfaceScalarField phiU
7  (
```

```
8       "phiU",
9       (fvc::interpolate(U) & mesh.Sf())
10    + fvc::ddtPhiCorr(rAU, rho, U, phi)
11  );
12
13  adjustPhi(phiU, U, p_rgh);
14
15  phi = phiU +
16  (
17      fvc::interpolate(interface.sigmaK())*fvc::snGrad(alpha1
            )
18    - ghf*fvc::snGrad(rho)
19  )*rAUf*mesh.magSf();
20
21  while (pimple.correctNonOrthogonal())
22  {
23      fvScalarMatrix p_rghEqn
24      (
25          fvm::laplacian(rAUf, p_rgh) == fvc::div(phi)
26      );
27
28      p_rghEqn.setReference(pRefCell, getRefCellValue(p_rgh,
            pRefCell));
29
30      p_rghEqn.solve(mesh.solver(p_rgh.select(pimple.
            finalInnerIter())));
31
32      if (pimple.finalNonOrthogonalIter())
33      {
34          phi -= p_rghEqn.flux();
35      }
36  }
37
38  U += rAU*fvc::reconstruct((phi - phiU)/rAUf);
39  U.correctBoundaryConditions();
40
41  #include "continuityErrs.H"
```

The pressure equation is solved as referenced in the previous section. Note how the final equation is assembled in line 25. This specific piece of code can be confusing, as some of the variables are re-used to minimize the use of memory, hence, their name does no longer indicate what they contain.

To conclude with the PIMPLE loop, the turbulence equations are solved and the turbulent fields updated, starting from line 121 in **ihFoam.C**.

Finally, all the fields that are computed are written into the disk (line 127). Since all the porosity-related fields have been created with the *NO_WRITE* flag, to avoid the automatic writing to the disk when porosity is not activated, an explicit call to the write function has to be made. From line 129 in *ihFoam.C*, the *porosity* and *porosityIndex* fields are output when the porosity model is active and the output time is the correct one.

5.3 Boundary conditions

Apart from the wave generation and absorption procedures developed in this work, there are currently two others available that can be applied in OpenFOAM®.

The first and oldest approach is GroovyBC, which is freely available online [1] and distributed independently from OpenFOAM®. While it is not a specific boundary condition for wave generation, it accepts elementary mathematical expressions. Hence, it is suitable only to generate simple wave theories like Stokes I or II, provided that wave length is given or approximated explicitly.

This technique is rather simplistic, as it only accounts for purely wet or dry cells. The resulting waves show initial disturbances similar to steps due to this lack of partial cells, and need more time to regularize their profile. Moreover, no wave absorption procedure is available with GroovyBC. Therefore, the wave generation boundary will reflect the waves that impact on it, increasing the agitation. Also, due to the mass imbalance between wave crests and troughs, the water level will increase unbounded.

The second approach, Jacobsen et al. (2012), is one of the latests works presented. It is also freely available online [2] and distributed independently from OpenFOAM®. This library is specific for wave generation, therefore, it supports a large number of wave theories, accounting for wet, dry and also partial cells. It also includes wave absorption capabilities. Both, wave generation and absorption, are based in internal relaxation zones.

This tool is currently the most widely used by OpenFOAM® users. Validation of the wave generation and absorption has been published (Jacobsen et al. (2012), Jensen et al. (2014)). However, this technique has a clear disadvantage, as requires increasing the computational domain by approximately one or two wave lengths, depending on whether an absorption region is placed opposite to the wave generation zone. This is quite inconvenient because studies to be published report an increase in the solving time up to 50% with respect to active wave generation and absorption.

[1] http://openfoamwiki.net/index.php/Contrib_groovyBC
[2] http://openfoamwiki.net/index.php/Contrib/waves2Foam

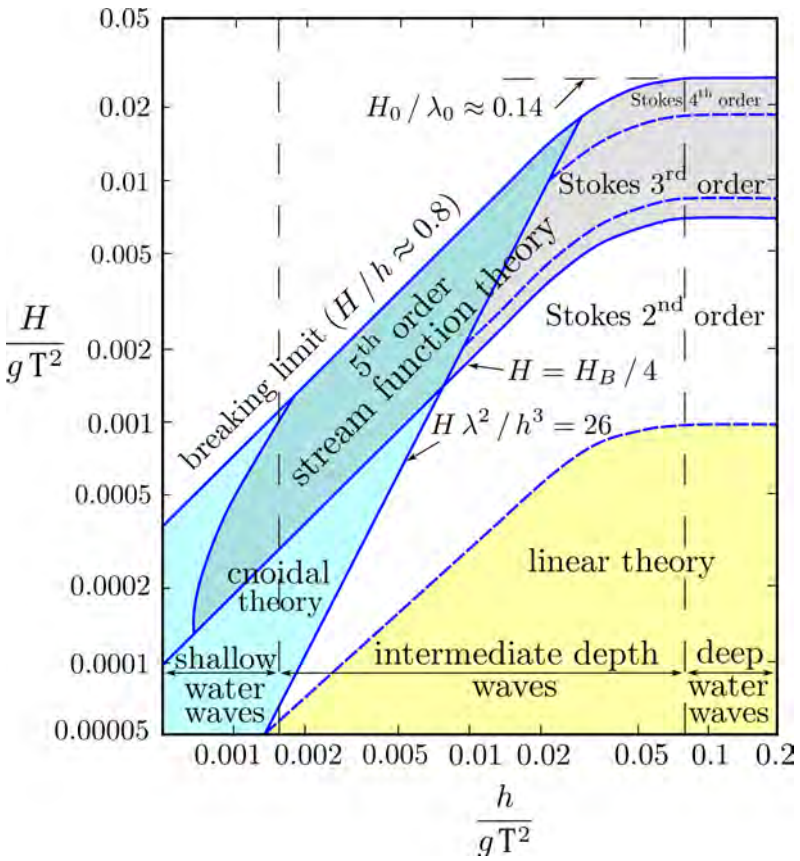

Figure 5.4: Wave theories range of applicability. Le Méhauté (1976). Taken from[3].

5.3.1 Static boundary wave generation

5.3.1.1 Introduction

The **IHFOAM** wave generation BC introduces several features such as active wave absorption and a specific module to replicate laboratory wavemakers. It has been coded from scratch to realistically generate waves at the boundaries according to a number of wave theories, including: Stokes I, II and V, cnoidal and streamfunction regular waves; Boussinesq solitary wave; irregular (random) waves, first and second order; and piston-type wavemaker replication. To choose among wave generation theories it is advised to use the classic graph by Le Méhauté (1976), shown in Fig. 5.4.

As a convention for the wave generation BCs to work appropriately, gravity has to act in the negative direction of the Z axis, and the lowest points of each wave generation boundary must be placed at the same level, but that level can be different from patch to patch. Angles are measured from the X axis, and increasing anticlockwise (towards Y).

[3] http://en.wikipedia.org/wiki/File:Water_wave_theories.svg

Theory	Reference	Comments
Stokes I and II	Dean and Dalrymple (1991)	
Stokes V	Skjelbreia and Hendrickson (1960)	
Cnoidal	Svendsen (2006)	Best fit solver.
Streamfunction	Fenton (1988)	No solver programmed. Its input is the output coefficients from Fenton (1988) program.
Solitary wave	Lee et al. (1982)	Boussinesq theory.

Table 5.2: Wave generation references.

η	free surface elevation
$[u, v, w]$	velocity components
L	wave length
T	wave period
h	water depth
k	wave number
c	wave celerity
ω	angular frequency
ψ	wave phase shift
θ	total wave phase
β	wave propagation direction

Table 5.3: Variables used in this chapter.

Table 5.2 is presented as a summary of the wave theories that are listed next. It includes the references used and some remarkable information about the solvers implemented within the boundary condition. Finally, all the common variables used in this part are referenced in Table 5.3.

5.3.1.2 Wave theories

Stokes I

Stokes I, Airy wave theory, small amplitude waves or linear waves is the most simple analytical solution for water waves. It was developed by Airy (1845) and still today is one of the most widely used, not only for its ease of implementation but also because it is accurate enough for some engineering approximations. Despite its narrow theoretical range of applicability, the practical use is wider, as this theory can also be further developed and extended to higher order, as presented on Section 5.3.1.2.

The main assumptions of this particular wave theory are as follows:

- Continuous, homogeneous, incompressible and inviscid fluid.
- Coriolis forces are neglected.
- Surface tension is neglected.
- Pressure at the free surface is uniform and constant.
- The flow is irrotational.
- The bottom is fixed and impervious.
- The relative wave height is small ($\frac{H}{h} << 1$).

Waves can be represented mathematically. The most important expression is the dispersion relation, a transcendental equation to obtain wave length (L) for a certain depth given a period:

$$L = \frac{g\,T^2}{2\pi}\tanh\left(\frac{2\pi h}{L}\right) \tag{5.26}$$

Other important relations are:

$$k = \frac{2\pi}{L} \tag{5.27a}$$

$$\omega = \frac{2\pi}{T} \tag{5.27b}$$

$$c = \frac{L}{T} \tag{5.27c}$$

$$L_0 = \frac{g\,T^2}{2\pi} \tag{5.27d}$$

The solution to this wave theory is based on a potential function, from which free surface elevations and the velocity field can be obtained. For a 2D wave, travelling in the positive direction of X axis the expressions are:

$$\eta = \frac{H}{2}\cos(kx - \omega t + \psi) \tag{5.28}$$

$$u = \frac{H}{2}\omega\frac{\cosh(kz)}{\sinh(kh)}\cos(kx - \omega t + \psi) \tag{5.29a}$$

$$w = \frac{H}{2}\omega\frac{\sinh(kz)}{\sinh(kh)}\sin(kx - \omega t + \psi) \tag{5.29b}$$

For these expressions to be applicable, the assumption that the lowest coordinate of the boundary is placed in $z = 0$ should be made. Nevertheless this is not general, and some simulations may have wave generating boundaries with different lowest levels. To account for it, this z coordinate may be viewed as a local one, $z = h^* + z^*$, in which the reference level for z^* is the initial still water level, and h^* is the local water depth in the current boundary.

Taking into account that 2D is a special case within the 3D scope there is a real need to extend this formulation to the general case. This is straightforward, setting the 2D case in the desired direction (β) and projecting the result in the X and Y axes, assuming that gravity always works in the Z axis. This process yields:

$$\eta = \frac{H}{2}\cos(\theta) \tag{5.30}$$

$$u = \frac{H}{2}\omega\frac{\cosh(kz)}{\sinh(kh)}\cos(\theta)\cos(\beta) \tag{5.31a}$$

$$v = \frac{H}{2}\omega\frac{\cosh(kz)}{\sinh(kh)}\cos(\theta)\sin(\beta) \tag{5.31b}$$

$$w = \frac{H}{2}\omega\frac{\sinh(kz)}{\sinh(kh)}\sin(\theta) \tag{5.31c}$$

where $\theta = k_x x + k_y y - \omega t + \psi$. Now $k_x = k\cos(\beta)$ is the projected wave number in the X axis and $k_y = k\sin(\beta)$ is the same for the other horizontal direction. From now on, only the 2D version of the wave theories will be presented, since the transformation to 3D is straightforward.

Should this wave theory be used outside its range, waves are likely to decompose and deform because free surface elevation and the velocity field are not those needed for equilibrium. This causes a secondary wave crest in the trough of the main waves, which

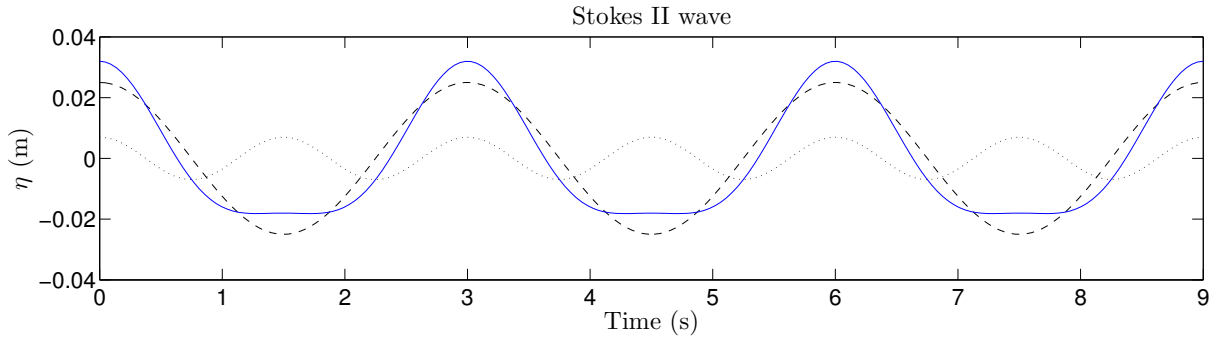

Figure 5.5: Stokes II wave theory: $H = 5$ cm; $h = 40$ cm; $T = 3$ s. Stokes I component is the dashed line, the second order contribution is the dotted line. The final wave is shown in a continuous line. The change in shape of the wave is evident.

does not appear in nature.

Stokes II

Stokes II is a further development of Stokes I wave theory, which adds a second order term to the previously studied theory. It is still very easy to implement, as only the dispersion relation has to be iteratively solved. The practical effect of the second term is the sum of another wave which oscillates twice as fast. The effect of the second order can be seen in Fig. 5.5, in which a 5 cm wave on 40 cm of water and 3 seconds of period is presented.

The resulting expressions for free surface and velocity components are:

$$\eta = \frac{H}{2}\cos(\theta) + k\frac{H^2}{4}\frac{3-\sigma^2}{4\sigma^3}\cos(2\theta) \tag{5.32}$$

$$u = \frac{H}{2}\omega\frac{\cosh(kz)}{\sinh(kh)}\cos(\theta) + \frac{3}{4}\frac{H^2\omega k\cosh(2kz)}{4\sinh^4(kh)}\cos(2\theta) \tag{5.33a}$$

$$w = \frac{H}{2}\omega\frac{\sinh(kz)}{\sinh(kh)}\sin(\theta) + \frac{3}{4}\frac{H^2\omega k\sinh(2kz)}{4\sinh^4(kh)}\sin(2\theta) \tag{5.33b}$$

with $\sigma = \tanh(kh)$.

Once again, if this theory is employed further outside its range of application a secondary wave crest will appear in the wave trough of the primary wave component.

Stokes V

The previous theories represent the smaller waves fairly well. However, as wave height increases they can no longer be considered of small amplitude. Therefore, another theory is necessary to be able to represent these finite height waves. There are a number of fifth order Stokes waves theories. Based on previous experience regarding wave generation, the theory presented in Skjelbreia and Hendrickson (1960) is applied in this work.

For the full development of the theory the reader is referred to the original paper, but the equations to solve and the expressions for free surface and velocity are given here. A system of two transcendental equations with two unknowns must be solved iteratively to obtain wave length (L) and the λ parameter that appear throughout the expressions. These two equations are:

$$\frac{\pi H}{h} = \frac{L}{h}\left[\lambda + \lambda^3 B_{33} + \lambda^5 \left(B_{35} + B_{55}\right)\right] \tag{5.34}$$

$$L = L_0 \tanh\left(\frac{2\pi h}{L}\right)\left(1 + \lambda^2 C_1 + \lambda^4 C_2\right) \tag{5.35}$$

where factors A_{ij}, B_{ij} and C_i depend on L, and have polynomial expressions. In the boundary condition, Newton-Raphson algorithm is used to solve the system. This is not always possible, specially out of range, so if no convergence is obtained the simulation stops and throws a fatal error.

In a practical sense there is a way to avoid N-R solver based on the fact that the resulting wave length is always greater than the linear theory one. This yields to a bound for Stokes V wave length, between the mentioned one and L_0. This interval can be divided into a great number of points, and for each of them two different λ values can be easily computed with Eqs. 5.34 and 5.35. The point which has the smallest difference between both values of λ will be the solution. For waves within the range of applicability, and using a high resolution for L, this approximation works fine. Outside that range the so called three crested waves might appear, as shown in Fig. 5.6.

The expressions for free surface and velocities are:

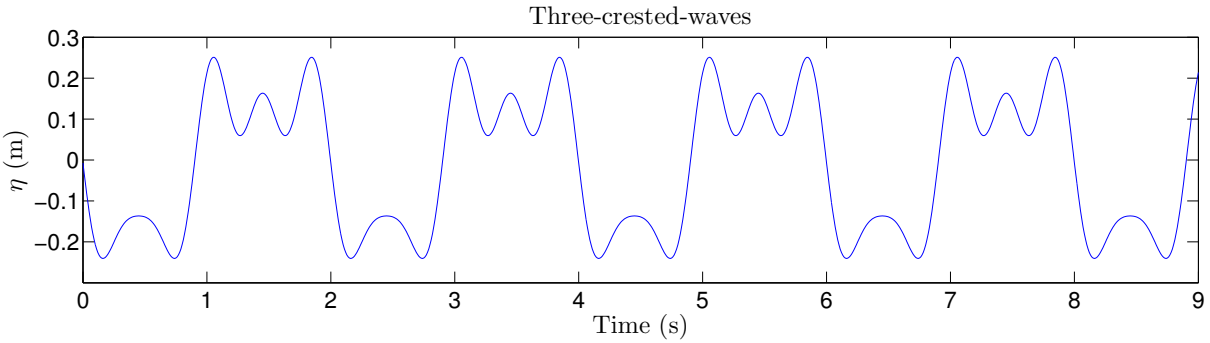

Figure 5.6: Three crested waves Stokes V wave theory: $H = 30$ cm; $h = 40$ cm; $T = 3$ s. Theory has been used out of range, as the wave is very close to breaking. Cnoidal or streamfunction should be used to realistically represent such waves.

$$\begin{aligned}\eta =&\lambda\cos(\theta)/k + \left(\lambda^2 B_{22} + \lambda^4 B_{24}\right)\cos(2\theta)/k + \left(\lambda^3 B_{33} + \lambda^5 B_{35}\right)\cos(3\theta)/k \\ &+ \lambda^4 B_{44}\cos(4\theta)/k + \lambda^5 B_{55}\cos(5\theta)/k\end{aligned} \tag{5.36}$$

$$\begin{aligned}u =&a_{vel1}\cosh(kz)\cos(\theta) + a_{vel2}\cosh(2kz)\cos(2\theta) + a_{vel3}\cosh(3kz)\cos(3\theta) \\ &+ a_{vel4}\cosh(4kz)\cos(4\theta) + a_{vel5}\cosh(5kz)\cos(5\theta)\end{aligned} \tag{5.37}$$

$$\begin{aligned}w =&a_{vel1}\sinh(kz)\sin(\theta) + a_{vel2}\sinh(2kz)\sin(2\theta) + a_{vel3}\sinh(3kz)\sin(3\theta) \\ &+ a_{vel4}\sinh(4kz)\sin(4\theta) + a_{vel5}\sinh(5kz)\sin(5\theta)\end{aligned} \tag{5.38}$$

in which the amplitude for each term is:

$$a_{vel1} = \frac{2\pi}{Tk}\left(\lambda A_{11} + \lambda^3 A_{13} + \lambda^5 A_{15}\right) \tag{5.39a}$$

$$a_{vel2} = 2\,\frac{2\pi}{Tk}\left(\lambda^2 A_{22} + \lambda^4 A_{24}\right) \tag{5.39b}$$

$$a_{vel3} = 3\,\frac{2\pi}{Tk}\left(\lambda^3 A_{33} + \lambda^5 A_{35}\right) \tag{5.39c}$$

$$a_{vel4} = 4\,\frac{2\pi}{Tk}\left(\lambda^4 A_{44}\right) \tag{5.39d}$$

$$a_{vel5} = 5\,\frac{2\pi}{Tk}\left(\lambda^5 A_{55}\right) \tag{5.39e}$$

Cnoidal

Cnoidal waves are a type of nonlinear regular waves with a distinctive shape. They are naturally present in nature, when wave length is large compared to the water depth. This leads to a particular and very recognizable wave shape, with very long and flat troughs and steep wave crests. Their starting point is the Korteweg-de Vries equation:

$$\frac{\partial \eta}{\partial t} + \sqrt{gh}\left(1 + \frac{3}{2}\frac{\eta}{h}\right)\frac{\partial \eta}{\partial x} + \frac{h^2}{6}\sqrt{gh}\frac{\partial^3 \eta}{\partial x^3} = 0 \tag{5.40}$$

This theory has two asymptotic limits. First, if wave length tends to infinity, a solitary wave will be obtained. Second, if the relative wave height is small, the results will match Stokes I theory. There are also a number of cnoidal wave theories in the literature, in this case Svendsen (2006) has been used.

Prior to obtaining free surface or velocities, Eqs. 5.41 must be solved to obtain the wave length (L) and the elliptic parameter (m):

$$\frac{c^2}{gh} = 1 + \frac{H}{mh}\left(2 - m - 3\frac{E_m}{K_m}\right) \tag{5.41a}$$

$$\frac{HL^2}{h^3} = \frac{16}{3}mK_m^2 \tag{5.41b}$$

$$c = \frac{L}{T} \tag{5.41c}$$

where K_m is the complete elliptic integral of the first kind and E_m is the complete elliptic integral of the second kind, both dependent on m. Eq. 5.41c is used to calculate the error of each iteration. The elliptical parameter m can take values between 0 and 1. When it reaches the lowest value, this theory is equivalent to Stokes I. And when m approaches 1 the resultant waves resemble a solitary wave in shape. Effectively, the range for cnoidal waves presented in Le Méhauté (1976) covers values of m between 0.5 and $0.\bar{9}$, therefore the implemented solver tests all the values in between with a 10^{-5} resolution for the smallest error. It is an assumable cost, since it is only performed once, and expressions are fully explicit then.

When the wave characteristics have been obtained, free surface is calculated using Eq. 5.42:

$$\eta = H\left[\frac{1}{m}\left(1-\frac{E_m}{K_m}\right)-1+cn^2\left[2K_m\left(\frac{x}{L}-\frac{t}{T}\right)\Big|_m\right]\right] \tag{5.42}$$

in which cn is Jacobi elliptic function. The expression for velocities involves knowing η in advance, and the ability to calculate several derivatives, which are obtained numerically. Velocity components are presented in equation 5.43.

$$u = c\frac{\eta}{h} - c\left(\frac{\eta^2}{h^2}+\frac{\overline{\eta^2}}{h^2}\right)+\frac{1}{2}c\,h\left(\frac{1}{3}-\frac{z^2}{h^2}\right)\eta_{xx} \tag{5.43a}$$

$$w = -c\,z\left[\frac{\eta_x}{h}\left(1-\frac{2\eta}{h}\right)+\frac{1}{6}h\left(1-\frac{z^2}{h^2}\right)\eta_{xxx}\right] \tag{5.43b}$$

where η_x, η_{xx} and η_{xxx} are the first, second and third derivatives of the free surface elevation with respect to x, respectively; and $\overline{\eta^2}$ is the mean over a wave period of the free surface elevation squared.

Streamfunction theory

When Stokes V or cnoidal wave theories are not applicable, usually a high order streamfunction solution can be used. And what is more, it can be extended to any order solving an extended system of equations. This approach allows the generation of waves very near to the breaking condition.

The specific procedure is not explained here; the reader may be referred to Rienecker and Fenton (1981) and Fenton (1988) for the details, but it is based on expressing the complex potential solution in terms of a Fourier series. The solver has not been coded within the boundary condition, instead a program called *Fourier*, developed also by Fenton and similar to the one presented in Fenton (1988) is used. It is coded in C and is currently available for download[4]. All it needs as input is the nondimensionalized wave height ($\frac{H}{h}$) and period ($T\sqrt{\frac{g}{h}}$) or wave length, plus the current magnitude, which can be taken as 0 when modelling a wave flume or tank. The output is formed by several wave parameters and two sets of components: 10 suffice for ordinary waves, but up to 32 can be computed for steeper ones. These, along with wave length and the mean fluid speed in the frame

[4] http://johndfenton.com/Steady-waves/Fourier.html

reference of the wave (also provided by the program) yield the free surface elevation and velocity field, therefore they constitute the input for the boundary condition.

Free surface is calculated using Eq. 5.44.

$$\eta = h \sum_{j=1}^{N} E_j \cos\left[j\left(k\,x - \omega\,t\right)\right] \tag{5.44}$$

where E_j are one set of the given coefficients. The velocity components are presented in Eq. 5.45.

$$u = c - \bar{U} + \sqrt{g h^3 k^2} \sum_{j=1}^{N} j B_j \frac{\cosh\left(jkz\right)}{\cosh\left(jkh\right)} \cos\left[j\left(k\,x - \omega\,t\right)\right] \tag{5.45a}$$

$$w = \sqrt{g h^3 k^2} \sum_{j=1}^{N} j B_j \frac{\sinh\left(jkz\right)}{\cosh\left(jkh\right)} \sin\left[j\left(k\,x - \omega\,t\right)\right] \tag{5.45b}$$

in which $\bar{U}$ is the previously mentioned mean fluid speed in the frame reference of the wave and B_j is the other set of coefficients.

Solitary wave

From the Korteweg-de Vries equation some solutions with permanent form can be obtained; this means that their shape does not change during propagation. The first of these solutions is the solitary wave, which is not an oscillatory wave, but a translational wave (i.e. all the particles of the wave move in the direction of propagation, because its shape is always over the still water level, without evident wave troughs).

There are a number of solitary wave theories. Some of them are reviewed in Lee et al. (1982), from which the expressions for velocities and free surface can been taken. Boussinesq theory is the chosen one, but any of them would be easily implemented and added.

The free surface expression is as follows:

$$\eta = H\,\mathrm{sech}^2\left[\sqrt{\frac{3H}{4h^3}} X\right] \tag{5.46}$$

in which $X = (x - c\,t)$, and the wave speed c is $\sqrt{g\,(h + H)}$.

The velocity components are straightforward, although they involve derivatives of η. They are presented in Eqs. 5.47.

$$\frac{u}{\sqrt{gh}} = \frac{\eta}{h}\left[1 - \frac{1}{4}\frac{\eta}{h} + \frac{h}{3}\frac{h}{\eta}\left(1 - \frac{3}{2}\frac{z^2}{h^2}\right)\frac{d^2\eta}{dX^2}\right] \tag{5.47a}$$

$$\frac{w}{\sqrt{gh}} = \frac{-z}{h}\left[\left(1 - \frac{1}{2}\frac{\eta}{h}\right)\frac{d\eta}{dX} + \frac{1}{3}h^2\left(1 - \frac{1}{2}\frac{z^2}{h^2}\right)\frac{d^3\eta}{dX^3}\right] \tag{5.47b}$$

Using the presented equations and assuming the boundary to be at $x = 0$, the free surface will start at the highest point of the solitary wave. In order to generate the full wave, an artificial lag in space has to be added. There is an obvious problem with this, as a solitary wave theoretical wave length is infinite. This lag in space is directly translated into a time lag. Therefore, there is a need to keep it as low as possible to reduce the simulation (and computational) time. Nevertheless the free surface decreases rapidly and an effective wave length can easily be defined. The usual criterion to calculate it is to set a percentage of the maximum wave height in which the simulation will start. For example if 1% is fine, the lag will be $l = \frac{3.5}{\sqrt{\frac{H}{h}}}$. Sometimes 5% is preferred, in this case the lag will be $l = \frac{2.5}{\sqrt{\frac{H}{h}}}$. Here the 1% criterion is used because 5% would involve half a cell of error in the case in which wave height is discretized using 10 cells.

Irregular waves

Waves in nature are seldom purely regular. For example, swell waves are more or less regular, but they also appear mixed with sea waves. In order to simulate real conditions, an irregular wave generating theory is needed. Most of the times a first order theory will suffice to represent the sea state, while other times second order interactions between first order components will be needed to get more accurate results.

First order

First order directional irregular waves are generated as a linear superposition of Stokes I waves for a given number of components (N), see Eq. 5.48. This approach is physically correct, as most of the times by discretizing a real wave spectrum with a large number of components, very small amplitudes are obtained. Each of the components is defined by its wave height (H_i), wave period (T_i), wave phase (ψ_i) and the direction of propagation

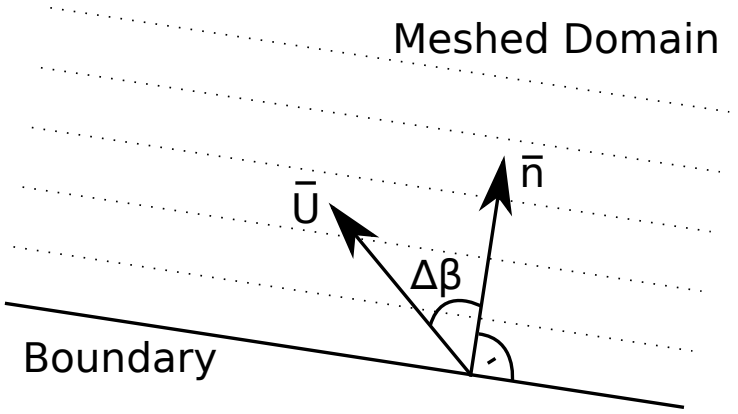

Figure 5.7:Δ β definition.

(β_i). Free surface and orbital velocity components are given by:

$$\eta = \sum_{i=1}^{N} \frac{H_i}{2} \cos\left(k_{x\,i}\, x + k_{y\,i}\, y - \omega_i t + \psi_i\right). \tag{5.48}$$

$$u = \sum_{i=1}^{N} \frac{H_i}{2} \omega_i \cos^2(\Delta\beta_i) \frac{\cosh(k_i z)}{\sinh(k_i h)} \cos(\theta_i) \cos(\beta_i) \tag{5.49a}$$

$$v = \sum_{i=1}^{N} \frac{H_i}{2} \omega_i \cos^2(\Delta\beta_i) \frac{\cosh(k_i z)}{\sinh(k_i h)} \cos(\theta_i) \sin(\beta_i) \tag{5.49b}$$

$$w = \sum_{i=1}^{N} \frac{H_i}{2} \omega_i \cos^2(\Delta\beta_i) \frac{\sinh(k_i z)}{\sinh(k_i h)} \sin(\theta_i) \tag{5.49c}$$

where $\theta_i = k_{ix}x + k_{iy}y - \omega_i t + \psi_i$. $\Delta\beta_i$ corresponds to the difference between each component direction and the vector normal to the boundary pointing into the domain, as shown in Fig. 5.7.

Despite the directionality, the boundaries are not capable of generating outward ($|\Delta\beta| > \pi/2$) or tangential ($|\Delta\beta| = \pi/2$) waves, so these should be left out, taking only angles smaller than $\pi/2$ on each side. For this purpose a classical square cosine function ($f = \cos^2(\Delta\beta)$) has been used. The resultant decreasing factor (f), as a function of the angle difference is shown in Fig. 5.8. This factor is multiplied by the velocities of each component at the boundary, as presented in Eq. 5.49.

Second order

Since with first order wave generation theory the group bound wave is not reproduced

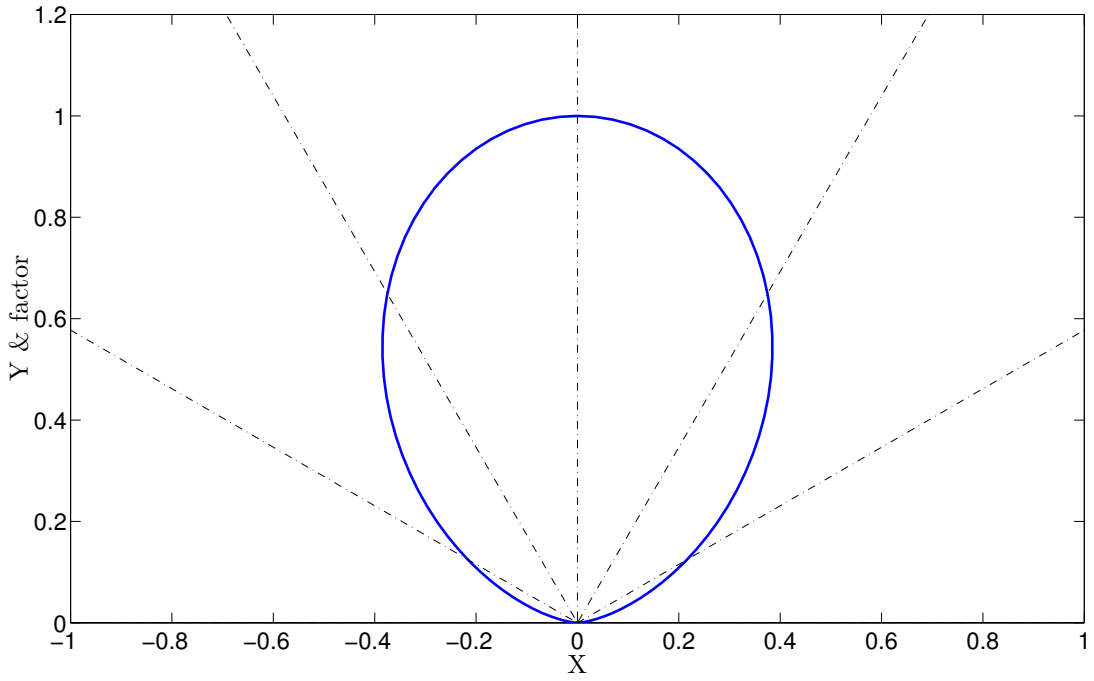

Figure 5.8: Square cosine decreasing factor function presented in blue continuous line. The X and Y axes have the same scale in order to evaluate the angle$\Delta\ \beta$. Only for this figure the angle reference is axis Y. The discontinuous lines are$\Delta\ \beta$ rays each 30°. The reduction factor is the ordinate of the cut point between the ray and the function. Angles greater than 90° and smaller than -90° have a decreasing factor equal to zero.

(Barthel et al., 1983), a correct wave representation needs to include second order effects. The absence of such a feature causes spurious free waves to be generated. Therefore, long wave effects are underestimated in shallow waters and overestimated in deep waters as stated in Sand (1982). Second order irregular wave generation takes into account the interaction between the individual primary wave components, two by two, and it is built on top of the first order method. Currently, it only supports components travelling in the same direction, therefore $\beta_i = \text{const}$.

In this case, the theory by Longuet-Higgins and Stewart (1960) completed with Baldock et al. (1996) is applied as in Torres-Freyermuth et al. (2010). The reader is referred to these papers for further details, as only a brief description will be given here. The second order effects are added to the first order free surface level (Eq. 5.50) and to the velocity. To account for all the velocity components simultaneously the final velocity potential (ϕ) expression is given here in Eq. 5.51.

$$\eta = \sum_{i=1}^{N} \eta_i + \sum_{n=1}^{N-1} \sum_{m=n+1}^{N} \frac{H_n H_m}{8g} [C \cos(\theta_n - \theta_m) - D \cos(\theta_n + \theta_m)] \tag{5.50}$$

$$\begin{aligned} \phi = & \sum_{i=1}^{N} \phi_i + \sum_{n=1}^{N-1} \sum_{m=n+1}^{N} \\ & \left[\frac{E \cosh[(k_n - k_m)(h + z^*)] \sin(\theta_n - \theta_m)}{g(k_n - k_m) \sinh[(k_n - k_m)h] - (\omega_n - \omega_m)^2 \cosh[(k_n - k_m)h]} \right. \\ & \left. - \frac{F \cosh[(k_n + k_m)(h + z^*)] \sin(\theta_n + \theta_m)}{g(k_n + k_m) \sinh[(k_n + k_m)h] - (\omega_n + \omega_m)^2 \cosh[(k_n + k_m)h]} \right] \end{aligned} \tag{5.51}$$

The only new variables introduced are C, D, E and F, which are defined in Longuet-Higgins and Stewart (1960), and given in Eqs. 5.52. C and E control the subharmonic generation while D and F generate the superharmonic interaction.

$$\begin{aligned} C = & \frac{[2\omega_1\omega_2 (\omega_1 - \omega_2)(\alpha_1\alpha_2 + 1) + \omega_1^3 (\alpha_1^2 - 1) - \omega_2^3 (\alpha_2^2 - 1)](\omega_1 - \omega_2)(\alpha_1\alpha_2 - 1)}{\omega_1^2 (\alpha_1^2 - 1) - 2\omega_1\omega_2 (\alpha_1\alpha_2 - 1) + \omega_2^2 (\alpha_2^2 - 1)} \\ & + \left(\omega_1^2 + \omega_2^2\right) - \omega_1\omega_2 (\alpha_1\alpha_2 + 1) \end{aligned} \tag{5.52a}$$

$$\begin{aligned} D = & \frac{[2\omega_1\omega_2 (\omega_1 + \omega_2)(\alpha_1\alpha_2 - 1) + \omega_1^3 (\alpha_1^2 - 1) + \omega_2^3 (\alpha_2^2 - 1)](\omega_1 + \omega_2)(\alpha_1\alpha_2 + 1)}{\omega_1^2 (\alpha_1^2 - 1) - 2\omega_1\omega_2 (\alpha_1\alpha_2 + 1) + \omega_2^2 (\alpha_2^2 - 1)} \\ & - \left(\omega_1^2 + \omega_2^2\right) + \omega_1\omega_2 (\alpha_1\alpha_2 - 1) \end{aligned} \tag{5.52b}$$

$$E = -\frac{1}{8} H_1 H_2 \left[2\omega_1\omega_2 (\omega_1 - \omega_2)(1 + \alpha_1\alpha_2) + \omega_1^3 \left(\alpha_1^2 - 1\right) - \omega_2^3 \left(\alpha_2^2 - 1\right)\right] \tag{5.52c}$$

$$F = -\frac{1}{8} H_1 H_2 \left[2\omega_1\omega_2 (\omega_1 + \omega_2)(1 - \alpha_1\alpha_2) - \omega_1^3 \left(\alpha_1^2 - 1\right) - \omega_2^3 \left(\alpha_2^2 - 1\right)\right] \tag{5.52d}$$

Constant velocity profile

The study of waves in experimental facilities is a very extended approach. In laboratories, waves are generated by moving elements and other physical processes as current or wind can also be reproduced with additional equipment. One of the most widely-spread wavemakers are piston-type for which the wave paddles move back and forth in a fixed

direction, generating a constant velocity profile along the water column.

The immediate way to treat piston-type wavemakers is by reproducing their movement. This dynamic condition will later be addressed in Section 5.3.3.

However, a static counterpart can also be developed. In this case, the present "wave theory" replicates the constant velocity profile generated by a piston-type wavemaker, without moving the boundary, applying a Dirichlet boundary condition. This implementation present some advantages, as it does not involve mesh movement and it can even replicate a current.

It must be noted that since the boundary condition generates a velocity profile that does not match that of a wave (except if the wave is in the linear shallow water regime), evanescent modes will be generated near the wavemaker, but their effect soon vanishes as the wave propagates away.

There are 4 main cases for this boundary condition depending on the input data. Nevertheless, these get converted and reduced to only 2 cases at the first time step of the simulation.

The first case (**tx**) requires a series of time and displacement of the wavemaker, which is the most usual output of experimental facilities. From these, velocity of the wavemaker is calculated as a first order forward derivative, as shown in Eq. 5.53.

$$U = \frac{X_{i+1} - X_i}{t_{i+1} - t_i} \tag{5.53}$$

in which for a given time t: $t_i \leq t < t_{i+1}$.

This expression is quite convenient because it does not require a homogeneous sampling rate. The resultant is the second type of input (**tv**), when a time series of velocities is provided.

The third and fourth cases are the same as before, but an additional series of free surface elevation at the wavemaker is also provided (**txeta, tveta**). Not all the experimental wavemakers are capable of providing such feedback, but it allows to connect the active wave absorption without further assumptions. To prescribe the free surface level, the time series is interpolated linearly.

5.3.1.3 Numerical implementation

Numerical implementation is common to all wave theories. Only a small change is made in the case of the piston-type wavemaker replication when no free surface is provided. The current approach takes into account three types of cells: wet cells, which have all the vertices below the free surface level; dry cells, which have all the vertices above the free surface level; and partial cells, in which the free surface is between the lowest and highest vertices of the cell.

Wave generation involves setting the values of velocity and VOF function (field *alpha1*, α_1 from now on), therefore their implementation is separate, but they share most of the source code. Pressure is not set directly, it is calculated using the *buoyantPressure* boundary condition. This special function available in OpenFOAM® calculates the normal gradient from the local density gradient. This ensures that the second derivative of pressure in the orthogonal direction to the boundary is zero.

During the first time step of the model, and only then, several processes are carried out. Wave generation variables are read and relevant variables are calculated using wave theory. Also the initial still water depth at the patch is measured, as the wet area of the patch (sum of the individual face areas times α_1) over the total patch area.

For the piston-type wavemaker replication, if free surface is not provided, the corresponding constant velocity profile along the whole water column is applied. This is done by multiplying such velocity by α_1 at each cell, in order not to introduce air velocity. No further considerations are made. If the free surface elevation is provided, it is interpolated linearly in time and the procedure is as in the general case, explained next.

For the rest of the cases presented, an expression to calculate the free surface is either provided or calculated by means of the corresponding wave theory. Consequently, at each time step, the theoretical and measured free surface levels can be compared in order to trigger active wave absorption. The following method takes into account the possibility of high amplitude reflected waves reaching the generation patch, and makes the simulation more stable.

In the next lines *zero gradient* is used to indicate that the boundary face value is set to the value of its owner cell or mathematically for any variable q: $\frac{\partial q}{\partial x_i} n = 0$, where n is the normal direction to the face. Please, note that it does not refer to the *zeroGradient*

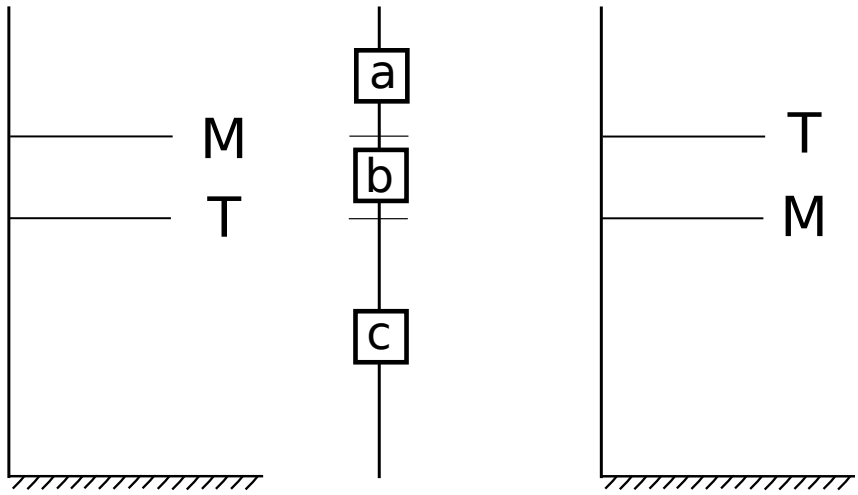

Figure 5.9: Water level in a wave generating patch. "M" stands for measured value, "T" stands for theoretical value. Three zones (a, b and c) and two interfaces are present in each case.

boundary condition provided in OpenFOAM®.

There are three different areas, which are indicated in Fig. 5.9, depending on whether the measured level is higher than the theoretical one (positive reflected wave, left panel on the figure) or lower (negative reflected wave, right panel). This disposition provides three different areas ("a", "b" and "c") and two interfaces between them. The implementation is explained next, and can be summarized as shown in Table 5.4.

Zone "a" is common in both cases, and corresponds to air ($\alpha_1 = 0$). Therefore, the faces within it have α_1 and velocity set to zero.

The interface between "a" and "b" is different depending on the case, because wave velocity is set only below the theoretical level. When M > T carries a zero gradient value for α_1 and zero velocity. If T > M, a special procedure is performed. The intersection between the theoretical water level and the cell is calculated to obtain the corresponding α_1 of the cell. Also the centroid of the cell wet part is obtained to calculate the velocity at that point. Velocity is set as the multiplication of both quantities. This is done to prevent inconveniently high air velocities at the interface, that tend to lower the Courant number and have negative impact in stability.

Zone "b" also depends on the case. When M > T, α_1 is set to zero gradient and velocity is directly zero. When T > M, α_1 is set to 1 when water flux is inwards and to zero gradient otherwise. Velocity is set to the theoretical value. This sometimes may cause water droplets to appear in the boundary, especially when the reflected amplitude

	M > T			**T > M**	
	α_1	U		α_1	U
a	0	0	a	0	0
a-b	$\frac{\partial \alpha_1}{\partial x_i} n = 0$	0	a-b	$\alpha_{1\,calc}$	$U \cdot \alpha_{1\,calc}$
b	$\frac{\partial \alpha_1}{\partial x_i} n = 0$	0	b	In $\rightarrow$ 1 Out $\rightarrow$ $\frac{\partial \alpha_1}{\partial x_i} n = 0$	U
b-c	$\frac{\partial \alpha_1}{\partial x_i} n = 0$	$U \cdot \alpha_{1\,calc}$	b-c	In $\rightarrow$ 1 Out $\rightarrow$ $\frac{\partial \alpha_1}{\partial x_i} n = 0$	U
c	In $\rightarrow$ 1 Out $\rightarrow$ $\frac{\partial \alpha_1}{\partial x_i} n = 0$	U	c	In $\rightarrow$ 1 Out $\rightarrow$ $\frac{\partial \alpha_1}{\partial x_i} n = 0$	U

Table 5.4: Overview of the boundary condition values depending on the zones established in Fig. 5.9.

is large (on the order of several cells).

The interface between "b" and "c" sometimes has water above (M > T) and sometimes should (T > M), but due to the reflected waves it does not. This condition changes its behaviour depending on this situation, as shown in Table 5.4 (left vs right table). In the first case, α_1 is set to zero gradient, and the velocity is calculated in the same way as in zone "a-b" for T > M, for the same reasons explained above. In the second case if water is flowing in, it is set to one, and to zero gradient otherwise. Velocity in this case is set to the calculated value.

Finally, the zone "c" is also common to both cases, as it is always under the measured and theoretical values. Therefore it corresponds to water ($\alpha_1 = 1$). If the flow is entering the domain, α_1 on the face is set to 1, otherwise it is set to zero gradient. This configuration is more stable than setting it always to 1, as it has been observed that this can more easily cause α_1 to reach negative values despite the fact that the MULES solver ensures boundedness between 0 and 1. Velocities are set to the theoretical value.

When an interface coincides with a cell, that cell is automatically an interface cell. Should both of the mentioned interfaces coincide within a cell (e.g. small reflected waves or even T = M), the priority of the cell is from below to the top, from "c" to "a".

The velocity and α_1 can be set in different ways, as decided by the user. The first and most obvious way is face by face. Each of them owns a cell which is formed by a number of points, and by a centroid, all of them having different coordinates. The zone of the face ("a"-"c") is checked using the highest and lowest points of the cell in the Z direction, while velocity is calculated using the centroid coordinate of the face. This boundary

condition also supports an automatic division of the generating patch in vertical slices. Such zones resemble the disposition of individual paddles within a wavemaker, and behave in the precise way to allow closer replication of such a device without the inconvenience of having to manually divide the boundary in advance. Cells within each of these zones lose their x and y coordinates in favour of the centroid of the paddle, but maintain their height, for α_1 and velocity calculation.

Additionally, if active absorption is connected, the face velocities get corrected adding the calculated value to the ones above, in the manner explained in the following section.

5.3.2 Static boundary active wave absorption

Active absorption of waves is one of the key features of physical and numerical experiments in coastal engineering. At prototype scale the waves can travel away from the study zone. However, in physical or numerical experiments this is not the case, the domains are either constrained in dimensions, such as in wave basins and flumes, or cannot be placed at an infinite distance because of computational restrictions. This situation causes inconvenient reflections that, if not handled adequately, could influence the experiment by distorting its results.

Active wave absorption systems can be divided into three categories: 2D, Quasi-3D and 3D. The details for each one are presented as follows.

5.3.2.1 2D Absorption

The 2D active absorption method is developed as appears in Schäffer and Klopman (2000). It is the easiest technique to be implemented considering the fact that the adjustment for the digital filter is immediate, as it is based on linear shallow water theory. Previous works on other numerical models (Torres-Freyermuth et al. (2010), Lara et al. (2011)) have shown that it works relatively well even when used for waves outside the shallow water range.

It is very convenient to use shallow water theory because the velocity along the water column height is constant, which matches the generation with a piston-type wavemaker. This also makes the evanescent modes cancel out because the velocity profile is the exact one for the progressive wave component. From this wave theory, Eq. 5.54 can be derived.

$$U\,h = c\,\eta \tag{5.54}$$

where U is the horizontal vertically–integrated (uniform) correction velocity and c is the wave celerity. U is the variable to solve for, and h and η are measurements, consequently there is a need to estimate wave celerity (c). This magnitude is dependent on the relative depth of the waves (kh) in the following way:

$$c = \sqrt{g\,h}\sqrt{\frac{\tanh(k\,h)}{k\,h}}. \tag{5.55}$$

Wave number (k) is very difficult to estimate from measurements, so the practical application of Eq. 5.55 is achieved by a digital filter assimilation. The use of digital filters for active wave absorption is widely used, for further information refer to Christensen and Frigaard (1994) and Troch and De Rouck (1999). More recently, in Wellens (2012), Eq. 5.56 is used as a rational approximation to Eq. 5.55.

$$c^* = \sqrt{g\,h}\,\frac{a_0 + a_1(k\,h)^2}{1 + b_1(k\,h)^2}. \tag{5.56}$$

Applying shallow water regime, as explained: $c = \sqrt{g\,h}$, yields $a_0 = 1$, $a_1 = 0$ and $b_1 = 0$.

In order to cancel out the reflected waves, the boundary must generate a velocity equal to the incident one but in the opposite direction. Arranging Eq. 5.54 so that the free surface corresponds to the reflected one η_R (the one to cancel out) leads to the active wave absorption expression presented in Eq. 5.57.

$$U_c = -\sqrt{\frac{g}{h}}\,\eta_R \tag{5.57}$$

in which U_c is the correction velocity that is applied to a vector perpendicular to the boundary, pointing into the domain; and the reflected wave height (η_R) is calculated by subtracting the measured elevation at the wavemaker (η_M) from the target one (η_T), according to the expected reflection-free wave generation: $\eta_R = \eta_M - \eta_T$.

This theory was first developed for wave flumes, where the results are usually two dimensional, but can easily be extended to three dimensions. If reflected waves propagate parallel to the wavemaker, the expected behaviour is exactly the same as in the 2D case.

If that is not the case, the absorption theory can be applied to the individual paddles of the wavemaker independently.

There is a problem, however, in absorbing in 3D with the 2D theory, as only the wave component perpendicular to the boundary can be absorbed. The other component, which is tangential to the wavemaker, continues to propagate along the boundary until it reaches a lateral dissipative device, if available. Otherwise it will reflect, as a plane wavemaker cannot absorb such a wave, because it can only introduce shear stresses.

5.3.2.2 Quasi-3D Absorption

Following the example presented in Schäffer and Klopman (2000) a method to absorb oblique waves is presented. This is only a correction of the already presented 2D absorption theory, enhanced by accounting for a known angle of incidence. The practical application is to reduce velocity by a factor $cos(\Delta\beta)$, as presented in Eq. 5.58.

$$U_c = -\cos(\Delta\beta)\sqrt{\frac{g}{h}}\,\eta_R \tag{5.58}$$

Note that when incidence is parallel to the boundary ($\Delta\beta = 0$), absorption velocity remains completely unaffected, since it is a true 2D condition. As waves approach the parallel direction, the theory is expected to underperform, never being able to absorb the tangential component of the wave as$\Delta\ \beta$ approaches 90°. This will ultimately lead to a stationary wave along the wavemaker if the situation is not handled correctly.

This method was developed for piston wavemakers, but it is modified here taking advantage of the numerical model capabilities, to obtain better performance. Instead of reducing the correction velocity and applying it to the direction perpendicular to the boundary, the total correction velocity is still the one calculated with Eq. 5.57, but applied to the desired direction. Generally, this new approach is able to absorb better than projecting the velocity and allowing the tangential component to flow along the boundary.

The performance of this boundary condition is outstanding, but there is a clear drawback: most of the times the direction of the incident waves cannot be anticipated, or radiation from the structure causes that direction to change either in time or along the boundary extents. Nevertheless, good performance is expected even for small deviations in the direction of the absorption (Schäffer and Klopman, 2000).

5.3.2.3 3D Absorption

Although both the 2D and Quasi-3D absorption theories can be used with reasonable results in 3D cases, a specific full 3D theory is needed to obtain lower reflection coefficients or to avoid wave radiation from the absorbing boundaries. The distinctive element of this method is that it uses the feedback additionally to evaluate wave directionality.

The following method is original and quite simple, furthermore it needs no tuning, but due to the complexity of measurements needed, it can only be applied to numerical models. Traditional 3D absorption theories for laboratory wavemakers rely on measuring free surface in front of the individual paddles and by calculating the derivatives or applying a digital filter to this data the directionality is estimated. This involves interconnection between wave paddles. The new method presented in this work eliminates the error introduced by the discrete calculation of derivatives, acting for each paddle independently.

As in the aforementioned methods, this one is also based on shallow water wave theory, i.e. such waves have a constant velocity field along the whole water column. As a result, averaging the horizontal components of velocity all over the water depth will theoretically yield the same value as in each point of a vertical line. The same principle is applied to the direction of the horizontal component of the velocity.

The practical application involves the calculation of a mean horizontal velocity with its mean direction for each vertical slice of the boundary. This velocity can be decomposed into two independent components: one normal to the paddle and another tangential to it. Also, the measured free surface level at that vertical slice is needed. Wave directionality cannot be inferred using these two components of velocity at the same time, since absorbing waves involves imposing a certain velocity on the boundary, which will completely distort the measurements. Hence, correction velocity can only be prescribed on the perpendicular direction to the paddle, as in the usual wave absorption theories using piston wavemakers, leaving the other component unmodified so that it can be measured. The implementation is presented graphically in Fig. 5.10.

Using simple calculations wave directionality can be obtained as follows:

$$|U_{calc}| = \sqrt{\frac{g}{h}}\,\eta_R. \tag{5.59}$$

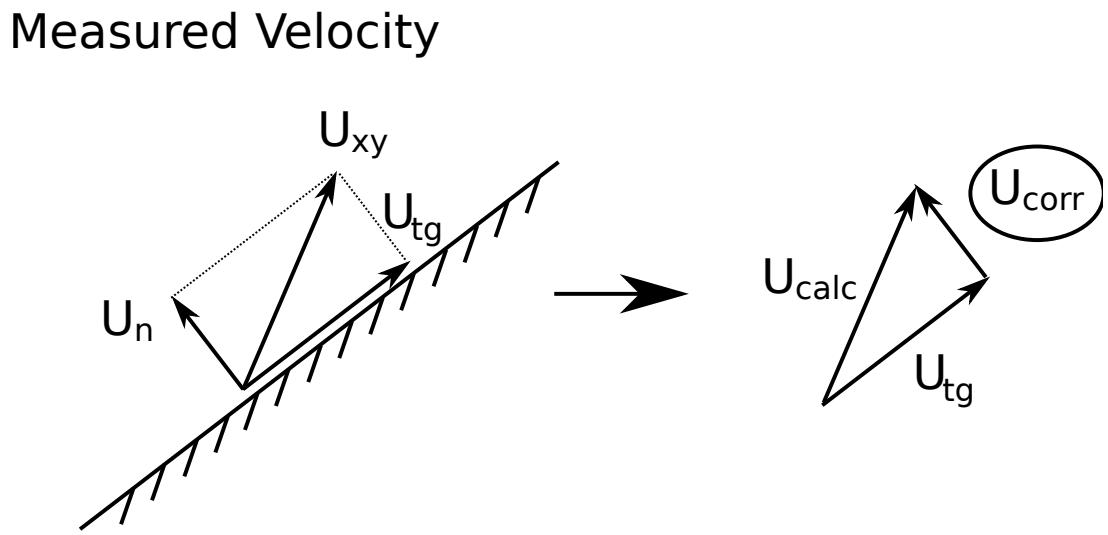

Figure 5.10: Sketch of the full 3D absorption theory.

where $|U_{calc}|$ is the total expected modulus of velocity, based on the measured free surface level minus the expected one. By decomposing it into the two horizontal components it is obvious that:

$$U_{calc}^2 = U_{corr}^2 + U_{tg}^2. \tag{5.60}$$

in which everything is known except for U_{corr}, the correction velocity that has to be applied in the perpendicular direction to the paddle in order to absorb the waves. To solve for U_{corr} modulus, the square root of a subtraction must be obtained:

$$U_{corr} = \sqrt{U_{calc}^2 - U_{tg}^2}. \tag{5.61}$$

It is easy to notice that when the tangential component of the velocity (U_{tg}) is greater than the total one there will be no real solution. To avoid the imaginary solution, if the value inside the square root is negative it is discarded and taken to be zero.

Once again, the problem of having a wave which propagates along the wavemaker is present. There are also two main problems related with corners. The first one is dealing with this tangential wave component which cannot be absorbed along the wave maker. The second is that if two absorbing boundaries converged in a 90° corner, the perpendicular component for the first will be the tangential one for the second and vice versa. This causes a stability problem because wave directionality cannot be correctly

estimated. A unique technique solves all these problems. This is to choose a number of paddles near the edges only capable of extracting water according to Eq. 5.57. The reason for limiting the in-flux of water in such parts is because in the case of an acute corner, water is pushed directly into a small space, causing the level to increase very rapidly, and most of the times reaching the top of the mesh, which will lead to loss of mass in that zone.

5.3.2.4 Numerical Implementation

The implementation of pure active wave absorption is easier, as only the velocities need to be prescribed. The pressure boundary condition is set to *buoyantPressure* again, and α_1 to *zeroGradient*.

Active wave absorption acting on any boundary works in the same way, including wave generation boundaries. This was shown in Fig. 5.2 (bottom left part), in which the correction velocity is added to the existing one: either the calculated velocity required by the wave theory, or 0 in case of a purely absorbent patch. Currently only 2D absorption theory is applicable to wave generating boundaries.

The practical application of the absorption theory consists of dividing the boundary into a given number of vertical elements. The minimum is one, a case in which the whole boundary will absorb globally. For each of the individual elements, the initial still water level is calculated and saved. Then, each time step the actual water level at each paddle is obtained and the correction velocity is calculated according to the previous theories (e.g. using Eq. 5.57 for 2D).

The correction velocity is then recalculated cell by cell, multiplying the obtained value (checking the paddle in which it is included) by the value of α_1 in that cell. This is done to prevent the propagation of air pockets close to the boundary. The resultant velocity is applied in the perpendicular direction to the face (for 2D and full 3D absorption) or to the given direction (Quasi-3D). If such velocity is positive (in-flux), only the cells below the measured ("M") water level are given this value, the rest are set to zero. Otherwise (out-flux) all the cells are set to the recalculated velocity value. The main reason for doing this is to gain stability, as if a water droplet from a splash was higher than the water level on the patch, it will not propagate when water is flowing into the domain. Otherwise,

and it will flow out.

5.3.3 Moving boundary wave generation

A new boundary condition (BC) has been developed to replicate the movement of piston-type wavemakers. The new module works in 2D (single paddle) or 3D (multi-paddle).

The only inputs that are required are the time series of displacement for each paddle. These signals can be theoretical (i.e. obtained by applying analytical expressions), case in which they must comply with the limitations of the device that they are trying to replicate (i.e. maximum velocity, acceleration and stroke). Alternatively, the signals may come from measurements of experimental facilities. In this case it is important to distinguish between the target and the feedback signal of the wave machine. The second one (if available) includes all the mechanical effects of the wavemaker as the response time (delay) and inertial effects. If active wave absorption is to be connected, the time series of water elevation at each paddle are also required. Again, these can come from theoretical values or from actual measurements from the free surface gauges mounted on the front of the paddles.

During runtime the BC performs several operations. First, it computes the limits of each paddle, dividing the boundary into a given number of vertical slices with equal width. It then distributes the vertices of the boundary between all the paddles, depending on their position.

Next, the displacement of such points is set according to the time series provided. The first problem arises at this stage because adjacent paddles in wavemakers move independently one from another and often have a different displacement. In fact they only present the same displacement when generating regular waves or long-crested irregular sea states, parallel to the wavemaker. Since multi-paddle devices are often used to generate oblique waves or short-crested irregular sea states, a technique to allow differential displacements between adjacent paddles in the numerical model is needed.

It must be noted that this problem is not trivial. Since the BC acts on the points of the boundary, a large difference in the displacement between two pairs of points that define a face may yield a warped cell that violates the mesh quality criteria. Therefore,

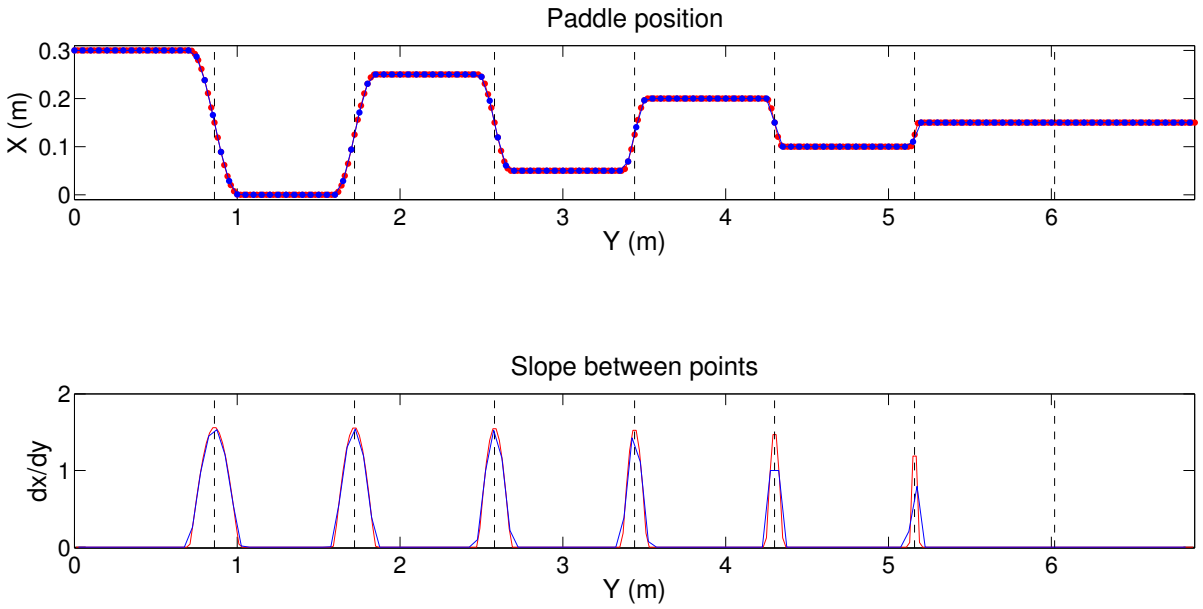

Figure 5.11: Effects of the numerical representation of different paddle displacements. Red line: 2 cm discretization. Blue line: 5 cm discretization.

the procedure that allows differential displacements must also provide a smooth variation between paddles, without forgetting that as the width of the smooth transition zone grows larger, the difference with reality also increases.

A compromise solution has been found to maximize the length of the boundary that remains flat and located where the laboratory paddle should be. A region of smooth transition is defined between each pair of paddles. This area presents a width that varies linearly with the difference in displacement between both paddles (Δd). Therefore, when larger displacements appear, the transition zone increases its width to avoid an excessive displacement between adjacent points, as noted previously. To ensure that the variation inside this region is continuous, a cosine interpolation (between 0 and π radians) has been chosen. This way, the derivative of the local difference in displacement between neighbouring points is always lower or equal to $\pi/2$. In theory, the maximum is always positioned at the interface between paddles and such value ensures that the skewness and non-orthogonality of the cells at that location are still adequate for the numerical model.

In Fig. 5.11 the technique described has been applied to represent a test case. The geometry depicted and coordinate system matches that of the wavemaker applied later in Fig. 6.13: 0.86 m-wide paddles in the Y direction, that move in the X direction, with a maximum allowed difference in displacement between adjacent paddles of 0.30 m. The

difference between the first two paddles (left side of the plots) is 0.3 m, decreasing 0.05 m for each subsequent pair, until the last two, that present the same displacement. Two different discretizations are plotted, a detailed one (2 cm) in red and a coarser one (5 cm) in blue. The top panel shows a horizontal slice of the deformed boundary. Note how the displacement takes place in the X direction and each point represents a node in the mesh. In the bottom panel the derivative of the displacement with respect to the Y direction is represented. The effect of the different discretizations is clearer in this graph. If the position were continuous, all the bell-shaped pikes would reach the $\pi/2$ maximum slope, and have a different width, according to$\Delta\ d$. However, as the displacement gets smaller, the resolution is not enough to fully describe the narrowest cosine curves. This fact does not mean that the errors increase, only that the displacement is not long enough to require such large slopes.

Finally, the target position may need to be corrected to perform wave absorption and/or to fulfil any physical limitations of the machine that is being replicated. The first case will be treated in depth in the following section. The latter involves checking that the velocity, acceleration and displacement of each paddle can be achieved by the physical wavemaker. Otherwise, the displacement has to be adjusted to remain within the limits. Of course, in case of testing an ideal wavemaker, the restrictions can be eliminated.

5.3.4 Moving boundary active wave absorption

Active wave absorption is needed to absorb the waves incident to the wave paddles, which will reflect back into the domain, otherwise. This system prevents an unbounded increase in the agitation, that will contaminate the results. In order to perform the absorption, the position of the paddles is corrected every time step according to the measured free surface elevation at each paddle.

The absorption procedure is based on a two-dimensional approach that appears in Schäffer and Klopman (2000). The starting point is a very simple digital filter, derived from linear theory in shallow water:

$$\mathbf{U}_c = -\sqrt{\frac{g}{h}}\,\eta_I\,\mathbf{n} \tag{5.62}$$

where $\mathbf{U}_c$ is the correction velocity that will absorb the incident wave, positive when

pointing towards the inside of the domain; g is the acceleration due to gravity; h is the water depth; η_I is the free surface elevation incident to the boundary, calculated by subtracting the measured (actual) elevation at the wavemaker from the target (expected) one; and $\mathbf{n}$ is a unit vector normal to the boundary and pointing inwards to the domain. As it can be noted, the bold variables indicate vectors.

Eq. 5.62 can also be written in differential form:

$$\frac{d\mathbf{X}_c(t)}{dt} = -\sqrt{\frac{g}{h}}\,\eta_I(t)\,\mathbf{n} \tag{5.63}$$

To translate this formulation into paddle displacement a uniform velocity along the entire time step (Δt) has been considered. Therefore, the correction velocity will yield the following correction in paddle displacement (ΔX_c):

$$\Delta\mathbf{X}_c = \mathbf{U}_c\,\Delta t \tag{5.64}$$

The negative sign in Eq. 5.62 indicates that to absorb a wave crest ($\eta_I > 0$) the velocity must be negative, causing a paddle movement that stretches the domain towards the outside.

Going back to Eq. 5.62, the cumulative correction displacement can be represented in terms of an integral from the start of the test ($t = -\infty$) to the current time (t), as in Schäffer and Klopman (2000):

$$\mathbf{X}_c(t) = -\sqrt{\frac{g}{h}}\int_{-\infty}^{t}\eta_I(t)\,dt\,\mathbf{n} \tag{5.65}$$

This equation implies an important phenomenon that needs to be taken into account when connecting active wave absorption, and this is the drift of the paddles. If the integration of $\eta_I(t)$ over a wave period is not exactly zero, this contribution will accumulate each wave period and the correction displacement will grow indefinitely.

Disregarding the drifting process can yield a saturation of wave paddle movement, if the piston reaches its maximum stroke. At that point waves can no longer be generated or absorbed because the paddle is not free to move as it should.

To avoid saturation, a so-called Drift Prevention System (DPS) has been implemented. The DPS checks when the 80% of the maximum forward or backward stroke is reached

and slowly pushes the paddle back to its initial position, while continuing to generate the target waves. The movement has to be very slow to minimize the effect on the short waves that still may need to be generated. When this system is activated, a smooth transition is desirable to avoid sudden changes that may lead to artificial effects. The solution is the same cosine function (between 0 and π radians), as applied before.

It must be noted that the static wave generation causes a net influx of mass. Therefore, active wave absorption needs to be connected on at least one boundary to prevent the rise of the mean water level.

Active wave absorption can be disconnected for the moving wave generation, unlike for the Dirichlet-type wave generation, because water interacts with a wall. This means that, even if it is moving, there is no flux across, so no variations of mass in the system are experienced.

5.3.4.1 Moving mesh

The new boundary condition provides the displacement of the points on the moving boundary. Since this technique works without changing the topology of the mesh, only mesh deformation procedures are involved. This means that the only additional field that needs to be solved is the point positions.

Before going any further, the boundary conditions that control the position of the points at the boundaries ($\mathbf{X}_\mathrm{p}$) must be discussed. Those boundaries connected to the moving wave generation boundary (generally two lateral walls, the bottom wall and the atmosphere boundaries) present a zero gradient BC to allow an unrestricted displacement. The rest of the boundaries (i.e. obstacles or the boundary opposite to the paddle), which should not move, have a fixed displacement BC, equal 0 in all the directions. This setup is sketched in Fig. 5.12.

Having defined the boundary conditions for point displacement, the internal vector field is obtained by solving a simple Laplacian equation:

$$\nabla \cdot (k \, \nabla \mathbf{U}) = 0 \tag{5.66}$$

where k is the diffusivity, either constant or variable in space; and $\mathbf{U}$ is the deformation velocity of the mesh points, so that when it is solved the new position for the points can

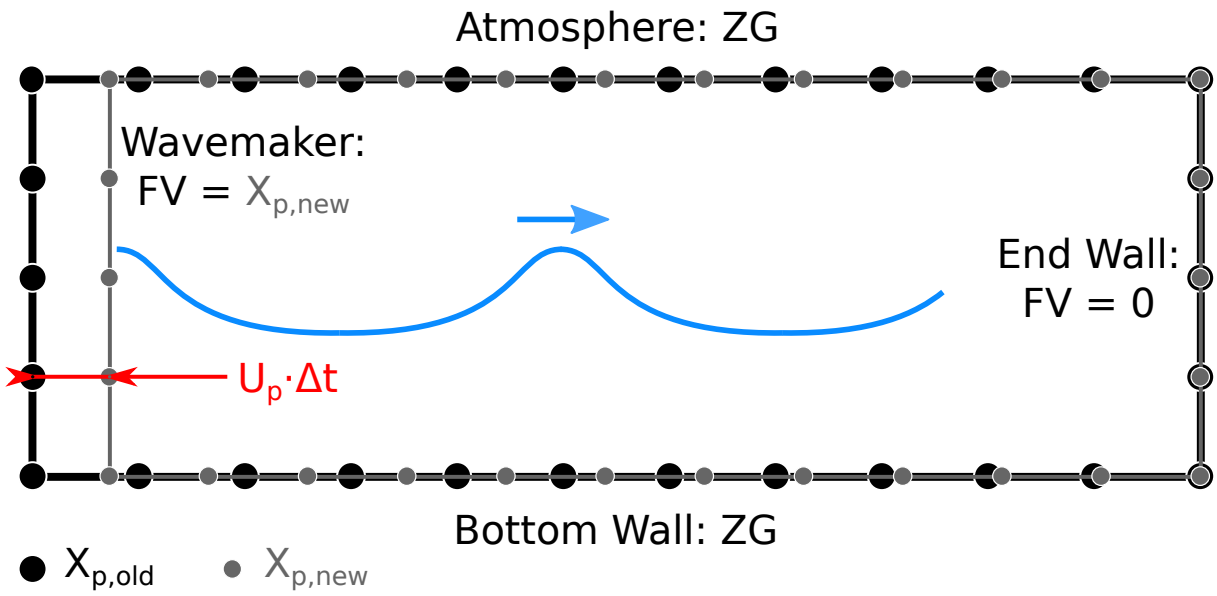

Figure 5.12: Dynamic mesh setup. FV stands for Fixed Value. ZG stands for Zero Gradient.

be obtained: $\mathbf{X}_{\text{new}} = \mathbf{X}_{\text{old}} + \mathbf{U}\Delta t$.

A variable diffusivity can help to re-distribute the motion of the boundary along the mesh. A diffusivity inverse to the distance from the moving boundary is often considered for moderate displacements (on the order of 10% of the total length). This means that the points of the mesh located closer to the dynamic boundary will move larger distances than those located far away from it.

Sometimes, a region of cells may need to be fixed. This is, for example, the case for cells that define a porous medium, as the armour layers or core of a breakwater. Deformation of such cells would result in an unphysical stretching of the structure. Options exist to preserve the geometry, freezing mesh deformation in sensitive areas.

The solving process of the Laplacian equation is followed by a number of additional operations, required by the finite volume technique. As previously mentioned, there are no topological modifications (e.g. changes in connectivity) but the volume of each cell and the areas of each face must be recalculated, and the fluxes need to be adjusted accordingly. Obviously, the full process has an impact on the performance of the model, increasing the computational cost. Generally, a 20% to 40% increment in runtime has been observed between moving boundary cases and their Dirichlet-type wave generation counterpart.

5.3.4.2 Boundary conditions for other fields

To conclude with the general framework of the numerical setup, the boundary conditions for the rest of the fields need to be discussed.

Since the moving boundaries are walls, the pressure and the VOF indicator function present the same boundary conditions as if they were static. The VOF function carries a zero gradient BC. Pressure needs the special boundary condition called *buoyantPressure*, present in OpenFOAM® to ensure the conservation of mass.

The moving boundaries have a particular BC for velocity, which ensures the dynamic no-slip behaviour, called *movingWallVelocity*. The result is that the moving wall is impermeable (zero flux across) and the velocity transmitted to the fluid is the instantaneous velocity at which the wall is moving.

Chapter 6

Validation of Wave Generation and Absorption Procedures

Numerical models need to be validated, to prove that they are capable of simulating phenomena in a physically-accurate way. **IHFOAM** has undergone an extensive validation process to demonstrate that the model is able to deal with wave generation and absorption.

In this chapter the performance of the wave generation and absorption boundary conditions, both static and dynamic, is tested in 2D and 3D cases.

6.1 Wave generation and active absorption - Static

Several cases have been simulated in order to test the model wave generation capabilities and the efficiency of the active absorption static boundary conditions implemented. First, the 2D absorption theory will be tested in 2D cases for solitary and regular waves. Then all the theories will be tested in 3D cases with oblique incidence of solitary waves. Finally an irregular wave case is analysed.

All the cases in the present section have been tested using a $k-\epsilon$ turbulence, as it is widely used. However, the results seem to be unaffected by it, as expected. This is because the first examples shown are not highly influenced by turbulence, as there is no wave breaking. Both $k-\epsilon$ and $k-\omega$ SST models have been considered in the validation cases in the following sections.

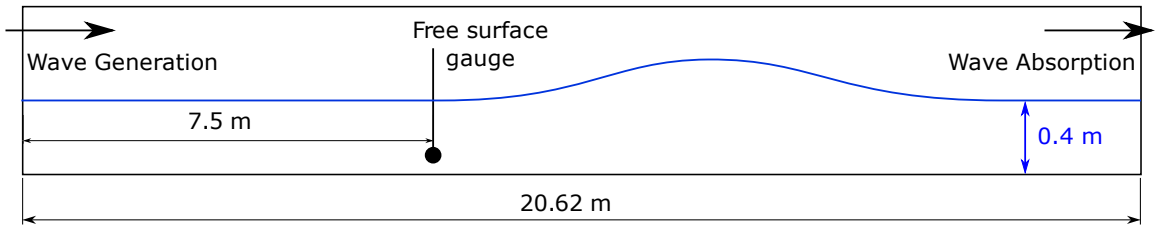

Figure 6.1: Schematic view of the 2D flume.

6.1.1 2D absorption of a solitary wave in a wave flume

All the 2D cases have been simulated using the same mesh, which is 20.62 m long, 0.58 m wide and 0.70 m high. The spatial resolution chosen is 2 cm on the horizontal direction and 1 cm on the vertical direction, which makes a fully structured and orthogonal mesh of 1031x70 cells.

The first tests were carried out by generating a solitary wave and absorbing it at the opposite end of the flume. Two wave heights were considered: 5 cm and 15 cm, both using Boussinesq theory. Water level is set at 0.40 m. A unique wave gauge is located 7.50 m away from the wavemaker and measures water elevation at 20 Hz. The schematic view of the flume is presented in Fig. 6.1.

Reflection coefficients are estimated as the quotient between the reflected wave and the initial wave at the gauge. As the reflected wave has to travel one way and back, its total displacement from the gauge is 26.24 m. Estimating a long wave celerity ($c = \sqrt{g\,h}$) the wave travels at approximately 2 m/s, so reflections are expected about 13 seconds later than the first pass. Nevertheless 60 seconds are simulated in order to check also the stability of the boundary condition when water is still. As the mesh is quite small (70,000 cells), the case runs on 1 processor (2.93 GHz), simulating the full 60 seconds in 1 hour and 30 minutes.

The results of the free surface level are shown in Fig. 6.2. At the top panel the free surface level at the only free surface gauge is presented. The lower panel shows the spatial and temporal variation of free surface level along the flume. The X axis corresponds to the length of the flume, while the vertical axis includes both space and time. Each line represents the free surface along the flume for a given time, every 0.10 seconds. The baseline for each one is placed at the time of the snapshot, and from it the free surface is represented in metres at the same axis, but amplified by a factor of 10. From the end

point of the figures until second 60, water shows smaller oscillations than the ones caused by the first reflection. The small oscillations that follow the soliton are an artificial effect of the wave generation boundary condition, and are generated as the solitary wave gains a stable profile, getting rid of several components.

For $H = 0.05$ m the peak of the solitary wave reaches the wave gauge at time $t = 6.40$ s with a height $\eta = 0.0461$ m. The biggest reflected wave is 0.0007 m in height and it reaches the gauge at $t = 20.80$ s. The reflection coefficient for the 5 cm wave is, then, 1.51%.

For the largest wave height case, the peak of the solitary wave reaches the wave gauge at time $t = 4.70$ s with a height $\eta = 0.1594$ m. The largest reflected wave is 0.0042 m in height and it reaches the gauge at $t = 18.55$ s. The reflection coefficient for the 15 cm wave results 2.63%.

In both cases the reflected wave is so small that it lies in the subgrid scale. Moreover, the long time simulated proves the stability of the boundary condition for very small free surface disturbances.

6.1.2 2D absorption of regular waves in a wave flume

These tests of regular waves in a flume have been simulated using the same 2D mesh as for the solitary waves. Six cases have been considered, as a combination of two wave heights: 5 cm and 15 cm; and three different wave periods: 2 s, 3 s and 4 s. Still water level was set at 0.40 m again. The case $T = 2$ s, $H = 5$ cm was generated using Stokes I theory, $T = 3$ s, $H = 5$ cm was generated with Stokes II and the rest of the cases with cnoidal theory. All of them present simultaneous generation and active wave absorption connected, apart from the active wave absorption on the other end.

This time there is a need for at least 3 gauges to accurately estimate the reflection of the boundary. Following Mansard and Funke (1980) method, the distances between the gauges are calculated based on the wave length in order to obtain a stable solution. The first gauge is always placed at $x = 7.50$ m. The distance between the first and second gauges is fixed: $X_{12} = \frac{L}{10}$. The distance between the first and third one is bounded: $\frac{L}{6} < X_{13} < \frac{L}{3}$ while $X_{13} \neq \frac{L}{5}$ and $X_{13} \neq \frac{3L}{10}$. To fulfil these restrictions $X_{13} = \frac{L}{4}$ has been chosen. For each of the wave periods there is an associated wave length, calculated using

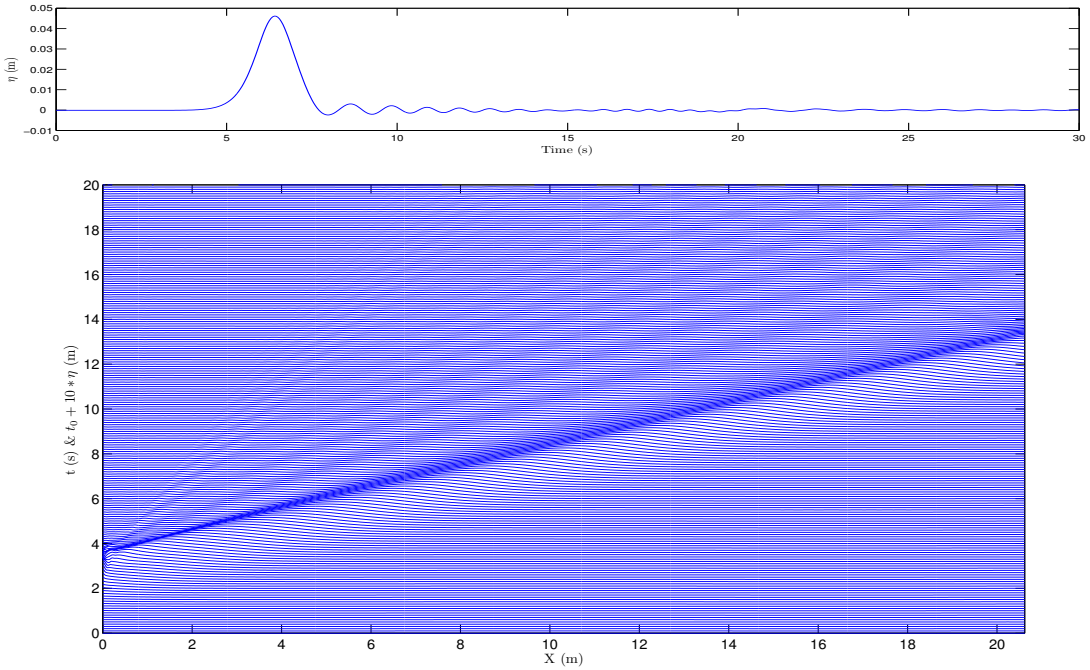

(a)

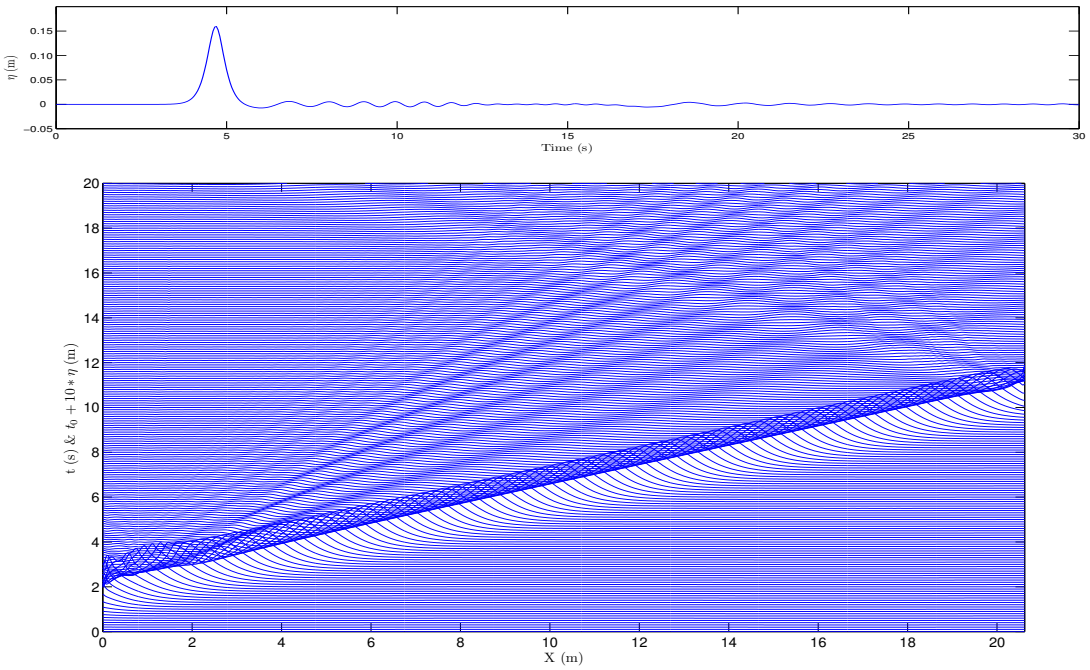

(b)

Figure 6.2: Solitary wave on a 2D flume with a 2D absorbing end: free surface at the gauge and spatial/temporal evolution. (a) $H = 5$ cm. (b) $H = 15$ cm.

T	L	X_{12}	X_{13}
2 s	3.70 m	0.370 m	0.924 m
3 s	5.77 m	0.577 m	1.441 m
4 s	7.79 m	0.779 m	1.948 m

Table 6.1: Regular waves in a 2D flume: wave lengths and gauges separation.

		H	
		5 cm	15 cm
T	2 s	4.6 %	11.2 %
	3 s	3.8 %	7.3 %
	4 s	2.3 %	6.7 %

Table 6.2: Regular waves in a 2D flume: reflection analysis given by waveLab® 3.

the dispersion relationship. On Table 6.1 wave lengths and distances between gauges for each wave period are given.

All the cases have been simulated for 120 seconds using 1 processor (2.93 GHz). The mean elapsed time is greater than double, compared with the previous case, as larger velocities inherent to the waves are present throughout all the simulation. The simulations are completed in less than 4 hours.

The reflection analysis is carried out using waveLab® 3 software, using the signal of the 3 gauges as input, and eliminating the first 5 waves to start with a steady state. The calculations of Mansard and Funke (1980) plus an inverse FFT in order to obtain the reflection coefficients in both the frequency and temporal domains have been carried out. The reflection results are presented in Table 6.2. Incident (regular continuous line) and reflected (bold continuous line) time signals for $T = 2$ s, $H = 15$ cm and $T = 4$ s, $H = 5$ cm cases, are shown in Fig. 6.3. The instantaneous reflection coefficient is also represented in dashed line.

The performance of these boundary conditions is very good, generally leading to reflection coefficients under or about 10% for the typical range of wave periods and heights on flumes. As expected, when period grows, the reflections decrease because waves are closer to the initial assumption: shallow water waves. For waves with smaller periods worse performance is expected. For higher periods the reflection coefficient will continue to decrease until the waves reach the shallow water condition. Following the work by Wellens (2012), explained in Eq. 2.75, will contribute to obtain a more even behaviour and better results along all the range of relative water depths.

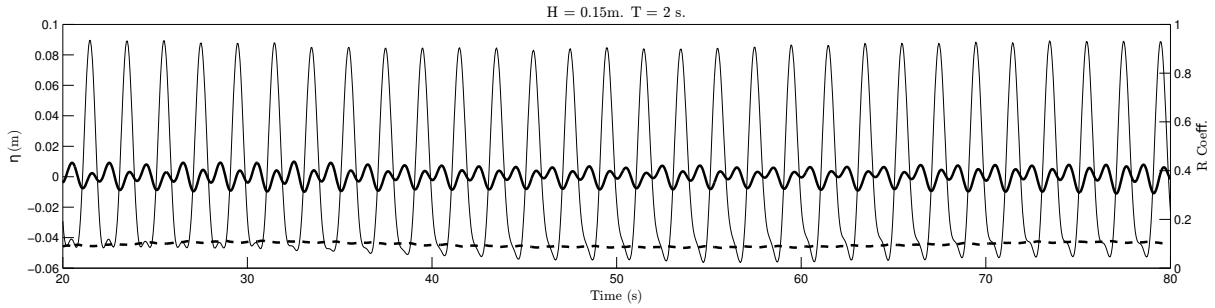

(a)

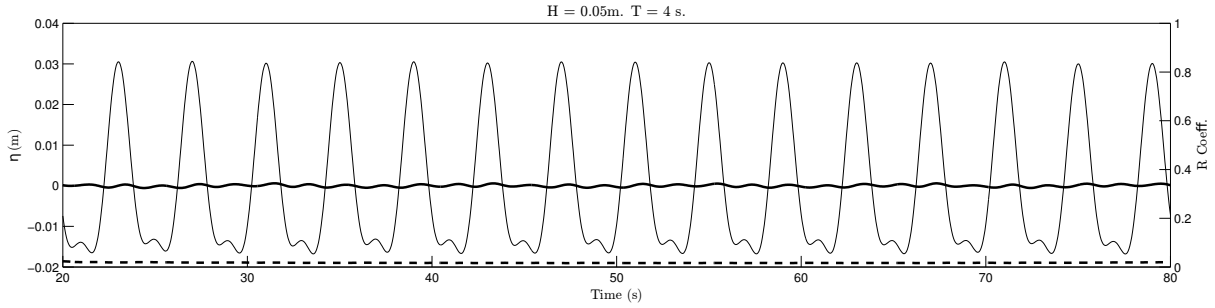

(b)

Figure 6.3: Reflection analysis of regular waves in a 2D flume for 2D absorption in the end. The regular continuous line is the incident component, the bold continuous line is the reflected component, both of them having the vertical scale on the left side. The dashed line is instantaneous reflection coefficient and its scale is on the right. (a) $T = 2$ s, $H = 15$ cm. (b) $T = 4$ s, $H = 5$ cm.

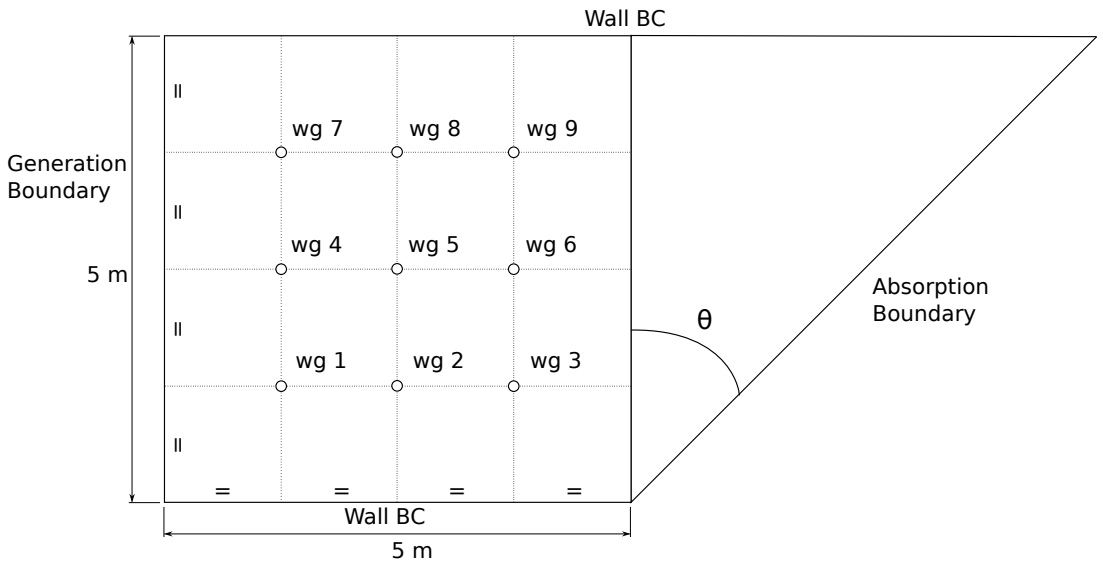

Figure 6.4: Geometry and wave gauges of the 3D wave tank. The figure is an application for $\theta = 45°$.

6.1.3 3D absorption of a solitary wave in a wave tank

Oblique incidence is obtained by setting up a special domain instead of generating waves with an angle, which can also be done. The wave tank has a geometry controlled by the angle of incidence (θ), while the dimensions specified in the right panel of Fig. 6.4 and the height (0.70 m) are fixed. The mesh is generated using the *blockMesh* utility, with the same parameters independently of angle θ: 125 cells in the X and Y directions and 40 cells on the vertical one. The resulting mesh has 625,000 cells and is structured but not always orthogonal. Resolution is dependent on θ. For the case of $\theta = 0$ the horizontal resolution is 4 cm and the vertical one is 1.75 cm. For all the cases tested using this mesh, nine free surface gauges have been placed. Their location and number are shown in Fig. 6.4, and coordinates can be obtained as all the combinations for X and Y with values 1.25, 2.5 and 3.75 metres. For reference, waves are always generated on plane $Y = 0$, so they propagate towards the positive values of X axis.

6.1.3.1 0 degree incidence angle, absorbent end

The first test is the 3D simulation of the 2D solitary wave case, with normal incidence ($\theta = 0°$). The tank is 5 by 5 metres. The solitary wave is 15 cm in height and simultaneous active wave generation and absorption is active. The boundary opposite to

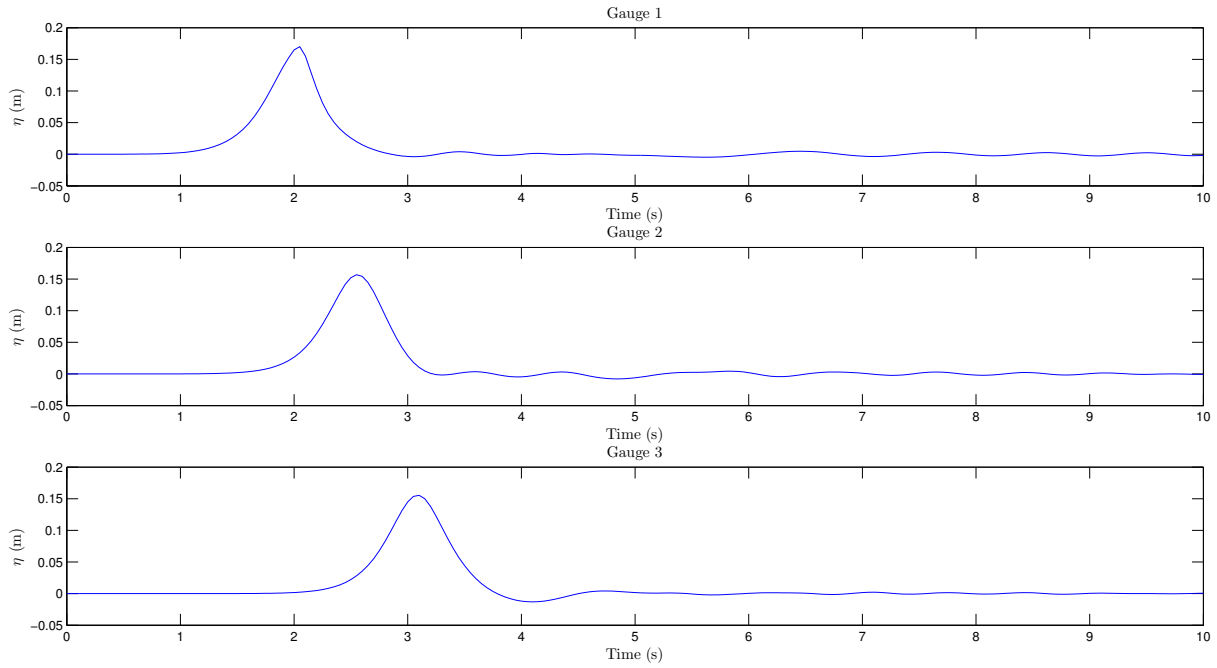

Figure 6.5: Free surface gauges for a solitary wave on a 3D tank with a 2D absorbing end. Incidence angle is 0°. The solution is fully 2D, so gauges 4–6 and 7–9 are the same as these ones shown.

wave generation is set to absorb incident waves, and it is automatically divided into 25 individual paddles, each of which is 5 cells wide and evaluates water level and corrected velocity independently. The lateral walls are set to no slip boundary condition. The case runs on 2 cores (2.93 GHz), and completes 10 seconds of simulation in 1 hour and 30 minutes.

The free surface elevation at the 3 first gauges is shown in Fig. 6.5. Only those gauges are presented because this is virtually a 2D case. It can be seen that the first gauge (top panel), which is the closest to the generation boundary, shows a wave with certain asymmetry due to local effects. In the next gauge (middle panel) the wave shape has a regular profile. The reflected wave is of the same order of magnitude of the perturbations that follow the soliton, and cannot be clearly distinguished. Nevertheless it can be measured, and the resulting reflection coefficient for the central gauge (number 5) is 4.39%.

The solution for the Quasi-3D case is identical, as the solitary wave propagates parallel to the paddle. The results for the full 3D case are also virtually the same as the case in 2D, since no velocities are expected to develop in the direction parallel to the wavemaker, therefore the resulting reflection coefficient for the central gauge is 4.13%. Both of them

are very close. However, the reflection coefficients are almost double compared with the value that was obtained in the 2D case. There are several reasons that explain this phenomenon. First, the tank domain is not as long as the flume and the free surface gauge is not located at the same relative location. Secondly, the discretization is different, as the flume cells are almost half in size with respect to the ones in the tank.

6.1.3.2 0 degree incidence angle, full absorbent walls

This case is identical to the previous one, but the lateral and end walls are set to absorbing boundaries with the same parameters as before (i.e. 25 individual paddles). Only 2D and full 3D absorption methods can be used, as Quasi-3D would introduce only shear stresses on the lateral faces. As it has already been mentioned, it is impossible to absorb a wave that propagates along a boundary.

The ideal behaviour for the lateral boundaries will be to actually behave like walls, hence the results will match those of the previous case. The 2D absorption theory calculates the velocity only by measuring water levels, as a result, it will take water out when the wave crest passes and pump water in when the wave trough arrives. The full 3D version is expected to reduce this effect. The purpose of this test is to evaluate the magnitude of these waves that get radiated from the lateral boundaries.

In Fig. 6.6 a cross comparison between the 2D theory (dashed line) and the full 3D theory (continuous line) is presented. It is clearly noticeable that the lateral boundaries disturb the wave in the first case, because as the wave propagates, water is being taken out of the domain. Wave height decreases significantly and the smaller troughs that follow the principal wave get maximized, especially along the center line (gauges 4–6) because the sum of the perturbations of both sides. Some of the differences between the gauges are up to 4 cm, more or less around 25% of wave height value. Solution continues to be symmetrical in both cases. The 3D theory (continuous line) can be assimilated as the reference case, because differences of 3 mm at most appear compared with the absorbent end case. If both cases were plotted in the graph, they would lie one on top of the other. Nevertheless those 3 mm increase the reflection coefficient by a 2%; namely 6.30%.

It can be concluded that the 2D boundary condition is not suitable for 90° incidence, because it generates great disturbances, while the newly developed full 3D theory deals

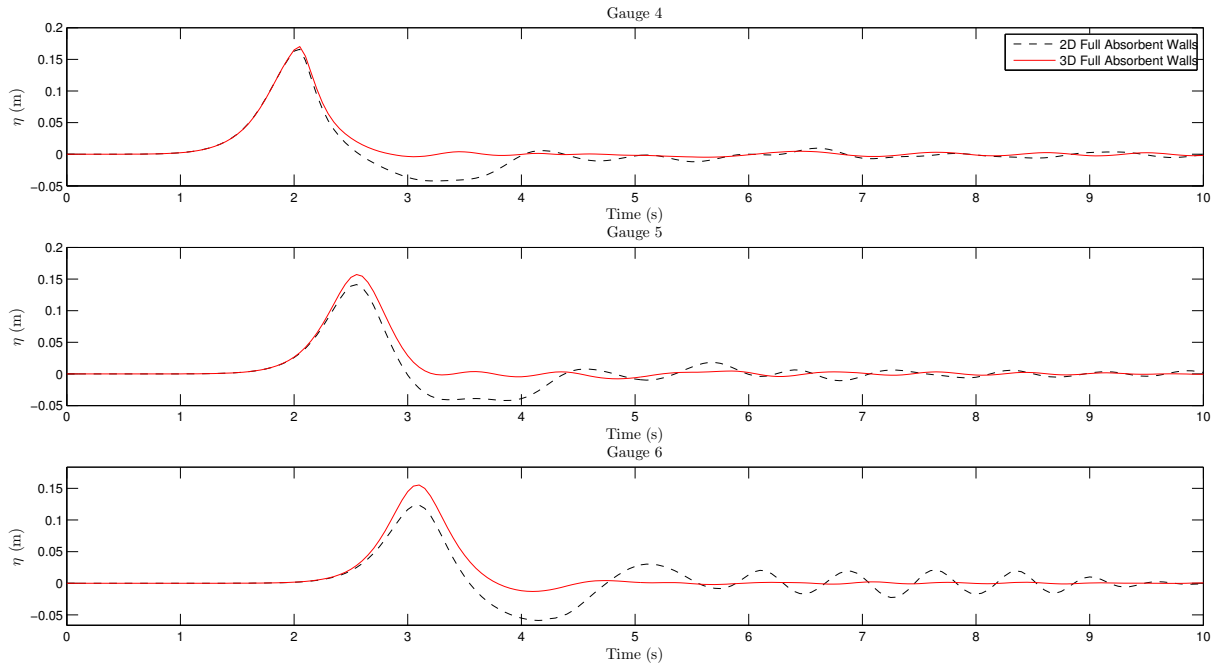

Figure 6.6: Comparison of free surface gauges between the solitary wave on a 3D tank. 2D absorbent walls (dashed line). 3D absorbent walls (continuous line).

correctly with such a situation.

6.1.3.3 45 degree incidence angle

The mesh for this case is exactly as shown in Fig. 6.4. The results for the 6 first gauges are shown in Fig. 6.7. Reflections are evident and three-dimensional, as the first triplet of gauges shows different reflected amplitudes between them and between the second triplet.

For 2D theory, and in order to avoid stability problems due to the corners, one paddle at each side of the acute end of the boundary is limited to out flux only. The reflection coefficient evaluated on gauge 5 results 7.65%. On gauge 3, towards the end of the series several re-reflected waves can be observed. They are created by the tangential wave component (parallel to the end patch), which gets reflected on the lateral walls because those are not absorbent. Performance is not as good as in the previous case where $\theta = 0°$ due to the tangential velocity component, but it is still very low.

Quasi-3D theory shows an outstanding performance, as reflected waves are barely noticeable. The reflection coefficient measured on gauge 5 is 4.09%, which is almost half compared with the one obtained using 2D absorption, and virtually the same as in the previously studied normal incidence case.

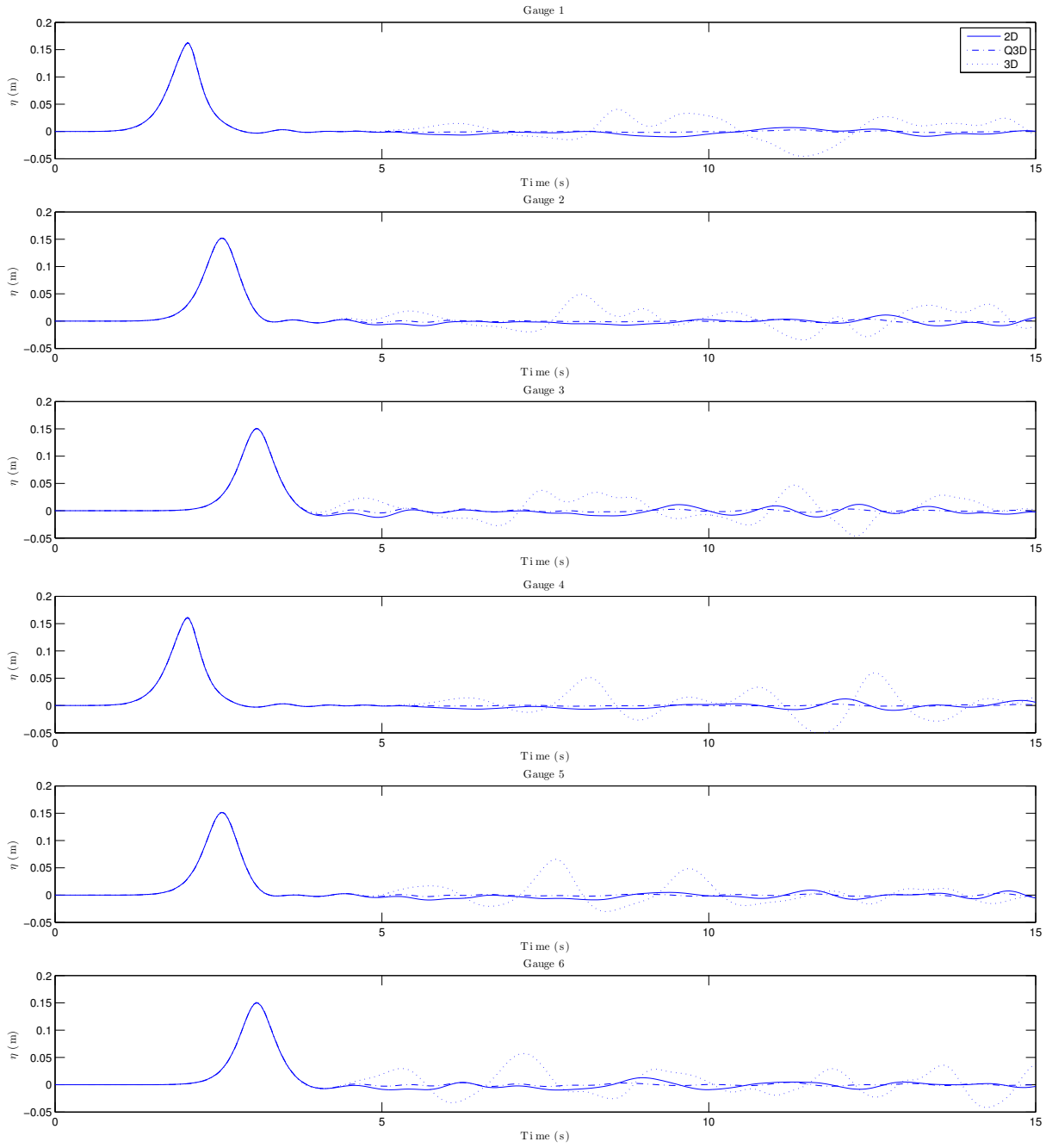

Figure 6.7: Free surface gauges for a solitary wave on a 3D tank with an absorbent end. Incidence angle is 45°. Comparison between all the absorption theories.

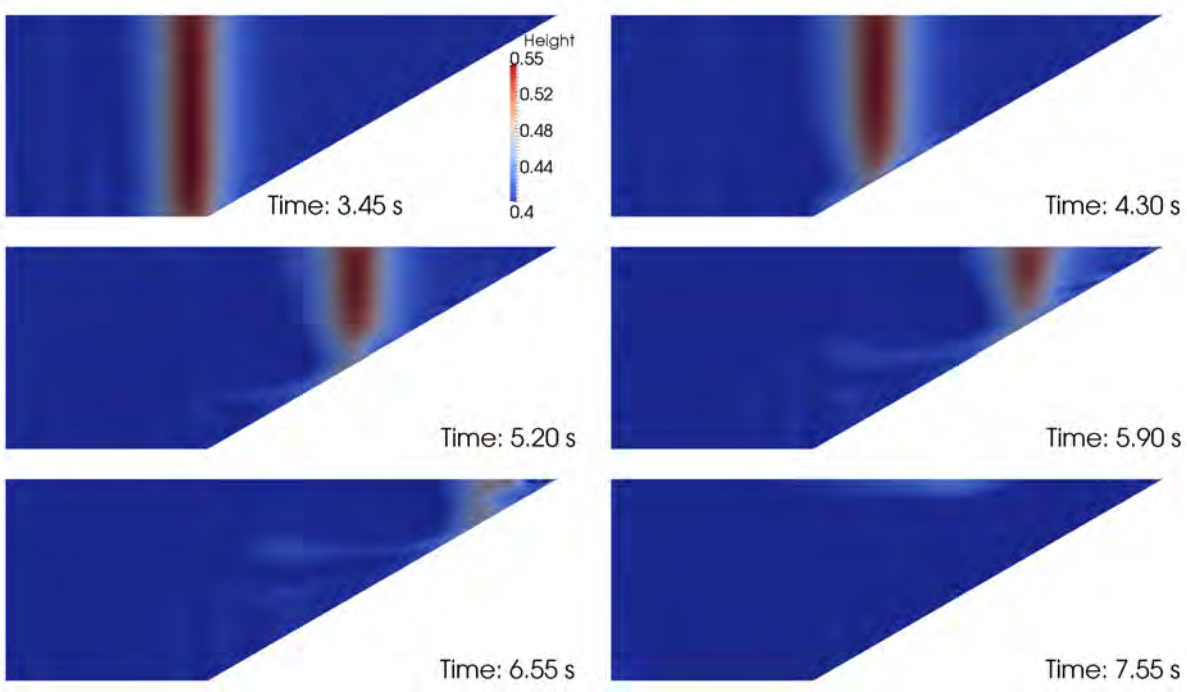

Figure 6.8: Free surface for the solitary wave on a 3D tank with a 2D absorbent end. Incidence angle is 60°.

Full 3D theory shows the worst performance amongst all of them, with a reflection coefficient on gauge 5 of 20.63%. In this case all the walls are absorbent to dissipate the tangential component of the wave and one paddle at each side of the acute end of the domain is limited to out flux only for each of the patches.

6.1.3.4 60 degree incidence angle

The last case is identical, but this time the incidence angle is set to 60°. Once again the behaviour is fully 3D. The reflection coefficients for gauge 5 are: for 2D, 3.64%; Quasi-3D shows the best performance with 2.58%; and full 3D reaches 13.92%.

The evolution of this case for the 2D absorption theory is presented in Fig. 6.8. As the wave flows along the absorbent end, small waves start to be radiated, but the goal to absorb the main wave is achieved. However, the spurious waves reach the longest lateral wall (see time 7.55 s) and then reflect towards the absorbent boundary again, were eventually they are dissipated.

6.1.4 3D absorption of directional irregular waves in a wave tank

Realistic sea states have little resemblance with the cases shown before. A real sea state can be described by means of a spectrum. The discretized spectrum can be defined in terms of wave components with wave height, period, phase and direction of propagation.

The synthetic spectrum that has been created for this case includes the typical features of a combined condition of a sea and a swell states, as it can be seen in Fig. 6.9(a). The mean direction of the sea state is 45°. The sea has a peak period of 1.5 seconds, while the swell presents a higher one, 5 seconds. Both of them have the same significant wave height, equal to 10 centimetres.

The mesh for this case is the same as for the 45° incidence wave tank, in which the waves corresponding to the theoretical spectrum are generated at the usual boundary featuring simultaneous active wave absorption. The rest of the vertical walls are set to fully 3D absorbent boundaries. No other absorption theories have been tested, since 2D absorption will radiate waves from the lateral boundaries. A similar case occurs for Quasi-3D absorption, the main direction of the waves generated coincides with the end wall, so if absorption direction were to be set it would be tangent to the wall. Moreover, it is very difficult to estimate an incidence angle at the walls in advance.

The case has been simulated for a total of 180 seconds (approximately 100 waves) in 9 days with 8 cores (2.93 GHz). Free surface is sampled at 20 Hz. The numerical gauges are placed, following the indications of the seven-element irregularly spaced array in Young (1994). Its central location is gauge number 5 in Fig. 6.4, and is chosen because it lies in the limit of the shadow zone of the spectrum. The 7 resultant signals are then analysed using waveLab® 3 built-in Bayesian Directional Spectrum Estimation Method (BDM). The resultant directional-frequency spectrum is shown in Fig. 6.9(b).

The comparison between both spectra is shown in Fig. 6.9. The top figure corresponds to the theoretical spectrum and the bottom one is the measured one.

The total energy of the theoretical spectrum (volume under the surface) is equal to 6.2316 10^{-4} m^2 rad. The measured energetic level is a 30% lower, totalling 4.361510^{-4} m^2 rad. This decrease of energy is caused by the chosen spectrum and point location, as the components beyond the 45° angle, reach that point affected by diffraction. This also confines the energy towards the 0° direction, reducing the directional dispersion. At

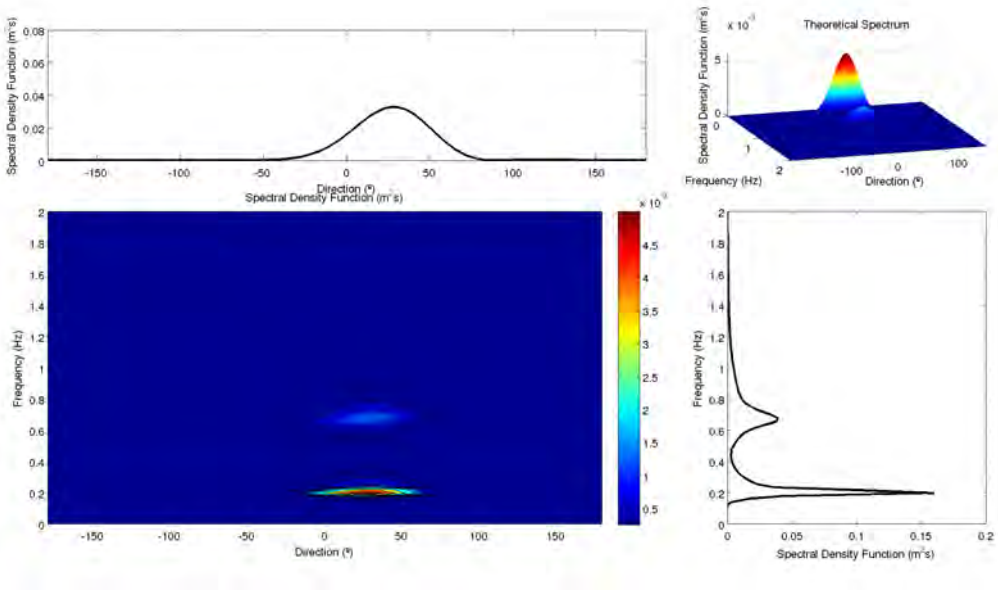

(a)

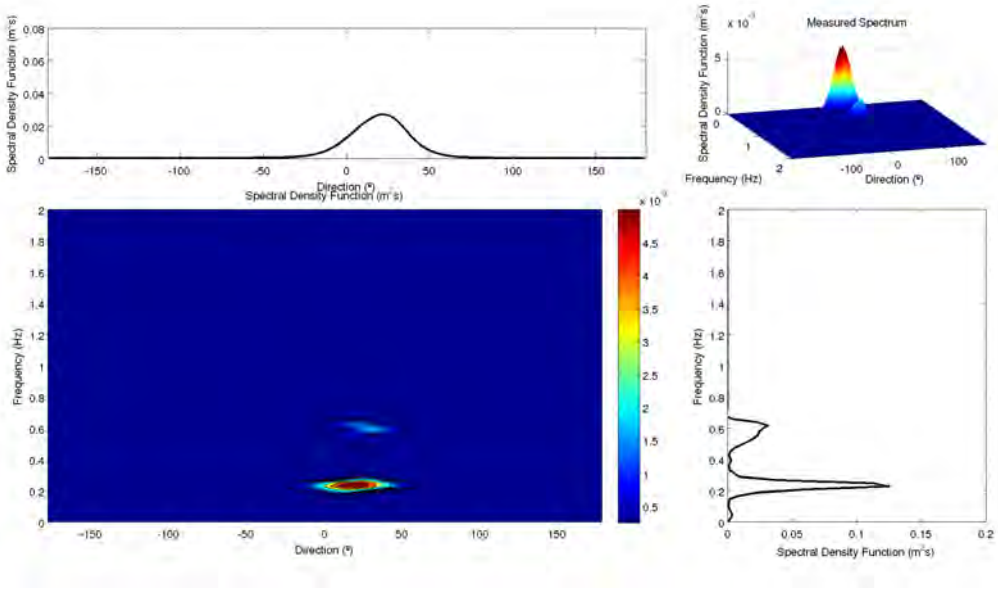

(b)

Figure 6.9: Theoretical spectrum (a) compared to the measured spectrum (b) of the irregular directional case.

	Sea		Swell	
	Theoretical	Measured	Theoretical	Measured
f (Hz)	0.6758	0.5950	0.1960	0.2257
θ (°)	31.17	31	27.15	19
SDF (m^2 s)	0.001538	0.001967	0.005540	0.006256

Table 6.3: Iregular waves in a wave tank: spectrum comparison. SDF stands for Spectral Density Function.

the same time, the frequency dispersion from the captured signal increases for the swell state and decreases for the sea state. Another remarkable fact is that the peaks of the sea and swell are correctly represented in frequency and direction, although the measured spectrum is more peaked, as it can be seen in Table 6.3. This means that the measured spectrum has higher and more pointed peaks, but less broad, as the total amount of energy is lower. The swell state is better reproduced, as the peak direction shows less deviation.

The snapshots in Fig. 6.10 show the evolution of the waves in the tank during 5 seconds. It can easily be appreciated that this is a short crested sea state, as no continuous wave fronts are present. Wave obliquity at the generation boundary can be seen in the last two snapshots. The correct behaviour of the absorbent end can also be observed comparing these two frames, especially at the acute end of the tank.

6.1.5 Conclusions

The newly implemented active wave generation and absorption have proven to be stable and to present very low reflection coefficients. The main advantage of this procedure over dissipation zones is clear, as it does not increase the computational cost or enlarge the domain.

Most of the reflection coefficients obtained are well below 10%. Whenever 2D absorption theory is not applicable because it radiates waves instead of absorbing them, a new 3D theory for wave absorption has been implemented. This one shows good performance for incidence angles close to 0° or 90°, although it is moderately reflective in between.

The previous two theories only absorb in the perpendicular direction to the boundary. Quasi-3D theory shows the clear advantage of absorbing in almost any direction with an outstanding performance. Its main drawback is that most of the times the incident wave

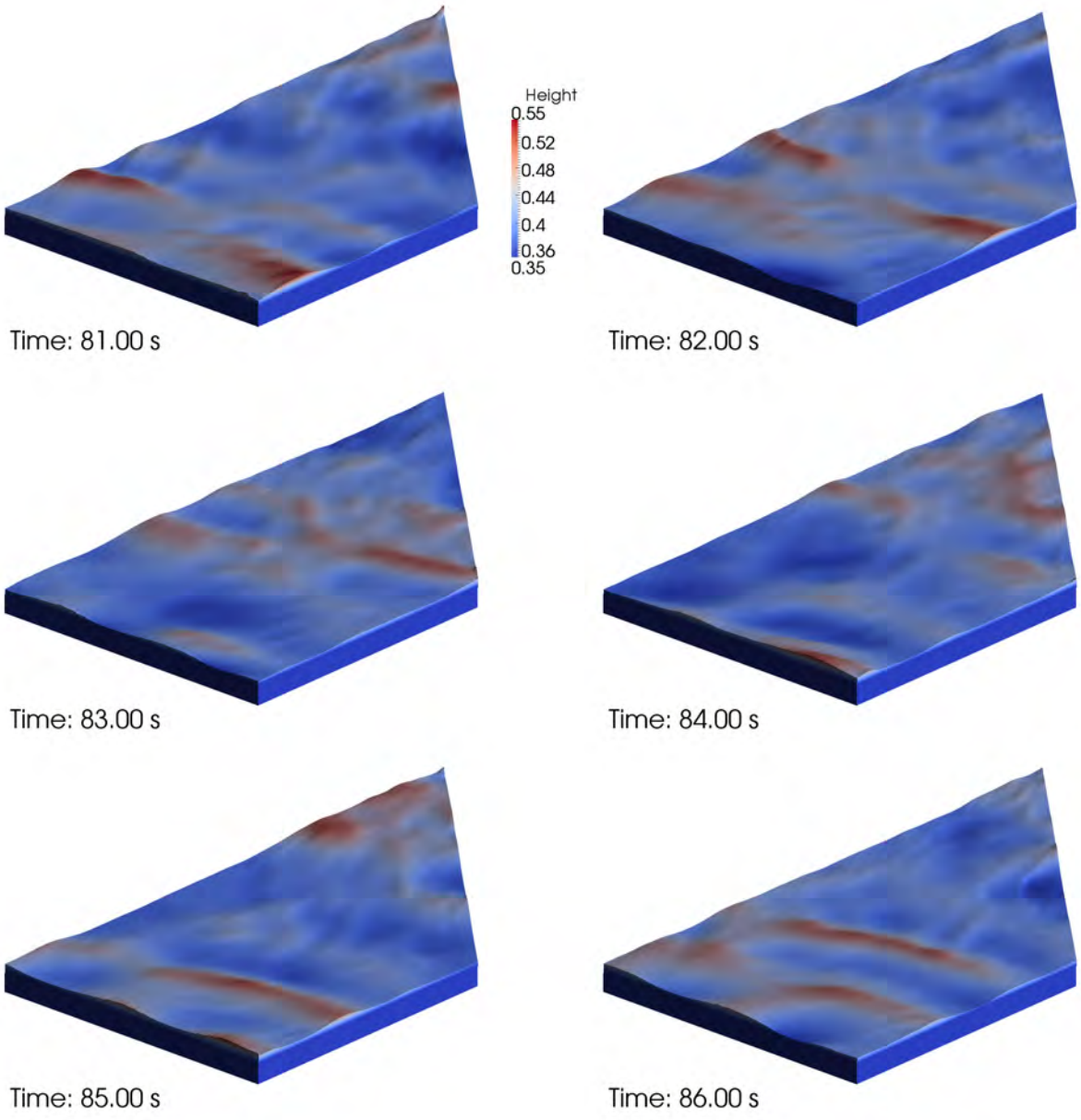

Figure 6.10: Free surface elevation for the irregular directional case.

direction cannot be anticipated or that it may vary within the same boundary.

6.2 Wave generation and active absorption - Dynamic

6.2.1 2D absorption of regular waves in a wave flume

Purely numerical experiments were carried out to test the performance of the active wave absorption procedure programmed on dynamic boundaries.

A 2D mesh to replicate a wave flume was developed. The domain extended 20.62 m in the X direction and 0.7 m in the Z direction. The initial discretization was kept constant and equal to 2 x 1 cm, totalling 72,000 cells. Waves were generated on the left boundary ($X = 0$) using the Dirichlet BC, including active wave absorption to avoid an increase of the water level in the flume. The wave theory was chosen according to Le Méhauté (1976) graph. On the other end of the flume a piston-type BC was placed and set only to absorb the incident waves.

Nine different regular wave cases were tested, as a combination of three wave heights (5, 10 and 15 cm) and three wave periods (2, 3 and 4 s). All the cases have been run with a water depth of 0.4 m and for 40 wave periods. The average simulation rate in a single processor resulted 40 s/h for the lowest wave height (smallest velocities) and 10 s/h for the highest wave height.

A reflection analysis applying Mansard and Funke (1980) method has been performed. This technique involves placing three free surface elevation gauges, with a given separation dependent on the wave period. Two results are included in Fig. 6.11. The analysis in the frequency domain has been performed for the last 30 wave periods of each simulation. the reconstruction of the results yields the total, incident and reflected time series of wave elevation, which are referred to the left axis scale. The analysis in the time domain covers 80% of the 30 wave periods and results in the time series reflection coefficient (green line), referred to the right axis scale. Small spurious disturbances caused by the digital filters are expected in the borders. The global reflection coefficient shown in the title of each graph and later reported in Table 6.4 is the result of averaging the time-domain series, excluding the zero values at each side.

The total reflection coefficients for each case are gathered in Table 6.4. The results

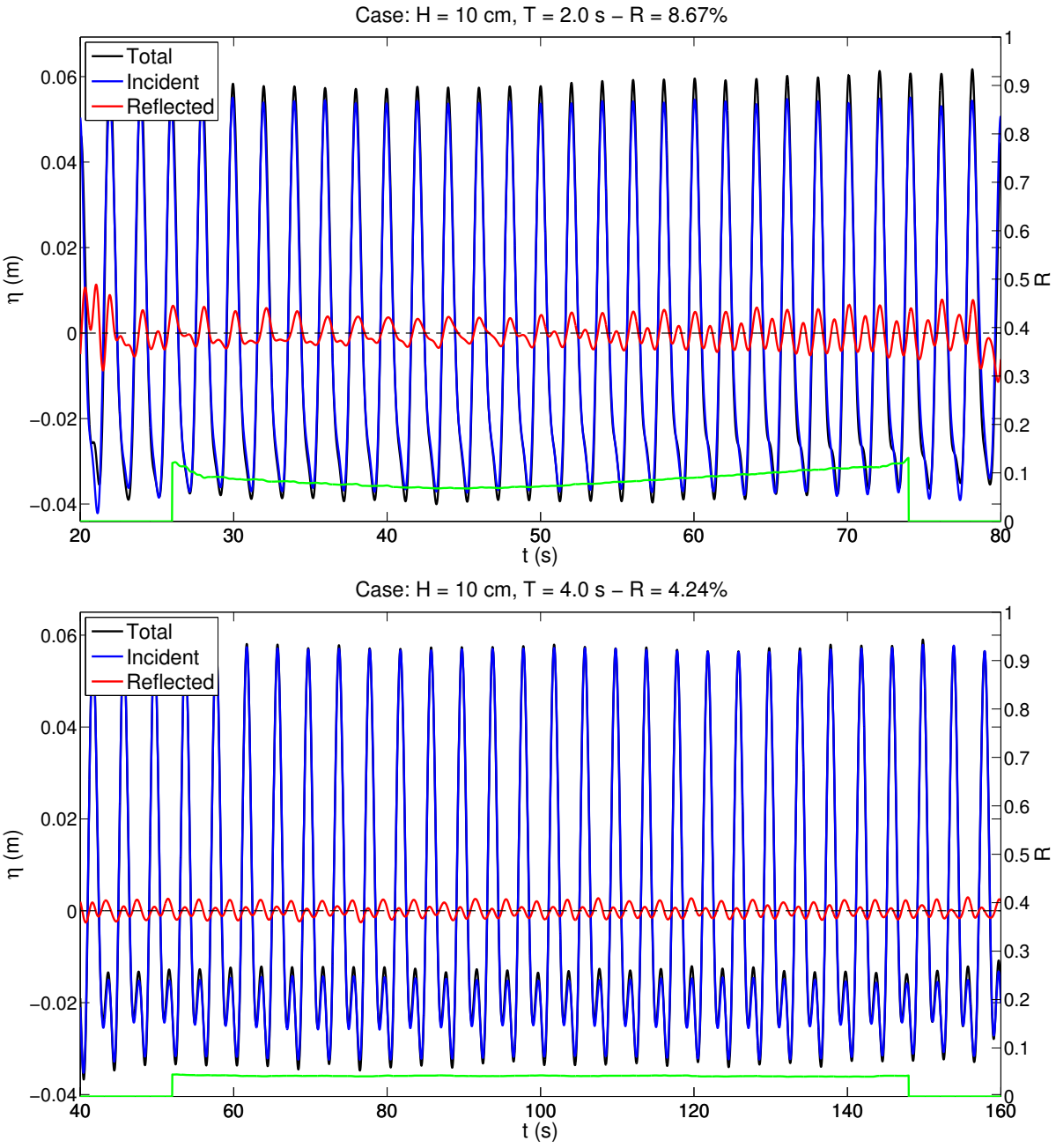

Figure 6.11: Incident-Reflected wave analysis.

		H		
		5 cm	10 cm	15 cm
T	2 s	5 %	9 %	15 %
	3 s	4 %	7 %	12 %
	4 s	3 %	4 %	6 %

Table 6.4: Regular waves in a 2D flume: wave lengths.

are similar to those reported before, generally smaller than 10%, except for those cases in which the wave conditions diverge from the assumptions of the absorption theory.

6.2.2 Simulation of wave focusings in 2D and 3D

In this section the new implementation of the moving boundary wave generation procedure for **IHFOAM** is validated against laboratory measurements.

6.2.2.1 Physical experiments

A set of physical experiments were carried out in the University of Cantabria small shallow water wave basin. The experimental facility testing area is 18.3 m long, 8.6 m wide and 1.2 m high. The total length of the tank is 28 m, as additional space exists behind the wave generation machine and a passive wave absorber formed by mesh screen layers mounted at the other end of the basin. Two photographs of the experimental setup can be seen in Fig. 6.12.

The wavemaker has 10 independent piston-type paddles, with a total stroke of 90 cm (± 45 cm from the initial position). The maximum allowed difference in displacement between adjacent paddles is 30 cm. Each paddle is equipped with a free surface elevation gauge mounted at its front face and a distance meter. The system is capable of performing active wave absorption.

A total of 20 resistive wave gauges (see top image in Fig. 6.12) were deployed and arranged as shown in Fig. 6.13. Auxiliary lines are plotted each metre in the graph, and the symmetry axis is represented in dashed line. The exact location of the gauges is gathered in Table 6.5.

Several experiments were carried out, including regular and solitary waves with different directions. Special tests in which the paddle displacements were calculated with external programs and introduced in the system to simulate different types of focused waves

Figure 6.12: University of Cantabria small shallow water wave basin. Experimental setup.

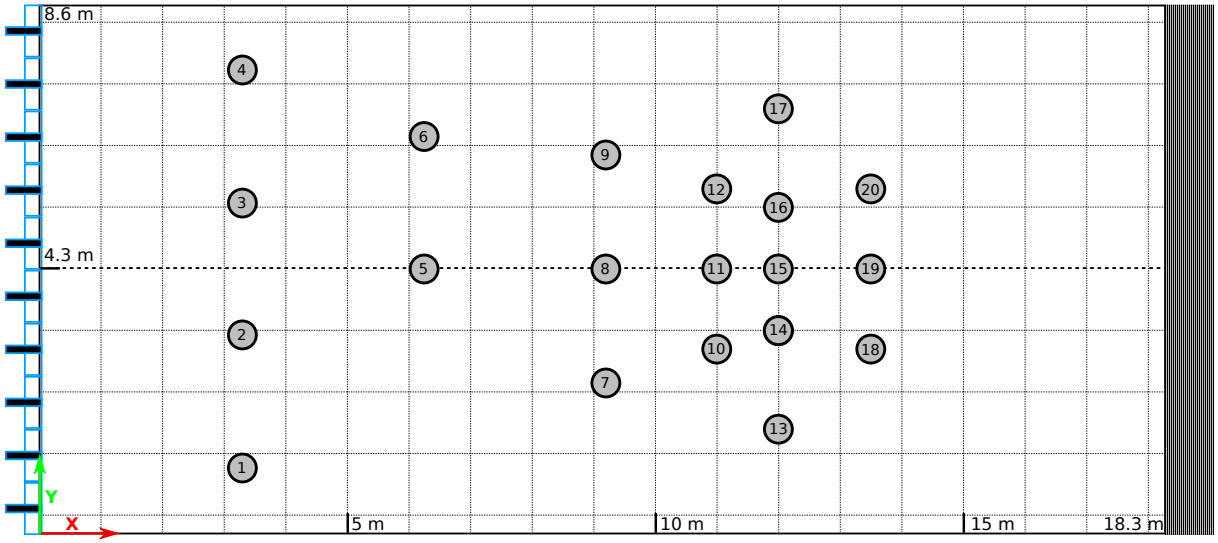

Figure 6.13: University of Cantabria small shallow water wave basin. Location of the free surface gauges.

Gauge	X (m)	Y (m)	Gauge	X (m)	Y (m)
1	3.30	1.07	11	11.00	4.30
2	3.30	3.23	12	11.00	5.60
3	3.30	5.37	13	12.00	1.70
4	3.30	7.53	14	12.00	3.30
5	6.25	4.30	15	12.00	4.30
6	6.25	6.45	16	12.00	5.30
7	9.20	2.45	17	12.00	6.90
8	9.20	4.30	18	13.50	3.00
9	9.20	6.15	19	13.50	4.30
10	11.00	3.00	20	13.50	5.60

Table 6.5: Location of the free surface gauges.

were also performed. Wave focusing experiments are becoming a standard in coastal and offshore engineering because they allow obtaining extremal results (e.g. impact of freak waves) by simulating a very short time series. However, they are a complex dynamic to simulate, as nonlinearity and second order effects play a significant role in the final results. The wave focusing cases are the main scope of this work.

A two-dimensional wave focusing (all the wave components propagating in a single direction) was tested with second order wave generation, according to Barthel et al. (1983) theory, as applied in Hughes (1993). The second order is relevant to suppress spurious free long waves, to generate just the long wave bound to the group, which travels at the group celerity. It has been proven that second order wave generation is specially needed to calculate run-up and overtopping effects accurately (Orszaghova et al. (2014)).

The two-dimensional wave group was created from a top hat spectrum: 50 evenly-spaced components between $T = 1.5$ s and $T = 2.0$ s and the same amplitude. The focused wave height was 13 cm. The wave generation properties were set to concentrate the energy at gauge number 15 ($X = 12$ m) at $t = 50$ s. The paddle displacement signals are shown in Fig. 6.14. In the top panel, the first and second order theoretical components appear separately. Note how a 15 s linear ramp transition has been introduced because the second order component does not start at the zero-position. After this shift, the wave focusing is expected at the same location, but at $t = 65$ s. In the bottom panel, the theoretical time series (blue line) is reconstructed. This signal has been used as input of the physical wavemaker. Superimposed, in red dashed line, the feedback signal from the actual experiment can be found. Note how the start is smoother, and how the end is tapered to end at the zero position.

A three-dimensional wave focusing was also performed. In this case the same top hat spectrum, with 50 evenly-spaced components between $T = 1.5$ s and $T = 2.0$ s and homogeneous amplitude was considered. Each paddle generates the same spectrum, but with a different direction (i.e. different phase shift). The focused wave height in this case was 25 cm and takes place at gauge number 5 ($X = 6.25$ m, $Y = 4.3$ m) at $t = 30$ s.

The still water depth was set to 0.4 m. The free surface was sampled at 100 Hz, while the displacement of each paddle was recorded at 50 Hz. Active wave absorption was not connected.

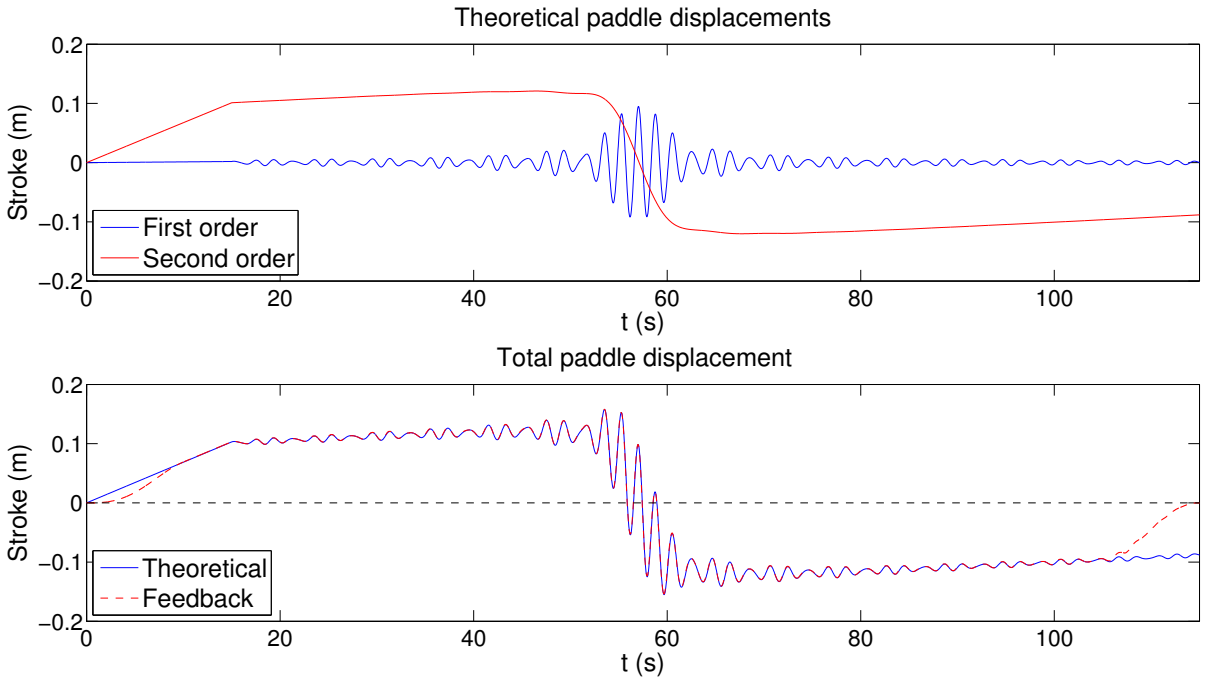

Figure 6.14: Time series of paddle displacement for the 2D wave focusing.

6.2.2.2 Repeatability analysis

Each of the tests was performed at least 4 times, in order to verify that they were fully reproducible. The results (i.e. time series of free surface elevation) have been analysed to quantify the variations between tests.

The first wave focusing is expected to be 2D, because all the paddles of the wavemaker move at once. However, in wave basins is quite common to get a spanwise oscillation even in 2D tests. The waiting time between two experiments was chosen to minimize this effect. In order to prove the two-dimensionality of the experiment, the analysis of the data has been performed in rows of gauges, located at the same distance from the wavemaker.

The repeatability analysis of the 2D focusing can be found in Figs. 6.15–6.17. The rows of free surface gauges can be identified in Fig. 6.13. The first one is [1, 2, 3, 4] and is represented in the top panels of Fig.6.15. Since 4 repetitions were performed, and 4 gauges are included in this set, the top panel shows 16 different free surface elevation time series. The time series of standard deviation analysis is included right below. For each time step, the 16 different elevation values are used to compute statistics. It can be noticed that correlation is very high for the first 50 s, in which the waves are very small. The maximum differences are experienced when the wave group passes. Nevertheless, the

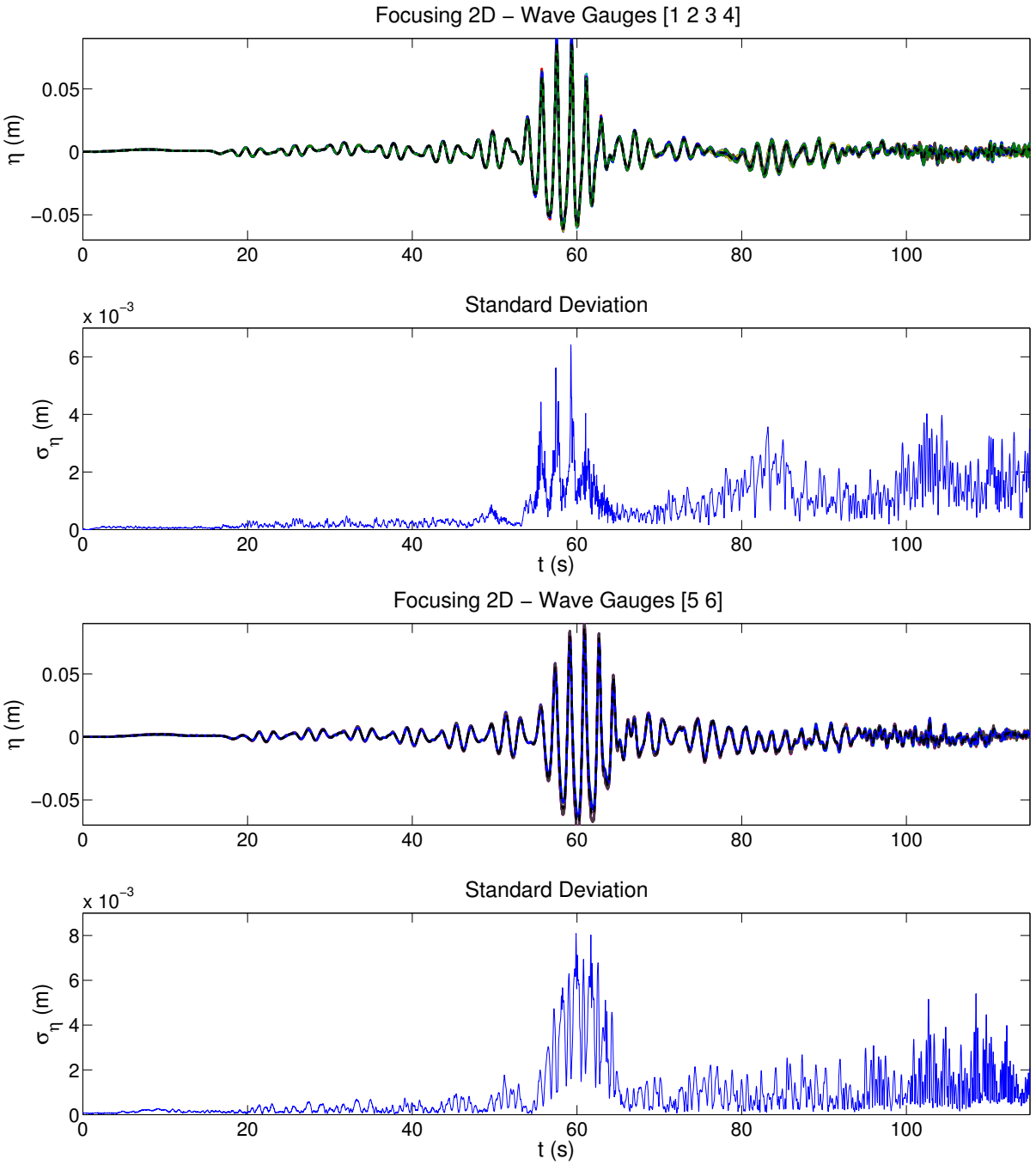

Figure 6.15: Wave focusing in 2D. Repeatability analysis. 4 time series per gauge are represented. Part I.

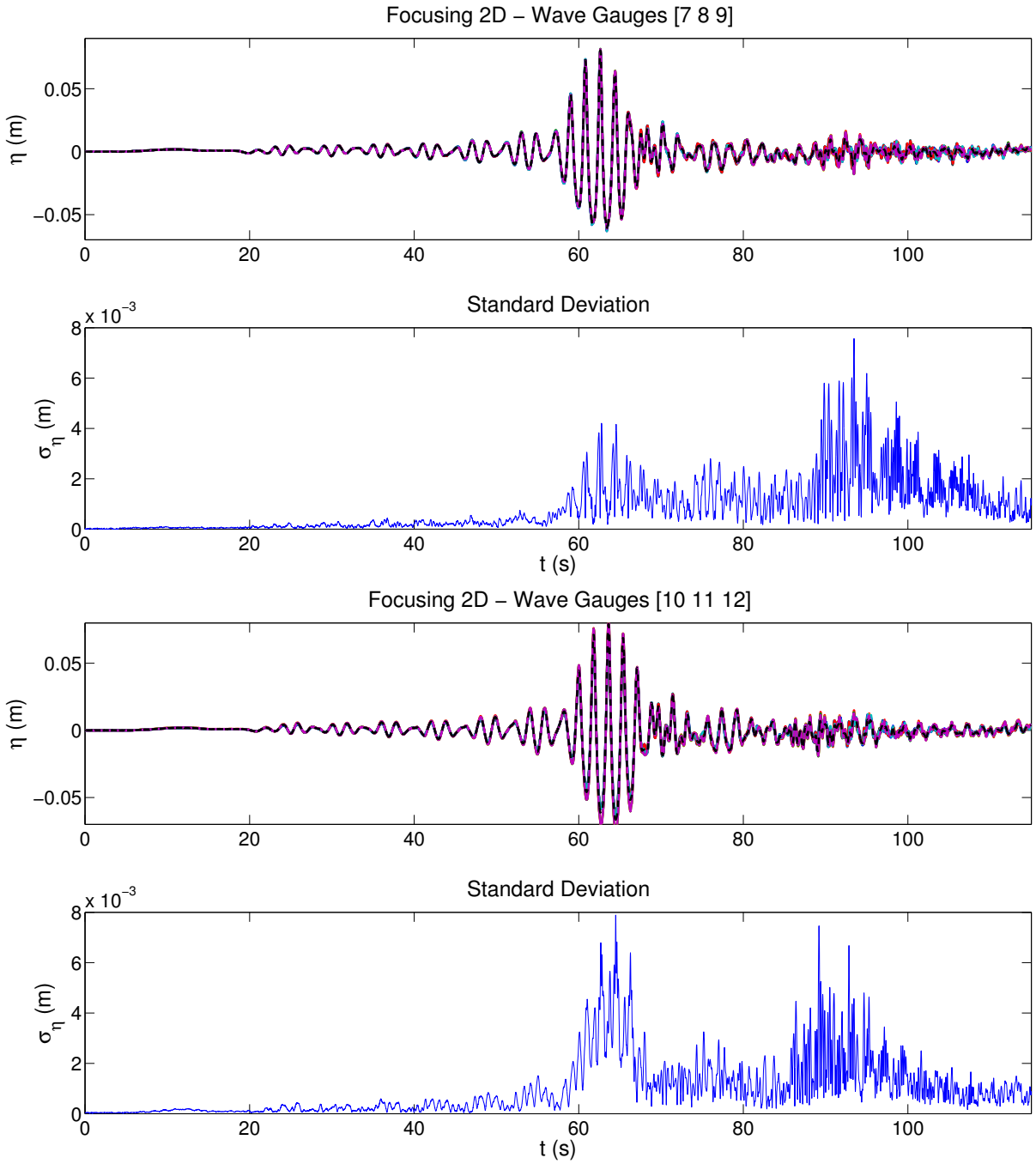

Figure 6.16: Wave focusing in 2D. Repeatability analysis. 4 time series per gauge are represented. Part II.

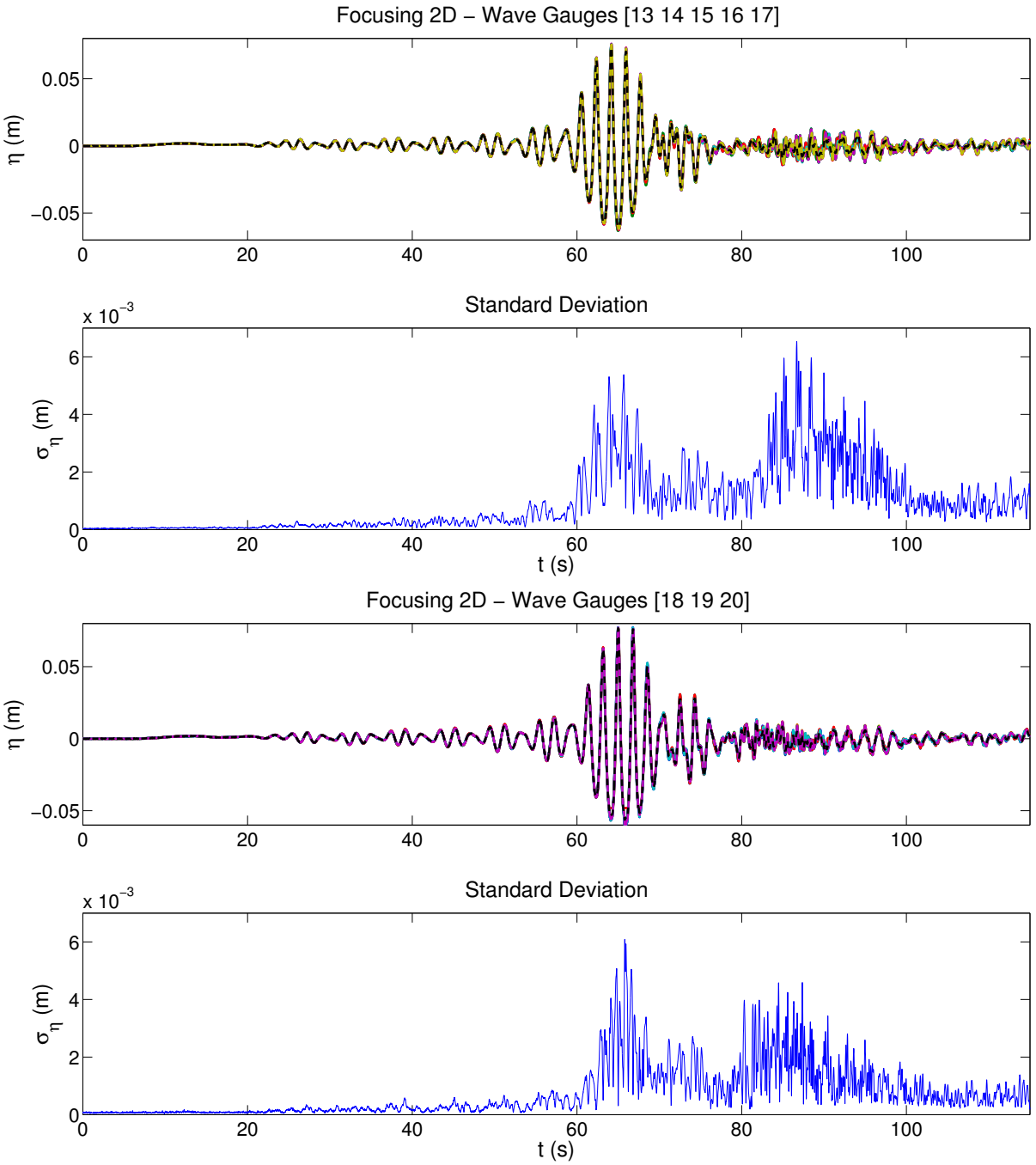

Figure 6.17: Wave focusing in 2D. Repeatability analysis. 4 time series per gauge are represented. Part III.

standard deviation barely reaches 6 mm, corresponding to less than a 5% deviation in terms of the maximum wave height of the group. The final part of the time series also presents large deviations, associated to the randomness of the wave field once the large waves have dissipated at the mesh screen zone. Since the most important dynamic of this test is the wave group, any effects occurring after it will be disregarded.

The second row of gauges is [5, 6], in the bottom panels of Fig.6.15. In this case, the standard deviation is calculated for 8 points (2 gauges, 4 repetitions) and increases up to 8 mm (9%) at the wave group. It must be noted that the alignment between the time series of different repetitions has been estimated, as the data acquisition system does not provide a time reference of the starting point of the simulation (i.e. the data acquisition and the wavemaker generation are not synchronized). The alignment has been performed selecting one of the time series as fixed and performing a correlation analysis on the rest. The time lag is estimated depending as the one that yields a higher correlation.

The third and fourth rows of sensors ([7, 8, 9] and [10, 11, 12]) are shown in Fig.6.16. The last two rows, [13, 14, 15, 16, 17] and [18, 19, 20] are represented in Fig.6.17. The results indicate that the standard deviation of the free surface elevation at the gauges where the focusing event takes place (13–17) is less than 5 mm.

The repeatability analysis of the 3D focusing can be found in Figs. 6.18 and 6.19. In this case, since the experimental setup and wave generation is symmetric, it is reasonable to anticipate that the results will also be. The repeatability tests have also been applied to the pairs of gauges at symmetrical locations. The repeatability at gauges 1 and 4 (Fig. 6.18, top panels) is excellent, not even reaching 1.5 mm when the wave group passes over them, and far below 1% with respect to the highest wave height of the group. Gauges 2 and 3, shown in the bottom panels of Fig. 6.18, also present a good correlation, with a mean standard deviation of 2.5 mm (1%) and a maximum around 8 mm.

Gauge number 5 (Fig. 6.19, top panels), where the wave focusing takes place, shows a high correlation that yields 4 mm at most of standard deviation (1.6%). Gauges 13 and 17 (Fig. 6.19, bottom panels) also present a good reproducibility behaviour, with a mean standard deviation of 2 mm.

The conclusion from this section is that the two-dimensionality assumption can be considered for the first case, and that the experiments are fully reproducible in the laboratory.

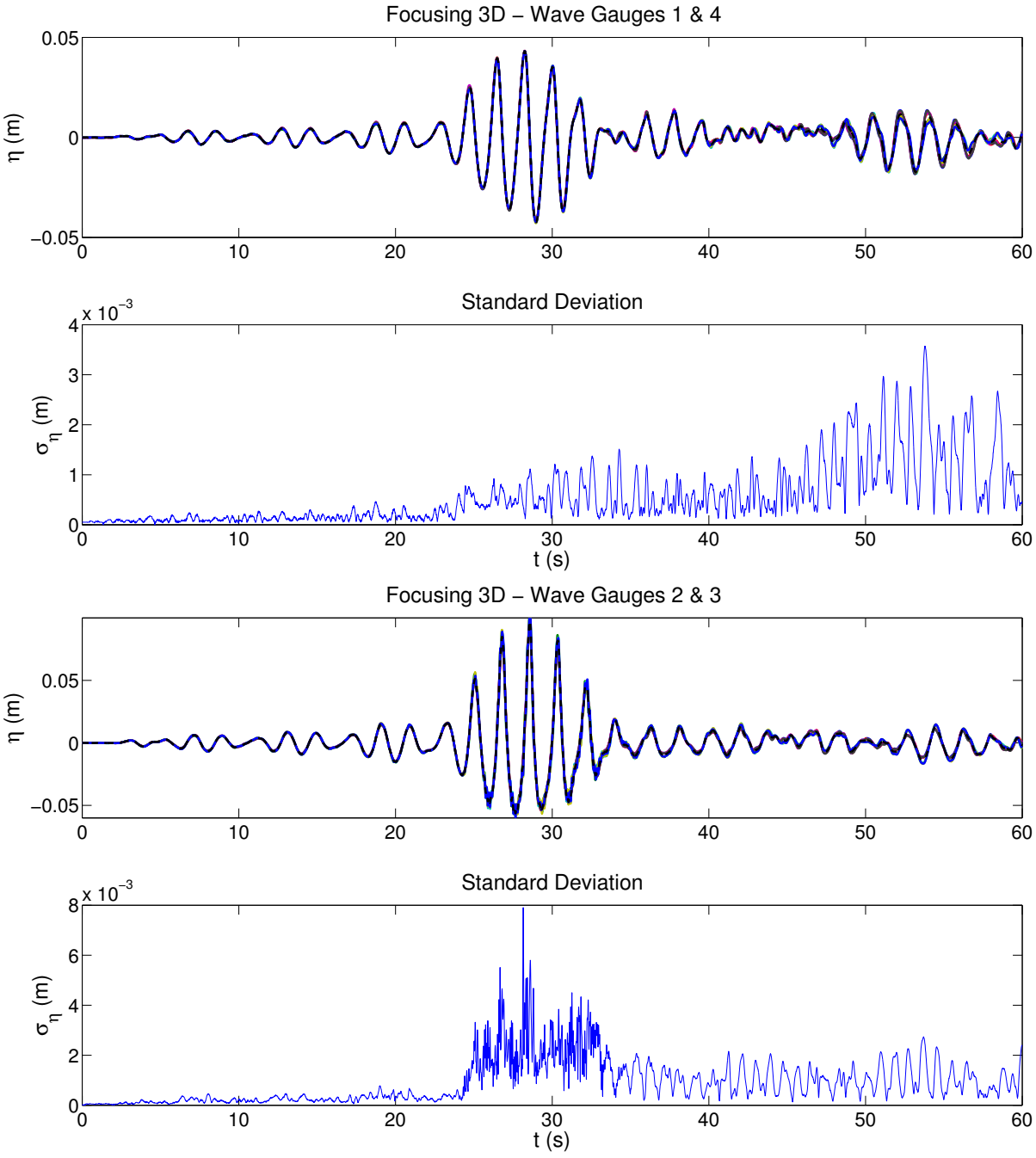

Figure 6.18: Wave focusing in 3D. Repeatability analysis. 4 time series per gauge are represented. Part I.

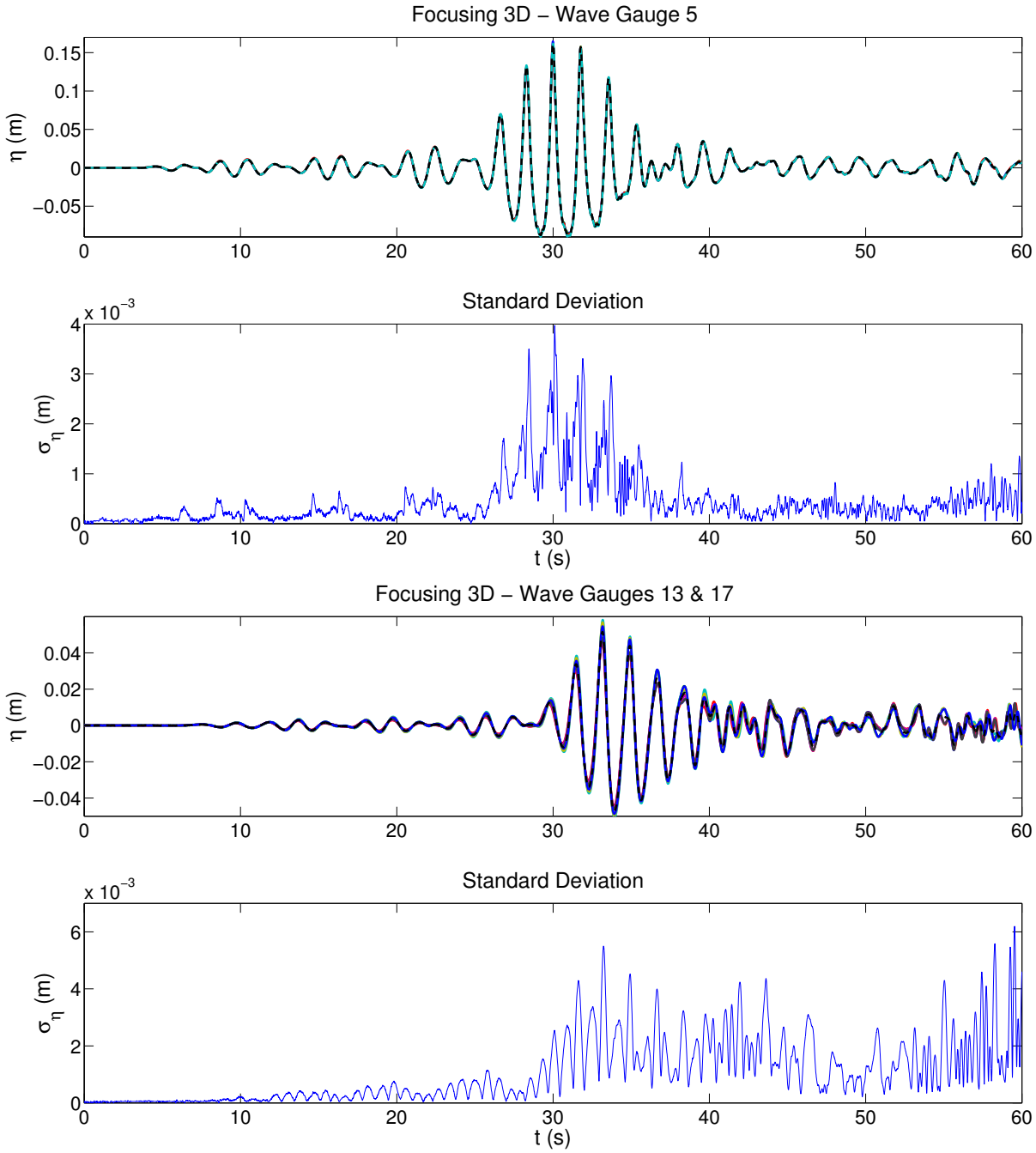

Figure 6.19: Wave focusing in 3D. Repeatability analysis. 4 time series per gauge are represented. Part II.

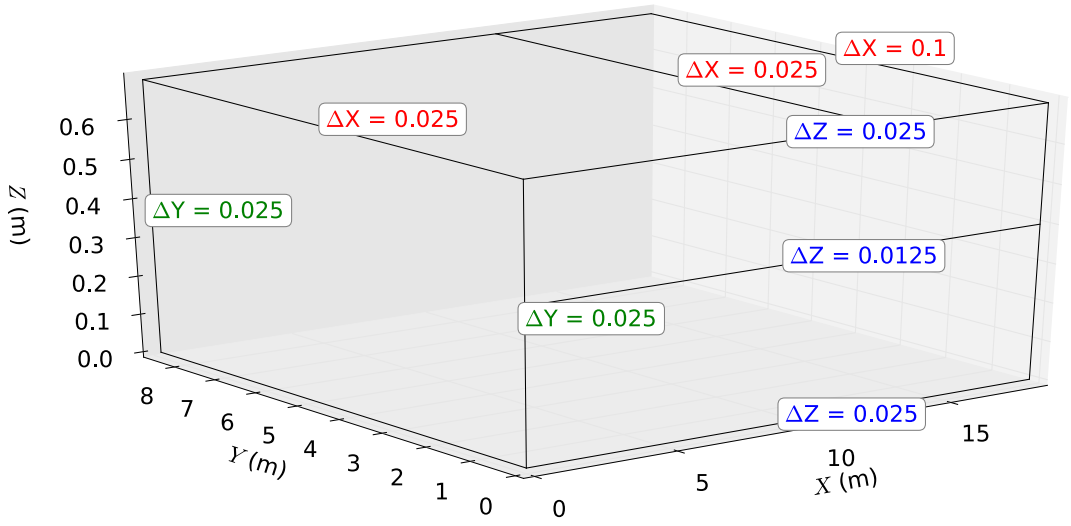

Figure 6.20: Variable mesh of the wave basin. Cell size in m.

Therefore, they should also be reproducible in the numerical model.

6.2.2.3 Numerical experiments

The effective area of the tank (18.3 x 8.6 x 0.7 m) has been reproduced numerically in 3D. The cell size varies along the X and Z axis, being constant in the Y axis. The variable discretization shown in Fig. 6.20 helps to save computational cost. The mesh is structured and orthogonal, and totals 8.1 million hexahedral elements.

The wave generation boundary is located at $X = 0$ m. The 10 paddles of the wave-making machine are replicated. Since the cell size in the Y direction is constant and equal to 0.025 m, each paddle is represented by 34 faces per horizontal row. The time series of the paddles displacement have been obtained from the measured signal, instead of using the theoretical signal, so that any machinery effects (e.g. response lag, inertia...) are taken into account. Active wave absorption has not been connected at the moving boundary.

The passive dissipative zone of the wave basin has been not reproduced. Instead, a static active wave absorption boundary opposite to the moving paddles has been applied. Turbulence has been modelled using $k - \omega$ SST.

The mesh deformation has been performed with a variable diffusivity, inverse to the distance from the wave generation boundary. Since no structure was being tested, no frozen zones have been defined.

A 2D mesh has also been generated to replicate the two-dimensional wave focusing.

This one corresponds to a single layer (Y plane) extracted from the 3D mesh, totalling 25,000 cells.

The 3D cases have been run in parallel using 96 processors (2.6 GHz) with an average simulation rate close to 1.5 seconds per hour. The 2D case can be run in a single processor, at a rate of 60 seconds per hour. However, the performance is not fully comparable, as the dynamics tested in 3D and 2D are significantly different.

6.2.2.4 Two-dimensional wave focusing results

The two-dimensional wave focusing simulation (115 s) takes 2 hours. The comparison between the numerical and experimental free surface elevation at one gauge on each row (6 different X-coordinate locations) is plotted in Fig. 6.21. The continuous red line represents the laboratory data and the black dashed line is the numerical time series. The long wave associated to each signal is also superimposed, amplified 10 times. It has been obtained by bandpass-filtering the time series with frequencies between 1/200 and 0.3 Hz.

According to the second order wave generation, a long wave trough is associated to the group. The numerical results show a high degree of accordance with the experimental measurements. The match between the long waves is almost perfect (1 mm difference for a total amplitude of 12 mm, or 8% relative error) up to the end of the group for the 3 first gauges (2, 5 and 6). The results for the last 3 gauges (11, 15 and 19) are as good in the beginning, but start to divert before the others. The variation can be explained by the difference between the absorption mechanisms of the laboratory and of the model. It is known that passive absorbers work adequately for short waves, but are less effective for long waves, which can pass through and get reflected at the end wall of the basin. On the contrary, active wave absorption presents a better performance for long waves. Hence, results for the long wave show growing differences with time, as the reflected components of the laboratory reach the gauges.

The long waves have been obtained by filtering the original signals measured. Therefore, the deviations between the experimental and numerical long waves are the result of differences in the unfiltered free surface elevation series. Noticeable discrepancies appear after the wave group for the mentioned reasons. However, since the dynamic of interest is the wave package itself, the study will focus on the instants previous to the end of the

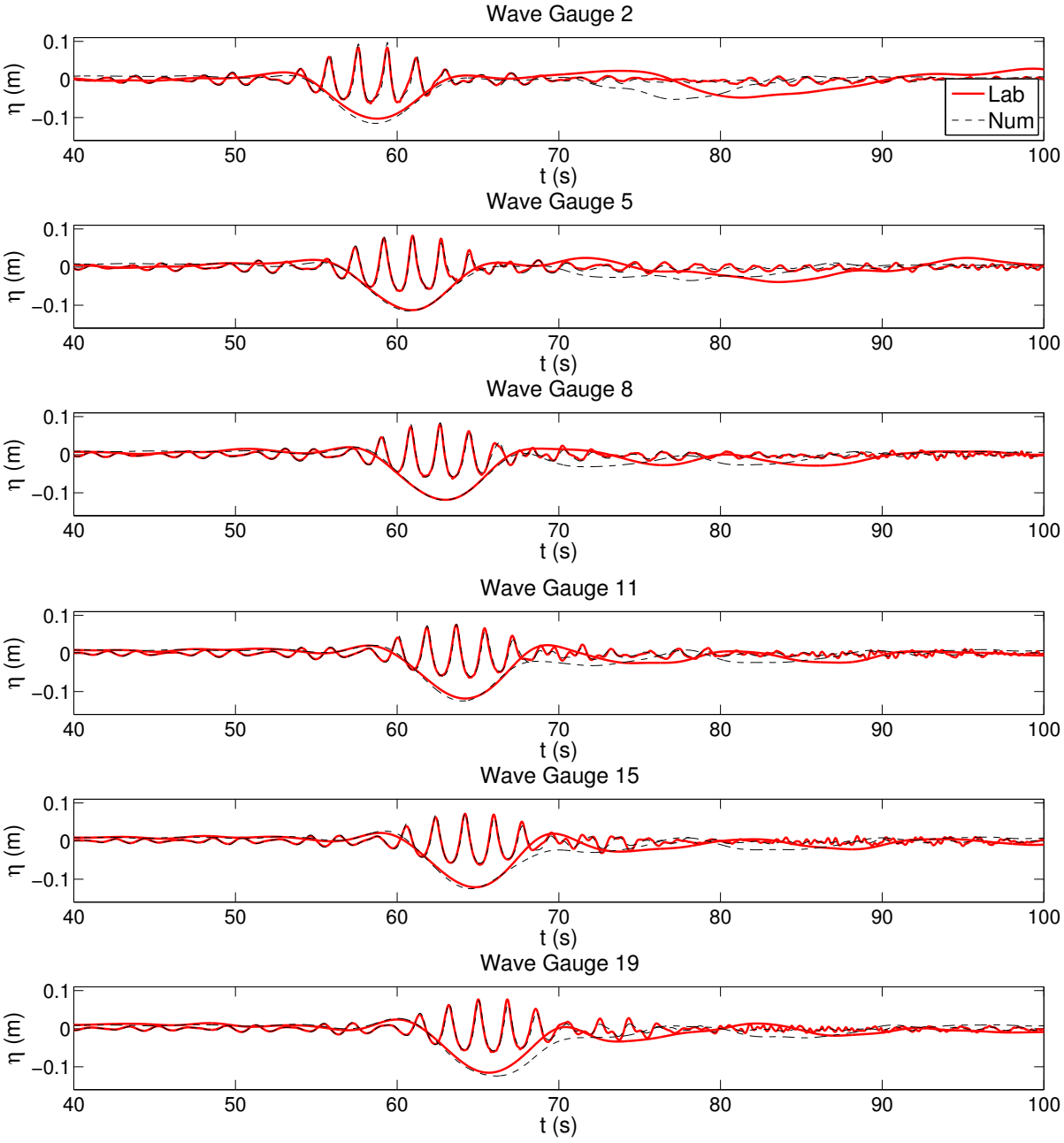

Figure 6.21: 2D wave focusing: free surface elevation comparison. Long wave amplified 10 times.

group.

As a general trend, the first two waves of the group are slightly overestimated, while the two last waves are underestimated. Nevertheless, the mean absolute error between the wave heights of the group along all the gauges is lower than 5 mm. Disregarding gauge number 2, the fit between the experimental and numerical central wave of the group is outstanding, with a maximum of 4 mm error (3% relative). The largest discrepancies appear at gauge number 2, the closest to the wave generation boundary. The shape of the numerical waves at that location is steeper (higher crests and shallower troughs). However, the difference in the wave height measured is barely 6 mm (4.6%). This difference is attributed to local effects of the wave generation procedure, as the match between the numerical and experimental wave profiles at the next gauge, number 5, is much better.

The local effects mentioned include minor processes of the experimental facility, as the flow that passes between paddles and between the paddles and the bottom of the basin are unaccounted for in the model. Others, which may be more significant, are the smooth variation at the numerical model boundary, but not for this particular case, as there is only one paddle. Finally, another significant effect may derive from the fact that the only magnitude that is measured experimentally is the position of the paddle, and not its velocity or acceleration. Therefore, an assumption of constant velocity during the time step has been made, which may yield accelerations quite different in the model than in the laboratory.

Moreover, the experimental setup for this particular case is far from ideal. Being effectively a 2D case, it could have been performed in a wave flume instead, as the water can easily oscillate transversally in wave basins. This may introduce some 3D effects that can contaminate the data. Fortunately, this seems not the case, at least until the wave group has already passed.

The main differences between this case and the one presented in Lara et al. (2011), which will later be reproduced successfully in Section 7.1.2, is that the group does not undergo heavy transformation in this case, as it propagates over a horizontal bottom. In the other test, the group experienced shoaling and breaking, after which the long wave bounded to the wave package was released. Nevertheless, the wave group in the present case shows some degree of deformation (asymmetry). The focusing, theoretically planned

at $t = 65$ s and $X = 12$ m (gauge 15), really takes place at $t = 64.21$ s. The use of a self correcting method as applied in Fernández et al. (2014), would be beneficial to ensure that the planned conditions are fully achieved.

6.2.2.5 Three-dimensional wave focusing results

The three-dimensional wave focusing simulation (60 s) takes 2 days. The comparison between the numerical and experimental free surface elevation at the gauges is split between Figs. 6.22–6.23.

Since the setup is symmetric, the gauges at symmetrical locations are represented in the same plot. No side distinction has been made for the laboratory gauges, both of them are represented with red dashed lines. The numerical gauges located at the left side (3, 4, 9, 12, 16, 17 and 20) are in blue line, while those at the right side (1, 2, 7, 10, 13, 14 and 18) are in black line. It can be observed that, actually, neither the laboratory or the experimental case are perfectly symmetric. Differences as high as 1 cm can be noticed between the numerical data (gauges 2 and 3) and as large as 2 cm between the experimental data (gauges 18 and 20).

The small variations in symmetrically-positioned gauges observed in the numerical model data are small and probably derive from the fact that the wave paddles at symmetrical locations do not share an identical movement due to local effects of the machinery. The higher differences in the experimental data are explained by the same reason, plus the uneven nature of the tank bottom and walls.

Fig. 6.22 includes the free surface elevation of the closest gauges to the wavemaker. The most important gauge is number 5, in which the focusing takes place, but the results are not as good as for the rest. The highest experimental wave height is 24.7 cm and noticeable differences appear after the first wave of the group. The wave troughs are not well captured, as differences of 2 cm (8% relative to wave height) can be found between the experimental and numerical solutions. Regarding the wave crests, only the first three waves of the group are accurately captured, while the following ones present errors up to 3 cm (12%). The cause of this problem is the large steepness of the waves at this gauge, reaching values close to 0.07.

These results indicate a limitation of the model: OpenFOAM® struggles to propagate

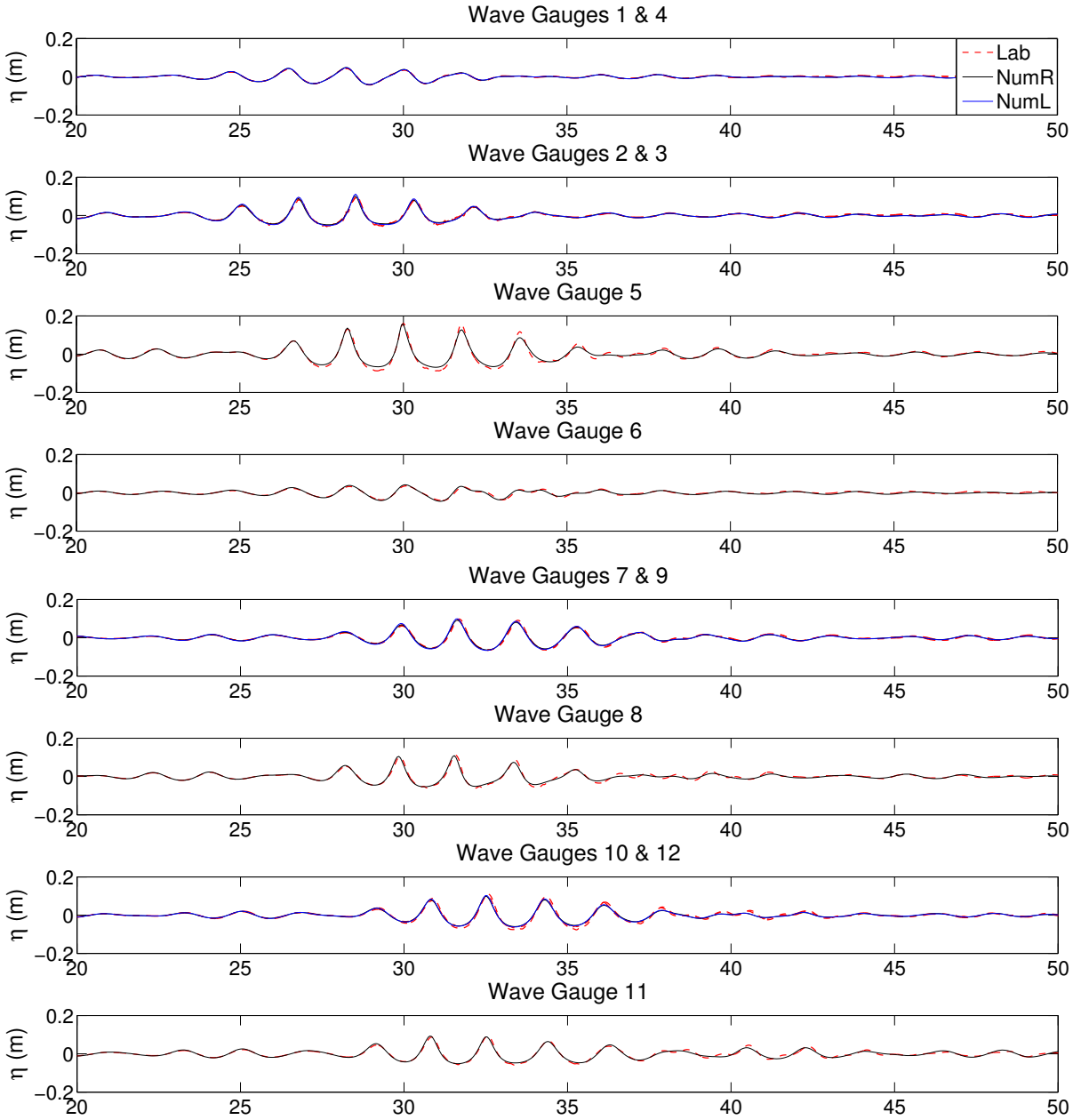

Figure 6.22: 3D wave focusing: free surface elevation comparison. Part I. NumL and NumR distinguish between the numerical gauges in symmetric positions, on the left and right side of the basin, respectively. See Fig. 6.13 for a reference.

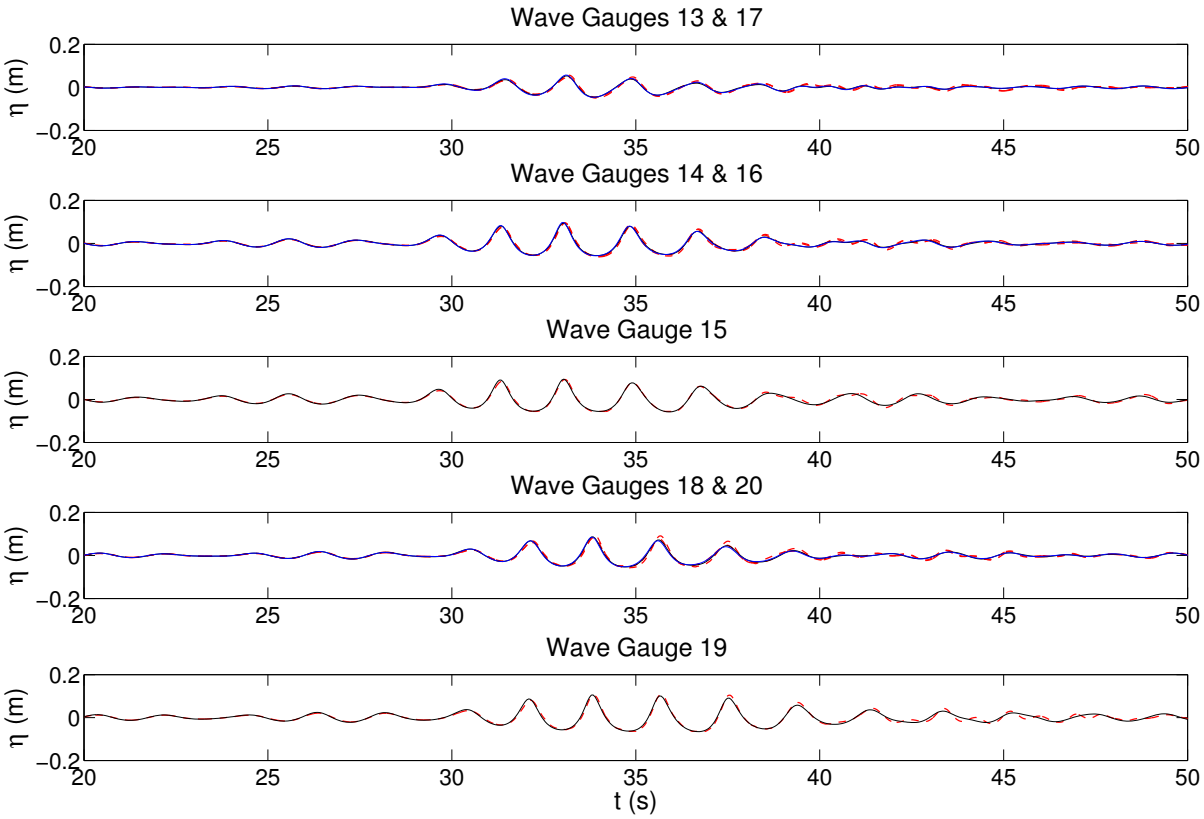

Figure 6.23: 3D wave focusing: free surface elevation comparison. Part II. NumL and NumR distinguish between the numerical gauges in symmetric positions, on the left and right side of the basin, respectively. See Fig. 6.13 for a reference.

steep waves. This is a well-known issue, already reported in Afshar (2010). The main driving mechanism is found to be the high artificial velocities that appear at the interface between water and air due to the large gradient of density. This issue is also connected to causing premature wave breaking over slopes (Jacobsen et al., 2012).

The rest of the gauges where wave steepness is lower, show a better performance. The accordance of the gauges of the first row (1–4) is excellent, enforcing the hypothesis that waves are generated correctly. The adequate result of gauge 6, in the same line as gauge 5, indicates that waves with a lower steepness propagate in a physically correct way. The gauges 7–11 prove the trend that as the steepness increases, so do the differences between the physical and experimental results.

Fig. 6.23 shows the furthest wave gauges from the wavemaker. The correlation is outstanding, especially for gauges 13, 15 and 17. As seen before, the differences grow larger for the last waves of the group. Errors in wave height for gauge 19 start at barely 2 mm and reach 1.5 cm (9% with respect to the 16.5 cm measured wave height). Regarding gauges 18 and 20, the match is almost perfect for one of the laboratory gauges, and up to 2 cm off for the other. A similar situation occurs for gauges 10 and 12 in the previous figure, proving that three-dimensional effects can have an influence, preventing fully symmetrical results.

A series of snapshots of the simulation are included in Fig. 6.24 with an amplification factor of 2 in the vertical direction. Two colour codes appear, one for the displacement of the paddles (X, in metres) and the other for the particle velocity at the free surface (U, in m/s).

The different displacement of each paddle and the smoothing function effects can clearly be seen in the top images. Note how the water elevation closer to the edges is initially higher ($t = 26$ s), and diffraction appears. Eventually, all the wave components focus at the symmetry plane of the basin. This effect can be first distinguished at $t = 27.25$ s, when the first wave of the group presenting large velocities (particle velocity on the crest of 1 m/s) has already converged at the centreline, and the second one, the highest wave of the group, is still split in two crests, close to the wavemaker. The still for $t = 30$ s shows the highest wave focused at the prescribed point (gauge 5). In the two panels on the bottom the evolution of the waves after the focusing can be seen. Since

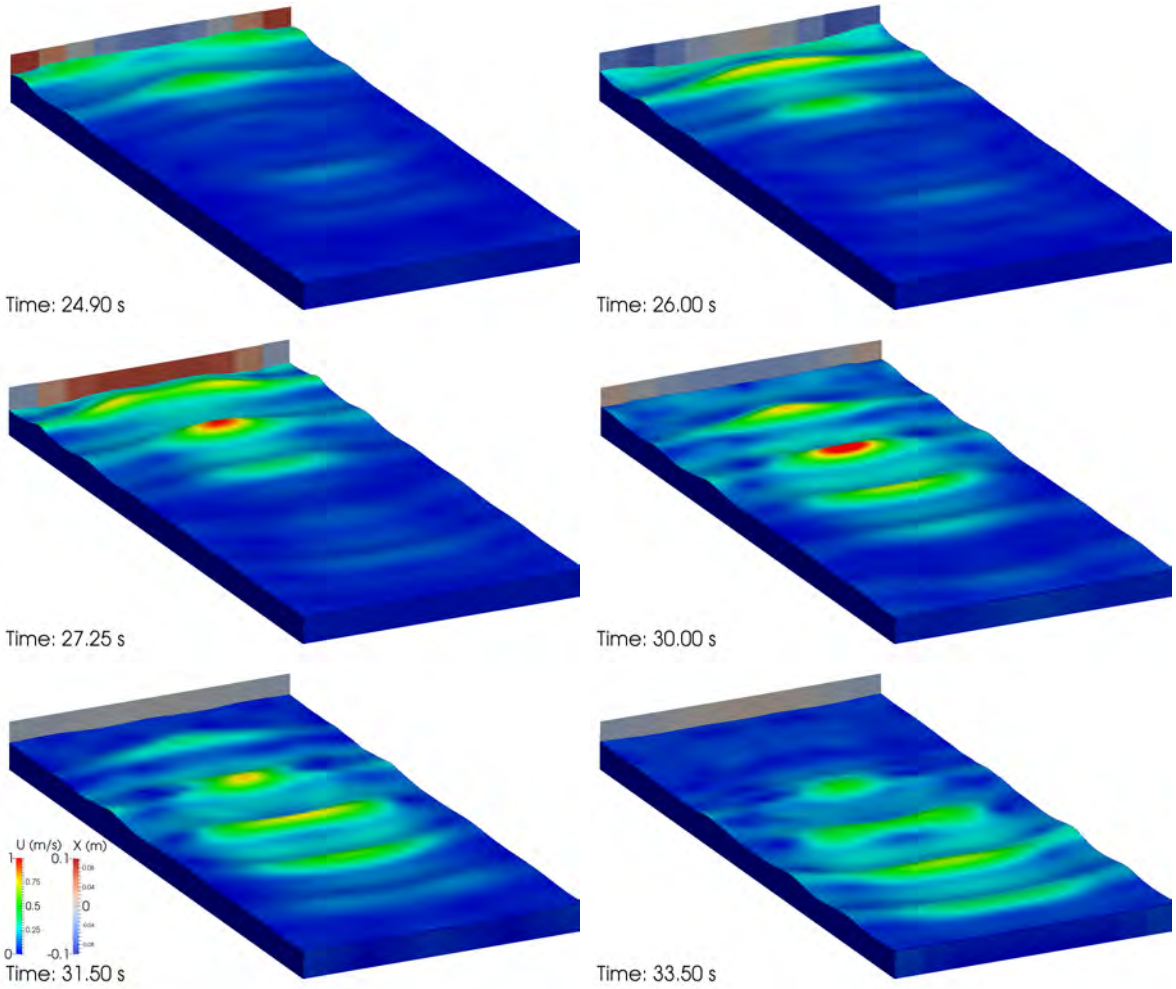

Figure 6.24: Generation and propagation of the three-dimensional wave group.

all the components generated continue travelling in their original directions, the waves decompose producing a longer crest first, and a split wave front next.

The effects of active wave absorption applied in the static boundary, opposite to the wavemaker, can also be noticed in the three last frames. A total of 10 vertical transects enable directional wave absorption, because each one absorbs the waves independently. Therefore, different velocities appear at the boundary, depending on the free surface elevation height at each transect.

6.2.3 Conclusions

A high degree of accordance has been found between the experimental and numerical for the 2D and 3D wave focusings. Small differences can be found close to the wave generation boundary, due to local effects. Other discordances derive from the different absorption methods applied (experimental passive wave dissipation vs numerical active wave absorption). This study has also unveiled the limitation of OpenFOAM® to simulate the propagation of very steep waves. Overall, the behaviour of the boundary condition is realistic. However, performance is lower than with the static wave generation routines, as the mesh updating routines add significant computational cost to the model.

Active wave absorption has been programmed applying a simple digital filter. The numerical results point out that the performance of this procedure for moving boundaries is as good as when applied for static boundaries. Reflection coefficients are generally smaller than 10%, and only larger for those cases in which the wave conditions are far from the original hypothesis.

Chapter 7

Validation of Coastal Engineering Processes

Validation is a mandatory process that numerical models must undergo to prove that they are capable of simulating physical phenomena in an accurate way. Extensive validation tests have been carried out with **IHFOAM**, comparing its results with experimental measurements to demonstrate that the model is able to deal with relevant coastal engineering processes.

In this chapter **IHFOAM** proves its capabilities to simulate some of the most important processes involved in wave transformation and interaction with impervious coastal structures. Then, porous media are introduced, to deal with the interaction of waves with porous coastal structures.

7.1 Wave transformation and interaction with impervious structures

The interest of this section is to present the practical application of OpenFOAM® to simulate coastal engineering processes.

Each of the individual cases is structured as follows. A brief introduction presenting the importance of the physical processes analysed is given first. Then, the laboratory experiments are described. Next, the numerical setup is described, including information about the mesh, the waves and the numerical sampling instruments. Finally, the numerical results are presented and compared with the existing laboratory data.

7.1.1 Pressure induced by a solitary wave on a vertical structure

One of the main variables that has to be correctly replicated by a numerical model in order to obtain relevant results for coastal engineering purposes is pressure. Stability of coastal structures is derived from the pressure laws. In order to assist the design of defense structures (specially non standard ones) the RANS models can be of great use. In this case a solitary wave, initially 2D interacts with a structure, generating 3D free surface evolution and pressure fields.

7.1.1.1 Description of the physical experiments

The physical experiments are presented in Lara et al. (2012). They were performed in the University of Cantabria wave flume, which is 20.62 m long, 0.58 m wide and 0.8 m high. Waves were generated by a piston-type wave maker.

Inside the flume, an impervious rectangular column made of methacrylate was placed. Dimensions were 30 cm in the cross-flume direction and 24 cm in the long-flume direction (Fig. 7.1). Some of the walls were drilled to accommodate pressure gauges. The closest face to the wave paddle was located 10.84 m away from the wavemaker mean position.

Eight pressure gauges were placed to measure the pressure exerted by the waves at the faces of the obstacle, with a sampling rate of 360 Hz. Their location is shown in Fig. 7.1(b). A total of 12 free surface resistive gauges were placed along the flume, as it can be seen in Fig. 7.1(a). The distribution is non symmetric because even though the test is carried out in a wave flume, it is not 2D. More gauges are placed downstream the structure, as the most relevant eddies travel in that direction. The sampling rate for the free surface gauges is also 360 Hz.

Several cases were tested, and efforts were done to prove the repeatability of the experiments. Still water depth varied from 0.25 m to 0.45 m depending on the case. Solitary waves and regular wave trains were tested. The solitary waves ranged from 5 to 14 cm in height, while regular cases considered 4 and 6 cm for four different wave periods (0.5, 1, 2 and 4 s).

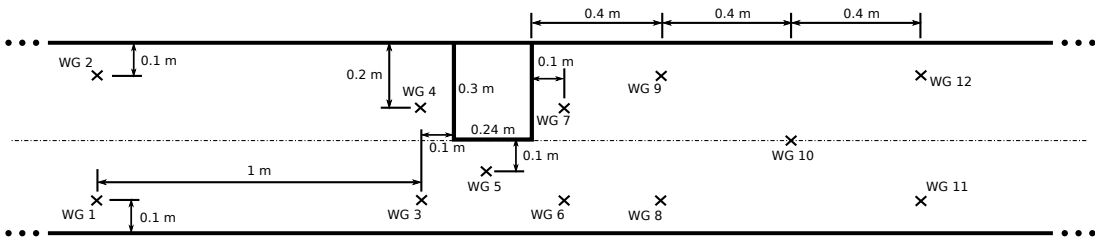

(a)

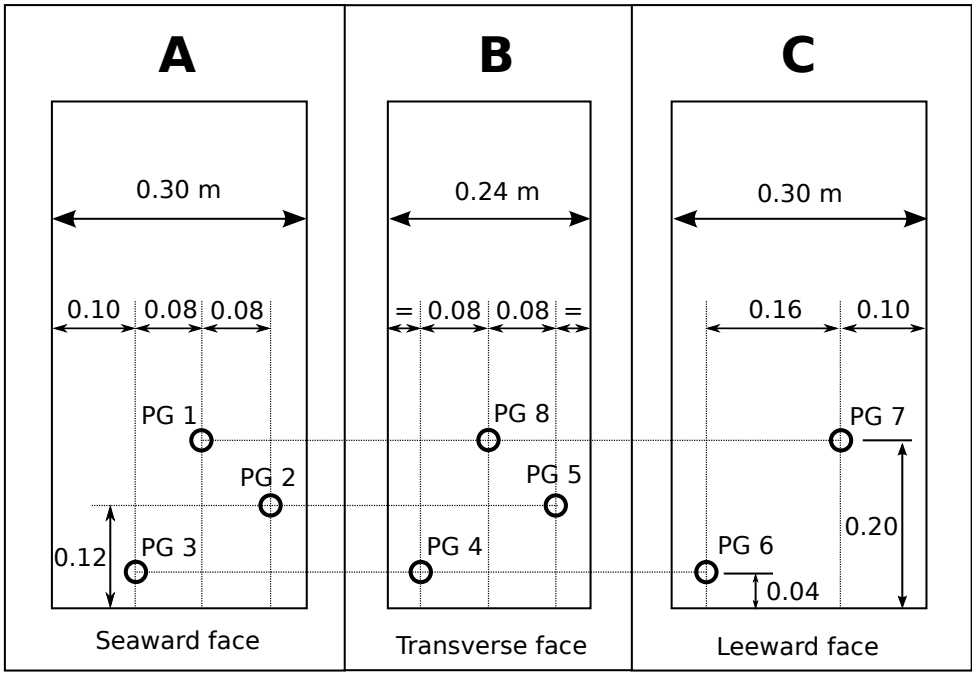

(b)

Figure 7.1: Position of the laboratory gauges. (a) Free surface gauges. (b) Pressure gauges mounted on the obstacle.

7.1.1.2 Description of the numerical experiments

The complete flume (20.62 x 0.58 x 0.8 m) is replicated in 3D. The longest length of the flume corresponds to the X axis, and it is meshed with a variable cell discretization.

This allows for better resolution in critical zones, as near the obstacle, while providing adequate resolution for other zones where dynamics are less restrictive. Resolution in the X direction starts with 3 cm from both ends (the wavemaker and the end of the flume), increasing up to 1 cm near the structure. This 1 cm discretization is kept constant from 2 meters away of the obstacle. The other horizontal and vertical directions feature a constant discretization of 1 cm. This mesh totals 5.5 million cells, with cell aspect ratio (H:V, X:Z) varying between 3 to 1. Turbulence is modelled using $k-\omega$ SST, since flow separation from the walls was clearly visible in the experiments.

The case with the highest solitary wave height (14 cm) has selected for numerical simulation because higher turbulent levels were expected in the vicinity of the structure. The solitary wave has beens generated using Boussinesq theory and without active absorption. This matches the laboratory setup, in which the paddle acts as a reflecting boundary once it has stopped. Data is acquired in the model at 20 Hz.

A series of 15 seconds has been simulated, including the first impact of the wave with the structure, but also the first reflection that reaches the obstacle again, generating two vortices each time. Simulation time is approximately 2 days using 8 cores (2.93 GHz). Mesh decomposition is handled by the scotch method[1], which is automatic.

7.1.1.3 Results

The results for the free surface gauges are shown in Fig. 7.2 and Fig. 7.3. The pressure gauges are presented in Fig. 7.4. The continuous line represents the laboratory measurements, while the dash-dot line shows OpenFOAM® results.

Regarding free surface, the solitary wave initially propagates in 2D along the flume, until it reaches the structure. From that moment, the gauges placed in the same x coordinate start to show a 3D behaviour (e.g. gauges 1–2, 3–4, 6–7, 8–9 and 11–12). In gauges 1 and 2 the shape of the solitary wave is highly influenced by the reflection of the impervious structure, and therefore, the profile is distorted, with a small overestimation of

[1] http://www.labri.fr/perso/pelegrin/scotch/

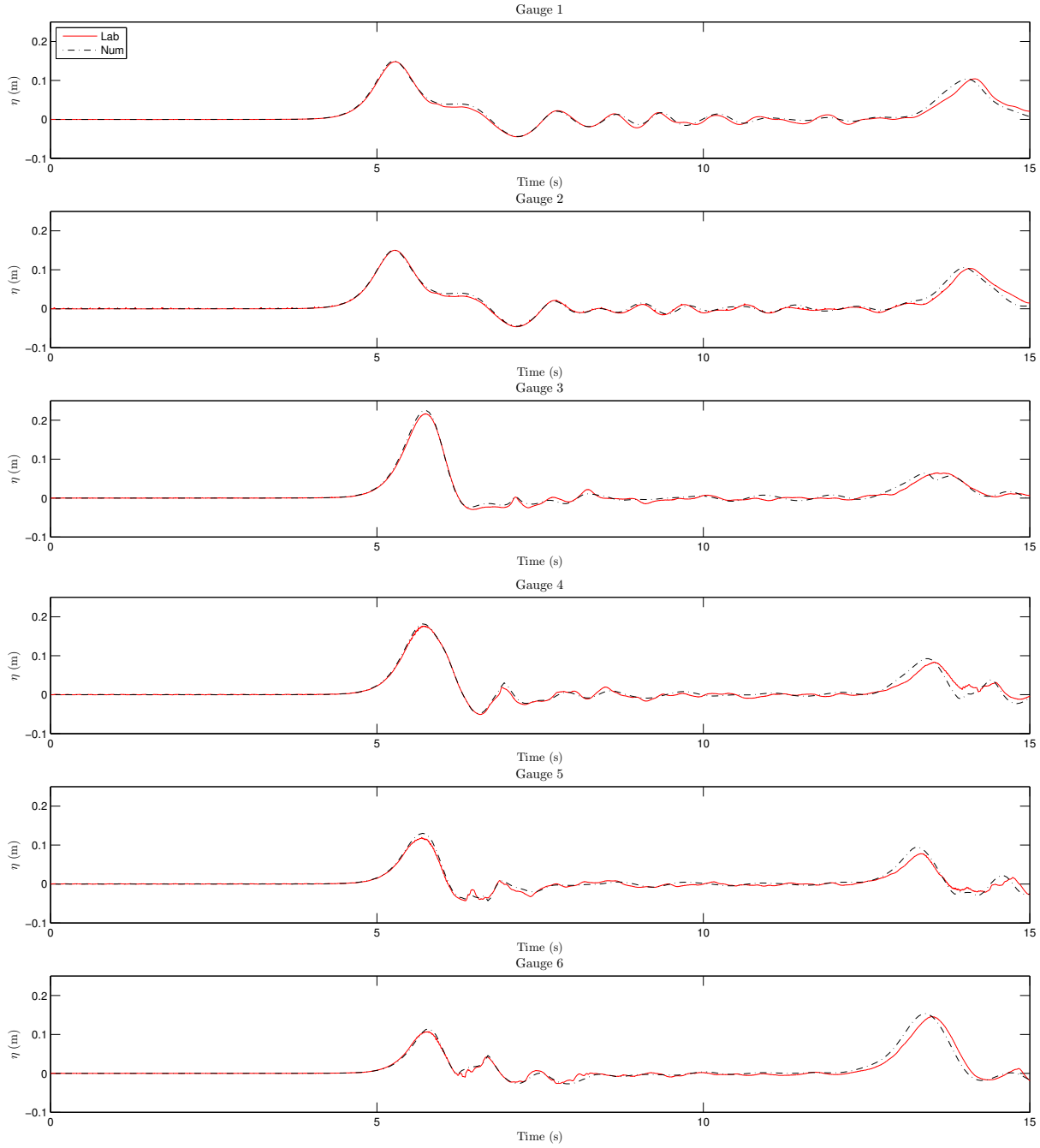

Figure 7.2: Solitary wave impacting on a vertical structure. Comparison of the numerical and experimental free surface elevation (Part I).

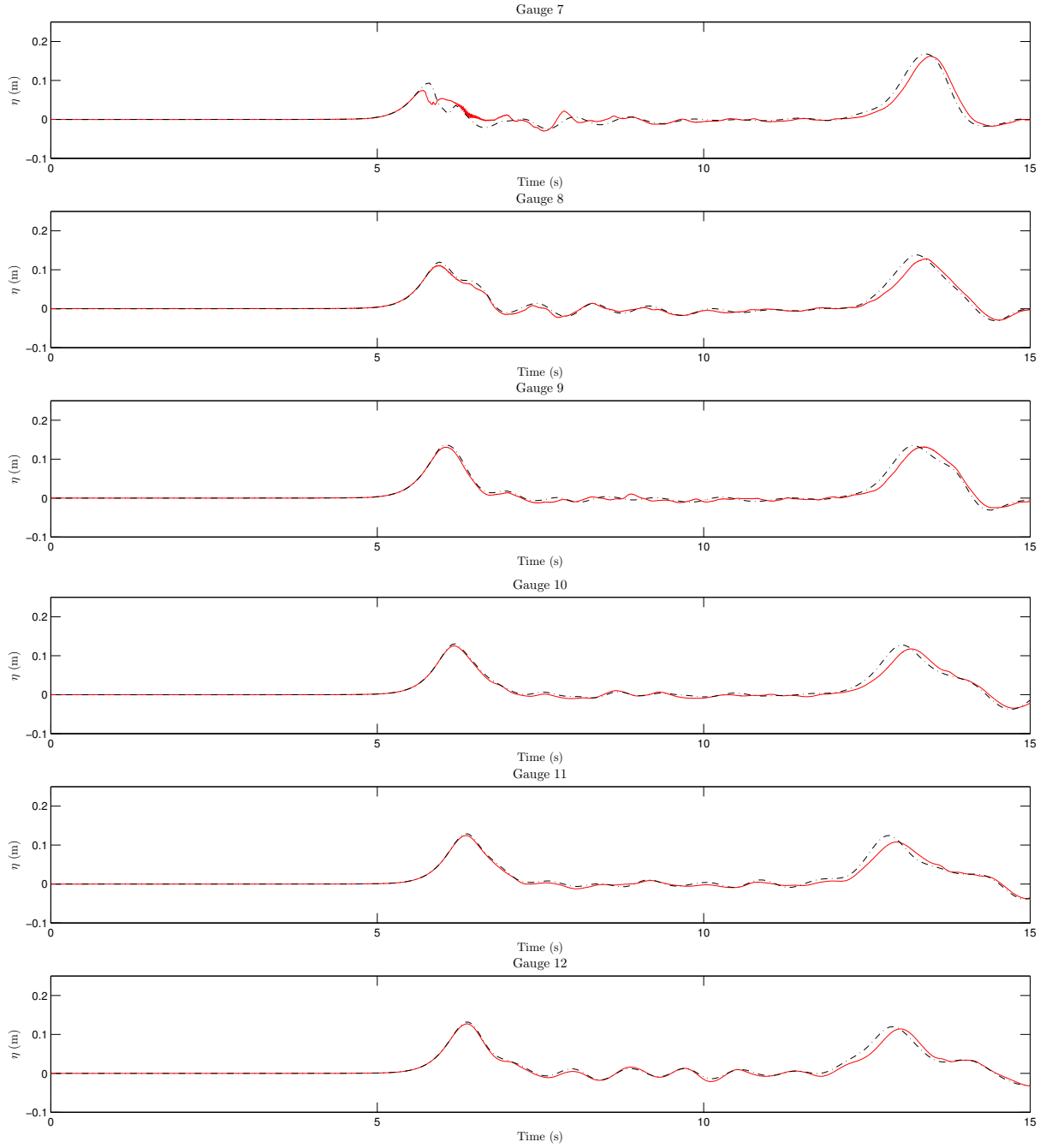

Figure 7.3: Solitary wave impacting on a vertical structure. Comparison of the numerical and experimental free surface elevation (Part II).

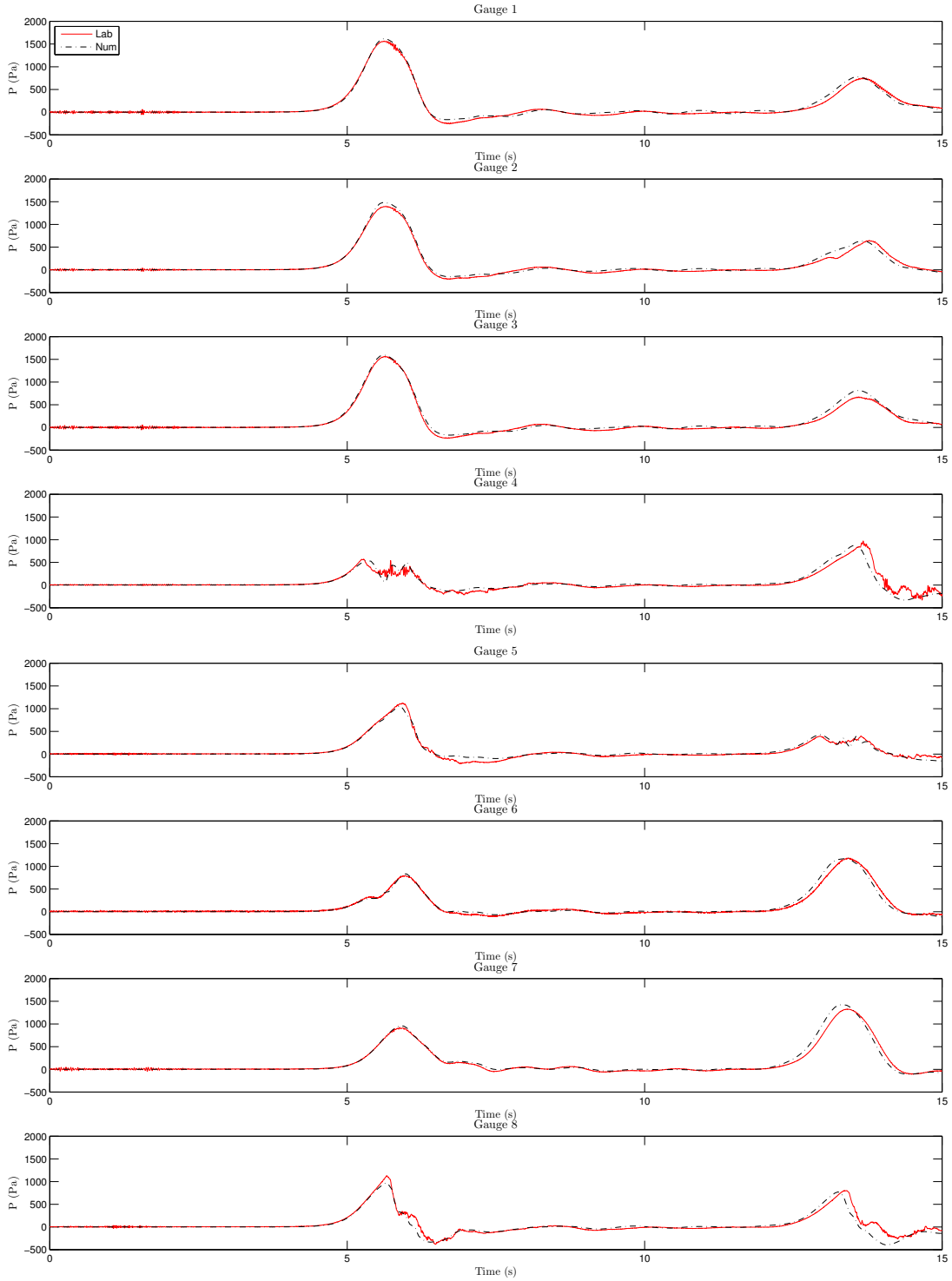

Figure 7.4: Solitary wave impacting on a vertical structure. Comparison of the numerical and experimental gauge pressure.

the numerical reflection. Gauge number 7 shows the worst agreement between both series, because of the location of the sensor, right in the place where big eddies are generated when the wave passes, as shown in Fig. 7.5. The process is so violent that the free surface is close to breaking, hence influencing the result of this gauge. Despite the fact that the free surface is not accurately captured at every time step, the general trend in the movement is adequate. Between the first solitary wave arrival and the second one, that corresponds to the reflection of the initial wave at the end wall of the flume, all the numerical gauges show a correct behaviour, representing small oscillations caused by reflections and eddies. In spite of the initial good results, there is a general disagreement between both series, systematic to all the gauges, and this is that the reflected numerical solitary wave reaches the gauges earlier than what it is observed in the experiments. Also the reflected numerical wave presents higher height for gauges from 4 to 12. A number of facts can cause the first effect. Some feasible causes are the change in celerity due to the higher wave amplitude or errors measuring the wave flume dimensions. The second effect is somehow less clear, nevertheless, it is very small, on the order of 1 cm (7%).

Fig. 7.5 shows the evolution of the free surface as the solitary wave passes for the first time around the impervious structure. The first large eddies appear due to high gradients in free surface elevation between the seaward and the leeward parts of the obstacle. As the wave propagates, the eddies detach from the corners and travel in the same direction. This causes an increase in water level in the vicinity of the eddies, which is finally dissipated radiating in all directions. A trapped air pocket can be seen at 6.90 seconds at the lateral wall of the flume. The numerical simulation has shown that the air trapped by the vortices reaches the bottom, confirming visual observations.

In Fig. 7.6 the dynamic pressure (excess in pressure respect to the initial hydrostatic loading) is presented for the same times in Fig. 7.5. For each instant, the top panels show the pressure at the different faces of the structure, as shown in Fig. 7.1(b). The bottom panel is a 3D view of the obstacle from the leeward side, which also includes bottom pressure. Free surface is also represented, as a white line. Positive pressure comes into sight as the wave gets closer, and negative pressure appears when the wave flows away.

The time evolution shows the generation of the vortices, that affect the whole structure from the free surface to the bottom, lowering pressure due to the larger velocities. It is

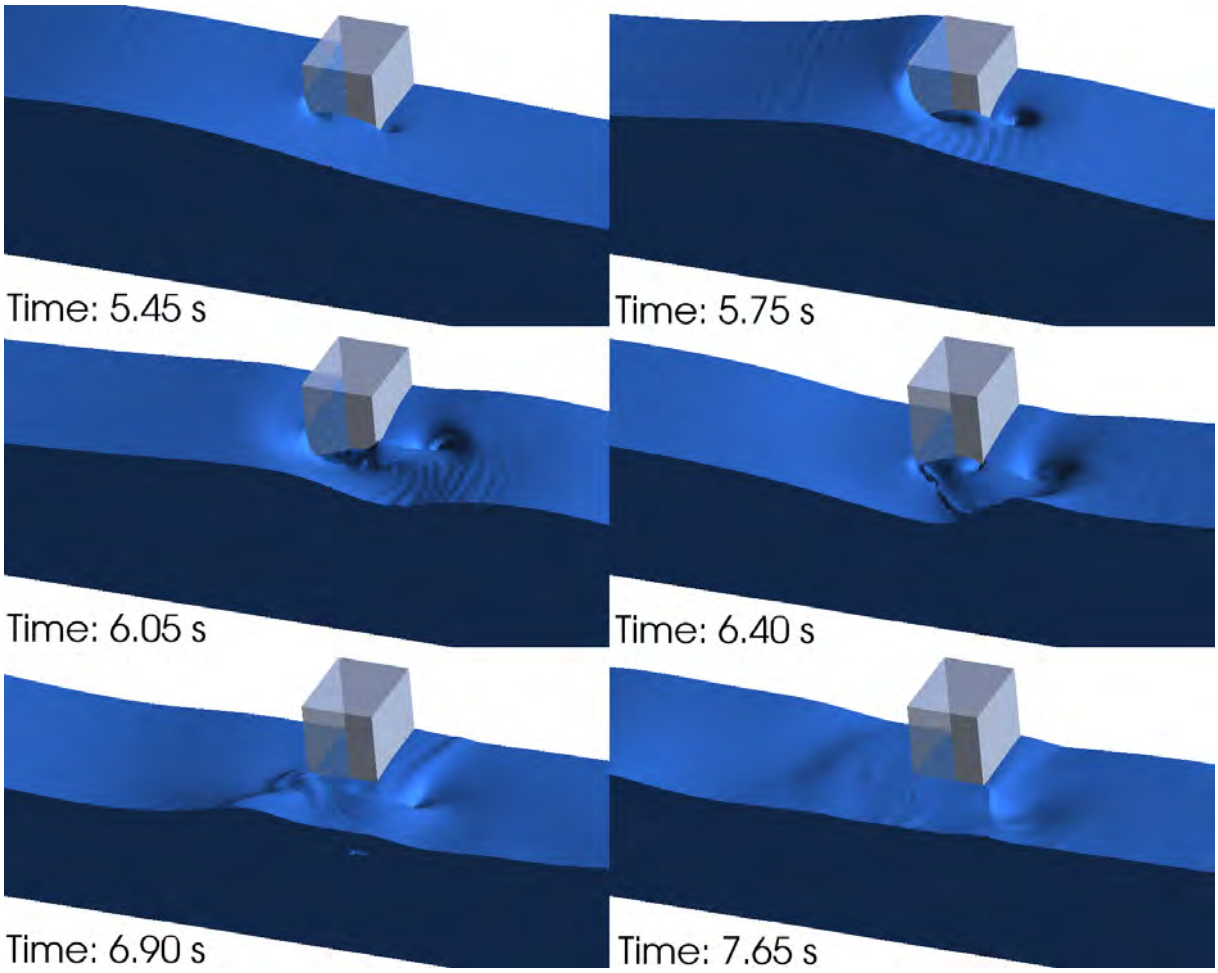

Figure 7.5: Solitary wave impacting on a vertical structure. Free surface evolution of the first impact of the solitary wave.

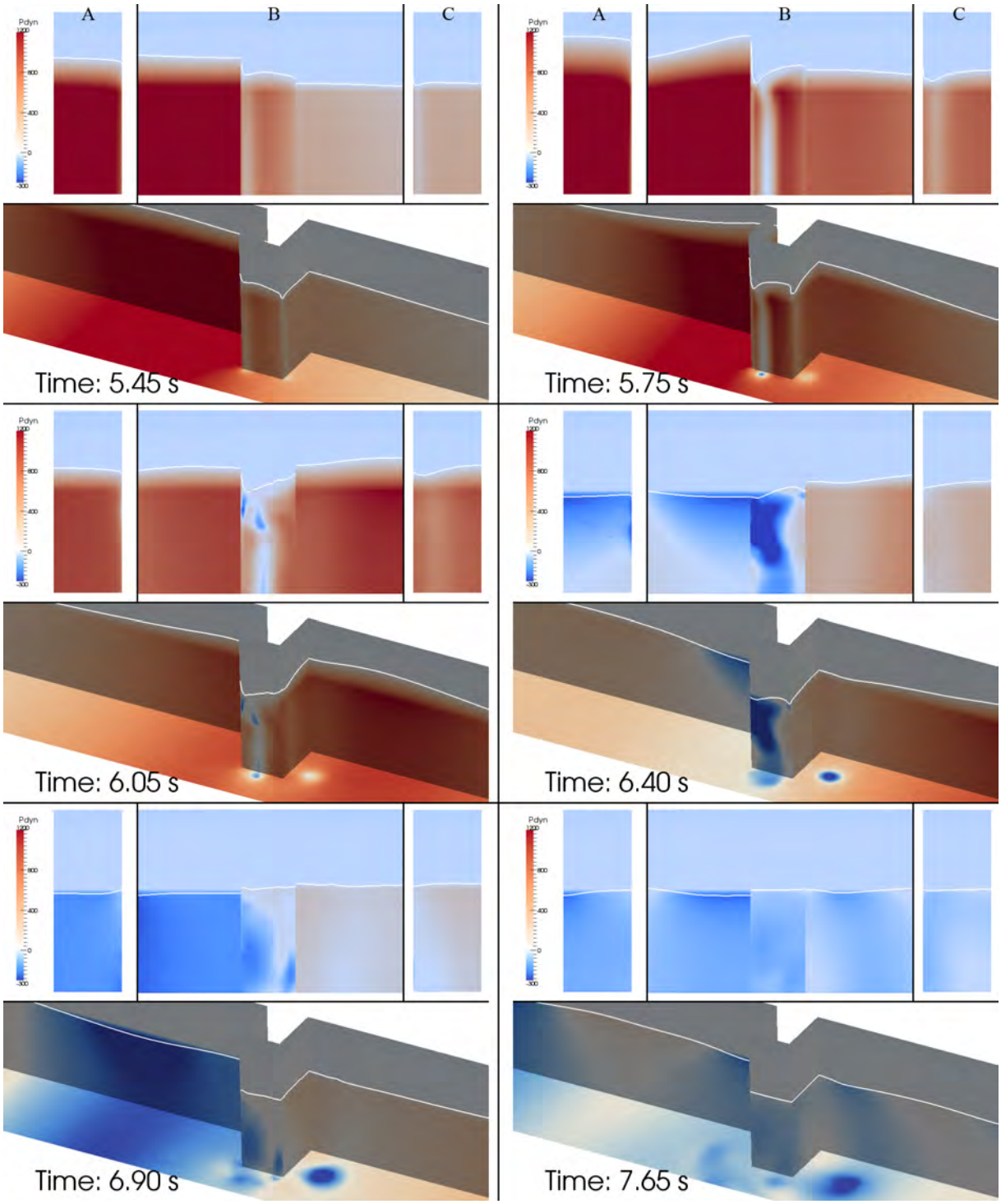

Figure 7.6: Solitary wave impacting on a vertical structure. Dynamic pressure evolution when the solitary wave interacts with the impervious obstacle. Units in Pa.

remarkable that the seaward vortex attaches to the transverse face of the structure, leading to its dissipation prior to the leeward eddy. The second vortex is generated by the leeward corner of the structure, and rapidly detaches from the face ($t = 6.40$ seconds). From that time it can be seen its influence on the bottom as a circular large drop in pressure, which is still moving away from the structure at the last time presented ($t = 7.65$ seconds).

7.1.2 Transient wave group

Wave breaking is one of the most difficult processes to replicate numerically, as it is a three-dimensional, turbulent and fully non-linear mechanism, highly dependent on the initial wave conditions. Prior to studying a full 3D case, the model accuracy is checked for a mere 2D simulation, with a peculiarity: second order wave generation, as accuracy of the waves is of special interest to study correctly the processes of the surf-zone. In this case the cross shore propagation of an infragravity wave induced by a transient focused short wave group over a sloping bottom is studied.

7.1.2.1 Description of the physical experiments

The physical experiments, along with a 2DV numerical replication are presented in Lara et al. (2011) and were also carried out in University of Cantabria wave flume, which has already been introduced in the previous case. The wavemaker movement was controlled using second order theory, as explained in Section 5.3.1. The still water level was set at 0.4 m.

The bathymetry resembled a steep beach profile in two parts, with a central horizontal section and was entirely built of plexiglass. The geometry along with the free surface gauges location is presented in Fig. 7.7.

Thirteen resistive wire gauges were placed within the flume, mounted on a carriage, to measure free surface elevation. The first three gauges, positioned between the wave paddle and the beginning of the slope, were used as control gauges. The rest of them were placed over the built bathymetry, to capture shoaling and breaking processes. Data was acquired at 60 Hz to provide a high temporal resolution.

Several cases were generated, defined by $N = 50$ individual wave components of equal amplitude, and uniformly spaced over a specified band of the frequency domain in order to

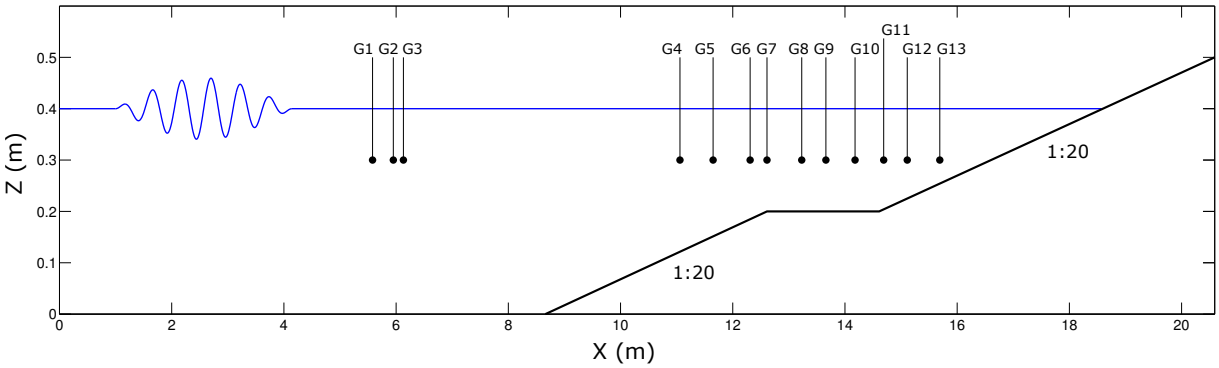

Figure 7.7: Experimental setup for the transient wave group tests. Bathymetry and free surface gauges location.

obtain a "top-hat" spectral shape. The control variables are defined as follows: component wave height $H_i = \frac{H}{N}$, where H is the total wave height; f_1 is the minimum frequency component, and f_N is the maximum one, in between them f_i varies linearly; the frequency bandwidth is$\Delta\ f = f_N - f_1$. A number of combinations were considered, refer to Lara et al. (2011) for further details.

7.1.2.2 Description of the numerical experiments

The wave flume has been replicated in 2D this time. The base for the mesh spans for the whole 20.62 m in length, and 0.7 m in height. Vertical cell resolution is constant, and equal to 0.5 cm. Horizontal resolution varies from 1.5 cm in the generation boundary up to 0.5 cm on top of the slopes, where more resolution is needed. Then the basic mesh is intersected with the bathymetry surface (using *snappyHexMesh*), and the resultant cells are refined (subdivided) twice to create a high density in resolution, allowing better inundation in the swash zone and a well defined boundary layer. The resultant mesh is completely smooth, which is a clear advance of OpenFOAM® with respect to the castellated approach used in Lara et al. (2011), as it also permits easier and more physical inundation in the swash zone. The final mesh has 250,000 cells.

A case which was not included in the original paper (Lara et al., 2011) was chosen to be reproduced numerically. The characteristics of the wave group are: $f_1 = 0.42$ Hz, $f_N = 0.77$ Hz, $H = 0.08$ m, and Iribarren number $Ir = 0.40$, defined as $\frac{\alpha}{\sqrt{\frac{H}{L_0}}}$, where $\alpha =$ 1:20 and $L_0 = \frac{gT^2}{2\pi}$ is the wave length in deep water. The wave focusing was calculated to occur in the constant depth bottom between the slopes, for $t = 100$ seconds. All the wave

components have been obtained and constitute the input. First order wave generation is the summation of the individual components using linear theory for each one. The second order interaction is considered and handled internally by the boundary condition following Longuet-Higgins and Stewart (1960).

IHFOAM is a two phase model, hence this simulation is affected by air as well, unlike the original numerical replication (Lara et al., 2011). $k-\epsilon$ and $k-\omega$ SST turbulence models were tested. In the end, no major differences were observed between the two. Numerical gauges were placed at the same locations of the laboratory test. Courant number was set to 0.3. A total of 200 seconds were simulated to have full description of the long wave generated, including its reflections. The full simulation finishes in 1 day in 4 (2.93 GHz) cores.

7.1.2.3 Results

The surface elevation on the free surface gauges is presented in Fig. 7.8 . The continuous line corresponds to the laboratory series and the dashed line is the numerical result. Only $k-\omega$ SST results are presented, as $k-\epsilon$ are virtually the same. The time series showing the transient wave groups are at scale 1:1, according to the scale on the left hand side. The long waves are also superimposed in the same figure, but they have been amplified by a factor of 10. They have been obtained filtering the original signal using a bandpass filter with frequencies between 1/200 and 0.3 Hz.

The agreement between both series is almost perfect. The wave group is extraordinarily well captured during the propagation and shoaling phases (gauges 1–7). Wave breaking also shows very good results, having only a somehow lower wave height towards the end of the group. The long wave is correctly replicated in the initial part along the whole set of sensors, which supports the idea of the good accuracy of the wave breaking process. Maximum absolute deviation is 3 mm, approximately a 3%. After the long wave gets reflected on the paddle and returns, the differences grow. This is likely to be caused by the movement of the physical paddle, as small variations of the length of the flume influence the long wave, and this effect is not present in the numerical simulation. When the results are compared with the simulation of IH-2VOF (Lara et al., 2011), it can be seen that there is an improvement, which may be caused by including the air effects or by

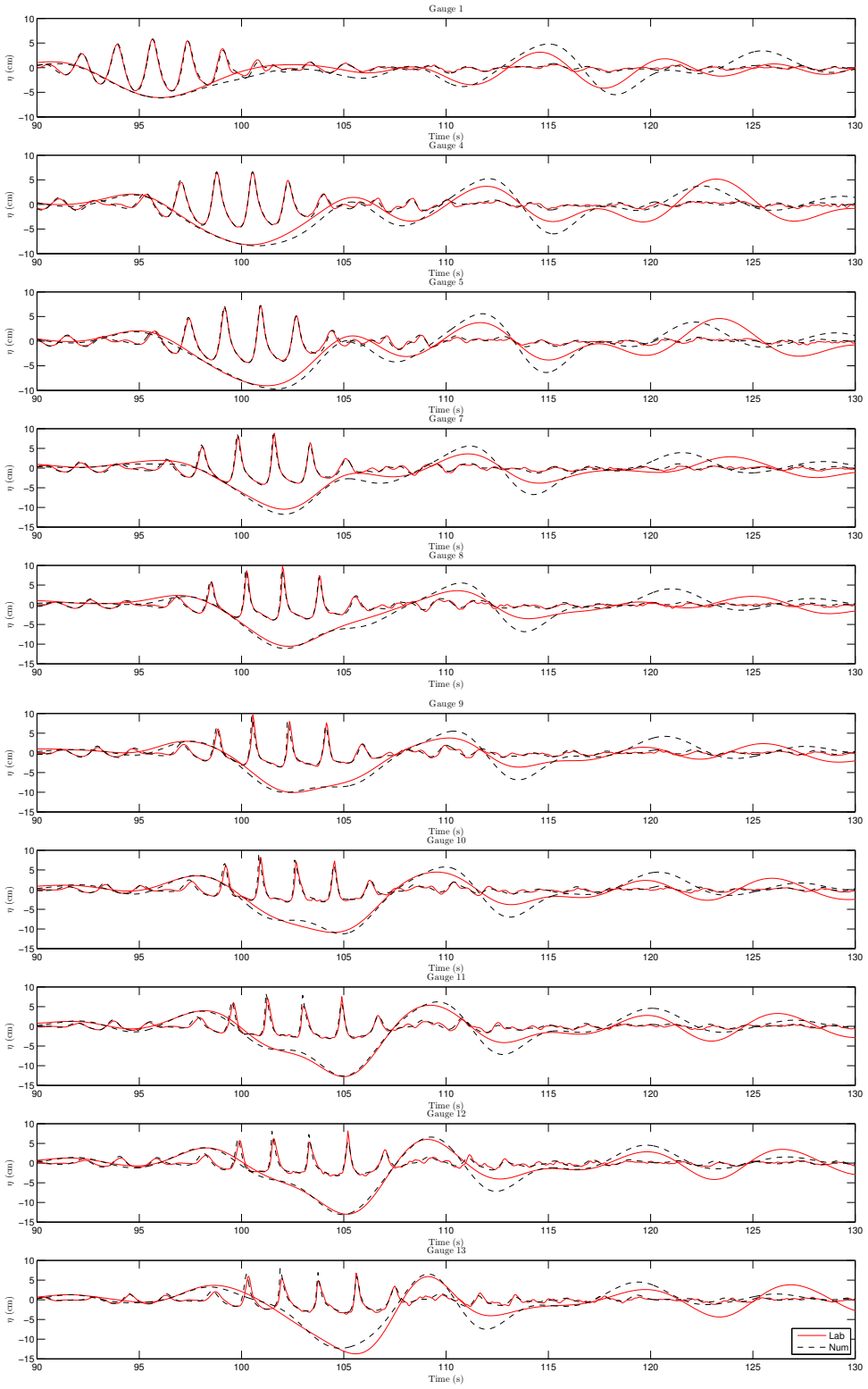

Figure 7.8: Transient wave group: free surface gauges.

the more accurate definition of the bottom. The latter one is due to the adaptative mesh approach followed by *snappyHexMesh* tool, that generates a smooth mesh by adapting and refining the cells intersected by a given surface (bathymetry), versus the old cutting cell method present in IH-2VOF, which yields sawtooth-type surfaces.

7.1.3 Breaking of a solitary wave in 3D

Wave breaking is always a full 3D process, but particularly when the bathymetry varies along the wave front direction. Now that this process has been studied in 2D with very accurate results, a special bathymetry is set up in this case in order to replicate 3D plunging breaking of a solitary wave. The goal of this simulation is to continue validating the model generation, and to check its performance when the wave breaks inducing 3D patterns in the wave flow. A solitary wave is chosen in order to better identify the wave generation, propagation and breaking in detail.

7.1.3.1 Description of the physical experiments

The physical experiment is part of Swigler (2009), and can currently be accessed online, as it is part of 2009 ISEC (Inundation Science & Engineering Cooperative[2]) workshop. The experiment was carried out at Oregon State University O.H. Hinsdale Wave Research Laboratory, that contains a large wave basin: 48.8 m long, 26.5 m wide, and 2.1 m deep. The 39 cm high solitary wave was produced with a piston-type wavemaker with 29 independent paddles, moving at once and acting as one. The bathymetry was made of smooth concrete in order to reduce the boundary effects due to friction.

The coordinate system of the laboratory was as follows: $x = 0$ m at the wavemaker and the positive X axis pointing towards the opposite end of the basin; the Z axis corresponds to the vertical upward direction, and $y = 0$ m was set at the symmetry line. The bathymetry was designed so that the wave breaking was symmetric with respect to the centre line of the basin, and it was formed of two superimposed geometries. The first was a 1:30 slope planar beach, which began at $x = 10.2$ m and extended to $x = 31$ m with a height of 0.95 m. On top of it, and beginning at the toe of the planar beach, a three dimensional shallow water shelf was built. When seen from above this element had

[2] http://isec.nacse.org

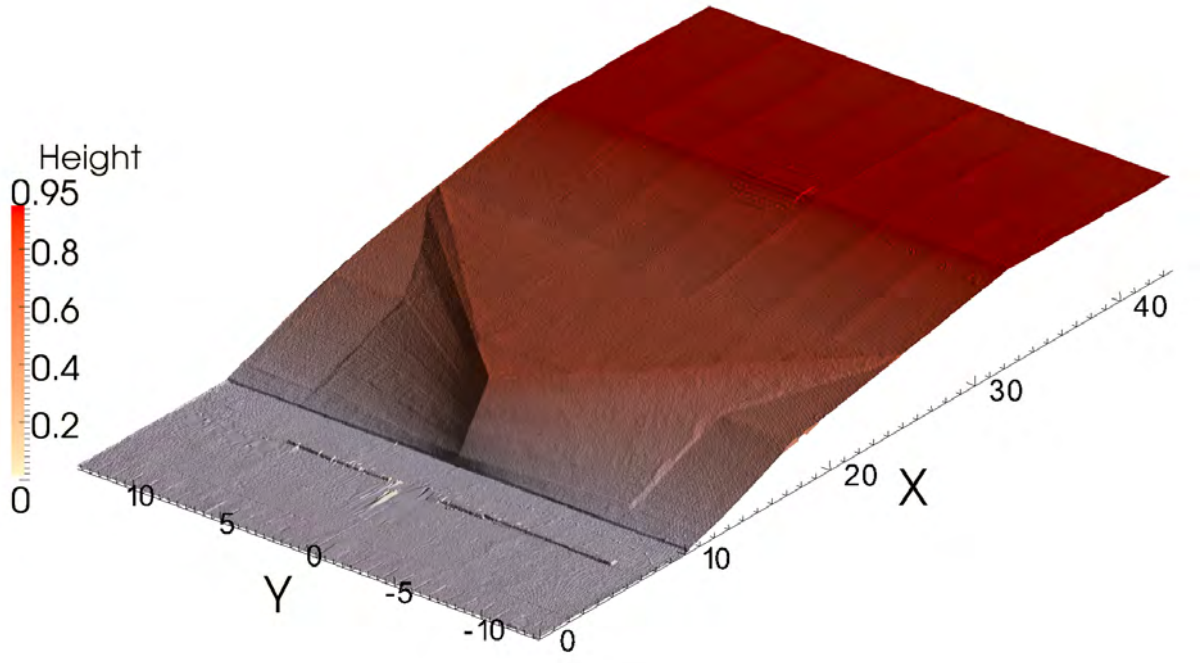

Figure 7.9: Bathymetry of the 3D solitary wave breaking case. The coordinate system is shown (units in metres).

a triangular shape, with its apex located at $x = 12.6$ m. The still water level was set at a depth of 0.78 m during all the experiments, so it intersected the built bathymetry at $x = 25.75$ m. This geometry can be seen in Fig. 7.9, note that the vertical scale has been amplified by a factor of 5.

Three types of measurement instruments were used during the experiments: 14 resistance wire wave gauges (WG) used offshore the shallow water shelf, 5 ultra sonic wave gauges (usWG) used onshore of the shallow water shelf to measure free surface elevation and 11 acoustic Doppler velocimeters (ADV) to measure fluid velocities. Both the WG and usWG were fixed on a bridge, which was moved to provide records in several positions. Data was obtained at a 50 Hz rate.

7.1.3.2 Description of the numerical experiments

The whole experimental facility was replicated numerically for the first test. Although Swigler (2009) stated that the bathymetry was fully symmetric, the one provided from the laser scanning was not, since minor differences existed in the initial horizontal bottom. As a result no symmetry was used in a first test. As stated, the basin is 48.8 m long,

26.5 m wide, and 2.1 m deep. The whole depth was not needed, therefore only 1.2 m in the vertical direction was meshed. Since 43.6 m was the effective length in which the experiment took place, the additional 5 metres were left out. In the end, the simulation results were found almost symmetric, hence for the second test only half of the domain was replicated.

The general discretization of the mesh is 0.10 m in the horizontal directions and 0.06 m in the vertical one. The cells intersected by the bathymetry and their neighbours were subdivided twice (0.025 m x 0.015 m) to obtain better resolution, which in this case will make the inundation of the swash zone easier, and will allow a better definition of the water film attached. Also cells between $z = 0.75$ and 1.2 m (wave propagation range) were refined, obtaining a discretization in that zone equal to 5 cm in the horizontal directions and 3 cm in the vertical one. The final mesh is near 12 million elements.

In the previous case no major differences appeared in the comparison between the performance of $k - \epsilon$ and $k - \omega$ SST. Therefore, for the first test, a Direct Numerical Simulation (DNS)(no turbulence model is considered) is carried out, although the reader must be aware of the fact that the cell discretization used is not fine enough to fully account for the turbulence effects. The reason to consider DNS was to check the influence of turbulence models in 3D wave breaking. Turbulence is modelled using $k - \omega$ SST in the second case, as it seems to work well in the case of swash flows (del Jesus et al., 2012). The second mesh is identical to the first one, but takes advantage of the symmetry by covering just one of the halves of the wave tank, hence having half of the number of cells.

In the simulation a 39 cm hight solitary wave was generated using the new boundary condition in the same way as in the first case. The simulation was parallelized into 36 processors (1.9 GHz). To simulate 15 seconds a total of approximately 7 days were needed. The time steps were very short because Courant number was enforced to be lower than 0.3 and cells in the swash zone were very small. Furthermore, the breaking process produces high velocities.

7.1.3.3 Results

All the available data were used to validate the model, i.e. water elevation at 17 points, 12 from the WG data set and 5 from the usWG. WG data is divided in two transects

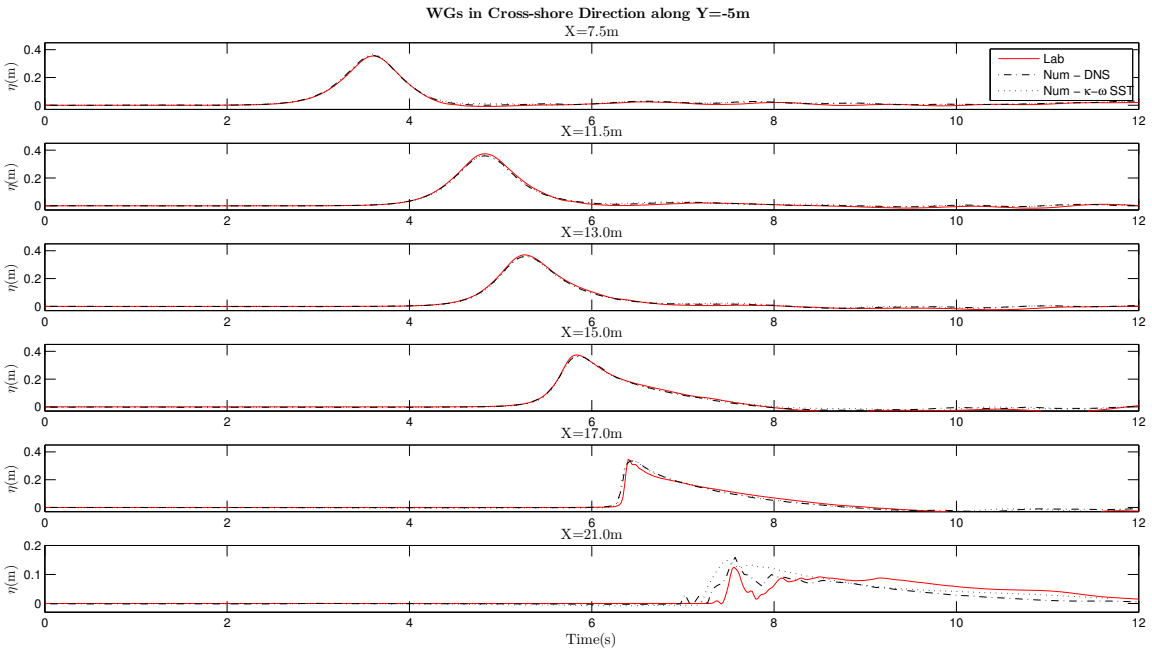

Figure 7.10: 3D solitary wave breaking case. WGs in cross-shore direction along y = -5 m.

along y = 0 m (centre line) and y = -5 m, with x = 7.5, 11.5, 13, 15, 17 and 21 m. This second transect is shown in Fig. 7.10. usWG records are presented in Fig. 7.11. In both figures laboratory and numerical results are plotted using a solid line, dash-dot line (DNS) and a dotted line ($k-\omega$ SST), respectively.

Fig. 7.10 shows very high agreement between the laboratory and the numerical series. This indicates, again, that the wave generation boundary condition is realistic, as the matching is almost perfect for the 4 top panels. As the wave is affected by shoaling and approaches the breaking point (x = 17 m) some differences arise, as the numerical wave front is less abrupt than the experimental one in both cases. Still, wave height is well captured. Once the wave is fully broken (x = 21 m) differences are larger. The free surface is properly replicated for the DNS case, while $k-\omega$ SST turbulence model tends to smooth the solution, increasing the differences with the experiments.

Regarding the longshore transects (Fig. 7.11) it can be seen that results are not as accurate as those from the previous gauges. All of these gauges are placed behind the breaking point, so they measure the shape of the bore. Apparently in the DNS some small disturbances arrive prior to the solitary wave front. Those are droplets of the broken wave that travel sliding on top of the free surface, and are clearly smoothed when

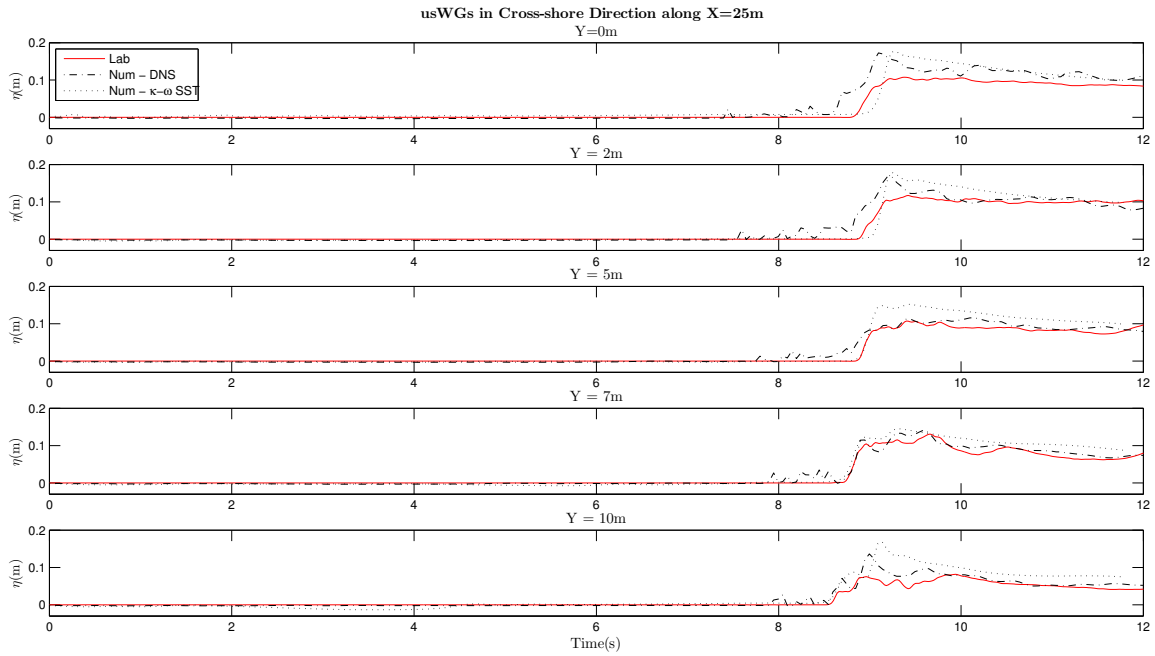

Figure 7.11: 3D solitary wave breaking case. usWGs in longshore direction along $x = 25$ m.

using the turbulence modelling. In the two cases the numerical wave height shows a higher amplitude than expected for the gauges closest to the central line ($y = 0$ and 2 m). DNS makes the bore travel somehow faster, while $k - \omega$ SST delays the arrival. Moving away from the centreline shows a general improvement in timing and height, especially for the DNS, except for the gauge located at $y = 10$ m. Once again the turbulent model solution is smoother, and shows higher differences with respect to the experimental profile.

It would be expected that the turbulent solution should lie below the DNS one, as it involves higher energy dissipation. However, the turbulence model changes the breaking point, which can be inferred from the bore arrival time at each gauge in Fig. 7.11. This change in the breaking point affects the places at which the broken wave bounces, possibly creating these unexpected results due to local effects.

Other issues that can also affect the comparisons are presented as follows. Air entrainment in the bore is one of the processes that may influence the results in two ways. First, a well known problem is that the laboratory results can be affected by uncertainties in the determination of the free surface level because resistive and ultra sonic gauges are not prepared to deal with immersed bubbles. On the top of that, air entrainment in terms of bubbles within the bore is not modelled in **IHFOAM** either. Another factor is that cells

are relatively large, so surface tension effects are not accurately represented. As a result, there is no generation of finger jets. Increasing the resolution will address this issue, as presented in Watanabe et al. (2005).

Snapshots of the evolution of free surface are presented in Fig. 7.12, starting at the time when the solitary wave is shoaling and right before breaking ($t = 6.15$ s). The evolution of the breaking wave, showing the three dimensional structures can clearly be seen (from $t = 7.75$ s). The last two panels in the bottom show the inundation of the slope. The formation of surface ripples, caused by the irregular bottom, is remarkable.

7.1.4 Rip current on a barred beach

The morphology of a beach is the dominant factor that controls wave breaking and the generation of water recirculating patterns. Transverse bar and rip is the morphological state in which the rip is clearly visible and with the strongest undertow current development. This is the case reproduced here, in which undertow and wave-current interaction are studied.

7.1.4.1 Description of the physical experiments

The physical modelling is included in Dronen et al. (2002). The experiments were carried out at ISVA's laboratory, in which the wave tank is 30 m long and 4 m wide. A bathymetry consisting of a bar with a rip channel was constructed. A sketch of the geometry can be seen in Fig. 7.13. An initial part with a horizontal bottom spanned until $x = 6$ m. Then the bar was placed on a plane with 1:27 slope, which continued until $x = 12.4$ m. The bar crest was 0.13 m high, 4.8 m long and 3 m wide, leaving a 1 m wide rip channel. Right before the final 1:17 planar beach (which started at $x = 14.3$ m), a 1.9 m horizontal section was built to act as the bar trough.

Several types of waves were generated, regular waves ranging from 6 to 20 cm in height and from 1 to 2 s in period. Irregular waves ranged 6 to 18 cm in H_{rms} and 1 to 2 s in peak period. Water depth varied from 5 to 15 cm at the highest point of the bar crest. In all of the experiments, at least 50 waves were generated prior to data acquisition in order to measure only once the steady state had developed. Free surface elevation, velocity and particle tracking were recorded.

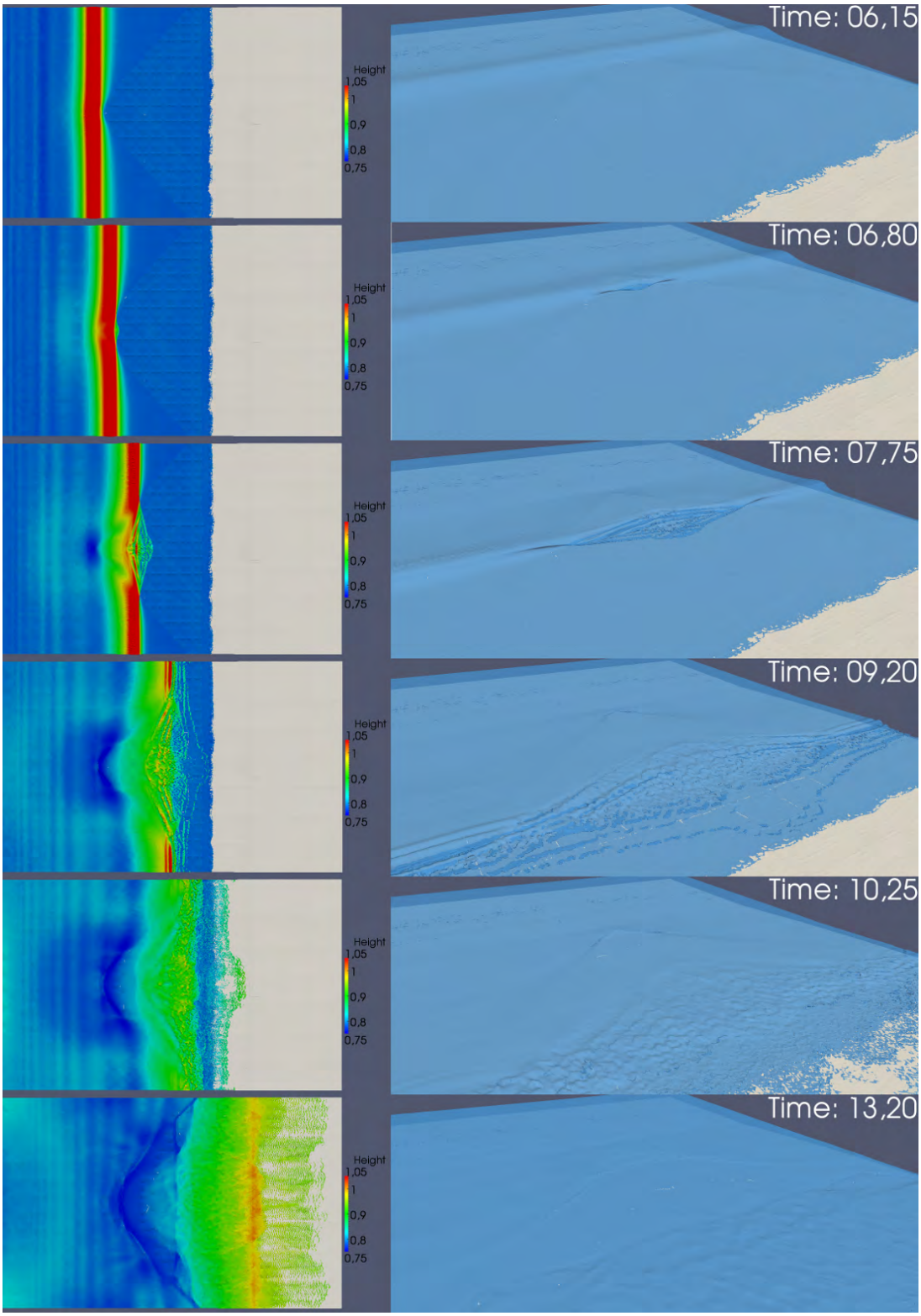

Figure 7.12: 3D solitary wave breaking case. Free surface evolution (DNS). Height in metres.

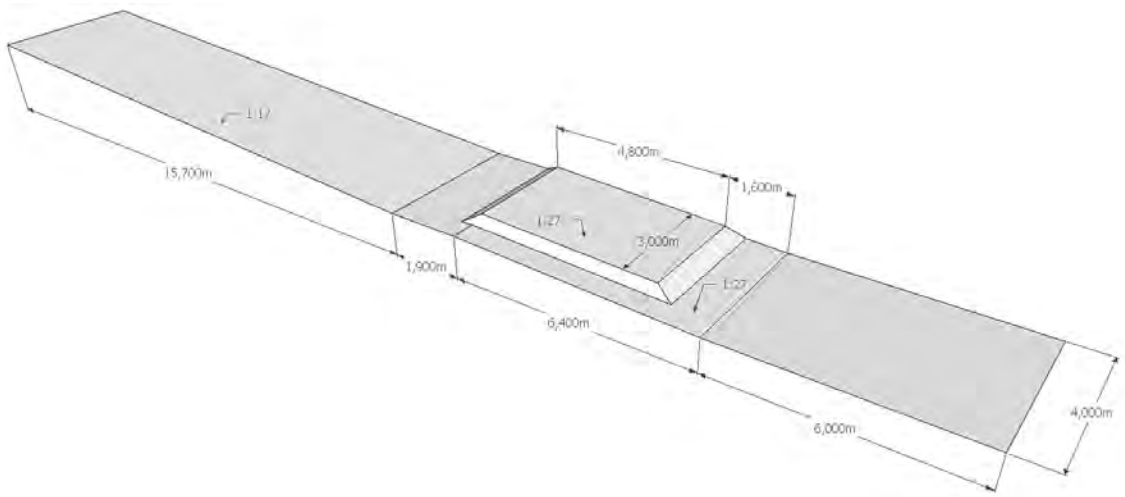

Figure 7.13: Rip current on a barred beach. Bathymetry reconstructed from the original data. Dimensions in metres.

7.1.4.2 Description of the numerical experiments

The mesh reproduces the complete domain: 30 m long, 4 m wide and 1.2 m high. The initial discretization is 10 cm in the horizontal directions and 4.8 cm in the vertical one. After the mesh is intersected by the bathymetry the cut cells are refined only once, since no run-up study is intended. The resolution in the bottom is, then, equal to 5 cm in the horizontal directions and 2.4 cm in the other one. The cells from 15 cm below and above the still water level are refined twice, resulting in 2.5 cm of horizontal resolution and 1.2 cm in the vertical one. This distance has been chosen to refine even the trough of the bar, and to account for shoaling effects, the expected increase in wave height experienced by the wave-current interaction and the increase in the mean level due to the nearshore set-up. It also refines the efficient swash zone of the final beach.

Since velocity measurements near the lateral walls are to be recorded and the resolution close to them is not sufficient to represent the boundary layer, the walls and the bottom have been modelled using a free slip boundary condition. The final mesh totals 3.1 million cells. A total of 90 seconds were simulated, which corresponds to 60 wave periods. Using 24 cores (2.6 GHz) almost 20 seconds were simulated per day.

The simulated case presents a regular wave train of $H = 15$ cm and $T = 1.5$ s, with 5 cm of still water depth at the highest point of the bar. This allows waves to be discretized by more than 12 cells in height. Waves were generated using Stokes II wave theory

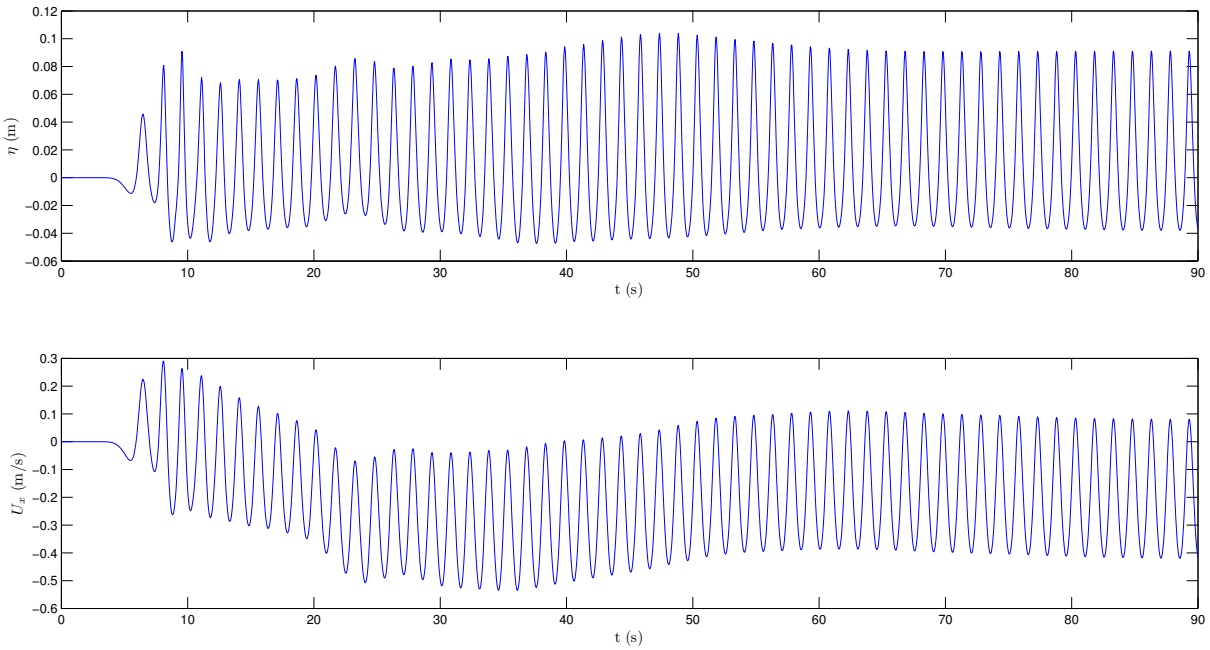

Figure 7.14: Rip current on a barred beach. Evolution of the free surface elevation (top panel) and cross-shore velocity at 1/3 of the water depth from the bottom (bottom panel), within the rip channel ($X = 10$ m, $Y = 3.5$ m).

with active wave absorption connected, without which this simulation could not be so accurate. It makes the whole boundary to behave as a single wavemaker, generating the target waves, ensuring at the same time that reflected energy flows out and that the free surface level does not rise.

Wave breaking starts once the waves reach the bar, so it is a major driving factor. Another very important dynamic to account for is inundation of the swash zone, which influences the nearshore circulation patterns. This makes the boundary region a very important part of the simulation. Therefore, turbulence was decided to be modelled using $k - \omega$ SST.

7.1.4.3 Results

Fig. 7.14 presents the free surface (top panel) and the cross-shore velocity evolution (bottom panel) of a point within the rip channel. This point is located at the middle of the rip, in both horizontal directions ($x = 10$ m, $y = 3.5$ m, see Fig. 7.16). Until $t = 25$ s, the water level rises as the wave set-up develops. From that point, the waves start to change due to the interaction with the opposing undertow current, which at that moment reaches its maximum value. The immediate result is that the waves increase in height.

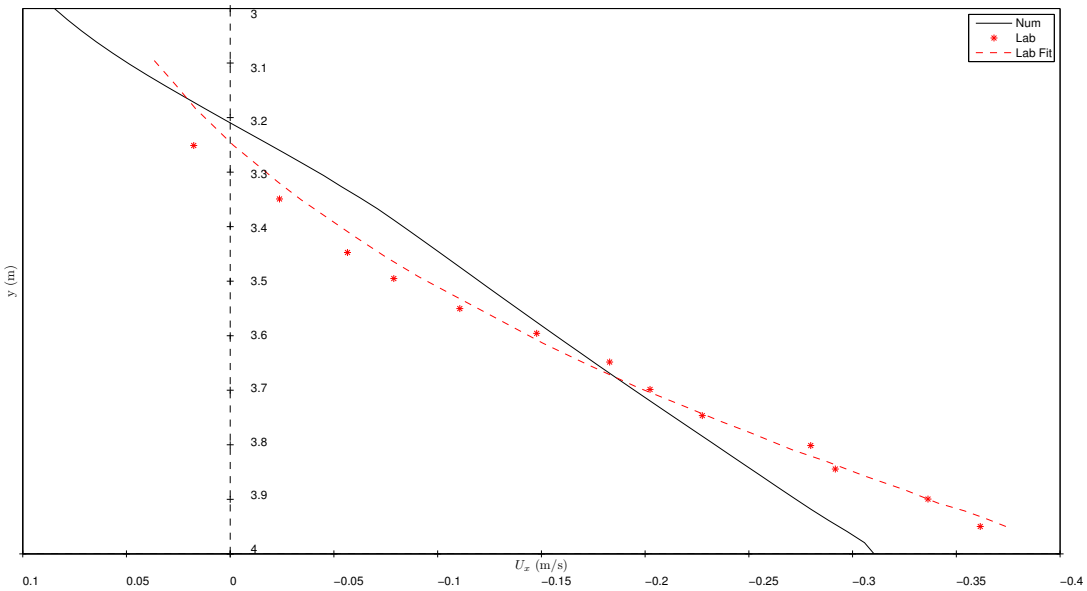

Figure 7.15: Rip current on a barred beach. Cross-shore velocity as function of long-shore positions at $x = 11.40$ m, at 1/3 of the depth from the bed.

The stationary state is approximately reached at $t = 60$ s, with a decrease in current magnitude and wave height. After that moment, 30 more seconds are simulated in order to obtain the results as the mean value over 20 waves. Such stationary state is achieved so early because of the linked wave generation and active wave absorption, otherwise the water level and the energetic level of the system would continue increasing.

In Fig. 7.15 the cross shore velocity in the rip channel as a function of long-shore positions at $x = 11.40$ m and 1/3 depth from the bed are represented, comparing them with the experimental results in Dronen et al. (2002). The asterisks represent measured data, and the dashed line is the best fit proposed by Dronen. The continuous line represents the numerical data. **IHFOAM** models correctly the velocity pattern within the cross section of the rip. The numerical shape is more or less linear, which contrasts with the apparent parabolic shape of the laboratory measurements. However, the results are close as only differences of at most 5 cm/s appear (15% relative error).

Fig. 7.16 presents the depth-averaged velocity on a regular grid. Although the wave conditions for this case and the presented magnitudes are different, this figure can be compared qualitatively with Fig. 4 in Dronen et al. (2002). In this case the upgrade of the resolution helps to visualize the water circulation pattern. The most intense currents do not appear within the rip channel, but in its vicinity, where water is taken from. The

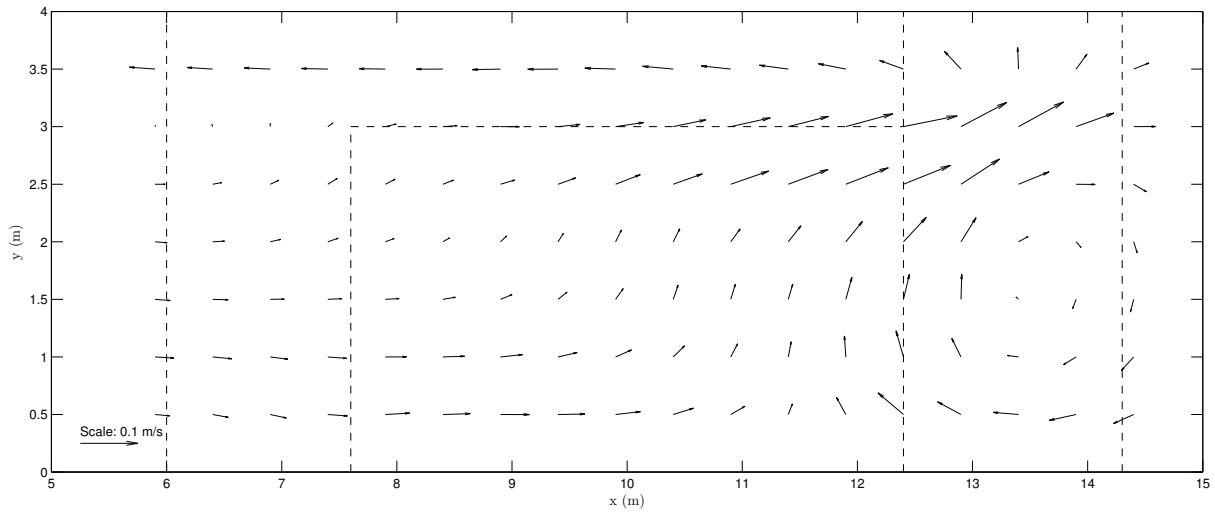

Figure 7.16: Rip current on a barred beach. Depth-averaged currents. Waves come from the left.

main circulation pattern is formed, as expected, by the onshore current along the bar crest and the offshore current in the rip. There is also a secondary circulation which happens at the bar trough, where water flows from the rip to the bar in the section close to the shoreline and in the opposite direction near the bar crest. This double circulation has been described in the literature, including Haller et al. (2002), Yu and Slinn (2003), Calvete et al. (2005) or Garnier et al. (2008), with topographically generated rip currents.

The evolution of the free surface and particle velocities along a wave period, showing the cross-shore velocity component on it, is presented in Fig. 7.17. The bar is represented as a rectangle. The top and bottom panels correspond to the same situation, as they are separated a full wave period (1.5 seconds). It can be noted that the largest negative velocities appear at the wave troughs within the rip channel.

The progress of the rip channel velocities from an early stage until the end of the simulation can be seen in Fig. 7.18. The change in wave shape due to the interaction with the current is clear, as waves show a higher steepness. Also the three dimensional evolution in the distribution of velocities can be noted, as current is stronger near the tank wall.

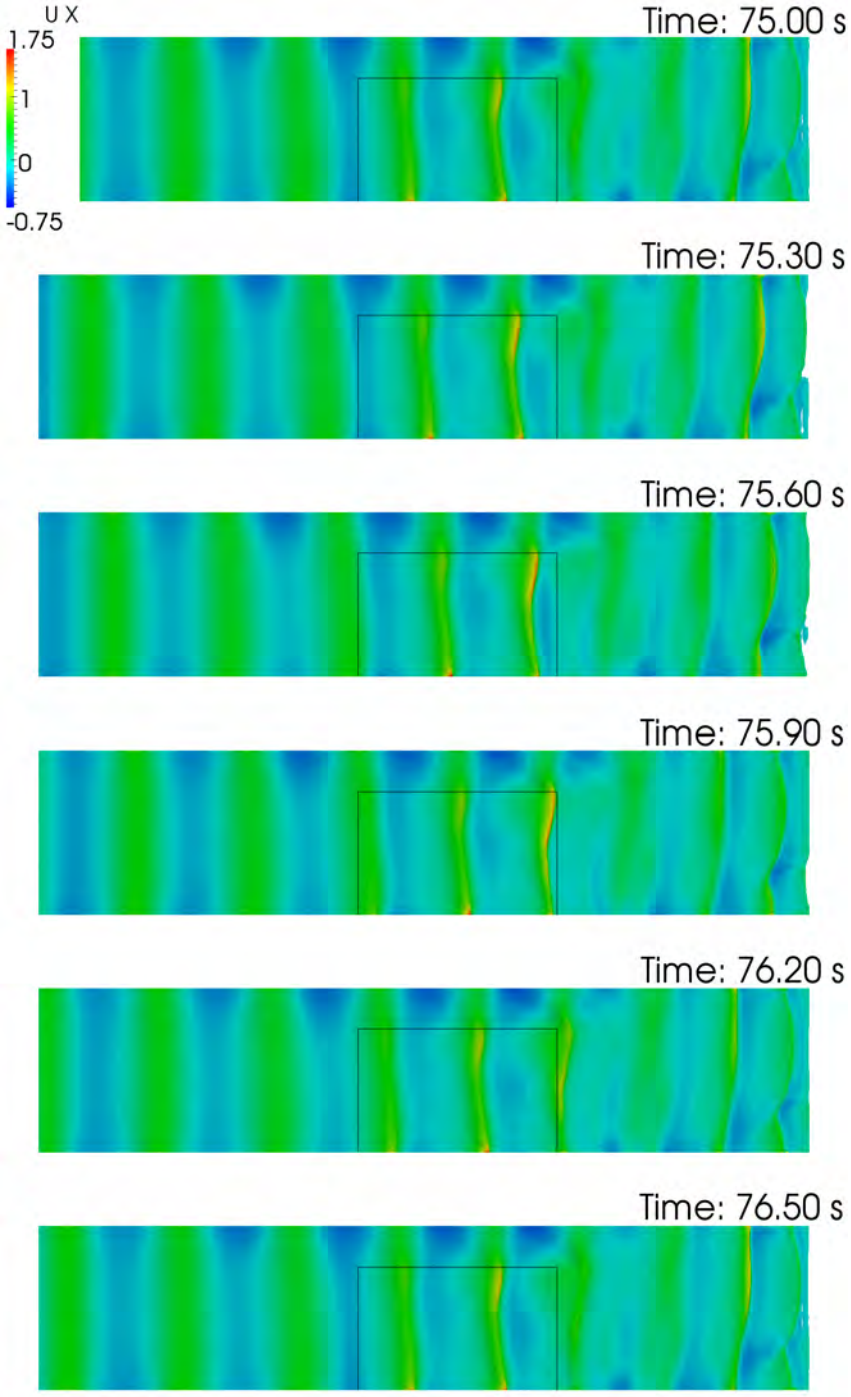

Figure 7.17: Rip current on a barred beach. Instantaneous cross-shore component of the velocity on the free surface. Units in m/s.

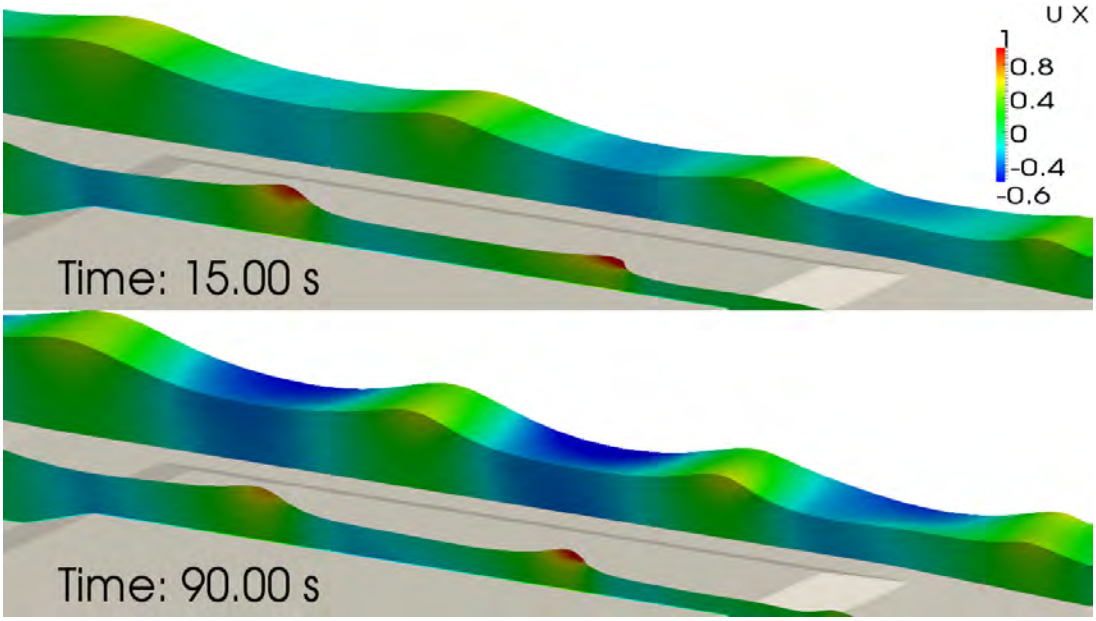

Figure 7.18: Rip current on a barred beach. Cross-shore velocity in a transect over the bar and within the rip channel. Units in m/s.

7.1.5 Run-up on a conical island

Wave run-up has always been a key parameter to calculate or to model in order to control the effect on structures that are built very near to the shoreline. Nowadays its importance has increased dramatically due to the devastation of recent tsunami events. A model which can simulate accurately run-up from a solitary wave can aid to design coastal structures such as seawalls, capable of reducing the damage in case of a tsunami. Another very important magnitude than can be evaluated using RANS models is shear stress, that indicates the dragging force produced by the waves and can be used to evaluate sediment transport and erosion. Here a highly 3D run-up pattern is induced by an initially 2D wave, in the absence of wave breaking.

7.1.5.1 Description of the physical experiments

This case is broadly used in literature to validate Boussinesq type models, as presented in Chen et al. (2000) or Tonelli and Petti (2010). The results of the experiment are included in Liu et al. (1995), but the physical experimental work was performed by Briggs et al. (1995). All the data can be accessed online at the NOAA Centre for Tsunami

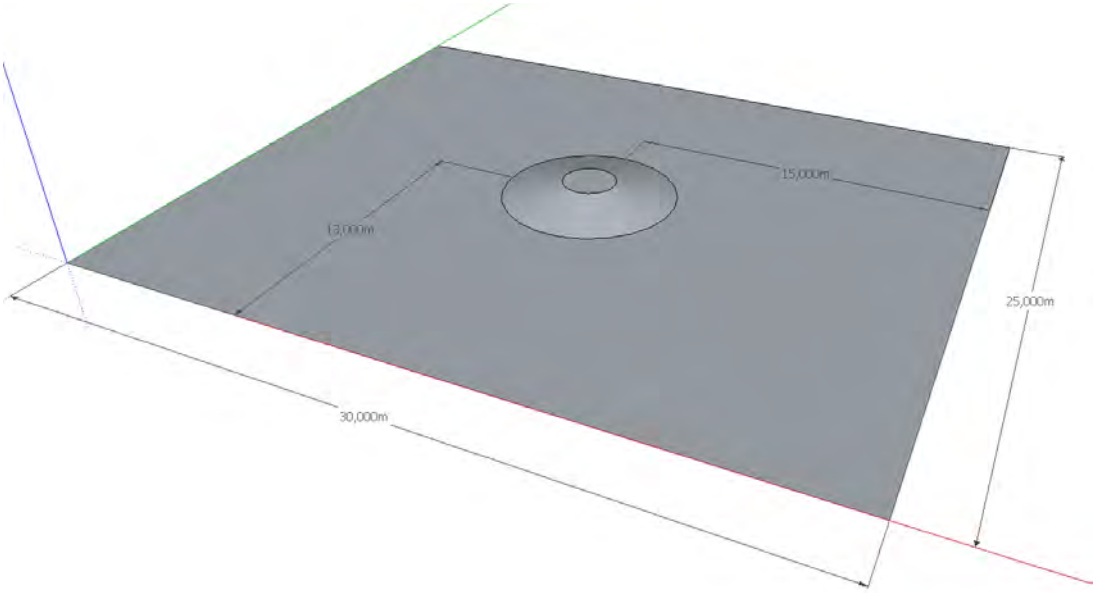

(a)

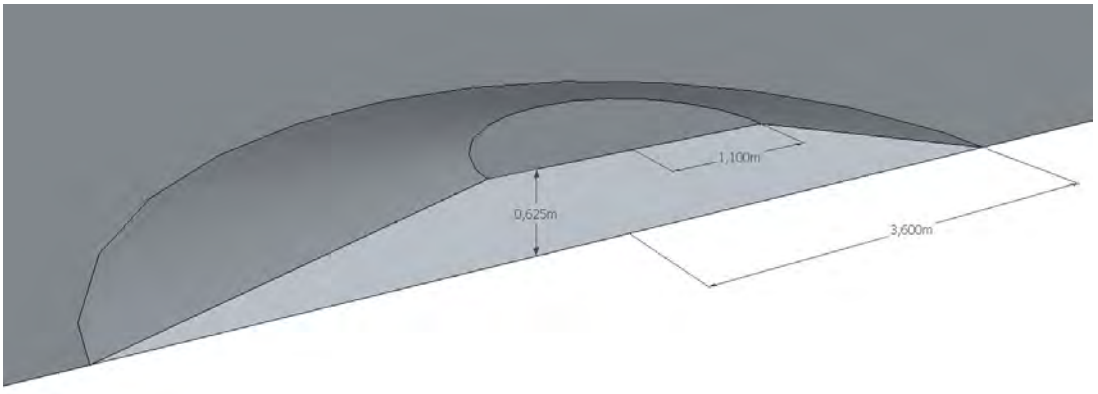

(b)

Figure 7.19: Run-up on a conical island: laboratory geometry (Briggs et al., 1995). (a) General view. (b) Section of the island.

Research web site[3], as it is part of a benchmark case.

Experiments were performed in a wave basin at the US Army Engineer Waterways Experiment Station, Coastal Engineering Research Center. The wave tank was 30 m wide and 25 m long. The island built inside was a frustum of a cone, with a bottom radius of 3.60 m and a slope of 1:4. Its center was located at $x = 15$ m, $y = 13$ m. The surface of the island and the floor of the basin were made of smooth concrete. The geometry of this case can be seen in Fig. 7.19.

[3] http://nctr.pmel.noaa.gov/benchmark/Laboratory/Laboratory_ConicalIsland/index.html

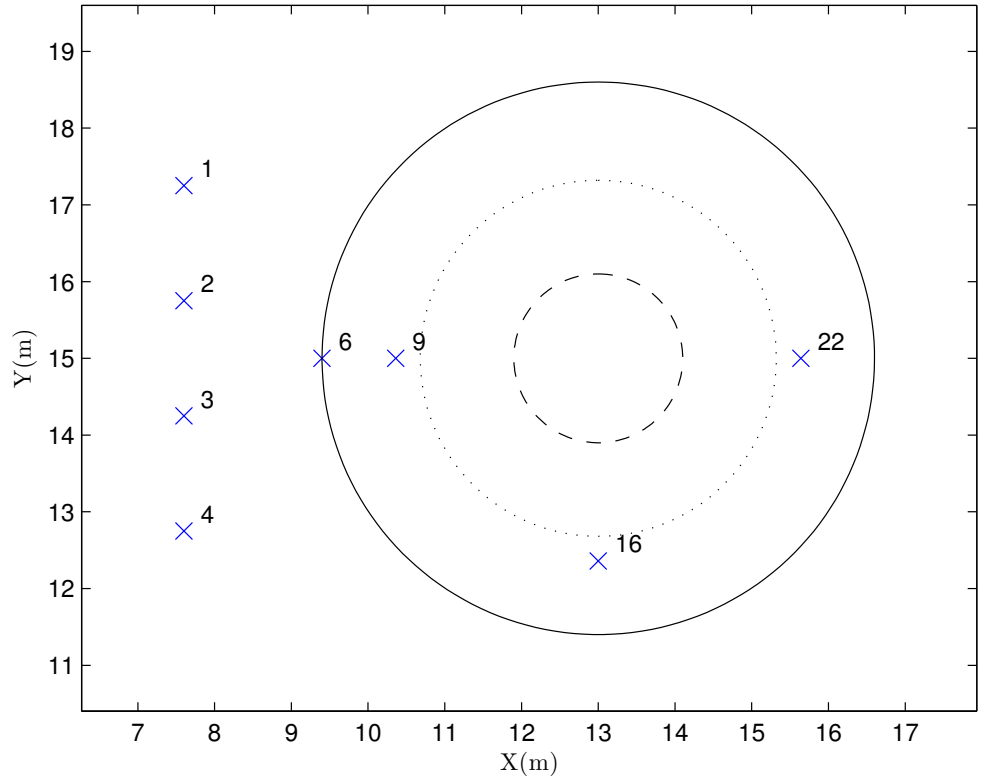

Figure 7.20: Run-up on a conical island: free surface gauges. Note that wave generation occurs in plane $Y = 0$, therefore, waves come from the left according to this figure.

The wavemaker was located at $y = 0$. Its total span was 27.43 m and it had 60 individual paddles. In this case all of them moved in phase to produce solitary waves. Two water depths were considered during the experiments: 0.32 m and 0.42 m. Three different solitary wave heights were tested in the case when the water depth was 0.32 m. In terms of wave nonlinearity, defined as wave height over water depth ($\epsilon = \frac{H}{h}$), the target values were $\epsilon = 0.05$, 0.1 and 0.2.

A total of 27 capacitive free surface gauges were placed inside the basin with a symmetric layout. Only gauges 1 to 4, 6, 9, 16 and 22 were available in the benchmark data. The position of these gauges is presented in Fig. 7.20. The data series are 60 seconds long, and include several reflections of the solitary wave at the walls of the tank.

Also 24 radial transects to the island are available to evaluate the run-up, but they were not evenly spaced. Sixteen were equally spaced every 22.5° around the perimeter. Then four radial transects with uneven spacing were located on the back side of the island to increase the resolution at that critical location where the two parts of the wave collide. The run-up experimental data can be seen in Fig. 7.22, as black dots.

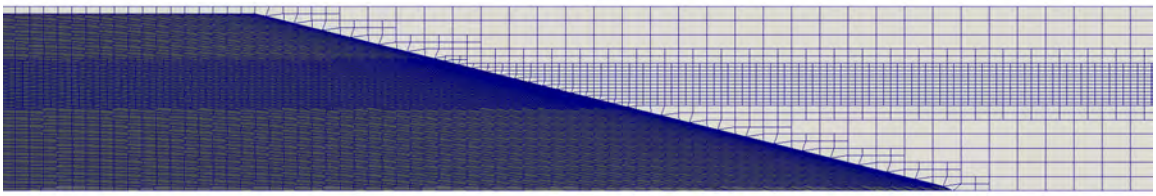

Figure 7.21: Conical island mesh seen from the symmetry plane. Note the base resolution, how it is refined once near the conical island, and twice covering the free surface variation area.

7.1.5.2 Description of the numerical experiments

Two numerical simulations for this case have been prepared. In order to save computational cost, and since the domain is fully symmetric, only half of the domain has been simulated. The mesh is 15 m in the X direction, 25 m in the Y direction and 0.65 m in the Z direction. This configuration guarantees 1 cell between the top of the island and the atmosphere. The basic mesh covers the mentioned domain with a discretization of 10 cm on the horizontal directions and 5 cm on the vertical one. From this orthogonal and structured mesh the island is removed using *snappyHexMesh*. Those cells intersected by the bathymetry get refined once. So do the cells between levels $z = 0.30$ m and 0.40 m, to increase the resolution near the free surface where the wave propagates. These cells (which also cover the effective swash zone) are refined twice to fulfil an adequate vertical representation of the solitary wave, which is very small in this experiment. The final mesh has nearly 8 million cells, and is presented in Fig. 7.21. The case was subdivided in 24 domains using scotch method, and the whole 15 second simulation finished in around 3 days with 2.6 GHz processors.

The case with the highest wave height was chosen, but the real wave height generated by the wavemaker was lower than the target value. Steepness equal 0.18 is used, because it is the experimental result. This yields a wave height of 0.058 m. Both turbulence models $k - \epsilon$ and $k - \omega$ SST were tested. In this case wave breaking is not present, so the comparison of performance is focused towards the inundation behaviour. Courant number was set to 0.3, and since the wave did not break the simulation showed a good evolution, with not too small time steps.

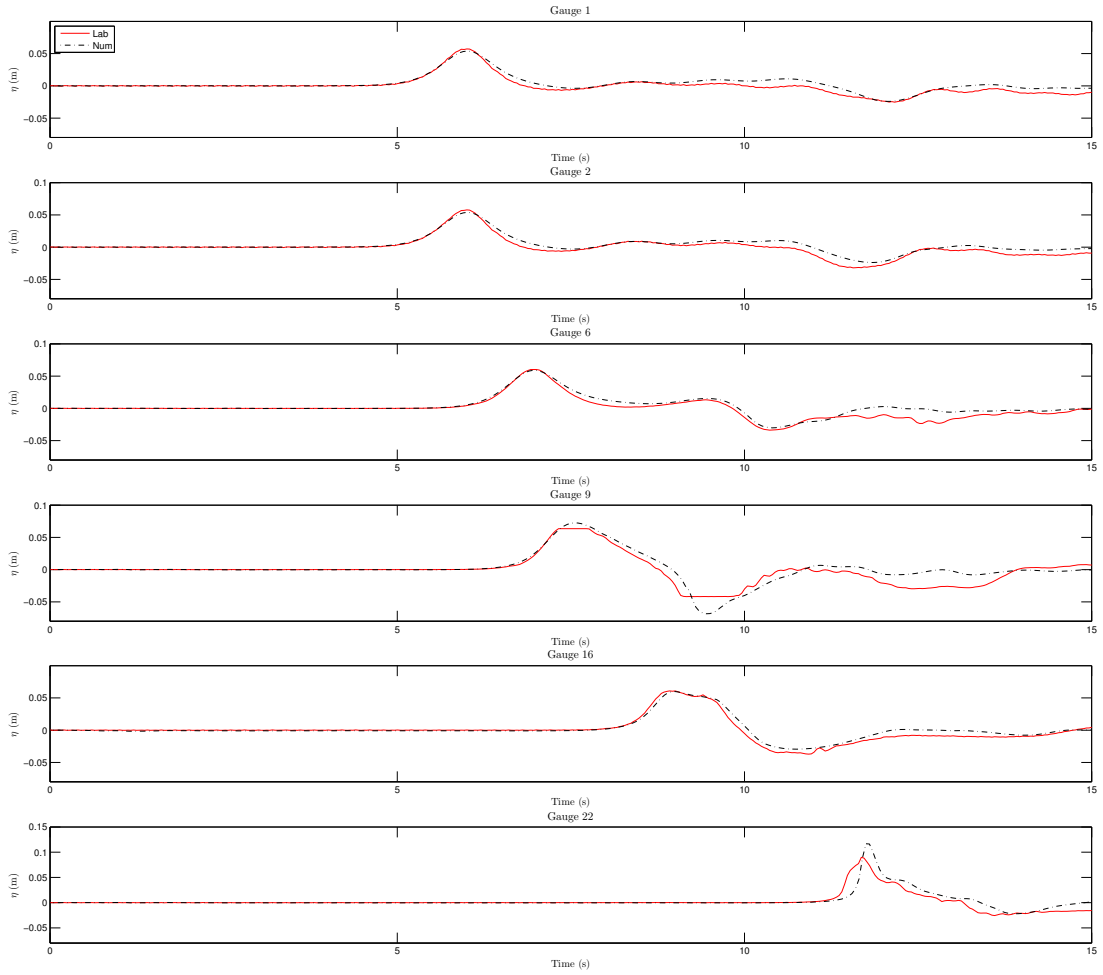

Figure 7.22: Free surface gauges on the conical island. The continuous line is the laboratory measurement and the dash-dot line is the numerical result for the $k-\omega$ SST case.

7.1.5.3 Results

The results from the free surface gauges are presented in Fig. 7.22. Sensors 3 and 4 are not represented because their location is symmetrical to 1 and 2. Only the results from the $k-\omega$ SST case are presented, because $k-\epsilon$ produces the same results, no difference can be observed due to the absence of relevant turbulent effects at the location of the free surface gauges.

From the first two free surface gauges the quality of the generated wave can be checked. The solitary wave is highly accurate in height, with an absolute difference in height of barely 3 mm (5% error). The shape of the wave is slightly different as the numerical wave decays less abruptly. This influences the reflected wave, which is smaller and can be noticed around $t = 12$ s. At the gauge number 6, which is located at the toe of the

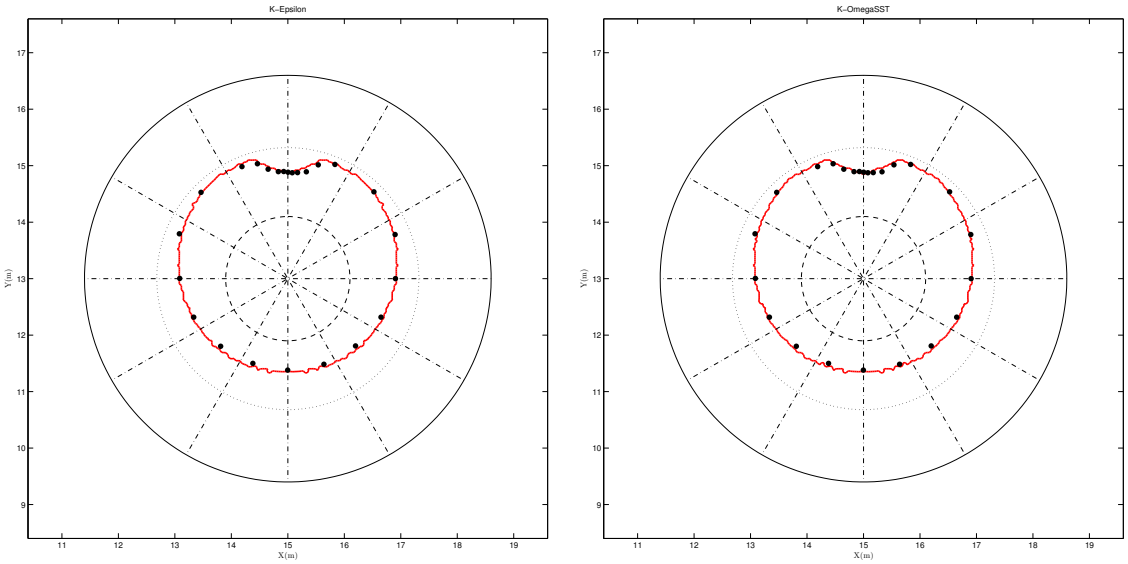

(a) (b)

Figure 7.23: Run-up on a conical island. Run-up results. The continuous bold line is the numerical result and the dots are the laboratory measurements. (a) $k-\epsilon$ turbulence model. (b) $k-\omega$ SST turbulence model.

island, and therefore is still not affected by shoaling, the wave height continues to be well captured and reflection is smaller again. The laboratory data of gauge number 9 presents some anomalies in the maximum and minimum values of the measurements, as if the wave gauge had reached its physical limits. The minimum value could happen if water level dropped more than 8 cm, but this is not the case. The gauge number 16 shows a high degree of accordance, while the higher water level due to the reflection is still present. The last gauge (number 22) exhibits the highest discordance between signals, as the numerical wave reaches the location late, in a more abrupt way and with a higher height. However, these discrepancies are not observed in the run-up, as explained later.

The maximum run-up line is plotted in Fig. 7.23 along with the laboratory discrete data. The numerical run-up is shown in continuous bold line and has been evaluated by checking the values of the VOF function within all the owner cells of the faces which constitute the conical island. A threshold value of 0.1 has been used to consider a cell as inundated. Surrounding it, the experimental data are presented as dots. The large circle represents the base of the conical island; the medium circle in dotted line is the initial water level and the smallest circle in dashed line is the top of the island. Radial auxiliary dash-dot lines are plotted every 30°.

Both turbulence models produce virtually the same result. This behaviour is as expected, because turbulence does not play a relevant role in this case since there is no wave breaking. The results are within 3 cm of the absolute error from the real measurements in the horizontal direction.

In Fig. 7.24 the evolution of shear stress on the bottom of the conical island is presented as a potential result to be studied in the future. This magnitude is important because it serves as an indicator of the erosion power of the wave. For each of the panels, the left semicircle presents $k-\omega$ SST results and the right one $k-\epsilon$. Differences are minimal between them. However, for $t = 9.70$ s and $t = 11.45$ s there is a different pattern on the swash zone due to a different disposition of small water droplets attached to it. The general behaviour shows that the largest shear stresses appear when water is retreating (compare $t = 7.90$ s vs $t = 9.15$ s), and when the wave advances in the lateral part of the island ($t = 9.70$ s).

7.1.6 Conclusions

The cases presented in this section show a physically correct behaviour. A high degree of agreement is obtained between the experimental and numerical results. Hence, it can be concluded that the wave generation boundary conditions developed present a realistic behaviour, and are capable of replicating all kinds of waves. Furthermore the model succeeds in reproducing the surf zone hydrodynamic processes tested in a very accurate manner.

The dynamic pressure results are as accurate as the free surface ones. This is important, especially in this case in which large eddies develop and influence pressures along the faces of the obstacle and down to the bottom.

Wave breaking is also correctly modelled. First in 2D, where the wave gauges results show an outstanding agreement, which involves that the energy transfer to the low frequency wave is very well replicated. Taking the air phase into account, and having a smooth and very refined bathymetry also helps to obtain better results than in the original paper (Lara et al., 2011).

As with regards the three dimensional plunging breaker simulation, the difficulty arises in the fact that it is highly influenced by turbulence and surface tension effects. For the

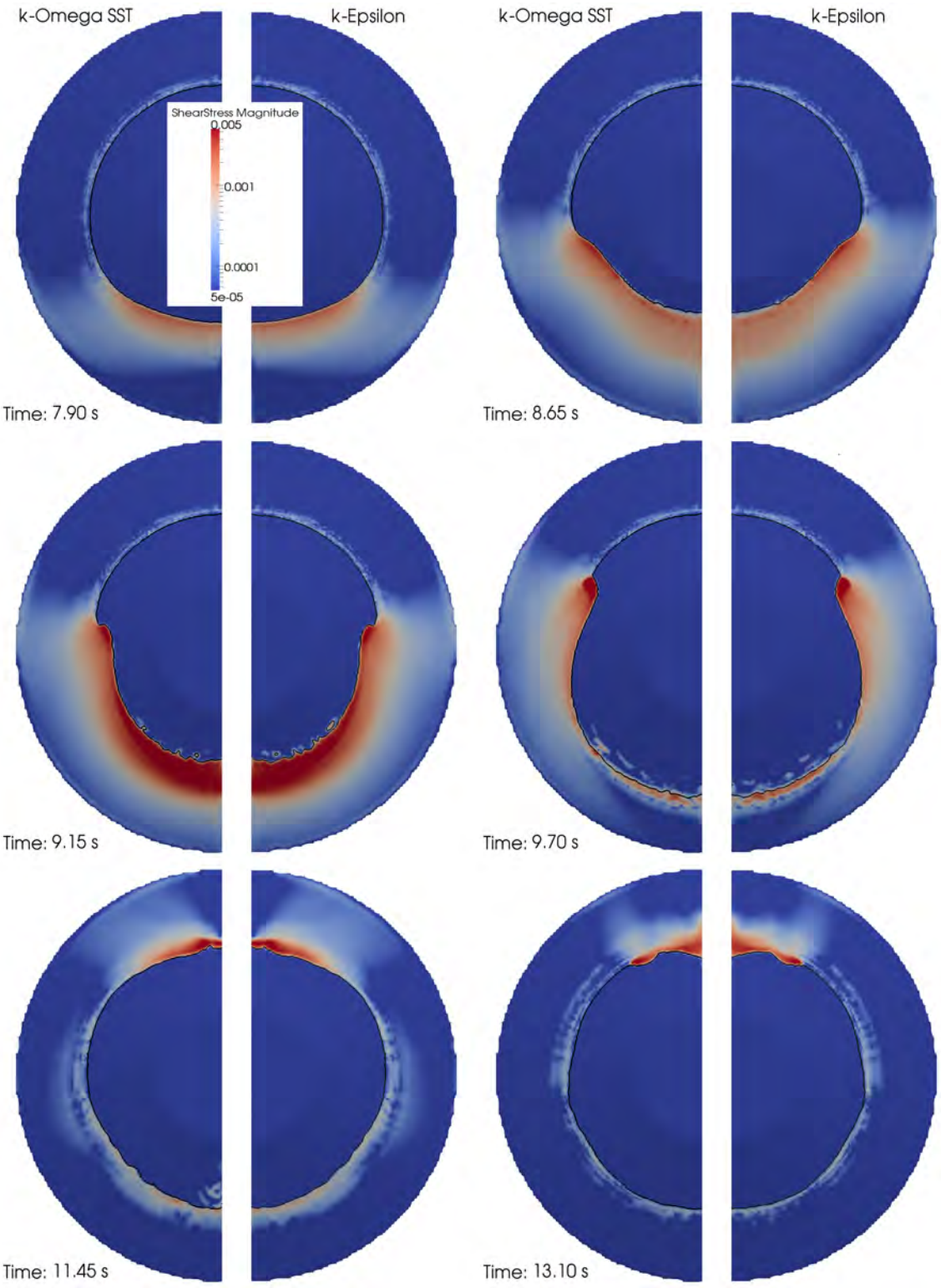

Figure 7.24: Run-up on a conical island. Shear stress (units in Pa) on the island.

current resolution the general performance is more than acceptable, but probably having smaller cells within DNS could improve the results, as presented in Lubin et al. (2003). Nevertheless, the breaking process generates three-dimensional structures, as expected.

The rip channel case proves again that **IHFOAM** can handle long time simulations, that are perfectly stable and do not suffer from an increasing mean water level. When waves break, the set-up appears. This accumulation of water causes an unbalanced distribution of the mean water level, which tends to be levelled by generating currents. The distribution of currents is coherent with what is observed empirically. The rip developed shows an undertow close to the experimental data, which is a promising result. The use of RANS models with **IHFOAM** is a very powerful approach to study all the detailed phenomena, as numerical probes can be placed anywhere without perturbing the flow, and may shed some light to finally discover why the secondary circulation appears.

Finally, wave run-up has also been correctly modelled. Similar or even better results are obtained with OpenFOAM®, compared to those presented in Chen et al. (2000) or Tonelli and Petti (2010) with other modelling techniques. The shear stresses on the conical island show a coherent distribution, and negligible differences between both turbulence models tested. The results are promising, but further analysis has to be carried out in the future.

7.2 Flow through porous media

The porous media closure model presented in Section 4.4 represents the linear and nonlinear drag forces induced by the porous obstacles as a value depending on the material characteristics (porosity and mean diameter) and on several calibration parameters (α and β). Calibration is needed to ensure that the porous media model is accurate and behaves in accordance with the underlying physics. Hence, a correct calibration is the first step towards validation.

The porous model also depends on another variable, C. However, the variation in the magnitude of C has proven to be of little importance in most of the cases (del Jesus, 2011). Therefore, according to recommendations and previous experience, a value of $C = 0.34$ is considered by default in this work.

In this section the new implementation of the VARANS equations for **IHFOAM** is validated against laboratory measurements. First, a sensitivity analysis of the porous parameters is carried out replicating the well-known Lin (1998) dam break experiments. The model is validated next in 2D under oscillatory flow in a wave flume, simulating the interaction of regular waves with a high mound breakwater from Guanche et al. (2009). Finally, the validation is extended to 3D wave interaction with a porous obstacle within a wave tank, as presented in Lara et al. (2012).

7.2.1 Two-dimensional porous dam break

These experiments carried out by Lin (1998) have been used as benchmark cases for numerical models featuring flow through porous media. Their simple setup and wide range of conditions make them especially suitable for these purposes.

7.2.1.1 Physical experiments

Lin (1998) tested a dam break flow through different porous materials. The experiments were performed inside a glass tank (considering an idealized 2D behaviour: 89 cm horizontally and 58 cm vertically), permitting the use of video recording techniques to obtain the free surface elevation all along the domain: inside and outside the porous medium.

Two different materials and three water heights were tested. The experimental setup was always the same, regardless of the porous medium type or water level tested. The main water body was confined on the left side of the domain, separated from the porous medium by a moving gate. This initial region spanned 30 cm in the horizontal direction. Right next to the water reservoir the porous medium extended for 29 cm. Finally, there was another clear flow zone between the porous medium and the end wall, spanning 30 cm. A base level of water of around 2.5 cm was set all over the tank bottom, outside the reservoir. A sketch of the initial state can be found in Fig. 7.25.

Two different porous materials were tested: crushed rocks and glass beads, to account for different material properties and flow regimes. The flow through the glass beads (GB from now on, $D_{50} = 0.3$ cm and $\phi = 0.39$) included two water elevations (15 and 25 cm) and was found to be laminar, and closer to a Darcy flow (del Jesus et al., 2012). However,

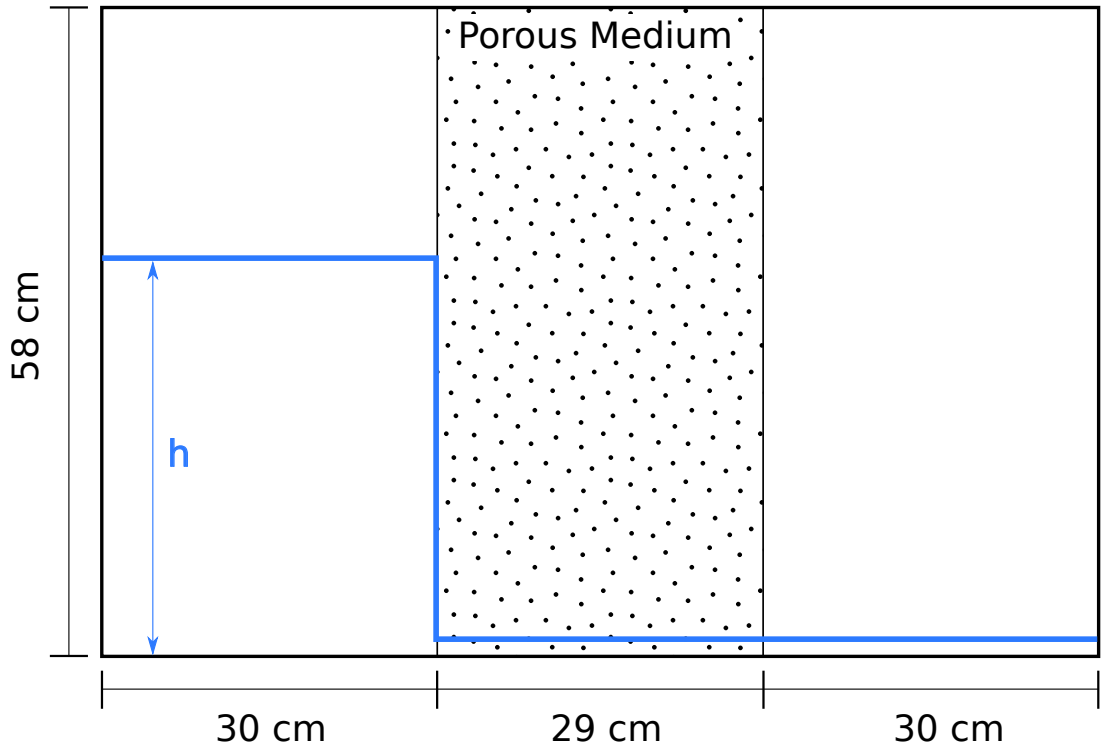

Figure 7.25: Sketch of the setup for Lin (1998) dam break experiments.

the flow through the crushed rocks (CR from now on, $D_{50} = 1.59$ cm and $\phi = 0.49$) was fully turbulent for water levels 15 and 35 cm, as velocities and pore size are greater.

The starting point of the experiments was the raising of the separation gate between the water and the porous medium.

7.2.1.2 Numerical experiments

The whole tank has been reproduced numerically in 2D. The cell size has been kept constant and equal to 5 mm throughout the domain. The mesh has 20,648 cubic cells and is structured, orthogonal and conformal.

The four cases presented in Lin (1998) have been reproduced: crushed rocks (CR15 and CR35) and glass beads (GB15 and GB25). With this set of simulations an extended range of flow regimes that can appear in coastal engineering are covered. On the one hand, turbulent flow (represented by CR35) appears very often, as wave breaking is most of the times a turbulent process. Furthermore, the crushed rocks material is closer to the ones found in rubble mound breakwaters. On the other hand, laminar flows (represented by GB15), close to Darcy's regime, can be found inside the breakwater cores, where velocities

Material	α
CR	[0, 50, 100, 500, 1000, 2000, 5000, 10000]
GB	[50, 100, 150, 200, 250, 300, 400, 500, 600, 1000]

Material	β
CR	[0.5, 1.1, 1.5, 2.0, 2.5, 3.0]
GB	[0.0, 0.1, 0.2, 0.3, 0.4, 0.5, 0.6, 1.0]

Table 7.1: Friction parameters of the sensitivity analysis.

are low enough. Transitional flows such as GB25 and CR15 complete the range.

The simulations start from rest, with the water and porous medium set at their initial location. Since there is no possibility to represent the raising of the gate that confines the water, no physical separation has been considered between the reservoir and the porous medium.

A number of α and β parameters have been considered as a way to validate the model choosing those with best performance and to carry out a sensitivity analysis. The value range for the friction factors is different depending on the material, therefore, the tested values are gathered in Table 7.1.

All the combinations between α and β have been simulated three times, as for each of the four base cases the turbulence has been taken into account using: Direct Numerical Simulation (DNS), $k-\epsilon$ and $k-\omega$ SST. Although the first simulation is called a DNS, since no turbulence model has been applied, it must be noted that the resolution is not fine enough to solve the whole scales of turbulence.

Each case has been simulated a total of 4 seconds, and the average case took less than 10 minutes to run in a single 2.5 GHz processor.

7.2.1.3 Results

Since the number of simulations is quite high (48 for each level of CR, and 80 for each case of GB, all of them for three turbulence models considered, totalling 768 simulations) the work process has been automatized following a methodology:

- Create the mesh.
- Set the porous media parameters and initialize the water level.

- Simulate the case.
- Obtain the free surface elevation.
- Calculate the errors.
- Assess the quality of the solution.

Three different error indicators are calculated based on the absolute value of the difference in free surface elevation between the physical experiment and the numerical simulation along the whole tank at an instant.

The results will depend highly in the time at which the errors are computed. If the calculation is fulfilled very early in the simulation, the expected differences are high due to the already mentioned issue with the gate separating the water and the porous medium. Similarly, if the comparison is carried out too late, the errors will be close to zero, as the system tends to equilibrium. A time between both bounds has been chosen, ranging from $t = 1.15 - 1.25$ s depending on the dynamics and data available for each case. This way the initial differences are diluted enough and the system is still evolving.

The applicability of this comparison technique is sensitive to any differences in the time reference (lag) that may exist between the experimental and numerical results. However, in view of the appropriate results, it does not seem the case.

The error indicators selected are:

1. Maximum absolute value of the deviation between both elevations.
2. Mean of the absolute value of the deviations along the whole width of the tank.
3. Absolute value of the area between both free surface elevations.

In all cases, the smallest value indicates the friction parameters with the best performance.

One may argue that the second and third error indicators are identical, but this is only true in the case of an even spatial sampling (constant dx). However, the sampling procedure applied yields more points where the free surface curvature is larger. In any case, since there are systematically more numerical sampling points than experimental

measurements, the laboratory free surface elevation between the given points is obtained by linear interpolation.

All the errors are represented as contour plots in the following test cases. However, two types of plots are presented. The first type features the absolute values calculated. The second type includes the same values, but non-dimensionalized by the global minimum (i.e. the best case shows a unit error, and the rest present higher values).

CR35

The results for the most turbulent case (crushed rocks, $h = 35$ cm) are shown first. This initial analysis will be thorough in terms of number of figures and thorough explanations. Since most of the implications derived from the analysis of the first set of data hold for the following cases, they shall be explained in a less detailed way.

The whole set of errors has been calculated for $t = 1.15$ s, and is shown in Fig. 7.26. The panels are arranged such that each row belongs to a different turbulence model (DNS, $k-\epsilon$ and $k-\omega$ SST from top to bottom) and each column is for an error indicator (maximum error, mean error and integrated error, from left to right), as already discussed.

For each panel, the vertical axis indicates the value of α friction factor while the horizontal axis is for β. The error magnitude is a contour plot. The color-value legend lies to the right of each panel. The simulations are the combinations of the α and β values shown in Table 7.1, and are represented as red points. The red dot surrounded by a red circumference identifies the best-fit case (smallest absolute error).

The first piece of information that can be extracted from Fig. 7.26 is that the results are virtually identical, regardless of the turbulence model used. Hence, only the results for the DNS cases will be shown from now on. Needless to say, as the current case is the most energetic and turbulent one, the differences between turbulence models in the following cases are expected to be even lower.

Regarding the best-fit friction factors extracted from Fig. 7.26, there is almost unanimity (8 out of 9 panels) to assure that the combination of $\alpha = 0$ and $\beta = 2.0$ yields the closest results to reality.

The deviation between the numerical and the experimental water surface at $t = 1.15$ s for this case is shown in Fig. 7.27. The porous medium zone is shadowed in gray and

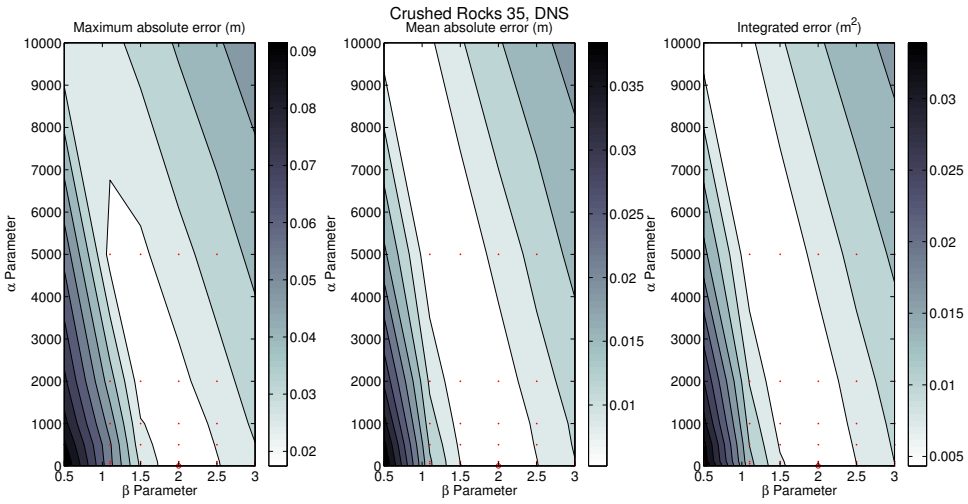

(a)

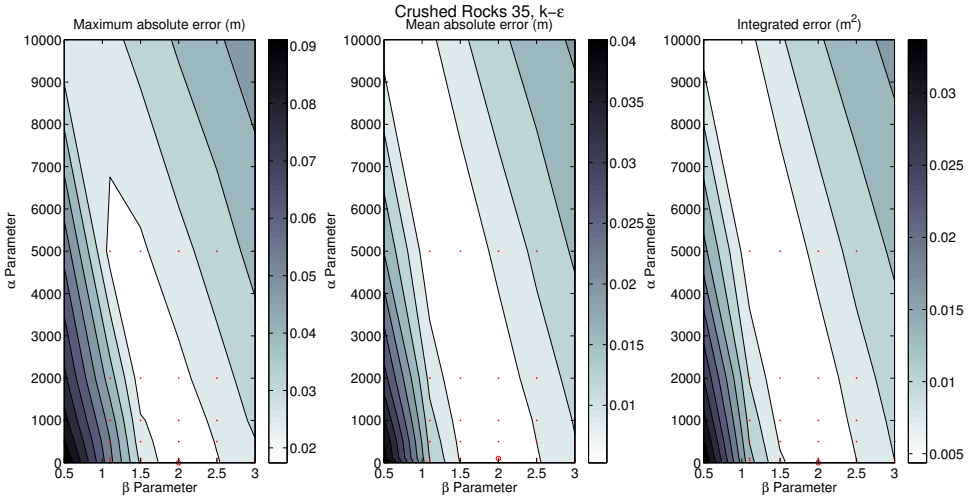

(b)

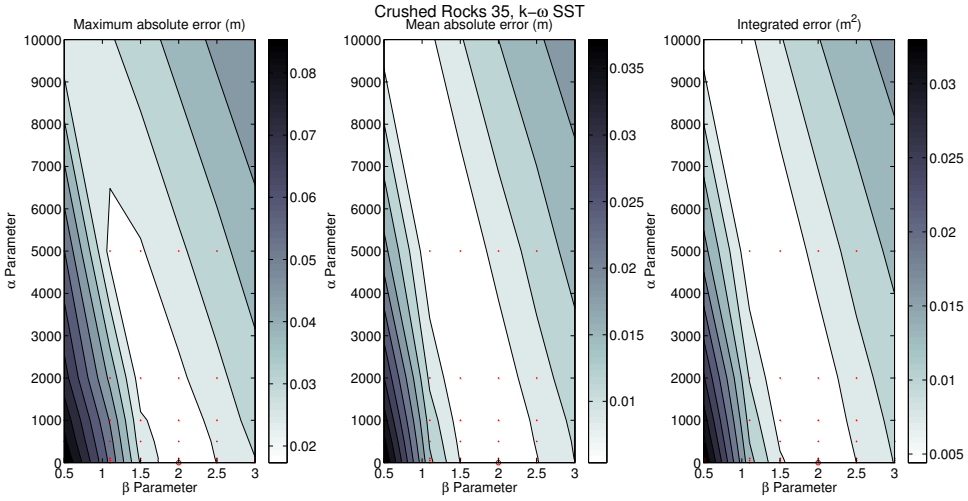

(c)

Figure 7.26: CR35 case errors for the whole α and β range. Panel (a): DNS. Panel (b): $k-\epsilon$. Panel (c): $k-\omega$ SST.

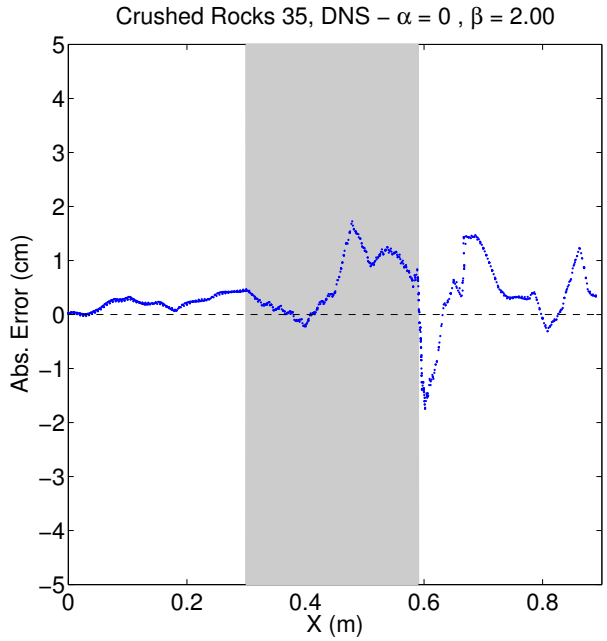

Figure 7.27: CR35 DNS deviation error for $t = 1.15$ s.

each of the blue points indicates a location at which the numerical free surface has been sampled along the whole tank (x axis). The y axis indicates the error between numerical and laboratory free surfaces, in cm.

The maximum absolute deviation between free surface elevation is 1.75 cm. Such magnitude corresponds to less than four cells in height and, as it can be seen in Fig. 7.27, it is located close to the interface of the porous medium, where water is flowing out. The hydrodynamics in that area are very complex to measure in the laboratory experiment and to simulate numerically.

The mean error is an aggregated indicator, because it takes into account the whole set of numerical points. Analysing Fig. 7.27 yields a mean error (in absolute value) of approximately 0.5 cm, on the order of magnitude of one cell.

Another implication that can clearly be extracted from Fig. 7.26 is that the minimum errors (brightest colour on the contour) are not localized around a small region, but forming a narrow band instead. This means that although the global minimum was found for $\alpha = 0$ and $\beta = 2.0$, there are other combinations that yield errors of the same order of magnitude. The slope of this region is roughly $d\alpha/d\beta = -10000/1$, indicating that a decrease of a unit in the β parameter can approximately be balanced with an increase in α of around 10000 (for these specific flow conditions and porous material).

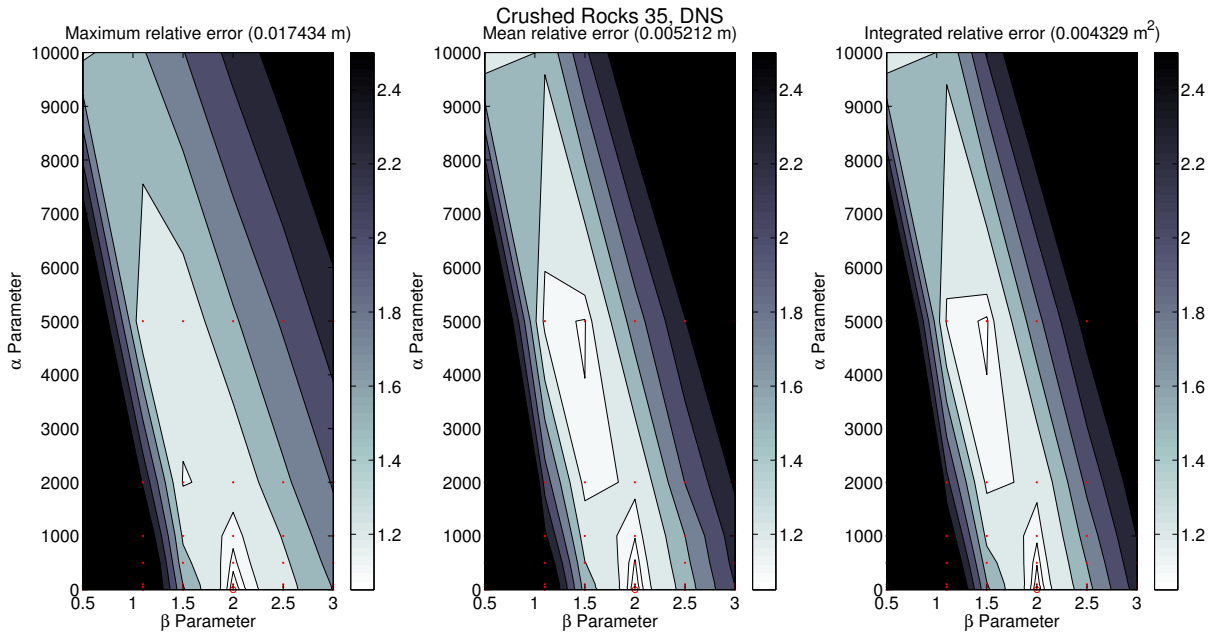

Figure 7.28: CR35 DNS relative errors for the whole α and β range.

For a more detailed analysis, Fig. 7.28 is introduced. The results are the same as presented on the top panel of Fig. 7.26, but instead of representing the absolute errors, these have been non-dimensionalized with the global minimum, so that all the magnitudes are relative to the best-fit parameters. With the new representation, the lowest errors resemble more a wedge that closes as α grows rather than a band, as noted previously. From these results it can be concluded that although $\beta = 2.0$ and $\alpha = 0$ yield the best performance, it is reasonable to assume α ranging up to 500 without significantly increasing the error.

The free surface elevation at the times for which experimental data exist is presented in Fig. 7.29. The porous medium is shaded in gray and contrasts with the clear flow region. Experimental results are shown as black circles, while numerical data are depicted as a blue dots. The spatial resolution is very high, which makes them to look as continuous line.

The numerical results agree quite well with the experimental data. Minor differences arise mainly during the first instants, because the lifting process of the gate is not immediate, and neither it is reproduced numerically. Therefore, these discrepancies appear at the initial snapshots, and are greater towards the bottom of the tank, where the pressure gradient is larger. However, as time advances, they get smaller and nearly vanish.

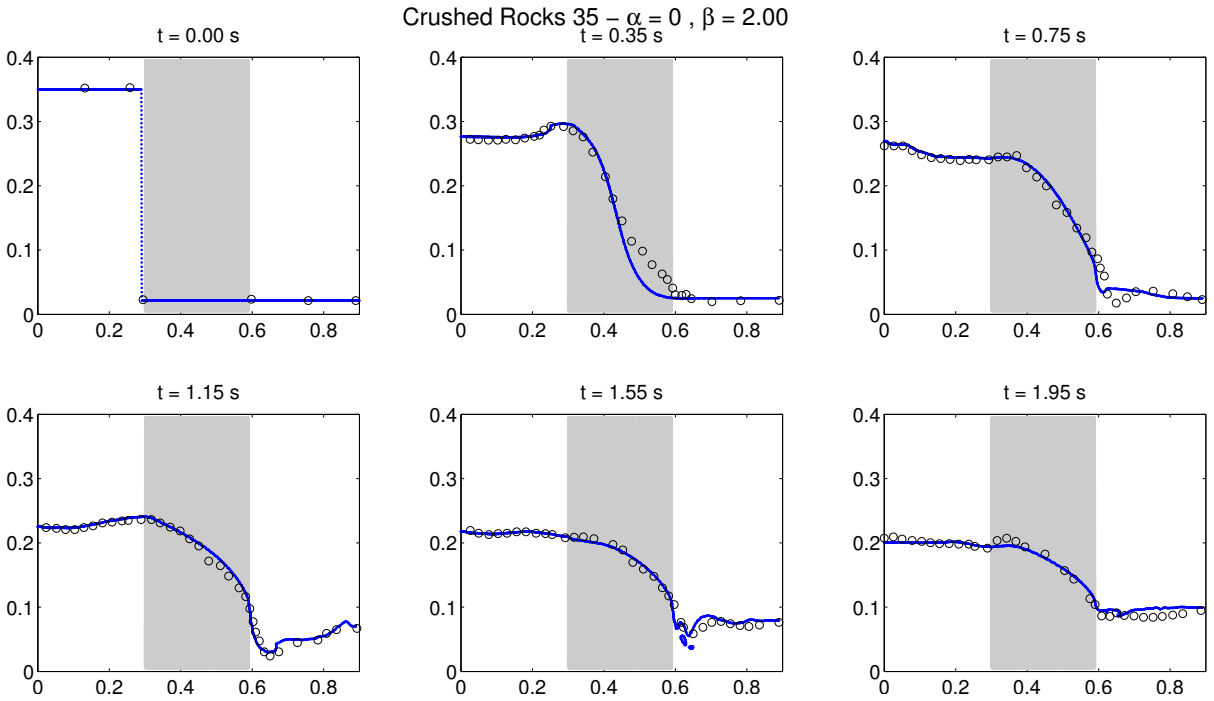

Figure 7.29: Validation case CR35: crushed rocks, $h = 35$ cm. $\alpha = 0$, $\beta = 2.0$. Laboratory data as circles, numerical data as points.

It is clear that the correct characterization of both friction parameters is the key factor to obtain a physical solution. Fig. 7.30 shows two alternative scenarios in which the friction factors are very low (left panel) and very high (right panel). The representation is analogous to Fig. 7.27. An insufficient drag leads to a water deficit on the initial reservoir and an excess on the other side of the porous medium, the flow rate is larger than it should because it is not refrained by friction (panel a). The contrary can also occur, as having excessive friction decreases the flow rate through the porous medium. This phenomenon is represented in panel b, in which the water level is higher in the initial reservoir.

Regarding the turbulence modelling, two snapshots showing the distribution of turbulent kinetic energy for $k - \epsilon$ and $k - \omega$ SST are presented side to side in Fig. (7.31). Black contour lines are represented for each negative integer power of 10.

It can be observed that, as a general trend, the k values are higher closer to the free surface, where the most energetic movements take place. The largest turbulence levels are obtained where the water flows out of the porous medium in both cases, as it experiences an acceleration. However, some differences between the two models can be spotted. First, the maximum turbulent kinetic energy level is not the same, as the $k - \omega$ SST yields significantly larger local values at the initial wall (where water bounces

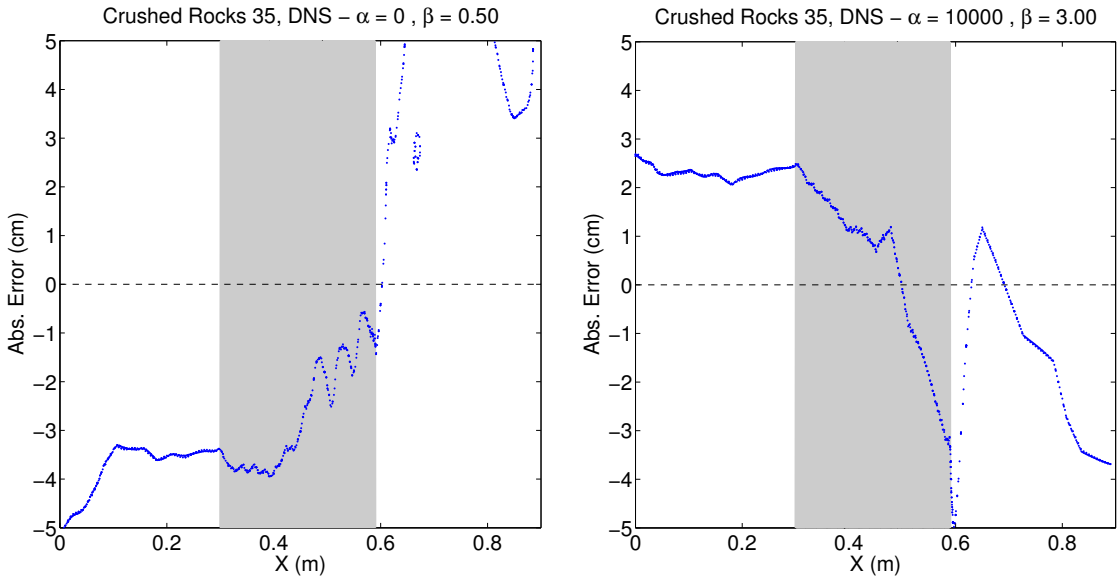

(a) (b)

Figure 7.30: CR35 DNS deviation error for $t = 1.15$ s. (a) Very low friction (b) Very high friction.

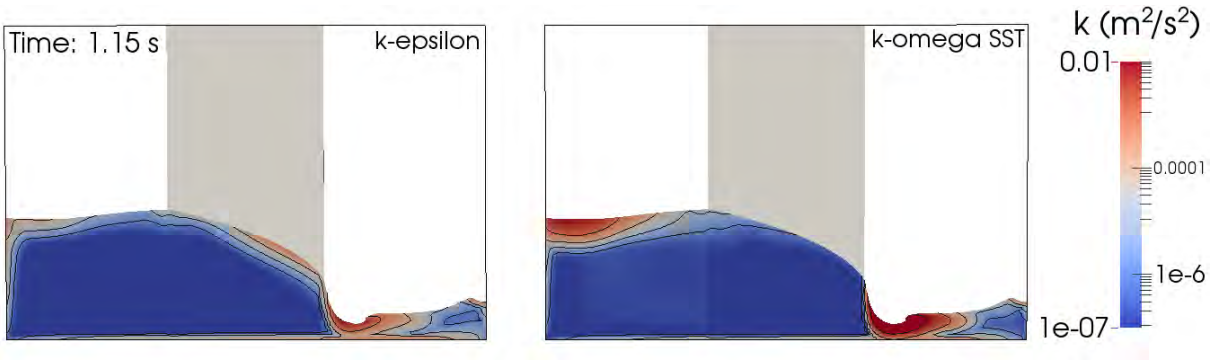

Figure 7.31: CR35: turbulent kinetic energy (k). Left panel: k–ϵ. Right panel: k–ω SST.

back and forth) and at the exit of the porous obstacle. The k pattern also differs slightly. While large values of turbulence are obtained at the free surface inside the porous medium for $k-\epsilon$, $k-\omega$ SST does not produce them.

CR15

The results for the crushed rocks material and $h = 15$ cm case are shown next. Similarly to the previous case, there are no significant differences between the DNS, $k-\epsilon$ or $k-\omega$ SST simulations. Hence, only the DNS results are included.

Fig. 7.32 shows the absolute and relative errors. As previously seen, the smallest

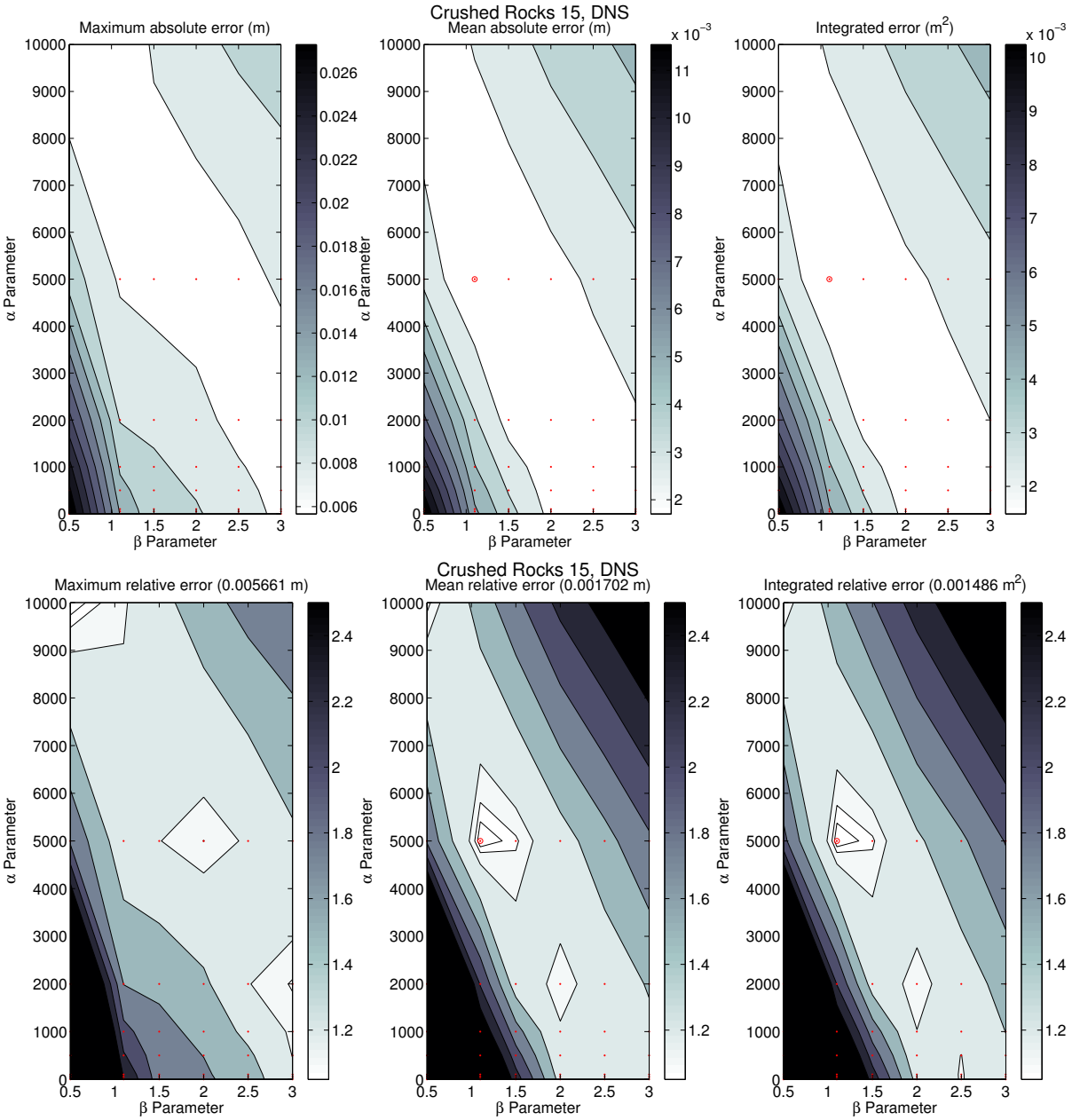

Figure 7.32: CR15 DNS case errors for the whole α and β range.

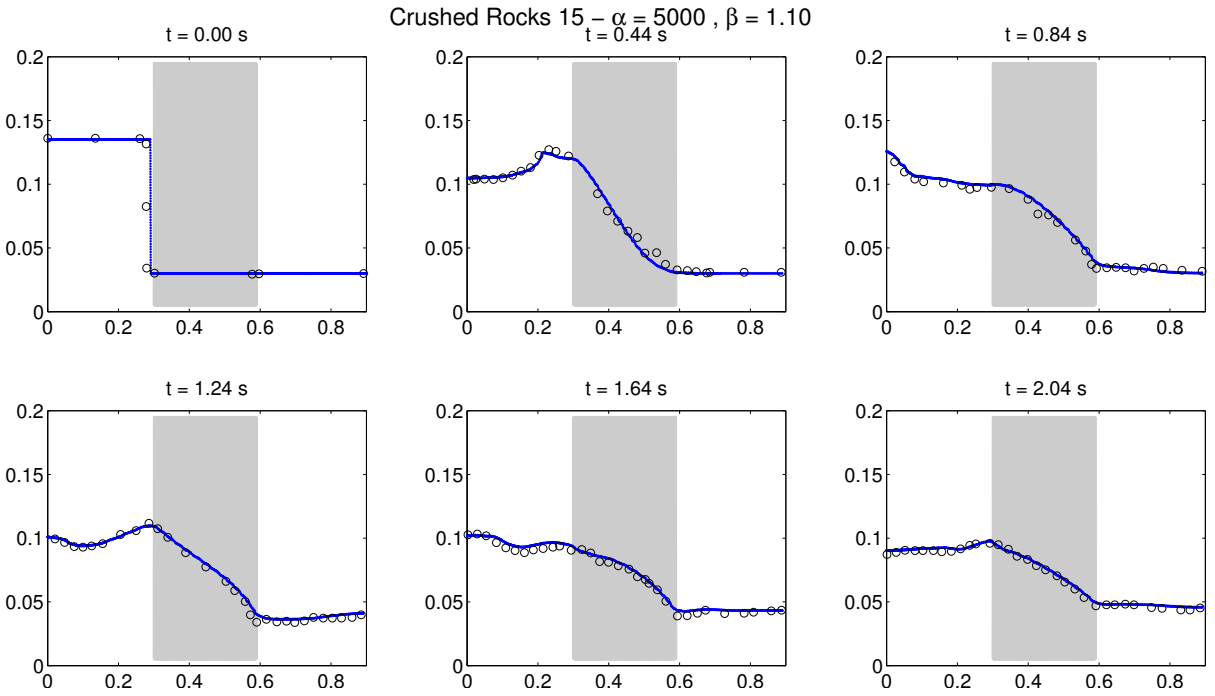

Figure 7.33: Validation case CR15: crushed rocks, $h = 15$ cm. $\alpha = 5000$, $\beta = 1.1$. Laboratory data as circles, numerical data as points.

errors (lightest color) form a band. In this particular case the slope of the region is approximately $d\alpha/d\beta = -10000/2$, half as steep as in CR35. This indicates that the flow is less turbulent, and the influence of the α parameter is larger than before.

There is a significant difference between the value of the best-fit friction factors between the individual and aggregated indicators. The maximum error method yields $\alpha = 10000$ and $\beta = 0.5$, while the other two return $\alpha = 5000$ and $\beta = 1.1$. As the second approach is preferred, the best-fit parameters are selected: $\alpha = 5000$ and $\beta = 1.1$.

The free surface elevation comparison is presented in Fig. 7.33. The agreement between both measurements is outstanding, presenting even better results than on the previous case (mean error: 1 mm vs 5 mm). The flow conditions are less turbulent, as the case presents a smaller pressure gradient, due to the lower initial water height. This flow regime presents no significant differences between the numerical and experimental data, even for the first time steps as it occurred in CR35. That difference is shown in Fig. 7.34 for $t = 1.24$ s. As it can be noted, the errors are significantly lower than 1 cm. The only remarkable difference occurs, again, at the outflow interface of the porous medium.

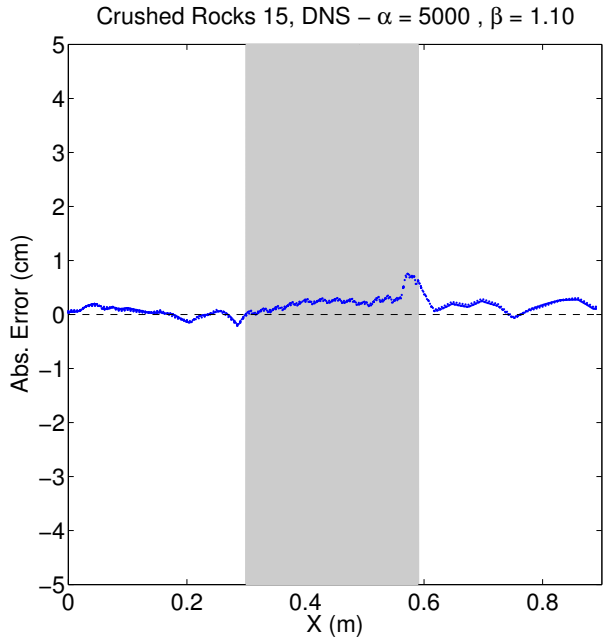

Figure 7.34: CR15 DNS deviation error for $t = 1.24$ s.

GB25

The results for the glass beads material and $h = 25$ cm, which corresponds to the second transitional state between fully turbulent and fully laminar flow, are studied next. As before, there are no significant differences between the DNS, $k - \epsilon$ or $k - \omega$ SST simulations, hence, only the DNS results are discussed.

The relative errors are represented in Fig. 7.35. The smallest errors band is less steep than on previous cases, with an approximate slope of $d\alpha/d\beta = -450/1$. Again, the flow is becoming more laminar, therefore, the influence of the α parameter is larger.

In this case all three indicators provide a different set of best-fit friction factors. The maximum error method yields $\alpha = 400$ and $\beta = 0.2$, the mean error method $\alpha = 500$ and $\beta = 0$, and the integrated error $\alpha = 500$ and $\beta = 0.1$. The selection is made in terms of the minimum mean error, as in the previous cases. In any case, the errors for $\alpha = 500$ and $\beta = 0$ are virtually the same as for the minimum of each criterion.

The evolution in time of the free surface is plotted in Fig. 7.36. As already commented, the flow rate is very low due to the type of porous material (glass beads). This effect is clear when comparing Fig. 7.36 with Fig. 7.33. Both of them start with the same water level on the right reservoir. However, the water elevation of the present case at $t = 4$ s is lower than CR15 for $t = 2.04$ s, even when its initial water height on the left reservoir is

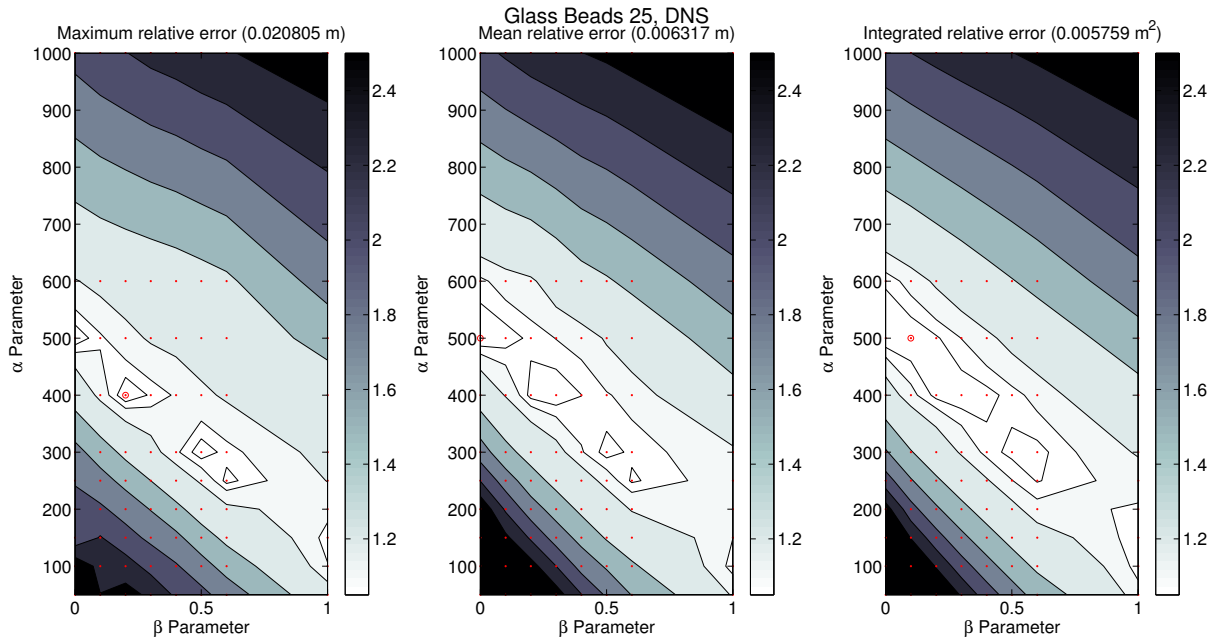

Figure 7.35: GB25 DNS case errors for the whole α and β range.

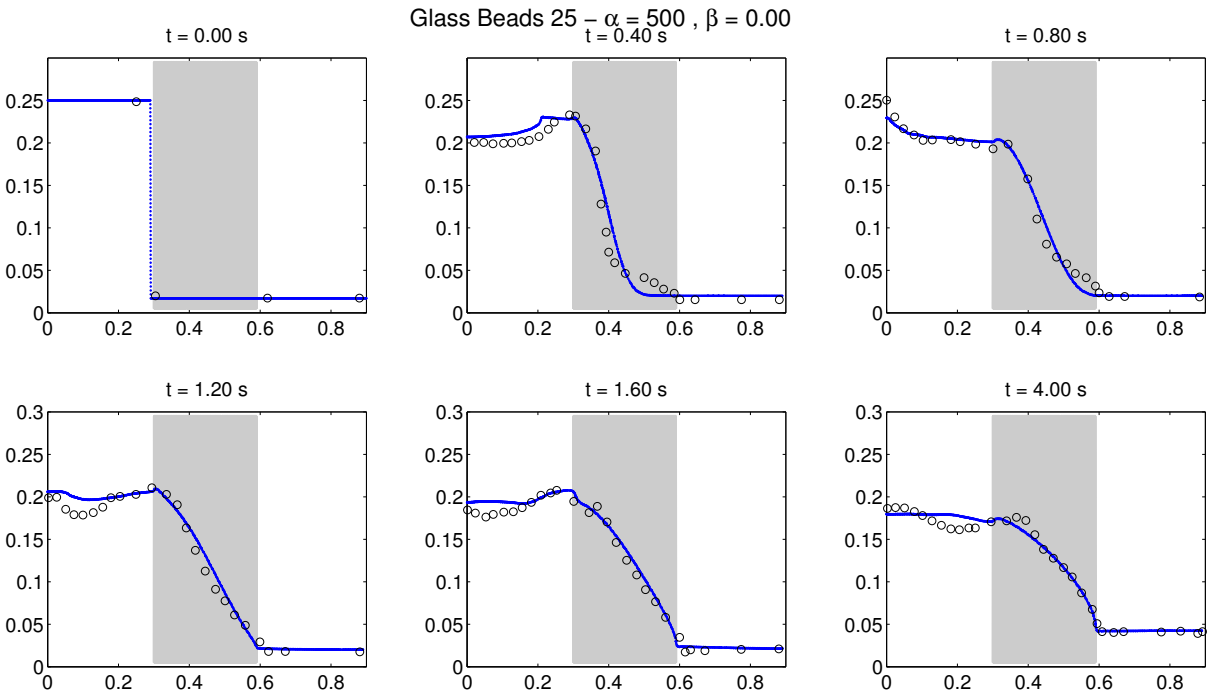

Figure 7.36: Validation case GB25: glass beads, $h = 25$ cm. $\alpha = 500$, $\beta = 0.0$. Laboratory data as circles, numerical data as points.

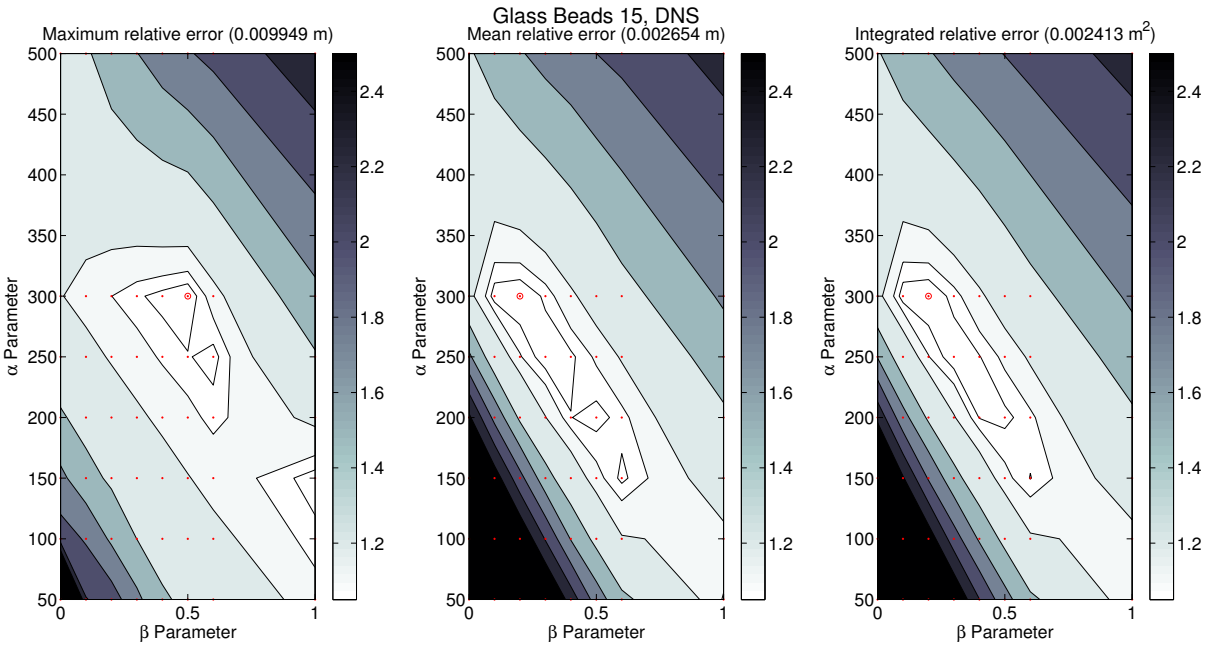

Figure 7.37: GB15 DNS case errors for the whole α and β range.

higher (25 cm vs 15 cm).

The agreement between the numerical and experimental series presents some similarities with the CR35 case. The initial time steps show some discordances towards the bottom of the porous medium. The effect of the moving gate is, again, the most plausible cause to explain them. As time advances, the differences vanish, as in CR35. However, some significant errors can also be noticed inside the left reservoir. As the flow rate is very low, the porous medium acts as a reflective wall for waves, not being able to damp the oscillation created in the process of elevating the gate. Since the phenomenon is not replicated numerically, the wave trapped in the model is smaller that the one in the experiment.

GB15

Finally, the results for glass beads and $h = 15$ cm is analysed. This is the most laminar case and only the DNS results are discussed.

The relative errors are represented in Fig. 7.37. This is the less turbulent case, hence, the slope is once again less steep: $d\alpha/d\beta = -350/1$. The change in slope is not very abrupt with respect to GB25, but indicates an increase in the influence of the α parameter.

As it happened in case CR15, the maximum error method yields a set of best-fit

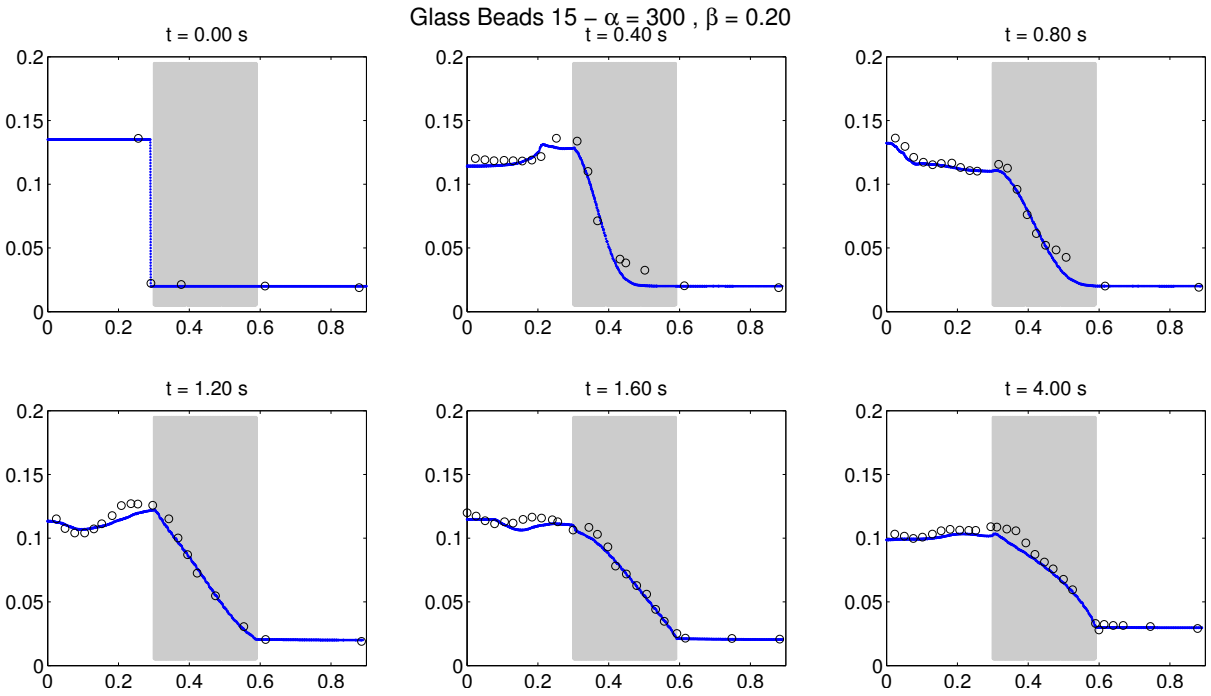

Figure 7.38: Validation case GB15: glass beads, $h = 15$ cm. $\alpha = 500$, $\beta = 0.0$. Laboratory data as circles, numerical data as points.

	CR35	**CR15**	**GB25**	**GB15**
α	0	5000	500	300
β	2	1.5	0	0.2

Table 7.2: Best-fit friction factors.

parameters ($\alpha = 300$, $\beta = 0.5$) different from the other integrated methods ($\alpha = 300$, $\beta = 0.2$). Accounting for the similar results, the minimum mean error is preferred and the selected friction parameters are $\alpha = 300$ and $\beta = 0.2$.

The free surface elevation comparison is shown in Fig. 7.38. As in the previous cases, the first time steps present minor differences near the bottom, due to the presence of the gate that contains the flow. The effect is no longer noticeable from $t = 1.20$ s. Other minor dissimilarities take place in the initial reservoir, but in general, the agreement is closer to reality than GB25.

7.2.1.4 Discussion

The best-fit friction factors for the materials and flow conditions tested are gathered in Table 7.2. The cases are ordered from turbulent to laminar, from left to right.

It is significant that the variation of the β factor is very small (units) compared to

that of the α factor (thousands). According to the previous section the simulations are more dependent on β than on α, as shown in terms of the slope of the lowest error band. Therefore, β, the non-linear friction factor, can be used as an indicator on how turbulent the flow regime is.

In that fashion, it can be concluded that flow through crushed rocks is significantly turbulent, requiring large values of β to accurately represent the conditions. On the contrary, flow through glass beads is more laminar, as a result, β is significantly smaller.

It is interesting to find out that β is slightly higher in the most laminar case, GB15, in which the hydraulic gradient is smaller, than in GB25. There is a simple explanation. First, a set of discrete simulations has been carried out, hence, the discretization in α and β may not be sufficient to find the optimum set of parameters. Moreover, the errors in the vicinity of the lowest error band are very small, and the choices in this section have been performed according to certain criteria from the countless number of them available.

7.2.2 Regular waves interacting with a high mound breakwater in 2D

The next validation case was presented in Guanche et al. (2009), and involves the interaction of regular waves with a rouble mound breakwater (as defined in Kortenhaus and Oumeraci (1998)), although accounting for its geometry it is closer to a high mound breakwater according to Oumeraci and Kortenhaus (1997).

7.2.2.1 Physical experiments

The physical experiments took place in the University of Cantabria's large flume. This facility is 60.0 m long (from the wavemaker mean position), 2.0 m wide and 2.0 m high. The flume bottom is horizontal. Originally, two different breakwaters were constructed and tested, however, here only the high mound breakwater is reproduced.

The caisson of the breakwater was made of concrete and spanned the whole width of the flume. It was 1.04 m long and 0.3 m deep, and its seaward side was located 45 m away from the wave paddle. This block laid on a gravel foundation which was 0.7 m high, and acted as the core of the breakwater. The core presented a 10 cm berm on the seaside. A 10 cm thick secondary armour layer made from a different type of gravel was present

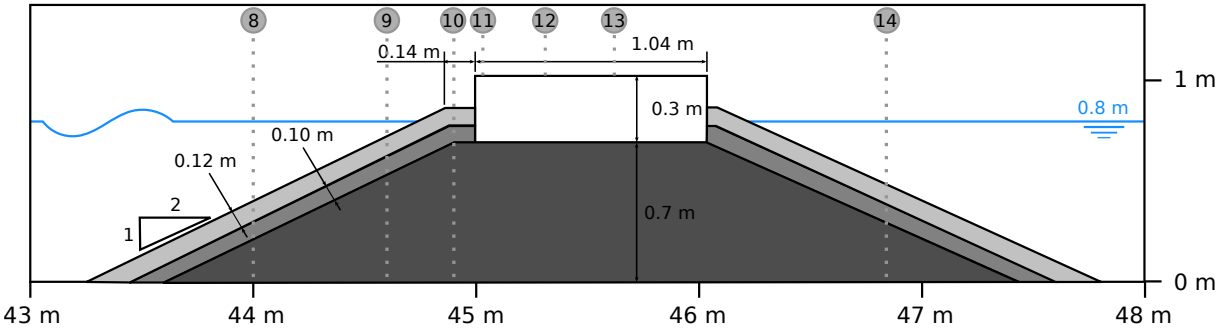

Figure 7.39: high mound breakwater section.

Material	D_{50} (m)	Porosity	α	β
Primary armour layer	0.12	0.5	50	0.6
Secondary armour layer	0.035	0.493	50	2.0
Core	0.01	0.49	50	1.2
Dissipation ramp	0.035	0.856	50	2.0

Table 7.3: Porous media physical properties and best fit parameters.

on both sides. The principal armour layer was 12 cm thick, and included a 14 cm long seaside berm. The slope of the porous materials was 2H/1V. A sketch of the geometry can be seen in Fig. 7.39. The specific physical properties of the porous media are given in Table 7.3.

A ramp was placed behind the breakwater to dissipate the transmitted waves. This device was made of metallic mesh screens, and will later be modelled as another porous medium.

Waves were generated using a piston-type wavemaker, which featured an AWACS system to deal with the waves reflected by the structure. The still water level was kept constant and equal to 0.8 m. Different wave conditions, including regular and irregular sea states, were tested. The reader is referred to Guanche et al. (2009) for further details.

Fourteen resistive water elevation gauges were placed along the centreline of the flume. Their location is indicated in Table 7.4. The first seven of them were placed in front of the structure. The rest were located on the structure. This last set is represented in Fig. 7.39, as vertical dotted lines. Notice that gauges 8–10 and 14 pierce the porous media, while those placed on top of the caisson lie on top of it. The last free surface gauge was positioned behind the breakwater, to measure transmitted energy.

Pressure was also measured at different locations on the caisson, as shown in Fig. 7.40, in which the sensors are represented as bold points. The first four pressure cells were

FS Gauges	X (m)	FS Gauges	X (m)	FS Gauges	X (m)
1	17.0	6	41.0	11	45.03
2	37.2	7	42.5	12	45.31
3	38.0	8	44.0	13	45.62
4	38.7	9	44.6	14	46.84
5	40.0	10	44.9		

Table 7.4: Free surface gauges location

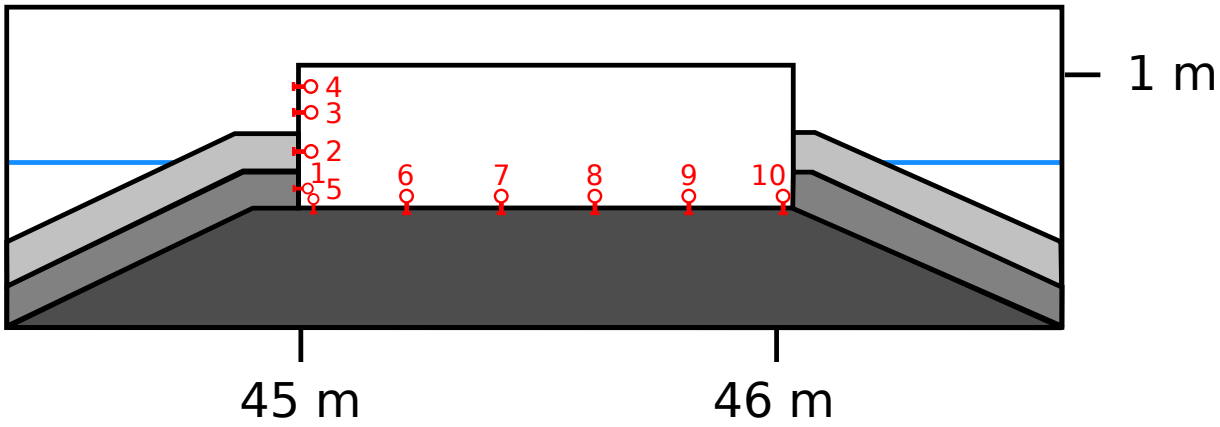

Figure 7.40: Pressure gauge distribution on the caisson.

placed on the seaside of the concrete prism, two of them within the armour layers and the other two on the clear part. The rest of the gauges were located below the caisson, in contact with the porous core.

7.2.2.2 Numerical experiments

The flume has been reproduced in its entirety in 2D: 60 m in length and 1.3 m in height. Three horizontal zones with different cell size grading have been defined. In the vertical direction the cell size is constant and equal to 1 cm throughout the flume.

The first zone represents the wave propagation area, and covers from the wave paddle ($X = 0$ m) to $X = 40$ m, close to the structure. The horizontal cell size in this sector varies from 4 cm close to the wave generation boundary to 1 cm close to the next area. This gradation saves computational cost by having less cells where they are not so important, as close to the generation boundary.

The next region is the interest zone, and it is located from $X = 40$ m to $X = 48$ m. The structure lies within, so the cell dimensions are chosen to obtain an adequate resolution. Cell size is constant and equal to 1 cm, which provides enough detail to represent the

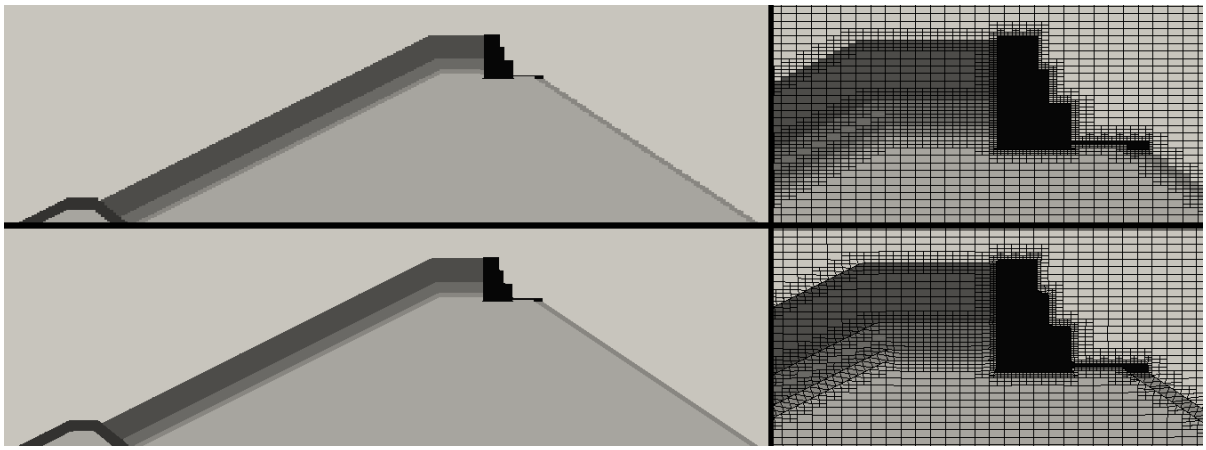

Figure 7.41: Castellated vs snapped porous media geometry setup.

processes taking place around the structure.

The final zone is where the energy that surpasses the structure is finally dissipated, and it covers the final 12 m. There, the cell size varies from 1 cm near the structure to 3 cm at the end wall. From the initial mesh that has been described, the caisson has been removed. The final mesh has over 355,000 hexahedral cells.

This case has been used to calibrate the porous media for oscillatory flow. The dissipative perforated ramp has been replicated by means of another porous medium. The numerical parameters have already been presented in Table 7.3. They have been chosen to obtain the best results after several tests.

The present porous media implementation requires that each cell can only contain one type of material. If a cell is at the interface between several materials, the one with higher presence should dominate and be chosen as representative of the cell. Since the meshes in OpenFOAM® are generally formed by hexahedral cells, the geometry resulting from irregular-shaped porous zones is *castellated* (i.e. sawtooth-type). This is not an inconvenience, as a strict application of the Volume-Averaging approach to a real geometry would yield smooth transitions between different zones, therefore, having a perfectly well defined interface line (*snapped* approach) would also be unrealistic.

Tests have been performed to compare the *castellated* and *snapped* approaches. In Fig. 7.41 the different meshes are shown in the top panels and bottom panels, respectively. The left panels feature the complete geometry of a complex breakwater, while the right panels show a detail of the mesh where differences are better observed.

Most of the results are very similar: free surface gauges, pressure around the structure,

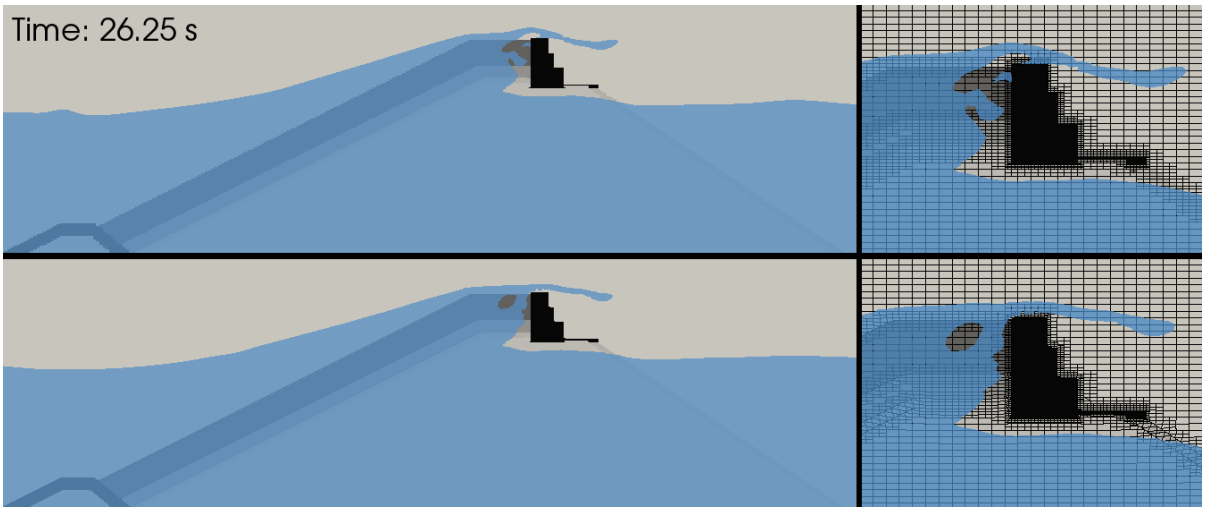

Figure 7.42: Castellated vs snapped setup. Overtopping comparison.

overtopping (as in Fig. 7.42). However, the *snapped* mesh is more prone to cell non-orthogonality errors and diminishes the stability of the model.

Therefore, the porous media have been set using a castellated setup in this case, as depicted in Fig. 7.46 (note that the vertical scale of the figure has been exaggerated).

The whole set of laboratory measuring instruments have been reproduced numerically. Free surface elevation has been probed at 14 locations, while pressure measurements have been taken at 10 locations.

The free surface elevation is equal to 0.8 m, and 20 cm in height and 3 s of period waves have been generated using the cnoidal theory.

Turbulence in this case is modelled using the volume-averaged $k - \epsilon$ model, so that the behaviour inside the porous media addresses both macroscale and flow patterns. The simulation has been run using 2 cores of a standard PC (2.5 GHz), and the 300 seconds were ready after 30 hours.

7.2.2.3 Results

One of the challenges of the simulation is to manage the wave transformation processes around the high mound breakwater such as wave reflected at the structure and the damped energy by means of wave breaking and flow percolation through the porous media. In order to deal with the high energy reflected from the structure (90%, as reported by Guanche et al. (2009)), the boundary conditions have been used to generate and absorb waves.

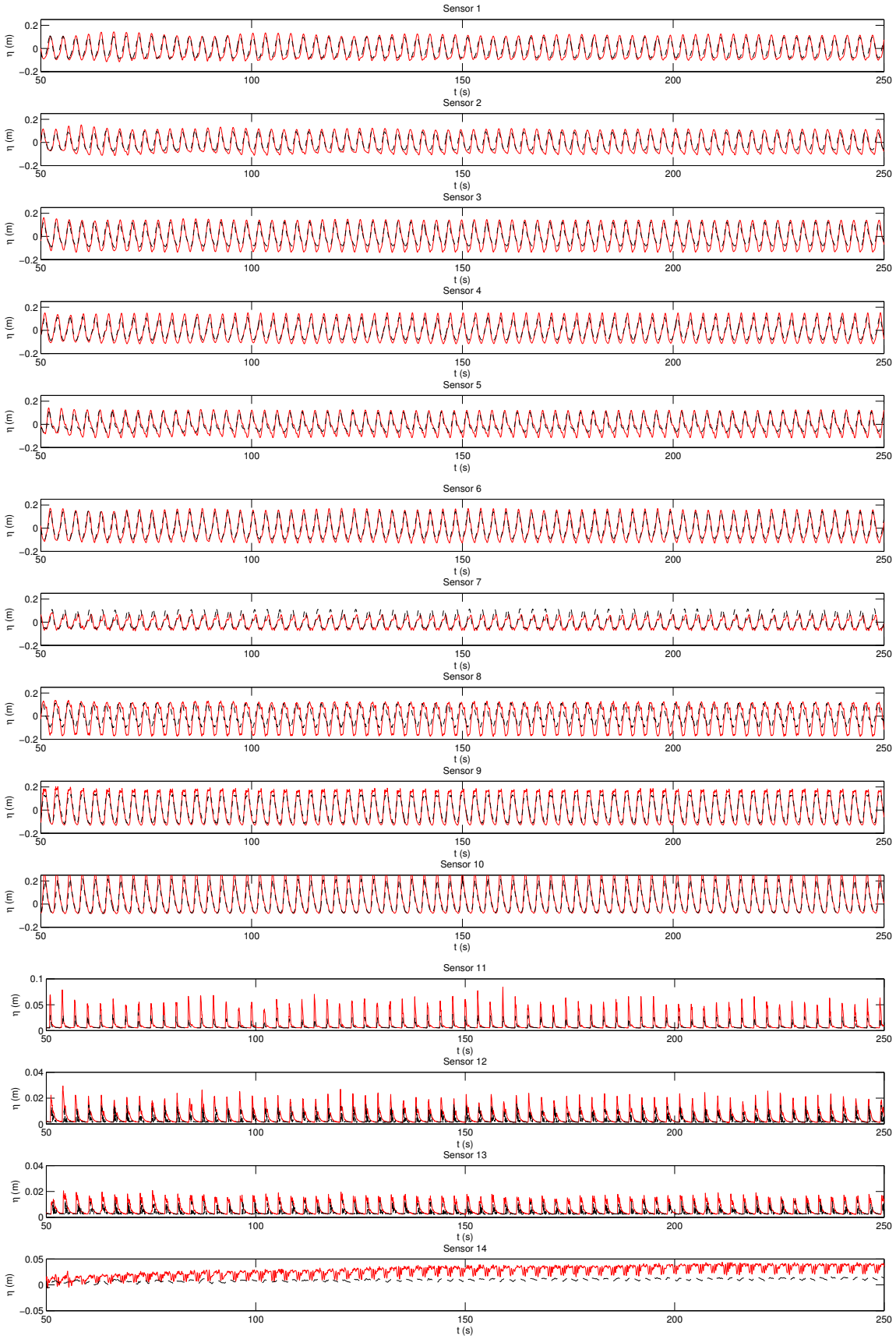

Figure 7.43: Regular waves interacting with a high mound breakwater in 2D: free surface elevation.

Results are presented in Fig. 7.43 for all the wave gauges reported in Table 7.4; ten in front of the structure, three over the caisson and an additional one leeward the breakwater to measure the transmitted wave by the combination of wave overtopping and flow percolation throughout the core.

A high degree of accuracy is demonstrated by the model in reproducing both wave phase and height. The wave profile, that reveals the existence of a quasi-steady wave pattern by the combination of an incident and reflected wave, is very well caught during the numerical simulations. Larger discrepancies are observed in gauges 8–10, which are located along the seaward breakwater slope. The simple definition of the porous slopes (see the white lines in Fig. 7.46) could induce such slight discrepancies. The use of incompressible two-phase flow modelling could also affect the wave evolution in the breaking zone, as the simulation is performed in a two-dimensional mesh. This implies that the air cannot escape sideways, as it does in reality, thus, the evolution of the wave during breaking can be modified. Such issue is not observed in three-dimensional simulations, as shown later.

The fluid layer on the top of the structure due to overtopping (gauges 11, 12 and 13) is well predicted in shape but a slight underestimation is observed. This may be a consequence of the deviations in wave evolution observed along the slope. The transmitted wave (gauge 14, bottom panel) is the most complex to reproduce, and is not well captured by the model.

From the results of the first gauges, it can be seen that the wave generation and absorption boundary conditions work adequately, as they manage to generate the target wave while absorbing the reflected energy, as the AWACS does in the laboratory.

Fig. 7.44 shows the time series of dynamic pressure. The comparison includes four pressure gauges along the vertical face of the caisson (gauge 1 to 4) and six gauges underneath the caisson (gauges 5 to 10). In general, the model is able to predict pressures accurately at every location, only with minor underestimations. It even captures the momentum damping induced at the core as waves propagate underneath the caisson towards the leeward side of the structure, presenting slight discrepancies in phase. The underestimation of the sensors may be another side effect of the mentioned underprediction of the wave height. Furthermore, additional differences on the sensors located at the front

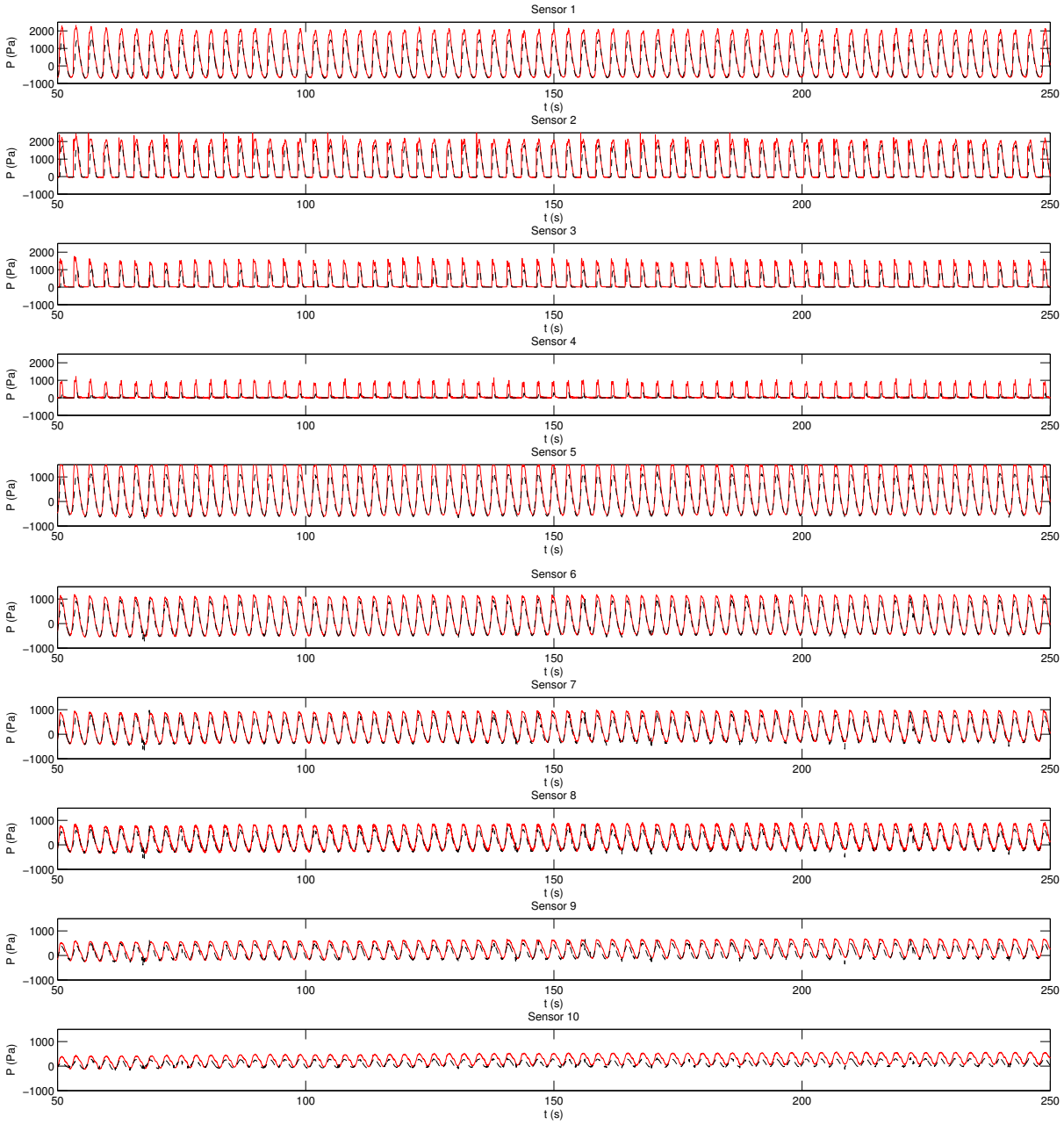

Figure 7.44: Regular waves interacting with a high mound breakwater in 2D: pressure series.

face may arise from the difference between the actual geometry of the armour layers and the homogeneous porous media considered. A laser scanning was carried out and the differences between the theoretical and real porous layers are clear comparing Fig. 7.46 versus Fig. B.5. In the second case, the pressure transducers are more exposed, hence, higher pressure values can be expected.

In Fig. 7.45, the most relevant stability variables are represented. The blue plots present the horizontal and vertical forces and the overturning moment (all per metre of width) time series acting on the caisson, from top to bottom. The black plots correspond to the safety coefficients against sliding (top) and overturning (bottom). For reference, the weight of the caisson is 6325 N per meter of width (for a concrete density of 2400 kg/m^3 and accounting for the submerged weight of the section located underwater).

The maximum horizontal dynamic force induced by the impact of waves is relatively small in comparison with the weight of the structure, only representing a 5%. The magnitude of the maximum vertical force doubles that of the horizontal component, increasing to 700 N. However, it only represents a 10% of the caisson weight. Accounting for both components of the force and the moments derived from them, large safety coefficients can be anticipated. The minimum safety coefficients allowed for the design of coastal structures are typically 1.4. In this case the lowest safety coefficient obtained corresponds to the overturning of the section and is 5.5. The safety coefficient against sliding is even higher, with a minimum value of 10. Clearly the structure is over-designed for this wave conditions, because the experiments were prepared to avoid any kind of movement of the caisson.

Two snapshots of turbulent kinetic energy around the structure are presented in Fig. 7.46. The top panel shows the instant when the first wave impacts the structure. The k level is greater around the free surface location (shown as a black line) and around the primary rock layer, presenting a uniform value along the whole depth. At this point the turbulence effects start to penetrate the core.

The bottom panel presents the same situation at a mean stage of the simulation. The turbulence distribution both around the free surface and the structure has clearly diffused. However, the turbulence level is more or less of the same magnitude. A turbulence level build-up is expected for very long simulations, as described in Jacobsen et al. (2012),

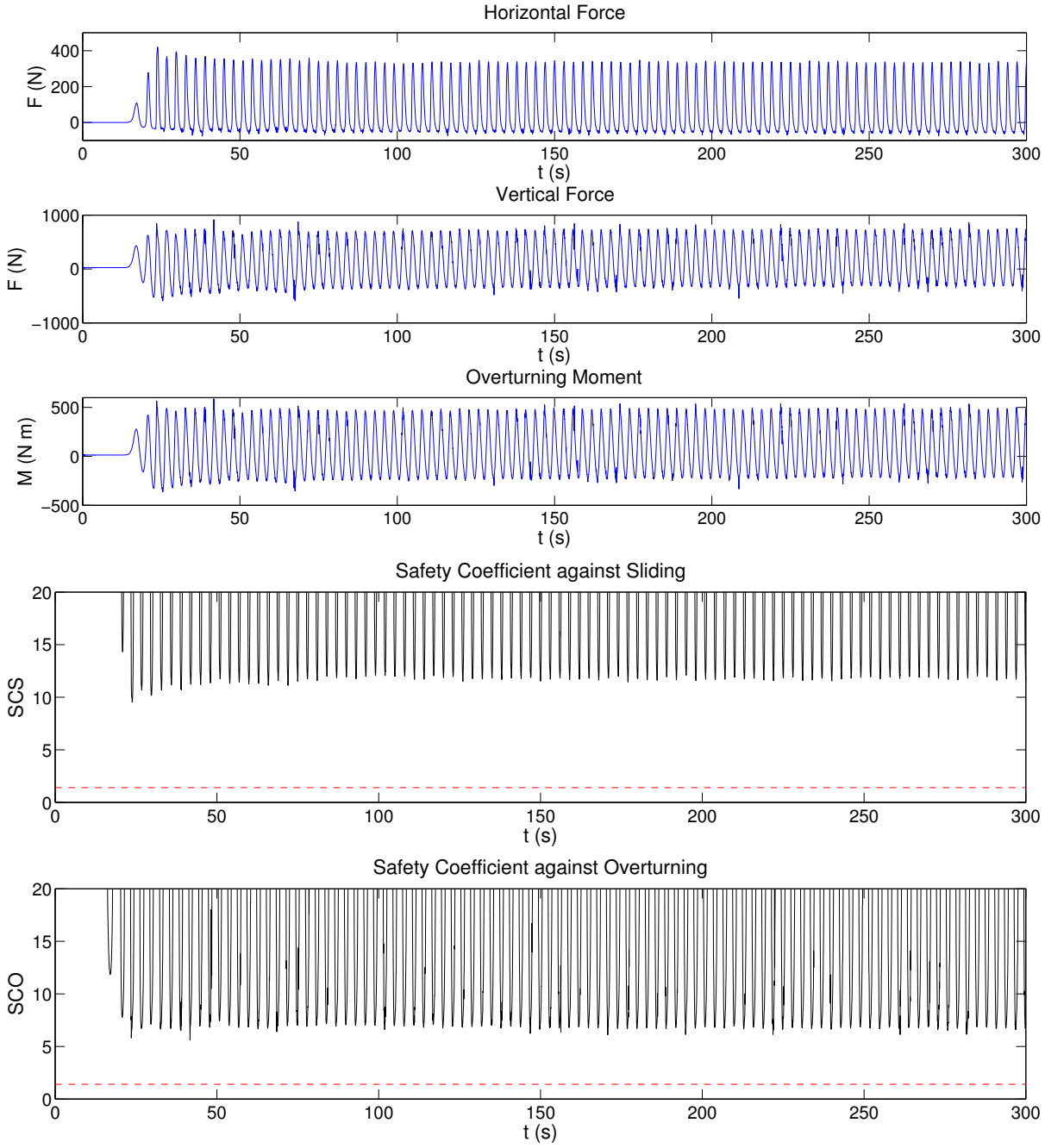

Figure 7.45: Regular waves interacting with a high mound breakwater in 2D: force and moments acting on the caisson and safety coefficients.

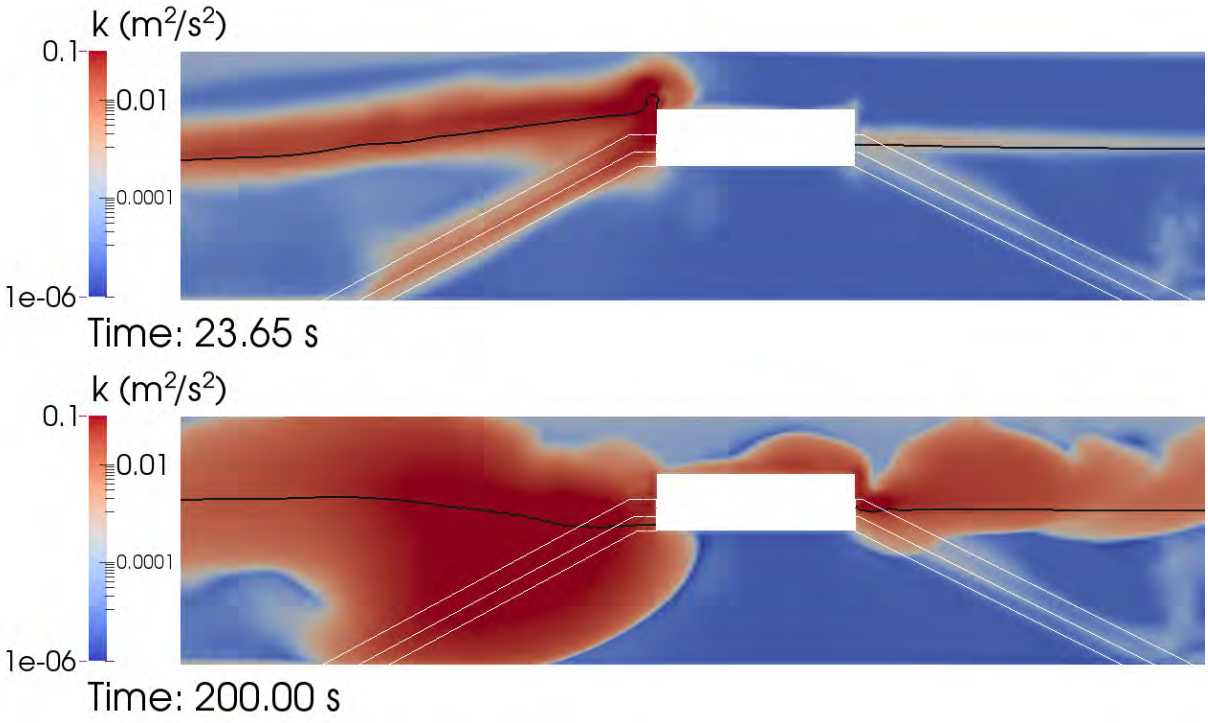

Figure 7.46: Turbulent kinetic energy level around Guanche et al. (2009) structure for the first wave impact and at $t = 200$ s.

because the production terms are formulated in a way that generates turbulence even for potential flows. Furthermore, the turbulence models were initially designed for stationary cases, and not for transient ones. It is interesting to remark that the k level is similar on the air and water phases. The turbulent effects have continued to propagate through the core of the structure. Nevertheless, as the flow inside is close to laminar, the majority of its volume continues to present low values of k.

The effect of this spurious turbulent kinetic energy level is an additional dissipation of momentum over that region, as the eddy viscosity is proportional to the square of k: $\nu_t = C_\mu \frac{k^2}{\epsilon}$. To solve this issue, Mayer and Madsen (2000) presented a technique in which the production term for k is not dependent on the strain rate, but on the vorticity. Therefore, the turbulent kinetic energy does not show such a dramatic growth as the simulation progresses. However, Mayer and Madsen (2000) work was applied to $k - \omega$ turbulence model.

7.2.3 Three-dimensional interaction of waves with a porous structure

Now that the capabilities of the model have been proven to work in two-dimensional cases it is time to extend the simulations to full three-dimensional ones. The interaction of waves with a vertical porous structure from (Lara et al., 2012) is now analysed.

7.2.3.1 Physical experiments

The physical modelling was carried out in the University of Cantabria's small shallow water wave basin, which is 17.8 m long, 8.6 m wide and 1.0 m high. The waves were generated by a piston-type wavemaker formed by 10 individual paddles that can move independently. However, all the cases had normal incidence of waves, so the whole set of paddles behaved as one. The remaining three walls of the tank were fully reflective and the bottom of the basin was completely flat.

A porous structure was built with a metallic mesh filled with a granular material. The mean stone diameter was 15 mm and the global porosity was 0.51. The shape of the structure was prismatic: 4 m long, 0.5 m wide and 0.6 m high, and resembled a porous vertical breakwater. The porous prism was attached to one of the lateral walls, and its seaward face was located 10.5 m away from the wavemaker. A general scheme of the setup is presented in Fig. 7.47.

The water depth was kept constant and equal to 0.4 m for all the experiments. A set of solitary waves (5, 7 and 9 cm of wave height) and cnoidal regular waves (5 and 9 cm of wave height; 2 and 4 s of wave period) were carried out.

Free surface elevation was measured at 15 locations, as depicted in Fig. 7.47. Pressure measurements were also taken at six points on the structure, shown in Fig. 7.48. These locations had been selected to assess the three dimensional effects.

7.2.3.2 Numerical experiments

The wave tank has been replicated numerically in its whole extension. The shape of the domain is a box (17.80 x 8.60 x 0.65 m), which makes the mesh orthogonal and conformal. The cell size varies in the X direction to save computational cost: from the

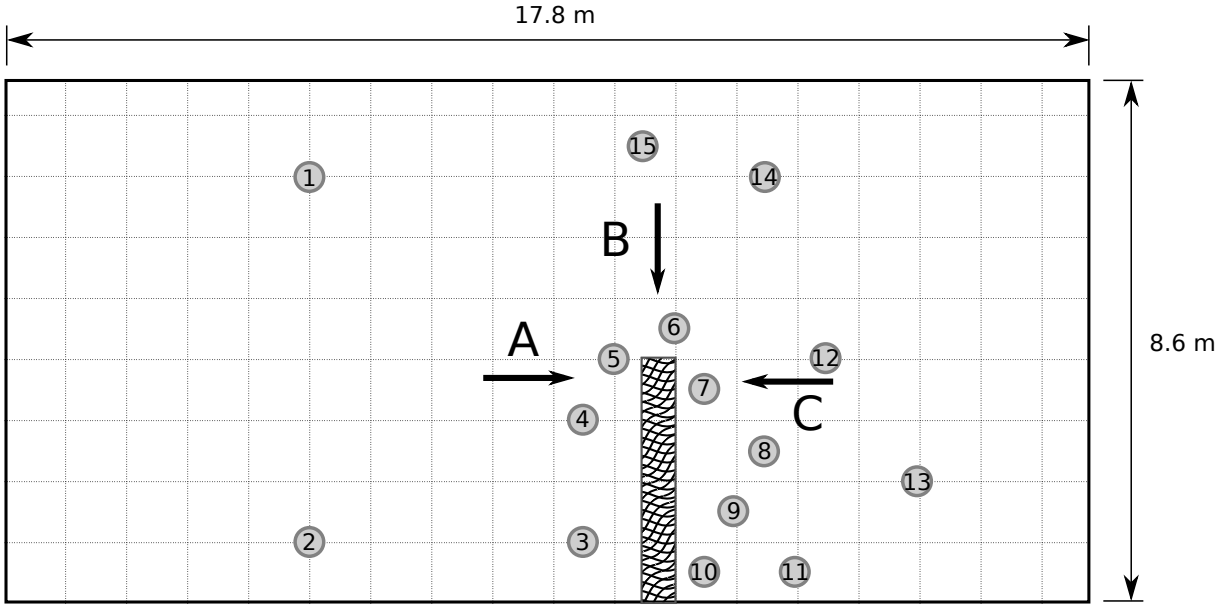

Figure 7.47: Three-dimensional interaction of waves with a porous structure. University of Cantabria's small shallow water wave basin. Sketch of the geometry and free surface elevation gauges. Auxiliary lines each metre.

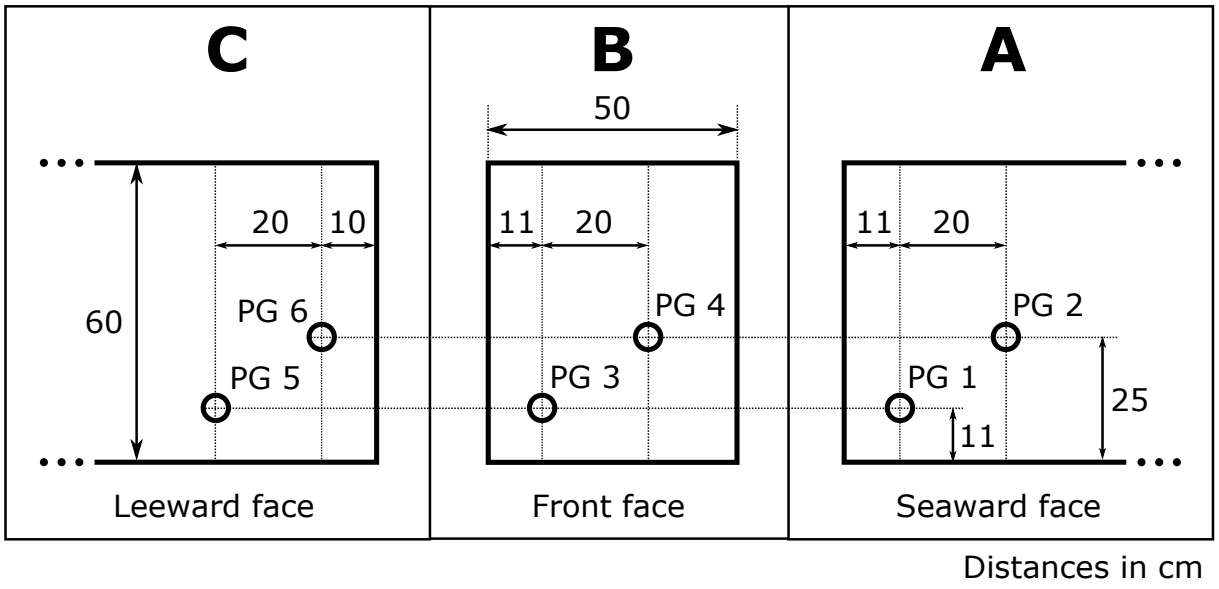

Figure 7.48: Three-dimensional interaction of waves with a porous structure. Location of the pressure gauges on the structure. Viewpoints according to Fig. 7.47. Distances in cm.

wave generation boundary to 1.5 m away from the structure$\Delta\ x$ varies from 2 cm to 1 cm. Then, it is kept constant and equal to 1 cm around the porous zone to obtain better details. Finally, from 1.5 m leewards the structure to the end of the tank the$\Delta\ x$ grows again from 1 cm to 2 cm. In the Y and Z directions the cell size is kept constant:$\Delta\ y =$ 2 cm and $\Delta z = 1$ cm. The total number of cells is slightly higher than 16.5 million.

The porous structure is treated as in the previous simulations. The situation resembles the dam break case, as the structure is perfectly defined by the cells, therefore, the castellated approach yields the exact geometry. The porosity variables are set to the best-fit values which previously represented crushed rocks: $\alpha = 0$ and $\beta = 2.0$.

Two wave conditions have been selected. First, a solitary wave of 9 cm in height is tested. In the original experiment the wavemaker was brought back slowly and then pushed forward suddenly to generate the wave. It eventually remains still at its final position until the end of the experiment. Therefore, the wave generation boundary has wave absorption disconnected, acting as a reflective wall. Next, 9 cm in height and 4 s in period cnoidal waves are generated, with active wave absorption connected. In both cases, 20 seconds are simulated in 12 hours using 128 processors (2.6 GHz).

Free surface elevation and pressure sampling has been carried out at the locations depicted on the experimental setup.

7.2.3.3 Results

In this section, the model reproduces the most relevant hydraulic processes to be considered in wave-structure interaction in a three-dimensional domain, which encompass wave reflection, wave dissipation, wave transmission resulting from wave penetration through the porous structure, wave diffraction and wave run-up on a porous structure.

Fig. 7.49 shows several snapshots of free surface elevation on the wave tank for different instants. The wave interacts with the structure from $t = 6$ s. The reflected, transmitted energy and the diffraction due to the gradient in wave height can be identified from $t =$ 7 s. The solitary wave gets reflected on the end wall at $t = 10$ s and continues to interact with the porous structure during the following instants.

Figs. 7.50–7.55 present the comparison of **IHFOAM** predictions versus laboratory measurements in the three-dimensional domain. Free surface and dynamic pressure time

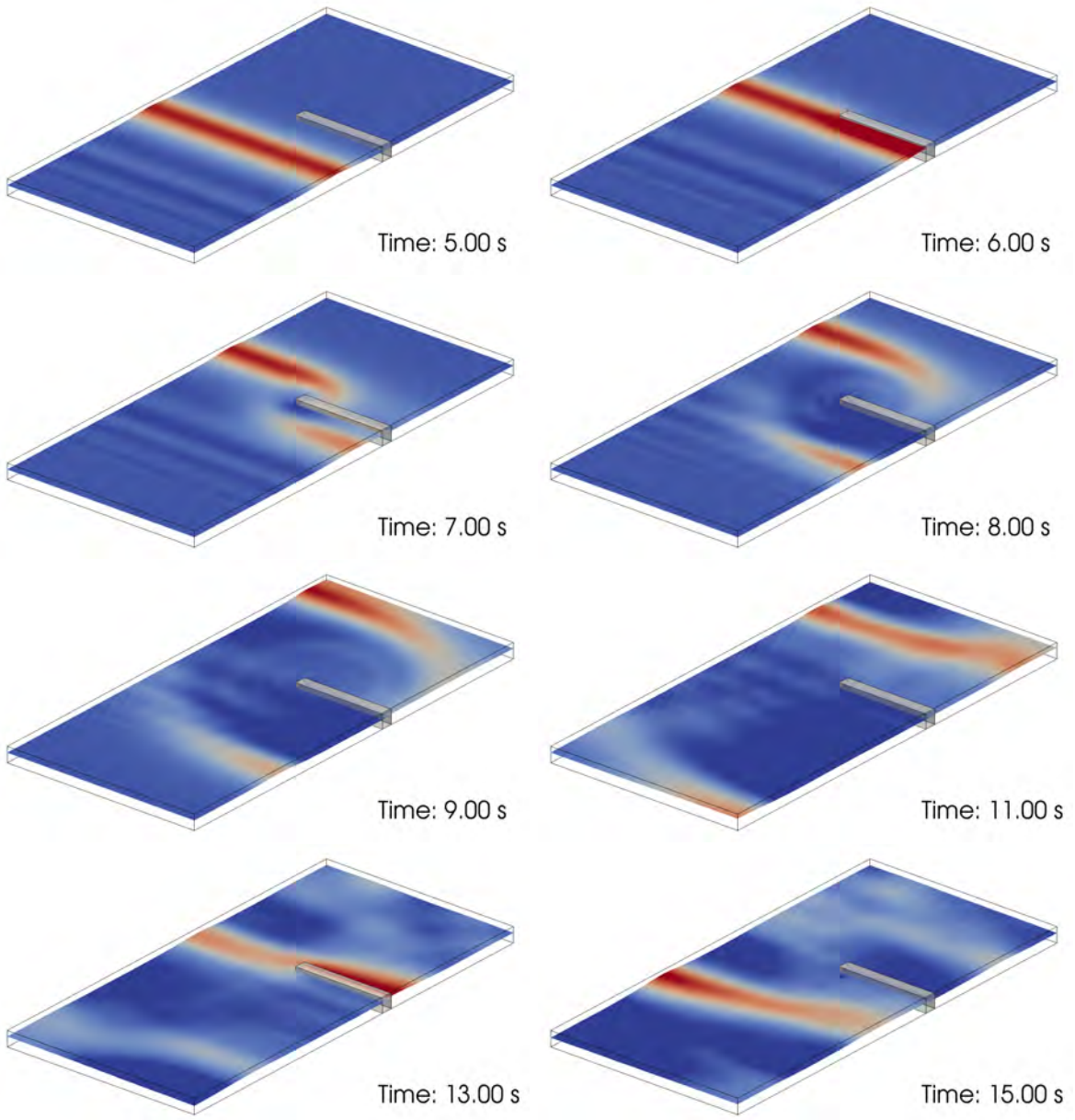

Figure 7.49: Three-dimensional interaction of waves with a porous structure. Solitary wave: free surface elevation.

evolution are studied for both cases.

The solitary wave validation is presented in Fig. 7.50 and (7.51). Several waves can be identified in the figures as a consequence of the reflected solitary wave at the basin walls. The model shows a high degree of accuracy in predicting both the free surface and pressure time series.

The model simulates quite well the energy reflected at the porous structure, as it can be seen on gauges 3 and 4 (Fig. 7.50), located seawards and close to the porous breakwater. The transmitted and diffracted wave height (see gauges 6, 7, 8 and 12) is perfectly reproduced numerically. The predictions for locations leewards the breakwater (see gauges 9, 10 and 11) also show a perfect match with measured data. A lag between the experimental and the numerical data is observed for the reflected wave towards the end of the series. The original solitary wave gets reflected at several locations on the basin: the end wall, the lateral walls and even on the wavemaker. Different reflections (and re-reflections) are in general terms well reproduced both in amplitude and shape. The lag was also reported by Lara et al. (2012) and it was attributed to discrepancies in several measurements, including the geometry of the breakwater, its location within the basin and slight variations in the location of the wave gauges. Another important factor is the reflections on the displaced wavemaker, as the numerical domain does not vary. The pressure measurements, presented in Fig. 7.51, show an almost perfect match with measurements.

Regarding the turbulence effects, several snapshots illustrate the evolution of the turbulent kinetic energy around the porous structure, as presented in Fig. 7.52. Two longitudinal transects and a plane 5 cm above the bottom are shown. The first snapshot (top left panel) shows the instant in which the solitary wave reaches the structure and starts to penetrate. The turbulent level is still relatively low. Outside the structure the k values are close to 0 outside the free surface interface zone and the corners of the structure, in which some vortices are starting to develop. A uniform base level of turbulence appears throughout the porous medium. The largest turbulence values occur near the interface of the structure, where the wave is impacting. The next time step (top right panel) shows the evolution of the system one second after. The turbulent energy base level has increased inside the porous medium. The most dissipative zone is located where the gradients of

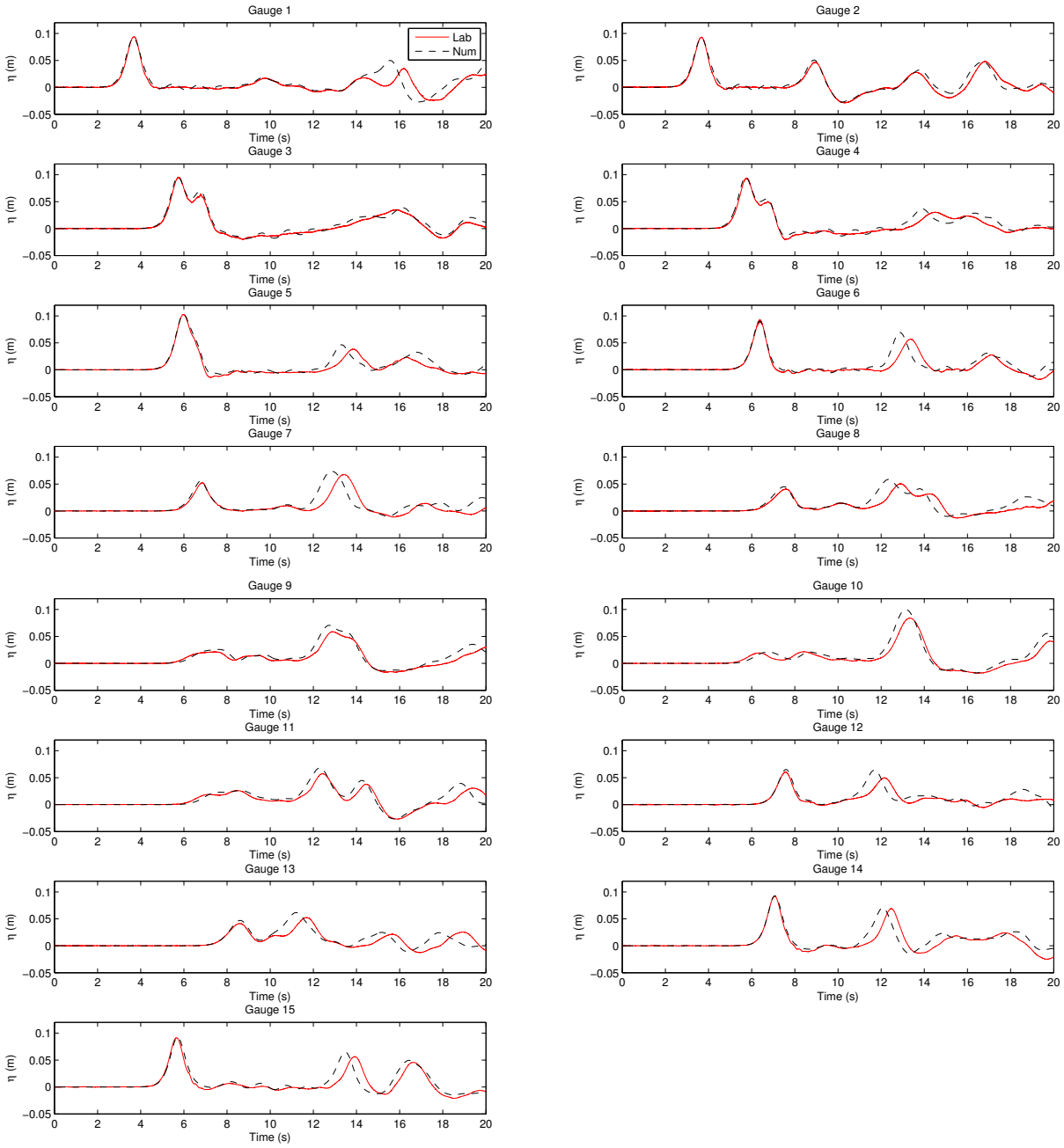

Figure 7.50: Three-dimensional interaction of waves with a porous structure. Solitary wave: free surface time series.

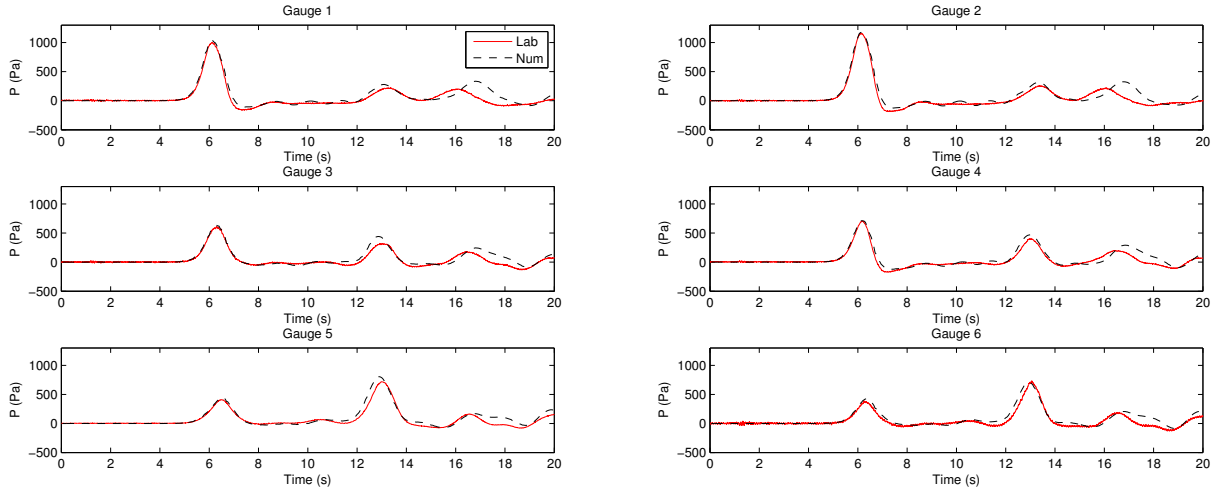

Figure 7.51: Solitary wave: pressure signals.

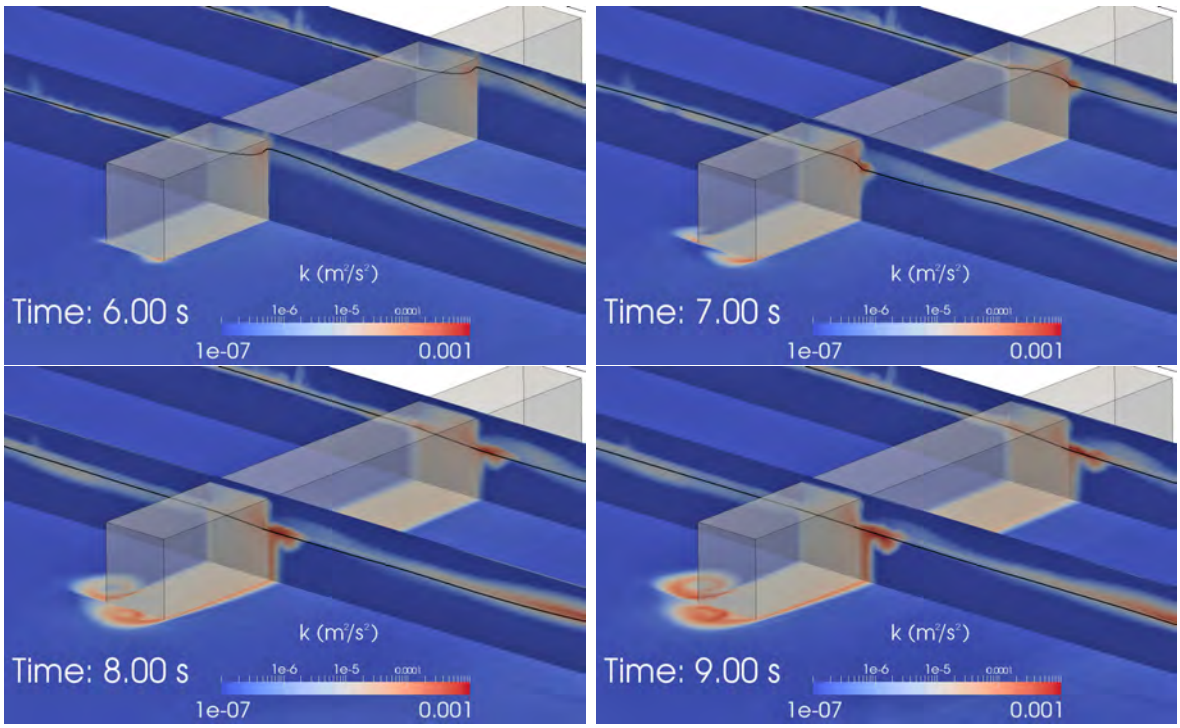

Figure 7.52: Three-dimensional interaction of waves with a porous structure. Solitary wave: turbulent kinetic energy generation.

free surface height are stronger. It is remarkable that there is also another zone outside the porous medium in which k is relatively large, and this is the area near the corners of the structure, where vortices appear. However, they do not detach, as expected, due to using $k-\epsilon$ as turbulence model, as it can be seen in the two final snapshots (bottom panels).

Fig. 7.53 shows free surface elevation along the wave tank for different instants. As observed for the solitary wave, complex processes such as the reflected, transmitted energy and the diffraction due to the gradient in wave height can be identified. Additionally, nonlinear wave-to-wave interaction is more clearly appreciated, as the wave generation boundary is continuously producing and absorbing waves. The gradient in wave height and reflections on the lateral and end walls yield complex free surface configurations as those depicted in $t = 15$ s and $t = 16$ s.

The regular wave validation is plotted in Figs. 7.54 and 7.55. A similar behaviour to the previous one is found in the comparisons between numerical data and laboratory measurements. The agreement is quite high, and the model properly reproduces the interactions between the incident and the reflected waves. Wave dissipation at the porous media seems to be well simulated because the reflected waves (gauges 3 and 4, in Fig. 7.54) and the transmitted waves (see gauges 9, 10 and 11) appear to be accurately captured in shape and in amplitude. The non-linear interactions between the incident waves with the multiple reflected waves at the boundaries are also reproduced by the model, as it can be seen towards the end of the signals presented in Fig. 7.54. The dynamic pressure measurements, plotted in Fig. 7.55, show also that the model provides a good representation of the wave-exerted pressure at the porous media.

As a summary, the overall agreement shown in the graphs is very good, proving that the model is capable of handling a three-dimensional scenario.

7.2.4 Conclusions

The validation of the model has been carried out for several cases. The comparison between the present formulation and del Jesus et al. (2012) surprisingly yields very similar results, but for radically different friction factors. These points out that the effects of disregarding the porosity in some terms of the momentum equation can be balanced by

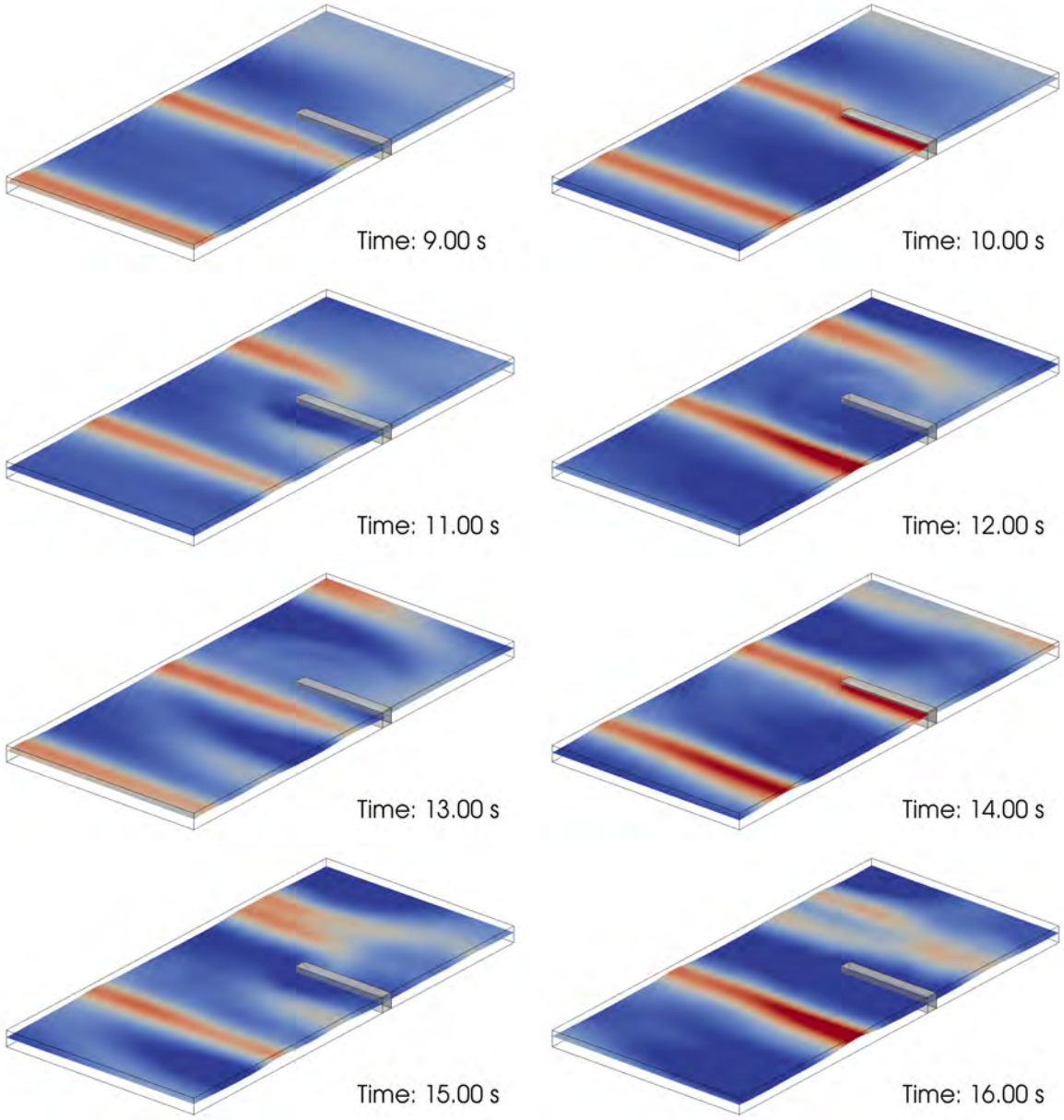

Figure 7.53: Three-dimensional interaction of waves with a porous structure. Regular waves: free surface elevation.

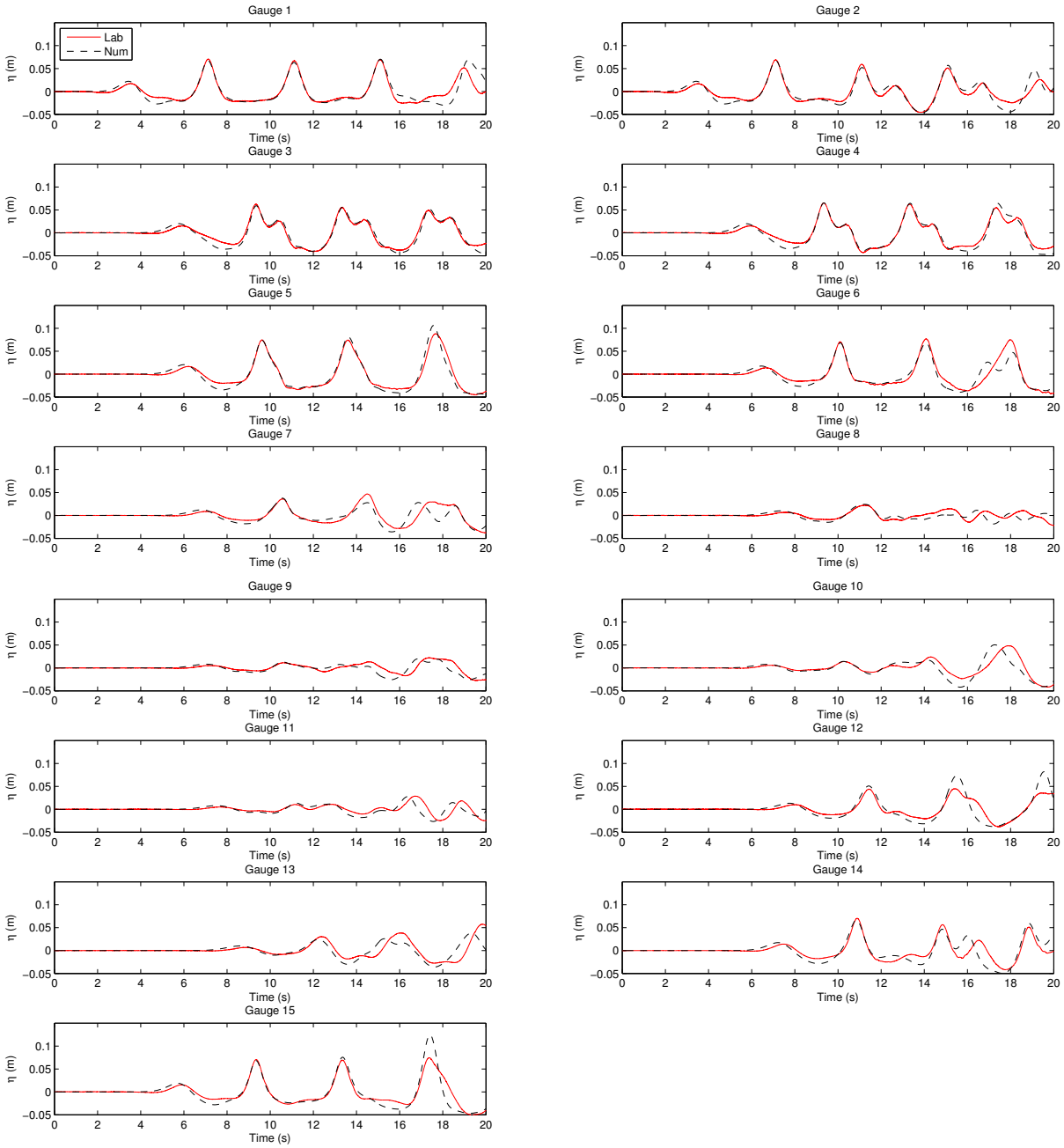

Figure 7.54: Three-dimensional interaction of waves with a porous structure. Regular waves: free surface time series.

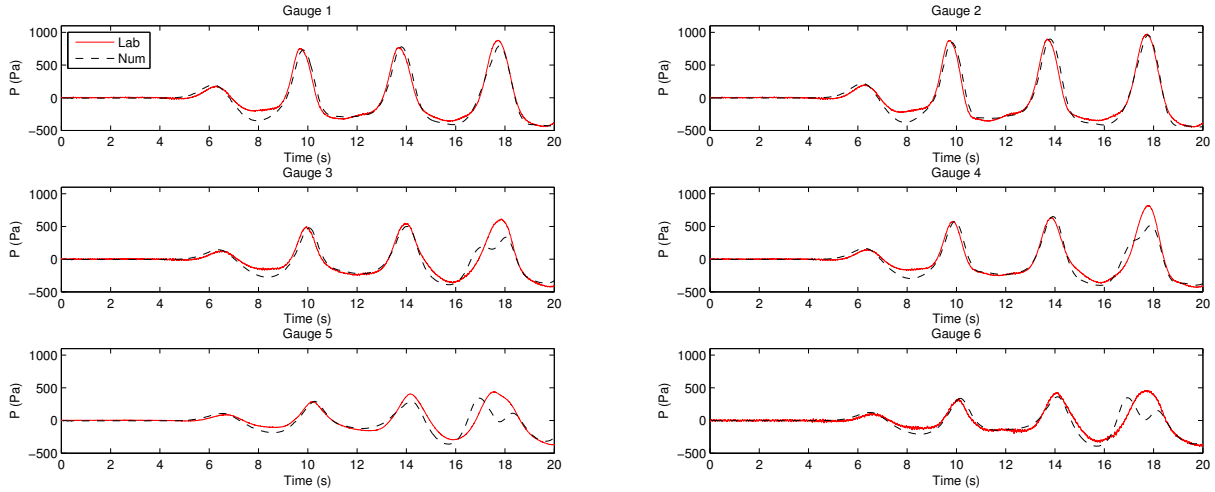

Figure 7.55: Three-dimensional interaction of waves with a porous structure. Regular waves: pressure signals.

larger drag forces without affecting much the quality of the solution.

First, a wide range of dam break flows through different porous materials have been simulated to calibrate the friction parameters. The absolute errors in free surface elevation are generally below 2 cm, which is to be seen as a very good result and as an indicator that the implementation in **IHFOAM** has been carried out correctly.

Further validation regarding wave interaction with porous structures has been considered. First, the 2D test case in which regular waves interact with a high mound breakwater shows very good results in the far field. Closer to the structure the comparisons are accurate, although discrepancies for wave height and pressure arise mainly due to the geometry of the breakwater. The 2D nature of the numerical case combined with the two-phase flow may also be another of the causes.

The three-dimensional comparisons for wave interaction with a porous structure in a wave basin show the potential of the model. The results for the solitary wave and the regular wave trains present a high degree of accordance with the laboratory data.

A special effort in assessing the effects of turbulence both inside and outside the porous media has also been carried out. Only the $k - \epsilon$ model has been used in the validation process because it is the only one with a closure model. The results indicate that turbulence is greater within the porous media, as it is generated when there is flow through. Spuriously high turbulent kinetic energy levels are also found in the free surface interface region.

Chapter 8

Application to Real Structures

The final part of this thesis is devoted to the application all the advances developed to simulate real structures at prototype scale.

Three-dimensional RANS models require a relatively large computational power to run. Although the run-times can be reasonable for test cases, as shown in the first part of this work, a 3D simulation of at least an irregular sea state of 1 hour is needed to design a non-conventional coastal structure based on the standards.

Nevertheless, at a typical **IHFOAM** rate of 2 seconds per hour, the whole simulation will take 75 days, a very long time for practical purposes. Moreover, the largest the domain, the largest the amount of output data that is produced each time step, so considerable storage capacity would be needed as well. In short, the current computational resources are not prepared yet to deal with such long simulations.

A methodology is needed to reduce the time and space domain of the simulation as much as possible, in order to rationalize the amount of computational resources needed and the simulation time required to obtain the results.

The first case is a simplified layout to test the benefits of applying the hybridization of two RANS models: **IH2VOF** in 2D and **IHFOAM** in 3D. The goal is not only prove that the hybridization of models can help reduce the run time significantly, but also analyze how stability and functionality variables can present large variations along a structure under three-dimensional conditions.

The second case is a complete application of an integral methodology to deal with a real coastal structure and environmental conditions (e.g. bathymetry, wave climate...). The methodology developed in the previous section is integrated into a much wider one,

that involves different numerical models and advanced statistical techniques to help reduce uncertainties linked to this kind of calculations.

8.1 Oblique waves interaction with a high-mound breakwater

A solution is proposed here by applying a 2D-3D hybrid methodology which not only will shorten the time and resources needed, but it will also overcome the current limitations inherent to applying semi-empirical formulations or 2D simulations only to design coastal structures.

8.1.1 Methodology

The first step of the methodology is to run a 2DV RANS simulation of a complete design sea state. A 1 hour irregular (random) sea state must be generated for the design wave height, period and frequency dispersion. The structure, idealized in 2D at this stage, should be numerically monitored throughout the simulation, so that the variables linked to the design limit state (i.e. instantaneous safety factors for sliding and overturning) can be obtained.

The initial 2D simulation serves as a method to investigate the most the critical wave effects on the structure, in terms of sliding and overturning. With the time series of pressures around the caisson, both instants can easily be obtained. From the experience, both of them occur almost at the same time, or at least within the same wave group. The majority of the times, this is the group that includes the highest wave of the sea state, although this is not always true, due to wave propagation and non-linear interaction of waves. Therefore, locating precisely this wave group is the main purpose to run the 2D RANS simulation.

This 2D simulation can be performed with **IHFOAM**. In this thesis the **IH2VOF** model (Losada et al. (2008b), Lara et al. (2011)), which has proven to yield accurate results, will be used instead. A typical 2D simulation of a 1 hour sea state at prototype scale with **IH2VOF** takes less than a day, unlike for **IHFOAM**, for which it would take approximately 5–10 times more time. Moreover, the postprocessing time for **IH2VOF** is

negligible, as it is prepared to obtain the results almost immediately after finishing the simulation.

The second step of the methodology is to run a 3D simulation of the same structure and sea state with **IHFOAM**, but restricted to the critical wave group. Since the system starts from rest, the simulation should begin around 5 mean wave periods prior to the target waves identified, so that the system is already "warmed up" when they reach the structure. With this simulation, the three-dimensional effects induced by the bathymetry or by the geometry of the structure will be taken into account.

Finally, once the 3D simulation has finished, the postprocessing procedure is carried out as usual, so the three-dimensional effects acting on the structure can be investigated and the 3D limit state regime obtained.

8.1.2 Description of the case of study

The main objective of these purely numerical simulations is to test the influence of the wave incidence angle (30°) on the limit state design variables (i.e. instantaneous safety factors for sliding and overturning) on a high mound breakwater.

The structure is a high mound breakwater located at 20 m water depth. It has been designed using Goda-Takahashi formulation (Goda, 1985) as applied in (Kim, 2009, chap. 18) for a maximum wave height of 8.1 m and a significant wave period of 10 s.

A sketch of the breakwater is presented in Fig. 8.1. The caisson, which complies with the safety prescriptions against sliding and overturning, has 7 m below and 6 m above still water level. The primary armour layer consists of two layers of concrete cubes of side 1.7 m (mean weight of 13 tons). The berm is three pieces wide and lies submerged 2 m below the sea surface. The secondary mantle is formed by two layers of rocks, with 0.8 m of nominal diameter (1.3 tons). The core is made of crushed rocks with a nominal diameter around 0.3 m. The estimated porosities are: 0.45 for the core, 0.5 for the secondary armour layer and 0.55 for the primary armour layer.

To simulate wave directionality the structure has been rotated within the domain. This way the base mesh would be the same and waves would always be generated in identical manner regardless of the incidence angle.

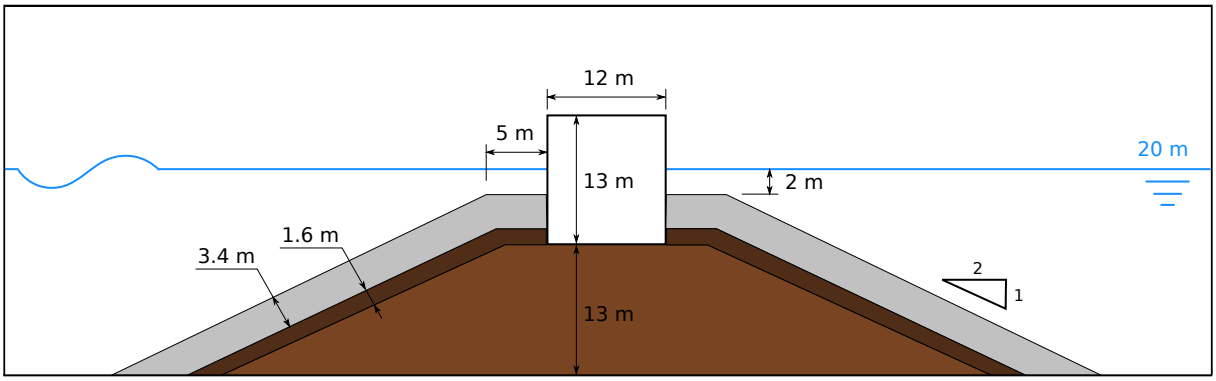

Figure 8.1: Section of the high mound breakwater.

8.1.3 Numerical setup

8.1.3.1 2D case

The numerical setup for **IH2VOF** corresponds to a slice of the hypothetical three-dimensional domain for 0° incidence angle, taking a plane normal to the Y axis. For the axes definition see Fig. 8.2. Since **IH2VOF** has its own meshing tool, the 2D and 3D meshes are generated independently. However, it is advised to mesh (or at least to sketch) the case in 3D first, so that both are as similar as possible in order to avoid a grid influence in the numerical simulations.

As sketched in Fig. 8.2, the caisson has been placed 200 m away from the wave generation boundary (right wall). The outflow boundary has active wave absorption condition connected and is located 133 m leeside of the structure (left wall).

The mesh is composed of three zones in the X direction and two zones in the Z direction, with variable cell sizes. First, a wave propagation zone was prepared in the X direction, in which$\Delta\ x$ varies from 1 m at the generation boundary to 0.25 m, 10 m away from the caisson. Next, a uniform zone in which$\Delta\ x$ is equal to 0.25 m spans for 80 m. The width of this second zone is chosen so that the structure lies within it on the 3D mesh, for the 30° rotation angle. Finally, a 75 m long zone leads to the absorbing boundary, grading the cell size from 0.25 m to 1 m. In the Z axis the vertical cell size varies from 0.5 m near the bottom to 0.25 m at the initial free surface level, and then it is maintained throughout the remaining height. The final mesh is orthogonal and conformal, and has less than 100,000 cells.

The wave forcing corresponds to an irregular sea state that follows a JONSWAP

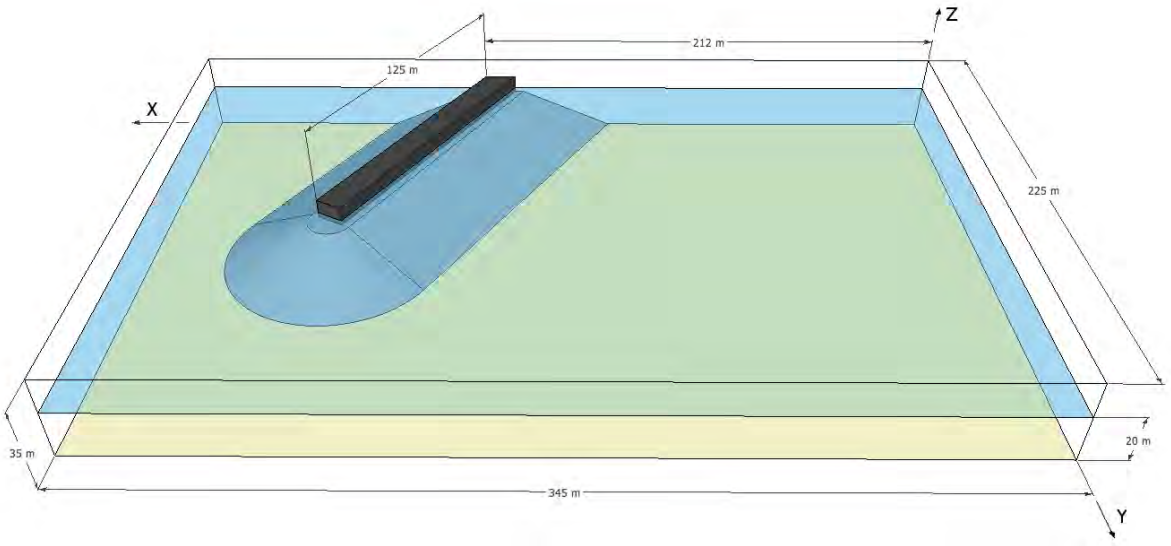

Figure 8.2: Three-dimensional sketch of the domain and the breakwater.

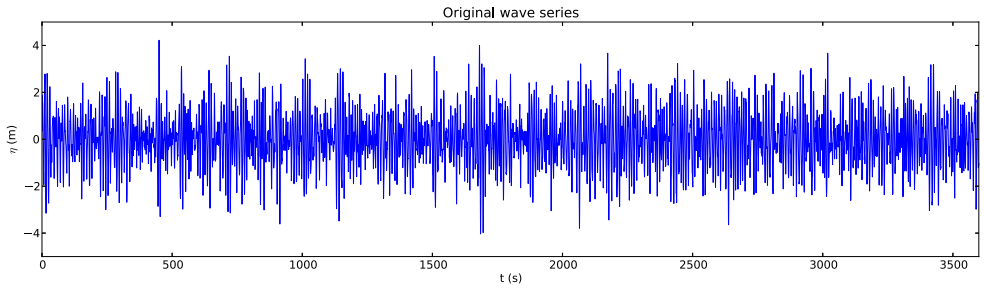

Figure 8.3: Irregular sea state.

spectrum of $H_s = 4.5$ m, $T_p = 10$ s and $\gamma = 3.3$. The random waves have been obtained based on an iterative process, ensuring that the sea state obtained is representative of the parameters provided. This is done reconstructing a free surface series, carrying out an upcrossing analysis and comparing the obtained values for H_s and T_p with the theoretical ones. On top of that, an additional condition regarding the highest wave height on the sea state, which must be at least 1.8 times H_s, was checked. A 2% error was allowed in this process.

The free surface elevation of the simulated sea state is presented in Fig. 8.3. An upcrossing analysis of the signal yields the maximum wave height: 8.04 m, which takes place at $t = 1707$ s. Afterwards it will be shown that the greatest event in terms of the total dynamic force on the caisson is associated to this particular wave.

The closure terms in the VARANS equations are implemented differently in **IH2VOF**, therefore, there is no direct equivalence between the porous media parameters used in it

and those applied in **IHFOAM**. Hence, a set of parameters which are known to work with rubble mound breakwaters were used. The estimated porosities and mean rock size previously introduced have been used.

The 1 hour sea state simulation is completed with **IH2VOF** in less than 19 hours.

8.1.3.2 3D case

The numerical mesh is created around an impervious obstacle (i.e. the caisson). The first step is to create a base mesh. Then, the obstacle is removed using *snappyHexMesh* and finally snapped to the original surface for a better definition of the obstacle, yielding the final mesh.

The base mesh has the shape of a box (345 x 225 x 35 m), and is orthogonal and conformal. It presents 3 zones in X, 2 zones in Y and 2 zones in Z, with variable cell size. Similarly to the 2D version, the zones in X and Z match. The major difference is that the discretization is half, so the cell sizes presented for the 2D case are multiplied by 2. Regarding the 2 zones in the Y direction, the first one spans for 135 m with constant resolution of 0.5 m, thus covering the area where the structure is located. Then, on the second zone, the$\Delta\ y$ grows up linearly to 1 m, 90 m away from the end of zone 1. Once the base mesh is ready, the structure is removed without performing additional refinement around its surface, yielding a mesh with 10 million elements.

The smallest cell in the 3D mesh is a cube of side 0.5 m, hence, the resolution is not very good. If the size of all the cells were half they would be equal to the ones in the 2D case. However, the base mesh would have near 80 million elements, and be very difficult to handle and would need enormous computational resources. A more convenient method is applied to obtain the required discretization: dynamic mesh refinement along the free surface.

The dynamic mesh refinement along the free surface is already provided in OpenFOAM®. Nevertheless, an improved version had to be developed so that it could be applied to meshes created with *snappyHexMesh*. The tool has been integrated in the solver, and refines the mesh by splitting the cells in halves. Refinement occurs at the interface between both phases, defined as the cells where α_1 ranges from 0.01 to 0.99 and their immediate neighbours. An example can be seen in Fig. 8.4. This system also handles un-refinement

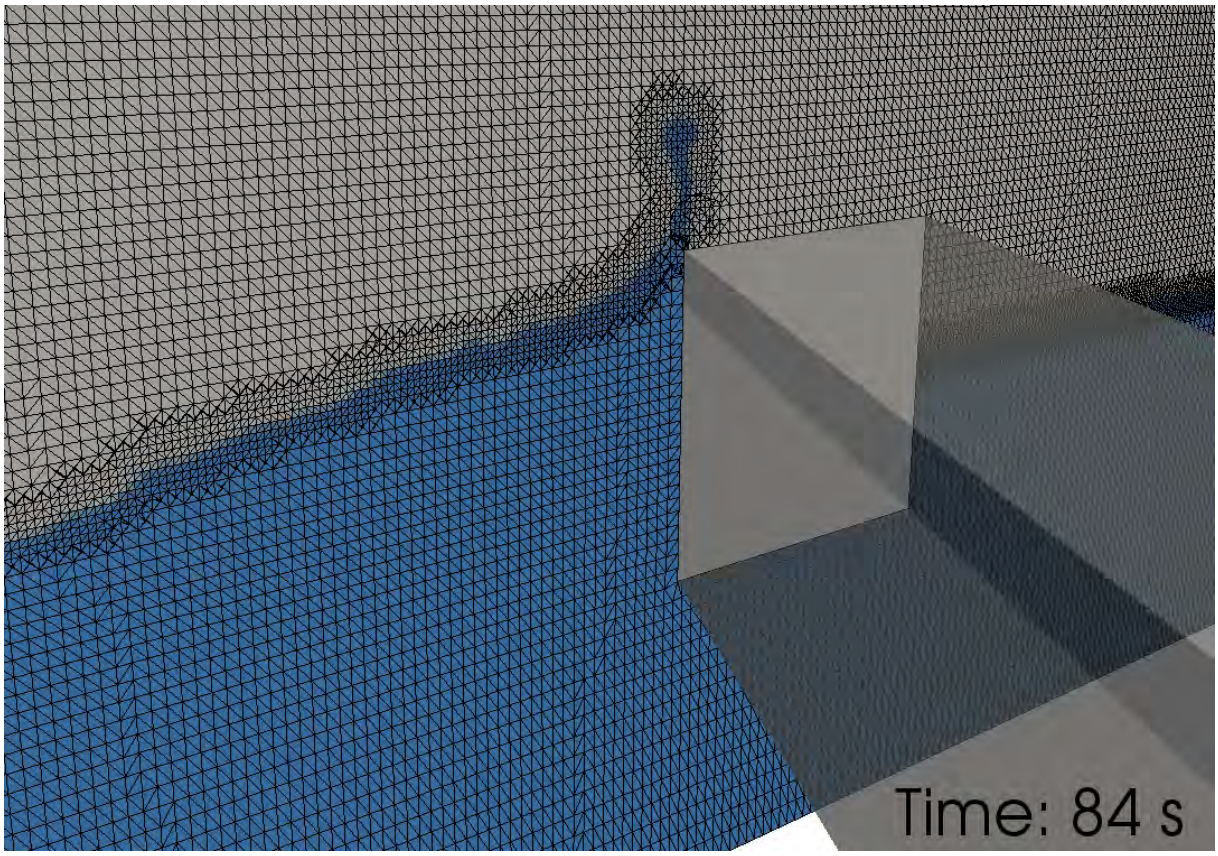

Figure 8.4: Dynamic mesh refinement. Most of the cells are hexahedral, as the triangulation shown is only a visualizing artefact. Water is the dark phase, and air is the light phase.

when necessary. The refinement process takes place each 10 time steps and it is not fast, as it almost doubles the time it takes to calculate a regular time step. During the simulation the number of cells varies constantly, but a mean of 20 million is obtained for this case.

Wave generation linked with active wave absorption takes place at the boundary located at $X = 0$, using the spectral components which lead to the free surface elevation signal in Fig. 8.3. The phases have been shifted accordingly to start at $t = 1625$ s in the **IH2VOF** simulation time, other than that, the data that feed the model are identical. Ten individual slices of the boundary are considered to actively absorb the incoming waves independently while generating, so that free surface variations along the generation boundary due to the reflection pattern can be handled. The boundary opposite to wave generation is purely absorbent. It is also divided in 10 slices which work independently for the same reason. The lateral boundaries are set to a free slip boundary condition, this

way the incoming waves do not get distorted.

The turbulence is modelled using the porous $k-\omega$ SST model, which is applicable in cases in which large flow separation can be expected. In this case such process will most likely take place on the rubble mound and on the breakwater front. All the fields are stored each 1 second for the first 70 seconds of simulation. As this is the warming up time, no more resolution is needed. From $t = 70$ s until the end of the simulation ($t = 110$ s), all the fields are saved at 20 Hz.

The simulation rate is of more or less 200 seconds per week, parallelizing the case into 96 processors (2.6 GHz).

8.1.4 Numerical results

8.1.4.1 2D case

As it mentioned before, the 2D simulation has been run first to calculate the critical instant for the structure in terms of sliding and overturning. The pressure time series around the structure are integrated to calculate the time series of forces and moments to which the structure is subjected. Then the safety factors are calculated as follows:

$$C_{SD} = \mu \frac{\mathrm{W_{Caisson}} - \mathrm{Uplift}}{\sum \mathrm{F_{Horizontal}}} \tag{8.1}$$

$$C_{OT} = \frac{\mathrm{Mom._{W.\ Caisson}}}{\sum \mathrm{Mom._{Horizontal\ F.}} + \mathrm{Mom._{Uplift}}} \tag{8.2}$$

where C_{SD} is the safety coefficient against sliding, in the same manner that C_{OT} is the safety coefficient against overturning. $\mathrm{W_{Caisson}}$ is the weight of the caisson, Uplift denotes the uplift force and $\mathrm{F_{Horizontal}}$ considers the rest of the horizontal forces. Mom. stands for momentum, and the subscript indicates the force by which it is produced. Finally, μ is the friction factor between the caisson and the core, which takes the typical value of 0.7.

The two-dimensional results are presented in Fig. 8.5. The sliding coefficient is shown in the upper panel, while the overturning coefficient is shown in the lower panel. The lower dashed line indicates the minimum threshold which may never be surpassed. The global minimum of the time series is marked with a circle. It can be noted that it occurs at the same instant ($t = 1707$ s) for both panels, therefore it can be concluded that in this

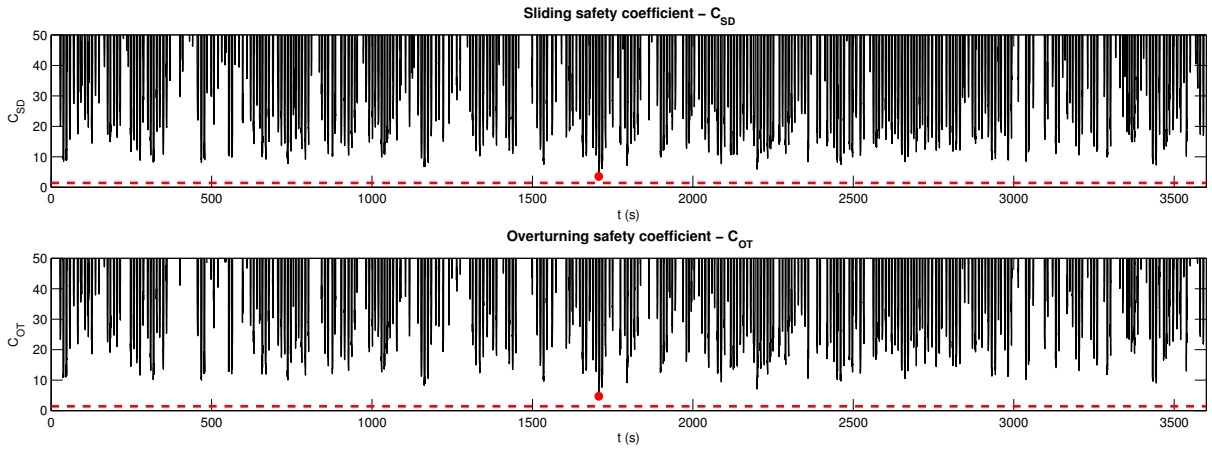

Figure 8.5: Evolution of safety coefficients on the caissons for the 2D case. The global minimum is marked with a circle.

particular case the limit state is linked to the highest wave group. This analysis yields the shifting time before the 3D simulation is started ($t = 1625$ s, as already mentioned).

8.1.4.2 3D case

In this section the three-dimensional results are analysed. The breakwater has been divided in 5 independent caissons of 25 m in length, as presented in Fig. 8.6.

The evolution of the safety coefficients against sliding and overturning are calculated for each of the caissons first. The dynamic pressure distribution is obtained all along the breakwater, considering 1-m-long slices (i.e. 25 profiles per caisson) and a 10 cm resolution between points. The integration of the 3D pressure yields the forces and the moments that act on the caisson. Finally, the safety coefficients are calculated.

The safety coefficients (top panels) and dynamic forces (lower panels) for the five caissons are plotted in Fig. 8.7. As it can bee seen, both safety coefficients (sliding represented as a continuous line and overturning as a dash-dot line, in the top panels for each caisson) evolve similarly, having more or less the same shape when the seaside force presents a crest (see lower panels, in continuous line). The sliding coefficient decreases as well when the minimum in the seaside force is obtained, associated with a wave trough. However, the magnitude is smaller than for the previous case. It is remarkable that the uplift force (dotted line, lower panels) is in phase with the seaside force, while the leeside force (dash-dot line, lower panels) presents a phase lag dependent on the location of the caisson.

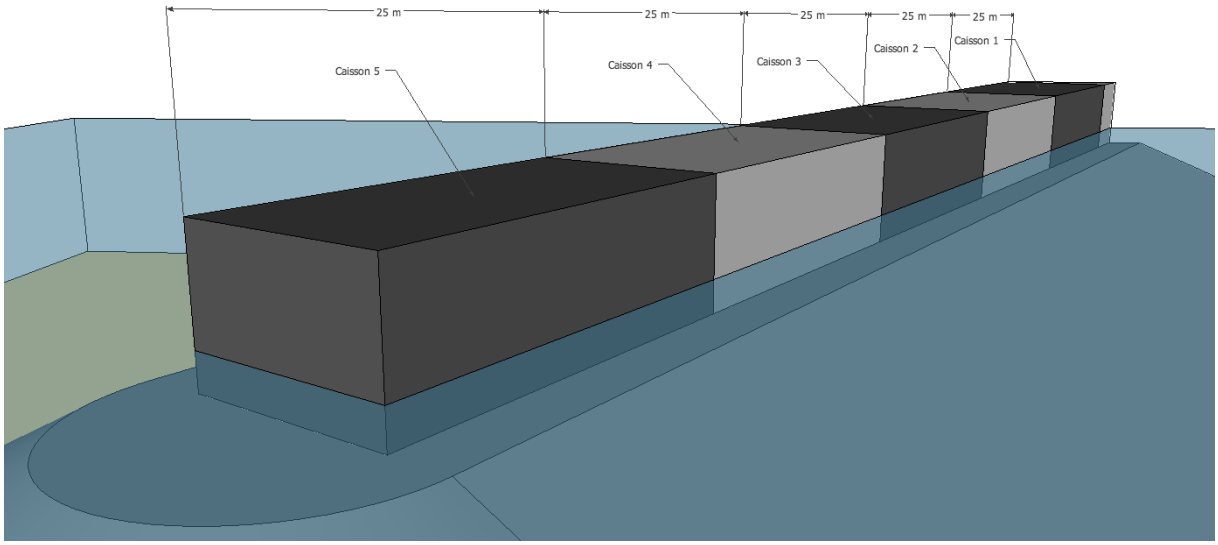

Figure 8.6: Individual location of the caissons.

The minimum safety coefficients have been extracted and gathered in Table 8.1, along with the time of occurrence. For the first 4 caissons, the critical instant is associated to the first of the two high waves of the group. For the caisson number 5, which is located at the breakwater head, the second wave impact is of larger magnitude. Although the first impact is also considered, the second is the most critical and is named *Caisson 5 Prime*. The values in Table 8.1 show that the breakwater is never in danger of failing for this extreme design sea state, as the safety coefficients are larger by far than the 1.4 design value.

The Goda-Takahashi pressure distribution (Takahashi et al., 1994) has been calculated using the sea state significant wave height as a starting point and the 30° incidence correction angle (Tanimoto et al., 1976). There is also another factor that has been taken into account. The correction term presented in Burcharth and L. (1999) [Eq. 5] reduces the effective pressure acting on the caisson, as it takes into consideration that due to the oblique incidence the maximum pressure does not take place along the whole caisson at once. The calculation for long-crested waves yields a factor of 0.983, which is less than a 2% reduction.

Although the mean measured pressure distribution among the 25 sections is close to the theoretical one, the formulation yields safety factors 3.3 and 3.34 for sliding and overturning, respectively. The theoretical sliding coefficient is systematically higher than

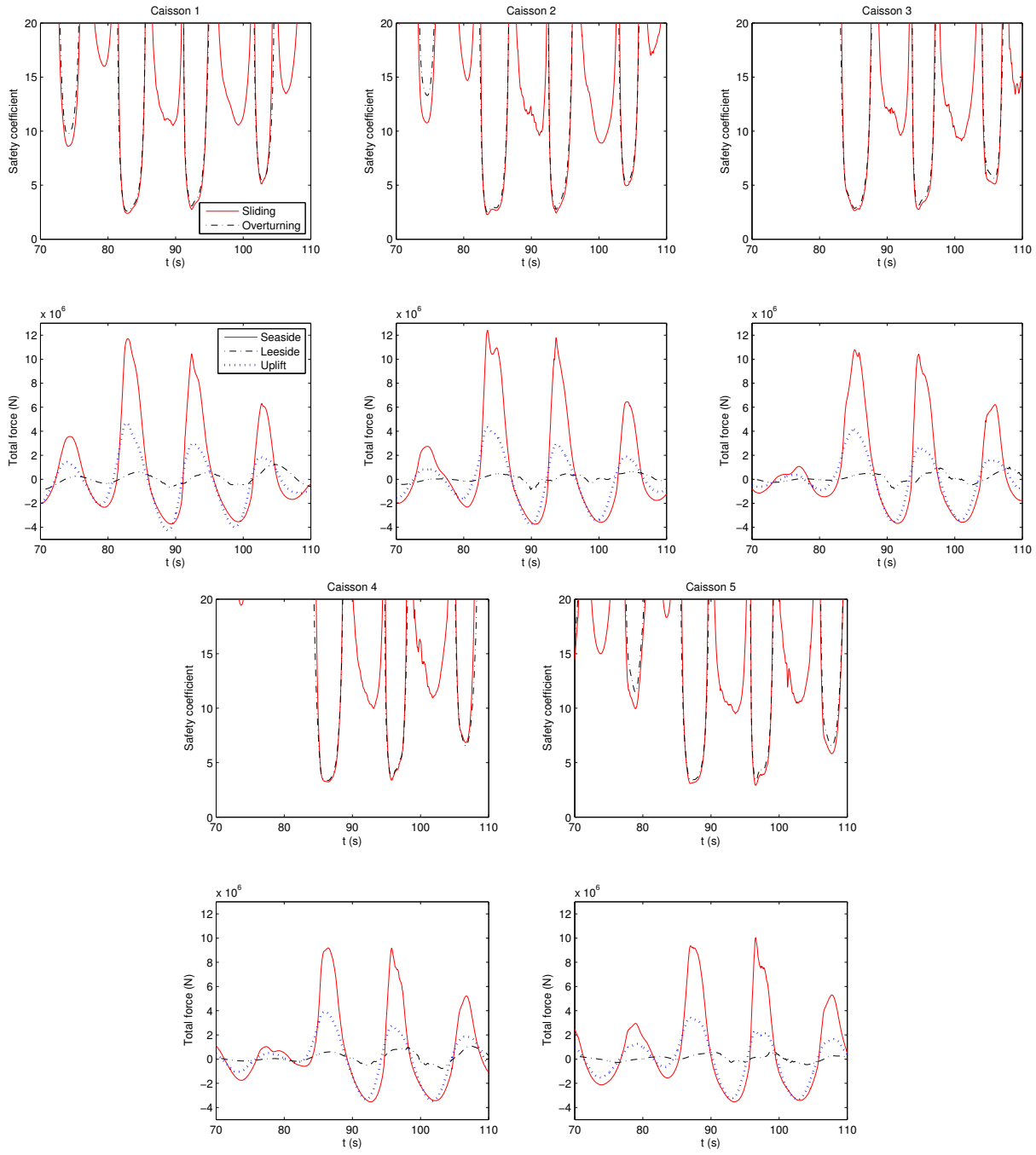

Figure 8.7: Evolution of safety coefficients and total forces on the caissons.

	Sliding		**Overturning**	
	SC	t (s)	SC	t (s)
C1	2.39	82.3	2.59	82.3
C2	2.26	83.0	2.48	83.0
C3	2.64	84.6	2.86	84.65
C4	3.23	85.9	3.36	85.85
C5	3.08	86.45	3.36	86.45
C5′	2.92	95.95	3.35	95.95

Table 8.1: Minimum safety coefficients on the caissons.

the ones obtained numerically. This indicates that the three dimensional effects are not negligible, as they are not on the safe side.

Fig. 8.8 includes the seaward, leeward and uplift pressure distribution on each of the caissons for the most critical instant. The Goda-Takahashi expected pressure distribution for this incidence angle (dashed line) is also plotted. The mean numerical pressure is represented scaled as a dash-dot line, while the maximum and minimum pressures along the caisson are represented as dotted lines.

The seaside pressure laws for caissons 1 and 2 resemble in shape and magnitude the theoretical approach by Goda and Takahashi. For the rest of the caissons the numerical pressure is noticeably smaller than the theoretical one, probably because of the three-dimensional effects induced by the reflection of the waves. Nevertheless, the first wave impact yields a consistent shape all along the breakwater. In general, the seaside pressure towards the top part of the face is smaller in the numerical model. This indicates that Goda-Takahashi predicts a higher run-up and splash. The uplift pressure is also systematically found smaller (from 20% to 50%) depending on the location. The second impact is shown for case *Caisson 5 Prime* (bottom right panel) only. The shape of the mean pressure is not so linear, but more pointed with smooth transitions, and large variations appear between the smallest and largest values. In fact the maximum pressure shows a very pronounced peak which almost doubles the pressure predicted by Goda-Takahashi.

In order to understand better the process of the waves impacting the caissons the reader is referred to Fig. 8.14, which will later be used to explain the overtopping pattern. This figure features snapshots of the first wave of the group, which causes the worst safety scenario for caissons 1–4. It is noticeable that this wave is not broken and it does not break onto the structure either. What is interesting to note is that the splash is turning

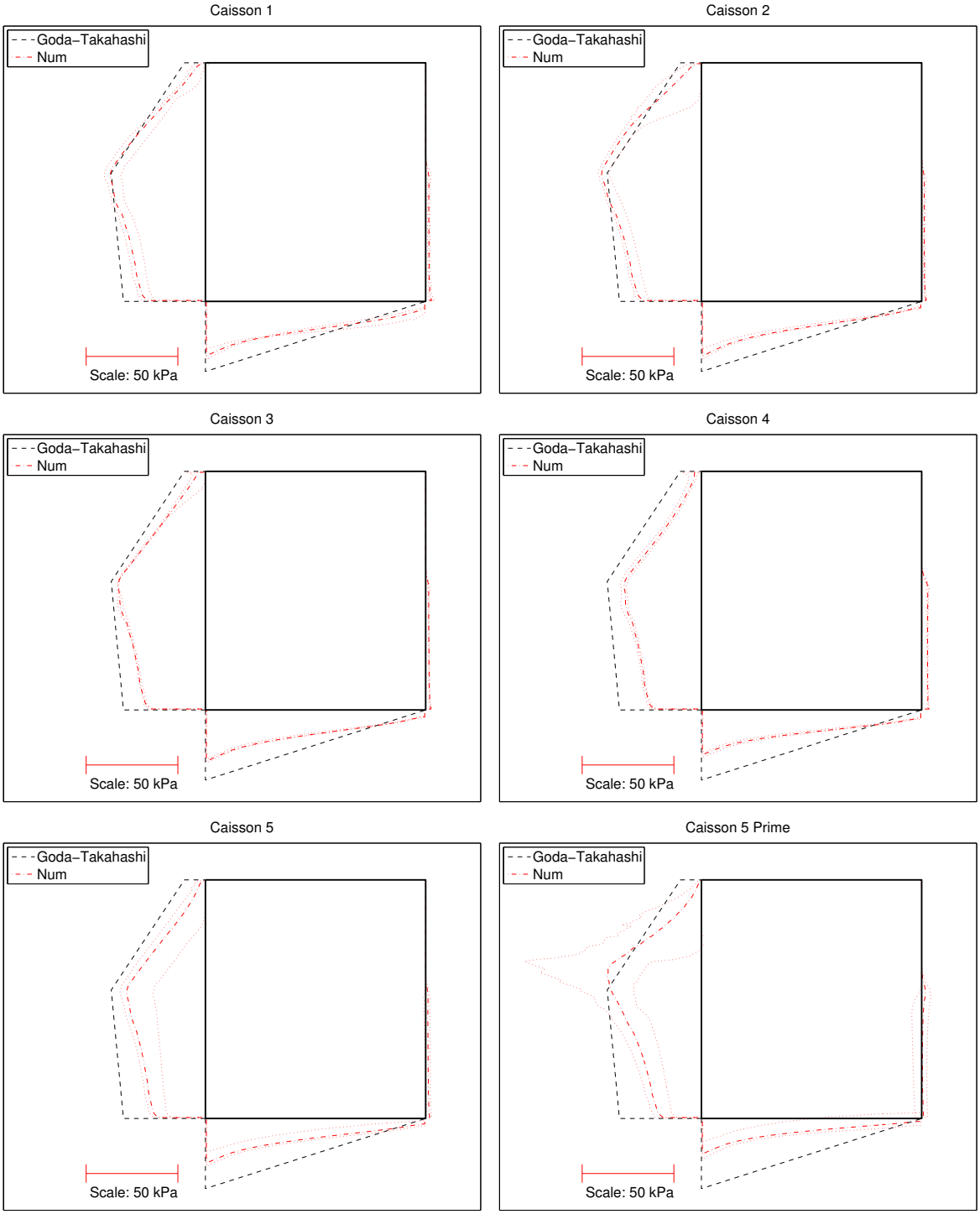

Figure 8.8: Pressure distribution on the caissons for the most critical instant.

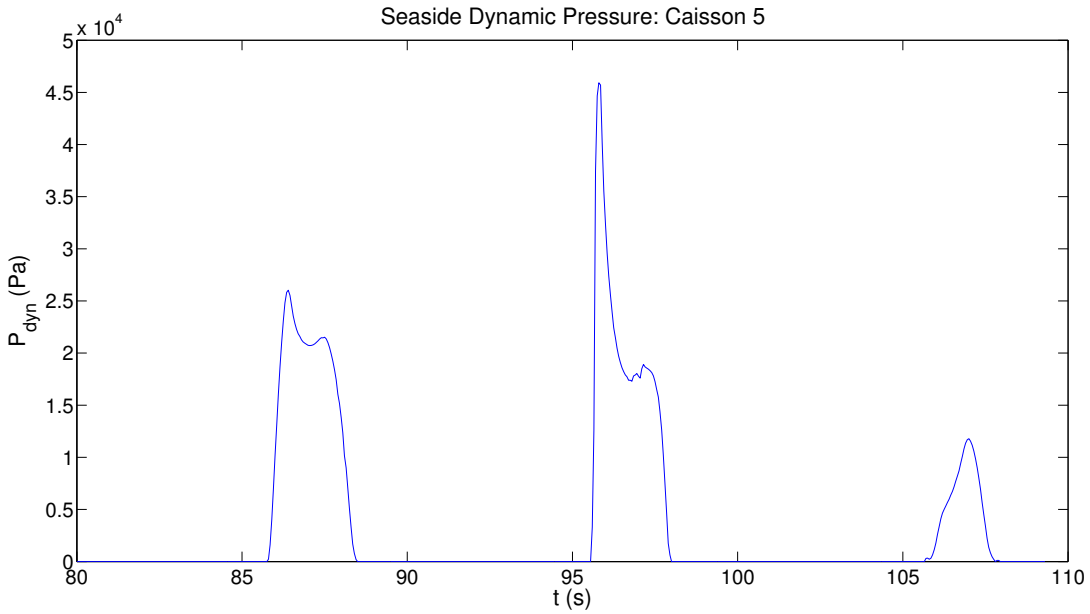

Figure 8.9: Dynamic pressure in the midpoint ($X = 112.5$ m, $Z_{\text{local}} = 6.5$ m) of the seaside wall of caisson 5.

backwards conforming the reflected wave that propagates away already broken (see $t =$ 86 and 88 s). The interaction between the reflected wave and the second wave of the group makes that the latter one arrives completely broken to the structure (barely visible in the center of Fig. 8.13).

The time series of the dynamic pressure acting on the midpoint ($X = 112.5$ m, $Z_{\text{local}} =$ 6.5 m) of the seaside wall of caisson 5 is presented in Fig. 8.9. The result is in accordance with the observations made in the previous paragraph regarding the two main waves. The first wave produces a non-impulsive impact. The second wave presents a large spike, which is almost double than the subsequent sustained pressure, and is the result of a broken wave impact. This proves that even though **IHFOAM** is a solver for two incompressible phases, impulsive pressure peaks can be detected. Furthermore, treating the wave breaking in 3D makes the air to scape sideways (unlike in 2D simulations) when impacting, which yields a more realistic pressure distribution.

In Fig. 8.10 the dynamic force acting on a vertical slice located in the middle of the seaside face of each caisson is presented in the left panel. The theoretical force given by the Goda-Takahashi formulation is represented in a horizontal red dashed line. The instantaneous dynamic pressure distribution on such slices for the instant with the largest force (marked with the vertical black dashed line in the left panel) is shown in the right

panel. The first impact is more or less even throughout the whole structure, presenting small variations only, inherent to the three-dimensionality of the processes. The second wave is more interesting. It shows a peak resulting from the localized impulsive impact, and is decreasing towards the breakwater head, as the wave is losing height due to the local breaking process.

The instantaneous pressure distribution in the right panel (blue dots) is quite different from the ones shown in Fig. 8.8. The comparison with the Goda-Takahashi distribution, represented as a black dashed line, confirms the impulsive nature of the impact, that can be inferred from the distinctive shape of the pressure law. However, as it has already been pointed out, the impulsive effects are so localized that the most restrictive safety factors occur for the first wave impact.

The difference between the impacts on caisson 5 (first wave) and 5 prime (second wave) is more clear in Fig. 8.11. In it the whole three-dimensional pressure distribution around the fifth caisson (top panel) and a contour of dimensionless dynamic pressure on the seaside wall ($P_{dyn}/(\rho g H_s)$, bottom panel) are plotted. The left panels show the first impact and the right panels show the second one. No pressure scale has been included because of the perspective, but the reader is either referred to the bottom panel or to Fig. 8.8 (lower panels) for an order of magnitude. The first impact presents an even pressure distribution throughout the seaside wall of the caisson, just showing a slight increase in pressure where the wave crest is located (X_{local} between 7.5 and 15 m), right at the initial water level (white dashed line). The second impact presents a large peak close to the end of the caisson, much larger in magnitude (almost double than that on the left panel). The effect is very concentrated and located one metre above the initial water level. The leeside and bottom faces do not show significant changes between both cases. However, the front wall presents a noticeable depression for the second impact due to the drag induced by the greater flow separation.

The evolution of the free surface around the structure for the first remarkable wave impact is shown in Fig 8.12. The free surface is coloured according to the module of the water particle velocity. The wave starts to impact on the first caisson ($t = 82$ s) and continues propagating towards the breakwater head. Overtopping can be observed starting at $t = 84$ s encompassed with wave reflection, which propagates away from

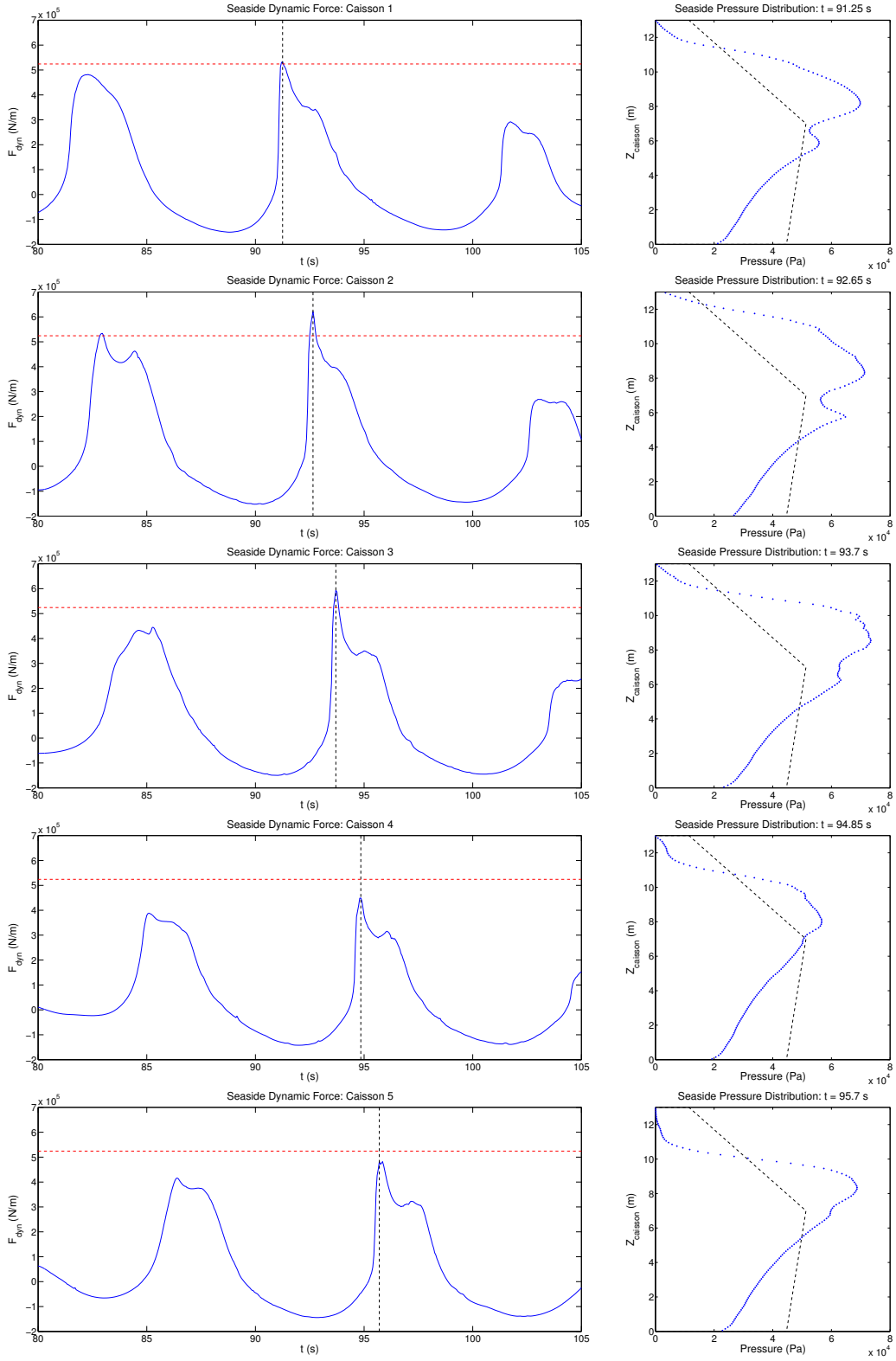

Figure 8.10: Dynamic force acting on a vertical slice (left panel) and dynamic pressure distribution for the instant with the largest force (right panel).

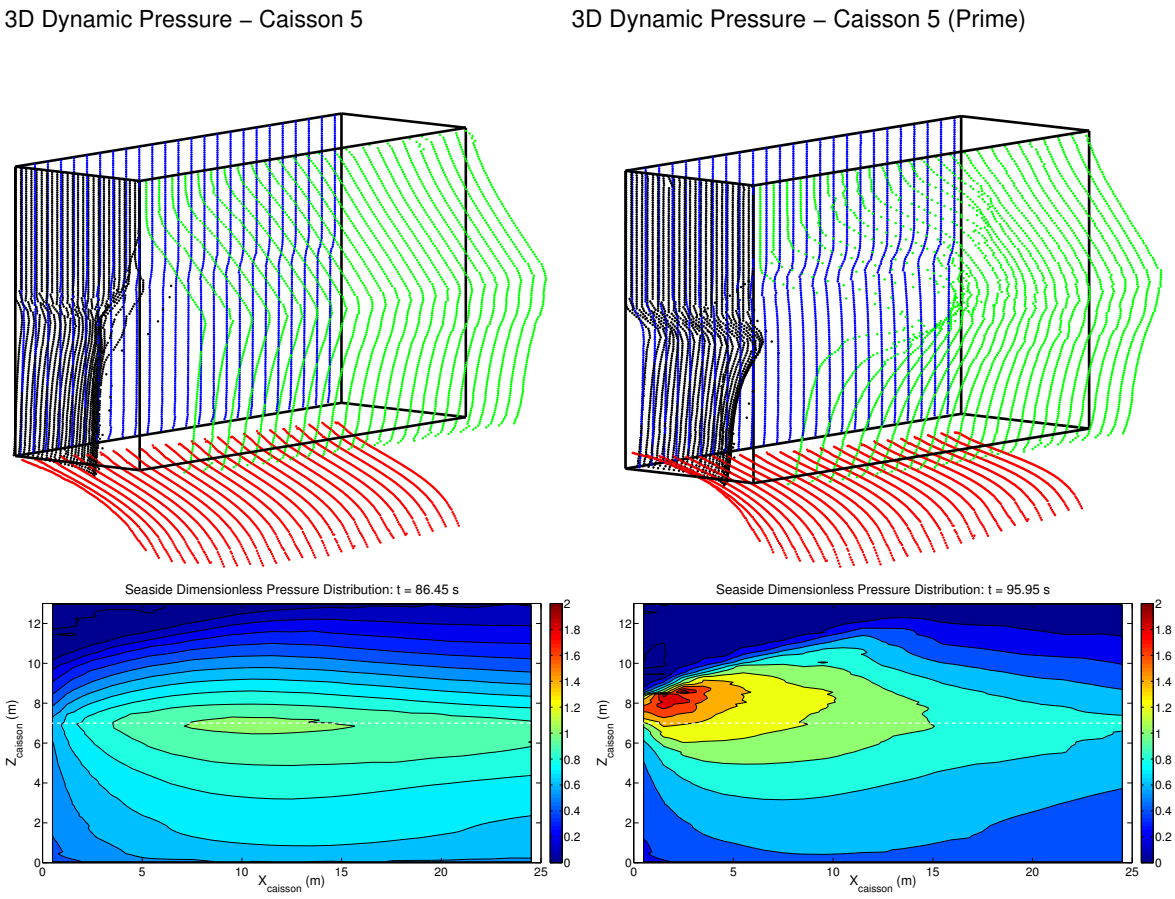

Figure 8.11: 3D pressure distribution on caisson 5 for the two critical instants. Lower panel represented with a local coordinate system.

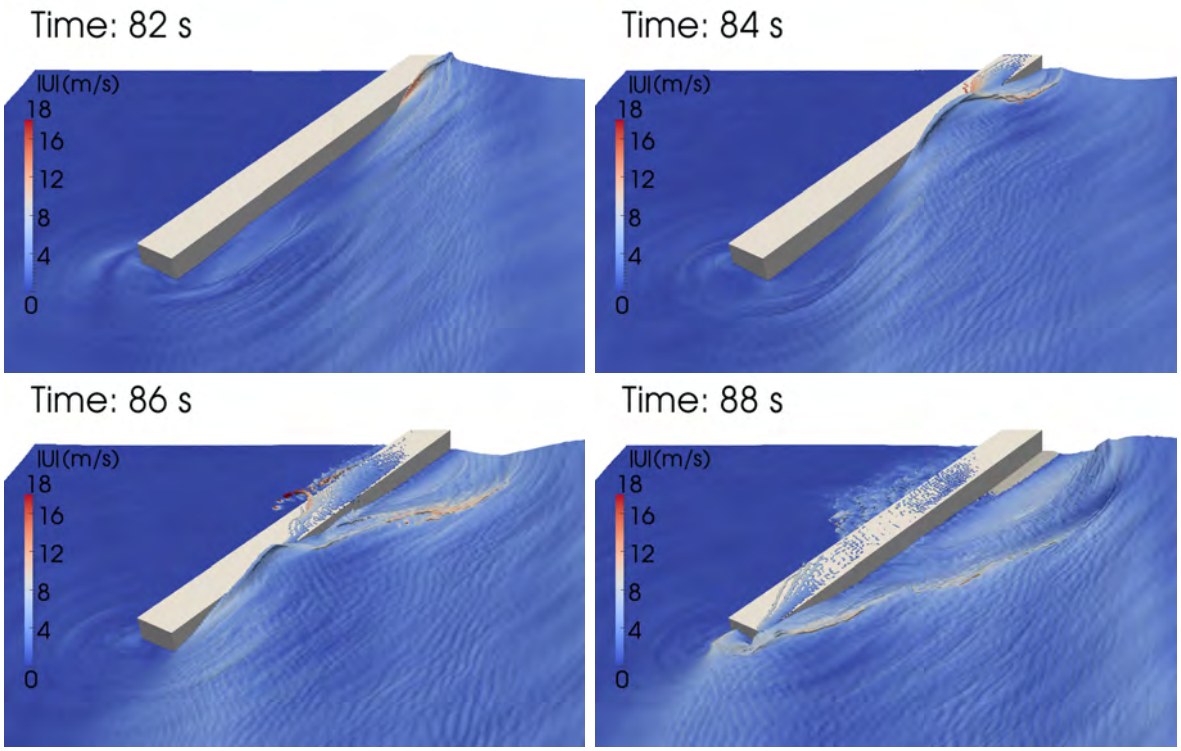

Figure 8.12: Free surface around the breakwater for the critical wave impact and water particles velocity module.

the caissons. Wave diffraction at the breakwater head can be distinguished in all the snapshots. The second high wave to reach the structure can be spotted in the last frame, interacting with the reflected wave prior to impacting the structure. The primary armour layer appears dry on this last picture, towards the zone of caisson 1, due to the arrival of the wave trough.

A more detailed view of the strongest impact on caisson 5 is presented in Fig. 8.13. The incoming wave is already broken, and even some pockets of air are trapped and can be seen in the snapshot. This can also be inferred from the shape of the seaside force (Fig. 8.7,caisson 5, bottom panel). Therefore, the pressure distribution corresponds to impulsive loading.

The whole sequence of overtopping can also be observed in Fig. 8.13 starting from the breakwater head. First, the wave impacts and splash occurs. In this case it reaches 5 m above the crest level. The splash continues to advance and falls gradually, impacting the surface of the breakwater. Finally, it falls on the other side of the caisson.

A quantitative analysis of the overtopping is presented in Fig. 8.14. The instantaneous overtopping discharge rate is plotted as a function of the simulation time and the local

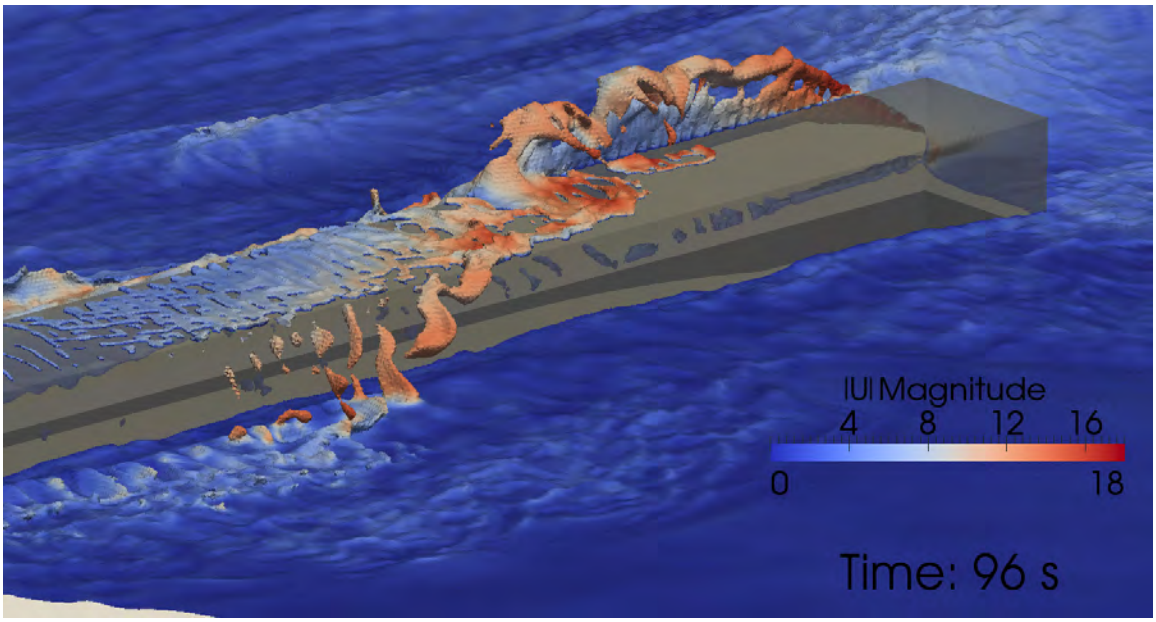

Figure 8.13: Critical wave impact for caisson 5.

coordinate on the breakwater. The caisson 1 starts at Dist = 0 m and the caisson 5 ends at Dist = 125 m. A total of 125 measurements have been taken over the breakwater at a 20 Hz sampling rate. The three-dimensional effects are clear. The first wave produces a maximum overtopping rate of around 9 m^3/s between the first two caissons. Then it is reduced drastically and becomes more or less even for the rest of the caissons (2.5 m^3/s). The second wave is influenced by the previous (reflected) wave, as the overtopping rate for the first caissons is cut almost a half. The rest of the caissons suffer from an increase of overtopping rate. The effect is more pronounced on the last caisson, in which it is almost triple. The results point out that overtopping is a magnitude highly dependent on the location and on the preceding waves, so in order to study it from a statistical point of view, very long simulations will be needed.

Another relevant variable that can be studied is the velocity of water particles, as there are studies (Tørum, 1994) that correlate the velocity magnitude above the breakwater primary armour layer with the forces occurring at each of its elements.

In the left panel of Fig. 8.15 the distribution of particle velocities on a plane 10 cm above the bottom is represented. The right panel shows the same situation but with a different color scale, as the velocities on the outer layer of the breakwater are superposed. As expected, the velocity is lower inside the porous media and it continues to decrease until it reaches the core due to increasing frictional effects. The places where the horizontal

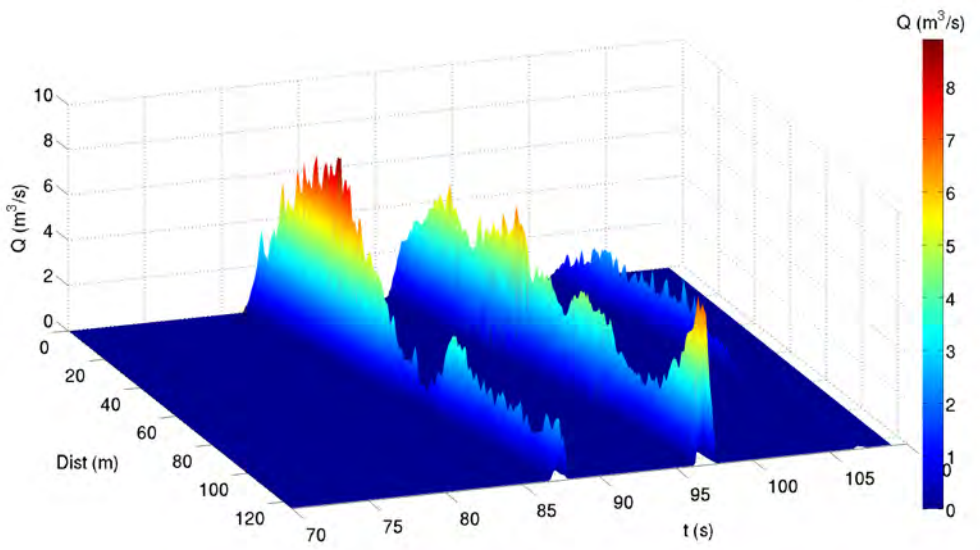

Figure 8.14: Space-time series of instantaneous overtopping discharge rate.

particle velocity changes direction are easily distinguished with a dark blue colour, between the red zones. Trying to follow them from the top boundary of the figure yields to the conclusion that the water particle velocities increase above the porous media, due to the effective decrease in water depth.

The rocks are subjected to a velocity on the order of 2 m/s at this instant, which recalling from Fig. 8.13 corresponds to the critical state for caisson number 5. Two locations present high values: the breakwater head near the free surface, and the seaside berm, where the water is retreating. These results are promising and can lead to the analysis of stability of the amour layers.

Relevant turbulent variables around the structure are presented in Fig. 8.16. A number of slices of the domain have been obtained to better visualize the results. The turbulent kinetic intensity (k) is larger in the vicinity of the breakwater and close to the free surface, a result of the high turbulence levels in the air, induced by the overtopping events which have occurred and are occurring at that instant (see Fig 8.12). No significant k levels are present inside the porous media, although on the first slice a part of the interface between the primary armour layer and the clear region shows a noticeable value. It can be concluded that the use of a $k-\omega$ SST model, which does not include the closure terms for the porous media, yields marginally smaller dissipation inside the porous materials, unlike $k-\epsilon$ according to the results presented in previous validations.

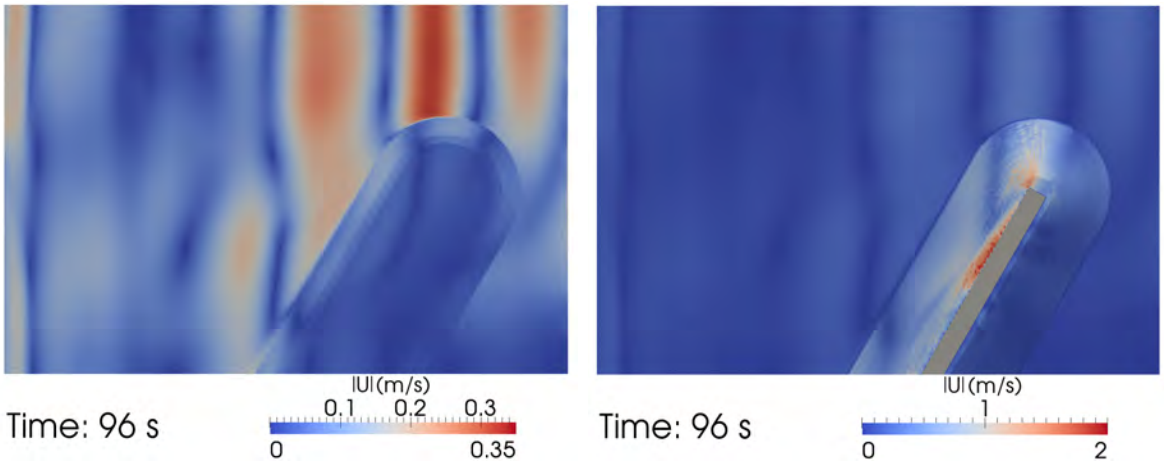

Figure 8.15: Particle velocity distribution around the structure. Left panel: at 10 cm from the bottom. Right panel: at 10 cm from the bottom and on the primary armour layer.

Regarding ω (turbulence eddy frequency), the values are also high near the breakwater, but also throughout the air region all over the domain. The region leeward the breakwater shows smaller ω levels, as the agitation in that zone is not as high as in the exposed area. It is important to note that the ω level increases due to the variation of porosity between the different layers of the breakwater.

8.1.5 Conclusions

The use of the 3D numerical simulations is specially indicated for cases where semi-empirical formulations and 2D simulations may not accurately represent the existing physical processes, as they overcome most of the limitations of both.

An innovative hybrid methodology (2D-3D) has been presented to optimize the simulation time needed to check the three-dimensional effects of wave-induced processes on coastal structures. This methodology results in a significant speed-up (x36 approximately) in simulation time and in a rationalization of the computational resources. If it was not for the hybrid methodology proposed in here these sea-state-long simulations would be virtually unaffordable.

The high mound breakwater simulation yields highly three-dimensional results. The mean pressure laws present a high degree of accordance with those provided by the Goda-Takahashi formulation. However, the safety coefficients obtained are, most of the times, lower than those from the theory. This indicates that the three-dimensional effects are

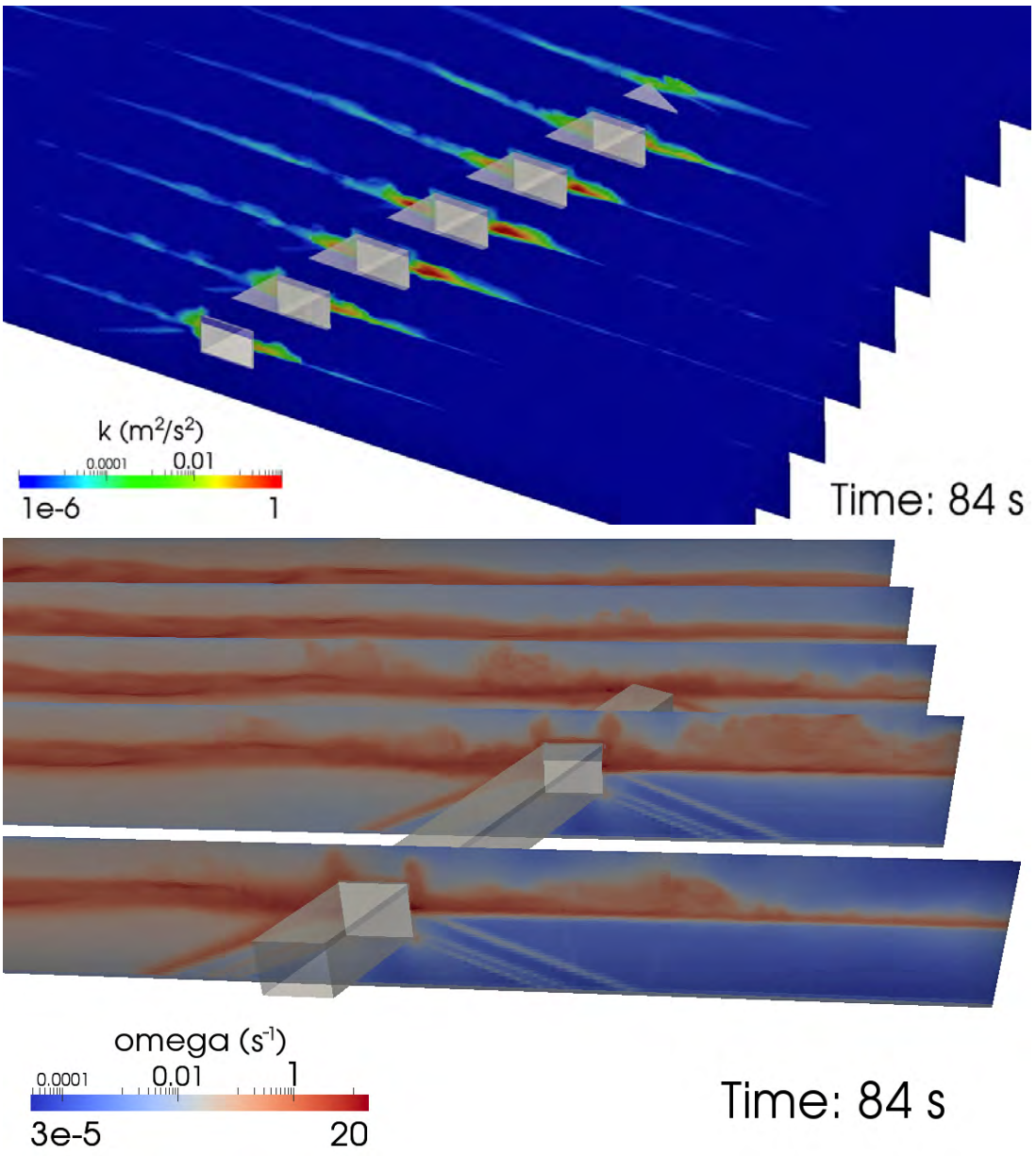

Figure 8.16: Relevant turbulent variables around the structure. Waves come from the left.

not negligible. Impulsive forces are obtained for the second wave on the group, but they introduce limited local effects, so in general the lowest safety factors are induced by non-impulsive loads. The overtopping discharge rate is completely dependent on the location of the section, but also on the preceding waves. To obtain more significant results, long simulations must be carried out.

The turbulent kinetic intensity distribution is concentrated around the structure, where the largest values are present. This fact reveals that the turbulence is an important process to consider in coastal engineering wave-structure simulations, and especially when flow through porous media is present.

Potential results for future studies regarding stability of the rubble mound have been shown. The model successfully shows, according to reality, that water velocities are smaller inside the porous media, and that the critical zones in terms of stability are the seaside berm and the front primary armour layer close to the free surface.

8.2 Irregular waves interaction with a real breakwater

The final case highlights the potential of the model with a three-dimensional analysis of the outer breakwater of the Port of Laredo (Cantabria, Spain). Such a complex layout, including the real geometry of the structure and the bathymetry, requires a methodology that defines the steps needed to establish the conditions to be tested in detail.

8.2.1 Work methodology

The work methodology presented next is a step forward in the simulation of real coastal structures with respect to that of the previous section.

The methodology, which involves a large number of sophisticated tools and numerical models, is sketched in Fig. 8.17 and is developed as follows:

1. Characterization of the wave climate at a location near the structure, not affected by nearshore coastal processes (refraction, diffraction...) or wave breaking. It can be based on observational data, on measurements of a buoy or on reanalysis. It is

convenient to have a calibrated database and as extensive as possible.

2. Selection of a cluster of waves from the database, applying statistical classification techniques as SOM, k-means, MaxDiss...

3. Propagation of the selected cluster from the original point to the structure, using a phase-averaged model.

4. Reconstruction of the wave climate at the structure, and selection of the design sea state, according to the standards. In Spain this is performed according to the ROM (Recommendations for Maritime Structures).

5. Determination of the design sea state at the original point.

6. Propagation of the design sea state from the original point to the structure, using a model in the time domain (non phase-averaged). The result is a time series of free surface and velocities.

7. 2D RANS simulation using the results from the time domain model as input.

   (a) Calculation of the variables that determine the structural stability: safety coefficients against sliding and overturning.

   (b) Identification of the wave groups that induce the minimum safety factors.

8. 3D RANS simulation of the most unfavourable groups.

   (a) Detailed three-dimensional study of the interest variables: run-up, overtopping, forces, safety coefficients...

8.2.2 Application of the methodology

The whole process applied to the Port of Laredo is illustrated in Fig. 8.17 with real images. The starting point is the wave climate from the DOW database (Camus et al., 2013) at a deep water location near the port. By means of the MaxDiss algorithm, 214 of the most energetic sea states have been selected. The propagation of this cluster (step 3) has been performed with the spectral model OLUCA. The goal was to obtain the characterization of the storms at the structure.

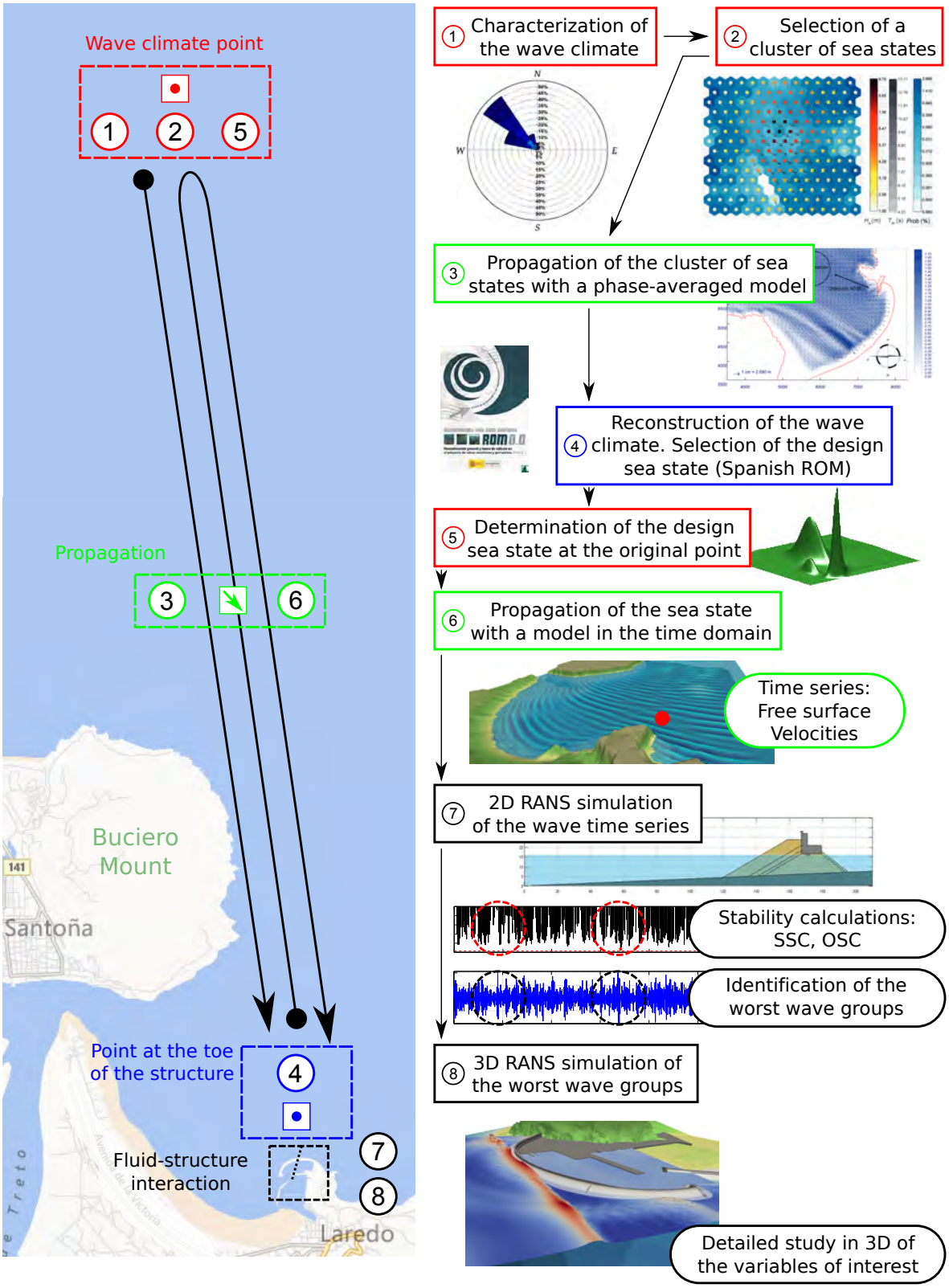

Figure 8.17: Work methodology for modelling real structures in 3D.

According to the Spanish ROM, the Port of Laredo has to be designed for a return period of 475 years. The wave climate at the structure yields a significant wave height of 6 m for that condition, applying a GEV fit. Such wave height is linked to a wave period of 18 s, with a dominant direction of NW in deep water. The diffraction of the waves at the cape formed by the Buciero Mount and the refraction at a submarine canyon, that concentrates the waves, cause that they end up reaching the structure with N15E direction. It is observed that the highest most likely wave for these wave conditions (10.8 m) is compatible with the water depth (8 m + 5.5 m of tide) at the structure, and corresponds to the highest wave that can reach the structure without breaking.

Once the design sea state has been selected, it is propagated with the **IHBouss** model (step 6), that solves the Boussinesq equations, not taking wave reflection into account. The results are time series of free surface elevation and velocities at several locations, approximately one wave length far from the structure. These data are used as input to force the waves on the **IH2VOF** RANS model (step 7). The 2D simulation provides an idealized representation of the complex structure, from which safety coefficients against sliding and overturning can be obtained. Thereafter, the wave groups that induce the minimum safety coefficients are identified, to be simulated in detail with the 3D model. Finally, only the critical instants are simulated in **IHFOAM**, forcing the wave generation with the time series obtained in **IHBouss**.

As background, the Port of Laredo is a recently constructed structure, inaugurated in 2011. The exterior breakwater consists of three linked curves in plan view and it is capped by a concrete crown wall, as shown in Fig. 8.17. The primary armour layer (1:2 slope) is formed by concrete cubes of 65 t, increasing to 70 t at the exterior part of the breakwater head. Underneath this layer, a secondary (concrete cubes of 6 t) and tertiary (crushed rocks between 300–1000 kg) layers and the core (1–100 kg) can be found. The shoreward rubble mound (crushed rocks between 300–1000 kg) has a 1:1.5 slope. The crown wall is founded at +5.5 m. The most exposed area reaches +17 m and includes a recurved wall. Towards the breakwater head the crest elevation decreases to +14 m, and the recurved wall disappears.

The **IHFOAM** mesh is oriented in the wave propagation direction (N15E) and covers an extension of 500 x 700 x 34 m. The lowest point of the mesh corresponds to the -11

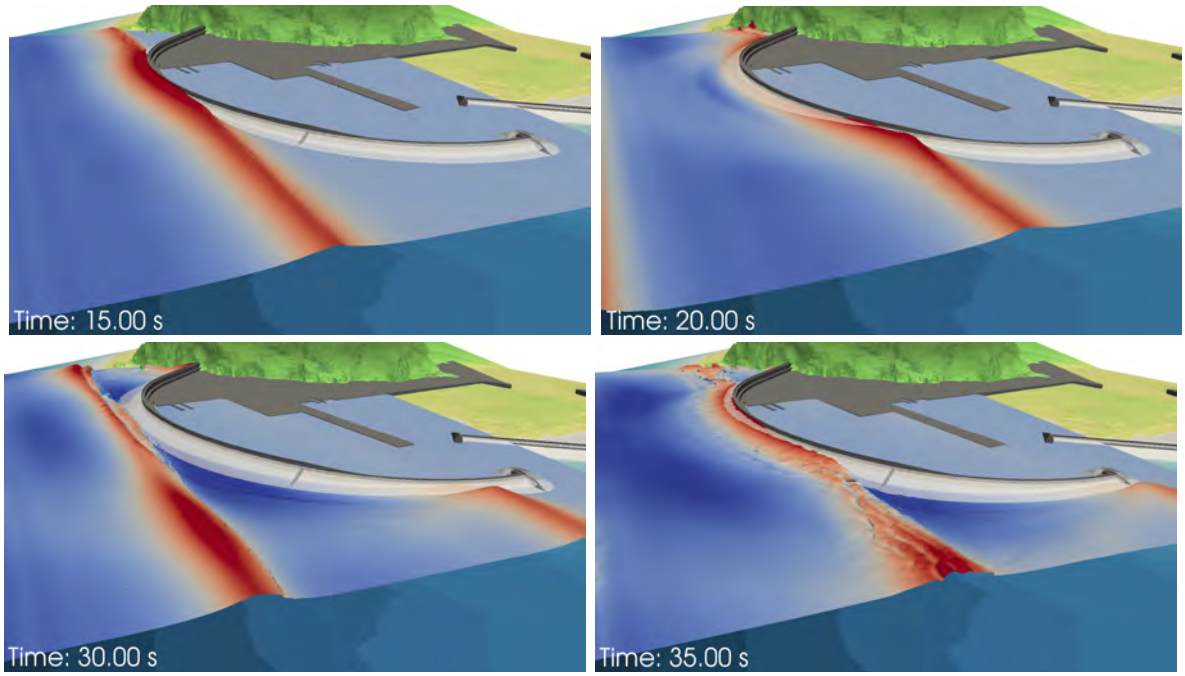

Figure 8.18: Propagation and impact of the wave group against the breakwater of Laredo.

m level of the bathymetry. The wave generation boundary is located at approximately one wave length from the breakwater. The general cell size is 1.5 x 1.5 x 1 m, whereas the interest zones (around the structure and close to the free surface) provide finer detail: 1 x 1.5 x 0.5 m. To better define the crown wall and to obtain great detail of flow and pressure around it the adjacent cells are refined up to 0.25 x 0.375 x 0.125 m. This mesh totals 10 million cells. The model performance is about 25 s per day using 128 processors.

8.2.3 Numerical results

In Fig. 8.18 some snapshots with a general view of the breakwater show the wave group propagating. The first wave of the group induces the worst effects, as the second one reaches the structure already broken due to its higher wave height. Some complex processes can be observed. For example, the impact of waves on the cliff($t = 20$ s), the interaction between incident and reflected waves ($t = 30$ s), the propagation of a bore ($t = 35$ s) or diffraction at the breakwater head ($t = 35$ s).

In Fig. 8.19 the effects of the first wave impact are shown. Important three-dimensional processes can be observed. The free surface when the wave impacts the breakwater and it reaches the highest elevation is plotted in the top left panel. Although the projected

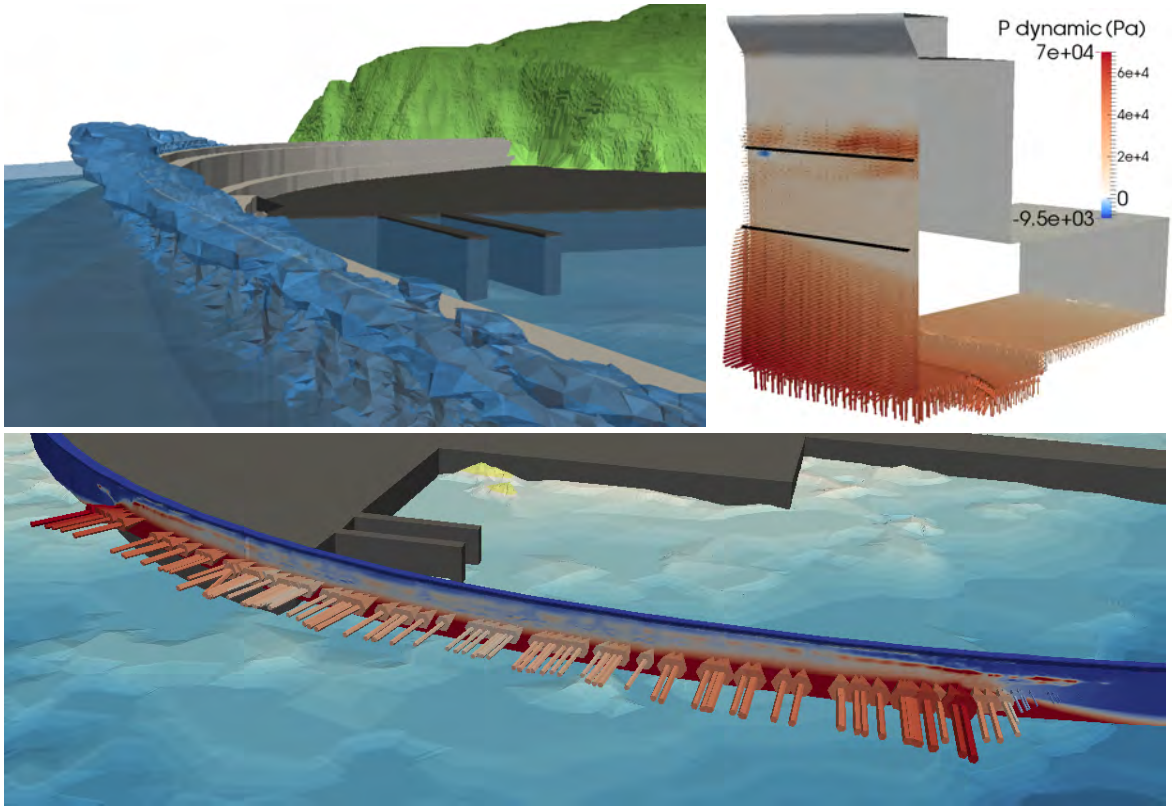

Figure 8.19: Three-dimensional results: overtopping, pressures and forces acting on the breakwater.

water level is well above the crown wall crest, overtopping is almost nonexistent. This is because only the splash exceeds the crown wall level, hence, it is deflected by the recurved wall. The effect is that the vertical momentum of the wave at the impact point gets projected towards the seaside, thereby preventing the overshoot of the structure. The role that the trapped air plays interacting with the structure can also be noted, as the contact zone between the primary armour layer and the crown wall presents pockets of trapped air along the whole breakwater.

In the panel immediately on the right the pressure acting on a section of 5 m of crown wall has been plotted. The black lines delimit the primary armour layer. The pressure distribution varies both along the horizontal and vertical directions. The protecting role of the primary armour layer is specially relevant, as the dynamic pressure (overpressure with respect to the rest state) inside it is almost zero. Above its upper limit, positive impact pressures appear, as well as a localized zone of negative dynamic pressure, probably caused by an air pocket trapped in the mantle. Also of note is the great complexity of the uplift pressure, due to the heel of the crown wall. In the bottom panel the pressure acting on the whole breakwater and some arrows that indicate the total horizontal force on different sections are shown. The force is calculated by the integration of pressure on the defined transects. The largest forces at that instant are located were the wave front impacts transversely to the crown wall.

A detailed stability analysis has also been performed accounting for several sections along the trace of the structure, as presented in Fig. 8.20. Since the breakwater of the Port of Laredo is curved, it is possible to analyse the effects of the wave incidence angle from 0 to 90 degrees all at once. The top panel includes a perspective of the breakwater with the sections studied. Each of them is 5 m wide (analogous to the view in Fig. 8.19). The colour code (red/blue) indicates the position of the section, since there are two different locations for which the waves impact at 15, 30 and 45 degrees, one at each side of the reference section (normal incidence: 0 degrees, painted black).

The variable geometry of the crown wall can be observed in the second panel. The sections are to scale, and three typologies can be distinguished. On the plots below, the section weight and moment against overturning per unit length are shown. The section number 1 includes a recurved wall, and is high (+17 m coronation level) but narrow, so

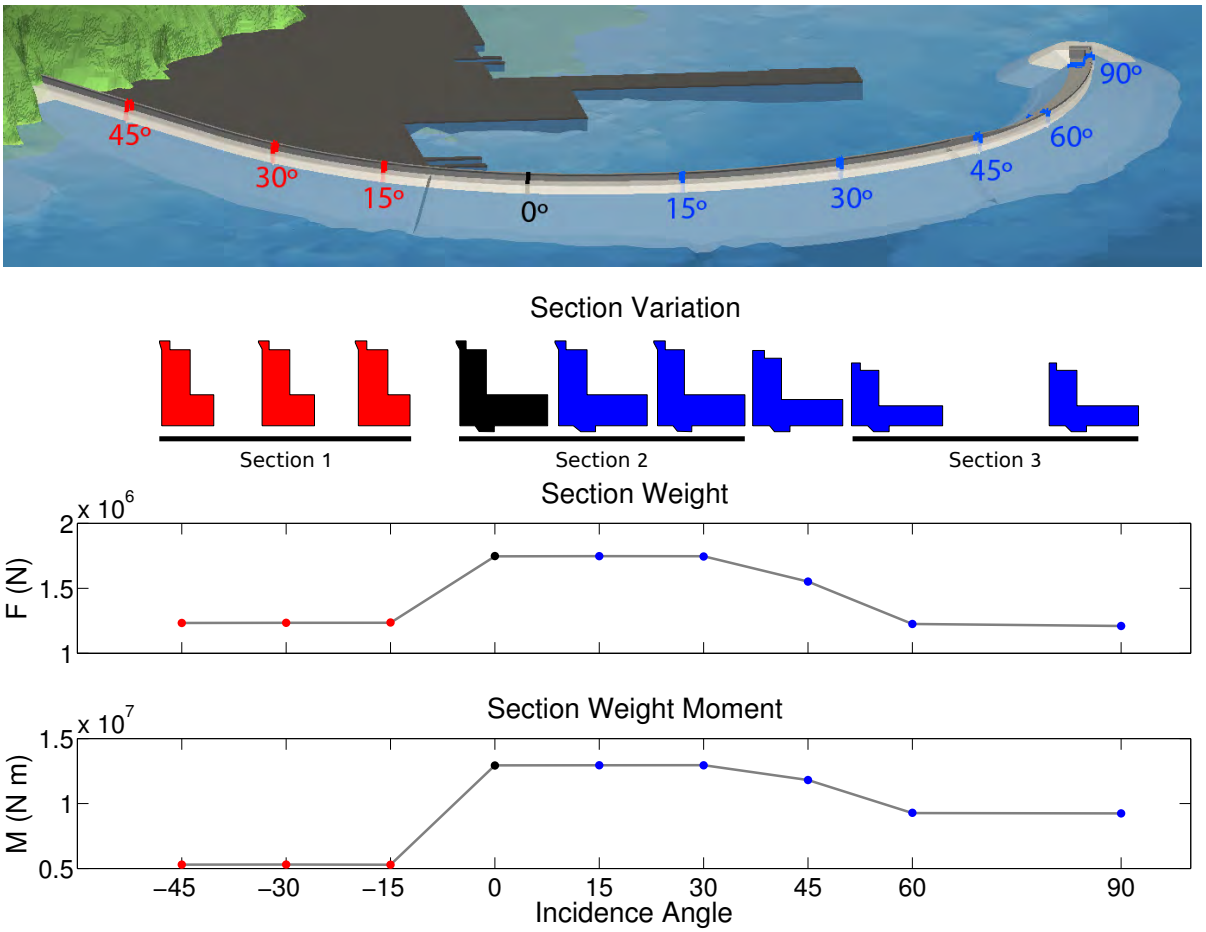

Figure 8.20: Laredo breakwater reference sections.

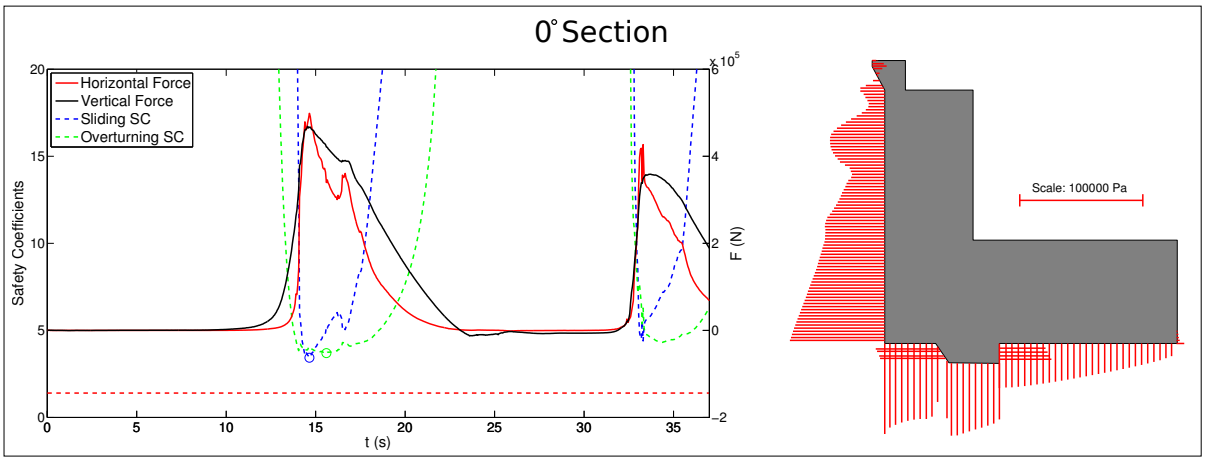

Figure 8.21: Three-dimensional stability results on the breakwater reference section.

it presents low weight and moment. Two section transitions are needed to accommodate the variations. The first one involves an increase in the width of the section, after an access ramp to the crown wall. Then, the section number 2 possesses a larger weight and moment against overturning, while maintaining the slab depth, total height and recurved wall until the 30 degree (blue) section. The second transition goes from 30 to 60 degrees. The coronation level drops to +14 m, the recurved wall disappears and the slab depth decreases, while maintaining the section width. Therefore, the weight diminishes significantly, mildly affecting the moment. From 60 to 90 degrees the section number 3 does not change.

Fig. 8.21 shows the time evolution of the horizontal and vertical forces, and the safety coefficients against sliding and overturning in the left panel. The scale on the right of the plot is for the forces (i.e. the mean value on the section per linear metre of width). The scale on the left is for the safety coefficients.

The horizontal force is shown in red continuous line, and it presents spikes when the wave impacts. The vertical force, in black line, is smoother and similar in magnitude to the horizontal one. The safety coefficient against sliding is represented in a blue dashed line. Its global minimum (blue circumference) is associated to the first impact, with a value equals 3.4, far away from the critical value accepted by the Spanish ROM standard (1.5, red horizontal dashed line). The overturning safety coefficient minimum (green circumference) takes place instants later, and it is not as critical as the sliding one.

In the right plot the pressure law acting on the section at the critical instant (lowest

safety coefficient against sliding) is represented. Its shape is almost hydrostatic where the mantles protect the section, and it presents two local maxima at the exposed part, caused by the impact of the wave front. Negative pressures appear at the recurved wall, originated by the drag of the deflected splash.

In Fig. 8.22 the maximum forces (top plots) and minimum safety coefficients (bottom plots) are compared for the different incidence angles. The green dashed line is the expected evolution taking the normal incidence (0 degrees angle) as a reference and applying a cosine factor, as in the formulation by Takahashi et al. (1994). The grey dashed line indicates the minimum safety coefficient allowed by the Spanish ROM.

The evolution of the maximum horizontal forces is similar in both directions (blue/red) and the results are always below the green line. However, the evolution of the maximum vertical forces is different depending on the side, as the red ones are up to 30% higher than the blue ones. Two factors can explain this variation. The first one is the local effects due to the bathymetry. The second one is geometry variations (e.g. the section number 1 in Fig. 8.20 has water on the seaside only, as on the other side there is the port esplanade; this may lead to an accumulation of water on the core and larger uplift pressures). On top of that, the distance between sections on either side is not homogeneous, as the breakwater has three different curvatures.

The value of the minimum safety coefficient against sliding is growing in the blue side with an almost perfect fit to the green line, which indicates that the structure is more stable as the incident angle increases from normal incidence. The red values are significantly lower, as the vertical forces, already introduced, are larger. Again, the local effects are the most plausible cause to explain the differences. Nevertheless, the overall minimum safety coefficient is 2, so there is still a safety margin.

The minimum safety coefficient against overturning is approximately constant along the whole breakwater. This behaviour is mainly caused by the variations in the breakwater section to optimize the costs, already introduced in Fig. 8.20. The affection is larger than for the sliding safety coefficient, as the range of variation of the stabilising moment is also wider. The red part is, again, the most critical due to the large uplift pressure and smaller weight moment.

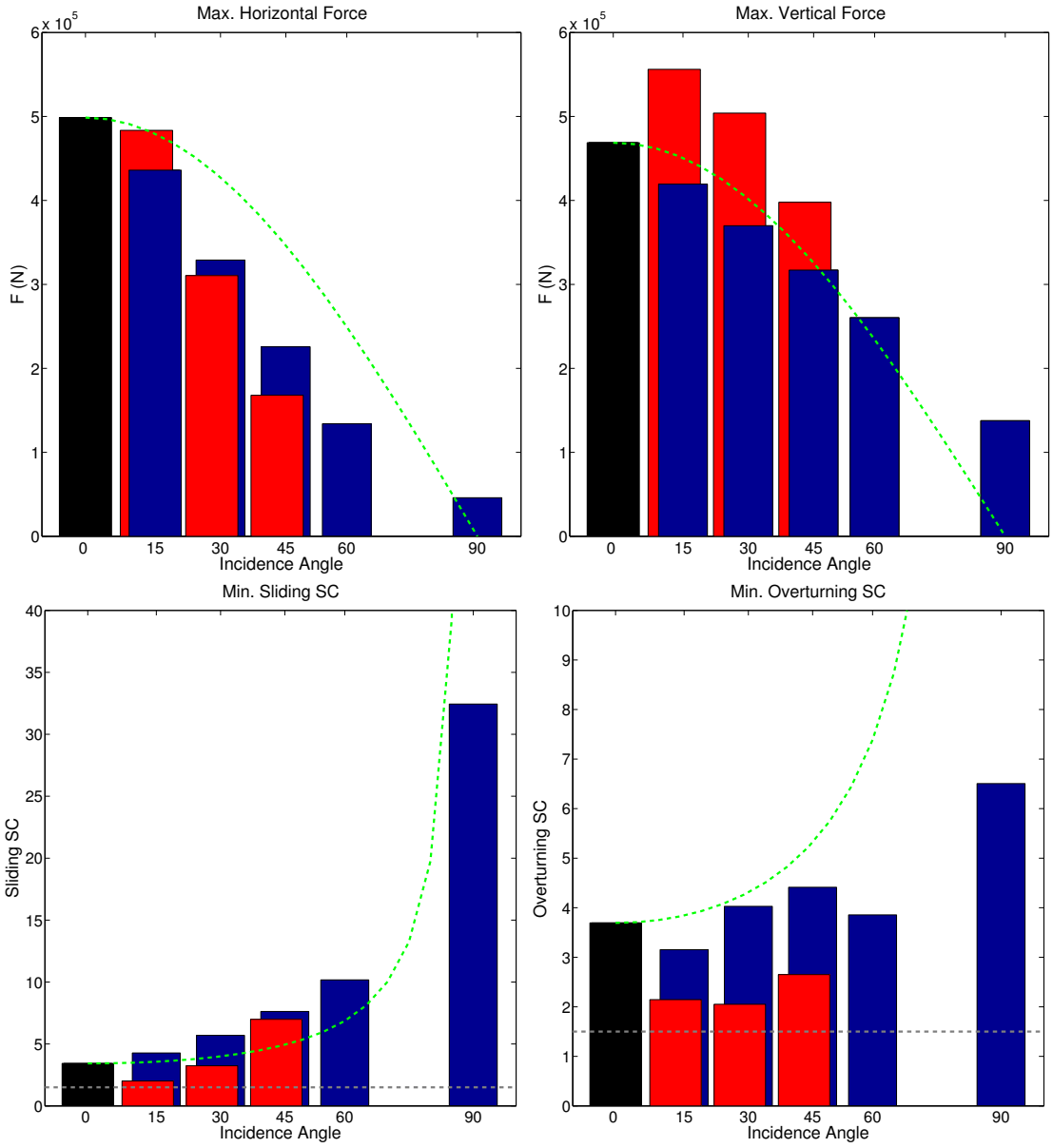

Figure 8.22: Forces and safety coefficients variation with the incidence angle.

8.2.4 Analysis of the design

Based on the three-dimensional data, and if this alternative were a predesign of the structure, the next step would be to study and propose a modified section, lightened where the safety coefficients have large values. This way, the safety coefficients could be reduced (within a safe margin) and an optimized structure would be obtained: as functional and stable as before, but more economic in terms of material.

A long list of factors has to be considered when planning an optimal structure. The most important idea is that a perfect design from the theoretical point of view would be the most expensive alternative to build. This is because the casting of a regular crown wall is a semi-automatic process with sliding formwork procedures. Changing the section continuously would inhibit the automatic procedures, involving higher costs (in terms of time, formwork-related materials and adjustments needed) than the actual savings in concrete. Furthermore, delaying or slowing down the construction of the crown wall would increase the risk of destruction. Should a storm arrive during construction, the structure would be fully exposed to the waves, which may overtop and wash away the materials.

These initial considerations yield clear conclusions: for short breakwaters a single section is probably the safest and cheapest option. For long breakwaters, having a number of different sections may be more beneficial. The key factor in the latter case would be to design all the sections in a way that they can all be cast with small variations of the same modular formwork, so it will be straightforward to operate and amortize.

The relevant question is now how to define when a breakwater is “short” or “long”. The answer is not trivial, as it needs an integral economical and risk analysis. The main factors that have to be taken into account are:

- Additional time and money to design and build the formwork.
- Additional time to operate the custom formwork.
- Additional time needed to build the transition between sections.
- Time restrictions included in the contract.
- Climatic risk (damage) due to additional times.

- Money savings in terms of concrete.

In this specific case, the breakwater of Laredo is 730 m long and features three different sections and two transitions (see Fig. 8.20). In view of the results the layout is reasonably optimal. The section number 1 is crowned at +17 m, it includes a recurved wall and the base slab is short and lacks a heel. The section number 2 is identical to section 1, but the base slab is longer and it includes a heel to prevent sliding. The section number 3 is crowned at +14 m, it does not have a recurved wall and the base slab is thinner; other than that, the widths of the vertical wall and the base are equal to the previous one. The similar shape of all the sections, mainly varying the heights of some elements, is a convenient design to easily adapt the formwork, saving time and money.

The total amount of concrete to build the crown wall is approximately 47000 m^3. If the entire breakwater were constructed with the same section (number 2), 57000 m^3 would be needed instead, resulting in a heavily over-designed structure. The optimization performed by the original designers involves a 20% saving in terms of concrete, which considering a typical cost of 130 €/m^3, it translates into 1,300,000 €.

A lighter section could be considered towards the breakwater head, but a new change in the formwork for such a small portion would increment the cost and time needed for the construction, not compensating the small savings on the material.

8.2.5 Conclusions

The methodology to simulate real structures in 3D combines all sorts of advanced tools and statistical techniques to reduce the uncertainty associated to wave-structure interaction calculations.

The **IHBouss** model propagates the sea states taking into account the local effects caused by the bathymetry and the wave-to-wave interaction. A time series is obtained at the structure, unlike other models that provide a phase-averaged spectrum.

The combined use of the **IH2VOF** and **IHFOAM** models has also demonstrated remarkable advantages in rationalizing the computational resources and in obtaining competitive simulation times. Applying 2D modelling to select the worst cases takes on added significance with the integration in this global methodology, as it is the key to enable the use of the 3D model.

Finally, the application of **IHFOAM** to simulate a complete structure is a milestone in the field of numerical modelling, as it is the first time that a real complex structure is modelled using a 3D RANS approach. This is only possible because just a small fraction of the sea state, the selected worst instants for the structural stability, need to be simulated.

The three-dimensional results of the detailed study indicate the correct operation of the breakwater. No overtopping has been detected and the safety coefficients are in accordance with the standard. For that reason, the current design can be considered an optimal solution.

Chapter 9

Conclusions

9.1 General conclusions

This work has been devoted to fill the gaps that were found in the state of the art of numerical modelling of coastal structures. Three specific objectives can summarize the goals of the thesis, as gathered in Chapter 3. These are the main conclusions that can be extracted from them.

In the first part of this work OpenFOAM®, a free, open source and multipurpose CFD code, consolidated, widely used and rapidly extending has been upgraded to deal with wave generation and absorption.

In view of the results in Section 6.1, a reliable wave generation and a stable active wave absorption system for static boundaries have been achieved with **IHFOAM**. Moreover, this technique has been proven as one of the most advanced in the state of the art, and especially advantageous with respect to internal wave generation and absorption.

The new boundary condition includes the most widely used theories, which cover the full spectrum of water waves, and both first and second order irregular wave generation. Furthermore, as real sea states are random and three dimensional, one of the advances presented is the capability of generating any frequency-direction wave spectrum, discretized in its components.

Active wave absorption presents an outstanding performance and is able to deal with large amplitude reflections reaching the boundaries. This technique has also been linked to wave generation, therefore, enhancing the stability of long simulations by decreasing the energy of the system and correcting the increasing water level due to the excess of

water in the wave crests.

The development of a moving wave generation boundary condition for **IHFOAM** is another of the novelties of the present thesis. This procedure can help to achieve more detailed numerical simulations, as it can replicate the functions of laboratory piston-type wavemakers, including active wave absorption.

The movement of the numerical multi-piston wavemaker can be prescribed according to theoretical data or as provided by the feedback signal of a laboratory device. Active wave absorption can be connected to prevent the reflections of waves incident to the moving boundary. The physical constraints of the actual machines have been taken into account (e.g. maximum stroke, velocities, accelerations...) so that realistic pre-tests can be carried out with theoretical signals.

Comparisons of the **IHFOAM** simulations against laboratory data have been presented in Section 6.2. A 2D and 3D wave focusing experiments have been successfully replicated. The results show a high degree of accordance between both sets of data, although limitations of OpenFOAM® to simulate the propagation of very steep waves have been unveiled. Overall, the behaviour of the boundary condition is realistic.

Active wave absorption is also applicable in moving boundaries and its performance is as good as when applied as a Dirichlet-type boundary condition. Reflection coefficients are generally smaller than 10%, and only larger for those cases in which the wave conditions are far from the original hypothesis. However, the efficiency of moving boundary conditions is lower because the mesh updating routines add significant computational cost to the model.

A new set of volume-averaged Reynolds averaged Navier–Stokes equations has been derived. The new formulation takes into account the effects of porosity gradients, as in Jensen et al. (2014). The novelty of the present derivation relies in considering the effect of time-varying porosity to permit the simulation of, for example, moving sediment. Another advantage presented in this thesis is that two turbulence models, $k-\epsilon$ and $k-\omega$ SST, have been volume averaged to account for turbulence inside porous media. $k-\epsilon$ includes a closure model, therefore the additional turbulence production within the porous media can be considered. No closure model is available for $k-\omega$ SST yet.

The implementation of the equations in OpenFOAM® includes a drag formulation

developed for coastal engineering and overcomes known bugs (i.e. failure to conserve mass) in the regular versions of the OpenFOAM® solver. In view of the results, it can be concluded that Objective 1 (develop a three-dimensional numerical model capable of simulating coastal engineering processes) has been successfully achieved.

Validation is one of the strong points of this thesis and is addressed in Chapters 6 and 7. The validation of the generation and absorption boundary conditions has already been commented on the previous lines, but it must be noted that without the new boundary conditions developed in this work, it would be impossible to obtain some results shown.

In Section 7.1, **IHFOAM** has been validated by testing several relevant coastal engineering benchmark cases. The five tests considered show globally a realistic behaviour, as the comparison between the laboratory and numerical signals presents a high degree of agreement. Moreover, in Section 7.2, the two-phase flow through porous media feature is calibrated and validated. Again, the results indicate that **IHFOAM** is a suitable tool for wave-structure interaction, not only because of the good results obtained for surf zone hydrodynamics and on the structures, but also for the reasonable computational resources needed. Objective 2 (validate the three-dimensional numerical model to prove that it is capable of simulating coastal engineering processes) is fulfiled.

The great power of RANS models lies in applying them to assist in the design of real structures, overcoming the limitations of semi-empirical formulations and experiments. This is Objective 3 of this work.

In Chapter 8, two steps forward are taken. An innovative hybrid methodology (2D-3D) has been presented, first, to optimize the simulation time needed to check the three-dimensional effects of wave-induced pressure, overtopping and turbulence acting on coastal structures. The critical conditions within a sea state are detected with a 2D RANS model (**IH2VOF**) to reproduce them later on with **IHFOAM**, thus, resulting in a significant speed-up (x36 approximately) in simulation time and in a rationalization of the computational resources.

Next, the 2D-3D methodology has been integrated into a global hybrid framework to study wave action on real structures. The final methodology encompasses wave databases, sophisticate statistical tools, simple and advanced wave propagation models and, of course, 2D and 3D RANS numerical modelling. The importance of this methodology is that it

allows obtaining magnitudes linked to the limit state of coastal structures in 3D.

The results demonstrate the importance of local effects and the enormous capabilities of performing three-dimensional numerical modelling to assist in the design of real structures.

Hybrid modelling is shaping up as a key factor in the future of coastal structure design, as it is especially useful for non-conventional structures. With the methodology presented in this work, composite modelling (laboratory + numerical model) can now be fully developed and applied in the coastal engineering framework, helping to overcome laboratory scale effects and reducing the uncertainty linked to this kind of calculations.

In short, **IHFOAM** has proven to be a valuable instrument to assess the three-dimensional effects in simulations of real coastal structures at prototype scale. Undoubtedly, the generalization of these technologies in the near future will constitute a breakthrough in the design of optimal structures, with enhanced stability and functionality, more environmentally friendly and cost efficient.

9.2 Scientific contributions

This work has yield several contributions to science in the form of publications and conference presentations.

In Higuera et al. (2013a) the wave generation and absorption procedures for static boundaries were presented. This work is a breakthrough in the coastal engineering field, as precise implementation details that can be applied to any RANS model are given. Its companion paper, Higuera et al. (2013b), included the extensive validation cases gathered in the first part of Chapter 7. The importance of this paper relies in that it is the first time that OpenFOAM® is validated as a tool for three-dimensional numerical modelling of coastal processes.

The implementation and validation of the VARANS equations by del Jesus et al. (2012) were presented in Higuera et al. (2014a). As already commented, discrepancies with the classic volume-averaging procedure were found later and have been corrected in this thesis. The comparison of former and new results can be found in Apendix B.

Higuera et al. (2014b) is an application of the first hybrid methodology, that shows

the capabilities of **IHFOAM**. To the authors knowledge it is the first time that three-dimensional pressure laws and overtopping discharge time series are obtained numerically along a whole structure.

Higuera et al. (2015) has been submitted for publication and includes all the details for the implementation and validation of dynamic-boundary wave generation and absorption.

9.3 Technology transfer

IHFOAM development started in 2011 as a slightly modified version of *interFoam* solver. As a part of the work during this thesis, an extensive training course that includes all the materials to learn how to use OpenFOAM® and **IHFOAM** was prepared. So far 5 editions of the course have been taught for attendants from academia and consultancy companies in Santander, Madrid and Chennai (India).

The first version of **IHFOAM** was released along with a training course in October 2012. This solver included an early version of the wave generation and absorption libraries developed in this work, but it lacked porous media flow.

IHFOAM version 2.0 (current version) was publicly released for free under the GNU GPL license on 15th July 2014, with significant improvements and new features. Download instructions can be found in the model website[1].

Thanks to the continuous improvements, **IHFOAM** qualifies as one of the most advanced numerical models in the state of the art, fully apt to simulate wave-structure interaction processes, as proven in this thesis. Some of **IHFOAM** most relevant practical applications are reviewed in Fig. 9.1.

The model is also a perfect example of technology transfer between research institutes and companies. The download statistics from the web site indicate that **IHFOAM** is currently being used by more than 280 users in 49 different countries (Spain, USA, Canada, Denmark, UK, China...)

[1] http://ihfoam.ihcantabria.com/source-download/

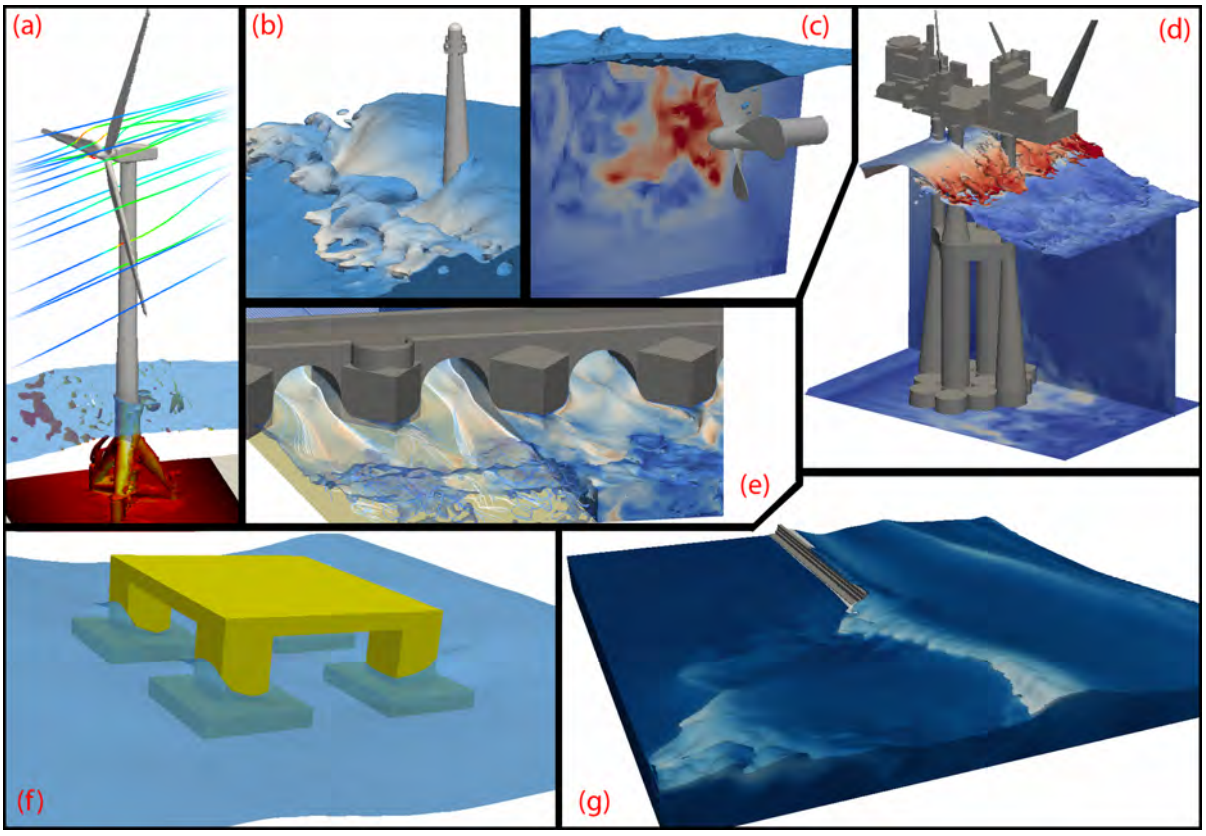

Figure 9.1: **IHFOAM** most relevant capabilities: (a) wind turbine offshore foundations (hydrodynamics + aerodynamics); (b) wave interaction with impervious structures, as lighthouses; (c) external dynamics, as ship propellers; (d) wave impact on offshore platforms; (e) river hydraulics around bridges; (f) floating offshore structures; (g) porous coastal structures.

9.4 Future work lines

IHFOAM development continues, adding new features, enhancing those that are currently there and fixing bugs.

Future work lines involve continue studying the possibilities that OpenFOAM® can offer in all the fields related with waves (e.g. coastal, offshore, renewable energies...) with special emphasis on trying to couple the code with others for additional capabilities and better performance.

The most advanced future line at this point, although not included in this thesis, is sediment transport with **IHFOAM**.

The new version of the solver includes the full implementation of the VARANS equations in Chapter 4, including the time-varying porosity.

The approach to treat sediment is also novel, individual particles that are tracked using the DEM Lagrangian algorithm (Discrete Element Method) and interact between them and with the fluid in a so-called four-way coupling (the fluid drives the particle movement and the particles also drive the flow).

A practical application, the scour caused by a constant current (0.5 m/s) of water behind a cylinder (10 cm in diameter), is shown in Fig. 9.2.

In the top panel, the path that has already been eroded below the white cylinder can be noticed. It is remarkable that some of the sediment particles (1 mm in diameter) get into suspension. The middle panel presents the streamlines and the interface of the sediment. The lower panel shows an earlier snapshot, with vertical profiles of velocity and vorticity contours. High vorticity values are found around the structure and in the scour hole that it is still growing.

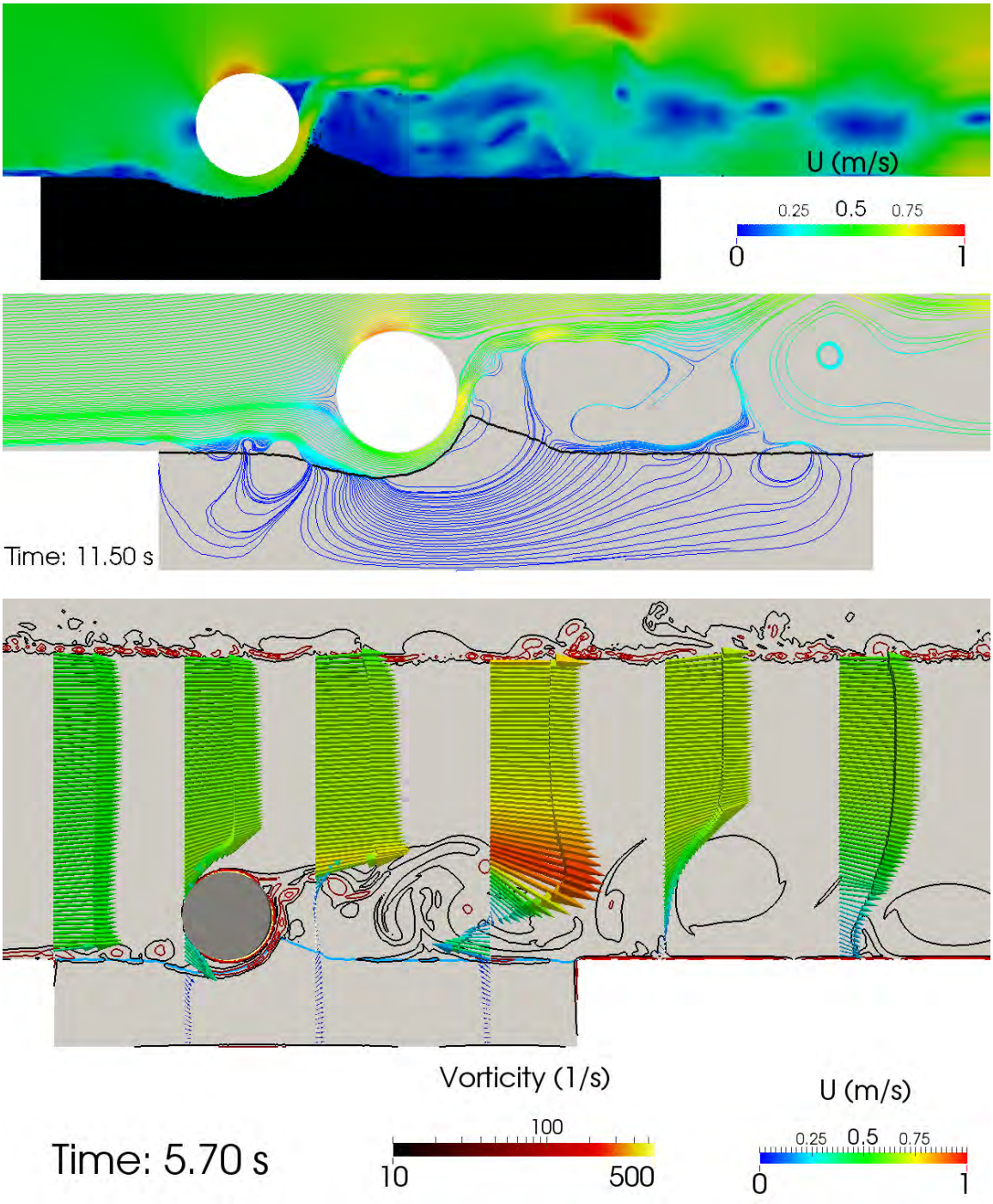

Figure 9.2: Volume averaging domain for several phases and obstacles.

Appendix A

Volume-Averaging Reference

A.1 Basic algebra

Volume averaging composite variables (δ) is one of the most important techniques applied in this work. Recalling Eq. 4.10 and before the derivations themselves, three terms are going to be identified in each case: $\delta = \langle \delta_k \rangle^f + \delta_k'' + \delta_k'^*$, the main terms, the first order terms and the second order terms. The expressions in Table 4.1 and Eq. 4.9 will be applied in the following derivations. In all the cases the final volume average has two main contributions:

$$\langle \underline{\delta} \rangle = \left\langle \langle \delta_k \rangle^f \right\rangle + \cancelto{0}{\langle \delta_k'' \rangle} + \langle \delta_k'^* \rangle \tag{A.1}$$

The first term ($\left\langle \langle \delta_k \rangle^f \right\rangle$) will be part of the general volume-averaged expression, while the terms resulting from the last element ($\langle \delta_k'^* \rangle$) will be included in the closure terms.

In all the derivations the assumption by Gray (1975) and Whitaker (1996) that the volume-averaged value constant within the control volume will be applied.

Product of two variables

The volume averaging of a product of two variables is the easiest expression to compute:

$$\delta = a\,b = \left(\langle a \rangle^f + a'' \right) \left(\langle b \rangle^f + b'' \right) = \langle a \rangle^f \langle b \rangle^f + a'' \langle b \rangle^f + \langle a \rangle^f b'' + a'' b'' \tag{A.2}$$

The three aforementioned terms can easily be identified:

$$\langle \delta_k \rangle^f = \langle a \rangle^f \langle b \rangle^f \tag{A.3}$$

$$\delta_k'' = a'' \langle b \rangle^f + \langle a \rangle^f b'' \tag{A.4}$$

$$\delta_k'^* = a'' b'' \tag{A.5}$$

Finally, volume-averaging the composite variable:

$$\langle \underline{\delta} \rangle = \langle a\, b \rangle = \left\langle \langle \delta_k \rangle^f \right\rangle + \cancelto{0}{\langle \delta_k'' \rangle} + \langle \delta_k'^* \rangle =$$
$$\left\langle \langle a \rangle^f \langle b \rangle^f \right\rangle + \langle a'' b'' \rangle = \phi \left\langle \langle a \rangle^f \langle b \rangle^f \right\rangle^f + \langle a'' b'' \rangle$$
$$= \phi \langle a \rangle^f \langle b \rangle^f + \langle a'' b'' \rangle = \frac{1}{\phi} \langle a \rangle \langle b \rangle + \langle a'' b'' \rangle \tag{A.6}$$

This expression can be applied for specific cases when one of the variables (k) is a constant (i.e. $k'' = 0$) and when both variables are the same (i.e. volume average of a squared variable):

$$\langle k\, a \rangle = \frac{1}{\phi} \langle k \rangle \langle a \rangle = \langle k \rangle^f \langle a \rangle = k \langle a \rangle \tag{A.7}$$

$$\left\langle a^2 \right\rangle = \frac{1}{\phi} \langle a \rangle^2 + \langle a'' a'' \rangle \tag{A.8}$$

Product of three variables

The previous derivation can also be extended to a triple product. Note that third order terms are dropped:

$$\begin{aligned}\delta = a\,b\,c &= \left(\langle a\rangle^f + a''\right)\left(\langle b\rangle^f + b''\right)\left(\langle c\rangle^f + c''\right)\\ &= \langle a\rangle^f \langle b\rangle^f \langle c\rangle^f + a''\langle b\rangle^f \langle c\rangle^f + \langle a\rangle^f b''\langle c\rangle^f + \langle a\rangle^f \langle b\rangle^f c'' +\\ &\qquad a''b''\langle c\rangle^f + a''\langle b\rangle^f c'' + \langle a\rangle^f b''c'' + \cancelto{O(\theta^3)}{a''b''c''}\end{aligned} \tag{A.9}$$

The three terms are as follows:

$$\langle\delta_k\rangle^f = \langle a\rangle^f \langle b\rangle^f \langle c\rangle^f \tag{A.10}$$

$$\delta_k'' = a''\langle b\rangle^f \langle c\rangle^f + \langle a\rangle^f b''\langle c\rangle^f + \langle a\rangle^f \langle b\rangle^f c'' \tag{A.11}$$

$$\delta_k'^* = a''b''\langle c\rangle^f + a''\langle b\rangle^f c'' + \langle a\rangle^f b''c'' \tag{A.12}$$

And the final expression:

$$\begin{aligned}\langle\underline{\delta}\rangle = \langle a\,b\,c\rangle &= \left\langle\langle\delta_k\rangle^f\right\rangle + \cancelto{0}{\langle\delta_k''\rangle} + \langle\delta_k'^*\rangle =\\ &\left\langle\langle a\rangle^f \langle b\rangle^f \langle c\rangle^f\right\rangle + \left\langle a''b''\langle c\rangle^f + a''\langle b\rangle^f c'' + \langle a\rangle^f b''c''\right\rangle =\\ &\phi\left\langle\langle a\rangle^f \langle b\rangle^f \langle c\rangle^f\right\rangle^f + \langle a\rangle^f \langle b''c''\rangle + \langle b\rangle^f \langle a''c''\rangle + \langle c\rangle^f \langle a''b''\rangle\\ &= \frac{1}{\phi^2}\langle a\rangle\langle b\rangle\langle c\rangle + \frac{1}{\phi}\langle a\rangle\langle b''c''\rangle + \frac{1}{\phi}\langle b\rangle\langle a''c''\rangle + \frac{1}{\phi}\langle c\rangle\langle a''b''\rangle\end{aligned} \tag{A.13}$$

Quotient of two variables

The volume averaging of a quotient requires a more sophisticate approach. First, the denominator needs to be approximated to second order with the Taylor rule:

$$\frac{1}{\langle b\rangle^f + b''} = \frac{1}{\langle b\rangle^f} - \frac{b''}{\left(\langle b\rangle^f\right)^2} + \frac{\left(b''\right)^2}{\left(\langle b\rangle^f\right)^3} + O\left[\left(b''\right)^3\right] \tag{A.14}$$

Then, dropping third order terms:

$$\delta = \frac{a}{b} = \frac{\langle a\rangle^f + a''}{\langle b\rangle^f + b''} = \left(\langle a\rangle^f + a''\right)\left(\frac{1}{\langle b\rangle^f} - \frac{b''}{\left(\langle b\rangle^f\right)^2} + \frac{(b'')^2}{\left(\langle b\rangle^f\right)^3}\right)$$

$$= \frac{\langle a\rangle^f}{\langle b\rangle^f} + \frac{a''}{\langle b\rangle^f} - \frac{\langle a\rangle^f b''}{\left(\langle b\rangle^f\right)^2} - \frac{a''b''}{\left(\langle b\rangle^f\right)^2} + \frac{\langle a\rangle^f (b'')^2}{\left(\langle b\rangle^f\right)^3} + \cancel{\frac{a''(b'')^2}{\left(\langle b\rangle^f\right)^3}}^{O(\theta^3)} \tag{A.15}$$

Identifying the three terms:

$$\langle \delta_k\rangle^f = \frac{\langle a\rangle^f}{\langle b\rangle^f} \tag{A.16}$$

$$\delta_k'' = \frac{a''}{\langle b\rangle^f} - \frac{\langle a\rangle^f b''}{\left(\langle b\rangle^f\right)^2} \tag{A.17}$$

$$\delta_k'^* = -\frac{a''b''}{\left(\langle b\rangle^f\right)^2} + \frac{\langle a\rangle^f (b'')^2}{\left(\langle b\rangle^f\right)^3} \tag{A.18}$$

And the result:

$$\langle \underline{\delta}\rangle = \left\langle \frac{a}{b}\right\rangle = \left\langle \langle \delta_k\rangle^f\right\rangle + \cancel{\langle \delta_k''\rangle}^{0} + \langle \delta_k'^*\rangle =$$

$$\left\langle \frac{\langle a\rangle^f}{\langle b\rangle^f}\right\rangle - \left\langle \frac{a''b''}{\left(\langle b\rangle^f\right)^2}\right\rangle + \left\langle \frac{\langle a\rangle^f (b'')^2}{\left(\langle b\rangle^f\right)^3}\right\rangle =$$

$$\phi\left\langle \frac{\langle a\rangle^f}{\langle b\rangle^f}\right\rangle^f - \frac{\langle a''b''\rangle}{\left(\langle b\rangle^f\right)^2} + \frac{\langle a\rangle^f \langle b''b''\rangle}{\left(\langle b\rangle^f\right)^3}$$

$$= \phi\frac{\langle a\rangle}{\langle b\rangle} - \phi^2\frac{\langle a''b''\rangle}{\langle b\rangle^2} + \phi^2\frac{\langle a\rangle\langle b''b''\rangle}{\langle b\rangle^3} \tag{A.19}$$

Quotient of a squared variable

Another useful expression is the quotient of a squared variable. Third and fourth order terms are dropped:

$$\delta = \frac{a^2}{b} = \frac{\left(\langle a\rangle^f + a''\right)^2}{\langle b\rangle^f + b''} =$$

$$\left[\left(\langle a\rangle^f\right)^2 + 2\ \langle a\rangle^f\ a'' + (a'')^2\right]\left(\frac{1}{\langle b\rangle^f} - \frac{b''}{\left(\langle b\rangle^f\right)^2} + \frac{(b'')^2}{\left(\langle b\rangle^f\right)^3}\right)$$

$$= \frac{\left(\langle a\rangle^f\right)^2}{\langle b\rangle^f} + \frac{2\ \langle a\rangle^f\ a''}{\langle b\rangle^f} + \frac{(a'')^2}{\langle b\rangle^f} - \frac{\left(\langle a\rangle^f\right)^2 b''}{\left(\langle b\rangle^f\right)^2} - \frac{2\ \langle a\rangle^f\ a''b''}{\left(\langle b\rangle^f\right)^2}$$

$$- \cancel{\frac{(a'')^2\, b''}{\left(\langle b\rangle^f\right)^2}}^{O(\theta^3)} + \frac{(b'')^2\left(\langle a\rangle^f\right)^2}{\left(\langle b\rangle^f\right)^3} + \cancel{\frac{2\ \langle a\rangle^f\ a''\,(b'')^2}{\left(\langle b\rangle^f\right)^3}}^{O(\theta^3)} + \cancel{\frac{(a'')^2\,(b'')^2}{\left(\langle b\rangle^f\right)^3}}^{O(\theta^4)} \tag{A.20}$$

The three terms are as follows:

$$\langle \delta_k\rangle^f = \frac{\left(\langle a\rangle^f\right)^2}{\langle b\rangle^f} \tag{A.21}$$

$$\delta_k'' = \frac{2\ \langle a\rangle^f\ a''}{\langle b\rangle^f} - \frac{\left(\langle a\rangle^f\right)^2 b''}{\left(\langle b\rangle^f\right)^2} \tag{A.22}$$

$$\delta_k'^* = \frac{(a'')^2}{\langle b\rangle^f} - \frac{2\ \langle a\rangle^f\ a''b''}{\left(\langle b\rangle^f\right)^2} + \frac{(b'')^2\left(\langle a\rangle^f\right)^2}{\left(\langle b\rangle^f\right)^3} \tag{A.23}$$

Finally, the volume-averaged expression:

$$\langle \underline{\delta} \rangle = \left\langle \frac{a^2}{b} \right\rangle = \left\langle \langle \delta_k \rangle^f \right\rangle + \cancelto{0}{\langle \delta_k'' \rangle} + \langle \delta_k'^* \rangle =$$

$$\left\langle \frac{\left(\langle a \rangle^f\right)^2}{\langle b \rangle^f} \right\rangle + \left\langle \frac{(a'')^2}{\langle b \rangle^f} - \frac{2\ \langle a \rangle^f\ a''b''}{\left(\langle b \rangle^f\right)^2} + \frac{(b'')^2 \left(\langle a \rangle^f\right)^2}{\left(\langle b \rangle^f\right)^3} \right\rangle =$$

$$\phi \left\langle \frac{\left(\langle a \rangle^f\right)^2}{\langle b \rangle^f} \right\rangle^f + \frac{\langle a''a'' \rangle}{\langle b \rangle^f} - \frac{2\ \langle a \rangle^f\ \langle a''b'' \rangle}{\left(\langle b \rangle^f\right)^2} + \frac{\left(\langle a \rangle^f\right)^2 \langle b''b'' \rangle}{\left(\langle b \rangle^f\right)^3}$$

$$= \frac{\langle a \rangle^2}{\langle b \rangle} + \phi \frac{\langle a''a'' \rangle}{\langle b \rangle} - 2\,\phi \frac{\langle a \rangle\ \langle a''b'' \rangle}{\langle b \rangle^2} + \phi \frac{\langle a \rangle^2\ \langle b''b'' \rangle}{\langle b \rangle^3} \quad \text{(A.24)}$$

A.2 Single phase vs multiphase approach

The first step to prove that the volume averaging procedure for a single phase is applicable when dealing with a multiphase flow tracked by the Volume Of Fluid (VOF) technique is applying it to the fluid properties. The intrinsic volume average of the density of one or more incompressible fluids (ρ) is going to be proved equal to the density itself: $\langle \rho \rangle^f = \rho$.

For a single incompressible fluid, the density is constant everywhere by definition, hence, the intrinsic average of a constant is the same constant.

For n-phase incompressible flows the proof is also simple, but additional indicator functions are needed. The current case is sketched in Fig. 4.2. When accounting for water and air, only a single indicator function is needed (α) and the fluid properties, as density, can be formulated as follows:

$$\rho = \rho_\alpha \alpha + \rho_\beta (1 - \alpha) \quad \text{(A.25)}$$

where ρ_α and ρ_β are the (constant) densities of both fluids. Volume-averaging the density results in:

$$\langle \rho \rangle^f = \rho_\alpha \langle \alpha \rangle^f + \rho_\beta (1 - \langle \alpha \rangle^f) \quad \text{(A.26)}$$

In the present case the indicator function (α) is defined as the volume of water per volume of the total fluid mixture (water plus air) inside the control volume. Therefore, this variable can be thought of as an already-volume-averaged variable. Then, following Gray (1975) and Whitaker (1996) approximation to consider the volume-averaged value constant within the control volume will result in $\langle\alpha\rangle^f = \alpha$, finally yielding $\langle\rho\rangle^f = \rho$.

The final step is to demonstrate that volume averaging the conservation of mass equation yields the same result when applied to the single and multiphase versions. The starting point of the multiphase approach is taken from Ni and Beckermann (1991). The expression is identical to Hassanizadeh and Gray (1979), but it includes the volume fraction (ϵ), as introduced in Section 4.2. The general equation that holds for any phase (k) is:

$$\frac{\partial \rho_k \epsilon_k}{\partial t} + \frac{\partial \rho_k \epsilon_k u_{k_i}}{\partial x_i} = 0 \tag{A.27}$$

Since the fluids are considered incompressible in this work, ρ_k is a constant and it can be left out, simplifying the calculations:

$$\frac{\partial \epsilon_k}{\partial t} + \frac{\partial \epsilon_k u_{k_i}}{\partial x_i} = 0 \tag{A.28}$$

Following the same guidelines as in Section 4.3.1, it is easy to obtain the volume-average of Eq. A.28:

$$\frac{\partial \epsilon_k}{\partial t} + \frac{\partial \epsilon_k \langle u_{k_i}\rangle^f}{\partial x_i} = 0 \tag{A.29}$$

Now, all the equations for each phase are added up:

$$\frac{\partial \epsilon_\alpha + \epsilon_\beta + \epsilon_\gamma + \epsilon_\delta}{\partial t} + \frac{\partial \epsilon_\alpha \langle u_{\alpha_i}\rangle^f + \epsilon_\beta \langle u_{\beta_i}\rangle^f + \epsilon_\gamma \langle u_{\gamma_i}\rangle^f + \epsilon_\delta \langle u_{\delta_i}\rangle^f}{\partial x_i} = 0 \tag{A.30}$$

Several conditions help to streamline the expression:

- Eq. 4.16: $\epsilon_\alpha + \epsilon_\beta + \epsilon_\gamma + \epsilon_\delta = 1$
- In VOF: $u_{\alpha_i} = u_{\beta_i} = u_i$

- Static obstacles: $u_{\delta_i} = 0$
- Eq. A.29: $\frac{\partial \epsilon_k \langle u_{k_i} \rangle^f}{\partial x_i} = -\frac{\partial \epsilon_k}{\partial t}$
- Eq. 4.17: $\phi = \epsilon_\alpha + \epsilon_\beta$
- Eq. 4.19: $\phi_{\text{DY}} = 1 - \epsilon_\gamma$
- Eq. 4.4: $\langle a \rangle = \phi \, \langle a \rangle^f$

yielding:

$$\begin{aligned}
\cancelto{0}{\frac{\partial \gamma}{\partial t}} + \frac{\partial \epsilon_\alpha \langle u_{\alpha_i} \rangle^f + \epsilon_\beta \langle u_{\beta_i} \rangle^f + \epsilon_\gamma \langle u_{\gamma_i} \rangle^f}{\partial x_i} = \\
\frac{\partial (\epsilon_\alpha + \epsilon_\beta) \langle u_i \rangle^f}{\partial x_i} + \frac{\partial \epsilon_\gamma \langle u_{\gamma_i} \rangle^f}{\partial x_i} = \frac{\partial (\epsilon_\alpha + \epsilon_\beta) \langle u_i \rangle^f}{\partial x_i} - \frac{\partial \epsilon_\gamma}{\partial t} = \\
\frac{\partial (\epsilon_\alpha + \epsilon_\beta) \langle u_i \rangle^f}{\partial x_i} + \frac{\partial (1 - \epsilon_\gamma)}{\partial t} = \frac{\partial \phi \langle u_i \rangle^f}{\partial x_i} + \frac{\partial \phi_{\text{DY}}}{\partial t} \\
= \frac{\partial \phi_{\text{DY}}}{\partial t} + \frac{\partial \langle u_i \rangle}{\partial x_i} = 0 \quad \text{(A.31)}
\end{aligned}$$

which is identical to Eq. 4.30.

Appendix B

Comparison with del Jesus et al. (2012) Formulation

In Section 4.6, a discussion between del Jesus et al. (2012) and the current VARANS formulation is carried out. It is clear that most recent derivation is correct from a mathematical point of view.

This appendix presents the results that were obtained validating **IHFOAM** with the VARANS implementation of del Jesus et al. (2012). These results were initially presented in Higuera et al. (2014a). A direct comparison can be carried out with the outputs from the new implementation, already presented in Section 7.2.

B.1 Two-dimensional porous dam break: CR35

The first case is the porous dam break. Only the crushed rocks material and $h = 35$ cm was considered for the initial validation work. The best-fit friction parameters for that case were $\alpha = 10000$, $\beta = 3.0$, versus the new ones: $\alpha = 0$, $\beta = 2.0$. A full description of the case is available at Section 7.2.1.

Fig. B.1 presents the free surface elevation at different instants along the tank, and is comparable with Fig. 7.29. No differences can practically be spotted until $t = 1.55$ s, and at that point the major discrepancy is some trapped air bubbles in Fig. 7.29, that barely affect the free surface above. At $t = 1.95$ s the variation in the flow discharge through the porous medium can be noticed. For the selected best-fit friction parameters the validation for del Jesus et al. (2012) formulation allows marginally less volume of

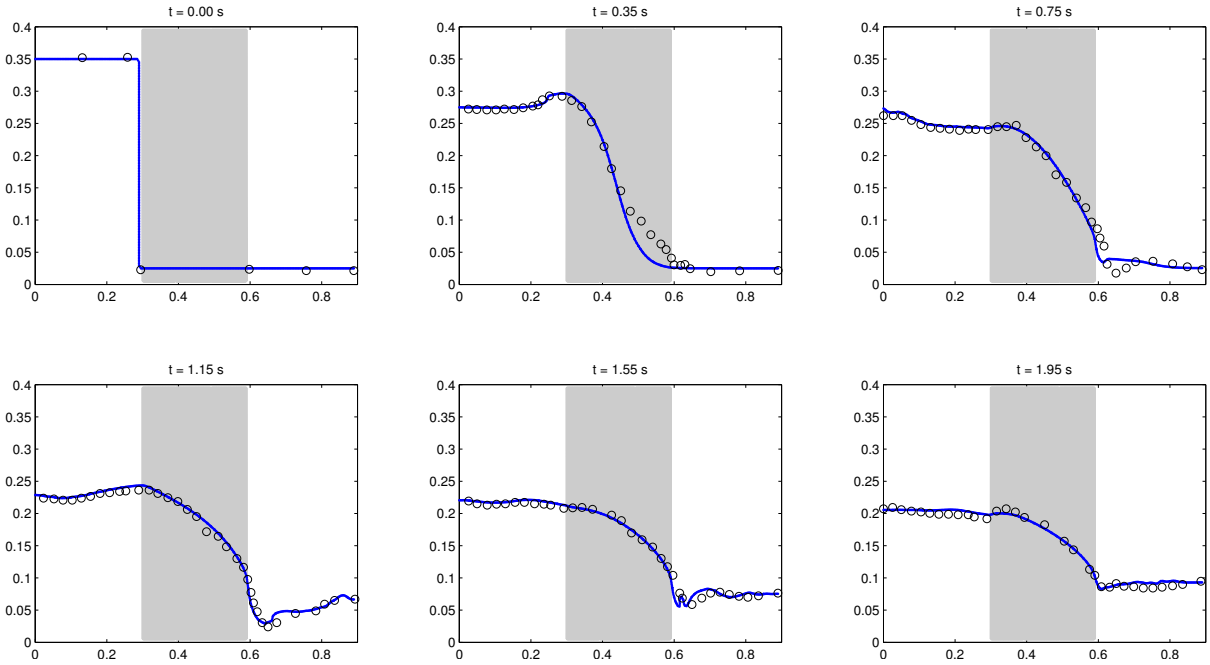

Figure B.1: Validation case for del Jesus et al. (2012) formulation: crushed rocks, $h = 35$ cm. $\alpha = 10000$, $\beta = 3.0$. Laboratory data as circles, numerical data as points.

water to pass through the porous medium. However, this is not a significant result, as with a finer tuning of the friction virtually the same results could be obtained.

In Fig. B.2 the distribution of turbulent kinetic energy (k) for the volume-averaged $k - \epsilon$ turbulence model (Higuera et al., 2014a) is presented. The figure can be compared with Fig. 7.31 (left panel). It must be noted that the comparison is between the initial derivation of the volume-averaged $k-\epsilon$ model (Higuera et al., 2014a) and the most recent one. Black contour lines are represented for each negative integer power of 10.

Some interesting differences can be observed when comparing both snapshots. The general trend is to obtain higher values of k closer to the free surface and to the bottom. This behaviour is observed in both cases in the clear flow regions. However, significant differences arise inside the porous medium. del Jesus et al. (2012) formulation yields an approximately constant value (0.01) along the whole obstacle, whereas the base value of the new formulation is negligible. Furthermore, the maximum value of the new formulation is five times smaller than with del Jesus et al. (2012) formulation, and in takes place at the same location: when the flow accelerates as it emerges from the porous obstacle. Without actual measurements it is not possible to assess the quality of each solution, although it must be noted that the current formulation has been averaged as intended by

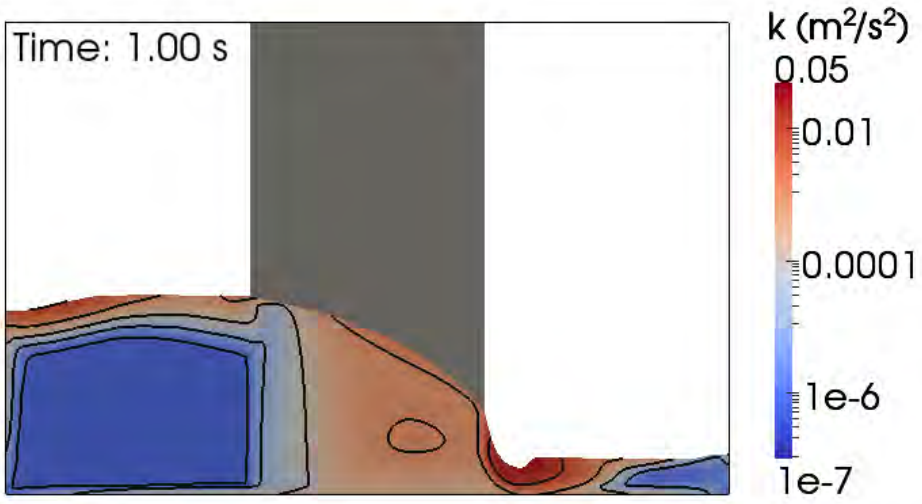

Figure B.2: CR35, del Jesus et al. (2012) formulation: turbulent kinetic energy (k).

Slattery (1967) and Whitaker (1967).

B.2 Regular waves interacting with a high mound breakwater in 2D

The second case is the simulation of regular waves interacting with a high mound breakwater in 2D. The best-fit friction parameters for del Jesus et al. (2012) formulation case were $\alpha = 5000$, $\beta = 1.0$–3.0, while the new ones result: $\alpha = 50$, $\beta = 0.6$–2.0. A full description of the case is available at Section 7.2.2.

There is a main difference between the two simulations, which can easily be spotted comparing Fig. 7.46 and Fig. B.5. In Fig. B.5 the layout of the main porous layer is uneven because a laser scan was carried out in the laboratory, and the original geometry had been replicated. In Fig. 7.46, the principal layer has been set to the theoretical shape (Fig. 7.39).

In Fig. B.3 the comparison between the numerical and experimental free surface elevation series is plotted. The new results are presented in Fig. 7.43. A high degree of accuracy is achieved in both cases, with larger discrepancies in gauges 8–10. The transmitted wave (gauge 14, bottom panel) is the most complex to reproduce, and is not well captured anyway. The change in the VARANS model does not induce any significant

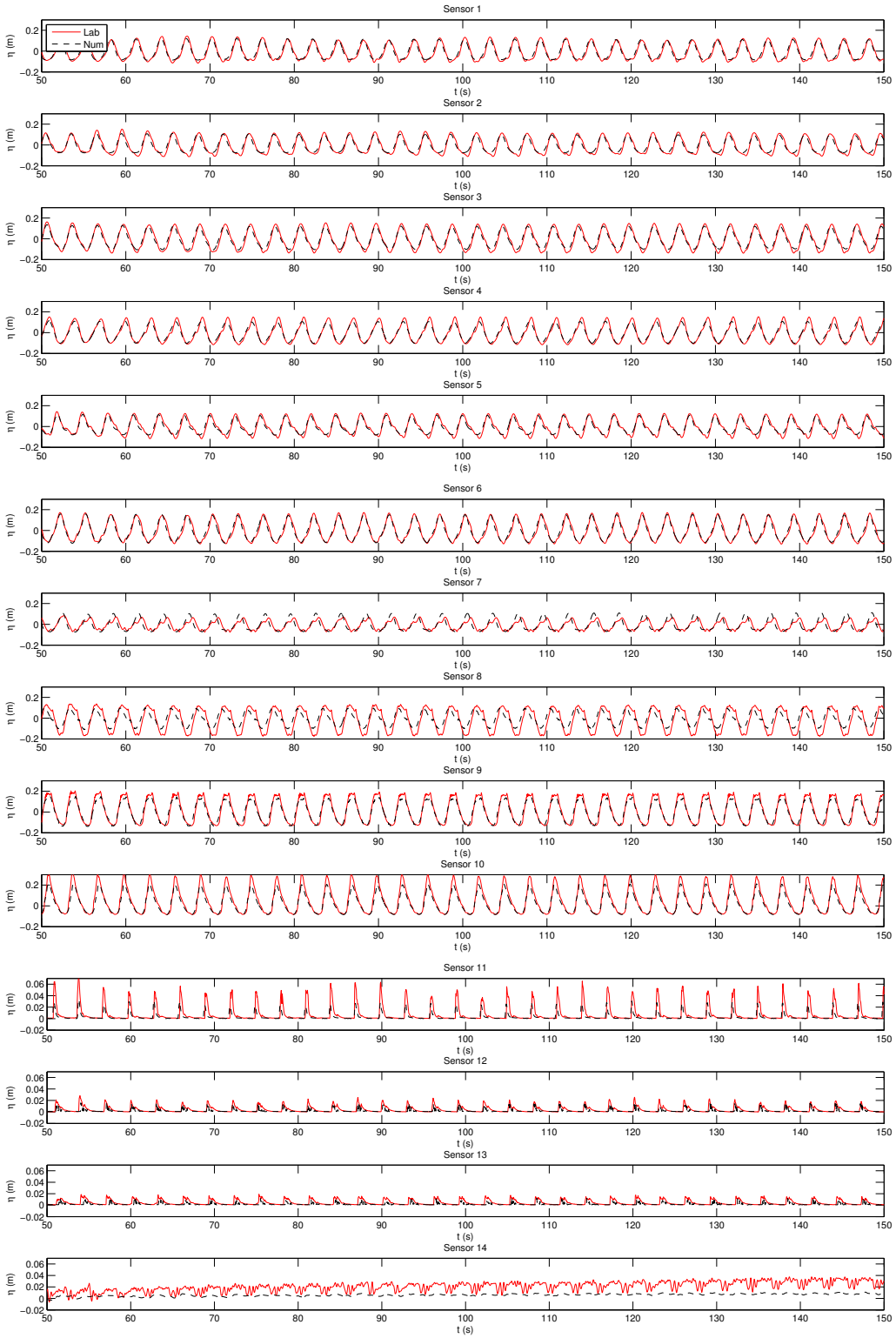

Figure B.3: Regular waves interacting with a high mound breakwater in 2D: free surface time series. del Jesus et al. (2012) formulation.

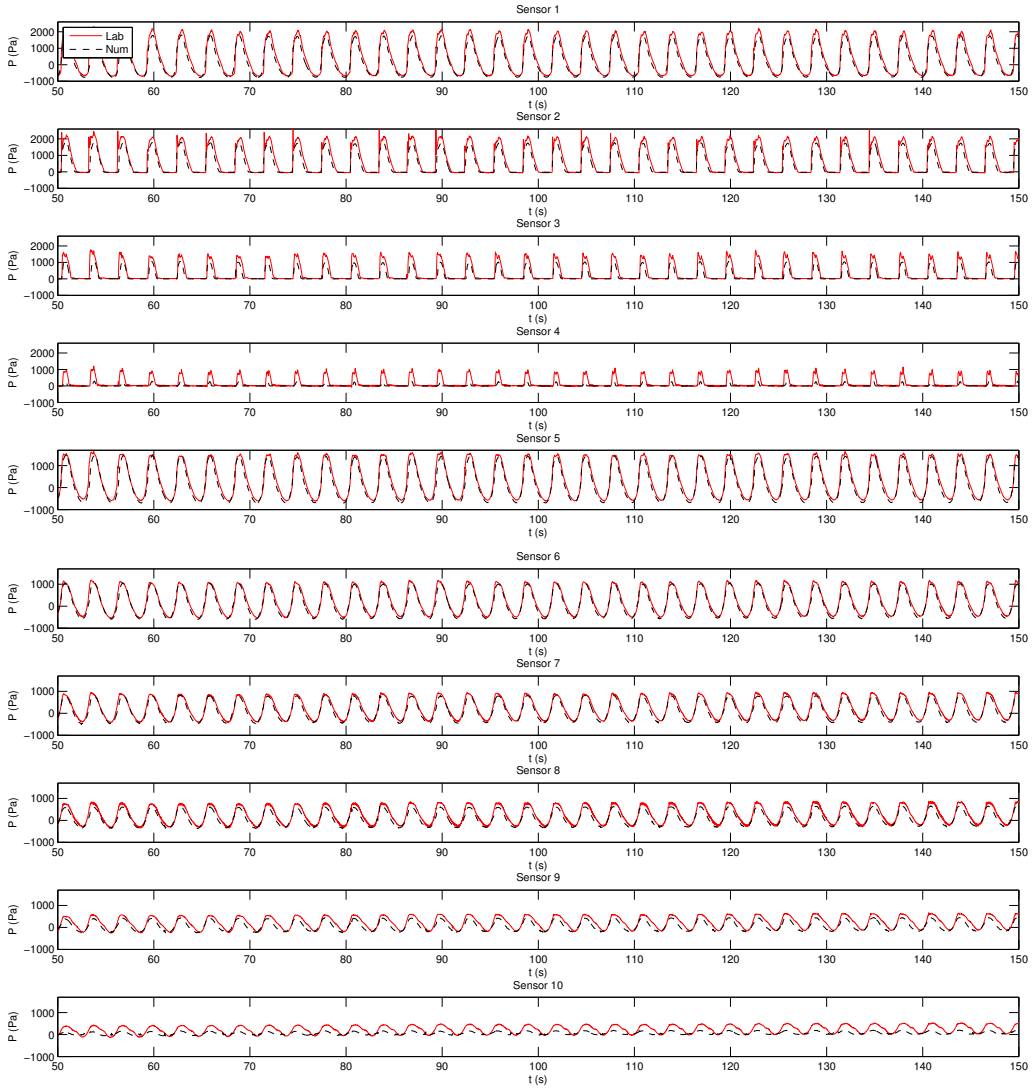

Figure B.4: Regular waves interacting with a high mound breakwater in 2D: pressure series. del Jesus et al. (2012) formulation.

changes, neither in wave amplitude or phase.

Fig. B.4 shows the time series of dynamic pressure. The new results can be compared with Fig. 7.44. In general, the model is able to predict pressures accurately at every location, only with minor underestimations, appearing in both cases. Some gauges, especially those located at the front face of the caisson, present a marginal improvement in Fig. B.4. The reason may be the principal armour layer geometry from the laser scanning, which leaves them more exposed, hence, higher pressure values are measured in **IHFOAM**.

Two snapshots of turbulent kinetic energy around the structure are presented in Fig. B.5. The figure can be compared with Fig. 7.46. Both of them show the turbulent kinetic energy around the structure at the instant when the first wave impacts the

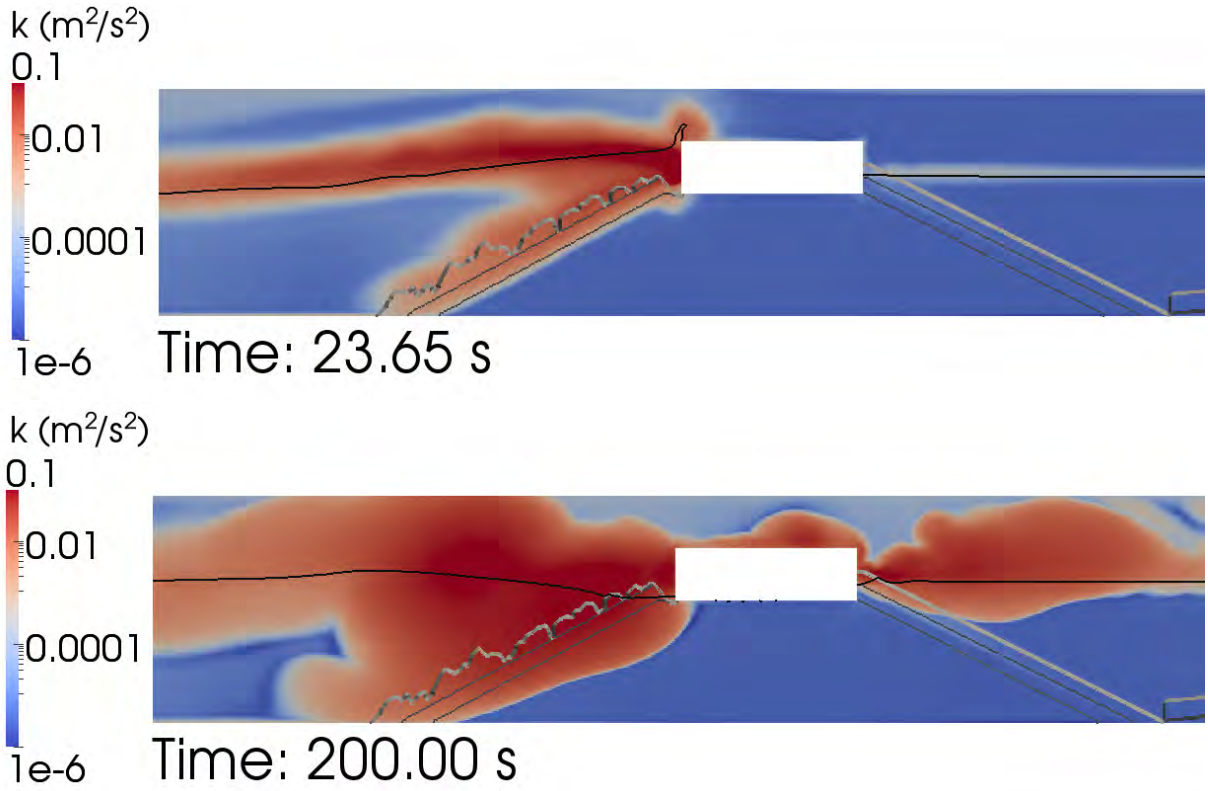

Figure B.5: Turbulent kinetic energy level around the structure for the first wave impact and at $t = 200$ s. del Jesus et al. (2012) formulation.

structure (top panel) and at $t = 200$ s (bottom panel). Free surface is represented as a black line.

At $t = 23.65$ s the results are almost identical for both models, in magnitude and distribution. The k level is higher where the free surface is moving and at the primary rock layer. At this point the turbulence starts to penetrate the core.

At $t = 200$ s the distribution of k is widely spread around the free surface and primary layer, and its magnitude is approximately homogeneous. The same turbulence build-up reported in Jacobsen et al. (2012) is experienced for the old model. Surprisingly, the turbulence inside the core advances less in Fig. B.5 than in Fig. 7.46, especially towards the bottom. However, the vast majority of the core continues to present low values of k, due to the laminar flow.

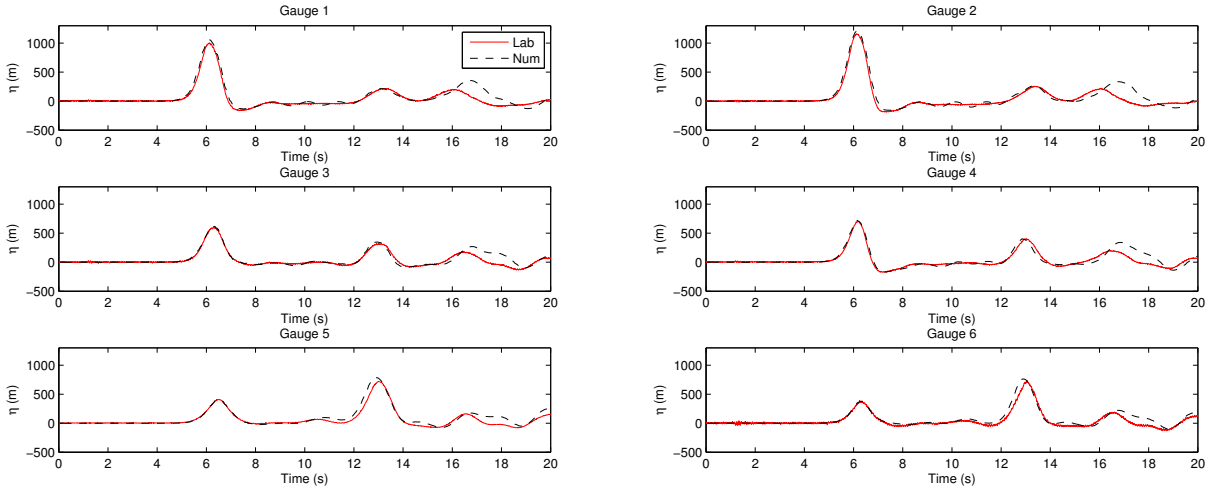

Figure B.6: Solitary wave: pressure signals. del Jesus et al. (2012) formulation.

B.3 Three-dimensional interaction of waves with a porous structure

The last case is the three-dimensional interaction of waves with a porous structure in a wave tank. The best-fit friction parameters for that case were $\alpha = 20000$, $\beta = 1.5$, versus the new ones: $\alpha = 0$, $\beta = 2.0$, those obtained for the CR35 case. A full description of the case is available at Section 7.2.3.

In Figs. (B.6)–(B.7) the time series of pressure and free surface elevation are shown for the solitary wave case. The results can be compared with Figs. (7.50)–(7.51). There are no major differences in any case. However, a slightly higher correlation between the numerical and experimental time series is obtained for del Jesus et al. (2012) formulation for pressure. On the contrary, the new formulation yields results marginally closer to reality for free surface elevation. According to the results, it seems that, again, both formulations are suitable, only fine tuning is needed to obtain the best results.

Fig. B.8 shows the turbulent kinetic energy around and inside the porous structure as the solitary wave impacts and surpasses it. The results are comparable with Fig. 7.52. There are no relevant differences for $t = 6$ and 7 s. The only dissimilitude appears for $t = 8$ and 9 s and is not related with the shape or magnitude of the vortices, but with the turbulence level at the front face of the structure. In Fig. 7.52 the magnitude of k is noticeably higher at the impact face. However, this variation does not induce significant

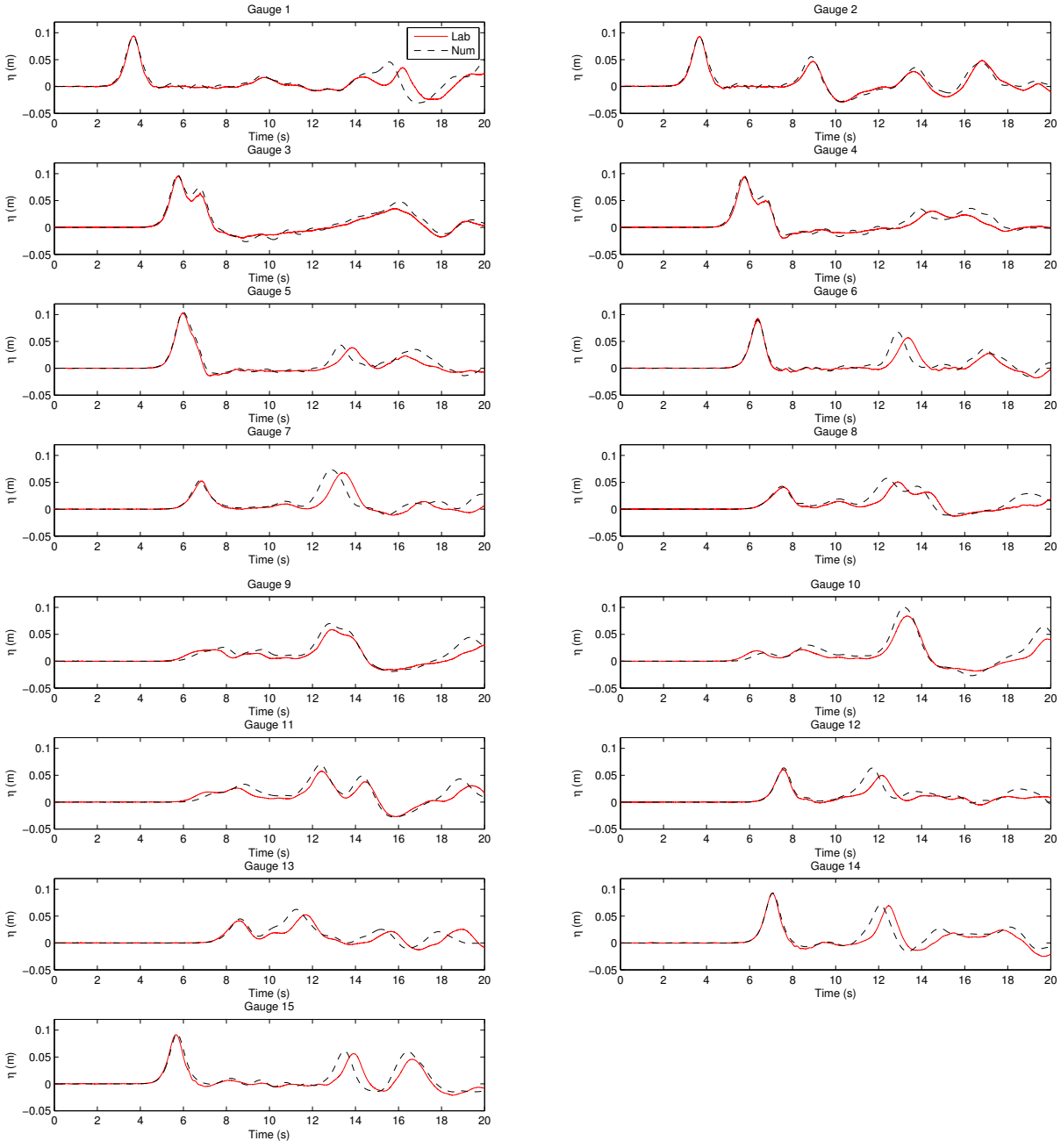

Figure B.7: Solitary wave: free surface elevation. del Jesus et al. (2012) formulation.

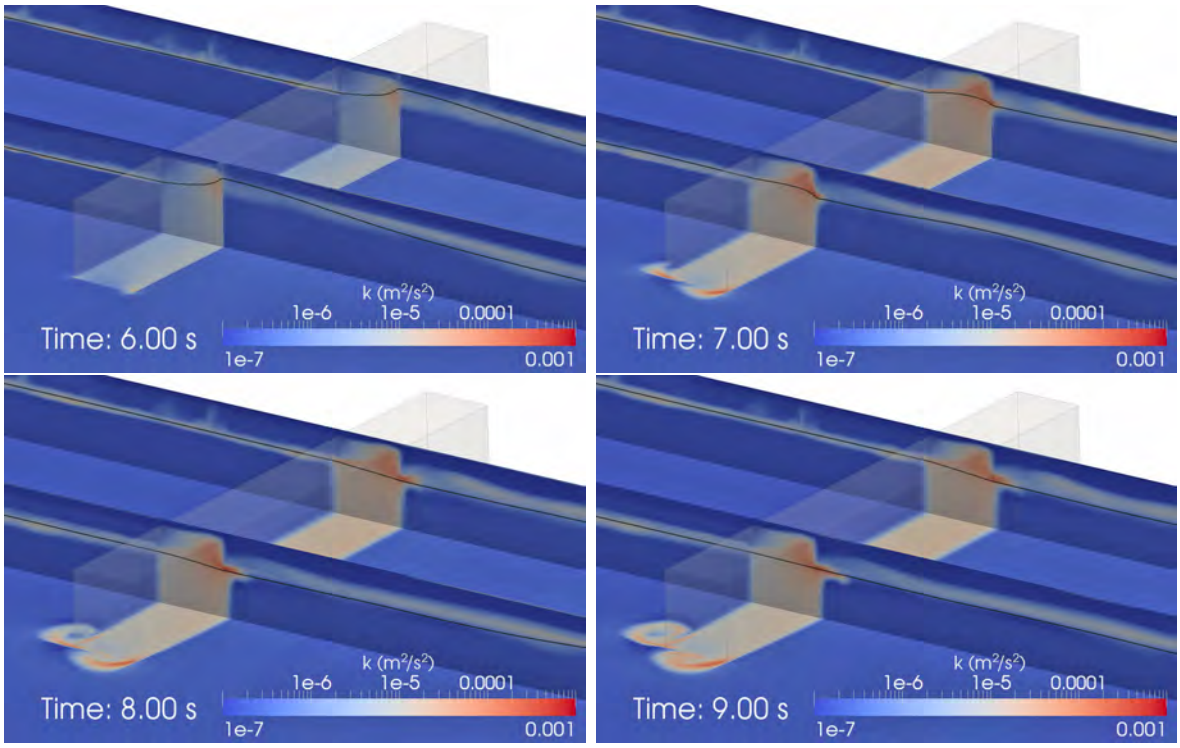

Figure B.8: Solitary wave: turbulent kinetic energy generation. del Jesus et al. (2012) formulation.

changes in free surface or pressure.

Figs. B.9–B.10 show the time series of pressure and free surface elevation for the regular waves case. Comparisons can be made with Figs. 7.54–7.55. Showing no major differences in any case, the best results are obtained for the new formulation.

B.4 Conclusions

In view of the results and despite the fact that del Jesus et al. (2012) derivation of the VARANS equations does not comply with the application of the volume averaging defined by Slattery (1967) and Whitaker (1967), the results obtained with it, both with **IH3VOF** (del Jesus et al., 2012) and with **IHFOAM** (Higuera et al., 2014a), are as good as those obtained with the new formulation.

The only major differences between the numerical setup is the large variation on the friction parameters α and β, that even reach several orders of magnitude. The final numerical results are, in both cases, acceptable and close to reality.

The explanation to this behaviour is simple, the numerical implementation overcomes

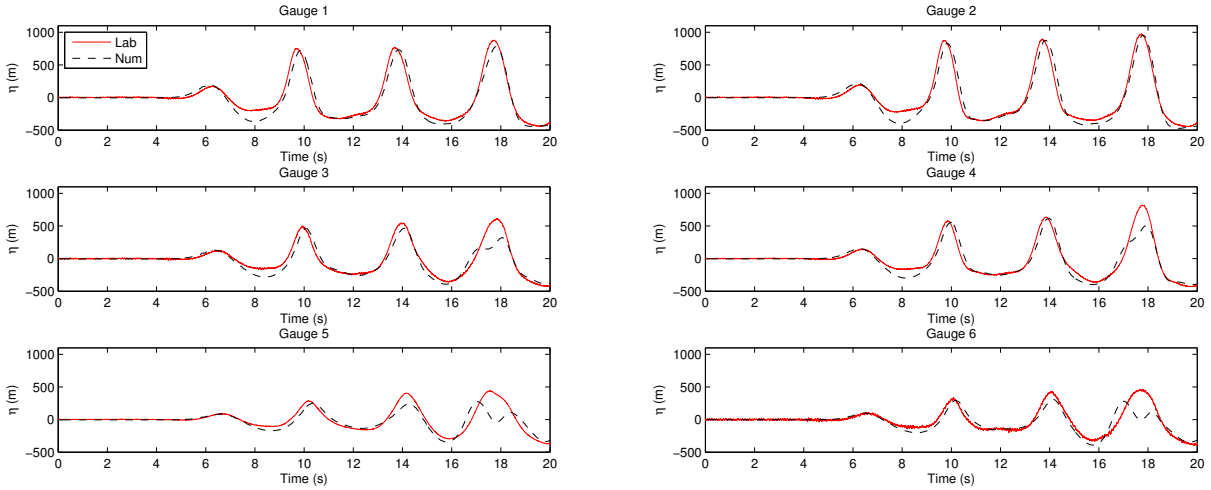

Figure B.9: Regular waves: pressure signals. del Jesus et al. (2012) formulation.

and corrects the mathematical flaws, yielding minor differences only, that can be balanced with higher levels of friction. Moreover, the largest differences are small and expected to be located at the interfaces of the porous media, where measurements are difficult to make due to important local effects.

As a conclusion, these facts enforce that both formulations are applicable, and only fine tuning is needed in α and β to obtain the best results.

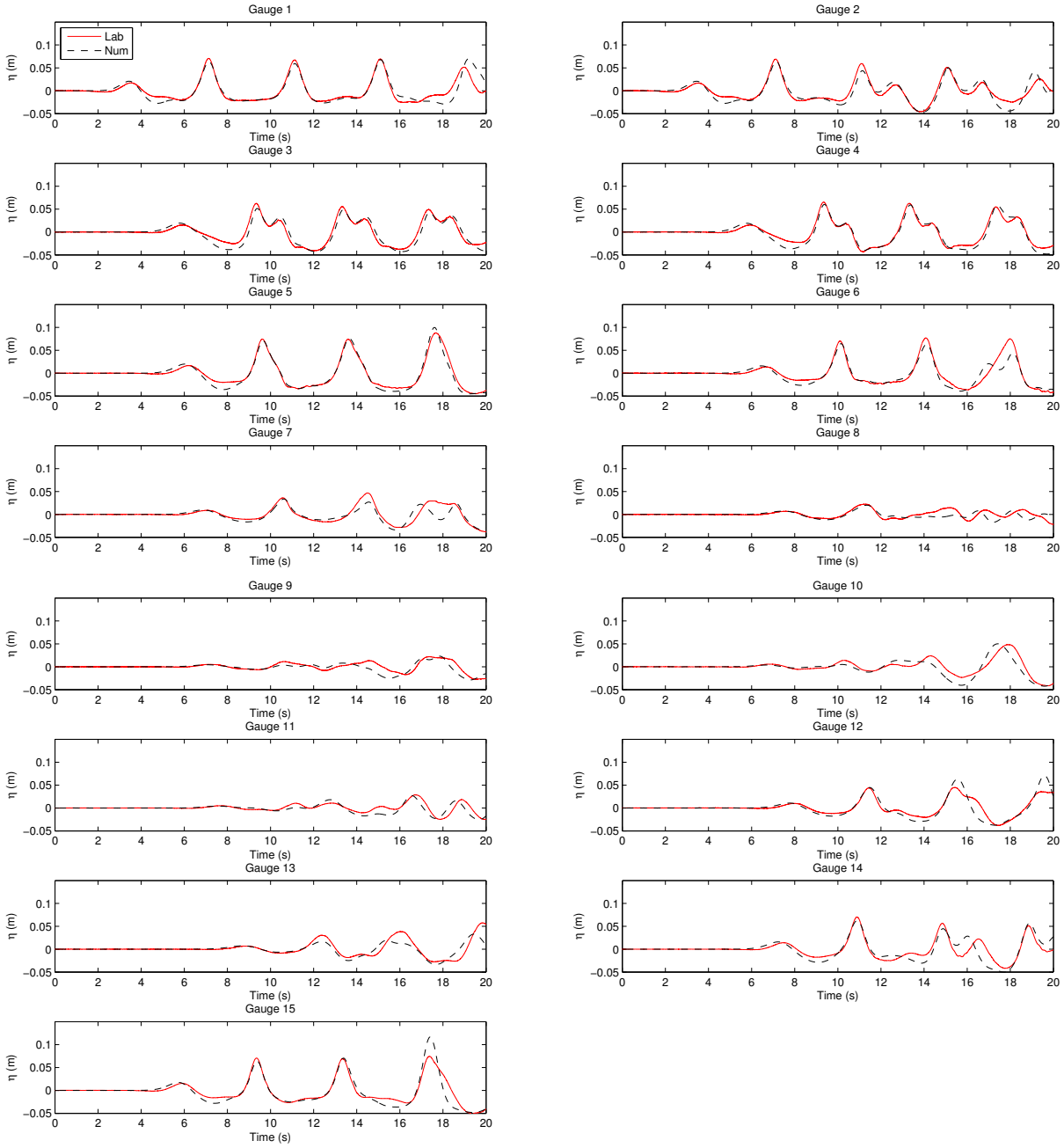

Figure B.10: Regular waves: free surface elevation. del Jesus et al. (2012) formulation.

Bibliography

Afshar, M. A. (2010). Numerical wave generation in OpenFOAM. Master's thesis, Chalmers University of Technology.

Airy, G. B. (1845). Tides and waves. In *Encyclopedia Metropolitana. Article 192*, pages 241–396.

Antoniou, A. (2006). *Digital signal processing: signals, systems and filters.* McGraw-Hill.

Baldock, T. E., Swan, C., and Taylor, P. H. (1996). A laboratory study of non-linear surface waves on water. *Philosophical Transactions of the Royal Society A*, 354:649–676.

Barthel, V., Mansard, E. P. D., Sand, S. E., and Vis, F. C. (1983). Group bounded long waves in physical models. *Ocean Engineering*, 10(4):261–294.

Becker, M. and Teschner, M. (2007). Weakly compressible SPH for free surface flows. In *Proceedings of the 2007 ACM SIGGRAPH/Eurographics Symposium on Computer Animation*, SCA '07, pages 209–217. Eurographics Association.

Berberovic, E., Hinsberg, N. P. v., Jakirlic, S., Roisman, I. V., and Tropea, C. (2009). Drop impact onto a liquid layer of finite thickness: Dynamics of the cavity evolution. *Physical Review E*, 79, 036306 - 15 pages.

Biésel, F. and Suquet, F. (1951). Les appareils generateurs de houle en laboratoire. *La Huille Blanche*, 5:723–737.

Bogdanov, I. I., Guerton, F., Kpahou, J., and Kamp, A. M. (2011). Direct pore-scale modeling of two-phase flow through natural media. In *Proceedings of 2011 COMSOL Conference, Stuttgart, Germany.*

Briggs, M. J., Synolakis, C. E., Harkins, G. S., and Green, D. (1995). Laboratory experiments of tsunami runup on a circular island. *Pure and Applied Geophysics*, 144:569–593.

Bullock, G. N. and Murton, G. J. (1989). Performance of a wedge-type absorbing wavemaker. *Journal of Waterway, Port, Coastal and Ocean Engineering*, 115(1):1–17.

Burcharth, H. and Andersen, O. (1995). On the one-dimensional steady and unsteady porous flow equations. *Coastal Engineering*, 24(3-4):233–257.

Burcharth, H. F. and L., Z. (1999). *MAST III / PROVERBS : Probabilistic Design Tools for Vertical Breakwaters: FINAL REPORT: Volume IIa Hydraulic Aspects. Chapter 4: Pulsating Wave Loads. Section 4.3: 3D Effects Force Reduction of Short-Crested Non-Breaking Waves on Caissons.* Technical University of Braunschweig.

Calvete, D., Dodd, N., Falques, A., and van Leeuwen, S. M. (2005). Morphological development of rip channel systems: Normal and near normal wave incidence. *Journal of Geophysical Research*, 110(C10006, 18 pages).

Camus, P., Mendez, F. J., Medina, R., Tomas, A., and Izaguirre, C. (2013). High resolution downscaled ocean waves (DOW) reanalysis in coastal areas. *Coastal Engineering*, 72:56–68.

Chen, Q., Kirby, J. T., Dalrymple, R. A., Kennedy, A. B., and Chawla, A. (2000). Boussinesq modelling of wave transformation, breaking and runup. II:2D. *Journal of Waterway, Port, Coastal, and Ocean Engineering*, 126:48–56.

Choi, B. H., Kim, D. C., Pelinovsky, E., and Woo, S. B. (2007). Three-dimensional simulation of tsunami run-up around conical island. *Coastal Engineering*, 54(8):618–629.

Choi, J. and Yoon, S. B. (2009). Numerical simulations using momentum source wavemaker applied to RANS equation model. *Coastal Engineering*, 56:1043–1060.

Christensen, E. D. and Deigaard, R. (2001). Large eddy simulation of breaking waves. *Coastal Engineering*, 42(1):53–86.

Christensen, M. and Frigaard, P. (1994). Design of absorbing wave-maker based on digital filters. *Proceeding, Waves - Physical and Numerical Modelling, Vancouver*, (100-109).

Clarke, D., Hassan, H., and Salas, M. (1986). Euler calculations for multielement airfoils using cartesian grids. *AIAA Journal*, 24:353–358.

Cruz, E. C., Isobe, M., and Watanabe, A. (1997). Boussinesq equations for wave transformation on porous beds. *Coastal Engineering*, 30:125–156.

Dalrymple, R., Herault, A., Bilotta, G., and Farahani, R. (2010). GPU-accelerated SPH model for water waves and other free surface flows. *Proceedings 32nd International Conference on Coastal Engineering, Shanghai.*

Dalrymple, R. A. and Rogers, B. D. (2006). Numerical modeling of water waves with the SPH method. *Coastal Engineering*, 53:141–147.

Darcy, H. (1856). *Les fontaines publiques de la ville de Dijon.*

de Lemos, M. J. S. and Pedras, M. H. J. (2001). Recent mathematical models for turbulent flow in saturated rigid porous media. *Journal of Fluids Engineering*, 123:935–941.

Dean, R. G. and Dalrymple, R. A. (1991). *Water Wave Mechanics for Engineers and Scientists.*, volume 2 of *Advanced Series on Ocean Engineering*. World Scientific, Singapore.

del Jesus, M. (2011). *Three-dimensional interaction of water waves with maritime structures.* PhD thesis, University of Cantabria.

del Jesus, M., Lara, J. L., and Losada, I. J. (2012). Three-dimensional interaction of waves and porous structures. Part I: Numerical model formulation. *Coastal Engineering*, 64:57–72.

Dronen, N., Karunarathna, H., Fredsoe, J., Sumer, B., and Deigaard, R. (2002). An experimental study of rip channel flow. *Coastal Engineering*, 45:223–238.

Engelund, F. (1953). On the laminar and turbulent flow of ground water through homogeneous sand. *Transactions of the Danish Academy of Technical Sciences*, 3.

Ergun, S. (1952). Fluid flow through packed columns. *Chemical Engineering Progress*, 48:89–94.

Farahani, R., Dalrymple, R., Hérault, A., and Bilotta, G. (2014). Three-dimensional SPH modeling of a bar/rip channel system. *Journal of Waterway, Port, Coastal and Ocean Engineering*, 140(1):82–99.

Fenton, J. D. (1988). The numerical solution of steady water wave problems. *Computers & Geosciences*, 14(3):357–368.

Fernández, H., Sriram, V., Schimmels, S., and Oumeraci, H. (2014). Extreme wave generation using self correcting method - revisited. *Coastal Engineering*, 93:15–31.

Forcheimer, P. (1901). Wasserbewegung durch Boden. *Z. Ver. Deutsch. Ing.*, 45:1782–1788.

Garnier, R., Calvete, D., Falques, A., and Dodd, N. (2008). Modelling the formation and the long-term behavior of rip channel systems from the deformation of a longshore bar. *Journal of Geophysical Research*, 113(C07053, 18 pages).

Gerritsen, H. and Sutherland, J. (2011). *Users guide to physical modelling and experimentation. Experience of the HYDRALAB network.*, chapter Composite Modelling. IAHR.

Goda, Y. (1985). *Random seas and design of maritime structures.* University of Tokio Press.

Goda, Y. and Ippen, A. P. (1963). *Theoretical and experimental investigation of wave energy dissipators composed of wire mesh screens.* Hydrodynamics Laboratoy Report No. 60, Department of Civil Engineering, Massachusetts Institute of Technology.

Gray, W. G. (1975). A derivation of the equations for multi-phase transport. *Chemical Engineering Science*, 30:229–233.

Grilli, S. T., Vogelmann, S., and Watts, P. (2002). Development of a 3D numerical wave tank for modeling tsunami generation by underwater landslides. *Engineering Analysis with Boundary Elements*, 26(4):301–313.

Guanche, R., Losada, I. J., and Lara, J. L. (2009). Numerical analysis of wave loads for coastal structure stability. *Coastal Engineering*, 56(5-6):543–558.

Ha, T., Lin, P., and Cho, Y.-S. (2013). Generation of 3D regular and irregular waves using Navier-Stokes equations model with an internal wave maker. *Coastal Engineering*, 76:55–67.

Haller, M. C., Dalrymple, R. A., and Svendsen, I. A. (2002). Experimental study of nearshore dynamics on a barred beach with rip channels. *Journal of Geophysical Research*, 107(C6, 14, 21 pages).

Harlow, F. and Welch, J. E. (1965). Numerical calculation of time-dependent viscous incompressible flow of fluid with a free surface. *Physics of Fluids*, 8:191–203.

Hassanizadeh, M. and Gray, W. G. (1979). General conservation equations for multiphase systems: 2. Mass, momenta, energy, and entropy equations. *Advances in Water Resources*, 2:191–203.

Higuera, P., Lara, J. L., and Losada, I. J. (2013a). Realistic wave generation and active wave absorption for Navier–Stokes models: Application to OpenFOAM. *Coastal Engineering*, 71:102–118.

Higuera, P., Lara, J. L., and Losada, I. J. (2013b). Simulating coastal engineering processes with OpenFOAM. *Coastal Engineering*, 71:119–134.

Higuera, P., Lara, J. L., and Losada, I. J. (2014a). Three–dimensional interaction of waves and porous coastal structures using OpenFOAM. Part I: Formulation and validation. *Coastal Engineering*, 83:243–258.

Higuera, P., Lara, J. L., and Losada, I. J. (2014b). Three–dimensional interaction of waves and porous coastal structures using OpenFOAM. Part II: Applications. *Coastal Engineering*, 83:259–270.

Higuera, P., Losada, I. J., and Lara, J. L. (2015). Three-dimensional numerical wave generation with moving boundaries. *Coastal Engineering (Submitted)*.

Hirakuchi, H., Kajima, R., and Kawaguchi, T. (1990). Application of a piston-type absorbing wavemaker to irregular wave experiments. *Coastal Engineering in Japan*, 33(1):11–24.

Hirt, C. W. and Nichols, B. D. (1981). Volume of fluif (VOF) method for the dynamics of free boundaries. *Journal of Computational Physics*, 39:201–225.

Hsu, T., S. T. and Liu, P. (2002). A numerical model for wave motions and turbulence flows in front of a composite breakwater. *Coastal Engineering*, 46(1):25–50.

Hughes, S. A. (1993). *Physical models and laboratory techniques in coastal engineering.*, volume 7 of *Advanced Series on Ocean Engineering*. World Scientific, Singapore.

Hur, D.-S., Lee, K., and Yeom, G. (2008). The phase difference effects on 3D structure of wave pressure acting on a composite breakwater. *Ocean Engineering*, 35(17-18):1826–1841.

Issa, R. I. (1986). Solution of the implicitly discretised fluid flow equations by operator-splitting. *Journal of Computational Physics*, 62(1):40–65.

Jacobsen, N. G. (2011). *A full hydro- and morphodynamic description of a breaker bar development.* PhD thesis, Technical University of Denmark (DTU).

Jacobsen, N. G., Fuhrman, D. R., and Fredsøe, J. (2012). A wave generation toolbox for the open-source CFD library: OpenFOAM. *International Journal for Numerical Methods in Fluids.*, 70(9):1073–1088.

Jamieson, W. W. and Mansard, E. P. D. (1987). An efficient upright wave absorber. In *Coastal Hydrodynamics 87, ASCE*, pages 124–139.

Jasak, H. (1996). *Error analysis and estimation for the finite volume method with applications to fluid flows.* PhD thesis, Imperial College of Science, Technology and Medicine.

Jensen, B., Jacobsen, N. G., and Christensen, E. D. (2014). Investigations on the porous media equations and resistance coefficients for coastal structures. *Coastal Engineering*, 84:56–72.

Keulegan, G. H. (1972). *Wave damping effects of fibrous screens.* Research report H-72-2, US Army Engineer Waterways Experiment Station, Vicksbourg, Mississippi.

Kiku, M., Nakamura, T., Kawasaki, K., and Mizutani, N. (2014). Introduction of immersed boundary model to 3-D numerical wave tank 'CADMAS-SURF/3D'. *Journal of Japan Society of Civil Engineers, Series B3 (Ocean Engineering)*, 70(1):33–43. in Japanese.

Kim, S.-H., Yamashiro, M., and Yoshida, A. (2010). A simple two-way coupling method of BEM and VOF model for random wave calculations. *Coastal Engineering*, 57(11-12):1018–1028.

Kim, Y. (2009). *Handbook Of Coastal And Ocean Engineering.* World Scientific, Singapore.

Kissling, K., Springer, J., Jasak, H., Schütz, S., Urban, K., and Piesche, M. (2010). A coupled pressure based solution algorithm based on the volume-of-fluid approach for two or more immiscible fluids. In *V European Conference on Computational Fluid Dynamics, ECCOMAS CFD.*

Klinghammer, C., Lomonaco, P., and Higuera, P. (2012). Design optimization for a passive mesh screen wave absorber for the CCOB. In *33rd International Conference on Coastal Engineering, Santander, Spain.*, volume 5, pages 4179–4189.

Klopman, G., Reniers, A., Wouters, J., and de Haan, T. (1996). Active multidirectional wave absorption. *Abstract, International Conference on Coastal Engineering, Orlando, Florida*, pages 798–799.

Kortenhaus, A. and Oumeraci, H. (1998). Classification of wave loading on monolithic coastal structures. *Proceedings of the 26th International Coastal Engineering Conference*, (26):867–880.

Kothe, D. B., Williams, M. W., Lam, K. L., Korzekwa, D. R., and Tubesing, P. K. (1999). A second-order accurate, linearity-preserving volume tracking algorithm for free surface flows on 3-D unstructured meshes. In *In Proceedings of the 3rd ASME/JSME*, pages 99–7109.

Kundu, P. K. and Cohen, I. M. (2004). *Fluid Mechanics*. Elsevier Science, San Diego.

Lara, J. L., del Jesus, M., and Losada, I. J. (2012). Three-dimensional interaction of waves and porous structures. Part II: Model validation. *Coastal Engineering*, 64:26–46.

Lara, J. L., Garcia, N., and Losada, I. J. (2006a). RANS modelling applied to random wave interaction with submerged permeable structures. *Coastal Engineering*, 53:395–417.

Lara, J. L., Losada, I. J., and Guanche, R. (2008). Wave interaction with low mound breakwaters using a RANS model. *Ocean Engineering*, 35:1388–1400.

Lara, J. L., Losada, I. J., and Liu, P.-F. (2006b). Breaking waves over a mild gravel slope: experimental and numerical analysis. *Journal of Geophysical Research*, 111(C11019, 26 pages).

Lara, J. L., Ruju, A., and Losada, I. J. (2011). Reynolds averaged Navier–Stokes modelling of long waves induced by a transient wave group on a beach. *Proceedings of the Royal Society A*, 467:1215–1242.

Larese, A., Rossi, R., and Oñate, E. (2014). Finite element modeling of free surface flow in variable porosity media. *Archives of Computational Methods in Engineering*, pages 1–17.

Larese, A., Rossi, R., Oñate, E., and Idelsohn, S. R. (2008). Validation of the particle finite element method (PFEM) for simulation of free surface flows. *Engineering Computations: International Journal for Computer-Aided Engineering*, 25(4):385–425.

Le Méhauté, B. (1976). *Introduction to Hydrodynamics and Water Waves.* Springer-Verlag, New York.

Lee, J. J., Skjelbreia, E., and Raichlen, F. (1982). Measurement of velocities in solitary waves. *Journal of Waterway, Port, Coastal and Ocean Engineering*, 108:200–218.

Lin, P. (1998). *Numerical modeling of breaking waves*. PhD thesis, Cornell University.

Lin, P. and Liu, P.-F. (1999). Internal wave-maker for Navier–Stokes equations models. *Journal of Waterway, Port, Coastal, and Ocean Engineering*, 125:207–215.

Liu, P.-F., Cho, Y.-S., Briggs, M. J., U., K., and Synolakis, C. E. (1995). Runup of solitary waves on a circular island. *Journal of Fluid Mechanics*, 320:259–285.

Liu, P.-F., Lin, P., Chang, K., and Sakakiyama, T. (1999). Numerical modeling of wave interaction with porous structures. *Journal of Waterway, Port, Coastal, and Ocean Engineering*, 125:322–330.

Liu, P.-F. and Losada, I. J. (2002). Wave propagation modeling in coastal engineering. *Journal of Hydraulic Research*, 40(3):229–240.

Liu, X., Lin, P., and Shao, S. (2015). ISPH wave simulation by using an internal wave maker. *Coastal Engineering*, 95:160–170.

Longuet-Higgins, M. S. and Stewart, R. (1960). Change in the form of short gravity waves on long waves and tidal currents. *Journal of Fluid Mechanics*, 8:565–583.

Losada, I. J., Gonzalez-Ondina, J. M., Diaz, G., and Gonzalez, E. M. (2008a). Numerical simulation of transient nonlinear response of semi-enclosed water bodies: model description and experimental validation. *Coastal Engineering*, 55(1):21–34.

Losada, I. J., Lara, J. L., Guanche, R., and Gonzalez-Ondina, J. M. (2008b). Numerical analysis of wave overtopping of rubble-mound breakwaters. *Coastal Engineering*, 55(1):47–62.

Lubin, P., Vincent, S., Caltagirone, J.-P., and Abadie, S. (2003). Fully three-dimensional direct numerical simulations of a plunging breaker. *Comptes Rendus Mecanique*, 331(7):495–501.

Luppes, R., Veldman, A. E. P., and Wellens, P. R. (2010). Absorbing boundary conditions for wave simulations around offshore structures. *V European Conference on Computational Fluid Dynamics (ECCOMAS CFD 2010), Lisbon.*

Lynett, P. J. and Liu, P. L.-F. (2002). A two-dimensional, depth-integrated model for internal wave propagation over variable bathymetry. *Wave Motion*, 36(3):221–240.

Mahmoudi, A., Hakimzadeh, H., and Ketabdari, M. J. (2014). Simulation of wave propagation over coastal structures using WCSPH method. *Journal of Marine Engineering*, 2:1–13.

Mansard, E. P. D. and Funke, E. R. (1980). The measurement of incident and reflected spectra using a least squares method. *Coastal Engineering*, pages 154–172.

Maric, T., Marschall, H., and Bothe, D. (2013). voFoam - A geometrical volume of fluid algorithm on arbitrary unstructured meshes with local dynamic adaptive mesh refinement using OpenFOAM. *arXiv preprint arXiv:1305.3417.*

Márquez, S. (2013). *An Extended Mixture Model for the Simultaneous Treatment of Short and Long Scale Interfaces.* PhD thesis, Universidad Nacional del Litoral.

Marrone, S., Colagrossi, A., Le Touzé, D., and Graziani, G. (2010). Fast free-surface detection and level-set function definition in SPH solvers. *Journal of Computational Physics*, 229(10):3652–3663.

Mayer, S., Garapon, A., and Søresen, L. S. (1998). A fractional step method for unsteady free-surface flow with applications to non-linear wave dynamics. *International Journal for Numerical Methods in Fluids*, 28(2):293–315.

Mayer, S. and Madsen, P. A. (2000). Simulation of breaking waves in the surf zone using a Navier-Stokes solver. In *Proceedings of the 27th International Coastal Engineering Conference (ICCE), Sydney, Australia*.

Mendez, F. J., Losada, I. J., and Losada, M. A. (2001). Wave-induced mean magnitudes in permeable submerged breakwaters. *Journal of Waterway, Port, Coastal and Ocean Engineering*, 127:7–15.

Menter, F. (1994). Two-equation eddy viscosity turbulence models for engineering applications. *AIAA Journal*, 32(8):1598–1605.

Milgram, J. S. (1970). Active water-wave absorbers. *Journal of Fluid Mechanics*, 43(4):845–859.

Mindel, J. E., Collins, G. S., Latham, J.-P., Pain, C. C., and Munjiza, A. (2007). Towards a numerical wave simulator using the two-fluid interface tracking approach combined with a novel ALE scheme. In *Proceedings of the Fifth International Conference on Coastal Structures, Venice, Italy*, pages 1465–1476.

Mittal, R. and Iaccarino, G. (2005). Immersed boundary methods. *Annual Review of Fluid Mechanics*, 37:239–261.

Mohd-Yusof, J. (1997). Combined immersed-boundary/B-spline methods for simulations of flow in complex geometries. *Center for Turbulence Research Annual Research Briefs*, pages 317–327.

Nakayama, A. and Kuwahara, F. (1999). A macroscopic turbulence model for flow in a porous medium. *Journal of Fluids Engineering*, 121:427–435.

Ni, J. and Beckermann, C. (1991). A volume-averaged two-phase model for transport phenomena during solidification. *Metallurgical Transactions B*, 22(B):349–361.

Nikora, V., McEwan, I., McLean, S., Coleman, S., Pokrajac, D., and Walters, R. (2007a). Double-averaging concept for rough-bed open-channel and overland flows: Theoretical background. *Journal of Hydraulic Engineering*, 133(8):873–883.

Nikora, V., McLean, S., Coleman, S., Pokrajac, D., McEwan, I., Campbell, L., Aberle, J., Clunie, D., and Koll, K. (2007b). Double-averaging concept for rough-bed open-channel and overland flows: Applications. *Journal of Hydraulic Engineering*, 133(8):884–895.

Noh, W. and Woodward, P. (1976). SLIC (Simple Line Interface Calculation). In *Proceedings of the Fifth International Conference on Numerical Methods in Fluid Dynamics June 28 - July 2, 1976 Twente University, Enschede*, volume 59 of *Lecture Notes in Physics*, pages 330–340. Springer Berlin Heidelberg.

Okumura, H. and Arikawa, T. (2014). A Study of CUDA/MPI Parallel Computations for CADMAS-SURF/3D. In *Proceedings of the Twenty-fourth International Ocean and Polar Engineering Conference Busan, Korea, June 15-20, 2014*, volume ISOPE-I-14-430, pages 420–425.

Orszaghova, J., Borthwick, A. G. L., and Taylor, P. H. (2012). From the paddle to the beach - a Boussinesq shallow water numerical wave tank based on Madsen and Sørensen's equations. *Journal of Computational Physics*, 231(2):328–344.

Orszaghova, J., Taylor, P. H., Borthwick, A. G. L., and Raby, A. C. (2014). Importance of second-order wave generation for focused wave group run-up and overtopping. *Coastal Engineering*, 94:63–79.

Ouellet, Y. and Datta, I. (1986). A survey of wave absorbers. *Journal of Hydraulic Research*, 24(4):265–280.

Oumeraci, H. and Kortenhaus, A. (1997). Wave impact loading - tentative formulae and suggestions for the development of final formulae. *Proceedings 2nd task 1 Workshop, MAST III, PROVERBS-Project: Probabilistic Design Tools for Vertical Breakwaters, Edinburgh, U.K.*, pages Annex 1.0.2., 13 pp.

Polubarinova-Kochina, P. (1962). *Theory of ground water movement*. Princeton University Press.

Reynolds, O. (1895). On the dynamical theory of incompressible viscous fluids and the determination of the criterion. *Philosophical Transactions of the Royal Society of London A*, 186:123–164.

Rienecker, M. M. and Fenton, J. D. (1981). A Fourier approximation method for steady water waves. *Journal of Fluid Mechanics*, 104:119–137.

Rudman, M. (1997). Volume-tracking methods for interfacial flow calculations. *International Journal for Numerical Methods in Fluids*, 24(7):671–691.

Rusche, H. (2002). *Computational fluid dynamics of dispersed two-phase flows at high phase fractions.* PhD thesis, Department of Mechanical Engineering, Imperial College of Science, Technology & Medicine, London.

Salter, S. H. (1981). Absorbing wavemakers and wide tanks. *Proceeding, Directional Wave Spectra Applications, Berkeley, California*, pages 185–202.

Salter, S. H. (1984). Physical modelling of directional seas. *Proceeding, Symposium Description and Modelling of Directional Seas, Copenhagen, Denmark*, 31.

Sand, S. E. (1982). Long waves in directional seas. *Coastal Engineering*, 6:195–208.

Schäffer, H. A. and Jakobsen, K. P. (2003). Non-linear wave generation and active absorption in wave flumes. *Proceeding, Long Waves Symposium, XXX IAHR Congress, Thessaloniki*, pages 69–77.

Schäffer, H. A. and Klopman, G. (2000). Review of multidirectional active wave absorption methods. *Journal of Waterway, Port, Coastal and Ocean Engineering*, pages 88–97.

Schäffer, H. A. and Skourup, J. (1996). Active absorption of multidirectional waves. *Proceeding, 25th International Conference on Coastal Engineering, Orlando, Florida*, 1:55–66.

Schäffer, H. A. and Sørensen, O. R. (2006). On the internal wave generation in Boussinesq and mild-slope equations. *Coastal Engineering*, 53(4):319–323.

Schäffer, H. A., Stolborg, T., and Hyllested, P. (1994). Simultaneous generation and active absorption of waves in flumes. *Proceeding, Waves - Physical and Numerical Modelling, Vancouver*, pages 90–99.

Shao, S. (2010). Incompressible SPH flow model for wave interactions with porous media. *Coastal Engineering*, 57(3):304–316.

Skjelbreia, L. and Hendrickson, J. A. (1960). Fifth order gravity wave theory. *Proceedings 7th Coastal Engineering Conference*, pages 184–196.

Slattery, J. C. (1967). Flow of viscoelastic fluids through porous media. *American Institute of Chemical Engineers Journal*, 13(6):1066–1071.

Smagorinsky, J. (1963). General circulation experiments with the primitive equations. *Monthly Weather Review*, 91:99–164.

Sun, F., Tan, M., and Xing, J. T. (2012). Air-water two phase flow simulation using smoothed particle hydrodynamics.

Sussman, M., Almgren, A., Bell, J., Colella, P., Howell, L., and Welcome, L. (1999). An adaptive level set approach for incompressible two-phase flows. *Journal of Computational Physics*, 148:81–124.

Sussman, M. and Puckett, E. G. (2000). A coupled level set and volume-of-fluid method for computing 3d and axisymmetric incompressible two-phase flows. *Journal of Computational Physics*, 162(2):301–337.

Sussman, M., Smereka, P., and Osher, S. (1994). An level set approach for computing solutions to incompressible two-phase flow. *Journal of Computational Physics*, 114:146–159.

Svendsen, I. A. (2006). *Introduction to Nearshore Hydrodynamics.*, volume 24 of *Advanced Series on Ocean Engineering*. World Scientific, Singapore.

Swigler, D. T. (2009). Laboratory study investigating the three-dimensional turbulence and kinematic properties associated with a breaking solitary wave. Master's thesis, Texas A&M University.

Takahashi, S., Tanimoto, K., and Shimosako, K. (1994). A proposal of impulsive pressure coefficient for design of composite breakwaters. *Proceedings of the International Conference on Hydro-technical Engineering for Port and Harbour Construction.*, pages 489–504.

Tanimoto, K., Moto, K., Ishizuka, S., and Goda, Y. (1976). An investigation on design wave force formulae of composite-type breakwaters. *Proceedings of the 23rd Japanese Conference on Coastal Engineering.*, pages 11–16. (in Japanese).

Tonelli, M. and Petti, M. (2010). Finite volume scheme for the solution of 2D extended Boussinesq equations in the surf zone. *Ocean Engineering*, 37(7):567–582.

Torres-Freyermuth, A., Lara, J. L., and Losada, I. J. (2010). Numerical modelling of short- and long-wave transformation on a barred beach. *Coastal Engineering*, 57:317–330.

Tørum, A. (1994). Wave-induced forces on armor unit on berm breakwaters. *Journal of Waterway, Port, Coastal and Ocean Engineering*, 120(3):251–268.

Troch, P. and De Rouck, J. (1998). Development of 2D numerical wave flume for simulation of wave interaction with rubble mound breakwaters. *Proceedings 26th ICCE, Copenhagen.*

Troch, P. and De Rouck, J. (1999). An active wave generating-absorbing boundary condition for VOF type numerical model. *Coastal Engineering*, 38(4):223–247.

van der Meer, J. W. (1987). Stability of breakwater armour layers–design formulae. *Coastal Engineering*, 11(3):219–239.

van Gent, M. R. A. (1995). *Wave interaction with permeable coastal structures.* PhD thesis, Delft University.

Vanneste, D. (2012). *Experimental and numerical study of wave-induced porous flow in rubble-mound breakwaters.* PhD thesis, Ghent University.

Ward, J. (1964). Turbulent flow in porous media. *Journal of the Hydraulics Division*, 90:1–12.

Watanabe, Y., Saeki, H., and J., H. R. (2005). Three-dimensional vortex structures under breaking waves. *Journal of Fluid Mechanics*, 545:291–328.

Wei, G. and Kirby, J. T. (1995). Time-dependent numerical code for extended Boussinesq equations. *Journal of Waterway, Port, Coastal and Ocean Engineering*, 121(5):251–261.

Wei, G., Kirby, J. T., and Sinha, A. (1999). Generation of waves in Boussinesq models using a source function method. *Coastal Engineering*, 36(4):271–299.

Wellens, P. (2012). *Wave simulation in truncated domains for offshore applications.* PhD thesis, Delft University of Technology.

Whitaker, S. (1967). Diffusion and dispersion in porous media. *American Institute of Chemical Engineers Journal*, 13(3):420–427.

Whitaker, S. (1986). Flow in porous media I: a theoretical derivation of Darcy's law. *Transport in Porous Media*, 1:3–25.

Whitaker, S. (1996). The Forcheimer equation: a theoretical development. *Transport in Porous Media*, 25:27–61.

Young, I. R. (1994). On the measurement of directional wave spectra. *Applied Ocean Research*, 16:283–294.

Yu, J. and Slinn, D. N. (2003). Effects of wave-current interaction on rip currents. *Journal of Geophysical Research*, 108(C3).

Zijlema, M. and Stelling, G. S. (2011). Swash: an operational public domain code for simulationg wave fields and rapidly varied flows in coastal waters. *Coastal Engineering*, 58(10):92–1012.